Quantitative landslide hazard assessment with remote sensing observations and statistical modelling

Romy Schlögel

UNIVERSITÉ DE STRASBOURG

UNIVERSITY OF STRASBOURG

ÉCOLE DOCTORALE DES SCIENCES DE LA TERRE, DE L'UNIVERS ET DE L'ENVIRONNEMENT

PhD Thesis presented by

ROMY SCHLÖGEL

For obtaining the degree

Doctor of the University of Strasbourg (PhD)

Quantitative landslide hazard assessment with remote sensing observations and statistical modelling

Public defence on February 12th, 2015

Examination committee

Prof. Pascal Allemand	Université Claude-Bernard, Lyon I Laboratoire de Géologie de Lyon, Terre, Planètes, Environnement (LGTPE)	*Reviewer*
Prof. Olivier Maquaire	Université de Caen Basse-Normandie Littoral, Environnement, Télédétection et Géomatique (LETG)	*Reviewer*
Dr. Erwan Pathier	Université Joseph Fourier, Grenoble Institut des Sciences de la Terre (ISTerre)	*Oral examiner*
Dr. Cécile Doubre	Université de Strasbourg Institut de Physique du Globe de Strasbourg (IPGS)	*Oral examiner*
Prof. Frédéric Masson	Université de Strasbourg Institut de Physique du Globe de Strasbourg (IPGS)	*Thesis co-director*
Dr. Jean-Philippe Malet	Université de Strasbourg Institut de Physique du Globe de Strasbourg (IPGS)	*Thesis co-director*

IPGS Strasbourg

Ecole et Observatoire des Sciences de la Terre

à ma mèroum…

REMERCIEMENTS - ACKNOWLEDGEMENTS

Ce travail de recherche est l'aboutissement d'un peu plus de 3 ans et demi de recherche au sein de l'Institut de Physique du Globe (IPGS) de l'Ecole et Observatoire des Sciences de la Terre de Strasbourg (EOST). Bien qu'il soit à la base un projet personnel, je tiens à remercier toutes les personnes qui y ont participé, sans l'appui desquelles, il n'aurait pu être mené à bien.

Je tiens d'abord à remercier mon responsable et co-directeur de thèse, le Dr. Jean-Philippe Malet, chargé de recherche au Centre National de la Recherche Scientifique (CNRS), pour sa rigueur, son esprit de synthèse et sa connaissance scientifique dans le domaine des glissements de terrain et de la vallée de l'Ubaye. J'adresse également mes remerciements au Dr. Cécile Doubre d'avoir accepté de me former aux techniques d'interférométrie radar, pour les discussions intéressantes en vue de l'amélioration des résultats ainsi que pour sa patience et son écoute. Je tiens également à remercier le Pr. Frédéric Masson, directeur de l'EOST, d'avoir accepté le rôle de directeur de thèse.

Je remercie également les membres du jury, le Pr. Olivier Maquaire, professeur au LETG de l'Université de Caen Basse Normandie et directeur du laboratoire de GEOgraphie PHysique et ENvironnement (GEOPHEN), le Pr. Pascal Allemand du Laboratoire de Géologie de Lyon, Terre, Planètes, Environnement (LGTPE) de l'Université Claude-Bernard, Lyon I, ainsi que le Dr. Erwan Pathier, chercheur à l'Institut des Sciences de la Terre (ISTerre) de l'Université Joseph Fourier de Grenoble, d'avoir donné de leur temps pour évaluer ce travail.

I was fortunate to collaborate and discuss with scientists from many disciplines thanks to the CHANGES-ITN. I thank Dr. Paola Reichenbach for hosting me and supervising me at CNR-IRPI (Perugia) during the several secondments. These stays allowed interesting scientific discussions in slope-unit delineation (Dr. Massimiliano Alvioli, Dr. Evan Marchesini), landslide mapping (Dr. Michele Santangelo, Dr. Federica Fiorucci, Dr. Francesco Bucci), rainfall thresholds (Dr. Maria Teresa Brunetti), frequency-size distribution analysis and logistic regression models (Dr. Mauro Rossi) and remote sensing techniques for landslide detection (Dr. Alessandro Cesare Mondini). I also feel really fortunate for having the opportunity to be a part of this Formosat-II research proposal enrolling Italy and Southeast Asian countries. Big hug to all the Italians for the good moments we spent together in Perugia: Marco, Stefano, Massimo, Elisabetta, Veronica, Federica, Frida, Antonio and Ale.

This scholarship also allows me to go to many conferences in France, Austria, Belgium, Norway and Italy were I was glad to meet interesting people and discuss about natural hazard. I would be glad to exchange more in the near future with the colleagues from the Romanian Academy (Dr. Mihai Micu, Dr. Martha Jurescu and Dr. Dan Balteanu). I also really enjoyed spending time with you on volcanoes and landslides, working at the research station or looking at the stars. Warm hug to Mihai for all the support! I was also lucky to exchange with the other ESRs of the project (Thea Turkington, Zar Chi Aye, Tess Spargue, Korbinian Breinl, Ziga Malek, Roxana Lilian Ciurean, Haydar Hussin, Veronica Zumpano, Kathrin Prenger-Berninghoff, Juliette Cortes Arevalo, Catrin Promper and Marie Charrière), unfortunately not enough but maybe in the future?

Ces neuf campagnes de terrain dans la vallée de l'Ubaye ont été pour moi une expérience unique, dans un cadre exceptionnel, je remercie Messieurs Georges Guiter et Michel Perron du Service de Restauration des Terrains de Montagnes (RTM) de l'antenne de Barcelonnette pour le partage de leur connaissance des mouvements de terrain de la vallée, leur soutien logistique et la mise à disposition de leurs observations de terrain et données de mesures. Un tout grand merci aussi à toutes les personnes avec qui j'ai eu la chance de passer quelques moments sur le terrain, au cours des campagnes de reconnaissance, pour les mesures GPS et LiDAR ou encore la mise en place et configuration des appareils photos et digisnap: Alexandre Mathieu, Julien Gance, André Stumpf, Tomas Dewez, Grégoire Skupinski, Patrice Ulrich, Benjamin Koenig et Marie Charrière. Merci également à Monsieur Claude Chardenal du Sauze pour son accueil et la mise à disposition de son matériel et à Monsieur Jean-Luc Printemps pour son accueil au centre Séolane. Je remercie également Thomas Lebourg du Laboratoire

GéoAzur de l'Université de Nice-Sophia Antipolis de m'avoir guidée sur le glissement de la Clapière et donné les informations et données nécessaires pour son étude. Merci également à Edouard Palis pour son aide concernant l'interprétation des données de tachéométrie.

J'ai pu également bénéficier de nombreux échanges avec des chercheurs, maitres de conférences et professeurs, qui m'ont parfois bien plus que montré la voie et donné l'envie de continuer à apprendre et me surpasser. Je remercie tout d'abord le Prof. Hans Balder Havenith, de l'Université de Liège, de m'avoir donné le gout du risque (naturel) et d'avoir continué à me soutenir et me faire confiance. J'en profite d'ailleurs pour m'excuser de n'avoir pas pu consacrer plus de temps récemment à notre article en commun. J'adresse également mes remerciements au Dr. Alexandre Remaître pour le partage de sa connaissance de l'Ubaye et les échanges qui ont suivi ses relectures de mes écrits. Merci également au Dr. Céline Bourdeau pour son soutien continu depuis notre rencontre sur les montagnes kirghizes, au Prof. Mustapha Meghraoui d'avoir échangé avec moi et proposé son aide, au Dr. Christophe Zaroli pour ses conseils mathématiques, au Dr. Noël Gourmelen pour son apport lors de l'apprentissage du logiciel d'interférométrie StamPS, au Dr. Marc-Henri Derron pour ses conseils pertinents en interférométrie radar, au Dr. Cédric Wemmer pour ses cours d'initiation au langage IDL, au Dr. André Stumpf pour son aide avec IDL, au Dr. Julien Gance pour ses idées en matière de reprojections de plans, au Dr. Julien Travelletti, de m'avoir passé le flambeau et montré quelques clés pour l'utilisation du LiDAR et le traitement des données sous Polyworks et au futur Dr. Aline Deprez pour sa connaissance de NSBAS ayant permis de débugger des scripts.

J'adresse aussi mes plus sincères remerciements aux doctorants, post-doctorants (ou juste EOSTiens) rencontrés à l'Université de Strasbourg, qui m'ont permis d'échanger sur nos thématiques d'études communes mais aussi, en dehors des murs, lors de moments plus festifs et toujours d'un grand soutien psychologique : Aline, J-R, Khac, Marilyn, Abeer, Sheldon, Jana, Christine, Semih, Julie, Alexandra, Zacharie, Aurore, Julia, Pierre, Cécile, Eve-Agnès, Basile, Paul, Maximilien, Nadège, Arne, Fred, Olivier, Karim, Elise et Sylvain. Thank you for everything my dear Esra, I enjoyed so much the time we spent together here (and in Turkey). Big hug to Juan, it was really nice to be your officemate as well as Elena.

Je n'oublie pas non plus le soutien des amis rencontrés dans cette belle ville et qui m'ont fait passer d'agréables moments de décompression et détachée quelque peu de cette addiction à la thèse. Merci à Léa pour les pauses gourmandes, Fred pour les cafés matinaux dans la bonne humeur, à Caro pour ton sens de l'humour et ta répartie, ainsi qu'à ton cher Val, à Deby pour ces quelques fous rires et danses endiablées, à Amine pour ta gentillesse ainsi que pour les quelques conseils dans Illustrator, à Karim et Adela pour les bons petits plats (enfin presque tous), ainsi qu'à Mélanie, Nesma, David, Olivier, Nico, Adrien, Xin et Emeline. Grazie a te, professore Roberto. Sans oublier ma petite espagnole, Rebe, pour son soutien, son sourire et les 'parties de golfe', dommage que tu aies déserté Strasbourg : muchas gracias. J'adresse également un remerciement sincère aux membres de l'association JED-Togo et aux enfants du village de Koveto que j'aurai aimé aider bien plus encore.

Merci aussi aux amis namurois, liégeois, montois, bruxellois et chimaciens : Bene&Jean, Bastien, Nat&Steve, Fred&Dourou, Raph, Jérôme, Hubert&Caroll, Sébastien, Hoan, Nico, Jean-Charles, Marty, d'être venus me voir à Strasbourg ou d'avoir simplement pris de mes nouvelles lors de ces années d'expatriations. Je ne sais pas comment remercier mes quatre poulettes, amies de toujours, pour leur soutien continu : Pam, Pri, Caro et Marie, qu'est-ce que vous avez pu me manquer les filles !

J'exprime également ma plus profonde gratitude à mon meilleur ami, Jean, de m'avoir supportée toutes ces années, coachée quotidiennement, aidée dans tous les domaines, depuis tous les pays traversés, ne t'en fais pas l'histoire ne s'arrête pas là, bizhug ! Un immense merci à ma famille, mes trois frangins d'avoir continué à me taquiner mais aussi et surtout à mes parents, pour leur inconditionnel soutien et dévouement. Je ne serais jamais arrivée jusque-là sans toi, ma courageuse mèroum, cette thèse t'est dédiée.

RÉSUMÉ LONG

• Introduction

Contexte de la recherche

Un mouvement de terrain est un phénomène géologique où une masse de terrain se déplace le long d'une pente ou d'une surface de rupture sous l'effet de la gravité. Ces mouvements de terrain font des dégâts matériels ou humains partout dans le monde. Leurs effets sont d'autant plus importants lorsqu'ils affectent des zones densément peuplées et plus ou moins vulnérables (selon le nombre de personnes, le type d'habitations ou d'infrastructures et l'activité économique exposés). Alors que les 'mouvements de versant' recouvrent une grande variété de phénomènes naturels : allant des laves torrentielles aux écroulements rocheux, nous nous intéresserons ici à un type spécifique de mouvement de versant : les glissements de terrain. Entre 2004 et 2010, 2.620 glissements de terrain dévastateurs ont été enregistrés à travers le monde, causant au total 32.322 victimes (Petley, 2012). Quelle que soit la région du monde, les mécanismes déclenchant les glissements de terrain restent difficiles à identifier avant la rupture proprement dite, comme l'a démontré le déclenchement inattendu de l'impressionnant glissement d'Oso (Washington, États-Unis) tuant 43 personnes en mars 2014. En Europe, on dénombre également de nombreux sinistres tous les ans, principalement dus aux intenses et/ou longues périodes pluvieuses représentant le principal facteur déclenchant des glissements de terrain. Les séismes peuvent également déclencher (ou favoriser le déclenchement) de grands glissements de terrain, comme ceux qui se sont produits après le tremblement de terre de mai 2008 dans la région de Wenchuan (Mw = 7,9), et ont tué plus de 20.000 personnes (Yin et al., 2009). Ce constat met donc en évidence l'importance et l'enjeu scientifique de prédire l'occurrence spatiale et temporelle des glissements de terrain et de leur(s) facteur(s) de déclenchement pour (1) identifier les zones les plus susceptibles de déclencher un glissement de terrain, (2) mettre en place des systèmes d'alerte performants et (3) choisir et dimensionner des ouvrages de protection.

Compte tenu de la diversité et de la complexité des glissements de terrain (Varnes and IAEG, 1984), il paraît difficile d'utiliser une méthodologie unique pour la création d'inventaires des événements de type glissement de terrain. Ces inventaires constituent la base d'une analyse quantitative (Guzzetti et al., 2012) même si leur élaboration a toujours une part importante de subjectivité et dépend de la méthode utilisée (Wills and McCrink, 2002). Le type de glissement de terrain, son occurrence temporelle et spatiale ainsi que son intensité (exprimée en termes de vitesse de propagation par exemple) sont des éléments essentiels à intégrer dans l'inventaire. A l'échelle régionale, la caractérisation détaillée des évènements est chronophage, coûteuse et dépendante des données disponibles. Les cartographies d'inventaires sont généralement produites par des méthodes conventionnelles (campagnes de terrain, photo-interprétation) ou par des techniques plus novatrices (modèles numériques de terrain à très hautes résolution et précision, images satellitaires optiques ou radar). Les progrès technologiques dans le domaine de la télédétection, en termes de résolution spatiale et spectrale et de répétitivité des mesures, ont largement amélioré les connaissances des aléas gravitaires en facilitant leur cartographie et leur surveillance. Dans ce contexte, la télédétection passive a largement prouvé son utilité, en termes d'efficacité et de rentabilité, notamment pour la connaissance et cartographie rapide de glissements de terrain, déclenchés par d'autres aléas naturels et localisés dans des zones reculées (Lu et al., 2011; Mondini et al., 2011; Lacroix et al., 2013). La télédétection active (imagerie radar terrestre, aéroportée ou spatiale) est, quant à elle, fréquemment utilisée pour identifier les glissements de terrain et mesurer leur cinématique. Par exemple, l'interférométrie radar permet d'obtenir une cartographie précise des déplacements dans la ligne de visée du capteur. Elle est particulièrement bien adaptée à la surveillance opérationnelle de mouvements lents, dénudés de végétation, avec des mesures répétées à intervalles courts. Cette technique comporte cependant de nombreuses limitations : couverture spatiale et temporelle limitées, influence du couvert végétal, effets atmosphériques variables et coûts opérationnels parfois importants.

Les méthodes d'évaluation de l'aléa et du risque ne sont pas standardisées à travers le monde mais il existe un consensus décrivant les approches possibles (van Westen et al., 2006). L'approche dite "expert" (ou "directe") consiste à laisser le géomorphologue définir, sur base de son expérience, l'importance à attribuer aux variables contrôlant l'occurrence du phénomène. En France, la procédure des Plans de Prévention des Risques (PPR) prévoit l'utilisation de méthodes directes (MATE/METL, 1999). L'approche quantitative (ou "indirecte"), complexe à mettre en œuvre, requiert (1) la maîtrise d'outils et de méthodes statistiques sophistiquées et (2) une importante base de données (événements et facteurs de contrôle). Elle utilise des outils statistiques intégrés aux Systèmes d'Information Géographique (SIG) pour identifier les relations entre la localisation du phénomène et ses facteurs de contrôle (facteurs de prédisposition). Depuis 2008, le "*Joint Research Center*" (groupe européen d'experts en glissements de terrain dirigé par Vladimír Šucha et localisé dans des institutions scientifiques en Belgique, Espagne, Italie, Allemagne et Pays-Bas), au travers de son rapport *"Guidelines for landslide susceptibility, hazard and risk zoning for land use planning"* (Fell et al., 2008a, 2008b) recommande l'utilisation des méthodes indirectes pour les procédures de cartographie de la susceptibilité, de l'aléa et du risque dans un cadre opérationnel.

Objectifs et cadre de la recherche

Considérant les progrès technologiques dans le domaine de la télédétection (active et passive) pour l'observation des glissements de terrain, en termes de détection/cartographie et de suivi temporel, l'objectif de ce travail de thèse est de proposer une méthodologie pour l'évaluation quantitative de l'aléa glissement de terrain par l'usage de données multi-sources, de télédétection et de modélisations probabilistes. Les objectifs principaux de cette recherche sont :

- de créer un inventaire multi-dates de glissements de terrain par des techniques variées et complémentaires (analyse de photographies aériennes et de cartes géomorphologiques, interférométrie radar, campagnes de terrain) ;
- de caractériser l'évolution morphologique des glissements observés ;
- de modéliser l'occurrence spatiale et temporelle des glissements pour des unités spatiales d'analyse appropriées ;
- d'identifier les relations entre les facteurs de prédispositions et les facteurs de déclenchement (météorologiques).

Les techniques et méthodologies de travail seront évaluées à l'échelle locale (1:5.000-1:2.000) et régionale (1:25.000-1:10.000) dans la moyenne vallée de l'Ubaye dans les Alpes du Sud. Les archives les plus anciennes consultées datent de 1850, alors que la plupart des données multi-sources disponibles dans cette région couvrent la période 1950-2010.

Cette thèse a été menée à l'Université de Strasbourg, au sein de l'Institut de Physique du Globe de Strasbourg (IPG, UMR 7516 CNRS-UNISTRA), sous la supervision du Dr J.-P. Malet, du Dr C. Doubre et du Professeur F. Masson. Elle a été a été financée par le projet européen Marie Curie (FP7) CHANGES, "*Changing Hydro-meteorological Risks as Analyzed by a New Generation of European Scientists*". En plus des différents cours intensifs organisés dans le cadre du projet permettant aux jeunes chercheurs d'interagir, une collaboration avec des chercheurs de l'Institut de Recherche pour la Protection Hydrogéologique (CNR-IRPI) de Pérouse (Italie) a pu être établie.

Le catalogue des glissements de terrain et les mesures in-situ ont été élaborés par le service RTM-04 (Restauration des Terrains en Montagne) du Département des Alpes-de-Haute-Provence. Les données GNSS ont été fournies par l'Observatoire français des glissements de terrain (OMIV : Observatoire Multidisciplinaire des instabilités de Versants : http://omiv.unistra.fr). Les mesures tachéométriques acquises dans la vallée de la Tinée ont été fournies grâce à un accord avec le Cerema (Centre d'études et d'expertise sur le risque, l'environnement, la mobilité et l'aménagement). Les images ALOS/PALSAR ont, quant à elles, été fournies par l'Agence Japonaise d'Exploration Aérospatiale (JAXA) et l'Agence Spatiale Européenne (ESA) dans le cadre du contrat C1P.8859. Neuf campagnes de terrain ont été

réalisées dans la vallée de l'Ubaye au cours de la période 2011-2013 pour la reconnaissance des glissements de terrain et la cartographie, la validation des signaux D-InSAR ainsi que l'acquisition de données GPS et LiDAR en collaboration avec d'autres doctorants et collègues de l'IPGS-EOST (Université de Strasbourg). En 2012, une visite de terrain sur le glissement de terrain de La Clapière (vallée de la Tinée) a été initiée par le Dr T. Lebourg (Laboratoire Géoazur, Université de Nice-Sophia Antipolis).

Contenu de la thèse

Cette thèse s'articule en quatre chapitres : les deux premiers définissent la terminologie utilisée et décrivent les méthodes d'analyse et la zone d'intérêt, le troisième présente la méthodologie de création de l'inventaire en intégrant des articles scientifiques et le quatrième aborde le calcul probabiliste de la susceptibilité et de l'aléa à l'échelle de différentes unités cartographiques (Fig. R1).

Le **chapitre 1** détaille les concepts abordés pour la reconnaissance des phénomènes gravitaires et pour l'étude de l'aléa glissement de terrain selon la réglementation française en vigueur. Les différentes unités spatiales d'analyse sont présentées ainsi que les méthodes d'estimation de la susceptibilité et de l'aléa.

Les contextes géographique, géologique, climatique, hydrologique et géomorphologique de la zone d'étude sont présentés dans le **chapitre 2**. Les aléas naturels affectant cette région sont présentés en détaillant des glissements de terrain actifs observés (La Valette, Poche, Super-Sauze, Aiguettes, Pra-Bellon, Adroit et Sanières).

Le **chapitre 3** présente les événements observés selon l'échelle considérée, en termes :

- de caractérisation de la cinématique à l'échelle du glissement par interférométrie radar ;
- de détection des glissements pour la création d'inventaires par interférométrie radar et d'interprétation visuelle de données multi-sources.

Ce chapitre s'appuie sur deux articles scientifiques développant et appliquant une méthodologie d'interprétation de la cinématique de grands glissements de terrain en utilisant des images radar en bande L (ALOS/PALSAR). Cette méthodologie propose une interprétation des différences de phase obtenues pour l'analyse détaillée des zones de déplacements de glissements de terrain actifs et complexes (La Valette et Poche en Ubaye et la Clapière dans la vallée de la Tinée). En effet, les valeurs de différences de phase positives correspondent à des déplacements s'éloignant du satellite, indiquant les zones d'ablation (ou de subsidence) alors que les valeurs de différences de phases négatives correspondent à des déplacements se rapprochant du satellite, identifiant les zones de transit ou d'accumulation. L'interférométrie radar combinée à des données *in situ* a donc permis de cartographier l'extension réelle des zones instables et de déterminer les vitesses (ou changements de régime de vitesses) de déplacement des différentes unités. La deuxième partie de ce chapitre décrit la méthodologie de création d'un inventaire multi-dates, par comparaison et combinaison de données multi-sources (rapports d'expertises, ortho-photographies, cartes géologiques et géomorphologiques, données dendrogéomorphologiques, campagnes de terrain, données InSAR). Des fonctions de densité de probabilité considérant la surface (ou l'aire d'extension) des glissements de terrain permettent d'analyser et de quantifier leur intensité. L'occurrence temporelle des glissements de terrain (en termes de déclenchement ou de réactivation) est également calculée sous forme de probabilité de dépassement (ou de non-dépassement) pour différentes périodes de retour grâce à la loi de Poisson.

Le **chapitre 4** détermine la susceptibilité et l'occurrence temporelle (incluant une probabilité de taille minimale) pour la zone d'étude. Une méthodologie de subdivision de la zone d'étude en unités spatiales d'analyse appropriées est proposée et appliquée à des modèles numériques de terrain de résolution différente (entre 5 et 25 m). L'occurrence spatiale des glissements de terrain est évaluée par régression logistique sur base d'une classification des unités de pente. L'occurrence temporelle est calculée pour différentes périodes de retour (à partir d'un intervalle d'analyse de 53 ans) et en tenant compte d'une évolution d'aire d'extension minimale (500 m^2). L'intensité des phénomènes a été estimée en calculant

l'aire nouvelle affectée dans l'unité d'analyse. Finalement, les résultats de la modélisation sont validés sur la base des glissements de terrain cartographiés dans la vallée. L'aléa est ensuite analysé à l'échelle locale pour différentes zones cibles et pour une période de retour de 10 ans.

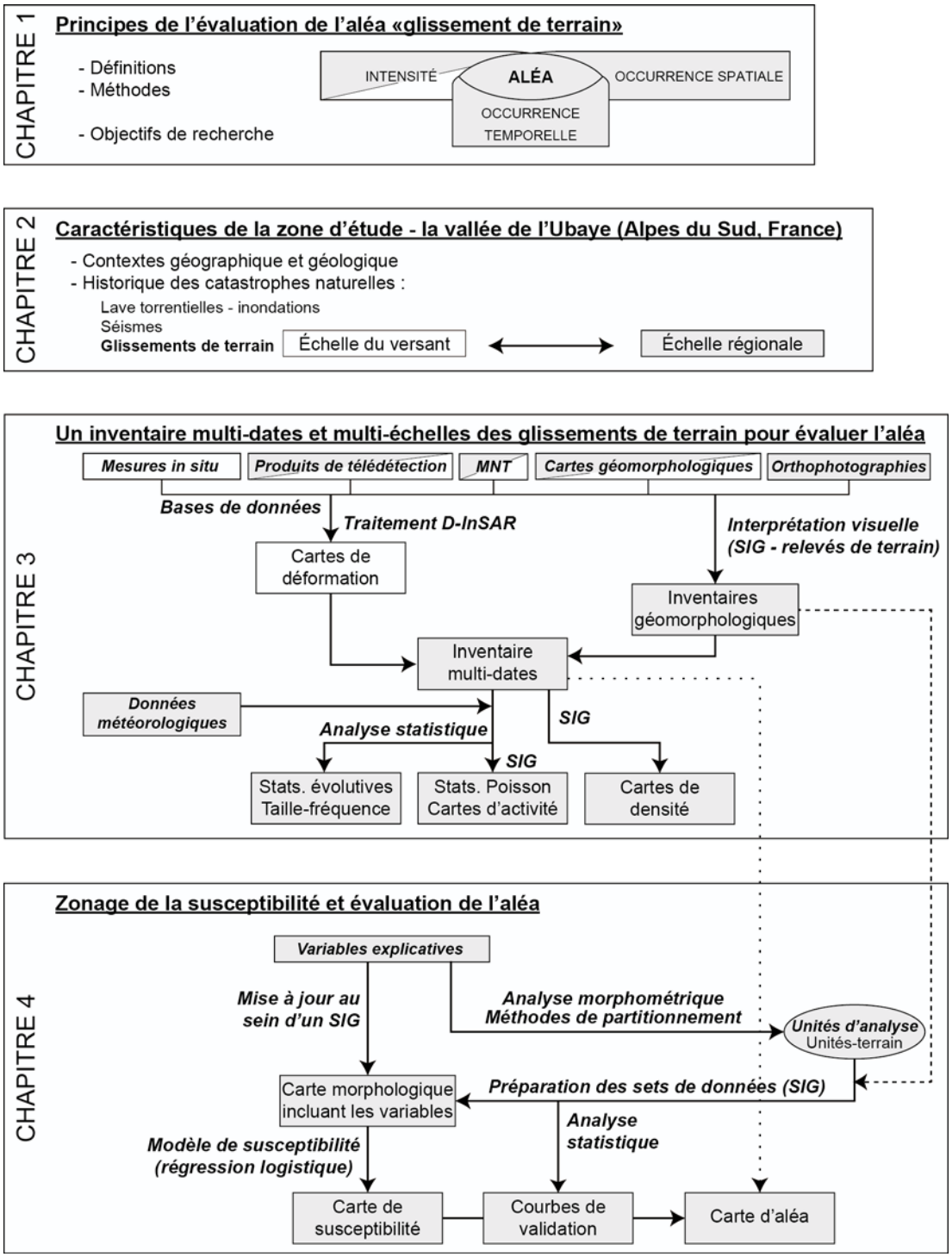

Figure R1 : structure du travail de recherche en quatre chapitres et présentation des méthodes et outils employés dans chacun d'entre eux.

- **Chapitre 1 : principes d'évaluation de l'aléa « glissement de terrain »**

Ce chapitre présente les concepts clés requis pour l'analyse des risques de glissements de terrain ainsi qu'un état de l'art des techniques utilisées pour l'évaluer qualitativement et quantitativement. Tout d'abord, les termes utilisés pour reconnaître, décrire et classer les glissements de terrain à une échelle d'étude donnée (régionale, locale ou à l'échelle du versant) sont précisés. Deuxièmement, les méthodes pour cartographier et inventorier les glissements de terrain selon des méthodes traditionnelles ou avancées sont discutées. Troisièmement, les différentes unités d'analyse (délinéation du territoire ou grille régulière) pour analyser la susceptibilité et l'aléa « glissements de terrain » sont décrites. Quatrièmement, les méthodes qualitatives et quantitatives permettant d'évaluer de façon relative cet aléa, par exemple via l'occurrence spatiale, sont détaillées. Cinquièmement, les méthodes permettant de quantifier l'aléa « glissement de terrain » en termes d'occurrence temporelle et d'intensité sont discutées. Enfin, la dernière partie conclut sur les limites rencontrées au cours de l'évaluation de l'aléa « glissement de terrain » ; elle décrit également les objectifs spécifiques et les aspects novateurs de cette recherche, comme suit :

(1) Un inventaire « multi-dates» a été créé à l'échelle régionale par comparaison des données multi-sources et comprend un indice de végétation afin de déterminer la (ré)activation des glissements de terrain au fil du temps ;

(2) Une méthode guidée par l'analyse géomorphologique a été mise en place afin d'interpréter les données InSAR à l'échelle régionale et à l'échelle du versant afin de détecter différents secteurs instables et évaluer leur évolution cinématique et spatiale ;

(3) Des données InSAR ont été combinées à des mesures au sol à l'échelle du versant afin de déterminer différents champs de vitesses associés à des glissements de terrain profonds complexes et de les relier à la géologie structurale ;

(4) La morphométrie des pentes et des sous-bassins a montré son influence sur la délinéation des unités de terrain ;

(5) L'unité d'analyse et l'effet des données d'élévation affecte l'évaluation de la susceptibilité aux glissements de terrain ;

(6) L'activité des glissements de terrain et de la probabilité de dépassement fondés sur un inventaire multi-dates a été estimée pour évaluer la récurrence des glissements de terrain en fonction de leur intensité, ainsi que certains événements potentiellement déclencheurs ;

(7) Les fonctions de densité de taille ont permis de comparer les relations entre la fréquence et l'aire des glissements de terrain en fonction de la subdivision de l'inventaire selon la situation géographique, la géologie et la période de temps considérée ;

(8) La susceptibilité des glissements de terrain a été évaluée grâce à un modèle multivarié considérant différentes variables dépendantes ;

(9) Les facteurs de prédisposition, où des glissements de terrain se sont produits et évoluent, ont été analysés ainsi que la combinaison de l'occurrence temporelle avec l'intensité des événements afin d'évaluer l'aléa de glissement de terrain sur certains secteurs d'intérêt de la vallée de l'Ubaye (décrits dans le chapitre 2).

• Chapitre 2 : caractéristiques de la zone d'étude – la vallée de l'Ubaye

Le chapitre 2 décrit dans ses deux premières parties les caractéristiques géographiques, géomorphologiques et géologiques de la zone d'étude. La troisième partie aborde les risques naturels observés dans la vallée, et préférentiellement les différents types de glissements de terrain rencontrés. Elle évalue l'impact de la géomorphologie sur la distribution des glissements de terrain.

Localisée dans les Alpes du Sud, la région se divise géologiquement selon un axe transversal ouest/est, divisant le domaine externe constitué de massifs cristallins (Ecrins et Queyras au nord, Argentera et Mercantour au sud) et de formations géologiques autochtones du domaine interne formé de plusieurs nappes de chevauchements. La vallée de l'Ubaye constitue donc une zone géologiquement complexe où se juxtaposent plusieurs ensembles structuraux. Cette activité tectonique a largement contribué à la genèse du bassin et à la dissymétrie de ses versants. Le bassin de Barcelonnette forme véritablement une 'cellule' enclavée entre ses massifs environnants et drainée par le cours moyen de l'Ubaye (Fig. R2a).

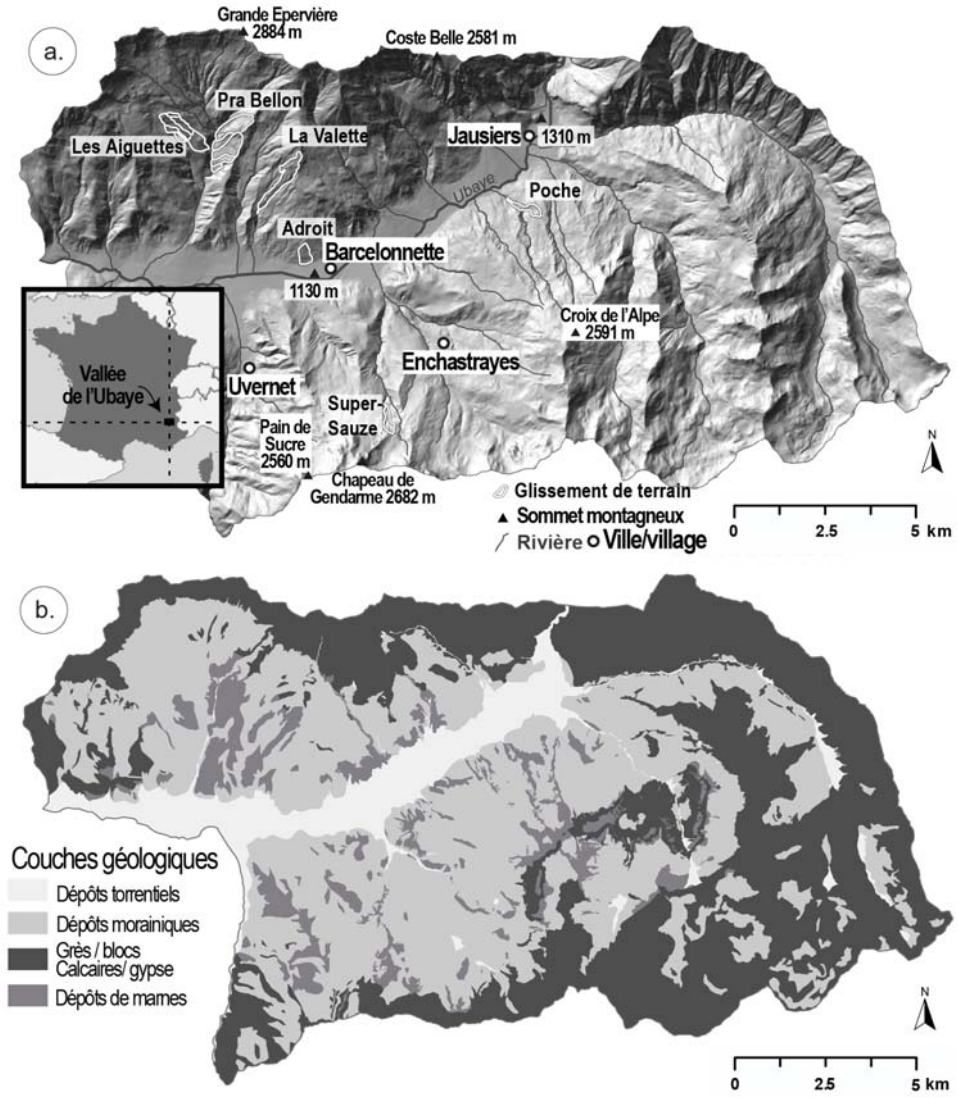

Figure R2 : la vallée de l'Ubaye dans le sud des Alpes-de-Haute-Provence. (a) Localisation des villages, sommets et glissements de terrain de Les Aiguettes, Pra Bellon, La Valette, Adroit, Poche et Super-Sauze (b) couches géologiques superficielles (dépôts torrentiels et morainiques), altérées ou remaniées (marnes noires ou chaos de blocs) ou compétentes et en place (calcaire et grès).

L'érosion préférentielle a permis de dégager les formations autochtones du Mésozoïque de la zone dauphinoise ouvrant ainsi sur une fenêtre géologique. Celle-ci est ouverte entre deux nappes de chevauchement (Autapie et Parpaillon) constituée de grès ou calcaire, et recouvre le bedrock autochtone, constitué de marnes noires (Fig. R2b). Ces « Terres Noires » callovo-oxfordiennes sont tendres et finement feuilletées. Les sources et concentrations d'eau dues à la faible perméabilité des marnes noires favorisent des surfaces de rupture au contact des formations superficielles ou des flyschs. Aussi, leur changement rapide d'état ou de consistance favorisent la susceptibilité aux mouvements de terrain.

Ensuite, plusieurs glissements de terrain actifs et potentiellement dangereux, représentatifs de la région étudiée, sont présentés ainsi que les études qui y ont été menées. Il s'agit des glissements de Les Aiguettes, de Pra Bellon, de La Valette et de Sanières dans la partie nord et de ceux de Poche et de Super-Sauze dans la partie sud (Fig. R2a).

- **Chapitre 3 : un inventaire multi-dates et multi-échelles de glissements de terrain pour l'évaluation de l'aléa**

L'objectif de ce chapitre est de créer un inventaire multi-dates et multi-échelles des glissements de terrain en considérant différentes sources d'information (cartes géomorphologiques, données acquises par télédétection, observations de terrain) à l'échelle du versant et à l'échelle régionale. Ce chapitre est divisé en trois sections : (1) principes d'analyse multi-échelles de glissements de terrain, (2) caractérisation des cinématiques de glissements à l'échelle du versant : une méthodologie guidée géomorphologiquement pour l'analyse d'interférogrammes d'images en bande L, et (3) création d'un inventaire multi-dates de glissements de terrain à l'échelle régionale par combinaison de données multi-sources. Enfin, ce chapitre se conclut par une synthèse des résultats de recherche sur l'interprétation de l'inventaire multi-dates à différentes échelles.

La section 3.1 présente le cadre de l'analyse multi-échelles de la recherche. Il présente les données disponibles et les techniques d'analyse. La section 3.2 met l'accent sur l'analyse des événements de glissements de terrain à l'échelle de pente. Elle présente une méthodologie guidée par une approche géomorphologique pour interpréter la cinématique de vastes et complexes glissements de terrain à l'aide de la bande L d'images SAR (Fig. R3).

Les images ALOS/PALSAR sont traitées avec les algorithmes ROI_PAC et NSBAS afin de créer des interférogrammes, enroulés ou déroulés. Les résultats DInSAR sont combinés aux mesures au sol pour cartographier l'étendue de la déformation de certaines pentes instables. La première partie de cette section décrit le développement de la méthodologie requise pour interpréter les signaux InSAR selon les différents types de glissements de terrain. Les taux de déplacement et l'évolution géomorphologique des glissements de terrain sont évalués pour la période 2007-2010. La deuxième partie de cette section est une application de ce cadre méthodologique à un glissement de terrain profond complexe actif contrôlé par les structures (à savoir, le glissement de La Clapière). L'information obtenue à partir de déplacement D-InSAR est ensuite intégrée dans un inventaire régional multi-dates créé à partir d'autres sources de données.

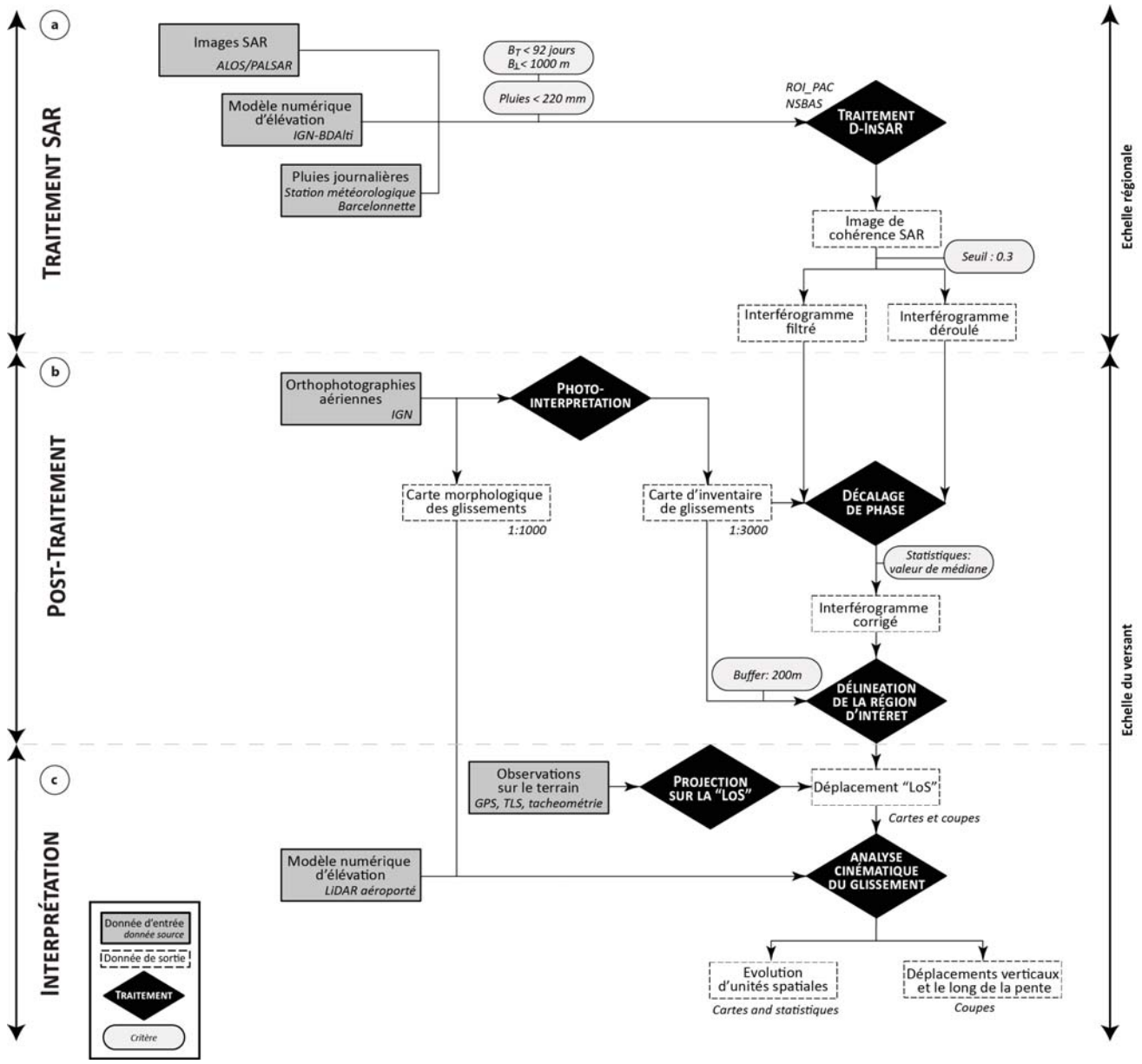

Figure R3 : Organigramme de traitement d'images radar à synthèse d'ouverture (SAR) pour l'interprétation de la cinématique des glissements de terrain à l'échelle du versant. (a) Les images ALOS/PALSAR, sélectionnées en fonction d'une ligne de base perpendiculaire inférieure à 1000 m, une ligne de base temporelle inférieure à 92 jours et un cumul de pluies inférieur à 220 mm entre deux acquisitions, ont été traitées par les algorithmes proposés dans NSBAS et ROI_PAC afin d'obtenir des images de cohérences ainsi que des interférogrammes filtrés et déroulés en fonction d'un seuil de cohérence de 0.3. (b) Les interférogrammes ont été corrigés manuellement en soustrayant la valeur de la médiane des zones stables à proximité des glissements de terrain considérés entourés d'un « buffer » de 200 m. (c) L'analyse des déplacements mesurés le long de la ligne de visée du satellite et reprojetés le long de la verticale ou le long de la pente pour estimer la cinématique de glissements de terrain complexes et l'évolution d'unités spatiales au cours du temps.

Cette sous-section inclut les articles scientifiques cités et résumés ci-dessous :

Schlögel, R., Doubre, C., Malet, J-P., Masson, F. (2015a). Landslide deformation monitoring with ALOS/PALSAR imagery: A D-InSAR geomorphological interpretation method. Geomorphology 231, 314-330.

L'objectif de cet article est de proposer une méthodologie guidée par la géomorphologie pour interpréter les interférogrammes créés par Interférométrie Radar Différentielle à Synthèse d'Ouverture (D-InSAR) à partir de la bande L des images ALOS/PALSAR. Les interférogrammes sont utilisés pour estimer le champ de déformation de deux glissements de terrain rapides et grande ampleur (Poche et La Valette, dans le sud-est de la France). Les valeurs de phase, enroulées ou déroulées, sont interprétées pour différents types de mouvements (rotationnel, translationnel et

complexe) et deux gammes de vitesses de déplacement de surface. Les sous-unités cinématiques sont identifiées pour d'une part, les glissements de terrain et d'autre part, les zones concernées par un élargissement ou une rétrogression. Les vitesses de déplacement calculées par l'InSAR sont cohérentes avec les mesures réalisées au sol et avec les estimations du déplacement effectuées grâce aux bandes C et X des capteurs satellitaires SAR. Les résultats démontrent le potentiel de la bande L des capteurs interférométriques ALOS/PALSAR pour la surveillance des glissements de terrain actifs avec des changements importants de l'état de surface du sol et recouverts par la végétation.

Schlögel, R., Malet, J.-P., Doubre, C., Lebourg, T. (2015b). Structural control on the kinematics of the deep-seated La Clapière landslide revealed by L-band InSAR observations. Landslides 1-14.

L'objectif de cet article est de documenter le champ de déformation du glissement profond de La Clapière pour la période 2007-2010 à partir de la combinaison d'interférogrammes SAR en bande L, de mesures réalisées au sol grâce à une station totale et d'identifier les structures géomorphologiques à l'échelle du versant. Les interférogrammes sont calculés pour des paires d'images ALOS/PALSAR acquises avec un intervalle temporel de 46 jours, et sont traités avec des algorithmes ROI_PAC et NSBAS. Le déroulement de phase est réalisé en intégrant les mesures quotidiennes de déplacement de la surface sur une série de 50 cibles. Les valeurs de phase, enroulées et déroulées, sont interprétées pour différents types de mouvement (subsidence sur la partie sommitale, accumulation en pied de glissement). Les résultats démontrent le potentiel de la bande L de l'imagerie ALOS/PALSAR pour la surveillance des glissements de terrain actifs caractérisés par une structure cinématique complexe et par des changements importants dans la rétrodiffusion radar de la surface du sol au cours du temps.

La section 3.3 présente la création d'un inventaire multi-dates sur base de données multi-sources pour l'évaluation statistique des périodes de retour et de l'intensité des glissements de terrain (voir organigramme en Fig. R4). D'abord, la méthode d'interprétation visuelle utilisée pour identifier les glissements de terrain est expliquée. Elle est basée sur l'analyse des caractéristiques des glissements de terrain décrites dans les rapports techniques ou mises en évidence sur les photographies aériennes, les cartes géomorphologiques, les modèles numériques d'altitude, les cartes de déformation InSAR et les observations de terrain. L'incertitude des données est prise en compte en considérant la résolution des ortho-photographies. L'incertitude de cartographie des glissements de terrain actifs est estimée en considérant une zone « buffer » dépendant de la visibilité mesurée par l'observateur et fonction de la couverture végétale (ex. glissement de terrain difficilement visible sous forêt). L'inventaire multi-dates permet d'acquérir une information cruciale sur les glissements de terrain réactivés durant certaines périodes de temps qui sont fonction des périodes d'acquisitions des données d'entrées. La Figure R5 montre le résultat de cet inventaire. L'intensité et la période de retour des événements sont évaluées grâce à plusieurs techniques statistiques. Enfin, les relations entre l'occurrence des glissements de terrain et les facteurs météorologiques potentiellement déclencheurs sont discutées.

Cette sous-section inclut l'article scientifique cité et résumé ci-après :

Schlögel, R., Malet, J.-P., Remaître, A., Reichenbach, P., Doubre, C., (2015c). Analysis of a landslide multi-date inventory in a complex mountain landscape: the Ubaye valley case study. NHESS 15, 2369-2389.

Nous proposons une méthodologie (1) pour élaborer un inventaire multi-dates des glissements de terrain dans une zone montagneuse affectée par plusieurs types de glissements de terrain avec différents degrés d'activité, et (2) pour estimer l'occurrence temporelle et l'intensité des glissements de terrain à travers l'analyse d'indicateurs morphologiques. L'inventaire, couvrant la période 1956-2010, est construit pour la partie centrale de la vallée de l'Ubaye (Alpes françaises du Sud) sur la base de l'analyse des documents multi-sources (cartes géomorphologiques, rapports historiques des événements de glissements de terrain, enquêtes de terrain, série d'ortho-photographies et d'images satellitaires SAR). Les incertitudes dans l'interprétation des documents et les caractéristiques morphologiques des glissements de terrain sont prises en compte par rapport à l'échelle des documents sources.
Plusieurs indicateurs morphologiques sont calculés pour décrire quantitativement l'évolution des glissements de terrain (longueur, superficie, altitude relative, distance entre l'escarpement et le pied du glissement). Les fonctions de densité fréquence-superficie sont calculées pour estimer les modifications dans les distributions des glissements de terrain. Un modèle de Poisson est utilisé pour estimer la probabilité de réactivation des glissements de terrain observés. L'inventaire multi-dates proposé et les statistiques qui y sont associées fournissent des informations supplémentaires par rapport au catalogue d'événements établi et géré par les autorités locales.

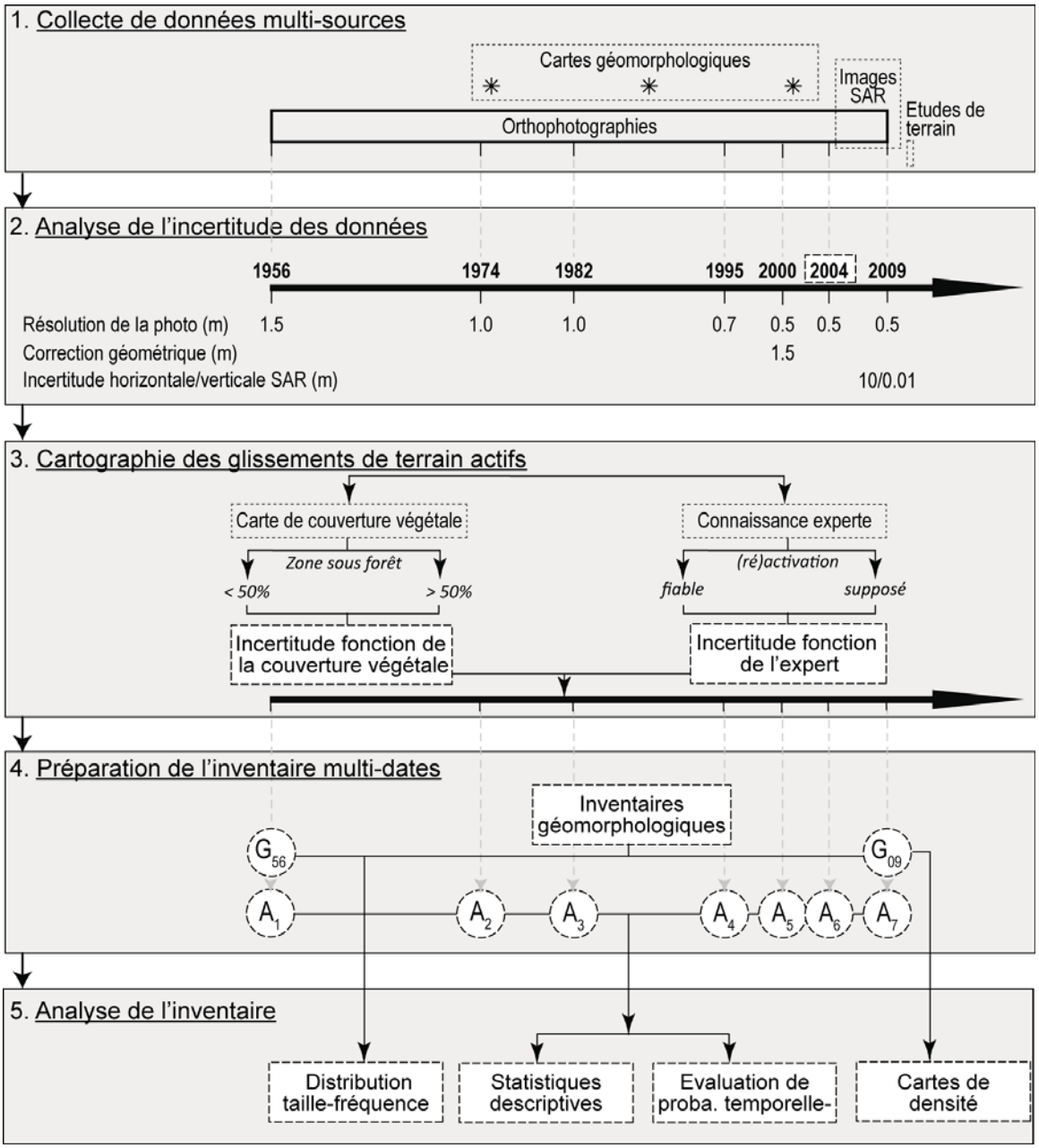

Figure R4 : Différentes étapes pour la préparation et l'analyse de l'inventaire multi-dates de glissements de terrain : (1) la collecte de données multi-sources couvrant différentes périodes temporelles, (2) l'analyse de l'incertitude de ces données en termes de résolution spatiale et de correction géométrique, (3) la cartographie des glissements de terrain en considérant une incertitude induite par la difficulté de visualisation en zones sous forêt et les connaissances du géomorphologue, (4) la préparation de l'inventaire multi-dates constitué d'inventaires géomorphologiques desquels les glissements de terrain actifs pour les différentes périodes de temps considérées sont distingués (voir Fig. R5), et (5) l'analyse statistique de cet inventaire pour estimer la densité par type de glissement de terrain, des distributions particulières de fréquences de taille de mouvement en fonction de la lithologie affectée ou de la localisation des phénomènes, l'évolution temporelle du nombre et de l'aire des glissements actifs ainsi qu'une estimation de leur probabilité de réactivation pour une période de retour de 5, 10, 25 ou 50 ans.

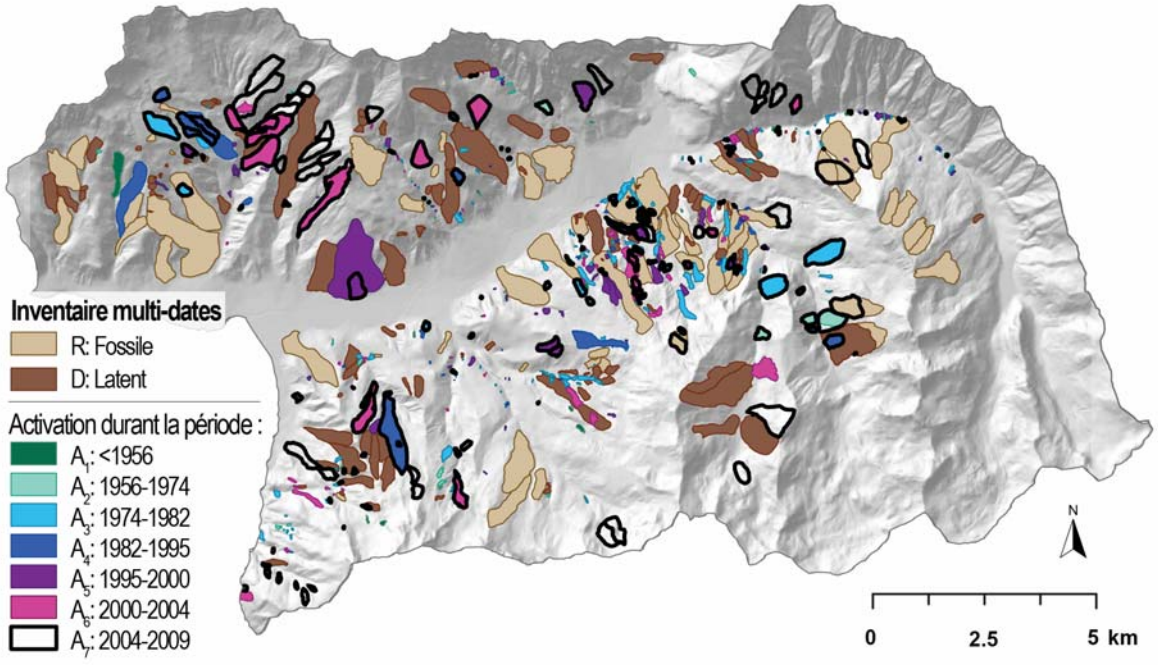

Figure R5 : Inventaire multi-dates des glissements de terrain actifs durant la période pré-1956 (A_1), entre 1956 et 1974 (A_2), entre 1974 et 1982 (A_3), entre 1982 et 1995 (A_4), entre 1995 et 2000 (A_5), entre 2000 et 2004 (A_6), et entre 2004 et 2009 (A_7).

Ce chapitre met en évidence la difficulté de gérer de nombreuses sources d'information acquises à différentes périodes mais aussi leur complémentarité en termes de cartographie des différents types de glissements de terrain. Les résultats de leur cartographie et l'analyse cinématique par interférométrie radar à l'échelle du bassin versant montrent le champ de déformation réel et ses caractéristiques pour étudier un type particulier de glissement de terrain et connaitre sa vitesse. Cette étude démontre que la méthodologie est applicable pour analyser des glissements de terrain actifs et complexes. Les cartes de déformation du sol générées à l'aide de l'InSAR permettent de détecter des compartiments de glissements ainsi que des structures profondes jouant un rôle dans la déstabilisation des pentes. Les phases interférométriques enroulées et déroulées sont capables de détecter ces structures et les déformations du sol qui y sont associées. La vitesse du glissement peut également être estimée en tenant compte d'une connaissance a priori du terrain qui permet de guider le processus de déroulage (*unwrapping*) de la phase interférométrique. Ces résultats constituent une information pertinente pour connaitre l'activité et l'intensité des glissements de terrain pendant la période 2007-2010. Ces sous-inventaires de glissements actifs sont une information précieuse dans la création d'un inventaire multi-dates de glissements de terrain à l'échelle régionale.

Cet inventaire multi-dates a donc été préparé par l'analyse par photo-interprétation de données de sources différentes. Par simple comparaison de sets de données, il révèle les glissements de terrain nouveaux et réactivés pour différentes périodes entre 1956 et 2009. Des statistiques descriptives et des paramètres attributaires de mobilité ont été calculés de manière à caractériser les phénomènes. L'évolution de l'activité des glissements de terrain de la vallée de l'Ubaye est ensuite comparée aux archives constituées par d'autres techniques d'analyse (ex. un catalogue ponctuel d'événements "glissement de terrain", un set de données issues de la dendrochronologie) afin d'évaluer son exhaustivité. Les fonctions de densité de fréquence d'aire montrent des distributions distinctes suivant la localisation du glissement affectant des couches géologiques particulières, suivant la zone nord ou sud considérée et en fonction de son degré d'activité. La récurrence du phénomène a également été calculée pour différentes périodes de retour sur base des surfaces actives durant les 53 années étudiées. La comparaison des événements enregistrés entre 1956 et 2009 avec la base de données historiques (1850-2012) montre que l'archive disponible est incomplète. En effet, notre analyse visuelle

des glissements de terrain nouveaux et réactivés permet de détecter davantage d'activations que le catalogue historique. Ceci démontre que, même si elle est fastidieuse et chronophage, l'interprétation visuelle des données de télédétection est toujours indispensable pour l'évaluation de l'aléa "glissement de terrain". Des événements météorologiques ont également pu être corrélés à des périodes d'activité importante liées aux glissements de terrain. L'analyse de probabilité d'excédence montre que sur une période de retour de 50 ans, il y a plus de 60 pourcents de chance d'avoir un nouvel événement "glissement de terrain" sur les parties du territoire déjà instables. Cette observation statistique basée sur l'analyse visuelle de données multi-sources met en évidence la fréquence importante des glissements de terrain dans la vallée de l'Ubaye.

Les limites des méthodologies mises en évidence dans ce chapitre dépendent de l'échelle de travail. La méthode DInSAR utilisée pour identifier et caractériser les glissements de terrain présente des limites dues à plusieurs facteurs induisant une haute décorrélation du signal, tels que :

- Les taux de vitesse élevés de certains compartiments instables (par exemple, la zone d'ablation du glissement de terrain de La Valette) ;
- La combinaison de propriétés SAR et des caractéristiques du terrain, induisant un résultat affecté par une déformation du signal (« *layover* ») selon l'orientation et l'angle de certaines pentes ;
- La présence de végétation dense (y compris avec un capteur utilisant la bande L) ;
- Les conditions climatiques changeantes dans ce contexte montagneux (comme la présence de neige ou les précipitations intenses) ;
- La ligne de base temporelle qui ne peut excéder 46 jours pour les analyses cinématiques quantitatives ;
- La ligne de base perpendiculaire entre certaines acquisitions, qu'il est souhaitable de maintenir inférieure à 1.200 m.

Notons que la méthodologie InSAR ne permet de détecter que les glissements de terrain actifs. Par conséquent, elle ne peut pas être utilisée pour constituer des inventaires de glissements de terrain. Dans cette étude, les signaux InSAR correspondant à la partie active de glissements de terrain sont recartographiés à plus haute résolution (1:3.000) selon la géomorphologie du terrain. Ces nouveaux polygones, qui correspondent à des glissements de terrain actifs, ont été introduits dans l'inventaire géomorphologique de l'année 2009. Malheureusement, en raison des propriétés géométriques (*layover*, pentes cachées par rapport à l'angle d'incidence du satellite), ils ne constituent pas un inventaire complet des mouvements actifs de la région pour une période donnée.

Après ces analyses d'activité, d'intensité et de fréquence temporelle, l'occurrence spatiale doit être évaluée à l'échelle régionale. Dans le chapitre 4, différentes unités cartographiques d'analyse ont été délimitées sur base de différents modèles numériques de terrain. Ensuite, les modèles de susceptibilité des glissements de terrain ont été calculés en fonction des unités d'analyse afin d'évaluer l'aléa relatif dans la vallée de l'Ubaye. Calculée sur base d'une grille à mailles carrées dans ce chapitre, la probabilité de dépassement temporel peut également être évaluée en fonction des unités de terrain issues des délinéations. Ensuite, l'intensité des glissements de terrain est estimée à partir des glissements de terrain qui manifestent une évolution de leur superficie, calculée dans la table des attributs de l'inventaire multi-dates. Trois composantes de l'aléa sont ainsi analysées à l'échelle locale et comparées à l'ensemble des glissements de terrain observés.

• Chapitre 4 : zonation de susceptibilité et prévision quantitative de l'aléa

Les objectifs de ce chapitre sont (1) d'évaluer l'effet de la délinéation en unités de pente en utilisant différents MNTs de résolution différente, (2) d'analyser l'effet des "unités terrain" sur la zonation de susceptibilité aux glissements de terrain et (3) de discuter l'aléa "glissement de terrain" à l'échelle de zones particulières à risque. Le chapitre est divisé en six sections et suit les différentes étapes d'analyse menant à la cartographie de l'aléa selon l'organigramme présenté à la Fig. R6.

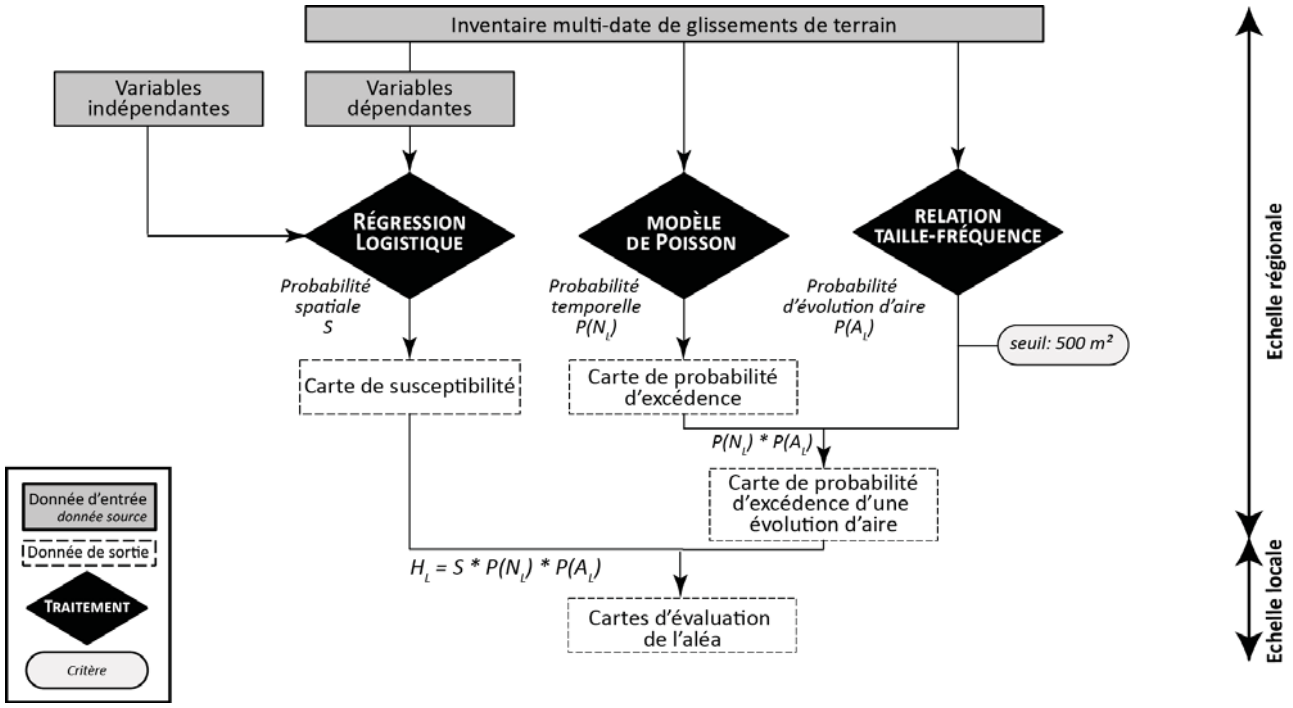

Figure R6 : Organigramme d'évaluation de l'aléa glissement de terrain par combinaison des estimations des probabilités spatiale *S*, temporelle $P(N_L)$ et d'évolution d'aire $P(A_L)$ incluant des variables dépendantes (glissements de terrain entiers ou zones d'ablation) et indépendantes (facteurs de prédisposition).

La section 4.1 se concentre sur les effets de la résolution des MNTs sur la délinéation des unités de terrain. Elle présente les différents modèles d'altitude disponibles et la méthodologie de partitionnement du terrain. Deux unités d'analyse différentes sont prises en considération pour l'évaluation de l'aléa : (i) une délinéation en unités de terrain avec une contrainte de superficie afin qu'elles restent représentatives de la morphologie locale et (ii) une délinéation en unités de pente créée en considérant les thalwegs et l'orientation des pentes.

Dans la section 4.2, les modèles de susceptibilité, appliqués aux différentes unités cartographiques, sont calculés par régression logistique.

Dans la section 4.3, les probabilités de dépassement temporel sont calculées pour les unités cartographiques grâce à la loi de Poisson. Ce modèle évalue la probabilité de déclenchement de glissements de terrain (à partir de l'inventaire multi-dates présenté au chapitre 3) pour différentes périodes de retour.

Dans la section 4.4, nous présentons une méthodologie pour évaluer l'intensité des glissements de terrain à l'échelle régionale. Leur mobilité est également calculée, et les probabilités temporelles supérieures à un seuil de taille de glissements de terrain sont estimées pour différentes périodes de retour.

L'aléa glissement de terrain est analysé à l'échelle locale sur la base de quatre secteurs préférentiels dans la section 4.5. Les probabilités d'occurrence des glissements de terrain sont examinées et discutés pour les bassins versants du Riou-Bourdoux, de Super-Sauze, de Poche et de Sanières.

Enfin, la section 4.6 aborde l'évaluation de l'aléa et les possibilités d'amélioration de la méthodologie.

Une cartographie exhaustive de la susceptibilité du territoire aux glissements de terrain peut aider les gestionnaires à évaluer la stabilité des pentes au point de vue des risques naturels et de l'aménagement du territoire. Malgré les recherches considérables réalisées au cours des deux dernières décennies sur la cartographie de la susceptibilité en utilisant des méthodes statistiques, les modèles de susceptibilité

physiquement basés et associés aux paramètres géotechniques sont les plus à même de représenter les conditions réelles du terrain. Les généralisations et simplifications couramment adoptées dans l'analyse statistique de la susceptibilité aux glissements de terrain et les hypothèses sous-jacentes réduisent la fiabilité des prévisions en raison principalement de la complexité des facteurs contrôlant le déclenchement et la réactivation des glissements de terrain. Cependant, les calculs préliminaires de la régression logistique utilisés dans cette étude comme outil d'analyse statistique multivariée ont donné des résultats satisfaisants. Bien que l'optimisation des paramètres pris en compte et des données supplémentaires (par exemple l'épaisseur du sol) permettraient d'augmenter les performances du modèle, une précision de ~ 78-79% a été estimée. Comme suggéré précédemment, une autre possibilité aurait été de tester une régression logistique basée sur une grille de pixels et d'analyser la pertinence des résultats obtenus.

Selon les conditions environnementales et les propriétés des glissements de terrain, la fonction de probabilité temporelle tenant compte d'un seuil de superficie est difficile à évaluer statistiquement. L'effet de la taille des unités de pente est un facteur important à considérer ainsi que le très petit nombre de nouveaux glissements de terrain au cours des cinquante dernières années. Dans cette recherche, un seuil d'aire de 500 m^2 a été considéré. Une autre possibilité pour analyser l'aléa aurait été de considérer un seuil plus grand. Il peut, par exemple, être choisi en fonction de l'évolution de la taille la plus faible des trois glissements de terrain actifs décrits dans le tableau R1 (par exemple 5.000 m^2). La probabilité de dépassement pour un glissement de terrain de grandeur donnée doit être analysée en fonction du seuil de taille ; mais dans notre zone d'étude, vu que le nombre de glissements de terrain actifs est faible, la probabilité temporelle (des réactivations de glissements de terrain) sera toujours sous-estimée. Malheureusement, cette loi statistique ne nous permet pas d'étudier de grandes réactivations. En effet, des évolutions surfaciques supérieures à 20.000 m^2 (comme à Sauze et à Poche ; voir tableau R1) sont difficilement contenues dans la même unité cartographique d'analyse (unités de pente) que le glissement de terrain initial.

Tableau R1 : Evolution de la superficie des glissements de terrain de Sauze, Poche et Sanières pour les périodes entre 1956 et 1974 (A_2), entre 1974 et 1982 (A_3), entre 1982 et 1995 (A_4), entre 1995 et 2000 (A_5), entre 2000 et 2004 (A_6), et entre 2004 et 2009 (A_7).

Evolution de l'aire des glissements de terrain (m^2)	A_2	A_3	A_4	A_5	A_6	A_7
Sauze	85.346	14.477	20.156	0	1.379	4.177
Poche	9.320	6.103	22.233	0	0	0
Sanières	650	0	2.785	0	0	4.129

A ce stade, nous imaginons trois possibilités pour améliorer la fiabilité des résultats, les rendant plus cohérents par rapport aux conditions du terrain. La première option pourrait être d'agrandir la taille des unités cartographiques. L'effet sera d'augmenter le nombre de petits glissements de terrain actifs à l'intérieur de ces unités et par conséquent d'augmenter la probabilité de dépassement d'un seuil donné. Toutefois, une résolution spatiale plus grossière de l'unité de cartographie ne peut pas être justifiée pour la cartographie des risques selon l'approche de PPRN. Une autre option pour considérer l'intensité dans l'évaluation de l'aléa est d'estimer la probabilité de dépassement sur base de mètres carrés (correspondant aux glissements de terrain) par an. Cependant, ce paramètre de vitesse n'a jamais été utilisé dans l'analyse statistique de glissements de terrain lents et donc, nous ne pouvons pas prédire une bonne précision des résultats. Enfin, la combinaison de la probabilité d'occurrence de modèles physiquement basés (intégrant des volumes de débris et/ou la vitesse) est une option non négligeable. Cependant, ce type d'analyse est dépendant de l'échelle et nous avons prouvé dans cette analyse que l'obtention d'informations précises à l'échelle régionale est une tâche fastidieuse et chronophage.

• Conclusions et perspectives

Cette recherche a démontré l'intérêt de combiner des données et des techniques multi-sources pour l'analyse des glissements de terrain à différentes échelles spatiales et temporelles. Les données acquises au sol et grâce aux techniques de télédétection ont été employées pour détecter et surveiller différents types de glissements de terrain. Les analyses statistiques ont été utilisées pour caractériser les événements observés et estimer l'aléa glissement de terrain pour différentes périodes de temps. Selon leurs types et les conditions environnementales, les glissements de terrain peuvent être actifs durant de très courtes ou de très longues périodes. Cette recherche a étudié la pertinence d'une combinaison de méthodes pour créer des inventaires multi-dates de glissements de terrain à l'échelle du versant (1:5.000-1:2.000) et à l'échelle régionale (1:10.000-1:25.000). L'analyse couvre la période 1850-2010, mais la plupart des données géospatiales utilisées concernent la période 1950-2010. Le site principal de l'étude est la partie centrale de la vallée de l'Ubaye (dans le bassin de Barcelonnette), et comprend une étude de cas dans la vallée de la Tinée.

Compte tenu de la diversité des systèmes de télédétection et des techniques modernes de traitement de l'image ainsi que les différentes approches d'évaluation de l'aléa, un état de l'art de l'analyse des glissements de terrain est proposé au chapitre 1. Cette revue bibliographique définit les concepts clés utilisés pour la reconnaissance des glissements de terrain ainsi que la méthodologie d'évaluation de l'aléa.

Le chapitre 2 aborde les caractéristiques géographiques, géomorphologiques et géologiques de la zone d'étude. Les risques naturels observés dans la région sont présentés ; l'accent est mis sur certaines zones de localisation préférentielle de glissements de terrains actifs.

Les inventaires de glissements de terrain servent de base à l'évaluation de l'aléa et du risque. Dans le cadre de cette recherche, des techniques avancées de télédétection (par exemple InSAR) et les techniques traditionnelles de cartographie (comme l'interprétation d'image, les campagnes de terrain) ont été utilisées. Malgré certaines limitations, l'InSAR est une technologie de télédétection rentable et adaptable qui peut compléter les méthodes standards. La création d'un inventaire multi-dates des glissements de terrain à partir de l'analyse multi-sources et multi-échelles de données multi-temporelles est présentée au chapitre 3. La cinématique et la répartition spatio-temporelle des glissements de terrain ont été analysées à différentes échelles.

Dans la première section du chapitre 3, des images SAR en bande L (acquises entre 2007 et 2010) sont utilisées afin de mettre en évidence les champs de déplacement des grands glissements de terrain à l'échelle de la pente. Une chaîne de traitement classique D-InSAR a été utilisée pour la création des interférogrammes, le filtrage de phase et le déroulement de phase. Les valeurs de phase, enroulées ou déroulées nous ont permis de détecter des schémas de déplacement de glissements de terrain complexes et actifs (sur les sites de La Valette, de Poche et de La Clapière). La méthodologie d'analyse guidée par une connaissance géomorphologique *a priori a* proposé une interprétation des signatures InSAR selon différents modes de déformation. En effet, les valeurs de phase positive (déplacement s'éloignant du satellite) indiquent les zones d'ablation caractérisées par un déplacement vertical prédominant (subsidence) tandis que les valeurs de phase négatives (déplacement vers le satellite) identifient les zones d'accumulation avec un déplacement principalement le long de la pente et donc, avec une composante horizontale prédominante. Même à l'échelle du versant, le processus de déroulement de phase fut une tâche difficile pour mettre en évidence les déformations importantes ($c > 0,4$ cm.jour^{-1}) dans un environnement montagneux avec une couverture végétale dense et des conditions météorologiques changeantes. Cependant, les modifications observées dans les champs de vitesse ont pu être estimées et validées par des mesures effectuées au sol. Le développement d'une méthodologie d'analyse guidée par la géomorphologie pour interpréter la phase interférométrique déroulée a prouvé son efficacité, mais a également montré les limites en termes de vitesse maximale détectée (en fonction de la longueur d'onde du capteur utilisé). Lorsqu'un déroulage de phase cohérent n'a pas été possible, la phase non-déroulée nous a donné des informations intéressantes sur l'influence

des structures géologiques sur les modes de déformation.

La deuxième section du chapitre 3 détaille la méthodologie pour préparer un inventaire multi-dates à l'échelle régionale à partir de l'interprétation de divers sets de données. Plusieurs descripteurs de glissements de terrain ont été utilisés pour documenter la localisation des glissements de terrain et leur évolution dans le temps et de l'espace. L'analyse comparative de divers ensembles de données est obligatoire pour créer un inventaire multi-dates cartographique complet. En supposant que tous les glissements de terrain fossiles, latents et actifs ont été cartographiés, l'inventaire multi-dates est analysé statistiquement sur plusieurs sous-périodes et sous-régions de la zone d'étude. La comparaison du nombre de (ré)activations enregistrées dans l'inventaire multi-dates avec des événements ponctuels enregistrés sur le terrain par les gestionnaires locaux des risques naturels (RTM) et d'autres géoscientifiques (par dendrochronologie par exemple) montre quelques divergences dues aux échelles spatiales et temporelles d'analyse. Par exemple, les périodes d'activité des glissements de terrain n'ont pas été déterminées aux mêmes dates avec les différentes techniques. La détermination des facteurs déclenchants dépend des propriétés des glissements de terrain et des conditions météorologiques (précipitations courtes et intenses ou continues). Les fonctions de densité de fréquence-surface indiquent des distributions différentes selon l'emplacement, la géologie et le niveau d'activité des glissements de terrain. L'estimation de l'évolution temporelle des réactivations de glissements de terrain avec un modèle de probabilité de Poisson nous a permis de calculer les probabilités de dépassement d'avoir au moins un événement sur différentes périodes de retour.

Le chapitre 4 présente la prévision de susceptibilité aux glissements de terrain et l'aléa dans la vallée de l'Ubaye en utilisant plusieurs unités spatiales de calcul. Une méthodologie pour délimiter les régions d'intérêt dans les unités appropriées de terrain a été proposée et testée. La procédure de délinéation a pour but de diviser les demi-bassins en unités en fonction d'un seuil de taille (compris entre 50.000 et 80.000 m^2) et disposant de propriétés géomorphologiques identiques. Le but était de fournir de petites unités de pente et de terrain et de tester l'impact de plusieurs résolutions de modèles numériques de terrain sur les statistiques des unités de terrain définies. Les probabilités d'occurrences spatiale et temporelle des glissements de terrain sont ensuite calculées à l'aide de modèles statistiques. Un modèle de régression logistique a été utilisé pour évaluer le zonage de la susceptibilité (S) pour les zones source de glissements de terrain d'une part et les glissements de terrain entiers d'autre part. Les résultats obtenus avec des unités de terrain ne sont pas pertinents (nombreux faux négatifs) et montrent une forte influence de la variable d'altitude (qui peut être redondante avec certains géotypes). Le zonage de susceptibilité aux glissements de terrain donne une bonne prévision des zones instables et génère moins de faux négatifs avec les unités de pente en utilisant un seuil de surface de 2% afin d'éliminer les petites parties de glissements de terrain se situant dans les grandes unités d'analyse et en considérant le glissement entier comme variable dépendante au lieu de la zone source uniquement. Cependant, la régression logistique attribue des valeurs très élevées de probabilité à un très petit nombre d'unités de pente (2,1%), contrairement à ce qu'on aurait pu attendre. Une précision de ~ 78-79% a été estimée, mais une optimisation des paramètres d'entrée (suppression de la variable d'altitude) et l'ajout de données supplémentaires (telles que l'épaisseur du sol) devraient augmenter les performances du modèle. $P(N_L)$ a été calculée en comptant le nombre d'événements se produisant dans une unité cartographique pour la période d'analyse. Elle montre une distribution dissymétrique en raison du fait que de grandes parties de la vallée ne sont pas affectées par les glissements de terrain au cours de cette période. Sur la base de l'inventaire multi-dates nous donnant des informations sur l'évolution des glissements de terrain (dont l'augmentation de la taille), la nouvelle taille de chaque glissement de terrain actif a été délimitée dans chaque unité de terrain pour chaque période d'analyse. Afin d'estimer la probabilité d'avoir un glissement de terrain d'une ampleur donnée, un seuil de taille (A_L) de 500 m^2 est choisi. Ce seuil d'évolution de surface a été déterminé systématiquement à partir de la détection visuelle du seuil de l'évolution sur les orthophotos. Enfin, une analyse de l'aléa glissement de terrain est proposée pour chaque site d'étude particulier caractérisé par des glissements de terrain actifs (Pra-Bellon, Sauze, Poche et Sanières). Selon le zonage de susceptibilité, seul le glissement de terrain de Pra-Bellon est situé dans une haute classe de susceptibilité alors que les autres sont compris dans des unités de pente à aléa modéré ou faible, en partie à cause de l'effet de la petite taille des unités

de pente, conduisant à un nombre artificiellement faible d'événements inscrits au sein de ces unités.

Des perspectives d'amélioration sont proposées pour modifier la délinéation des unités de pente (générant des unités cartographiques de plus grande taille) ou l'utilisation d'une grille de pixels. Comme les performances d'analyse multivariée sont limitées, les modèles de susceptibilité physiquement basés pourraient être utilisés car ils sont plus appropriés pour expliquer la réponse du terrain aux facteurs déclenchants en fonction des conditions réelles à l'échelle du versant. Ils ont cependant besoin de nombreuses données pour caractériser les paramètres mécaniques et géotechniques du versant de l'environnement local et ne sont pas facilement applicables à l'échelle régionale. Une autre amélioration pourrait être l'évaluation de l'aléa en considérant l'intensité des glissements de terrain en termes d'évolution annuelle relative de la zone de glissement totale (probabilité de dépassement qu'une portion donnée de l'unité d'analyse soit affectée par des glissements de terrain) ou d'évolution annuelle de la longueur de glissement.

CONTENTS

LIST OF FIGURES

LIST OF TABLES

Introduction

Research context: quantitative landslide hazard assessment

Landslides are one of the most dangerous hydro-geological hazards causing damages to natural and human environments. They can involve flowing, sliding, toppling or falling phenomena and most of the exhibit a combination of two or more types of movement (Varnes, 1978; Crozier, 1986; Hutchinson, 1988; Cruden and Varnes, 1996; Dikau et al., 1996). Landslides are observed both at the Earth's continental surfaces and in submarine environments.

Between 2004 and 2010, 2,620 fatal landslides were recorded worldwide, causing a total of 32,322 fatalities (Petley, 2012). The majority of human losses occurred in Asia (Fig. Ia). Some examples of fatal landslides occurring in 2014 are presented in Figure Ib-e. In December 2014, a landslide has been triggered by heavy rainfall in Central Java (Indonesia), causing 32 deaths and 76 missing persons (Fig. Ib). In Europe, intense and/or long rainfall events are the major triggering factors (ex. in Switzerland, a landslide destroyed a house and killed two people in October 2014; Fig. Ic). Earthquakes may also trigger numerous (and large) landslides all over the world, such as after the Wenchuan earthquake (Mw = 7.9) in May 2008, that caused more than 20,000 fatalities (Yin et al., 2009). In August 2014, the Yunnan earthquake (Mw = 6.1) triggered valley-blocking landslides and associated "quake lakes" which killed 589 people and injured more than 2,300 others in this landslide-prone region of China (Fig. Id).

Due to the diversity and complexity of landslide phenomena, a single methodology to identify and map landslides is difficult, if not impossible. Landslide inventory maps are produced using conventional methods and new (innovative) techniques (Guzzetti et al., 2012). Conventional methods used to prepare landslide maps include (i) geomorphological field mapping (Brunsden, 1985), and (ii) visual interpretation of stereoscopic aerial photographs (Rib and Liang, 1978; Brunsden, 1993; Cruden and Varnes, 1996). The recent methods for preparing landslide inventory maps are: (i) the analysis of very-high resolution digital models (DEMs), (ii) the interpretation and analysis of satellite images and, (iii) the use of new tools and methods based on remote sensing imagery to facilitate rapid field mapping. These recent methods seem to be less subjective and especially useful to assist time-consuming and expensive traditional mapping or field surveys over large areas.

The creation of event inventories is the basis of quantitative analyses (Guzzetti et al., 2012) even if their elaboration has always a part of subjectivity (Wills and McCrink, 2002). The landslide location, type and intensity (expressed in velocity rates for instance) have to be integrated in the inventory since these descriptors are required to produce landslide susceptibility, hazard and risk maps. Over large territories, the detailed characterization of landslide events is expensive, time-consuming and depends on the available datasets. Creating inventories for large areas (> 100,000 landslide events after the 1998 Mitch storm or the 2008 Wenchuan earthquake) are impossible to be collected without remote sensing techniques.

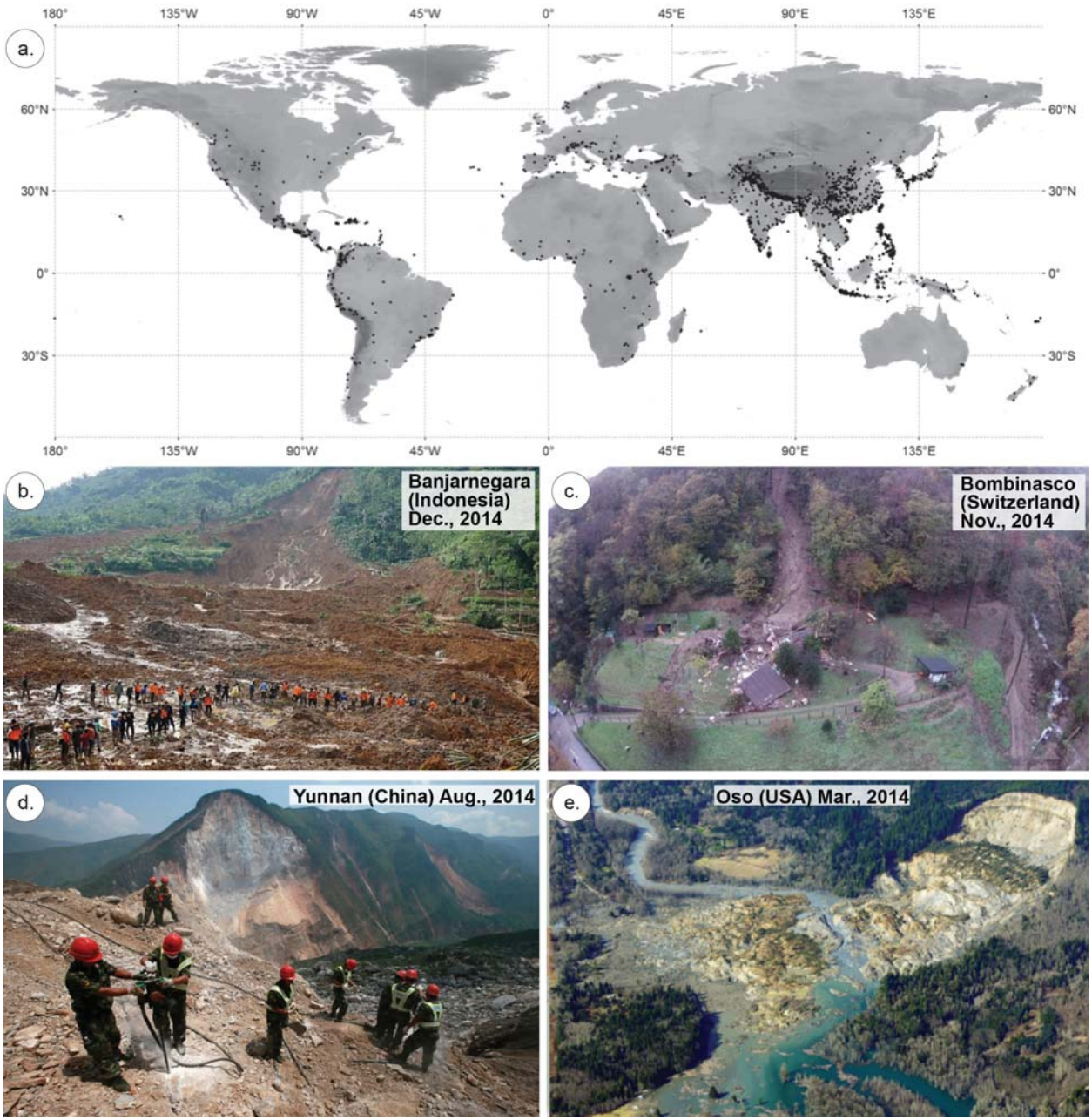

Figure I: Examples of fatal landslides. (a) Spatial distribution of fatal landslides over the period 2004-2010, each dot representing a single event (Petley, 2012). (b) Banjarnegara landslide in Java, Indonesia occurring in December 2014 (dead=32; missing=76). (c) Landslide in Bombinasco (Switzerland) killing 2 persons in November 2014. (d) Fatal landslides triggered after the 6.1 Yunnan earthquake in China occurring in August 2014. (e) Oso landslide triggered in the Washington state in March 2014 which destroyed 49 houses (dead=41; missing=2).

Remote sensing observations and Geographical Information System (GIS) are powerful tools to assess landslide hazard and are being used extensively in landslide researches during the last two decades (e.g. Mantovani et al., 1996; Metternicht et al., 2005; Canuti et al., 2004; Ferretti et al., 2011). Landslide inventory maps are prepared using various techniques and the selection of the appropriate technique depends on the purpose of the inventory, the size of the area covered and the time required to complete the inventory, the skills and experience of the investigators, and the available resources (van Westen et al., 2006; Stumpf, 2013; Mondini and Chang, 2014). Landslide detection and mapping strongly benefit from panchromatic, multispectral and synthetic aperture radar (SAR) images. In the field of optical imagery, high-resolution satellites (e.g. World-View, GeoEye, and Pléiades) offer a very powerful tool to create regional inventory maps with a low cost/benefit ratio (Casagli et al., 2005; Lu et al., 2011). Some

of the new methods are processed with object-oriented image classification methods (e.g. Martha et al., 2010; Lu et al., 2011; Stumpf et al., 2013) and change detection techniques (e.g. Mondini et al., 2011).

One of the most promising technique related to the measurement of ground movement is satellite radar interferometry (Tofani et al., 2013). Synthetic Aperture Radar (SAR) images proved useful to detect single large landslides that have changed considerably the topographic surface or the land cover (Singhroy et al., 1998; Czuchlewski et al., 2003; Lauknes et al., 2010), or to identify areas where multiple shallow landslides were triggered. Surface elevation data obtained from SAR sensors may also be exploited to study the displacement field(s) large event landslides. The joint analysis of SAR and optical (multi-spectral) information still represents an open field of research, with potential new applications for the detection and mapping of landslide events. SAR images combined with in-situ monitoring allow a better understanding of landslide geometry and kinematics (e.g. Pancioli et al., 2008; Peyret et al., 2008; Peduto et al., 2010; Strozzi et al., 2010). In this context, our work proposes to integrate active remote sensing images for the creation of landslide inventories.

A generic framework for Quantitative Risk Assessment (QRA) exists for landslides and includes from land use planning and zoning for urban development to "global or regional landslide risk management" (Fell et al., 2005). The most direct way of computing landslide risk is by quantifying each of the components of the hazard equation (Hungr et al., 2005; Corominas et al., 2008). The available methods for assessing the probability of landsliding have been reviewed by Mostyn and Fell (1997), Baynes and Lee (1998), Aleotti and Chowdhury (1999), Picarelli et al. (2005) and Corominas et al. (2008). Traditionally, two independent approaches have been used to assess the future occurrence of landsliding: the analysis of the potential for slope failure and the statistical treatment of the past landslide events. In order to zone the hazard level, the landslide frequency has to be determined at each land unit and for each potential landslide type (Corominas et al., 2008). The QRA based on magnitude-frequency has the advantage of not requiring the assessment of the stability conditions at the potential landslide source. If the frequency of the landslide triggering event is considered, the QRA requires prior assessment of the landslide susceptibility of the study area. Numerous research and operational works carried out by geoscientists all over the world demonstrated that different strategies and a combination of different methods and techniques have to be applied, depending on the type and number of landslides, the size and complexity of the study area, and the available data and resources. Despite a lot of developments in the last decades, methods of hazard and risk assessment are not completely standardized over the world (van Westen et al., 2006). Since 2008, the "*Joint Research Center - European Landslides expert group*" advice the use of quantitative approaches for susceptibility, hazard and risk mapping (*"Guidelines for landslide susceptibility, hazard and risk zoning for land use planning"*; Fell et al., 2008a, 2008b). However, the generation of quantitative risk zoning maps seems still a step too far even if its main use is in development planning and emergency response planning. For instance, authorities even change their priorities related to natural hazards after damaging event (hazard management in the Washington State - SR 530 Landslide Commission report - after the March 2014 Oso landslide; Fig. Ie). Constructing appropriate hazard maps is thus extremely challenging. The different approaches existing to evaluate landslide hazard (e.g. heuristic, semi-quantitative, quantitative) are detailed in the Chapter 1.

Research objectives

The objective of this work is to propose a quantitative assessment of landslide hazard (spatial and temporal probabilities of occurrence, intensity) from the analysis of a multi-date landslide inventory created with various data sources. The methodology associates the analysis of Earth Observation (EO) products and statistical modelling for the characterization of landslide hazard in a rural and mountainous region of the South French Alps (e.g. middle section of the Ubaye Valley: Barcelonnette Basin).

The detailed objectives are:

(i) to update existing landslide inventory maps and create a multi-date landslide database of the Barcelonnette Basin from the interpretation of time series of SAR images, aerial photographs, geomorphological maps, historical reports and field surveys;
(ii) to characterize the spatial and temporal occurrences (displacement pattern, geomorphological evolution) and the intensity of the observed events;
(iii) to identify relations among landslide predisposing factors and the landslide locations using statistical multivariate models;
(iv) to propose a quantitative assessment of hazards in a probabilistic framework for the creation of hazard maps.

The approach is multi-scalar as the methods have been developed at the slope (1:5,000-1:2,000) and regional (1:25,000-1:10,000) scales. The oldest archives available for this region are from 1850 whereas most of the geospatial data used in this research covers the period from 1950 to 2010.

Framework

The research was conducted at the University of Strasbourg at the *Institut de Physique du Globe de Strasbourg* (IPGS, UMR 7516 CNRS-UNISTRA), under the supervision of Dr. J.-P. Malet, Dr. C. Doubre and Prof. F. Masson. It has been carried out in the framework of the Marie Curie Research and Initial Training Network *"CHANGES: Changing Hydro-meteorological Risks as Analyzed by a New Generation of European Scientists"*, funded by the European Community's 7th Framework Programme FP7/2007-2013 under Grant Agreement No. 263953. The aim of this project was to understand how global change will affect the temporal and spatial patterns of hydro-meteorological hazards and associated risks in Europe. It also analysed how these changes could be assessed, modelled, and incorporated in sustainable risk management strategies, focusing on spatial planning, emergency preparedness and risk communication. This interdisciplinary and intersectorial project was an interesting opportunity to exchange and interact with young scientists of different nationalities during intensive workshops and international conferences. Several research stays have been carried out at CNR-IRPI (Perugia, Italy) under the supervision of Dr. P. Reichenbach. The joint work allowed us to delineate the landscape in different mapping units and propose susceptibility models (collaboration with Dr. M. Alvioli, and Dr. M. Rossi).

Landslide catalogue and *in-situ* measurements have been acquired by the RTM-04 (*Restauration des Terrains en Montagne*) service of the *Département des Alpes-de-Haute-Provence*. The GNSS data are provided by the French Landslide Observatory (*OMIV: Observatoire Multidisciplinaire des Instabilités de Versants*: http://omiv.unistra.fr). EDM measurements acquired in the Tinée valley were provided thanks to an agreement with the Cerema (*Centre d'études et d'expertise sur le risque, l'environnement, la mobilité et l'aménagement*). ALOS/PALSAR images are provided by the Japan Aerospace Exploration Agency (JAXA) and the European Space Agency (ESA) under the contract C1P.8859. Nine field campaigns were completed in the Ubaye valley over the period 2011-2013 for landslide recognition and mapping, validation of D-InSAR signals as well as GPS and LiDAR acquisitions with other PhD students and colleagues from the IPGS-EOST (University of Strasbourg). In 2012, a field visit on La Clapière landslide (Tinée valley) was realised, guided by Dr. T. Lebourg (Laboratory GéoAzur, University of Nice-Sophia Antipolis).

Outline of the thesis

The thesis is subdivided in four chapters (see Fig. II) addressing successively (1) the definition, criteria and techniques for the establishment of a landslide inventory and the quantitative assessment of landslide hazard, (2) the physio-geographical settings of the study area and the observed natural hazards, (3) the multi-technique procedure to create the multi-date landslide inventory and (4) the forecast of landslide susceptibility and hazard through statistical models.

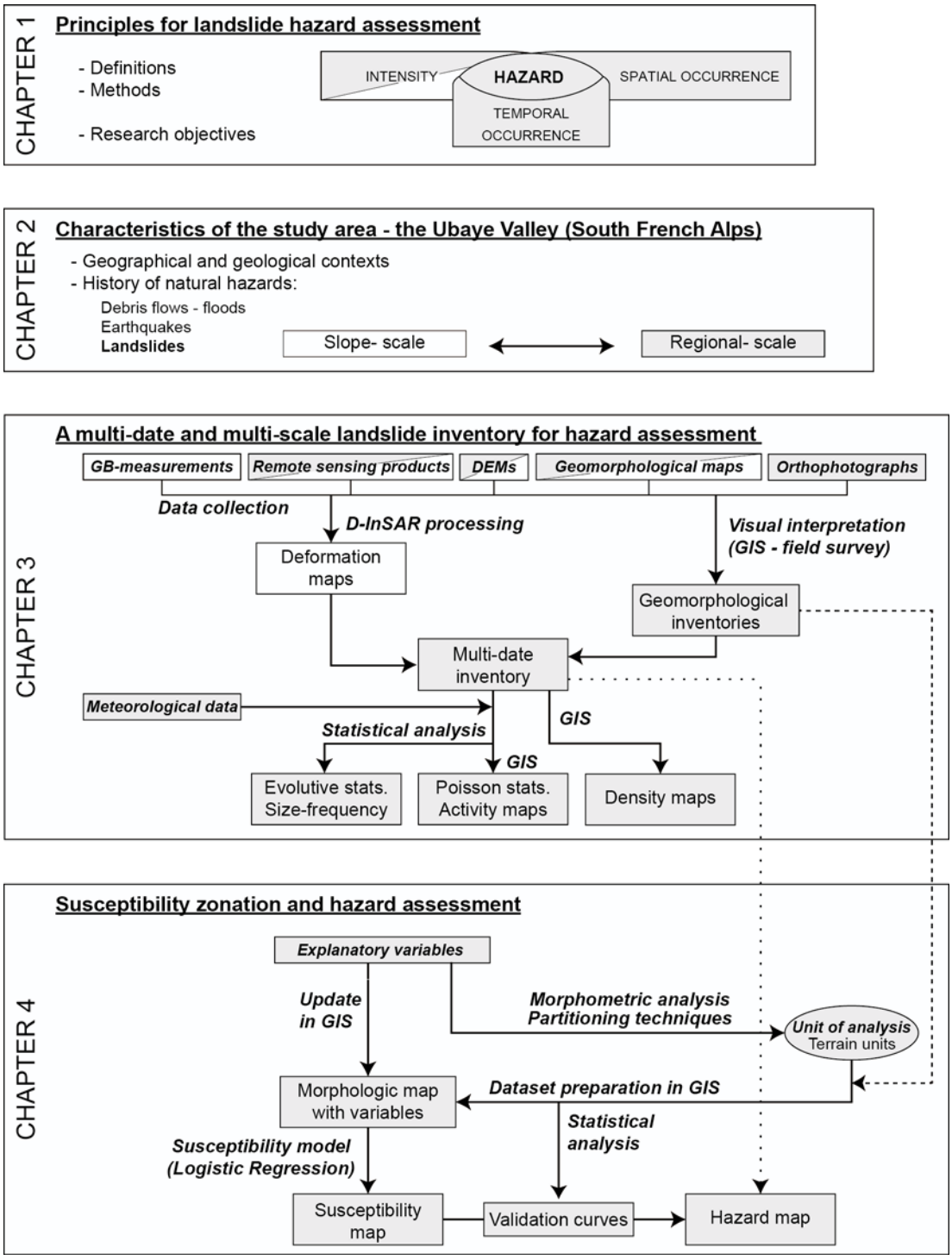

Figure II: Content of the manuscript with Chapter 1 dedicating to the principles commonly used for hazard assessment, Chapter 2 focusing on the study area; Chapter 3 detailing the procedure of inventory creation, including InSAR interpretation and Chapter 4 estimating the susceptibility and hazard using different terrain units.

The **Chapter 1** provides a review of the concepts used for the detection and recognition of landslides and the procedures for landslide hazard assessment in relation with international standards and the French policy regulation for natural risk mapping. The mapping units are presented as well as the techniques for susceptibility zonation and hazard assessment.

The **Chapter 2** details the geographical, geomorphological and geological characteristics of the study area. The natural hazards observed in the region are presented with focus on some active and monitored landslides (La Valette, Poche, Les Aiguettes, Pra-Bellon, Adroit and Sanières)

The **Chapter 3** analyses the kinematics and the spatio-temporal distribution of the landslides at different scales. First, the kinematic of large landslides is monitored by the interferometric analysis of L-band SAR images at the slope-scale. Second, a multi-date inventory is created at the scale of the region by the visual interpretation of geospatial data, the analysis of interferometric phase values and the analysis of historical reports. The chapter is organized along a published manuscript and two manuscripts currently under review. The first two manuscripts are detailing a geomorphologically-guided methodology developed to interpret the kinematics of large and active landslides by using L-band (ALOS/PALSAR) imagery. Radar interferometry combined with *in-situ* measurements allowed us to define the deformation field of unstable areas and to detect new sliding zones. Then, the methodology of multi-date inventory preparation is described. Probability density functions are calculated in order to estimate area-frequency relationships. The temporal occurrence of landslides is estimated with a Poisson probability model to compute exceedance probabilities for different return periods.

The **Chapter 4** forecasts the landslide susceptibility and hazard for the entire territory using several spatial units of calculation. A methodology to delineate the regions of interest into appropriate terrain units is proposed and tested. A logistic regression model is used to evaluate the spatial occurrence of landslides on the basis of several mapping units. Three statistical probabilities (spatial, temporal and temporal according to an intensity threshold) are examined to analyse the landslide hazard at regional scale (results of the spatial, temporal landslide occurrence obtained for the Ubaye valley). The results are discussed and compared on some local hotspots. Perspectives of improvement are proposed.

CHAPTER 1: Principles of landslide hazard assessment

This chapter provides the key concepts required to analyse landslide hazard as well as a review of techniques to assess it qualitatively and quantitatively. First, the terms used to recognize, describe and classify landslides at a particular study scale (i.e. regional, local or slope scale) are explained. Second, the methods to map and inventory landslides in traditional or advanced ways are discussed. Third, the different units of analysis (i.e. terrain or grid-based) to analyse landslide susceptibility and hazard are described. Fourth, qualitative and quantitative methods for a relative landslide hazard assessment, i.e. to evaluate spatial occurrence, are detailed. Fifth, methods to quantify landslide hazard assessment in terms of temporal occurrence and magnitude are discussed. The final section concludes on the limitations encountered to evaluate landslide hazard and the main goals and innovative aspects of this research.

1.1. Landslide recognition and description

1.1.1. Definition and study scales

A *landslide* is the movement of a mass of rock, debris, or earth down a slope, under the influence of gravity (Varnes, 1978; Cruden and Varnes, 1996). Mass movements are occurring over the world; their triggering factors are numerous and function of their type: intense or prolonged rainfall, earthquakes, rapid snow melting, and a variety of human activities. Landslides may involve a fall, a flow, a slide, a topple or a combination of two or more types of movements (Varnes, 1978; Crozier, 1986; Cruden and Varnes, 1996; Dikau et al., 1996). In this chapter, we explore issues of landslide inventory, landslide susceptibility, landslide hazard and briefly those of elements at risk, vulnerability and risk (see Fig. 1-1).

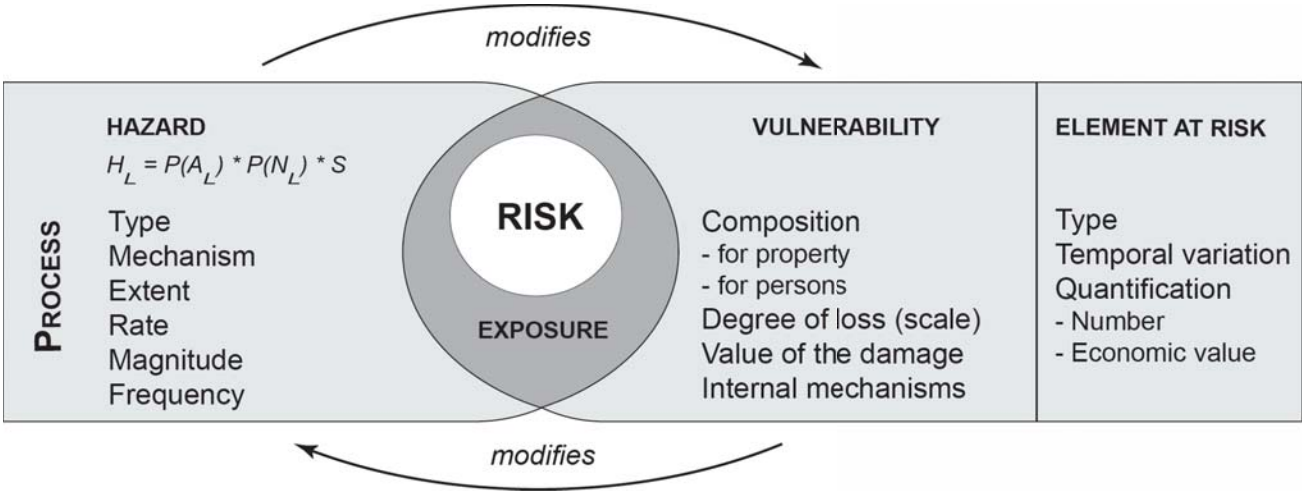

Figure 1-1: Concepts of hazard, exposure and vulnerability (with the element at risk) and risk.

A *landslide inventory* clusters information on the classification, location, size, activity and date of occurrence of individual landslides in an area (Hansen, 1984a; McCalpin, 1984; Wieczorek, 1984). The *landslide susceptibility* (*S*) is a quantitative or qualitative assessment of the classification, the extension (volume or area) and the spatial distribution of landslides which exist or potentially may occur in an area. Susceptibility may also include a description of the velocity and intensity of the existing or potential landsliding. The *landslide susceptibility zoning* involves the classification, the size and the spatial distribution of existing and potential landslides in the study area. It usually involves the

development of landslides inventory which have occurred in the past together with an assessment of the areas with a potential to experience landslides in the future, but without assessment of the frequency (annual probability) of occurrence. The *hazard* is the probability that a specific damaging event will happen and will cause an undesirable consequence (Cardona et al., 2003; Crozier and Glade, 2005; Fell et al., 2008a; Corominas et al., 2014). The description of landslide hazard includes the location, the extent, classification and velocity of the potential landslides and any resultant detached material as well as the probability of occurrence of a particular size of event $P(A_L)$ within a given period of time $P(N_L)$. The *landslide hazard zoning* takes the outcomes of landslide susceptibility mapping, and assigns an estimated frequency (annual probability) to the potential landslides (e.g. Gupta and Joshi, 1990).

The degree of loss to a given element or set of elements at risk within the area affected by the landslide hazard is defined as the *vulnerability* (Leone et al., 1996; Hearn and Griffiths, 2001; Glade, 2003; Glade and Crozier, 2005; Roberds, 2005; Li et al., 2010; Pascale et al., 2010). It is expressed on a scale of 0 (no loss) to 1 (total loss) and is a function of the intensity of the phenomenon (Canuti and Casagli, 1996). For property, the loss will be the value of the damage relative to the value of the property; for persons, it will be the probability that a particular life (the element at risk) will be lost, given the person(s) is (are) affected by the landslide. The *elements at risk* are the population, buildings and engineering works, economic activities, public services utilities, infrastructure and environmental features in the area potentially affected by the landslide hazard (Varnes and IAEG, 1984).

Finally, the *risk* is a measure of the probability and severity of loss to the *elements at risk*, usually expressed for a unit area, over a specified period of time (Dai et al., 2002; Fell et al., 2005; Leroi et al., 2005). The *landslide risk zoning* takes the outcomes of hazard mapping and assesses the potential damage to persons (annual probability the person most at risk loses his or her life) and to property (annual value of property loss) for the elements at risk, accounting for temporal and spatial probability and vulnerability (Finlay and Fell, 1997; Finlay et al., 1999; Chacón and Corominas, 2003; Cascini et al., 2005).

1.1.2. Classification criteria

1.1.2.1. Landslide types and geomorphological features

Any analysis of landslide hazard and risk has to apprehend the variety of landslide types and of the geologic, topographic, and climatic environments in which they occur. Geoscientists distinguish landslides that are triggered in rock formations from those occurring in coarse- or fine- textured unconsolidated soils or sediments (see Fig. 1-2). They further categorize landslides considering their failure mechanisms (falls, topples, slides, spreads and flows), water content and velocity (Varnes, 1978; Cruden and Varnes, 1996). According to Varnes (1978), movements that have a particular initial failure mechanism but one or more different styles of subsequent movement are called “complex landslides”. Failure types are recognized according to their specific morphologic features (e.g. main scarp, secondary scarps, crown, cracks, depletion zone, accumulation zone). The red lines in Fig. 1-2 show landslide types studied in the framework of this research.

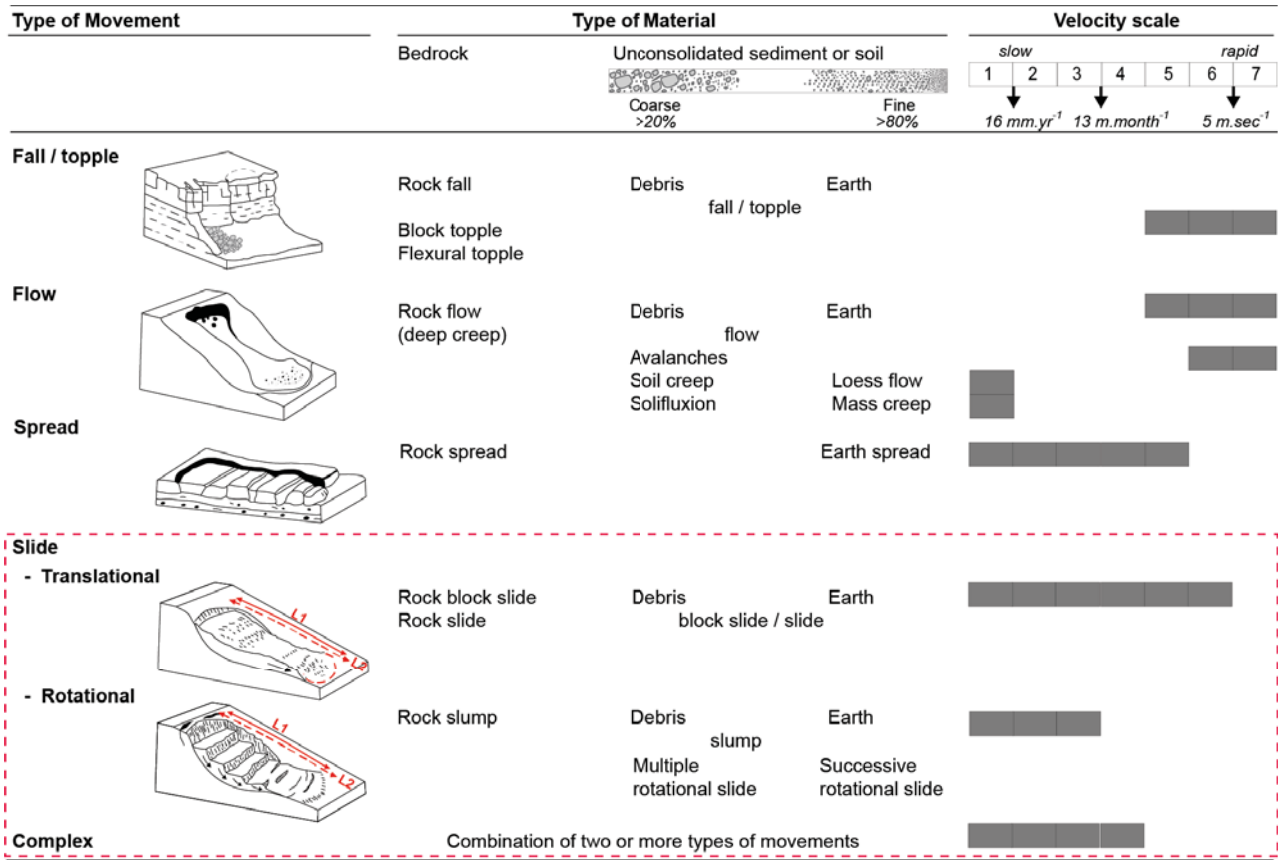

Figure 1-2: Landslide classification according to the type of movement, the type of material and the velocity scale (modified after Cruden and Varnes, 1996)

1.1.2.2. Velocity and size of landslides

The expectable displacement rates are closely linked to the landslide type and constitute a further criterion. Possible displacement rates vary by orders of magnitude ranging from a few millimetres per year to several meters per second (Cruden and Varnes, 1996). Therefore, landslide velocity scale can vary from very slow (e.g. soil creep) to very rapid (e.g. loess flow). According to the Cruden and Varnes (1996) classification, landslide velocity classes rank the risk on a scale from a low risk Class 1 (where mitigation works can reduce the risk from slow-moving slides), up to a Class 7 (where there is an expectation for the loss of life). This parameter has a strong influence on the applicable mapping technique and the choice of the observation frequency.

The landslide area spans the range from less than a few square metres (e.g. shallow soil slides) to hundreds and even thousands of square kilometres (e.g. large submarine failures). Defining a proxy to measure landslide magnitude is a challenge in hazard assessment. The frequency-size distribution can be calculated either on the basis of the area (e.g. Hovius et al., 1997; Pelletier et al., 1997; Guzzetti et al., 2002; Malamud et al., 2004) or the volume (e.g. Fujii, 1969; Hungr et al., 1999; Li et al., 2001; Guzzetti et al., 2003) of the failed materials. Landslide inventories usually give total landslide areas, with areas including both the failure and runout. It can be argued that just the landslide failure area or the landslide volume would be preferable (Malamud et al., 2004a). However, these quantities are often difficult to determine and their estimation is chiefly based on the type of failure, and the morphology and geometry of the detachment area and the deposition zone (Brunetti et al., 2009). Like for earthquakes, the frequency of the events and their magnitude present a power-law trend. Small landslides are represented at the high-frequency low-magnitude portion of the distribution and large landslides by the linear low-frequency tail.

1.1.3. Landslide abundance and evolution in time

Long-term evolution (i.e. over years or decades) of landslides can be measured considering spatial evolution and internal morphologic reshape of the slope. Lateral enlargement or retrogression over time shows their level of activity. According to the McCalpin (1984) classification, the age of the latest movement is identified in function of morphologic parameters of the landslides (see Fig. 1-3). However in mountainous context where vegetation is dense, landslides are not easily visible either in the field or by photograph analysis. Morphologic differences exist among landslide types, which can cause two slides of different type to appear similar, even if their ages are different. Landslides on surfaces of different aspect or slope are modified at different rates by different dominant slope processes. Geomorphic basis for landslide age classification considers the concept of deterministic, unidirectional landform change with time proposed by Davis (1899) in his "geographic circle" of youth, maturity and old age. A multi-temporal landslide inventory (or a multi-date landslide inventory) provides information on landslide evolution in time at medium or regional scales. A method to quantify the geographical (spatial) abundance of landslides is the preparation of landslide density maps. Indeed, landslide density (or frequency) maps measure the spatial distribution of slope failures (Campbell, 1973; DeGraff, 1985; DeGraff and Canuti, 1988). Depending on the type of mapping unit used to compute and portray the density, they can be based on statistical or geomorphological criteria (Guzzetti et al., 2000).

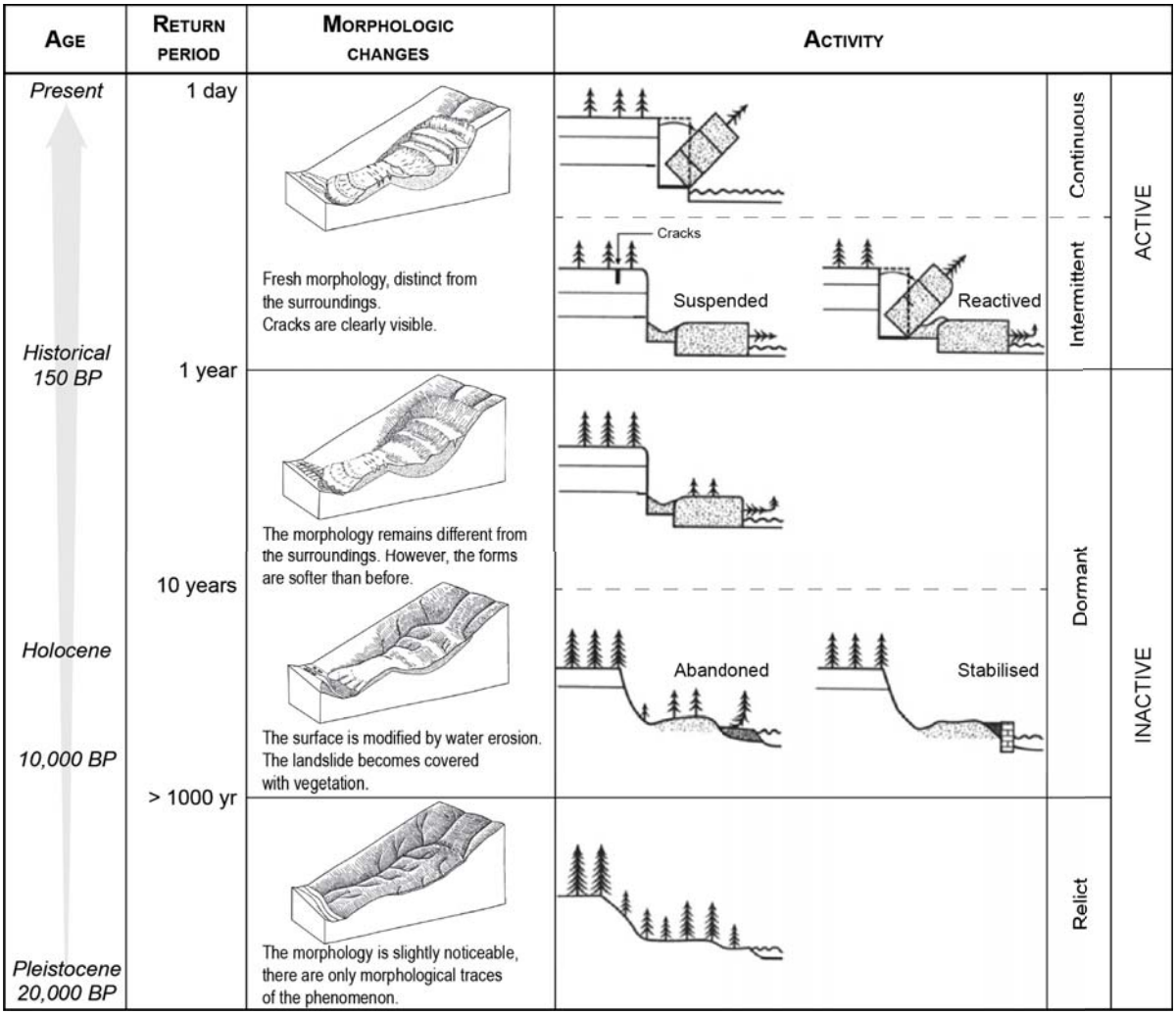

Figure 1-3: Classification of landslide activity levels in function of the geomorphological features (modified after McCalpin, 1984 and Thiery, 2007).

The short-term evolution (i.e. over days or months) of landslides mostly considers the analysis of parameters allowing us to assess their kinematics. Monitoring of landslide velocity is difficult without on site instruments, which is expensive and time-consuming. Other techniques (e.g. by remote sensing) described in the next section allow getting information about some landslide characteristics, like the type, the activity, the size, or the velocity rate, describing the sliding motion(s). In case of a complex landslide, sliding compartments can also move with different velocity rates in different directions, which is interesting to analyse and evaluate. Limitations according to slope angle, vegetation or particular climatic condition found in mountainous environment can be difficult to manage but some techniques, such as radar remote sensing, can allow us to deal with. Morpho-structural maps and kinematical analyses are often conducted at local or slope scales.

1.2. Creation of landslide inventories

As already mentioned, a *landslide inventory* records information on the classification, location, size, activity and date of occurrence of landslides visible in the landscape (Pašek, 1975; Hansen, 1984a, 1984b; McCalpin, 1984; Wieczorek, 1984; Guzzetti et al., 2000). Landslide maps can be prepared using different techniques (Guzzetti, 2006). The selection of a specific technique depends on the purpose of the inventory, the extent of the study area, the scale of the base maps, the resolution and characteristics of the imagery (e.g. aerial photographs, satellite images, LiDAR data), the skills and the experience of the geomorphologist, and the data source available to achieve the work (Guzzetti et al., 2000; van Westen et al., 2006). Two or more techniques can be combined to prepare an inventory map. Different types of possible inventories as well as techniques to map them will be detailed in this section.

1.2.1. Types of landslide inventory maps

1.1.2.1. Event inventory maps

Event inventory maps document the extent of populations of landslides caused by a single natural trigger, such as an earthquake (e.g. Wasowski et al., 2002; Parker et al., 2011), an intense rainfall event (Guzzetti et al., 2004; Cardinali et al., 2006; Mondini et al., 2013; see Fig. 1-4), or a rapid snowmelt event (e.g. Cardinali et al., 2000). Extension and magnitude of the landslide events are documented in those inventories, whereas they are key information of determining the dismantling of a mountain range and also reliable statistics of landslide size, chiefly landslide area (Guzzetti et al., 2002; Malamud et al., 2004b). These inventories can be represented as point type (e.g. Govi, 1977; Jibson and Keefer, 1989; Tibaldi et al., 1995; Keefer, 2000; Harp et al., 2011a, 2011b). In this case, a centroid point locates the landslide event (see example for the Barcelonnette area; Fig. 1-6a) and its characteristics are indicated in an attribute table.

1.1.2.2. Geomorphological inventory maps

A geomorphological inventory map details the sum of many landslide events over a period of some tens, hundreds or even many thousands of years (e.g. Galli et al., 2006; Fig. 1-5). It is typically prepared through the systematic interpretation of one or two sets of aerial photographs, at print scales ranging from 1:10,000 to 1:70,000, aided by field observations. Geomorphological inventory maps cover areas ranging from few tens to a few thousand square kilometres (see second map at Fig. 1-6a). Their preparation depends on the extent of the study area, the availability, scale and number of the aerial photographs, the complexity of the study area, and the time and resources available to complete the project. All different types of landslides are typically represented in a single map. Alternatively, a set of maps can be prepared, each map showing a different type of failure, i.e. deep-seated slides, shallow failures, debris flows, rock falls, etc. (Cardinali et al., 1990).

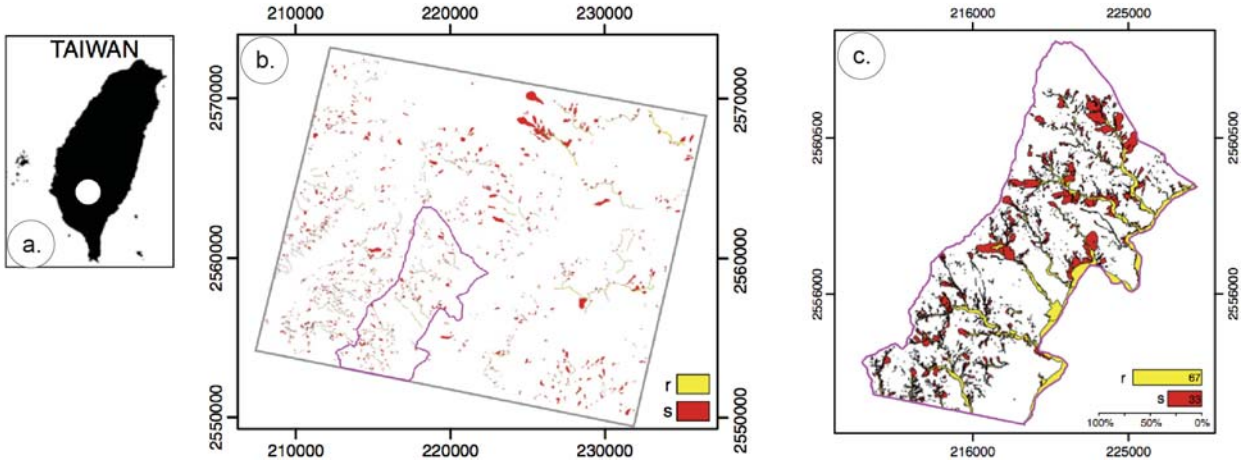

Figure 1-4: Example of event landslide inventory maps in Taiwan. (a) Location. (b) Pre-event landslide inventory map prepared through the visual interpretation of FORMOSAT-2 images showing landslides triggered by multiple rainfall events before March 16, 2009 in the study area and the surrounding region. (c) Post-event landslide inventory showing landslides identified visually on orthophotographs taken about 20 days after the Typhoon Morakot (Mondini et al., 2013).

1.1.2.3. Multi-temporal and multi-date inventory maps

A multi-temporal landslide map is the most advanced form of landslide inventory (Fausto Guzzetti et al., 2006). It includes the location and types of landslides in an area and shows their recent evolution in space and time. Preparing a multi-temporal inventory is a difficult and time consuming operation that involves the assimilation of multi-source data: (1) information obtained by systematically interpreting all the aerial photographs available for a study area, irrespective of age, scale and type of the photographs; (2) data from field surveys, conducted after landslide triggering events; (3) information on the occurrence of historical landslide events, obtained by looking at multiple archive and bibliographical sources; and sometimes, (4) information on ground movements obtained through *in situ* measurements and remote sensing technologies (detailed in the next section). Because of the difficulty and complexity in preparing a multi-temporal inventory, these maps are rare or of limited extent, ranging from few tens to few hundreds of square kilometres (e.g., Hovius et al., 1997; Cardinali et al., 2004; Guzzetti et al., 2005; Galli et al., 2008; Fiorucci et al., 2011).

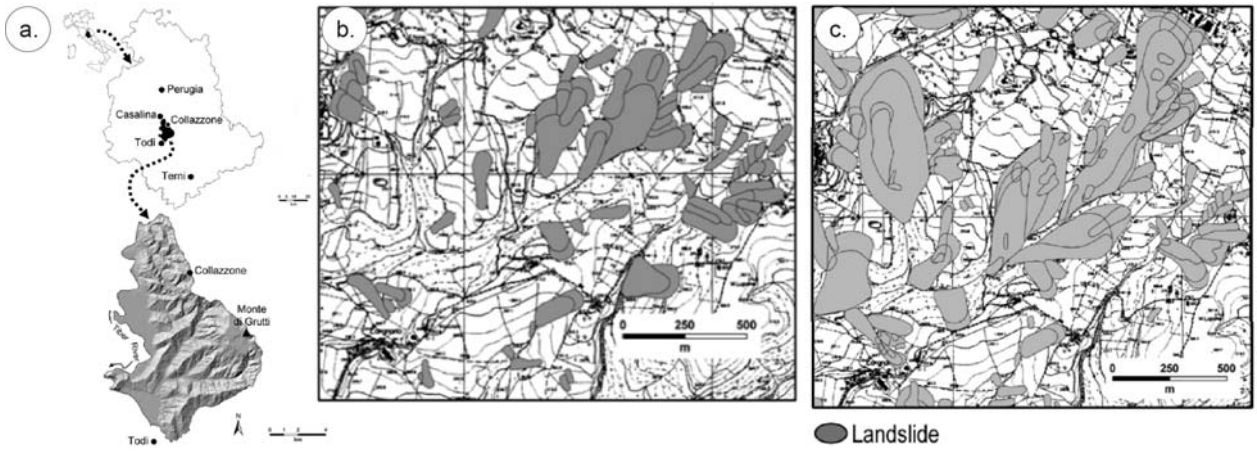

Figure 1-5: Inventory maps for the Umbria region, Italy. (a) Location. (b) Portion of the geomorphological inventory map (Galli et al., 2008). (c) Portion of the multi-temporal landslide inventory map prepared through the interpretation of 5 sets of aerial photographs (Galli et al., 2008).

Successful production of event-based and multi-temporal landslide inventories is often hampered by the lack of a timely coverage of aerial photographs. To overcome this limitation, investigators have

attempted to exploit satellite images to detect and map landslides (e.g., Huang and Chen, 1991; Mantovani et al., 1996; Lin et al., 2002; Hervás et al., 2003; Cheng et al., 2004; Nichol and Wong, 2005a, 2005b; Metternicht et al., 2005; Lee and Lee, 2006; Hong et al., 2007; Saba et al., 2010; Mondini et al., 2013).

An alternative, mixing event- and multi-temporal inventories, may be a multi-date inventory. In some areas of the world, there are a few major triggering events and landslides are more driven by the combination of forcing factors, which are often local and moderate. According to the climatic conditions of the area, the vegetation cover removed or disturbed after a landslide event can recover fast. In those conditions, the detection of landslide activation by conventional and remote sensing methods is difficult or even impossible. The multi-date inventory combines several geomorphological landslide inventories at several times (according to the available aerial images or orthophotographs). One inventory has been created at a particular time is considered as complete (combination of observations from several recognition fields, archive and multi-source data). The other inventories are created by comparison to this one: (1) new landslides are clearly visible; (2) lateral, downslope and/or upstream enlargement of old landslides are observed; (3) reactivation(s) inside landslide bodies is (are) distinguished. The base inventory can also be compared to past-data where landslides were smaller or not yet visible. This multi-date inventory can be divided according to their activity (see Fig. 1-3) in order to separate very-old, dormant and active landslides. For an accurate mapping, the geoscientist must be well trained to the visual analysis of the datasets and their changes over time according to his knowledge of the field. The final multi-date map can only represent typologically correct landslides which are completely new or old ones which have been reactivated between the considered periods of time (e.g. two available orthophotographs).

1.2.2. Conventional methods for the creation of landslide inventories

1.2.2.1. Visual analysis of aerial photographs

Brunsden (1993) wrote, "The landslide researcher's best friend is still the aerial photograph. Everyone is familiar with the (…) capabilities of this medium and there can be few studies carried out which do not use interpretation of air photos in some form". Mantovani et al. (1996) even concluded that aerial photographs are the most important remote sensing tools in landslide studies. For a trained geomorphologist, interpretation of the aerial photographs is an intuitive process that does not require sophisticated technological skills. The technology and tools needed to interpret aerial photographs are simple (e.g., a stereoscope; Fiorucci et al., 2011; Fig. 1-6b) and inexpensive, if compared to other monitoring or landslide detection methods (Guzzetti, 2004). More than two decades later, and despite significant technological innovation (see Section 1.2.3.), in many cases interpretation of the aerial photographs (or orthophotographs) remains the most common method to recognize precisely landslides, and to prepare paper maps or store them in computer systems. However, using conventional mapping methods, the production of seasonal and multi-temporal landslide maps is time consuming and resource intensive (Galli et al., 2008; see Fig. 1-5). In addition, the technique remains qualitative as it does not allows us to determine directly landslide velocities.

1.2.2.2. Field mapping

Mapping landslides in the field is part of standard geomorphological mapping (Brunsden, 1985). However, the detection of old landslides (see Fig. 1-3) is particularly difficult due to: (1) the size of the landslide, often too large to be seen completely in the field; (2) the viewpoint of the investigator, often inadequate to observe all parts of a landslide (e.g., the scarp, lateral edges, deposit, toe) with the same detail, and (3) the vegetation coverage or the dismantling by other landslides, erosion processes, and human actions, including agricultural and forest practices (Guzzetti et al., 2012).

Generally, field work is conducted to (1) identify and map landslides triggered by a specific event or in a period (e.g., Brabb et al., 1989; Baum et al., 1999; Cardinali et al., 2006; Santangelo et al., 2010);

(2) obtain general and specific information of the landslides (e.g. type, characteristics, orientations), to exploit for improved visual interpretation of the aerial photographs or satellite images (Guzzetti and Cardinali, 1990), and to (3) check (validate) inventory maps prepared using other techniques (Brunsden, 1985; Guzzetti et al., 2000; Cardinali et al., 2001).

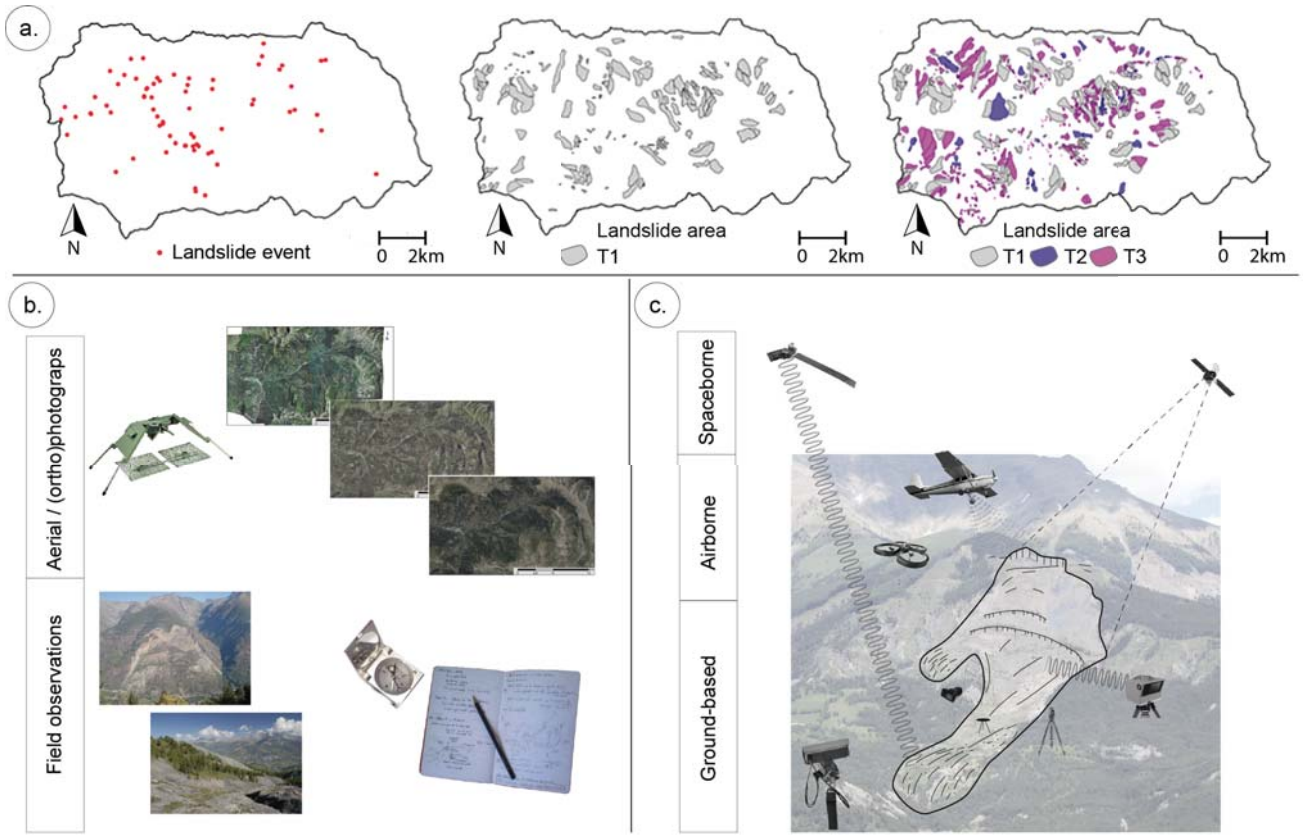

Figure 1-6: Landslide inventory maps created by conventional and advanced techniques. (a) Examples of landslide event, geomorphological and multi-date inventory maps; (b) Conventional methods used for the creation of landslide inventories (i.e. aerial photograph analysis and field observations); (c) Advanced spaceborne, airborne and ground-based technique for landslide mapping and monitoring (modified after Stumpf, 2013).

1.2.3. Advanced methods for the creation of landslide inventories and the quantification of landslide parameters

Over the past three decades, geophysical techniques and most notably remote sensing have become a key component of landslide investigation (Metternicht et al., 2005). According to the available platforms, remote sensing can be grouped in spaceborne, airborne and ground-based techniques (see Fig. 1-6c). Key developments comparing to the conventional methods are: (1) the advance in satellite image interpretation with the application of radar and laser technologies; and (2) the increased use of photogrammetry to allow remote collection of rock-slope property data (Petley, 2012). Throughout this period there has been a progressive improvement in the spatial resolution of the data available, cost, and geographic coverage. The different methods are stated in Table 1-2 and briefly explained below.

Electronic Distance Meter (*EDM*) equipment and the *theodolite* are classical tools for the monitoring of active landslides. They are currently used for displacement measurements at high temporal resolution and centimetre-level accuracy and often coupled to other techniques (Squarzoni et al., 2005; Fig. 1-7). EDMs can be operated automatically to measure displacement along the direction of the laser beam at distances up to 1,000 m with specifically designed prism targets (Malet et al., 2002). Since EDMs only allow to measure distances in the direction of the laser beam, they are typically combined with

tacheometer in integrated systems (i.e. *total stations*) and/or with defined prism targets (Castagnetti et al., 2013; Giordan et al., 2013).

Table 1-1: Information given by the several advanced ground-based, airborne and spaceborne methods and their associated references.

Method	Information	References
EDM/Total station	Distances, velocities	Malet et al., 2002; Squarzoni et al., 2005; Santangelo et al., 2010; Castagnetti et al., 2013; Giordan et al., 2013
TLS	Displacement fields, volumes, structures	Teza et al., 2007, 2008; Travelletti et al., 2008, 2010; Baldo et al., 2009; Oppikofer et al., 2009; Prokop and Panholzer, 2009
ALS	High resolution topography Landslide detection Regional risk analysis	Lineback Gritzner et al., 2001; McKean and Roering, 2004; Glenn et al., 2006; Razak et al., 2011; Van Den Eeckhaut et al., 2012; Giordan et al., 2013
Terrestrial SP	Features, changes	e.g. Kaufmann, 2012
Spaceborne DIC	Landslide detection and (semi-)automatic mapping, displacement fields	Singhroy and Molch, 2004; Leprince et al., 2008; Martha et al., 2010, 2012; Mondini et al., 2011, 2013; Stumpf and Kerle, 2011; Booth et al., 2013; Lacroix et al., 2013; Stumpf et al., 2013; Raucoules et al., 2013
Airborne DIC	Landslide detection, displacement fields	Casson et al., 2003; Delacourt et al., 2004, 2009; Debella-Gilo and Kääb, 2012
Airborne SP	Landslide features detection	Casson et al., 2005; Baldi et al., 2008; Dewitte et al., 2008; Strozzi et al., 2010; Fiorucci et al., 2011
Spaceborne SP	Features, changes, displacement fields	e.g. Stumpf et al., 2014
Terrestrial DIC	Features, structure, changes, displacement fields	e.g. Travelletti et al., 2012
Classical DInSAR	Deformation, 1-D displacement fields	Fruneau et al., 1996; Massonnet and Feigl, 1998; Squarzoni et al., 2005; Delacourt et al., 2009; García-Davalillo et al., 2013; Nikolaeva et al., 2014; Schlögel et al., 2015a
Advanced DInSAR	Deformation, 2-D displacement fields	*(PS)* Ferretti et al., 1999, 2011; Colesanti et al., 2003; Bovenga et al., 2012; Herrera et al., 2013; Ciampalini et al., 2014; *(SBAS)* Berardino et al., 2002; Tolomei et al., 2013; Calò et al., 2014; *(combined)* Hooper, 2008; Lauknes et al., 2010; Singleton et al., 2014; Wasowski and Bovenga, 2014
GB-InSAR	Deformation mapping, displacement fields	Tarchi et al., 2003; Strozzi et al., 2012; Pieraccini, 2013

Comparison of repeated *LiDAR* (Light Detection and Ranging) surveys should allow for the detection of active or recurrent slope failures over large areas (e.g. Glenn et al., 2006; Fig. 1-7). Laser scanning surveys may provide volumetric information important to erosion studies. Airborne laser scanning (*ALS*) can be an important data source for producing event and geomorphological landslide maps. It is also one of the few remote sensing techniques that allow us to investigate landslides under dense vegetation (Razak et al., 2011; van den Eeckhaut et al., 2012). However, the effort is hampered by the possibility of co-registering the different LiDAR surveys with sufficient topographic accuracy to measure the topographic changes caused by the movement of the landslides (e.g. of *TLS* in Baldo et al., 2009), and to resolve potential morphological ambiguities when the variations are small.

Stereo-photogrammetry (*SP*) relies on basic principles of image matching and stereo-vision. It targets the reconstruction of surfaces and displacement from multiple images acquired on the ground. Stereo- or multi-view camera setups (*terrestrial SP*) with multiple elevation data indicate a great potential of time-lapse stereo for landslide monitoring with a reported accuracy of ± 5 $cm.yr^{-1}$ (Kaufmann, 2012). Image correlation of monoscopic time-series (*terrestrial DIC*) has still relatively a few field applications to landslides. Most *DIC* techniques use a window-based search to match areas with a similar appearance among two images. Recently, Travelletti et al. (2012) demonstrated the possibility to monitor 2D surface displacement with a fixed installed camera including a detailed analysis of the sources of potential errors.

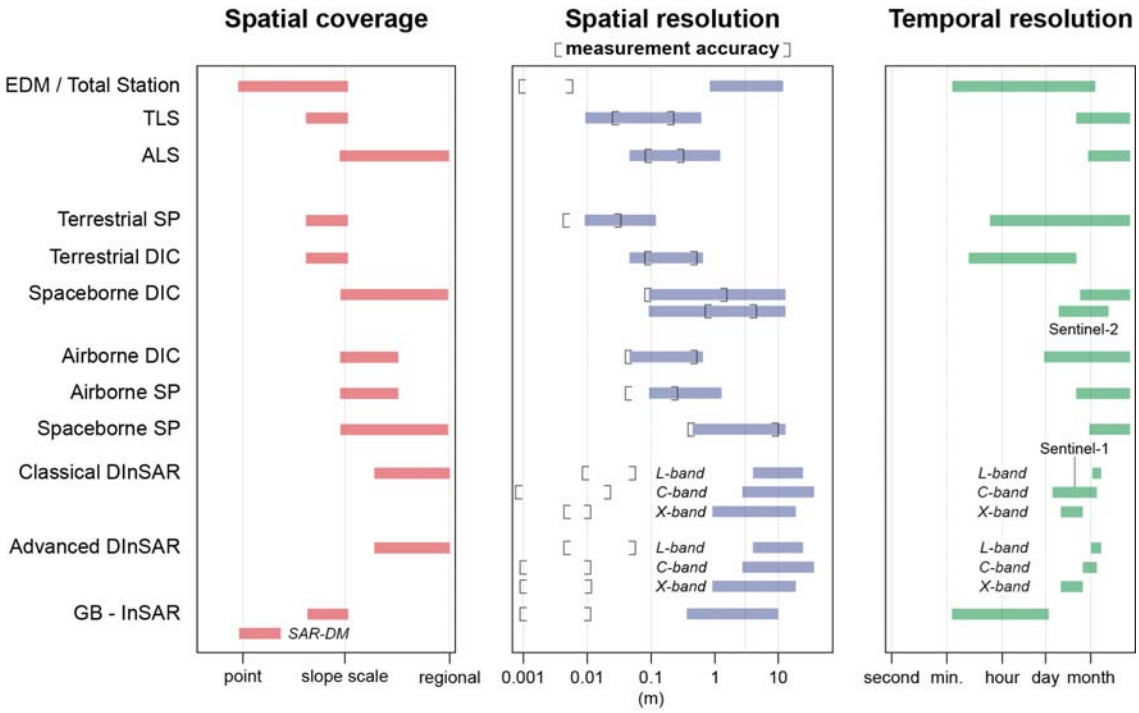

Figure 1-7: Capability of remote sensing techniques for landslide monitoring regarding (a) spatial coverage, (b) spatial resolution and measurement accuracy and (c) temporal resolution (modified after Stumpf, 2013).

High-resolution optical and SAR images from *airborne* and *spaceborne* platforms are commonly used for landslide inventory mapping (Guzzetti et al., 2012). 2D displacements are commonly derived using Digital Image Correlation (*DIC*) techniques from series of panchromatic satellite images or high resolution SAR amplitude images (*spaceborne DIC*) and from series of aerial images (*airborne DIC*). *Space-* and *airborne DIC* with optical images has been employed in numerous case studies using both VHR satellite images and aerial photographs (e.g. see Table 1-2) to measure 2D displacement with decimetre-level accuracy. They exploit mainly multi-spectral data, time-series of panchromatic images and in some cases also high-resolution SAR amplitude images (see examples at Table 1-2). Processing *DIC* requires precise co-registration and orthorectification which typically needs a number of well distributed tie points (image to image), ground-control points (GCPs, image to ground) with known 3D coordinates and an adequate Digital Elevation Model (DEM).

SAR sensors are active devices with the unique ability to extract information from an area during the night, and when clouds cover the area. In principle, this allows us to detect fresh landslides during or immediately after a triggering event. The limited ground resolution of the SAR sensors, the peculiar geometry of the acquisition, and the difficulty in processing the SAR data, hamper the possibility of using SAR data to detect and map small to medium size landsides in rugged terrain. However, SAR data proved to be useful to detect single large landslides that have changed considerably the topographic surface or the land cover (e.g., Singhroy et al., 1998; Lauknes et al., 2010), or to identify areas where multiple shallow landslides were mobilized by a triggering event in a catchment, providing valuable and timely information for post- event relief efforts, and erosion studies (Guzzetti et al., 2012). SAR Offset tracking can be applied on SAR images in L-, C-, and X-band but denser (spatially and temporally) and more accurate measurements can be obtained with VHR X-band satellites. TerraSAR-X and CosmoSkymed are also more flexible in acquisition programming and thus have better capability to acquire images for the same site from different orbits, and thus view angles (Raucoules et al., 2013). Surface elevation data obtained from SAR sensors (e.g. TerraSAR-X) may also be exploited monitoring complex displacement patterns of large landslides of up to 20 $m.yr^{-1}$ with a precision of 0.1 m (Raucoules et al., 2013). The joint analysis of SAR and optical (multi-spectral) information represents an open field of research, with potential new applications for the detection and mapping of event landslides.

Series of stereo-images are also exploited to reconstruct the topography of some landslides and monitor their kinematics. Airborne stereo-photogrammetry (*airborne SP*) has been applied in many studies to analyse archived aerial photographs typically for one particular landslide (e.g. Casson et al., 2005; Baldi et al., 2008; Dewitte et al., 2008). The parallax shift between multiple stereo-pairs allows reconstructing the surface and vertical changes; associated orthophotographs can be used to track horizontal displacements (Stumpf, 2013). Such techniques typically achieve decimetre-level accuracy and provide reliable information about horizontal displacement and vertical changes in the past. Nevertheless, they depend on the revisit time of the aerial surveys (typically several years). Spaceborne stereo-photogrammetry (*spaceborne SP*) follows similar principles than classical *airborne SP* but with lower geolocalisation accuracy and a 0.5-m spatial resolution. It has mainly been used for volume estimation after catastrophic failures and vertical errors (in the range 2–6 m) have been reported (e.g. Martha et al., 2010b).

Relevant information for landslide detection and monitoring can be extracted with Differential SAR interferometry (*DInSAR*). Classical SAR interferometry (*classical DInSAR*) exploits the phase difference between a pair of radar images with a temporal baseline depending on the repeat pass-cycle of the satellite. Precise explanation and limits of the technique and the *advanced DInSAR* methods will be explained in Chapter 3. Numerous case studies have shown that *classical* and *advanced spaceborne DInSAR* can be used to measure landslide deformation along the Line-Of-Sight (LOS) with accuracies in the range of centimetres to millimetres according to: the classical technique, the Permanent Scatterers approach (PS-InSAR), the Small Baseline approach (SBAS) and combinations of different advanced approaches or multi-sensors (e.g. see Table 1-2). Ascending and descending orbits of SAR satellites can be combined to retrieve full 3D displacements (Rocca, 2003). Many considerations regarding the site characteristics and displacement rates are rather fundamental and will also apply to future satellite missions. The upcoming Sentinel-1 data will provide publically available C-band images at a 12-day repeat-pass cycle and a large 250-km swath. They are eagerly awaited for their capabilities to measure faster displacement rates with higher precision and at lower costs (Rucci et al., 2012).

High-resolution airborne SAR has a great potential for displacement monitoring (*DIC* and *InSAR*), estimation of soil parameters, and the investigation of the 3D structure of vegetation and man-made objects. However, currently the processing chain is still rather complex and the costs for repeated surveys are very high (Reigber et al., 2012).

Ground-based (*GB*) *InSAR* systems are most currently operated in the Ku-band, while also systems with longer wavelength (X-band, C-band, S-band) are being tested. Operational commercial GB-SAR systems are available but the development is ongoing and proposed upgrades will significantly lower the systems costs and enhance the imaging frequency (Tarchi et al., 2003). In contrast to real-aperture radar, current SAR systems are faster and lighter (Pieraccini, 2013), whereas developing real-aperture prototypes (Strozzi et al., 2012) may give new performance perspectives in the near future.

1.2.4. Current limitations of ground-based measurements and satellite imagery for landslide mapping: quality and incompleteness of landslide inventory maps

In general, an event inventory map is more complete than a geomorphological inventory. Immediately following a landslide triggering event (i.e., a rainstorm, an earthquake or a snow melt event), the landslide morphology is generally well recognizable by conventional techniques allowing for the production of complete (or nearly complete) event inventories. In some cases, typical landslide features (e.g., the crown area, the lateral shear boundaries, or a bulging toe) may not be clearly identifiable, particularly where the landslide did not mobilize material after failure (Cardinali et al., 2000). Establishing the exact location of the landslide boundary is often impossible based solely on surface morphological information, especially for large and complex landslides. The problem may not be relevant when compiling small- to medium-scale event inventories, but becomes a problem in the preparation of large-scale event inventories (Guzzetti, 2006). In addition, old, dormant landslide bodies

reshaped by subsequent erosional processes, cannot easily be identified and correctly classified. The factor of uncertainty cannot be readily evaluated and explicitly incorporated in the subsequent phases of the analysis, as it depends on: (1) the skills of the investigator, (2) the quality and (3) the scale of the aerial-photographs and base maps used (Carrara et al., 1995). An error in mapping the boundary of a large landslide may affect significantly the measure of the size of the landslide, negatively affecting the frequency-area statistics that can be obtained from event inventory maps (see section 1.5.2).

Finally, the contribution of remote sensing, in the form of stereo aerial photograph and satellite image interpretations, largely improves the understanding of landslide characteristics (e.g., distribution and classification), factors (e.g., slope, lithology, geostructure, land use/land cover, rock anomalies) and displacement fields (e.g. 3D displacement). Nowadays, it becomes mandatory for mapping, monitoring, spatial analysis and hazard prediction, at local and regional scale (see Fig. 1-7).

1.3. Scale and spatial units of analysis

1.3.1. Working scale

Different working scales are used in the research on landslide hazard and risks. Indeed, five levels can be found in the literature: (1) the national scale; (2) the regional scale; (3) the medium scale; (4) the large scale and (5) the detailed or slope scale (van Westen, 1993; Soeters and van Westen, 1996). Table 1-2 summarizes the map scales of the landslide inventory, susceptibility, hazard, risk and an example of zoning application. For landslide risk assessment (Crozier and Glade, 2005), two embedded scales of analysis are required (Brand, 1988; Charlier and Decrop, 1997; Aleotti and Chowdhury, 1999):

(a) a detailed or large scale to focus on an unstable slope or site to have precise data and evaluate precise factor of safety or triggering factors (Maquaire, 2002; Malet, 2003);
(b) a medium or regional scale extended to a catchment to transpose the results obtained in (a).

Table 1-2: Scales for landslide zoning mapping and their applications (modified from van Westen, 1993; Soeters and van Westen, 1996; Maquaire, 2002).

Type	Extension	Typical scale	Example of zoning application
National	> 10,000 km2	1:1,000,000	National landslide inventory
Regional	> 1,000 km²	< 1:100,000	Landslide inventory and susceptibility to inform the general public and policy makers.
Medium	100-1,000 km²	1:50,000 – 1:25,000	Landslide inventory, density maps and susceptibility zoning for regional and local development. Preliminary hazard mapping (expert or statistical approaches).
Large	10-100 km²	1:25,000 – 1:5,000	Landslide inventory, susceptibility and hazard zoning for local areas (statistical or deterministic approaches). Preliminary risk zoning.
Detailed	< 10 km²	> 1:5,000	Advanced level hazard and risk zoning for specific areas (determinist approach).

Examples of transposition of results between scales are rare. Indeed, rock massifs are generally too complex in terms of hydrological or geomechanical properties which may induce a non-sense simplification. In addition, different landslide types with particular triggers often characterize an area. Two types of approaches are recognized for the different working scales (Soeters and van Westen, 1996; van Westen, 2004):

(a) The deterministic approaches (physically-based model) consider direct measurements of (geotechnical, hydrological, etc.) parameters of the slope. These models are essentially deserved to large or local scales (Chowdhury, 1976; Malet, 2003);
(b) The statistical approaches are based on spatial correlations between the mapped phenomena and the predisposing factors. These models are dedicated to medium or large scale of analysis (Carrara et al., 1995; van Westen et al., 2006).

These different approaches for landslide hazard assessment are described in sections 1.5 and 1.6 with a few focuses on detailed scale. In France, the regulatory landslide hazard zoning maps are those found in the "Plan de Prévention des Risques de mouvements de terrain" (PPRmt) methodology. In the regulated frame of the PPRmt, the hazard analysis and zoning is at 1:10,000 according to a qualitative expert investigation (Leroi, 1996; MATE/METL, 1999; Malet et al., 2006). The map divides the municipality into areas exposed to high risk, moderate risk or without predictable risk and is annexed to the "Plan local d'Urbanisme" (PLU). In Europe, first geomorphological analyses considering the landslide hazard were proposed in the years 70-80s in Kienholz (1977, 1978), Amadesi and Vianello (1978), Malgot and Mahr (1979), Ives and Messerli (1981), Rupke et al. (1988) or through ZERMOS maps at 1:25,000 (Antoine, 1977).

1.3.2. Representation of the terrain within the spatial unit

The selection of an appropriate unit of analysis is mandatory for landslide hazard assessment. It clearly depends on the study site (geomorphology, extension) and the available base maps (resolution, precision). The "terrain-unit" (or mapping unit or homogeneous domain) refers to a portion of the land surface which contains a set of ground conditions that differ from the adjacent units across definable boundaries (Hansen, 1984a; van Westen et al., 1993, 1997; Carrara et al., 1995; Luckman et al., 1999). At the scale of the analysis, the spatial unit represents a domain that maximises internal homogeneity and between-units heterogeneity (Guzzetti et al., 1999; Guzzetti, 2006). Various methods have been proposed to partition terrain for landslide susceptibility assessment and mapping (Meijerink, 1988; Carrara et al., 1995; Soeters and van Westen, 1996; Guzzetti et al., 1999; Guzzetti, 2006). According to the literature, all methods fall into one of the following seven groups: (1) grid-cells, (2) terrain units, (3) unique condition units, (4) slope units, (5) geo-hydrological units, (6) topographic units, and (7) political or administrative units. The first approaches will be detailed in the next section while the second considers the other methods (i.e. from 3 to 7). This selection of a mapping unit is important as it affects the way uncertainties in the input data are dealt with, the model fit, and the reliability of the obtained susceptibility zonation (Guzzetti et al., 1999). The main advantages and drawbacks of the different types of mapping units are known (e.g. van Westen et al., 1993; Carrara et al., 1995; Guzzetti et al., 1999; Van Den Eeckhaut et al., 2005; Guzzetti, 2006; see on Table 1-4) but only a few investigators have critically examined the influence of different terrain subdivisions on susceptibility zonation (Carrara et al., 1995; Carrara and Pike, 2008; van den Eeckhaut et al., 2009).

Table 1-3: Comparison of advantages and disadvantages of the main terrain-units for landslide hazard mapping (adapted from Carrara et al., 1995).

Unit of analysis	Consistency	Physical meaning	Technique	Rapidity of acquisition
Grid-cell	High	Low to medium	Automatic	High
Terrain unit				
- Unique condition unit	High	Medium	Automatic	High
- Slope-unit	High	Medium to high	Automatic	Low
- Geomorphologic unit	Low	High	Manual-Autom.	Low

1.3.2.1. Grid-cell approach

Many raster-based GIS users (e.g. Bernknopf et al., 1988; Mark and Ellen, 1995) implied the division of the region of interest into grid-cells of given size as terrain-unit of reference. In the susceptibility assessment processing, each cell has an assigned value from each considered predisposing factors. The main advantage of the technique is the fast and algorithmically simple computer processing and manipulation. In the 90', this technique was criticized because of its low accuracy due to the large cell-size required due to limited computing power. Nowadays, the trend of this technique is to use small grid-cells (e.g. same resolution than the available elevation data) to avoid special inaccuracy after processing a complex statistical technique over large areas. Numerous landslide hazard studies prefer

this technique instead of large grid-cell size (e.g. Carrara, 1983), which may result in a hazard map that is overly generalized (e.g. Nefeslioglu et al., 2008; Das et al., 2010; Pradhan, 2010; Motamedi and Liang, 2013). Large grid-cell sizes are used when the study area is a mountain range (Havenith et al., subm.), a country (Koukis et al., 2005; Malet et al., 2009, 2013) or a continent (Günther et al., 2007, 2013; Reichenbach et al., 2007).

1.3.2.2. Terrain units approach

The first technique is based on a partitioning of the study site into polygons of homogeneous slopes (i.e. slope-units; see Fig. 1-8a1). They can be catchments or sub-basins where only the topography is taking into account for the partitioning. Identification from a DTM is either manual or automatic (Carrara et al., 1988, 1995). Then, the information given by the predisposing factors are combined into the corresponding slope-unit (Fig. 1-8a2). Another technique exploits the basic function of a GIS to obtain a combination of factors stored in a single map or layer. Each combination, called Unique Condition Unit (UCU; Chung et al., 1995), is coded and represents the whole of the factors for a unique cell. In each cell, more there are factors, more there are units. The partitioning technique can also be based on main geomorphological units observed by an expert (Meijerink, 1988). Indeed, in natural environments, the interrelations between materials, forms and processes result in morphological boundaries which frequently reflect geomorphological and geological differences. Comparing to the others, this approach is purely expert-based and thus, not applicable generally (Carrara et al., 1995; see Table 1-2). However, the partitioning is possible in a GIS by combining the classified factors as polygons (van Westen et al., 2000, 2003; Clerici et al., 2002). Then, it requires a unique coding in order to obtain less 'unique' polygons with the same characteristics. This latter technique is rarely used in landslide susceptibility assessment.

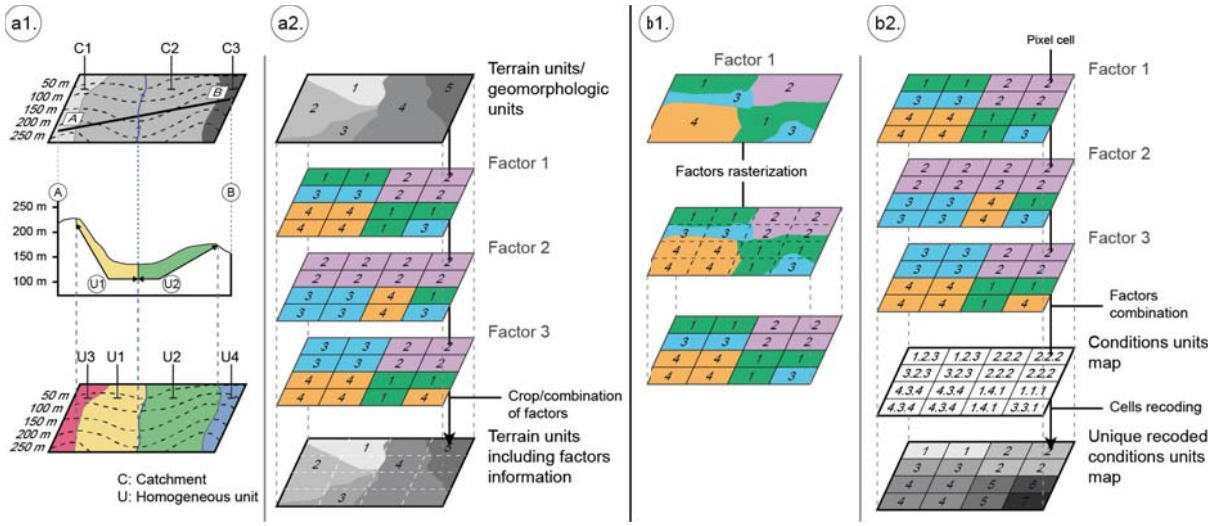

Figure 1-8: Terrain unit approaches. (a1) Homogeneous units based on the slope-unit principle proposed by Carrara (1988) and (a2) combination of predisposing factor for landslide susceptibility assessment into the TUs. (b1) Homogeneous units based on the rasterisation into grid-cells (pixels) and (b2) homogeneous units based on combination of factors (cell-format) resulting into Unique condition units as proposed by Chung et al. (1995).

1.4. Landslide conditioning factors

In the field of landslide analysis and hazard zoning, the expert defines the phenomenon and the roles played by the predisposing and the triggering factors. Indeed, landslides are controlled by mechanical laws that can be determined empirically, statistically or in deterministic fashion. Conditions that cause landslides (instability factors), are directly or indirectly linked to slope failures, can be collected and used to build predictive models of landslide occurrence (Crozier, 1986; Dietrich et al., 1995). Landslide

susceptibility using statistical methods allows us to correlate landslides location and some predicting variables (i.e. predisposing factors) to obtain susceptibility maps (e.g. van Westen, 1993; Carrara et al., 1995; Chung et al., 1995; Soeters and van Westen, 1996; van Westen et al., 2006; Rossi et al., 2010). Whereas triggering factors consist of variables that directly cause the slope failure. Therefore, they are mandatory in landslide hazard assessment as temporal probability is approached through long-term records of landslide-triggering factors (see Fig. 1-9). Different predisposing and triggering factors and their importance in landslide hazard is shown in Fig. 1-10.

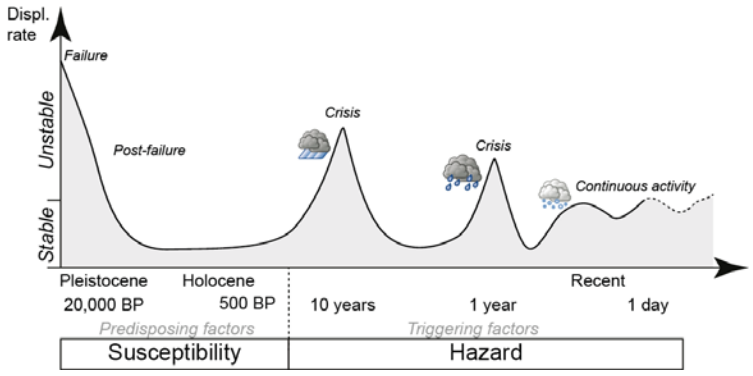

Figure 1-9: Potential phases of landslide activity according to the analysis of predisposing or triggering factors, for a susceptibility or hazard assessment, respectively (modified from Vaunat and Leroueil, 2002).

1.4.1. Predisposing factors

Hydrological and morphological parameters are generally obtained from DTM. Hydrological variables include the length, gradient, order and magnitude of drainage channel (for a review of these different factors see Sidle and Ochiai, 2006). Morphological variables include mean elevation, standard deviation of elevation, mean length, mean terrain gradient, standard deviation of terrain gradient, aspect, and terrain roughness. These independent variables can either be used independently and be kept in a pixel-cell based way or they may be included in a terrain-unit according to the chosen partitioning method. In the latter case, maximum, mean, standard deviation of parameters can be calculated for each terrain unit and derivative variables describing the shape of the slope unit profile (concave, convex, irregular, etc.) can also obtained (Rossi et al., 2010).

Lithological, structural and bedding information are obtained from a geological map (e.g. 1:10,000) but can also be completed by field measurements (e.g. fault orientations). The lithological information is usually divided lithological units of same properties. Bedding domains can also be considered in terms of the geometrical interaction between bedding attitude and the local slope (Cruden, 2003).

The vegetation cover is another major parameter that influences slope stability (e.g. Fuchu et al., 1999; Reid and Page, 2003). Indeed, it contributes to a better rainfall infiltration and reduces the grain-by-grain erosion of the soil; and plants roots increase the cohesion of the soil. However, in some cases, the presence of large trees on steep slopes can also increase the probability of landslides.

1.4.2. Triggering factors

Catastrophic landslides are mainly triggered by large earthquakes (for a review see Keefer, 2002) or heavy rain (see De Vita et al., 1998). Those are the only two triggering factors which can produce large clusters of individual landslides (Crozier, 1996). Earthquake triggering of landslides is very common but not quantitatively understood. Keefer (1984, 2002) observed from a worldwide catalogue of landslides and earthquakes that the minimum magnitude for an earthquake to trigger a landslide was M=4, and that the area where landslides occur increases with magnitude. Malamud et al. (2004a) found from a worldwide inventory that the minimum magnitude to trigger a landslide was M=4.3±0.4.

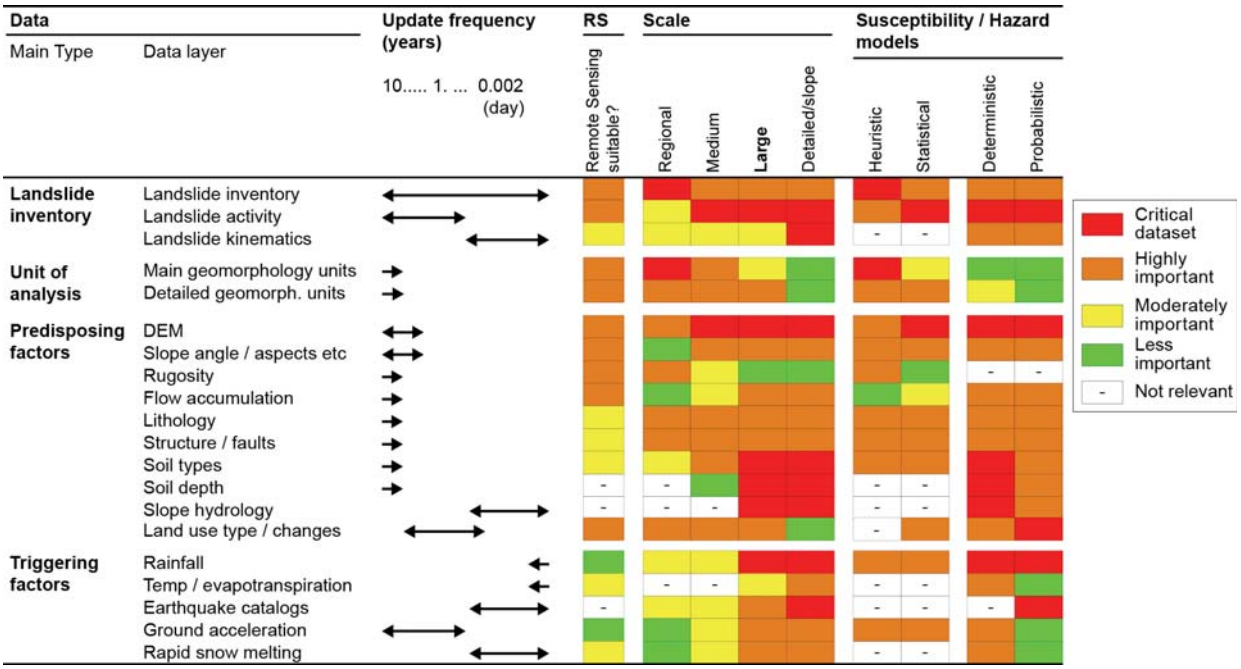

Figure 1-10: Schematic representation of basic data sets for landslide susceptibility, hazard and risk assessment with an indication of the ideal update frequency, an indicator of the usefulness of remote sensing for the data acquisition, an indication of the importance of the data layer at small, medium, large and detailed scales, related with the feasibility of obtaining the data at that particular scale and for hazard models, an indication of the importance of the data set for heuristic models, statistical models, deterministic models and probabilistic models (modified from van Westen et al., 2008).

Ground water level and pore pressure changes result from the infiltration from surface (rainfall, snowmelt, leaking pipe...), or exfiltration from bedrock, preferential flow and convergent flow leading to water accumulation (Tatard et al., 2010). This in turn leads to increased pore water pressure which reduces the soil strength and increases stress (Ray and Jacobs, 2007).

Other processes known to influence slope stability are freeze-thaw cycles (Matsuoka and Sakai, 1999; Frayssines and Hantz, 2006), snow-melt episodes (Sandersen et al., 1996; Frayssines and Hantz, 2006; Gruner, 2008), glacial and fluvial downcutting (Wieczorek, 2002), deglaciation (Wieczorek, 2002; Holm et al., 2004), neotectonic stresses (Ai and Miao, 1987; Julian and Anthony, 1996) and anthropic works (Smyth and Royle, 2000; Stark et al., 2005). In the latter case, an increase in slope angle (e.g. road cutting steepening hillslopes or other urbanization works) or an excavation of a cutslope toe indubitably contribute to the triggering of a landslide.

1.5. Methods for a relative estimation of landslide hazard (spatial occurrence)

The spatial probability of landslides can be estimated using a variety of statistical techniques. They are usually based on two assumptions: (1) that areas which have experienced landslides in the past are likely to experience them in the future and (2) that areas with a similar set of geo-environmental conditions as those of the failed areas are also likely to fail in the future (Guzzetti et al., 1999; Fell et al., 2008a). Therefore, quantitative estimates of the spatial location of future landslide sources depend on the detailed information on the distribution of past landslides and a set of thematic variables such as slope angle, aspect, lithology, etc. that has initiated these landslides. The second assumption facilitates in predicting the geographical location of future landslides in passive areas (i.e., areas presently devoid of landslides) provided the geo-environmental conditions remain the same. The above assumptions have been successfully used for statistically quantifying landslide susceptibility (LS) at a basin scale (Jaiswal et al., 2010).

1.5.1. Qualitative or knowledge-driven approaches

The qualitative analysis is a direct (or semi-direct) method in which the geomorphological map is renumbered to a hazard map or in which several maps are combined into one using subjective decision rules based on the experience of the earth scientist (Mantovani et al., 1996). Heuristic methods for spatial prediction of landslide occurrence can either be direct or indirect (see Fig. 1-11).

1.5.1.1. Direct mapping

In the direct method, very detailed geomorphological mapping is carried out, using uniquely coded polygons which were evaluated one-by-one by an expert to assess the type and degree of hazard (Barredo et al., 2000). Thus, the degree of hazard is determined by the geomorphologist mapping with care, based on his experience and knowledge of the terrain conditions. If the resulting map is checked statistically with the input landslide occurrence map, it can be stated that the percentage of misclassification is 0, which means that all landslides actually occur within the high hazard zones (van Westen et al., 1999). The main disadvantage of direct mapping is that the quality of the resulting hazard map is completely depending on the experience, skill, and commitment of one individual or mapping team. Due to this subjectivity, the reasoning behind the outlined hazard classes is often not presented on the hazard map.

Methodology recognized by French authorities for landslide risk assessment is based on this principle. It is applied at 1:10,000 scale for the elaboration of the "Plan de Prévention des Risques" (PPR; MATE/MATL, 1999). The expert defines the type of phenomenon, the role of the predisposing factors (e.g. slope gradient, lithology, land use) and the triggers (e.g. earthquake, rainfall, anthropic actions). This approach is the result of an analogical argument between the phenomenon and the role played by each factors. Some weights are attributed to them in agreement to his knowledge of the field and sometimes, some experiments or researches in order to evaluate the recurrence of the phenomenon over the next 100 years.

1.5.1.2. Indirect mapping

In indirect heuristic methods, individual factors assign specified weight values or ratings that are based on subjective criteria. The main limits or problems of heuristic methods are related to the subjectivity involved while one main advantage is that they can allow site specific evaluations of the causal factors, and avoid the generalization that is often used in data-driven ones (van Westen et al., 2003).

In the Fuzzy Logic method of landslide hazard zonation, each landslide explanatory variable is represented by a value between 0 and 1 based on the degree of association of these parameters with landslide occurrence (Champatiray, 2000). Weighs are assigned to the causative factors. Landslide events are outcome of several explanatory variables at a time which call for application of multivariate methods for a more accurate mapping.

Multi-criteria evaluation enables the integration of different data layers with different levels of uncertainty for landslide hazard mapping and zonation. Over the last two decades, there have been a number of multi-criteria decision rules implemented in the GIS environment including the weighted linear combination or weighted summation/Boolean overlay methods (e.g. Carver, 1991), the analytic hierarchy process (e.g. Banai, 1993), ordered weighted average (Yager, 1988), the ideal/reference point methods (e.g. Eastman, 1997) and the outranking methods (e.g. Joerin et al., 2001). The attempts of landslide susceptibility mapping have used GIS-based multi-criteria approaches including mainly the Boolean overlay and the weighted linear combination methods (Malczewski, 1999). According to Feizizadeh and Blaschke (2012), analytic hierarchy process performed good results in landslide susceptibility mapping.

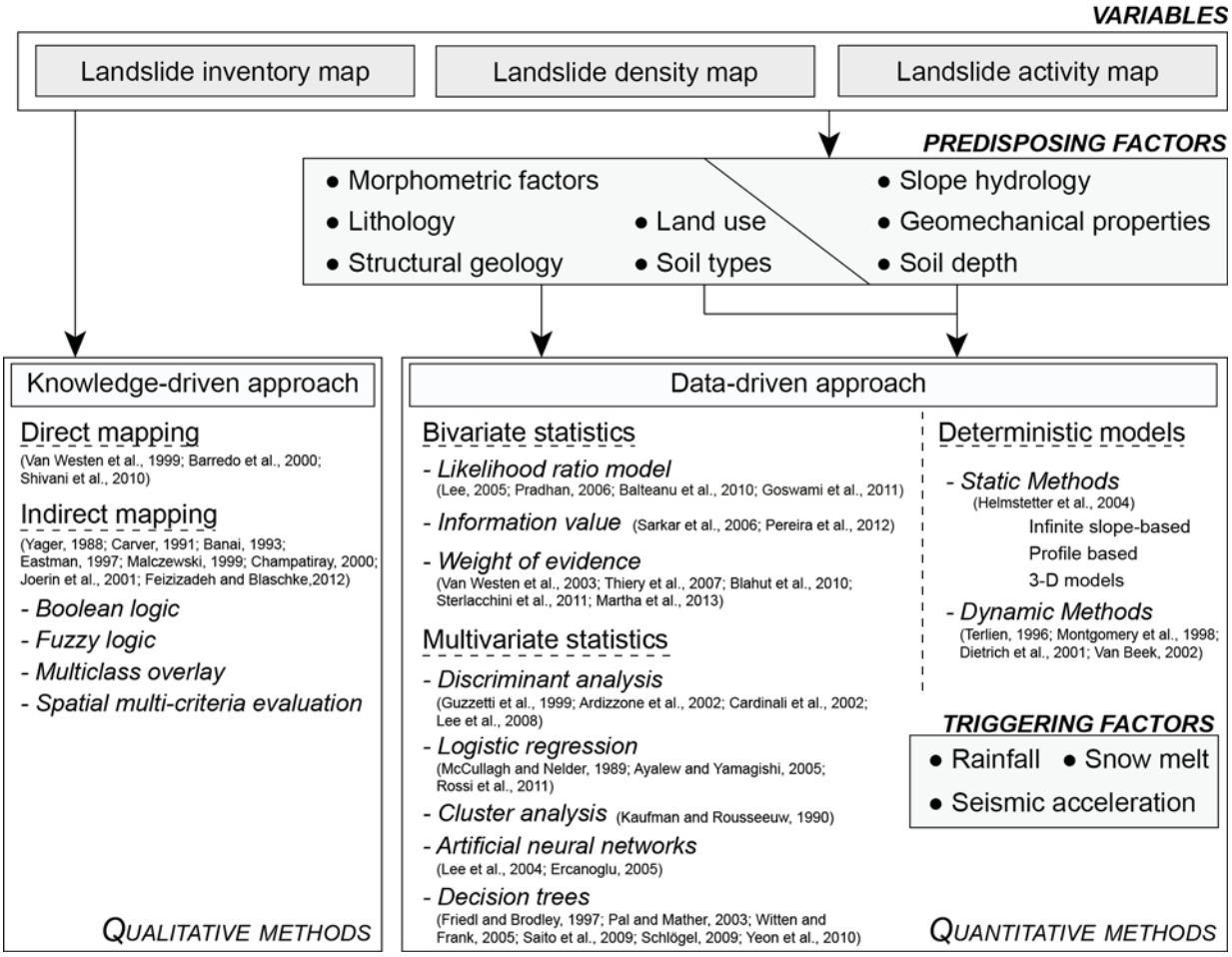

Figure 1-11: Qualitative and quantitative approaches for landslide hazard assessment

1.5.2. Quantitative or data-driven approaches

Quantitative approaches can be divided into statistical and deterministic analyses (see Fig. 1-11) according to Mantovani et al. (1996). The statistical analysis is an indirect method in which statistical analyses are used to obtain predictions of the mass movement from a number of parameter maps. Deterministic analyses are indirect methods in which parameters are combined in slope stability calculation.

1.5.2.1. Bivariate models

The bivariate statistical analysis compares each data layer of causative factor to the existing landslide distribution (Kanungo et al., 2009). Weights to the landslide causative factors are assigned based on landslide density. Frequency Analysis approach, Information Value Model (IVM), Weights of Evidence (WofE) Model, Weighted overlay model etc. are important bivariate statistical methods used in landslide hazard assessment mapping (Pardeshi et al., 2013).

Frequency (or *likelihood*) *ratio model* is based on observed relationships between the landslide distribution and each causative factor related to landslides. This method can be used to establish a spatial correlation between landslide location and landslide explanatory factors (Lee, 2005). The frequency ratio for each sub-class of individual causative factor is calculated based on their relationship with landslide occurrence. The LS index is computed by summing of frequency ratio values of each factor. Some studies show satisfying applications all over the world to assess landslide spatial distribution (Lee, 2005; Pradhan et al., 2006; Bălteanu et al., 2010; Goswami et al., 2011).

Information Value model (IVM) is based on relationships between landslide occurrence and related parameters (Sarkar et al., 2006). The information values are determined for each subclass of landslide related parameter on the basis of presence of landslide in a given mapping unit. Pereira et al. (2012) used IVM to evaluate the role of different combinations of landslide predisposing factors in the occurrence of shallow landslides in parts of Northern Portugal. IVM is also a useful method in determining the degree of influence of individual causative factor responsible for landslide occurrence.

In landslide susceptibility assessment, the *Weight-of-Evidence* (WofE) is a log-linear form of the Bayesian probability model that uses landslide occurrence as training points to derive prediction outputs. It calculates both unconditional and conditional probability of landslide hazards. This method is based on calculation of positive and negative weights to define degree of spatial association between landslide occurrence and each explanatory variables class. The WofE model has been used for landslide susceptibility since 1990's (Blahut et al., 2010). It uses different combinations of landslide causative factors in order to describe their interrelation with landslide distribution. WofE statistical method for landslide susceptibility modelling has proved to be a useful spatial data prediction model in many research works (e.g. van Westen et al., 2003; Thiery et al., 2007; Sterlacchini et al., 2011; Martha et al., 2013).

1.5.2.2. Multivariate models

Carrara et al. (1977, 1978) introduced two main approaches of multivariate analysis: (1) a statistical analysis of point data obtained from checklists of causal factors associated with individual landslide occurrences and (2) a statistical analysis performed on terrain units covering the whole study area. For each of the units, data on a number of geological, geomorphological, hydrological, and morphometrical factor is collected and analysed using multiple regression or discriminant analysis (Carrara et al., 1978, 1988, 1990, 1991, 1992; Carrara, 1983).

Discriminant analysis allows us to determine the maximum difference for each independent variable (e.g. predisposing factors) between landslide group and non-landslide group and to determine weights for these factors (Lee et al., 2008). In case of slope units partitioning, each one is classified into landslide affected and landslide-free classes and then relative importance of each variable is calculated. Results show relative importance of each variable in a discriminant function as a predictor of slope instability (e.g. Guzzetti et al., 1999; Ardizzone et al., 2002; Cardinali et al., 2002). Variables with high coefficient values are strongly associated with presence or absence of landslide. The goal is to establish a model to sort the mapping units into their appropriate groups with minimal error.

Among the wide range of statistical methods proposed in LS mapping, *logistic regression* (LR) analysis has proven to be one of the most reliable approaches (Ayalew and Yamagishi, 2005; Rossi et al., 2010). The model helps in establishing a multivariate relation between a dependent (landslide) and several independent variables, which are the predisposing factors for landslides. Basically, LR analysis relates the probability of landslide occurrence (having values from 0 to 1) to the "logit" Z (where $-1<Z<0$ for higher odds of non-occurrence and $0<Z<1$ for higher odds of occurrence). In its most simple form the LR model can be quantitatively expressed the probability of landslide occurrence as:

$$P_r = \frac{1}{1+e^{-z}} \tag{1}$$

where P is the probability of a landslide occurring, and z is the linear combination:

$$Z = \beta + \beta_1 X_1 + \beta_2 X_2 + \cdots + \beta_n X_n \tag{2}$$

The LR analysis assumes the term Z to be a combination of the independent set of geographical variables X_i (i =1,2,...,n) acting as potential causal factors of landslide phenomena. The coefficients i (i = 1,2,...,n) are representative of the contribution of single independent variables X_i to the logit Z. It has to

be noted that the LR approach does not require, or assume, linear dependencies between dependent term of *P* and the independent set of variables representing causal factors. P varies between 0 and 1 on an S-shaped curve as Z varies from −∞ to +∞ (Menard, 1995). An exponential equation and coefficients are estimated using maximum likelihood criterion and correspond to the estimation of the more likely unknown factors. Multivariate regression analysis plays a central role in statistics that make it one of the most powerful and commonly used techniques (McCullagh and Nelder, 1989). However, this approach inherently has some limitations such as generalizing and simplifying causal factors. In addition, this method does not take into account the temporal aspects of landslides and is not able to predict the impact of changes in the controlling conditions.

In the *cluster analysis*, the definition of clustering could be "the process of collecting objects into groups whose members are similar in some way" (Kaufman and Rousseeuw, 1990). As for any other problem in unsupervised learning, it deals with finding an unknown structure in a collection of unlabelled data. The goal of clustering is thus to determine the intrinsic grouping in a set of unlabelled data and to exploit this result in order to reduce the number of erroneous samples introduced in the training set. The procedure with a dataset partitioned into k clusters aims to maximize the similarity between objects in a cluster and its prototype and minimize the similarity between cluster barycentres. The simple Euclidean distance is often used to group similar data instances. In landslide susceptibility zonation the variables used in classification are not immediately comparable (Melchiorre et al., 2008).

Another technique is the use of *artificial neural networks* (ANN) for the determination of weight value in hazard assessment. The weight, either fixed or standard, is of relative importance among predisposing factors such as slope, curvature, and soil texture, and the rating is of relative importance among the classes of each factor (Lee et al., 2004). They should be determined based on objective analysis and not on subjective expert opinions. For instance, if slope is more important than soil texture in landslide occurrence, the relative importance value is the weight; and if a 30° slope is more hazardous than a 5° slope, the relative importance value is the rating. Due to their dynamic, flexible and nonlinearity-adaptable features, ANNs have an advantage of being able to deal with complex input-output relationships. Despite its black box features, ANNs can be used as a powerful tool when different types of landslides with complex mechanisms exist in medium or regional scale studies (Ercanoglu, 2005).

A *decision tree* is a technique for finding and describing structural patterns in data as tree structures and making predictions using the data (Witten and Frank, 2005). The main advantage is that a decision tree does not require the relationship between all the input variables and an objective variable in advance. A decision tree can also handle data measured on different scales, without any assumptions concerning the frequency distributions of the data (Friedl and Brodley, 1997). Data-mining tools are can be used to construct the decision trees based on an algorithm (e.g. C4.5) and detect landslides using satellite optical images (Schlögel, 2009). The decision-tree models are also useful for estimating landslide distributions (Saito et al., 2009) but even if some studies have given good predicting results (e.g. Yeon et al., 2010), their applications in landslide susceptibility are still limited.

1.5.2.3. Deterministic models

In deterministic analysis, the landslide hazard is evaluated using slope stability models, resulting in the calculation of factors of safety (van Westen et al., 1997). The development of several high-quality constitutive models for geomaterials and numerical codes combined with an increasing computer performance, allow us to predict, simulate and evaluate the behaviour or stability of any slopes submitted to different instability factors with relatively good accuracy (Fall et al., 2006). It requires a large amount of detailed input data, derived from laboratory tests and field measurements, and can therefore be applied only over small areas at large scales.

In some cases, *static methods* can be used but it assumes that the geometry of the landslides does not vary over time. In this condition, a static safety factor can be evaluated at each time step for a fixed calculation grid (Malet et al., 2007). For Vaiont and La Clapière landslides, to account for a progressive

slope failure (i.e., a time dependence in stability analysis), some researchers have taken a quasi-static approach in which some parameters are taken to vary slowly to account for progressive changes of external conditions and/or external loading (Helmstetter et al., 2004). But, it seems better to process dynamic deformation methods to increase the reliability of the impact assessments.

Dynamic methods in a GIS environment have been used by many investigators (Terlien, 1996; Montgomery et al., 1998; Dietrich et al., 2001; van Beek, 2002). Deterministic models are able to forecast the spatial and temporal frequency of slope failures with meteorological inputs. A dynamic hydrological model (e.g. related to shallow rainfall-induced landslides) simulates the pore pressure over time with a slope stability model that quantifies the susceptibility as the critical pore pressure threshold. The deterministic approaches for earthquake-induced landslides hazard analysis are generally based on the simplified Newmark slope stability model, applied on a pixel-by-pixel basis. This latter method is commonly used to evaluate LS in seismically active regions since it was shown that in some cases such geotechnical models can successfully predict the regional failure potential (Jibson et al., 1998; Miles and Ho, 1999). Havenith et al. (2006a) showed that the Newmark method produced LS values fitting particularly well with local landslide densities in the Suusamyr Basin (Tien Shan mountain range) if faults were considered as seismic sources.

1.6. Methods for a quantitative landslide hazard assessment

Assessing the probability of occurrence at a certain location within a certain period, is possible only when a relationship can be found between the occurrence of the landslide and the frequency of the triggering factors, such as rainfall or earthquakes.

1.6.1. Methods for the quantification of landslide temporal occurrence

The temporal frequency (or the recurrence) of landslide events can be established from archive inventories (Coe et al., 2000; Guzzetti et al., 2003) and from multi-temporal landslide maps (Guzzetti et al., 2005).

Before showing how to obtain the probability of landslide occurrence from archive inventories, it is convenient to establish an appropriate mathematical framework. As a first approximation, landslides can be considered as independent random point-events in time (Crovelli, 2000).

The Poisson distribution is a discrete distribution mainly used for the temporal occurrence of landslides. The probability of experiencing n landslides during time t is given by:

$$P\,[N_L\,(t) = n] = P_t = \; e^{(-\lambda t)}\,\frac{(\lambda t)^n}{n!} \qquad \text{with } n = 0, 1, 2, \ldots \qquad (3)$$

where $N_L\,(t)$ is the number of landslides that occur during time t in the investigated area, λ is the estimated average rate of occurrence of landslides, which corresponds to $1/\mu$, with μ the estimated mean recurrence interval between successive failure events. The model parameters λ and μ can be obtained from a historical catalogue of landslide events or from a multi-temporal landslide inventory map.

Hence, Guzzetti et al. (2005) derived the probability of experiencing one or more landslides during time t (i.e. the exceedance probability) as:

$$P_t = \; [N\,(t) \geq 1\,] = 1 - e^{(-\lambda t)} \qquad (4)$$

The Poisson model allows for determining the probability of future landslides for different times t (i.e., for a different number of years) based on the statistics of past landslide events, under the following assumptions (Crovelli, 2000): (1) the numbers of landslide events which occur in disjoint time intervals

are independent, (2) the probability of an event occurring in a very short time is proportional to the length of the time interval, (3) the probability of more than one event occur in a short time interval is negligible, (4) the probability distribution of the number of events is the same for all time intervals of fixed length, and (5) the mean recurrence of events will remain the same in the future as it was observed in the past. These assumptions, which may not always hold for landslide events, should be considered when interpreting (and using) the results of the Poisson probability model.

A binomial model can be adopted as an alternative to the Poisson model. The binomial probability model is a discrete-time model consisting of the occurrence or random-point events in time. In this model, time is divided into discrete increments of equal length, and within each time increment a single point-event may or may not occur.

Temporal probability calculation can be done for some grid-cells or terrain-units according to the chosen unit of analysis (section 1.3). The frequency of landslide occurrence for *x*-year period is obtained from multi-temporal inventory. For each unit, landslide recurrence values, i.e. the expected time between successive (re)activations, is evaluated based on past events.

1.6.2. Methods for the quantification of landslide intensity

1.6.2.1. Definition of landslide intensity

Landslide hazard is defined as the probability of occurrence of a landslide of a given magnitude, in a pre-defined period of time, and in a given area (Varnes and IAEG, 1984). The definition incorporates the concepts of spatial location ("where"), frequency of occurrence ("when", or "how of- ten"), and magnitude or intensity ("how large"). After answering to the "where" and "when" questions, magnitude refers to the prediction of the size and velocity of the landslide. In the scientific community, the investigators do not agree on a single measure for landslide magnitude or intensity (Hungr, 1997; Cardinali et al., 2002; Malamud et al., 2004a; Reichenbach et al., 2005). Malamud et al. (2004a) proposed using the total number of the triggered landslides, information available from accurate event inventory maps. In Guzzetti et al. (2009), the total volume of landslides occurred during an event (or a period) was used to measure the magnitude of a landslide even (or period). The magnitude m_L is defined as the logarithm (base 10) of the total landslide volume produced during the event (or period). Determining the volume is a more difficult task that requires information on the surface and sub-surface geometry of the slope failure. This information is difficult and expensive to collect. For hundreds to several thousand failures, the task is even more challenging (Malamud et al., 2004a). Empirical relationships to link the volume of landslides to geometrical measurements of the failures, i.e. landslide area, were adopted (Simonett, 1967; Hovius et al., 1997; Guthrie and Evans, 2004; Korup et al., 2005; Guzzetti et al., 2008, 2009; Larsen et al., 2010).

1.6.2.2. Magnitude Frequency (M-F) relations for landslides

Frequency of landslide event can be determined by dendro-geomorphological techniques but few attempts have been made to estimate landslide magnitude by analysing the spatial distribution of disturbed trees (Corominas and Moya, 2010). Ideally, this is achieved by using inventories of past landslide events recorded by conventional mapping techniques as described in 1.2.2 section. The magnitude-frequency (M-F) relationships for landslides have been discussed by a number of researchers (i.e. Hovius et al., 1997; Pelletier et al., 1997; Hungr et al., 1999; Guzzetti et al., 2002; Malamud et al., 2004; Picarelli et al., 2005). They have found that the M-F distribution of landslides appears to have a power-law similar to the one observed in seismology. The Gutenberg-Richter relationship between earthquake magnitude and cumulative frequency of earthquakes is expressed as:

$$\log N(m) = a - bM \tag{5}$$

where $N(m)$ is the cumulative number of earthquake events of magnitude equal or greater than M, and a and b are constants. This equation is equivalent to a fractal (power law) relationship between the number of earthquakes and the characteristic size of the rupture (Turcotte, 1997). Represented either by the area or by the volume of the deposits, magnitude-cumulative frequency (MCF) techniques have been developed for different landslide types and reviewed in Guzzetti et al. (2002), Malamud et al. (2004a) and Picarelli et al. (2005).

Frequency-area relationship appears to be robust and consistent across space and time and can be used to quantify the completeness of an inventory (Stark and Hovius, 2001; Guzzetti et al., 2002; Malamud et al., 2004a). It quantifies the number of landslides that occur at different sizes and can be analysed in terms of the frequency density function (f) of the landslides areas (A_L) using the equation proposed by Malamud et al. (2004a):

$$f(A_L) = \frac{1}{N_{LT}} \frac{\delta N_L}{\delta A_L} \tag{6}$$

where δN_L is the number of landslide with areas between A_L and $A_L + \delta A_L$.

In a log-log graph, this function shows the typical behaviour of natural event records (landslides, earthquakes, etc.) characterized by a more or less linear "tail" for the large size events, which can be fit by a power-law and a roll-over (inflection) for smaller events with decreasing frequency density for very small landslide areas. Pelletier et al. (1997) attributed the rollover shown by the probability density function (PDF) of landslide areas to a transition from a resistance controlled chiefly by friction for large landslides to a resistance controlled by cohesion for small landslides. As example, Fig. 1-12 shows the PDF of landslide areas in the Staffora basin (Guzzetti et al., 2005). Two estimates of the PDF are shown: (1) using the truncated inverse-gamma function of Malamud et al. (2004a) where 97.5% confidence intervals are also shown, (2) using the double-Pareto function of Stark and Hovius (2001).

Landslide frequency–area distributions allow quantitative comparisons of landslide distributions between landslide-prone regions and/or different time periods. PDF models the number of landslides occurring at different time periods for a study area (e.g. in the Maily-Say Valley, Kyrgyz Tien Shan, Havenith et al., 2006; Schlögel et al., 2011) or for comparison of different regions (e.g. in the European Alps, Wood et al., 2015). PDF can also be used to compare the influence of landslide location in natural or anthropogenic environments (Guns and Vanacker, 2014), in different lithology (Schlögel et al., 2015c) or at different distances from earthquake source area (Valagussa et al., 2014).

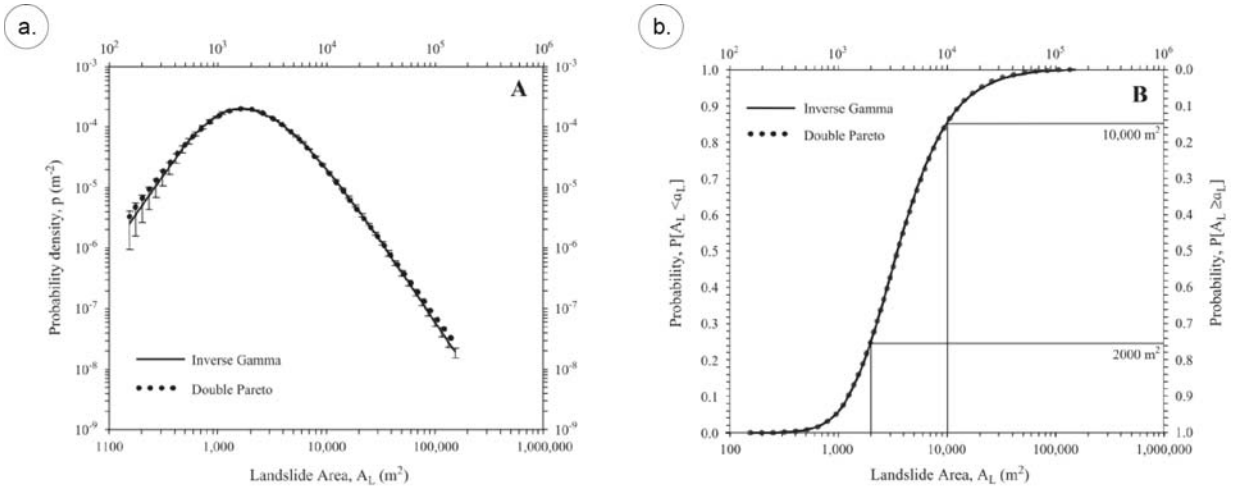

Figure 1-12: Probability density (a) and probability (b) of landslide area in the Staffora River basin (Guzzetti et al., 2005). Solid black line is a truncated inverse gamma function (Malamud et al., 2004a). Dotted line is a double Pareto function (Stark and Hovius, 2001). Error bars show 97.5% confidence intervals.

1.6.2.3. Deterministic evaluation of landslide runout

Runout modelling is rather complicated because between initiation and stopping the materials involves various transformations depending on the initial composition, the morphology of the path and the material incorporated during the flow (Savage and Hutter, 1991; Rickenmann, 2000; Iverson et al., 2004). The behaviour of the deposit and its parameters are often different from the initial material characteristics. As in many cases there is no information on velocities or flow type; the rheological regimes are difficult to estimate. The challenge will be to determine the rheological behaviour of different types of rapid gravity flows based on the morphology, distribution and sedimentological characteristics of the material deposited along the flow path, to qualify the expected mechanism and apply appropriate physically based models to simulate the corresponding flows (van Westen et al., 2006). Modelling the exact location of the source areas of debris flows and the spreading of material on the deposition fans is also challenging.

1.7. Current limitations for quantitative landslide hazard assessment and objectives of the research work

1.7.1. Limitations and uncertainties associated with multi-date inventories

In some conditions (e.g. where climate allows an important vegetal cover), detecting and mapping recent landslide activation is tricky. Although the multi-temporal landslide inventory seems to be the most accurate for a landslide hazard assessment, the available data information or the field conditions are sometimes not sufficient to create this kind of inventory. Some alternative techniques could be found to simplify the mapping technique procedure in application to the study area. Landslide multi-date inventory including a vegetation index may be a solution to take into account activation. Indeed, a simple index in the attribute table of the inventory may indicate if at a certain period, there is a visible activation or a stabilization of an already unstable slope. Initial polygons can therefore be enlarged or stay the same (with an indicator of the change) in a recent time or be diminished or identical (with an indicator of the change) in a past time according to the period considered. This technique allows us to deal with the delicate mapping of landslide with the invisible boundaries. However, underestimation in the size of the landslide activation is noticed. Frequency-area distribution may also be affected due to the lower number of small (to medium) active landslides. This is mainly due the fact that dormant landslide body (already observed in previous mapping) is still included into the other dates (constituting the multi-date) inventory. Therefore, the chosen susceptibility models of these data needs to consider the particular mapping when including landslide information as dependant variables as well as for the interpretation of the results.

1.7.2. Influence of the unit of analysis

Only a few investigators analysed at the impacts of mapping units partitioning for the susceptibility assessment (Carrara et al., 2008; Van Den Eeckhaut et al., 2009; Fig. 1-13). According to Van Den Eeckhaut et al. (2009), visual comparison of the landslide susceptibility maps shows that the geomorphological-unit-based assessment classifies a larger area as of high or very high susceptibility (23% of the study area) than the grid-cell-based assessment (10% of the study area). First, terrain-unit-based assessment predicts where an entire landslide is expected, whereas the grid-cell-based assessment forecasts only the location of the landslide initiation area. In the grid-cell-based susceptibility assessment with the location of old landslides, the lower parts of the landslide accumulation areas were not always identified as susceptible by the model. Second, terrain-units were designed to be larger than the mapped landslides (average area is 1×10^5 m^2 vs. 4×10^4 m^2), and were assigned a unique susceptibility value. Main differences occur where individual terrain-units encompass variable morphologies, including flat valley bottoms and plateaux free of landslides and sloped landscape with landslides or susceptible to slope failures (van den Eeckhaut et al., 2009).

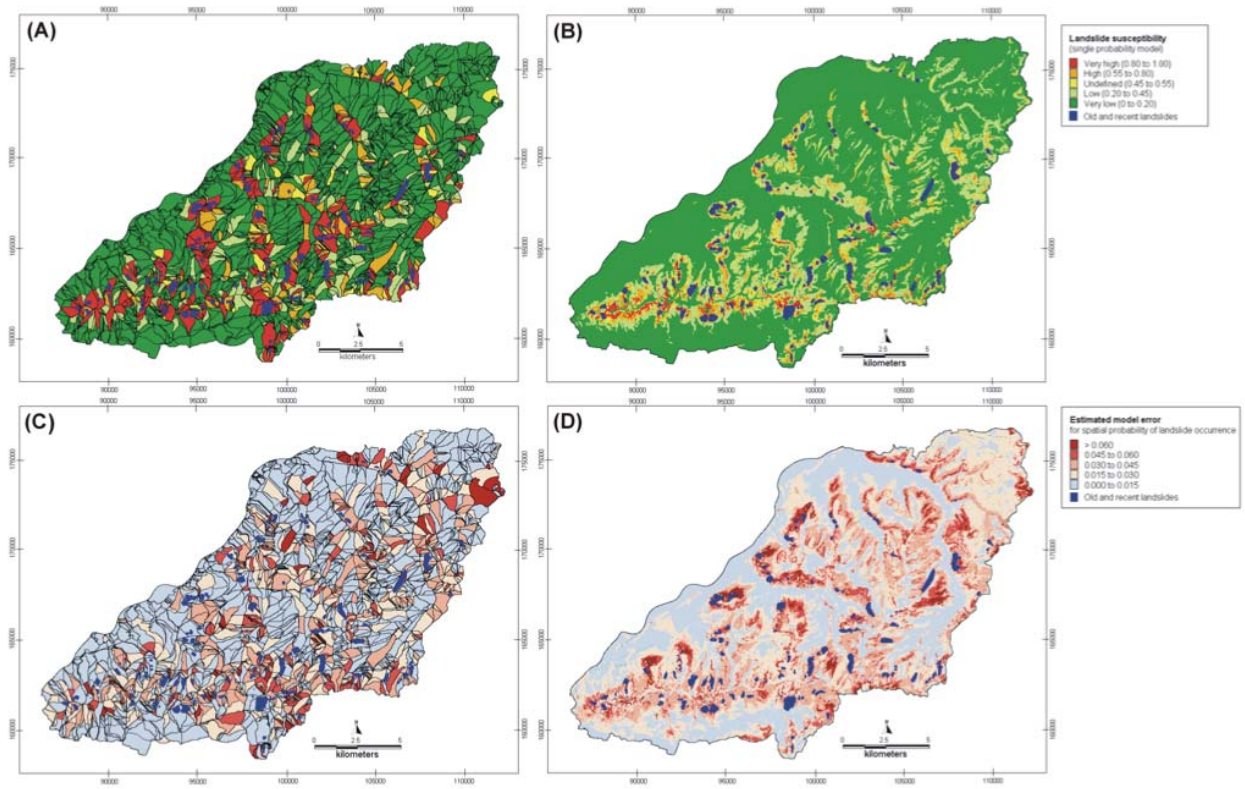

Figure 1-13: Landslide susceptibility assessment with different mapping units. (A) Topographic-unit-based susceptibility assessment (single probability estimate from the entire set of topographic units). (B) Grid-cell-based susceptibility assessment (single probability estimate from the calibration set of 958 grid cells). (C) Distribution of model error for topographic-unit-based assessment. (D) Distribution of model error for grid-cell-based assessment (van den Eeckhaut et al., 2009).

1.7.3. Limits of susceptibility assessment

In a knowledge-driven method, the geoscientist decides on which parameters and input maps are used, the weight of their classes or, of the input maps themselves. The definition of the importance of the factors is therefore subjective and the technique is not reproducible and remains qualitative. In the case of the data-driven method, the geoscientist decides on which criteria and input maps selection according to the state-of-the-art (see Fig. 1-9), the study site and the data availability. Weights are determined by comparing the input maps with known occurrence of the feature what we want to predict. Influence and importance of input data can be determined by different techniques, such as data mining techniques using decision trees (Schlögel, 2009). In both, bivariate and multivariate methods, results can be validated. However, as they are probability depended, stochastic models involve uncertainty. The models are valid under certain conditions defined by the properties and processes of the study area. The susceptibility map remains valid until any intrinsic or triggering factors change (e.g. road construction, climate change).

With single value at a given space and period of time, deterministic models show no (or a few) uncertainty. In static models, independent of time, time is frozen while dynamic models can simulate changes through time. These process-driven models are based on general physical laws but require many parameters to reflect the reality of the field, which are difficult to obtain over a large area. However, they have some limitations: overestimation of the area of failure (e.g. STARWARS/PROBSTAB), in case of lack of rainfall intensity data (usual in landslide-prone areas in developing countries) or lack of knowledge of initial conditions.

1.7.4. Limitations for the combination of temporal probability and intensity

For large areas, methods are mainly focused on answering the "where" question instead of validating the "when" and "where" according to a particular landslide size. Old landslide maps are rarely checked and/or updated. Thanks to a multi-temporal or multi-date inventory, it is possible to estimate differentiated return periods according to the years considered for mapping and thus, to obtain the temporal probability. The spatial probability that landslides would affect a particular area for a given temporal probability is calculated as the landslide density (in space domain) inside the landslide susceptibility class. This probability can be estimated by multiplying the temporal probability (1/return-period for annual probability) of having new landslide events by the spatial occurrence. This indicates the chance for grid-cell (or a terrain-unit) to be affected by an event. In this case, the assumption is that large events with a long return period would also trigger those landslides that could be induced by smaller events with shorter return periods. The scale of a study is also a limiting factor for hazard models, with a critical importance of accurate landslide inventory in heuristic models as well as landslide activity or rainfall data for probabilistic and deterministic approaches (see Fig. 1-10). In conditions where landslide can be either new or reactivated, susceptibility assessment is still mandatory. A susceptibility map remains useless unless it is spatially and temporally validated. If an area is already landslide-prone, landslide intensity and temporal occurrence is really important to assess.

1.7.5. Objectives of our research

According to the table of content presented in the previous section and the state-of-the-art established above, this research has the following objectives:

(1) The creation of a "multi-date inventory" (see § 1.2.1) at regional scale by comparison of multi-source data (§ 1.2.2) and including a vegetation index in order to determine landslides activation over time;
(2) The development of a geomorphologically-guided method to interpret InSAR data (§ 1.2.3) at regional and slope scales in order to detect different slides (red dotted rectangle in Fig. 1-2) and evaluate their kinematic and spatial evolution;
(3) The combination of InSAR and ground-based measurements (§ 1.2.3) at slope scale to determine different velocity fields of complex deep-seated landslides and link them to the structural geology;
(4) The influence of the morphometry of slopes and sub-basins on terrain-unit delineation (§ 1.3.2);
(5) The influence of the unit of analysis (§ 1.3.2; § 1.7.2) and the effect of the elevation data on susceptibility assessment;
(6) The characterization of landslide activity and exceedance probability (§ 1.6.1) based on a multi-date inventory to evaluate landslide recurrence according to their magnitude (§ 1.6.2.2), and some potential triggering events (§ 1.5.1);
(7) To assess probability density function of size to compare frequency-area relationships according to subdivision of landslide inventory according to geographical location, geology and period of time considered (§ 1.6.2.2);
(8) To evaluate landslide susceptibility with a multivariate model (§ 1.5.2.2) considering different dependant variables;
(9) The analysis of predisposing factors (§ 1.4.1) where landslides occurred and evolve, and the attempt to combine the temporal occurrence with the intensity of the events to evaluate the landslide hazard on some hotspots of the Ubaye Valley, French Alps (described in Chapter 2).

CHAPTER 2: Characteristics of the study area - the Ubaye Valley (South French Alps)

Chapter 2 describes the study area in terms of geographical, geomorphological and geological characteristics. First, the geographical context of the Ubaye Valley is introduced. Second, the geological information is presented through a description of the lithology and of the tectonic affecting the Mercantour massif. The third section discusses the natural hazards observed in the valley with a focus on the different landslide types. It addresses the control of geomorphology on landslide distribution. Several active and potentially dangerous landslides are presented, as representative of the region: Les Aiguettes, Pra Bellon, La Valette and Sanières landslides in the northern zone and Poche and Super-Sauze landslides in the southern zone.

2.1. Geographical context

The Ubaye catchment is located in the Alpes-de-Haute-Provence department (Southern French Alps; see Fig. 2-1). This 15-km wide and 25-km long area (2-2a) has elevations from 1000 to nearly 3000 m above sea level. It has representative climatic, lithological (Fig. 2-1d), geomorphological and land cover conditions of the Mercantour massif and is highly affected by natural hazards, especially landslides.

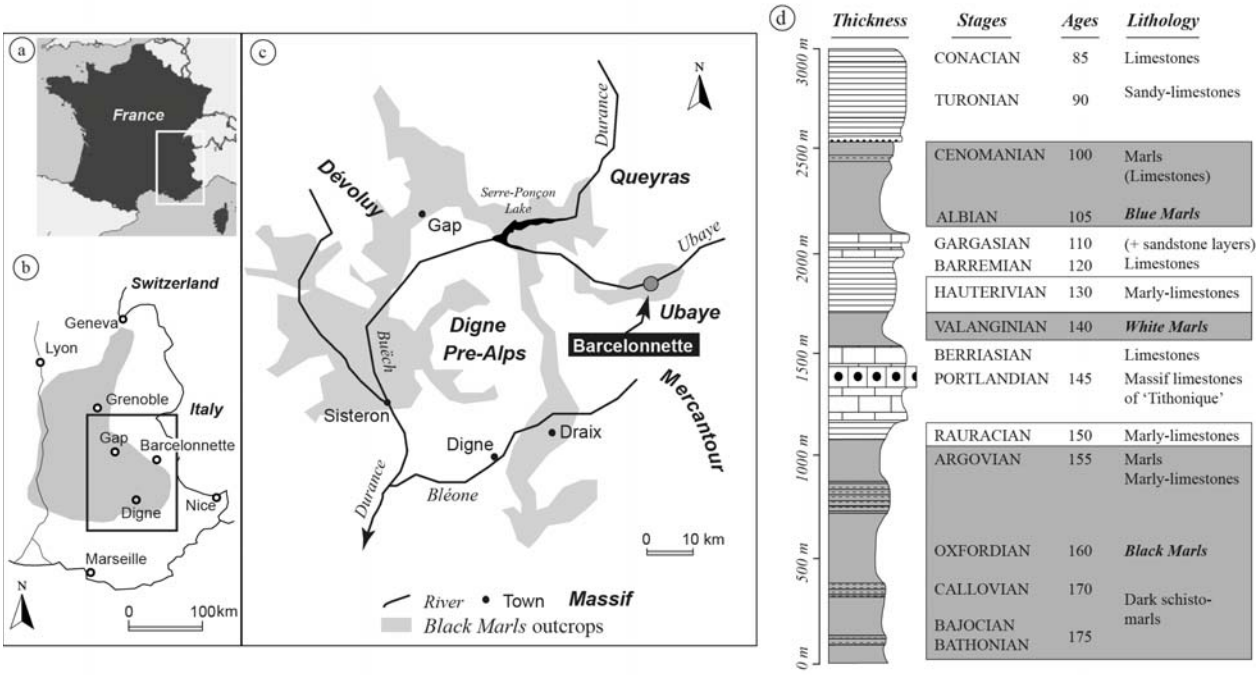

Figure 2-1: Location of the Ubaye Valley and extension of black marls facies in the South-East French Alps (a-c). Different types of black marls are represented in grey (b-c). Stratigraphy of the Dauphinois zone is shown in (d) (modified from Malet, 2003; Remaître, 2006).

The Ubaye River crosses the Barcelonnette basin from the East to the West (Fig. 2-2b). Many tributaries flow into it, such as the Bachelard River to the West (Fig. 2-3e). During the Würm glaciation the Ubaye Valley has been covered with ice, up to altitudes of approximately 2000 m (see Fig. 2-5c). In addition to the erosion activity of the glaciers, torrential erosion by the Ubaye River and the 26 active torrential streams have progressively carved out most the landscape (Fig. 2-2d). Hillslopes are characterized by very steep slopes (30-70°) and more gentle slopes (10-20°). The relief is irregular and associates alternating steep convex slopes, regular planar slopes and hummocky slopes:

- the steepest convex slopes (> 30°) are carved in the black marl outcrops and are, for most of them, gullied in badlands or affected by rock-block slides or complex slides (e.g. La Valette landslide to the North of Barcelonnette town; Fig. 2-2c);
- the regular planar slopes (10°-20°) are covered by thick morainic deposits (between 10 and 20 m), are usually cultivated and affected by rotational and/or translational slides (Légier, 1977; Weber, 2001);
- the hummocky slopes are generally covered by forests and/or by natural grasslands (see 2-3h).

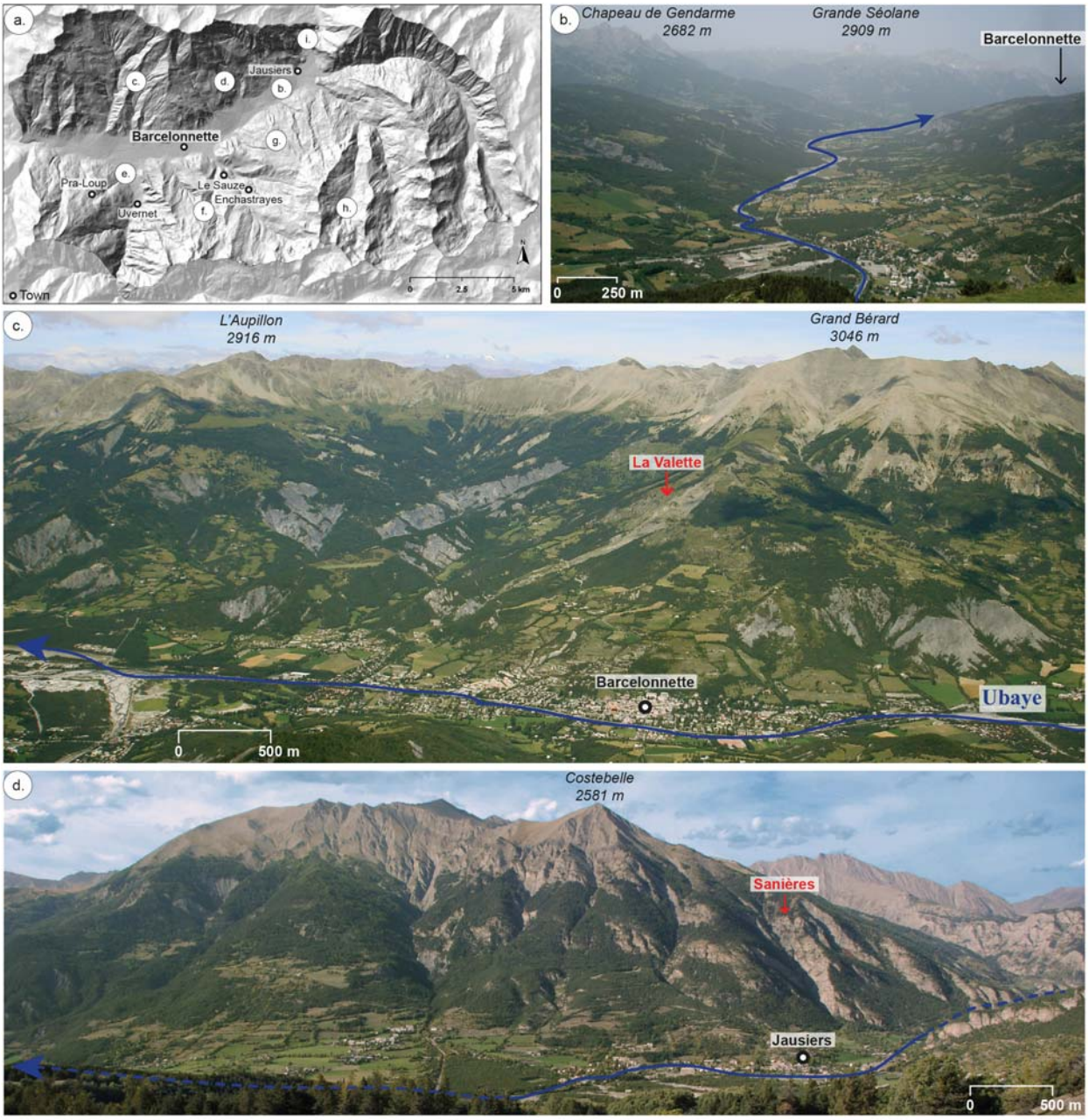

Figure 2-2: Examples of landscapes observed in the northern slope of the Ubaye valley. (a) Extension and topography of the valley with location of the views. (b) View in the west direction on Jausiers municipality showing right and left riverbank of the Ubaye. (c) View of the northern part of the valley with the Barcelonnette and the La Valette landslide (d) View of the NE part of the valley and Jausiers municipality.

Figure 2-3: Examples of landscapes observed in the southern slopes of the Ubaye valley. (e) View to the SW part of the area with the Bachelard River passing by Uvernet and reaching the Ubaye River and the Pra-Loup ski station. (f) View in the southern direction on the Super-Sauze landslide. (g) View on the Ubaye plain, the southern slopes and the Poche landslide. (h) View in the southern direction to the hummocky area of the Terre Plaine catchment covered by natural grasslands. (i) View of the eastern limit (Abriès sector) of the area of interest characterized by steeper slopes and harder rocks.

The Barcelonnette Basin has a dry and mountainous sub-Mediterranean climate with strong interannual rainfall variability of 712 mm (std. dev.: 152 mm) over the period 1928–2013, strong storm intensity during summer and autumn (over 50 $mm.h^{-1}$) and ca. 130 days of freezing per year (Maquaire et al., 2003). Highest monthly rainfall generally occurs in autumn (> 75 $mm.month^{-1}$ in October and November). During winter (from the beginning of December to the end of March) precipitation is mainly snow but it is considered as a dry period. Meso-climatic differences on a small scale emerge due to the east-west orientation of the valley (Remaître, 2006). Indeed, there is a distinct difference in evaporation, temperature and duration of the snow cover between the north-facing slopes and the

south-facing slopes: the south-facing slopes have the highest temperatures and evaporation, and the shortest snow cover period.

The economy of the Ubaye valley was based on crafts, little textile industry and feeding agriculture. During the 15th and 16th centuries, deforestation and soil erosion caused considerable damages. During the 18th and the 19th centuries the developing industries caused a growing need for timber. The logging of trees resulted in the deforestation of large areas. In the same period a part of the rural population migrated to the cities. In the Ubaye valley, the logged or abandoned agricultural areas were very prone to erosion. Torrentiality is the major hydrological factor throughout the Southern Alps and this valley is not an exception. Local risk managers from the "Service de Restauration des Terrains de Montagne" (RTM) conducted actions to stop the processing, i.e. by reforesting at the turn of the century. Actually, reforestation can only limit or restrict erosion where this is possible. When the substratum is sensitive to erosion (e.g. marls), the combination of the steep slope, the climatic conditions (e.g. intense rainfalls separated by long dry periods) make the reforestation precarious. The exodus occurred over almost two centuries; nowadays the economy is no longer based solely on agriculture. Tourism is sizeable with its related activities and especially winter tourism (e.g. at Pra-Loup and Super-Sauze winter resorts).

2.2. Geological context

2.2.1. Morphostructure of the area

The South French Alps are geologically divided in two units according to a W-E axis: (1) the external domain and (2) the internal domain (See Fig. 2-4; Evin, 1997). (1) is constituted by several crystalline massifs (Argentera-Mercantour-Ecrins) and some allochtonous formations. (2) is formed by several thrust sheets: "(sub-)briançonnaise" zones and a "piemontaise" zone to the extreme east.

The Ubaye valley is located in a complex area with structural geological groups (Légier, 1977; Weber, 2001; Fig. 2-4 and 2-5b). The alpine orogenesis contributes to the genesis of the catchments and the dissymmetry of the slopes. During the alpine Oligocene folding, the disappearance of the external magmatic bedrock allowed the progress of the overthrust on the external sedimentary domain over tens of kilometres in a NE/SW direction (Blanchard, 1950; Evin, 1997). This discordant displacement occurred more than 20 million years ago, between Eocene to Miocene. This tectonic activity allows the displacement of huge fragments of rocks, which are still visible in the Barcelonnette basin (see Fig. 2-5b):

- At the north-facing slopes: some fragments of limestones and flysches (klippes of the Parpaillon and Autapie thrust sheets) constitute the crests, such as the "Chapeau de Gendarme" at 2682 m of elevation. These geological formations are generally observed above 1800 m.
- At the south-facing slopes: allochtonous formations from the Parpaillon thrust sheet are observed (e.g. Aupillon: 2916 m, La Chalanche: 2984 m, Coste Belle: 2581 m. They are located up to 1600 m and more present comparing to the north-facing slopes. From ca. 2000 m, fragments of the basal overthrust, made of several flysches are visible. Upper crests, less affected by the overthrust, are located in the Parpaillon thrust sheet mainly constituted by the Helminthoid flysch rocks, described by Kerckhove (1969).

Some post-overthrust episodes of folding generated anticlines and synclines in the thrust sheets guiding the location and direction of actual streams (Weber, 2001). These deformations are dated from Superior Miocene and affected by normal faults, oriented NW-SE.

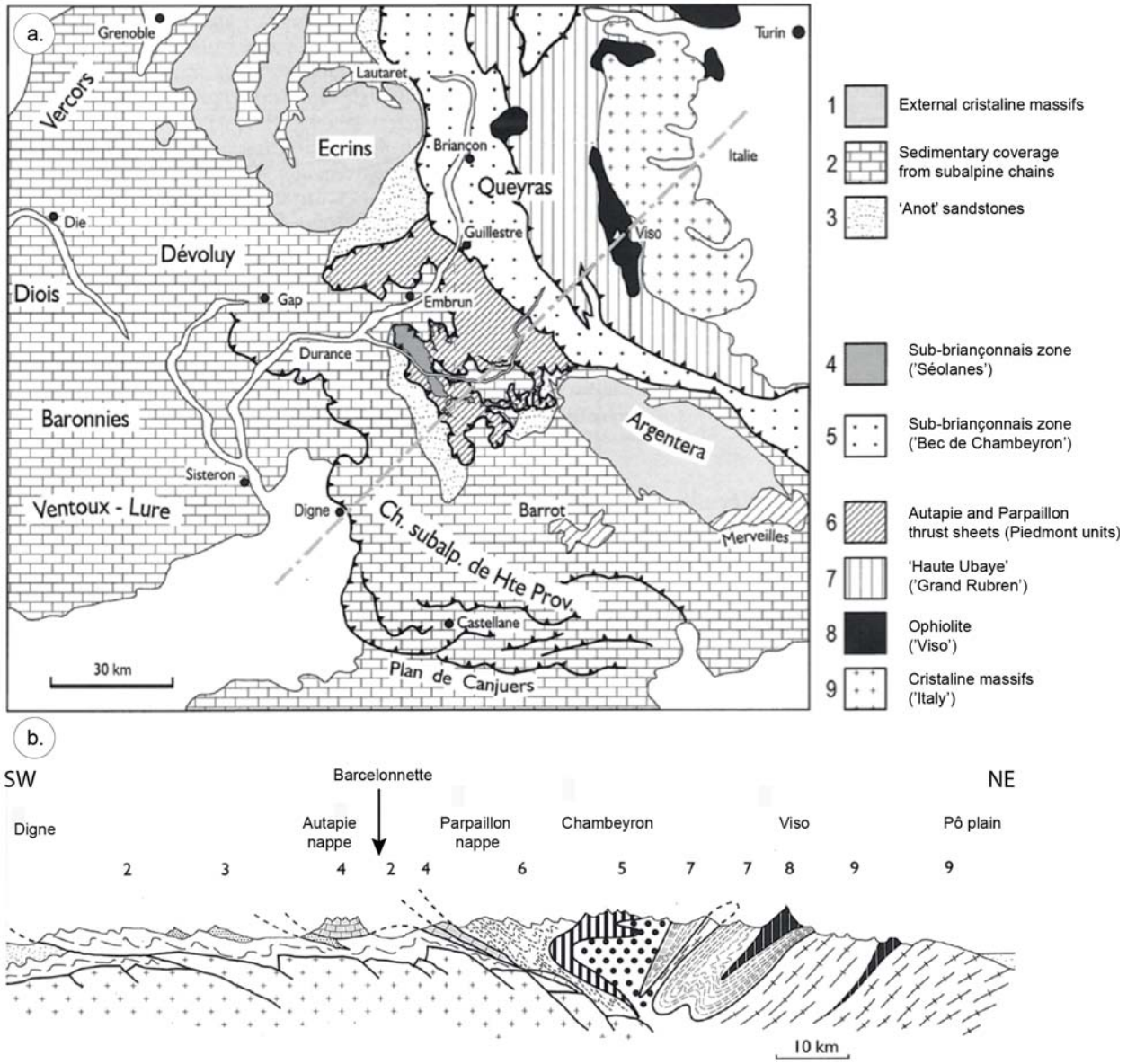

Figure 2-4: Geology of South French Alps (after Debelmas et al., 1983 and Evin, 1997). (a) Simplified geological map and (b) SW-NE oriented cross-section through crystalline massifs and thrust sheets.

2.2.2. Lithology and chronostratigraphy of the autochthonous bedrock

The Barcelonnette Basin is a geological window opened between two Eocene sheet thrusts (Autapie and Parpaillon), made of strong limestones or sandstones, and overlying autochthonous bedrock made of soft black marls (see Fig. 2-5a). Therefore, the thick Mesozoic sedimentary cover (about 7 km) may be separated into three thrust sheets and two superposed structural units (Fig. 2-5b):

(1) The lower structural unit is constituted by the sub-Briançonnais thrust sheets and the Autapie Helminthoid Flysch thrust sheet. The sub-Briançonnais thrust sheets display a very complex arrangement of numerous slices (Kerckhove, 1969; Maury and Ricou, 1983). Their facies range from Upper Triassic to Upper Eocene. This unit took place in the Ubaye valley during the early Oligocene and was folded during the late Oligocene.

(2) The upper structural unit is the largest Helminthoid Flysch thrust sheet (Parpailon Thrust sheet). The stratigraphy of this Upper Cretaceous flysch is well-known (Latreille, 1961; Kerckhove, 1969) and constitutes a thin (50-100 m) dark shale layer at the base overlain by 1000-2000 m of typical Helminthoid limestones. The Parpaillon Thrust sheet lies on an erosional surface which cross-cuts the Oligocene structures of the Digne thrust sheet. Consequently, the final position of the Parpaillon Thrust sheet in Embrunais-Ubaye probably occurred during the early Miocene (Kerckhove, 1969).

The 'Helminthoid Flysch' sequences of the Autapie and Parpaillon thrust sheets were deposited in the Ligurian Ocean at the end of Cretaceous time, which explains their Eocene tectonic history (Merle and Brun, 1984). Differential erosion revealed the autochthonous formations from the Mesozoic Age of the Dauphinois zone of the Western Alps. They form an anticline with a 20°-dipping involving formations from Superior Miocene. The sandstone bedrock is dated from Trias to Superior Eocene. We can observe Oxfordian-Callovian black marls, Valanginian white marls and Aptian-Albian blue marls over 220 km^2 in the Durance Basin (Fig. 2-1d). With a thickness of 300 m as minimum, the Oxfordian-Callovian black marls are divided into four groups according to their ages (Maquaire et al., 2003). The gentle slopes (10–30°) of the lower part (1100-1900 m a.s.l.) consist of these marls, mainly composed of fragile plates and flakes packed in a clayey matrix. This macrostructure of the bedrock and its mineralogy make them highly sensitive to the erosion and the formation of badlands. Their changes of state or consistency (rock state to plastic component to liquid according to the water content) make them a key predisposing factor for landslide susceptibility (Antoine et al., 1995; Malet, 2003; Remaître, 2006). They have also a low permeability and thus, host watercourse springs at the contact with Quaternary deposits (moraine) or flysches. Hydrological, geomechanical and rheological properties of the Oxfordian-Callovian black marls are detailed in Malet (2003) and Maquaire et al. (2003). Due to their sensitivity to erosion, several landslides (e.g. La Valette, Poche and Super-Sauze; Fig. 2-5a) occurred in the black marls or at their contact with morainic deposits.

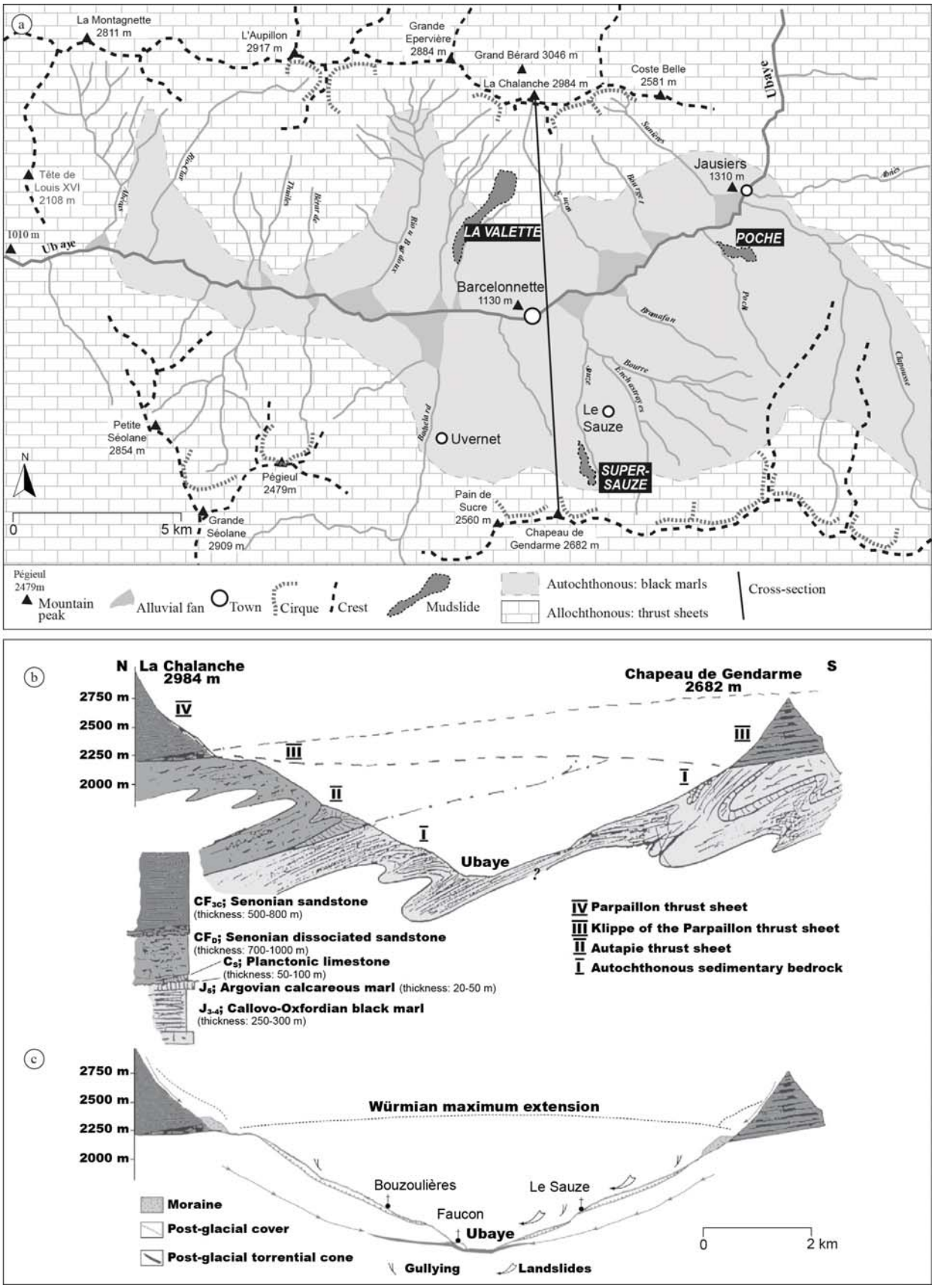

Figure 2-5: Morphological structure of the Ubaye Valley. (a) Location of the autochthonous and allochtonous formations observed. (b) Geological N-S oriented cross-sections with the four main structural units. (c) Geomorphology with maximal extension during the Würm glaciation, post-glacial cover with gullying and sliding processes are represented (modified after Maquaire et al., 2003).

2.2.3. Geomorphology of the landscape

2.2.3.1. Heritage of the glaciation

The morphology of the Ubaye valley is highly influenced by the heritage of the Würm glaciation and its post-effects overlying the Oxfordian-Callovian black marls (see Fig. 2-5c). In general, the Ubaye glacier and its tributary glaciers deposited those allochtonous formations. A 65-km long and 600-m high glacier limited to the west by the Durance glacier was present in the valley. Glacial deposits are observed all over the valley: kame terraces, rock glaciers (e.g. in the area of the "Chapeau de Gendarme" peak; Fig. 2-6a), morainic arcs, old glacial lobes (Fig. 2-6b), erratic blocks and rocks (Fig. 2-6d).

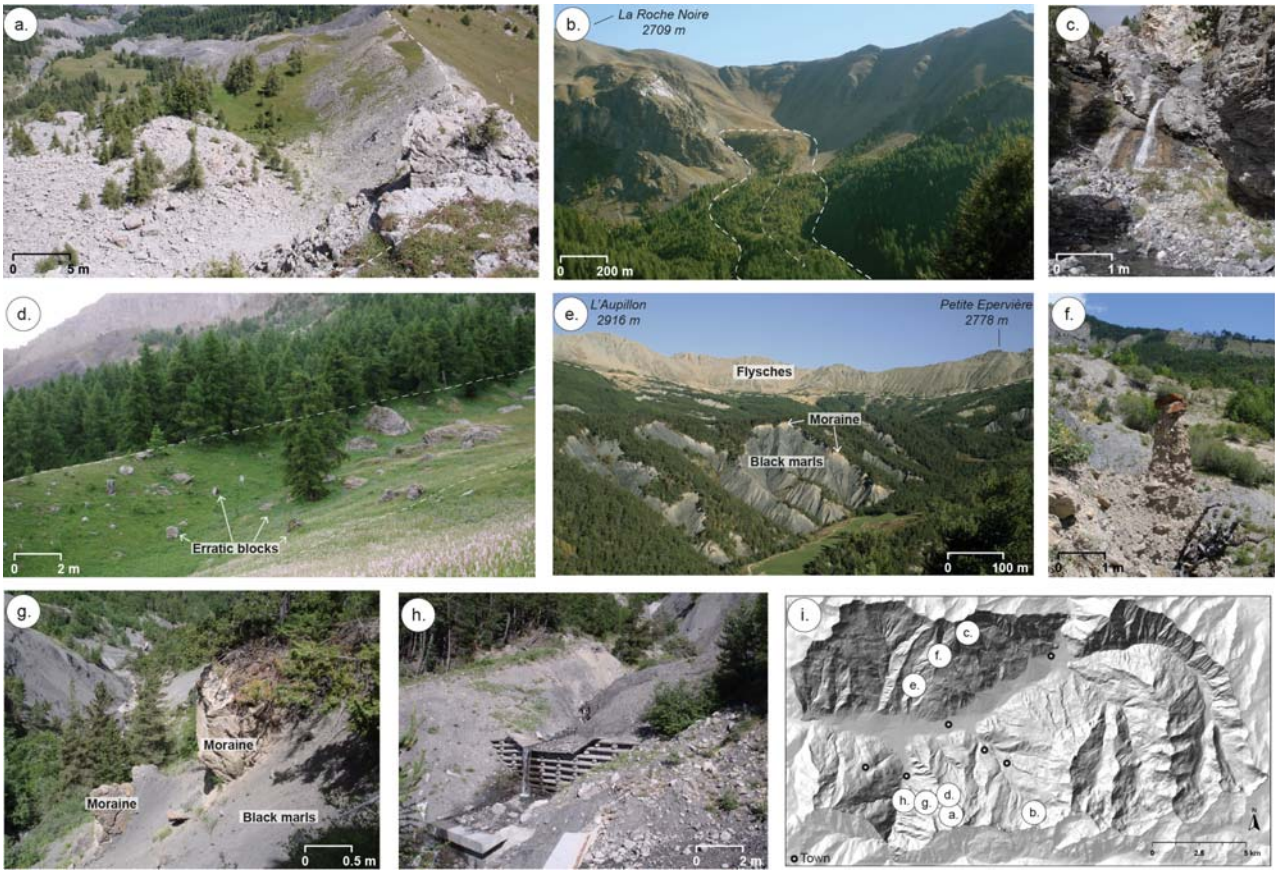

Figure 2-6: Geomorphological features due to glaciers and geology of the valley. (a) Rock glacier located below the "Chapeau de Gendarme" and "Bec Second" peaks. (b) Footprint of an old ice tongue downslope to the "La Roche Noire" peak. (c) Sanière torrent at its upper part. (d) Erratic blocks observed in the forest downslope to the "Chapeau de Gendarme" peak. (e) View on the 'badlands' oriented to the SE and located below the "La Chalanche" crest (1600 m of elevation). (f) Hoodoo (also called fairy chimney) formed within the thrust sheets constituted by different sedimentary rocks. It can be found close to the 'Faucon' catchment. (g) Morainic blocks observed in the marly slopes of the "Riou Chanal" catchment. (h) One of the numerous check dams constructed along the "Riou Chanal" torrent to control channel instability and prevent potentially disastrous debris flows. (i) Location of the previously described morphological features or elements of the landscape.

Glacial and periglacial formations are characterized by a discontinuous morainic cover presenting a width ranging from 1 to 25 m (Mulder, 1991). These deposits can be found at high elevation (up to 2400 m), especially on the north-facing slopes (upstream of Enchastrayes village, see Fig. 2-6). They are also overlying black marls, which form "badlands" at lower elevation (e.g. in Fig. 2-6e) or along the riverbanks of active torrents (e.g. in the Riou Chanal; Fig. 2-6g). Morainic deposits are difficult to date in both absolute and relative ways. They were also probably affected by large mass movements at the end of the Würmian and at the upper Holocene (Jorda, 1980).

2.2.3.2. *Morphometry and dissymmetry of the valley*

Below the mountain peaks surrounding the Barcelonnette Basin, slopes are often steeper than 45° and characterized locally by some circular water catchments (cirque) formed at the ice age. From those places, torrents (e.g. "Sanières" torrent in Fig. 2-6c) have their source and participate to the erosion of the slopes over a few metres, shaping the landscape of the valley (Miramont, 1998).

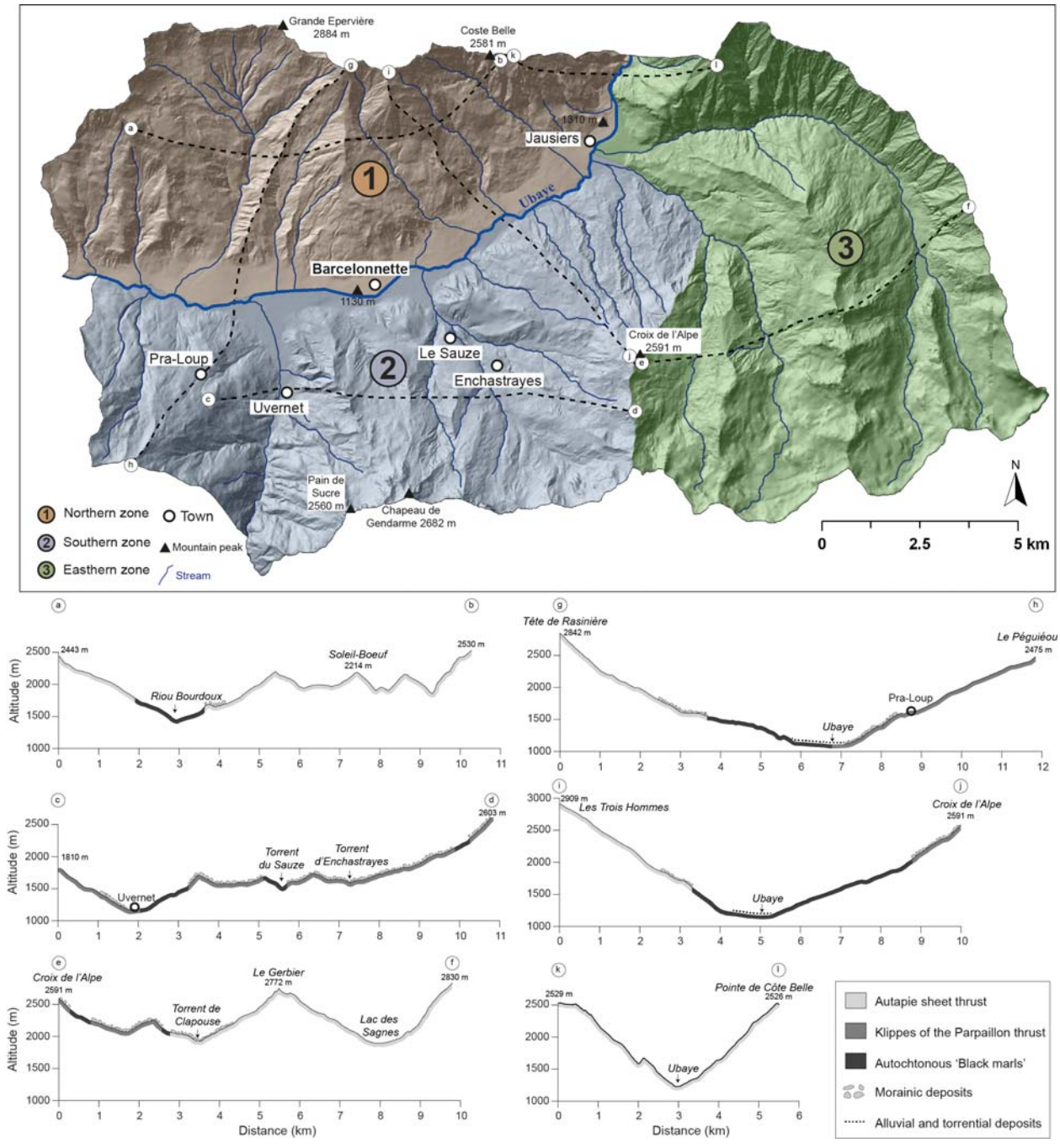

Figure 2-7: Extension of Barcelonnette Basin and simplified geological cross-section. Hillshaded view of the area divided into three zones (North, South, East) and cross-sections showing geology and dissymmetry of the relief.

Over roughly 8 km, from East to West, a dissymmetry of the right riverbank slopes vs. the left ones is observed (e.g. cross-section g-h; Fig. 2-7). To the West of the area, slopes are of around 25° to the North and ca. 30° to the South. Topography also depends on the aspect angles, as it is different considering the lateral tributary valleys:

- On the north-facing slopes (southern zone): the torrents incised moderately the valleys (e.g. the Poche and Sauze torrents and slopes are regular (Remaître, 2006);
- On the south-facing slopes (northern zone): the torrents incised intensively (up to 150-m width) the valleys. These slopes are more variable in angle and uneven than the north-facing ones (profile a-b in comparison to profile c-d; Fig. 2-7). Debris flows occur frequently in these torrents (Remaître et al., 2009) forming large alluvial fans (e.g. up to 1500 m; Remaître et al., 2002, 2005). Check-dams were constructed from 19th century in order to decrease the effect of debris flows (e.g. in the Riou Chanal, see in Fig. 2-6h). According to Remaître and Malet (2010), the role of series of check dams in regulating torrential and hillslope processes is fundamental.

2.3. Inventory of natural hazards observed in the valley

Due to the economic growth, the Barcelonnette area is a touristic place with expanding use of land in the flood plain area. The area is constantly suffering from many hazards including landslides, snow avalanches, debris flows and flooding.

2.3.1. Debris flows

There were several evidences of torrential events associated with debris flows (Flageollet et al., 1999; Maquaire et al., 2003; Remaître and Malet, 2010). They were controlled by the construction of several check dams designed to protect the inhabitants and to channelize the river within the boundary of the municipality. Debris flows are generally caused by heavy rainfall from either intense convection, or sustained frontal rainfall (Tarolli et al., 2012). Those rainfalls may trigger debris flows and flash floods in the same channels filled with sediments (van Asch et al., 2014). Both events can be approached similarly in the analysis of the threshold using atmospheric indicators (Turkington et al., 2014). Kappes et al. (2011) indicate a dominance of flash floods with 461 recorded events while only 100 debris flows have been registered. The spatial distribution of historical debris-flows shows that they have occurred mainly in the torrents located on the south-facing slope of the Barcelonnette Basin. Indeed, about 75% of the debris-flow events were recorded in four torrents: Riou-Bourdoux, Sanières, Faucon and Bourget. Some of the most recent and abundantly documented debris flows are those that occurred in the Faucon catchment (Faucon-de-Barcelonnette municipality) in 1996 and 2003, causing significant damage to roads, bridges and properties. This catchment has even experienced a total of fourteen debris flows since 1850 (Remaître et al., 2009).

2.3.2. Floods

Anthropic activities within the catchment had strong effects on the hydrologic behaviour and land erosion. Changing land use in the alluvial plain tended to aggravate these issues. Increasing the erosion loads from the slopes results in blocking of the check dams through sediment concentration. A renewed phase of flooding occurred when the area faced the regional event of flooding in 1957 (Liébault and Piégay, 2002). After this event, the municipality took protection measures which reduced the impacts of other meteorological events. The most recent peak discharge of the Ubaye River occurred in 2008. These damages have grabbed the attention of researchers and authorities for flood hazard assessment. Breinl et al. (2013) proposed a model to generate daily precipitation amounts and its application in risk management for the Ubaye valley.

2.3.3. Seismicity

The Barcelonnette Basin is one of the most seismically active areas of France (e.g. Jongmans and Campillo, 1993; Thouvenot and Fréchet, 2006; Daniel et al., 2011). The highest recorded earthquake occurred in April 5th, 1959 (Ms = 5.5) without precursor shaking. A seismic crisis affected the valley from January 2003 to November 2004 with more than 15,000 recorded earthquakes. From January

2012, 12,786 earthquakes were detected in the region with 2,473 earthquakes recorded between April 7th and April 18th 2014. A few landslide events are considered as co-seismic in this area. However after some earthquakes, when intense rainfall was also registered, the displacement of some active landslides increases (e.g. multiplied by a factor 5 at upper part of La Valette landslide after the April 7th, 2014 event).

2.3.4. Landslides

This section describes to the landslide activity at regional scale and addresses particular case studies. Numerous studies were conducted on landslides distribution in the Ubaye valley (e.g. Flageollet et al., 1999; Maquaire et al., 2003; Remaître et al., 2005; Thiery, 2007; Thiery et al., 2014). The area counts ca. 860 landslides whatever the degrees of activity considered (i.e. ca. 650 active, 127 dormant, 60 relict and 22 sackung landslides). The main active and dormant landslides are indicated in Fig. 2-8.

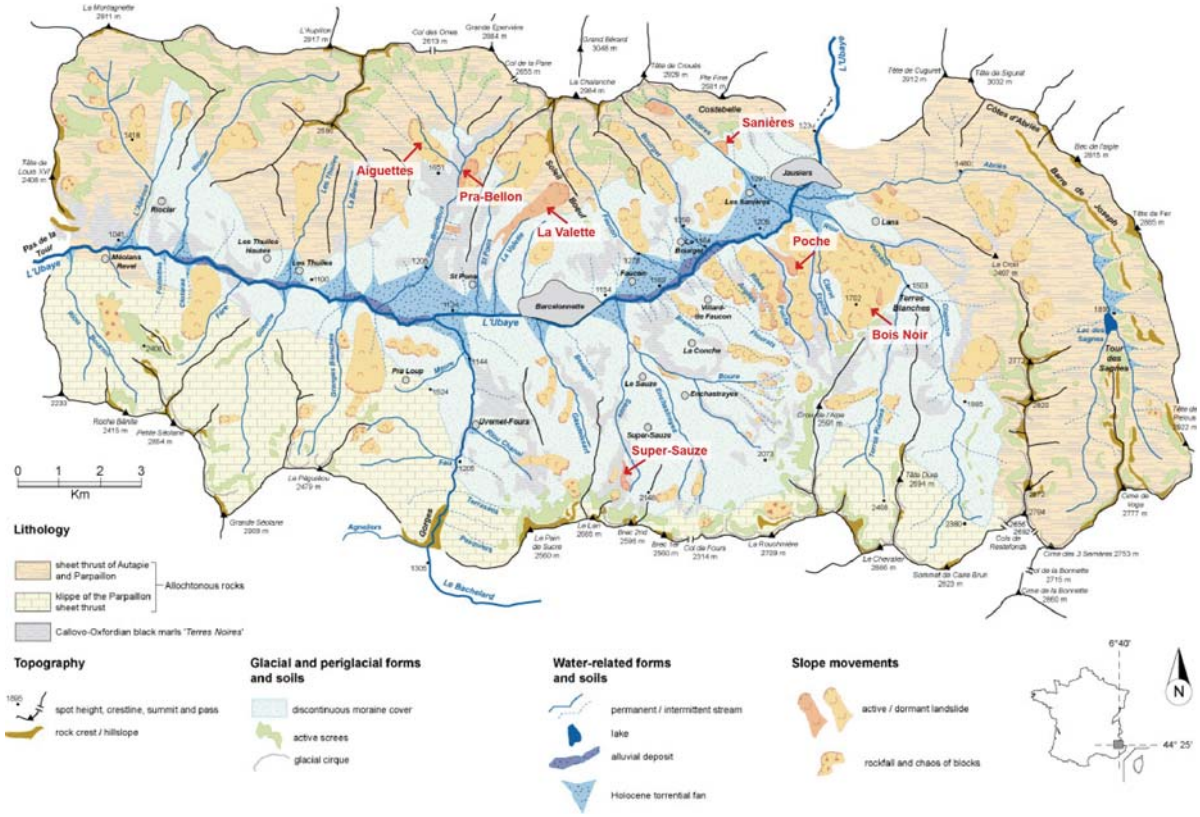

Figure 2-8: Simplified geomorphological map of the Barcelonnette Basin and location of the main active and relict landslides (after Remaître, 2006 and Kappes et al., 2011).

2.3.4.1. Distribution of landslides at the regional scale

The northern zone of the valley is affected by the La Valette landslide (see Fig. 2-5a, 2-8) triggered suddenly in February 1982. It is directly located uphill of the Barcelonnette municipality. Since the 1990's, it has been continuously monitored due to its frequent activity and the potential risk for the inhabitants. In that area, the Riou-Bourdoux catchment is the best-known torrent in the Ubaye valley. It is a small tributary of the Ubaye River but it has been considered as the most hazardous torrential area in France (Delsigne et al., 2001). Within this huge basin (i.e. 2,000 ha.) the Pra Bellon sector is particularly unstable and includes a landslide of several million cubic meters in slow and continuous movement. The Aiguettes landslide is dated from the previous glaciation it became really active in 1970 (see Fig. 2-8). Analysis of past events on the Aiguettes landslide was based on growth-ring series (Lopez-Saez et al., 2013a). Uphill, some instability is also observed at the La Pare slope. Recorded by

DInSAR measurement (2007-2009; see next chapter) and confirmed during a field campaign (2013), the entire slope seems unstable with the presence of cracks, scarps and counter-slopes.

Some instabilities are also observed in the municipality of Barcelonnette (e.g. on the way to the "Les Allemands" hamlet and at the swimming pool with the "Adroit" landslide). The Faucon catchment is mostly prone to debris flows (e.g. large events occurred in 1996 and 2003). To the east, DInSAR results have also revealed some instability on Costebelle sector. Most recently, in August 2013, a large rockslide has been triggered in the Sanières torrent and the municipality of Jausiers is directly threatened.

The southern zone of the Barcelonnette basin, between the municipalities of Jausiers and Enchastrayes, is affected by several landslips of various sizes, both active and dormant. In the forested sector of la Frache, the Bois Noir translational slide occurred after a period of excess cumulative rain at the beginning of the 1990s (Malet et al., 2007). However, it seems that a combination of distant multi-annual factors with seasonal or monthly parameters may be attributed to the triggering of the landslide (Flageollet et al., 1999). In addition, the construction of a forest road in 1981 may have increased susceptibility to landsliding (Lopez-Saez et al., 2011). The Poche landslide developed in black marls is observed in the Poche river basin (Fig. 2-8). Triggered in the 19th century and between 1956 and 1971, it remains active nowadays. To the southwest on the north-facing slope of the Barcelonnette Basin, the complex Super-Sauze landslide has developed in the soft clay-shales of a torrential basin (see Fig. 2-8). Triggered in the 1960's, it is really active and therefore, well instrumented and studied by scientific teams of all over the world.

Some landslides occurring in intensively fractured hard rocks also affect the Eastern zone drained by the Abriès torrent which is an asymmetric valley in highly fractured sandstones. The gentle slopes there (10–30°) are covered by moraine deposits and by coniferous forests or grasslands. These slopes are affected by shallow rotational or translational slides triggered by the undercutting of torrents (Thiery et al., 2007). In contrast, the steep slopes (30–70°) are characterized by bare soils and affected by rockfalls on sandstones (e.g. at the main road going to the "Col de la Bonnette").

2.3.4.2. Landslide case studies

Different landslide types are presented in details because of o their continuous activity, their potentiality of reactivation and/or their threat to the inhabitants of the valley. Some are located in the northern zone (i.e. the Aiguettes, Pra Bellon, La Valette, Adroit and Sanières landslides) and the others are in the southern zone (i.e. the Super-Sauze and Poche landslides; see Fig. 2-10). Table 2-1 references the landslide properties and geoscientists who have studied them. In addition to field observations (2011-2013), the researches already done on these case studies are briefly summed up here. Some landslides were also detected and/or studied kinematically thanks to DInSAR measurements in the next chapter.

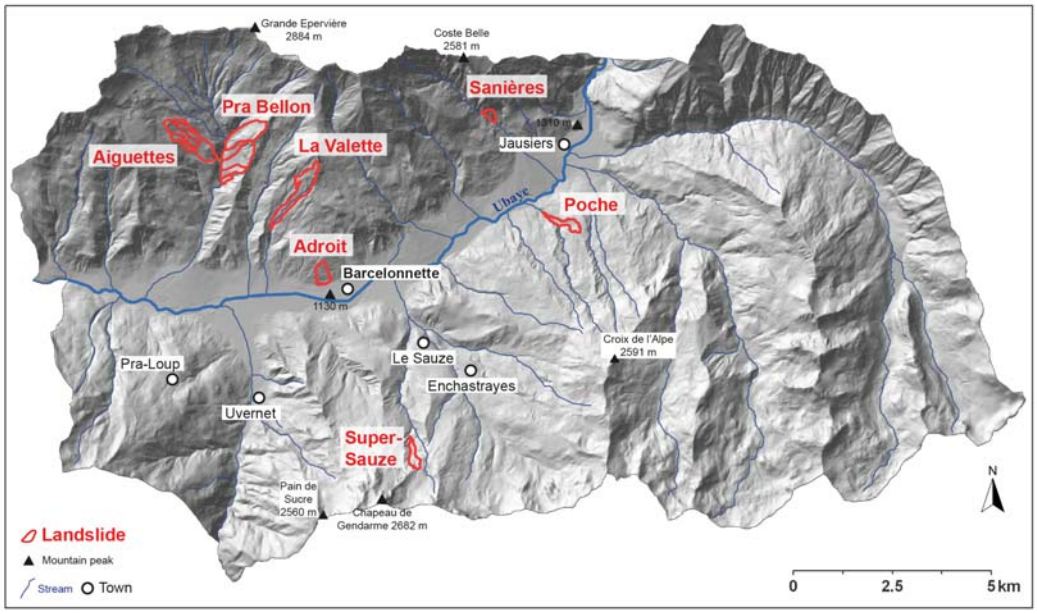

Figure 2-9: Location of case studies: the Aiguettes, Pra Bellon, La Valette, Adroit, Sanières, Poche and Super-Sauze landslides.

Table 2-4: Descriptive parameters of the landslide case studies.

Name	*Type*	*Triggering date*	*Elevation (m)*	*Extension (m)*	*Velocity* (cm.day^{-1})	*References*
Aiguettes	Translational	Late 19th century	1740-1980	800 (l) 400 (w)	?	Stien, 2001; Utasse, 2009; Lopez-Saez et al., 2013a; Corona et al., 2014.
Pra Bellon	Rotational	15th century	1470-1750	1750 (l) 450 (w)	5 (70s)	Braam et al., 1987; Caris and Van Asch, 1991; Weber, 1994; Dehn and Buma, 1999; Mathieu, 2009; Utasse, 2009; Lopez-Saez et al., 2012, 2013a.
La Valette	Mudslide Complex	1982	1240-2070	2000 (l) 200-500 (w)	0.3-0.6	Le Mignon and Cojean, 2002; Maquaire et al., 2003; Squarzoni et al., 2003; Delacourt et al., 2007; Leprince et al., 2008; Kappes et al., 2011; Hibert et al., 2012; Travelletti et al., 2012, 2013; Kurtz et al., 2014; Stumpf et al., 2014; Schlögel et al., 2015a.
Adroit	Rotational	2012-2013	1135-1300	550 (l) 300 (w)	0.1-0.9 (04-05)	Stien, 2001
Super-Sauze	Mudslide Complex	1960s	1740-2105	900 (l) 135 (w)	< 0.4	Flageollet et al., 1999; Malet et al., 2002, 2003, 2005, 2007; Maquaire et al., 2003; Malet, 2003 Casson, 2004; Delacourt et al., 2007; Travellett et al., 2008, 2012, 2014; Kappes et al., 2011; Tonnellier et al., 2013; Stumpf et al., 2014; Kurtz et al., 2014.
Poche	Mudslide Complex	> 1855	1200-1500	1200 (l) 150-300 (w)	< 0.4	Manné and Schwin, 1998; Schmutz, 2000; Guillon, 2001; Le Mignon and Cojean, 2002; Maquaire et al., 2003; Delacourt et al., 2007; Kappes et al., 2011; Mazeau, 2013; Stumpf et al., 2014; Kurtz et al., 2014; Schlögel et al., 2015a.
Sanières	Translational Rockslide	2013	1500-1650	435 (l) 200 (w)	?	Mathieu et al., 2014

A. <u>The translational Sanières rockslide</u>

The Sanières landslide is a large rockslide that occurred in early August 2013 in the lower part of the Sanières catchment, on the left side of the torrential channel (Fig. 2-11a). This stream is located on the right bank of the Ubaye River, about 2 km NW of the municipality of Jausiers. A large amount of debris has been mobilized during several days along a 475-m length cliff, reached and filled the downslope

channel (Fig. 2-11b). The slope is still unstable and the local stakeholders are expecting the formation of a debris-dam in the channel which could lead to a debris flow in case of failure, threatening directly the urban area of Jausiers (Fig. 2-11c). This unstable rockslide requires monitoring in order to track the evolution of the sliding processes and assess hazards.

Photogrammetry combining terrestrial and airborne LiDAR has been applied to monitor the evolution of the slide from August 2013 to April 2014. DEMs derived from ground-based pictures taken from the lower part of the slope did not include any stable area, preventing their georeferencing. Pictures obtained from airborne photogrammetry include stable areas and were georeferenced using the LiDAR aerial survey point-cloud. Preliminary displacement map created with an image matching technique is expressed in pixels. This technique was applied to two images pairs, in September 2013 just after the main slide event and in early November 2013 (Fig. 2-12). Then, a Structure from Motion technique could be used to generate DEM from the two aerial acquisitions (Westoby et al., 2012). As this landslide occurred very recently, its monitoring has just started and a few analysis has been done so far.

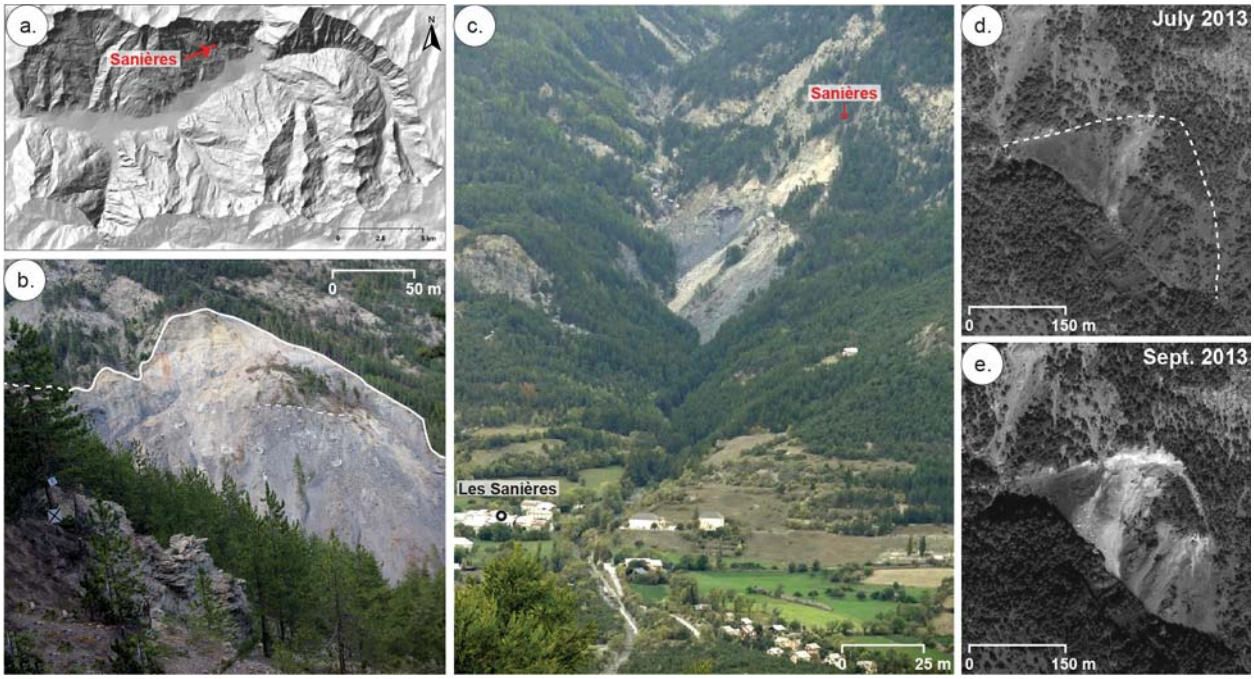

Figure 2-10: Morphology of the Sanières rockslide (a) Location (b) View on the head scarp to the NE. (c) View of the Sanières valley to the north. (d) Pre-event orthophotograph in July 2013. (e) Post-event orthophotograph in September 2013.

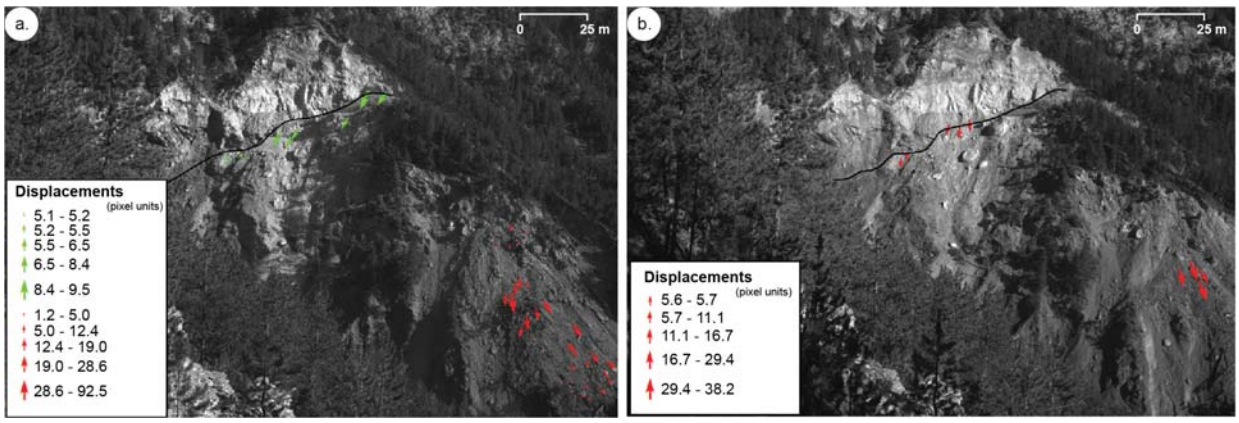

Figure 2-11: Displacement fields obtained by time series processing from pairs of images taken (a) in September 2013 and (b) in October/November 2013 (Mathieu et al., 2014).

B. The translational Aiguettes landslide

The Aiguettes landslide is located in the Riou-Bourdoux torrent. It is mainly characterized by a translational slide with a rotational component at its upper part (Fig. 2-13a). The Aiguettes landslide is 800 m long, 400 m wide and ranges from 1740 to 1980 m a.s.l. The site is characterized by irregular topography with a mean slope angle of ~20°. Geology is characterized by a 9-m thick top layer of morainic colluvium formed of blocks of Triassic limestone and dolomite buried in a sandy matrix (Fig. 2-13c). The colluvium is underlain by autochthonous Callovo-Oxfordian black marls (Stien, 2001; Utasse, 2009) which are very sensitive to weathering and erosion (Antoine et al., 1995). They principally constitute the three main scarps (Fig. 2-13b). Secondary scarps are observed in the ablation (see Fig. 2-13c) and intermediate areas as well as counter-slopes.

Vegetation is highly disturbed or completely removed in some active areas (e.g. Fig. 2-13e). In the whole site, tilted and deformed trees clearly indicate that the Aiguettes landslide has been affected by multiple reactivations in the past. According to Lopez Saez et al. (2013a), dendro-geomorphic data helps to define two activation phases in the 1880s and 1910s on the basis of trees growing on the landslide. In addition, they estimate the mean return period for the landslide at 0.11 event.yr^{-1} for the period 1891–2010. The number of reactivations clearly increases from 3 events for the period 1921–1970 to 7 events for the period 1971–2010 (Lopez-Saez et al., 2013a). Maximum decadal frequencies (3 events) are observed in 1971–1980. For the period 1980–1990, the Aiguettes reconstruction shows a complete absence of landslides whereas an increase in landslide frequency is observed at the regional scale, partly related to the triggering of mudslides at La Valette and Super Sauze (Malet, 2003). Moreover, analyses confirmed the primordial role of winter total precipitation (from December to April) in landslide triggering.

In 1995, local risk managers from RTM conducted some investigations and a draining system was installed (Stien, 2001). In October 2012, some field visits allowed us to notice that the landslide is locally really active (i.e. in its upper part; see Figs. 2-13b-e). In spring 2012, local risk managers conducted the construction of a new check dam in order to channelize the Aiguettes torrent (Fig. 2-13f) even if the risk for the inhabitants is limited.

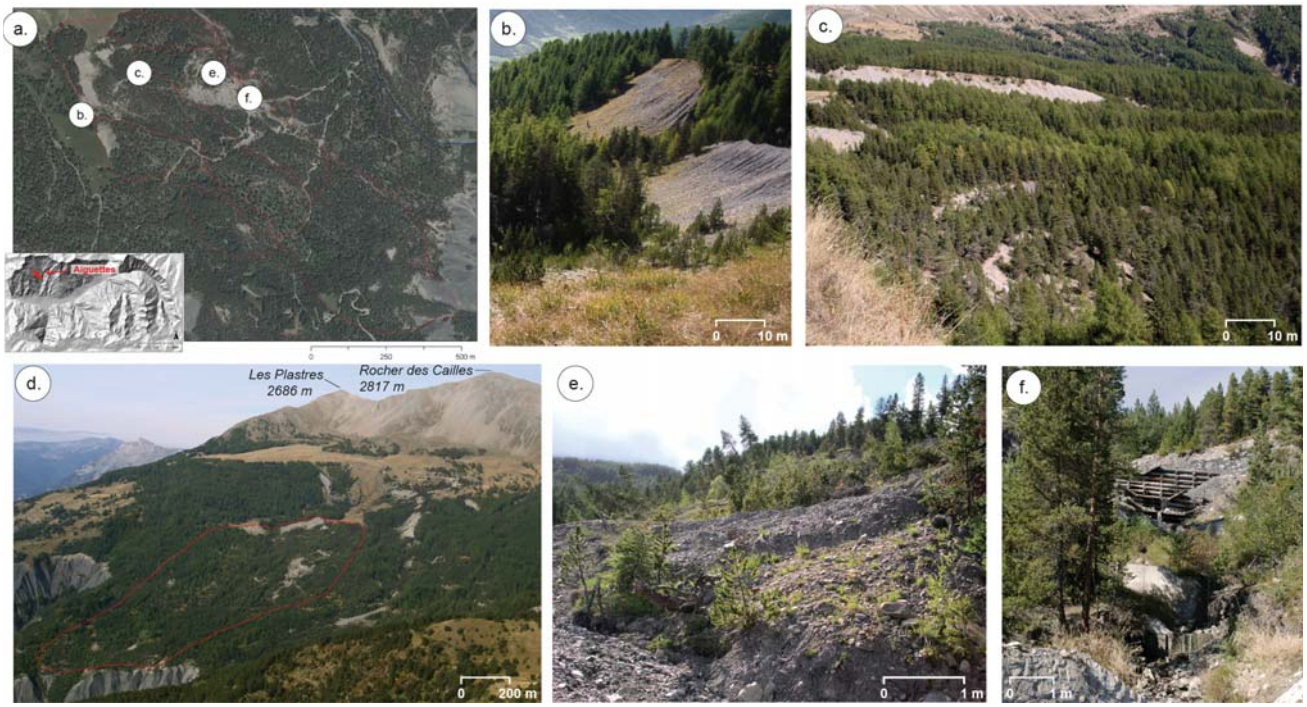

Figure 2-12: Morphology of Aiguettes landslide in the Riou-Bourdoux catchment. (a) Orthophotograph of 2009 locating the different slides and some features. (b) View to the southeast of the main scarp. (c) Ablation area of the

landslide with secondary scarps. (d) View of the whole landslide to the west direction, taken from the opposite crest. (e) View of the active part of the landslide body made of black marls almost free of vegetation. (f) Check dam constructed in October 2012 at the Aiguettes torrent.

C. The rotational Pra Bellon landslide

Like the Aiguettes landslide, the Pra Bellon sliding area (Fig. 2-14a) is located in the Riou-Bourdoux catchment, on the north-facing slope of the Barcelonnette basin, 3 km north of the Saint-Pons village. More precisely, a complex of embedded slides in a hilly vegetated area can characterize the entire slope (Fig. 2-14b, c and d), which makes complicated the kinematic analysis and the dating of the instability. With a length of ca. 1,000 m, a width of ca. 400 m and an altitude ranging from 1400 to 2200 m a.s.l., the active part of the Pra Bellon landslide (Fig. 2-14b) remobilised 1.5-2*10^6 m^3 of rocks. Slopes are constituted by weathered marls, flysches and covered by moraine deposits. The impermeable black marls are 300-m thick with a dip-angle of 20° NE. The Autapie overthrust passes through the "Bernarde" crest.

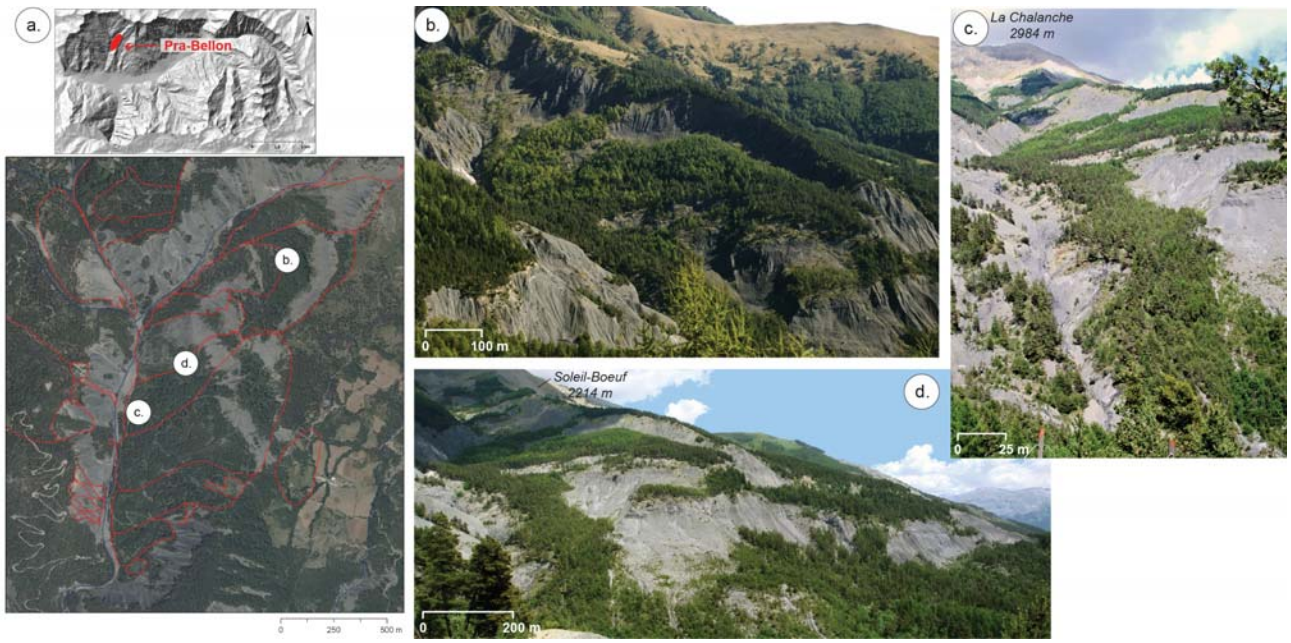

Figure 2-13: Morphology of Pra Bellon landslides sector in the Riou-Bourdoux catchment. (a) Orthophotograph of 2009 locating the different sliding compartments. (b) View to the northeast of uppermost sliding zone. (c) View from Riou-Bourdoux torrent the Ablation area of the landslide with secondary scarps. (d) View to the northeast direction of the landslide scarps.

The landslide probably started after previous glaciation with the melting of the ice cap (Braam et al., 1987). Its activity seems to date back to at least the 15th century when the area was almost completely deforested (Weber, 1994). In 1663, a main activation was recorded. Recent reactivations have been noticed between 1956-1963. Peaks of activity have been recorded during the period 1970-1973 with a downslope progression of the slide and velocities of 5 $cm.day^{-1}$. Between 1974 and 2009, some shallow translational landslides and debris flows occurred (Mathieu, 2009). Although precipitation certainly plays a crucial role in the triggering of both processes, intense rainfalls capable of generating debris flows in the Riou-Bourdoux catchment (Remaître, 2006) will not necessarily be sufficient to cause the Pra Bellon landslide to reactivate. Highest return periods associated with major probabilities of reactivation are mapped in the central part of the landslide body on each side of a recent earthslide (Lopez-Saez et al., 2012). Despite forest restoration efforts in the basin, the return period of landslides at Pra Bellon sharply increased over the last 50 years, and might one day threaten the inhabitants in case of landslide-dam.

D. The rotational Adroit landslide

The Adroit landslide is located to the right riverbank of the Ubaye River, overlooking the town of Barcelonnette. Fig. 2-15a shows the most active sliding area which is a part of an old bigger landslide of 1500-m length and 1300-m width. The soil is mainly clayed mixed with moraine deposits. The geology is constituted of weathered Callovo-Oxfordian marls. A hummocky topography with some deformation features is observed along the slope. Absence of cracks or clear scarps suggests that the main landslide is latent with a reactivated part (see Fig. 2-15b).

The landslide was triggered after the last glaciation and the decompression of the ground and became active in a lower extent from 2000 (Stien, 2001). Two houses were considered as unliveable due to the numerous fissures and the danger of the site. In 2001, an acceleration of the displacement, slumping the road, was registered upslope to the college. Nowadays the instability is still visible as shown by the Figs. 2-15c-f taken in October 2012. The meadows of the eastern border of the landslide are characterized by slope ruptures (Fig. 2-15c). Trees visible along the mapped area (e.g. in the forest and next to the road) are affected by the instability (Figs. 2-15d-f). The road to the south of the swimming pool was still affected by the movement in 2012 (see Fig. 2-15f) even if some remediation works were conducted in 2004-2005. Following a preliminary study made by the local risk managers attesting the landslide hazard, some piezometers and inclinometers were installed on the unstable slope. However, during the 6-month period of analysis, only millimetric displacements were recorded and hydrostatic levels did not change much. According to our knowledge, the landslide is still moving extremely slowly and some reactivation are expected which could affect the infrastructure.

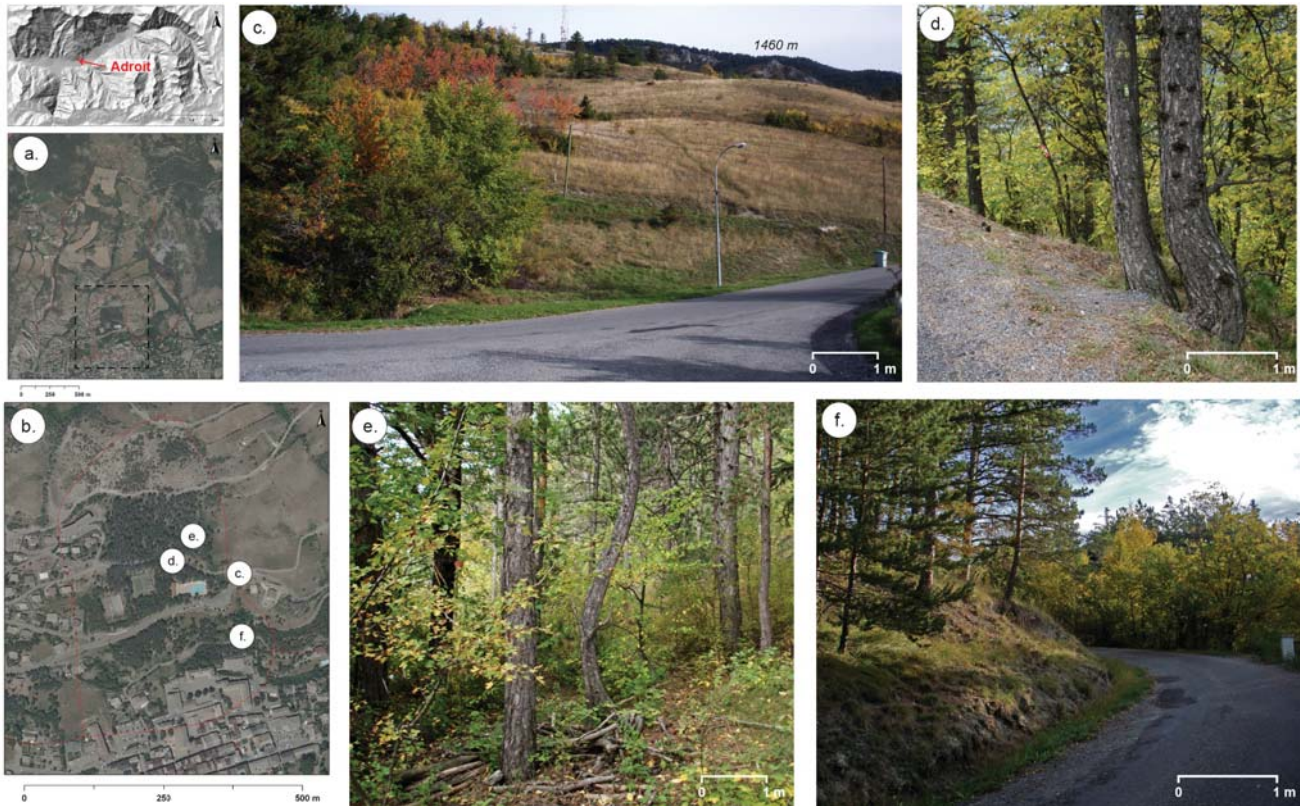

Figure 2-14: Morphology of the Adroit landslide located in the town of Barcelonnette. (a) Orthophotograph of 2009 locating the latent Adroit landslide by a dotted black rectangle focusing on (b) the active part of the landslide and the location of the pictures. (c) View to the eastern border of the active landslide showing some lateral scarps and cracks in the meadow. (d) Disturbed trees located close to the road to the north of the swimming pool. (e) Disturbed trees in the forest of the north of the swimming pool. (f) Disturbed trees along the road to the south of the swimming pool.

E. The complex La Valette mudslide

La Valette landslide affects an area located directly upslope of the municipality of Saint-Pons in the Barcelonnette basin (see Fig. 2-16a) and is an important threat for around 170 community housings located downstream. Triggered in March 1982, it is one of the most important with its 2-km length and 0.2-km width in the lower part. The whole mobilized material is estimated at $3.5*10^6$ m^3 with about one quarter in the lower part (Travelletti et al., 2009; Fig. 2-16b and c). The La Valette landslide is a case of reactivation of an older landslide and is characterized with a complex succession of individual slides as it is often observed in deep-seated landslides. The mean slope gradient is ca. 30° in the scarp area (Fig. 2-16e and f) and ca. 20° in the transit area (Fig. 2-16d). The maximum thickness varies from 35 m in the upper part to 25 m in the medium and lower parts (see Fig. 2-16b and c). For the period 2005–2010, the observed average displacement rate is comprised between 1 and 2 $m.yr^{-1}$.

Field observations and previous remote sensing studies indicate that the general pattern of movement shows higher displacements at the scarp and gradually decreasing displacements downslope (Squarzoni et al., 2003; Delacourt et al., 2007; Leprince et al., 2008; Raucoules et al., 2013; Stumpf et al., 2014; see Fig. 2-17). Using correlation of Pleiades images, Stumpf et al. (2014) estimated the horizontal displacement of the ablation area at ca. 0.82 m during two months in 2012.

Due to its high velocity rate and its potential threat in case of huge reactivation, the La Valette landslide is well studied. Several monitoring techniques are used to characterize its dynamics and mechanisms in relation to climatic and hydrologic conditions. Mitigation works have been constructed (drainage system, storage reservoir) and an early-warning system (cameras and captors) is maintained by RTM. Differential single-frequency GPS monitoring system was installed by the OMIV observatory in order to detect changes in real-time.

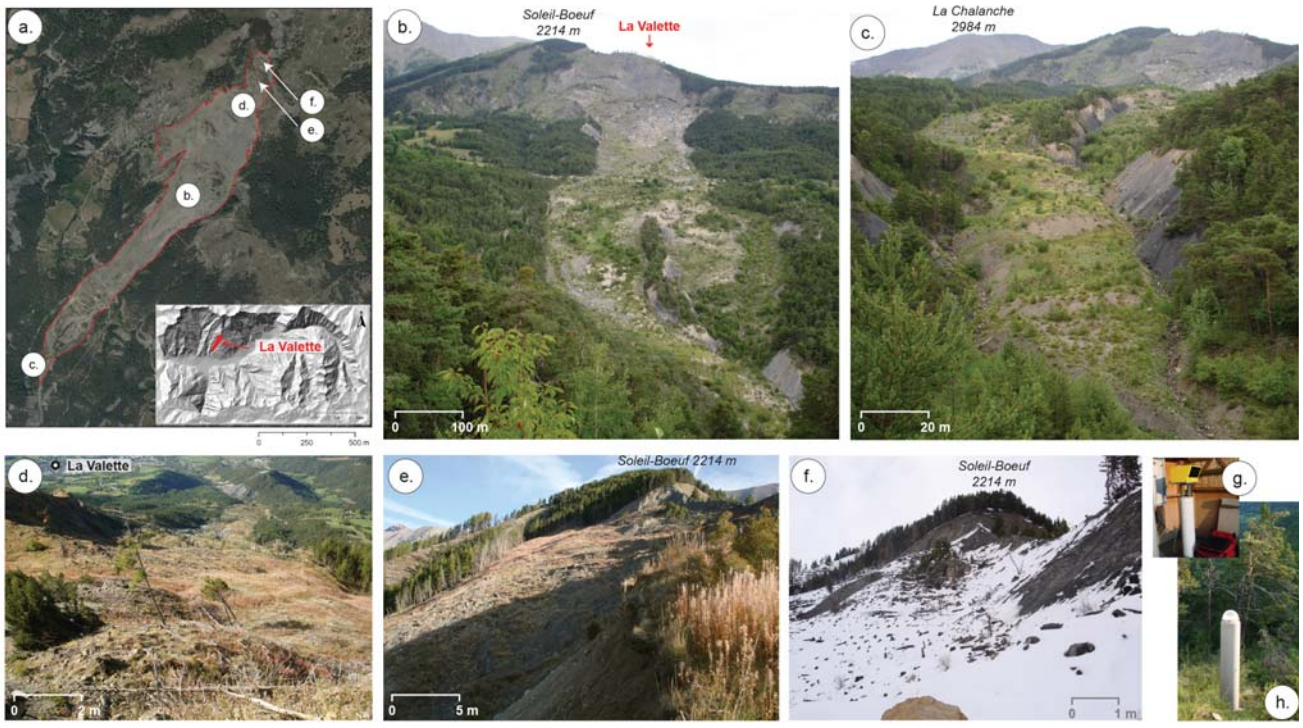

Figure 2-15: Morphology and monitoring of La Valette landslide. (a) Orthophotograph of 2009 showing the landslide in red and locating the picture views. (b) View to the northeast from the opposite crest showing the whole landslide body. (c) View from the lowermost part of the toe. (d) View to the southwest direction taken from the scarp, showing the sliding tongue. (e) View to the north of the ablation area and the main scarp. (f) View to the north of the main scarp covered by snow (April 2012). (g) LiDAR acquisition system temporarily installed on the opposite crest close to (h) the permanent dGPS antenna sending measurements in real-time.

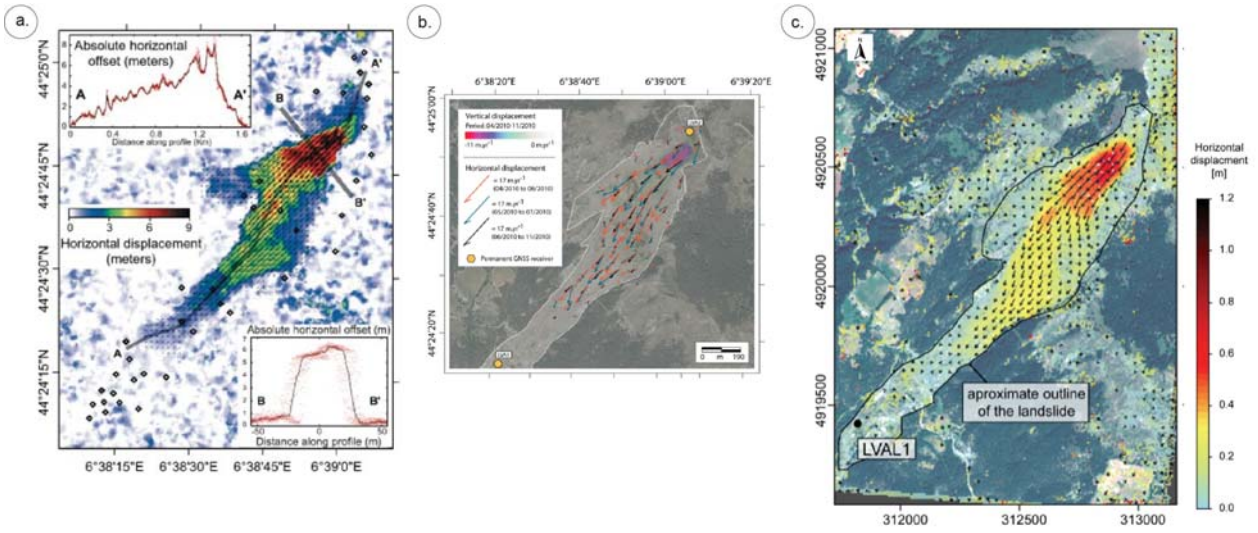

Figure 2-16: Displacement field of the La Valette landslide. (a) Absolute horizontal displacement from the correlation of two SPOT 5 images acquired on 19/09/2003 and 22/08/2004 (Leprince et al., 2008). (b) 3D displacement map for three sub-periods, i.e. between April and November 2010 derived from the correlation of X-band spaceborne images (Raucoules et al., 2013). (c) Horizontal displacement for the period 07/08/2012-05/10/2012 from terrestrial photogrammetry using GCPs (Stumpf et al., 2014).

F. The complex Poche mudslide

Contrarily to La Valette, the Poche landslide is located on the right riverbank of Ubaye in the north-facing slope of the Ubaye Valley, 5 km to the East of the municipality of Barcelonnette (Figs. 2-18a and b). Its triggering date is estimated in the middle of the 19th century, its extent characteristics are detailed in Table 2-1. The mean slope angle is ~15° in the ablation zone (Figs. 2-18 c and e) and ~20° in the accumulation zone (Figs. 2-18g and h). The maximum landslide depth, estimated both by seismic tomography and geotechnical boreholes, ranges from 10 to 25 m (Schmutz, 2000).

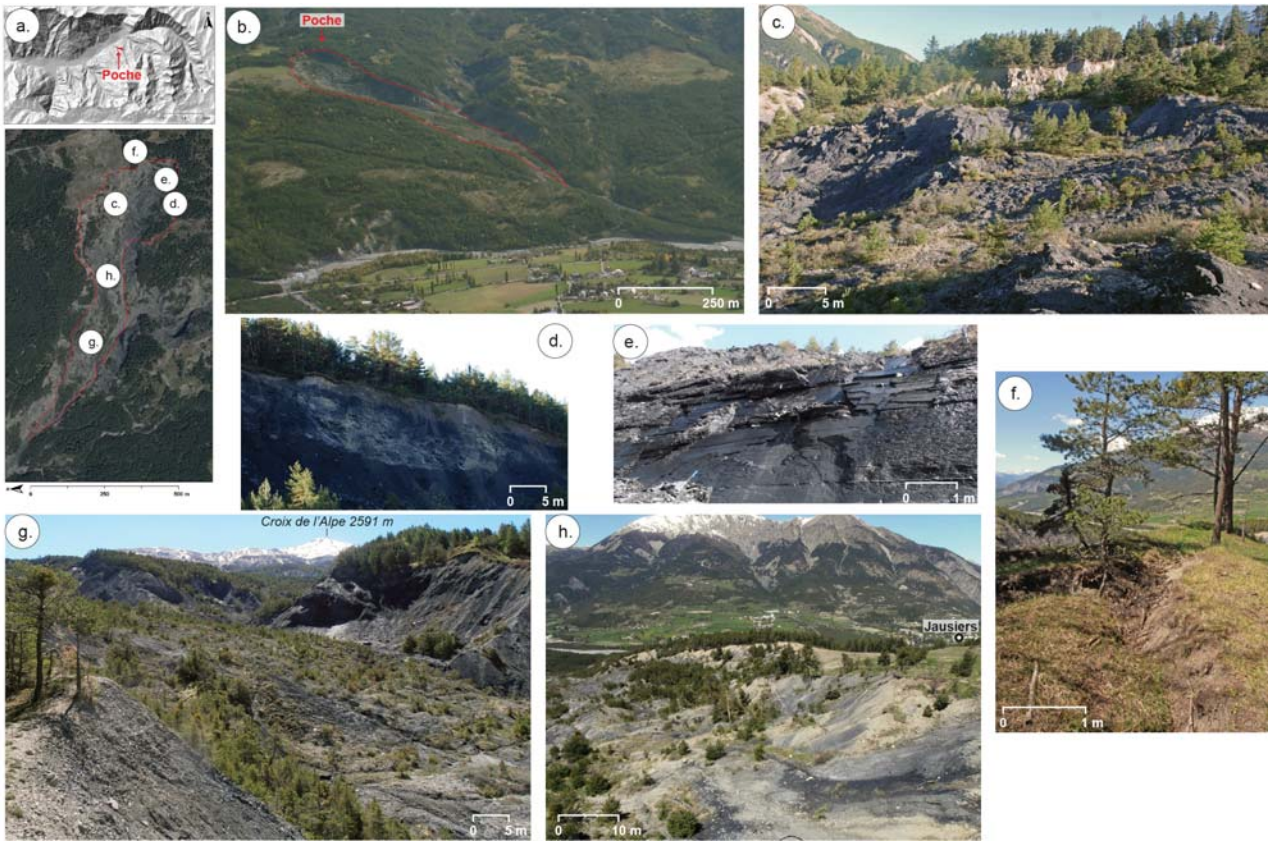

Figure 2-17: Morphology of the Poche landslide. (a) Orthophotograph of 2009 showing the landslide in red and locating the picture views (top represent the eastern direction). (b) View to the south from the opposite crest showing the whole landslide body (outlined in red). (c) View from the landslide body constituted by black marls to the NE part of the main scarp. (d) View of the southern main scarp and the contact between surficial soil, moraine deposits and black marls. (e) View on a rupture plan in the black marls dipping downslope. (f) View to northwest on a deep crack located close to the landslide crown (g) View to the south of the slowly moving landslide tongue. (h) View to the north from the top to the landslide body constituted by mixed moraine and marls deposits.

The landslide ablation zone consists of a combination of structural rock block slides to the South-East (see Fig. 2-18e) and a large rotational slide to the North-East. The 20°-dipping main scarp limits the ~10-m-thick moraine deposits and the Callovo-Oxfordian black marls (Le Mignon and Cojean, 2002; see Fig. 2-18c and d). The transit and accumulation zones present a flow-type morphology with the progressive burial of the thalweg of the Poche torrent (Fig. 2-18g). For the period 1993–2003, the displacement rates measured by total station on 10 benchmarks are ~1 cm.day^{-1} (Malet and Maquaire, 2003). In spring 2001 and 2008, higher displacement rates, up to 8 cm.day^{-1}, have been observed but nowadays, the average displacement stays below 0.4 cm.day^{-1} (Schlögel et al., 2015a). Former researches also testify high displacement rates, mainly at the middle part of the landslide (see Fig. 2-18). Nevertheless, no monitoring equipment is installed at Poche landslide but specialists from RTM regularly come to do some EDM measurements, especially to estimate a potential retrogression of the crown.

In the framework of this research, the kinematic and recent evolution of La Valette and Poche landslides were analysed by DInSAR measurements in the Chapter 3.

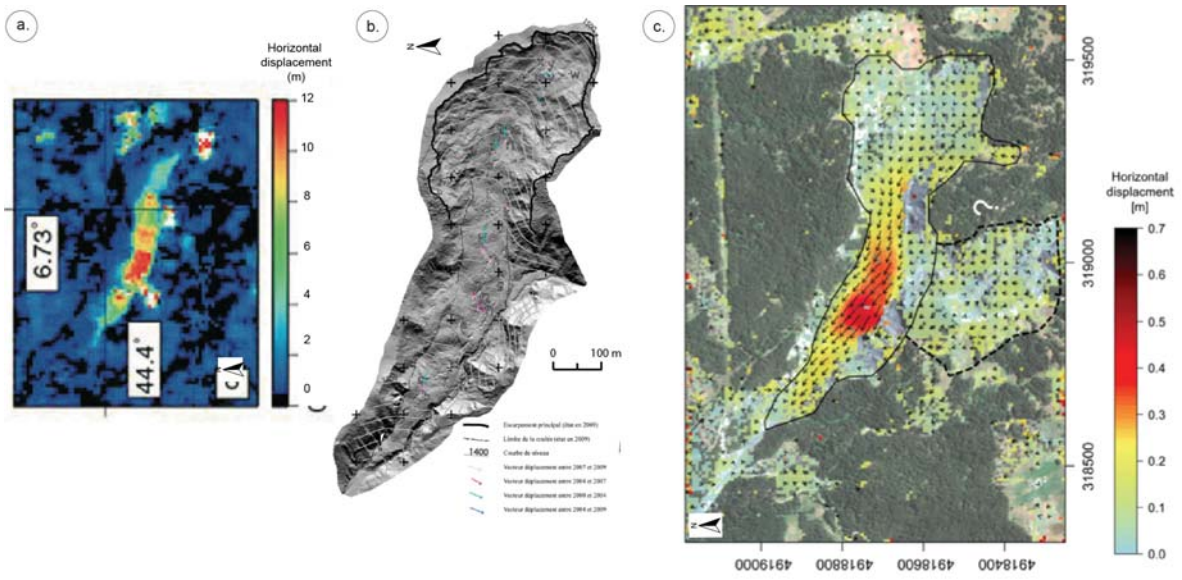

Figure 2-18: Displacement field of the Poche landslide. (a) Horizontal displacement for the period 09/19/2003–08/22/2004 derived from the correlation of SPOT5 images (Delacourt et al., 2007). (b) Horizontal displacement vector measured by comparing orthophotographs in 2000, 2004, 2007 and 2009 (Mazeau, 2013). (b) Horizontal displacement for the period 07/08/2012-05/10/2012 from terrestrial photogrammetry (Stumpf et al., 2014).

G. The complex Super-Sauze mudslide

The Super-Sauze landslide is located five kilometres to the south of Barcelonnette on the south-western border of the municipality of Enchastrayes and immediately next to the Super-Sauze ski resort. The Super-Sauze mudslide (Fig. 2-20) is a flow-like landslide characterized by a complex vertical structure associating a slip surface and a viscoplastic plug (Travelletti et al., 2008). Multidisciplinary observations (geology, geomorphology, geotechnics, hydrology; Flageollet et al., 1999) provide substantial information about its geology and geometry. Triggered in the 1960s, the Super-Sauze landslide is another example of complex landslides developed in soft clay-shales (silty-sand matrix) mixed with moraine debris. It is located in the headwater basin of the Sauze torrent between 2105 m and 1740 m for an average slope gradient of 25°. It has a length of ca. 900 m and an average width of 135 m. TEM measurements allow the estimation of maximal thickness of ca. 10m at the ablation zone and ca. 8 m at the accumulation zone (Schmutz et al., 2000). The total volume is estimated at 560,000 m^3 (Travelletti and Malet, 2012). Velocities lie in the range from 0.01 to 0.40 $m.day^{-1}$ with possible acceleration of up to 40 $cm.day^{-1}$ (Malet et al., 2002; see Fig. 2-20a).

Since the 1990s, the landslide is investigated by the University of Strasbourg (Flageollet et al., 1999). Several monitoring techniques (OMIV monitoring network) are used to characterize its dynamics and mechanisms in relation to climatic and hydrologic conditions. The kinematics of the landslide is currently monitored by dGPS, TLS and by a remote camera monitoring system (Fig. 2-20c; see some results on Fig. 2-21). Indeed, the displacements are spatially very variable all over the landslide, and directly correlated with the geometry of the covered paleotopography (Fig. 2-20d and e) and the presence of water. The paleotopography plays a role by delimiting preferential water and material pathways and thus, compartments with different kinematic, mechanical and hydrodynamical properties (Malet and Maquaire, 2003). The rate of displacement is directly controlled by the hydrological regime and period of high water levels (Travelletti et al., 2008).

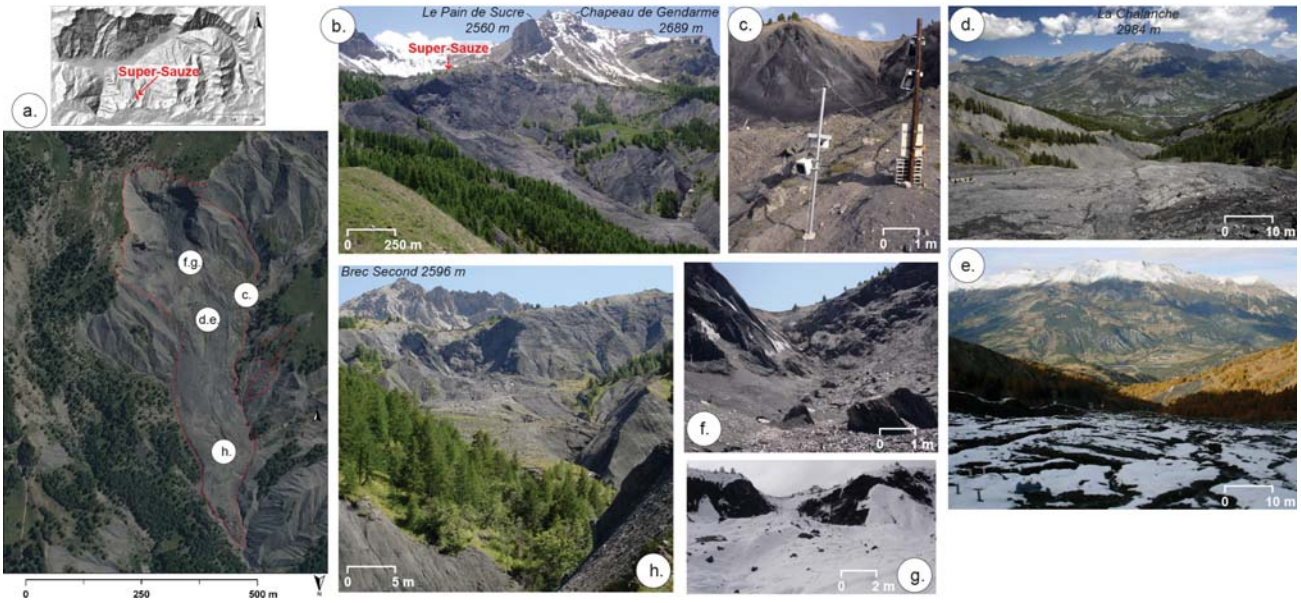

Figure 2-19: Morphology and monitoring of the Super-Sauze landslide. (a) Orthophotograph of 2009 showing the landslide in red and locating the picture views (top represent the southern direction). (b) View to the southwest from the opposite crest showing the whole landslide body. (c) View from the stable western border to the scarp of the landslide showing the camera-system installed in 2012. (d) Landscape and downslope view to the northern direction taken from the middle part of the landslide taken from the scarp, showing the sliding tongue. (e) Same view than d. showing the gullies presented at the sliding tongue (October 2011). (f) View to the south of the ablation area of the landslide with blocks of black marls. (g) View to the south of the main scarp covered by snow (April 2012).

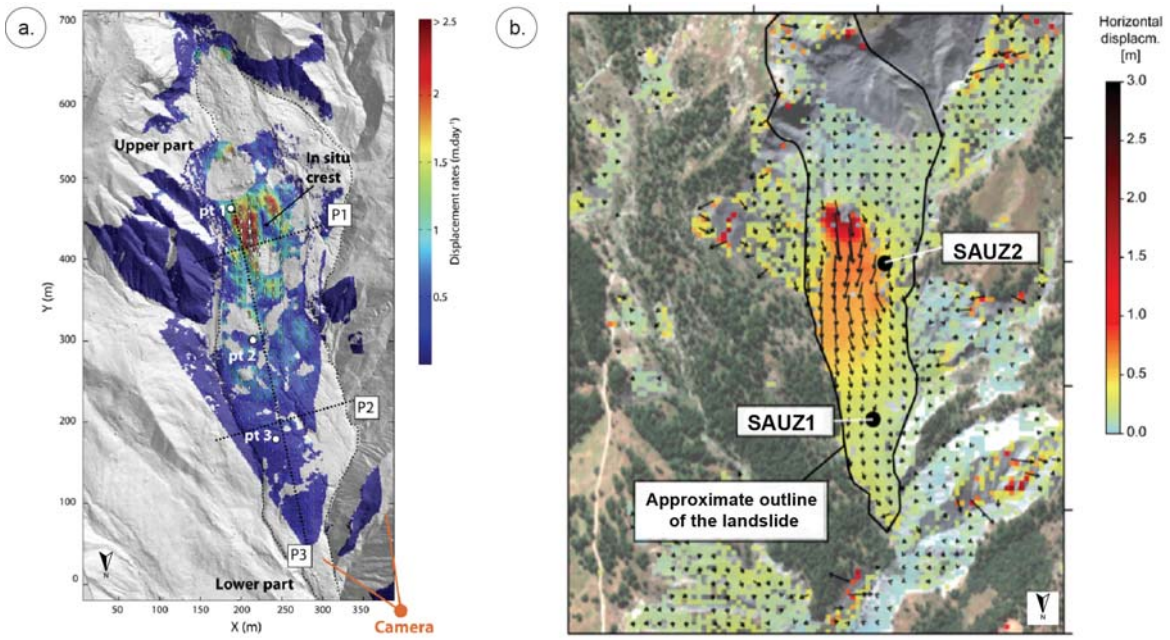

Figure 2-20: Displacement field of the Super-Sauze landslide. (a) Displacement rate measured for the period 1-4 June 2008 derived from correlation of terrestrial photographs (Travelletti et al., 2012). (b) Horizontal displacement for the period 07/08/2012-05/10/2012 from terrestrial photogrammetry using GCPs (Stumpf et al., 2014).

2.3.4.3. Climate-landslide relationships

The climate-landslide relationships have been analysed for the period from 1928 to 2003 in order to attempt to define climate conditions (and possibly rainfall thresholds) able to trigger or reactivate landslides in the study area (see Malet et al., 2007; Thiery, 2007). Annual rainfall was compared to periods of sliding activity of some landslides of the valley obtained from archives (RTM database of

events) and dendrochronology analyses (Lopez-Saez et al., 2011, 2012, 2013a, 2013b). Peaks of landslide activity can be explained by periods of high cumulative rain (like at the beginning of the 1990s) but it does not fit all the time. This can be partially explained by the dating technique. On longer time scale, datings of eccentricities of tree rings in some slopes of the study area demonstrated landslide frequencies of ca. 4 ± 2 years (Verhaagen, 1988; Buma, 2000), indicating climate characteristics favourable to a continuous activity of slope processes. Some relatively dry periods (e.g. period 1982-1990) are also characterized by the occurrence of landslides, testifying of the complexity of the landslide-climate relationships. Rainfall is one of the factors that accelerate or trigger landslides, together with other factors such as land use or tectonic activity (Corominas, 2000).

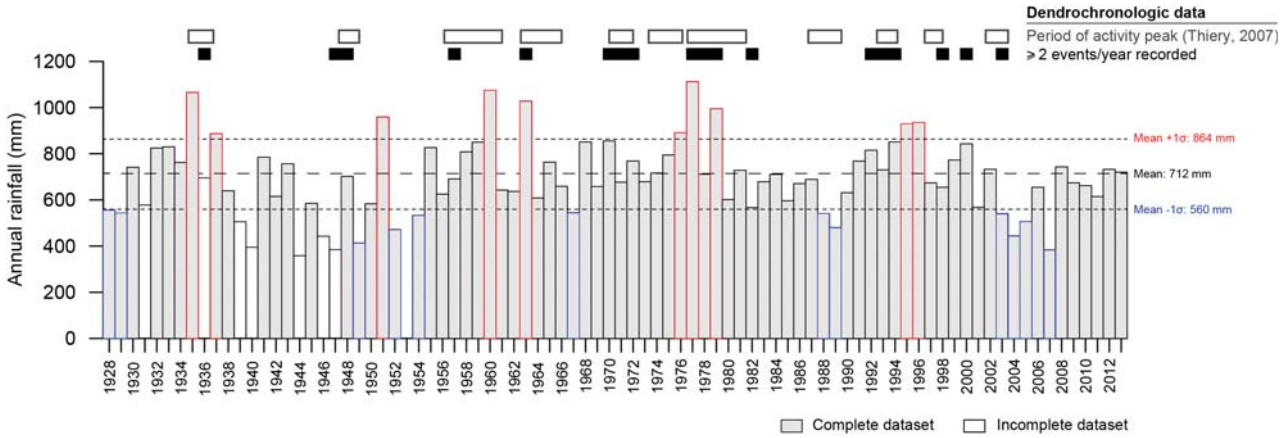

Figure 2-21: Annual rainfall (with mean and mean +/-1σ) at Barcelonnette rain gauge and landslide events recorded by dendrochronologic measurement showing periods of sliding activity and periods with at least two events registered by dendrochronologic data.

Relationships between landslide activity and meteorological conditions are discussed in Chapter 3. The next chapter also focuses on the interpretation methodology to monitor the Poche and La Valette landslides using passive remote sensing technique. The latter technique is also applied at regional scale and constitutes one of the multi-source data taken into account for the creation of the multi-date inventory and its statistical analysis.

CHAPTER 3: A multi-date and multi-scale landslide inventory for hazard assessment

The objective of this chapter is to create a multi-date and multi-scale landslide inventory by considering different sources of information (geomorphological maps, remote sensing data, field observations) at the slope- and regional scales. The chapter is divided in three sections.

Section 3.1 introduces the multi-scale analysis framework of the research. It presents the available observation data and the techniques of analysis.

Section 3.2 focuses on the analysis of landslide events at the slope scale. It presents a geomorphologically-guided methodology to interpret the kinematics of large and complex landslides using L-band SAR images. ALOS/PALSAR images are processed with ROI_PAC and NSBAS algorithms in order to create wrapped and unwrapped interferograms. DInSAR results are combined to ground-based measurements to map the extent of the deformation of some unstable slopes. The first part of this section depicts the development of the methodology to interpret InSAR signals according to different landslide types. Displacement rates and the geomorphological evolution of the landslides are evaluated for the period 2007-2010. The second part of this section is an application of the methodological framework to an active and complex deep-seated landslide controlled by structures (i.e. La Clapière landslide). The displacement information obtained from D-InSAR is then integrated in a regional multi-date inventory created from other data sources.

Section 3.3 presents the creation of a multi-date inventory for the statistical evaluation of landslide return periods and intensity. First, the visual interpretation method used to recognize the landslides is explained. It is based on the analysis of landslide features described in reports or observed on aerial photographs, geomorphological maps, elevation products, InSAR deformation maps and field surveys. Landslide intensity and return periods are evaluated using several statistical techniques. Then, relationships between the recorded landslide events and possible meteorological triggers are discussed.

The chapter highlights the complexity of handling numerous sources of information over different time periods but also their complementarity to map and analyse different landslide types.

This chapter is mainly based on the following scientific papers:

Schlögel, R., Doubre, C., Malet, J-P., Masson, F. (2015a). Landslide deformation monitoring with ALOS/PALSAR imagery: A D-InSAR geomorphological interpretation method. Geomorphology 231, 314-330.

Schlögel, R., Malet, J.-P., Doubre, C., Lebourg, T. (2015b). Structural control on the kinematics of the deep-seated La Clapière landslide revealed by L-band InSAR observations. Landslides 1-14.

Schlögel, R., Malet, J.-P., Reichenbach, P., Remaître, A., Doubre, C., (2015c). Analysis of a landslide multi-date inventory in a complex mountain landscape: the Ubaye valley case study. NHESS 15, 2369-2389.

3.1. Principles of multi-scale landslide analysis for hazard assessment

As introduced in Chapter 1, many types of landslide inventories exist, which can be created in different ways and at different scales (i.e. national, regional, slope). In the framework of this analysis, we will combine information on the evolution of landslides over several time periods at both the slope-scale (characterization of the slope kinematics; Fig. 3-1a) and the regional scale (detection, mapping and characterization of the landslide activity; Fig. 3-1b). The two analysis scales are combined for the elaboration of a multi-date landslide inventory used for the evaluation of the landslide return periods and intensity.

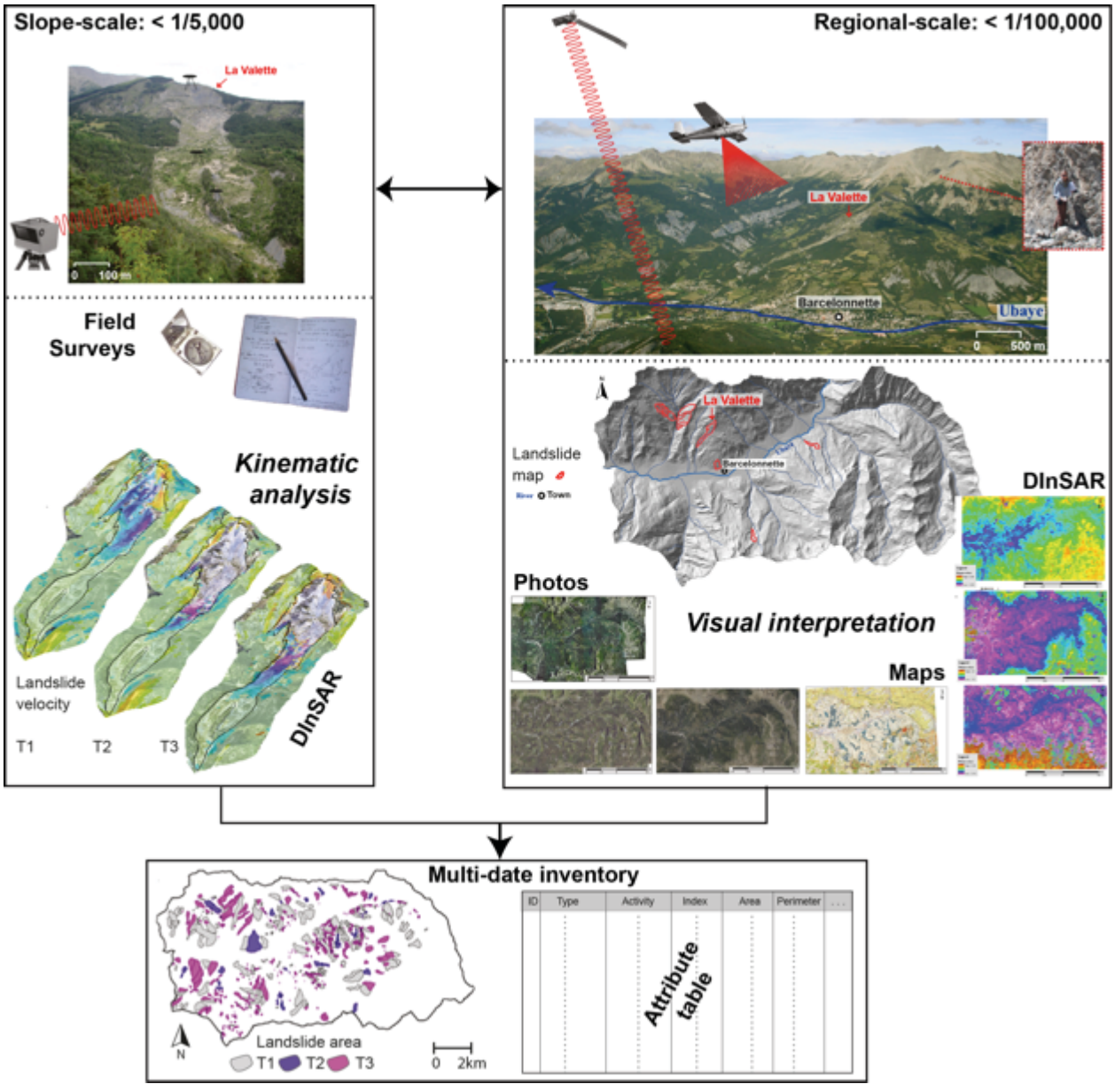

Figure 3-1: Combination of two analysis scales (slope, regional) for the creation of a multi-date landslide inventory.

According to the definition of *landslide inventory*, several parameters, like the location, the type and ideally the timing of the slope failures, are mandatory to analyse spatial and temporal patterns. They are studied to quantify long- and short-term evolution of slope movements and underline relationships to tectonic and hydro-meteorological processes (Guzzetti et al., 2012).

The creation of a landslide inventory encompassing multi-temporal information needs high quality and high-resolution data source as well as a good knowledge of the field. Visual image interpretation and field surveys are the prevailing methods for landslide inventory mapping but are very time consuming. Semi-automatic image analysis methods based on remote sensing techniques are proposed but their quality lacks behind the expert mappings (Guzzetti et al., 2012). For the moment, they are no common standards for the preparation of landslide inventory (Guzzetti et al., 2012) but it clearly depends on the skills of the expert and the purpose of the analysis.

For characterizing the landslide spatial occurrence, the landslide distribution and its relations to triggering factors, knowledge on the location and size of landslides is sufficient (Guzzetti et al., 2002; Harp et al., 2011a; Gorum et al., 2013). In the case of hazard analysis, detailed information on the landslide types and spatial features (e.g. source and runout sub-units) is required (Fell et al., 2008a; van den Eeckhaut and Hervás, 2012). In addition, large disagreements in the mapping can be observed among experts both in terms of total landslide affected areas (Carrara, 1993; Ardizzone et al., 2002; Galli et al., 2008; Fiorucci et al., 2011) and in terms of landslide classification. Such disagreements have to be critically quantified to ensure reproducible results and to provide measures of the uncertainties.

Considering the absence of established standard maps, the strong influence of geoscientist skills, the quality and availability of the observation data, we propose a multi-source data approach for the creation of the inventory. Indeed, we assume that more the dataset is complete, more the interpretation of the results will be relevant and representative of the field conditions. A large observation set of multi-source data covering the period from 1850 to the actual is used (see Fig. 3-2). According to the characteristics of the available data and the interpretation methods, we divided the periods of analysis in three: from 2007 to 2010 (see section 3.2), from 1956 to 2009 and from 1850 to 2012 (see section 3.3).

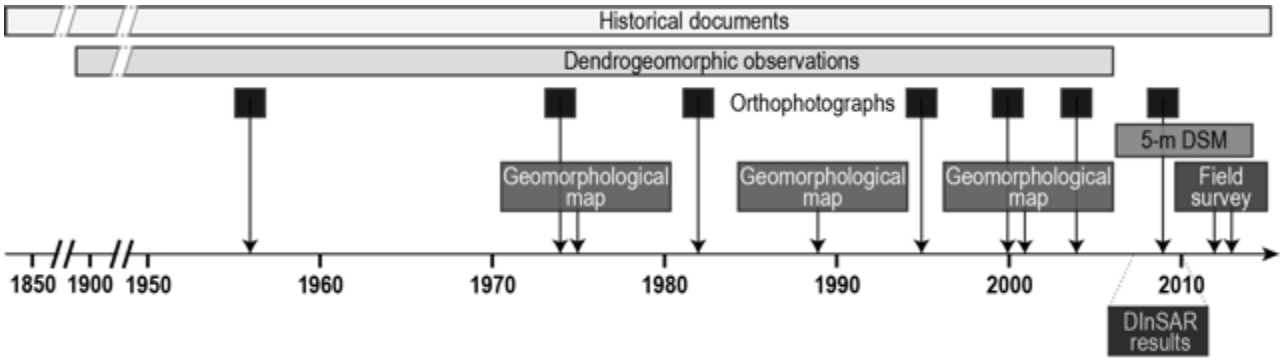

Figure 3-2: Timeline of the available observations.

The specific objectives of this chapter are the following:

- To detect and map the evolution of landslides by using different remote sensing techniques;
- To develop a method for analysing L-band SAR images to evaluate quantitatively the kinematics of several landslides, and validate the observations with in situ measurements;
- To prepare a homogeneous multi-date inventory for the three time periods at the regional scale by combining several landslide descriptors;
- To analyse the descriptors and evaluate the landslide return periods and intensity;
- To relate the periods of landslide activity to triggering factors mainly linked to meteorological events.

3.2. Characterization of landslide kinematics at the slope scale: a geomorphologically-guided methodology for the analysis of L-band SAR interferograms

This section illustrates some potential uses of SAR images for landslide mapping and monitoring despite significant challenges persisting in regard to the practical applicability of the technique to landslide investigations (e.g. Singhroy et al., 1998; Wasowski et al., 2002; Colesanti and Wasowski, 2006). Coherence loss (a problem typical of vegetated areas) and atmospheric effects are the most important factors that limit the usability of radar satellite images. Using higher spatial resolution sensors (e.g. RADARSAT 2, TerraSar-X) or low band frequency images (e.g. L-band; ALOS) seems more suitable for landslide applications (e.g. Strozzi et al., 2005), especially when long series of SAR images are not available.

We used ALOS/PALSAR images and a classical DInSAR technique (Fig. 3-3a) to investigate the landslides located in Fig. 3-3b. A resample 25-m DEM (Fig. 3-3b) was used for the InSAR processing chains (ROI_PAC and NSBAS) to produce deformation maps. Coherence maps (Fig. 3-3c) have been calculated as indicator of the decorrelation of the scene and used to create the filtered and unwrapped interferograms (Fig. 3-3d). More details on the InSAR technique can be found in Appendix 1.

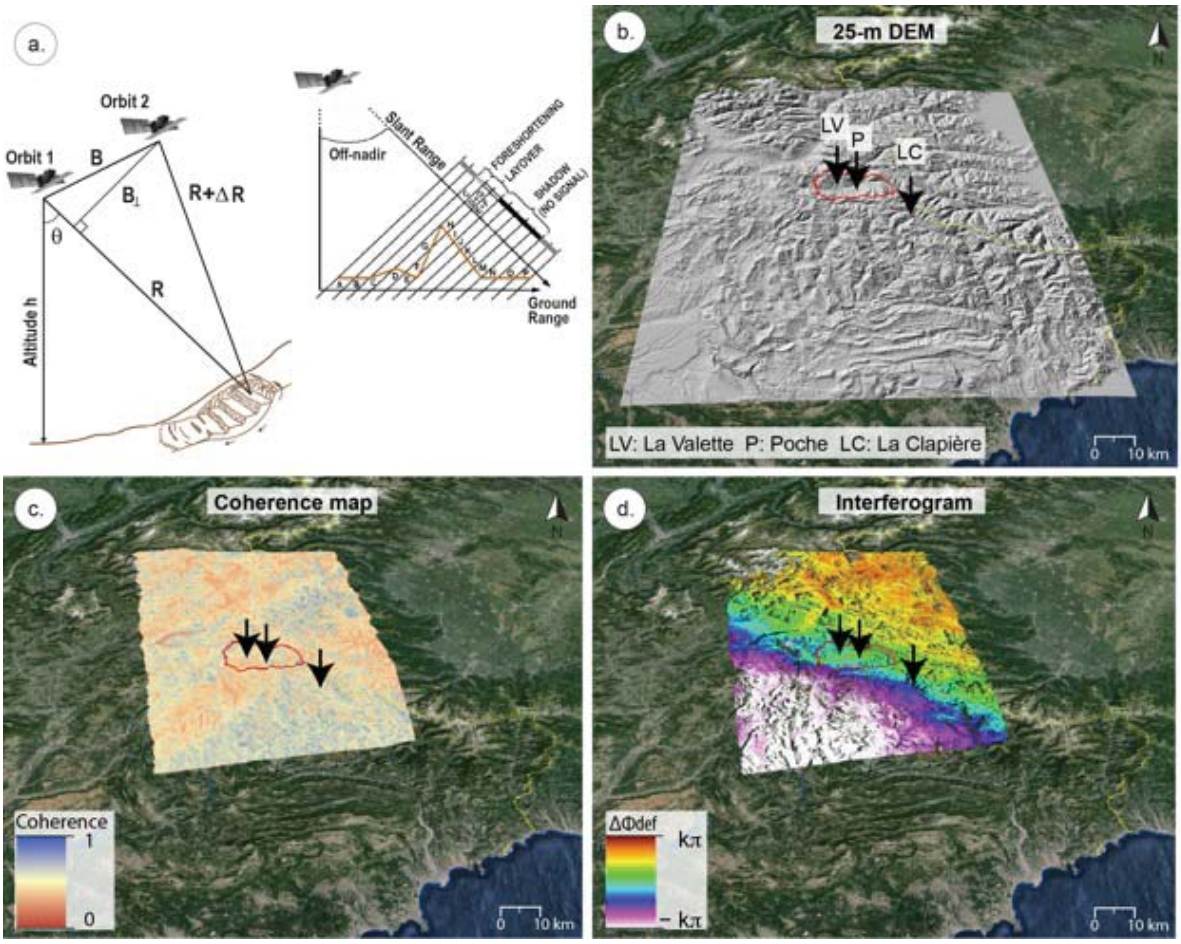

Figure 3-3: SAR interferogram imaging geometry in the plane normal to the Line of Sight (LoS) direction applied to landslide mapping. (a) Principle of DInSAR for landslide investigation (with B: Baseline, R: Distance along the Line of Sight, θ: incidence angle) and geometric distortion effects (Colesanti and Wasowski, 2006): foreshortening (range pixel C), layover (range pixels D, G, E, F) and shadowing (range pixels H–N). (b) Extent of the 25-m DEM resampled according to the L-band sensor resolution (i.e. around 10 m) and location of the La Valette, Poche and La Clapière landslides investigated in Section 3.2. (c) Example of coherence map. (d) Example of unwrapped interferogram.

According to the available SAR dataset and the complexity of the field conditions, we preferred to post-process manually the interferograms obtained by the classical DInSAR approach. Some residual noise and decorrelation due to the atmospheric contribution (Appendix 1) are observed in the interferograms. In order to compare them and to create velocity maps on the basis of stable areas, phase signals are corrected at slope scale. The post-processing procedure leading to the interpretation the interferograms in terms of slope deformation is detailed in Appendix 2. For this purpose, we have developed a GIS-toolbox (python code) to correct automatically the phase signal at slope-scale. The aim is to shift the phase value to zero for the slopes considered as stable on the basis of the previous inventory, by subtracting the median phase value (Φ_{med}) of the zone surrounding the landslide to the phase values of the whole area. The resulting phase for the wrapped interferograms is thus in the range [$-\pi-\Phi_{med}$, $\pi-\Phi_{med}$]. In all the deformation maps presented in this section, the stable areas are around a zero value which corresponds to a green colour. At the end of the procedure, deformation maps are created to characterize the kinematic evolution of landslides by comparison of results over time. While unwrapped interferograms allow us to obtain velocity maps, wrapped ones give us information about the deformation field(s) and deep structures. Validation of the results is based on ground-based measurements and field surveys. The two following sections are based on this methodology.

3.2.1. Development of the interpretation methodology on representative case studies: La Valette and Poche landslides

This section describes the development of the geomorphologically-based method to interpret L-band SAR interferograms for the analysis of landslide kinematics at slope-scale. The technique is applied to representative landslide types of the study area, namely the La Valette and Poche landslides (Fig. 3-3). This work is published in the peer-reviewed journal *Geomorphology*.

Geomorphology 231 (2015) 314–330

Contents lists available at ScienceDirect

Geomorphology

journal homepage: www.elsevier.com/locate/geomorph

Landslide deformation monitoring with ALOS/PALSAR imagery: A D-InSAR geomorphological interpretation method

Romy Schlögel *, Cécile Doubre, Jean-Philippe Malet, Frédéric Masson

Institut de Physique du Globe de Strasbourg, CNRS UMR 7516, Université de Strasbourg/EOST, 5 rue Descartes, 67084 Strasbourg, Cedex, France

ARTICLE INFO

Article history:
Received 31 May 2014
Received in revised form 7 November 2014
Accepted 21 November 2014
Available online 19 December 2014

Keywords:
Landslide
InSAR
ALOS/PALSAR
Displacement monitoring

ABSTRACT

The objective of this work is to propose a geomorphologically-guided method for the interpretation of L-band ALOS/PALSAR interferograms created by Differential Interferometric Synthetic Aperture Radar (D-InSAR). The interferograms are used to estimate the deformation pattern of two rapid and large landslides (Poche, La Valette; South East France). The wrapped and unwrapped phase values are interpreted for different movement types (rotational, translational, and complex sliding) and two ranges of surface displacement rates. Kinematic subunits are detected for both landslides, and zones affected by enlargement or retrogression are identified. The InSAR-derived displacement rates are consistent with ground-based measurements and with remote estimates of the displacement from C-band and X-band satellite SAR sensors. The results demonstrate the potential of L-band ALOS/PALSAR imagery for the monitoring of active landslides with important changes in the soil surface state and covered by vegetation.

1. Introduction

Landslides are one of the most significant geohazards in terms of socio-economic costs, threatening infrastructures and human settlements. The monitoring of their surface displacement is thus crucial for the prevention and forecast of landslides. In regions where large landslides ($>10^5$ m^3) cannot be stabilized and may accelerate suddenly, remote monitoring is often the only solution for surveying and/or early-warning. Techniques using high resolution (HR) to very-high resolution (VHR) space-borne optical and radar (SAR) images provide valuable information to investigate landslide kinematics measuring 1D Line-of-Sight (LoS) and 2D horizontal surface displacements (Delacourt et al., 2007). For instance, digital image correlation (DIC) of VHR optical satellite images has been used to estimate the horizontal component of the displacement with a centimetric accuracy (Booth et al., 2013; Stumpf et al., 2014). To yield a sub-pixel accuracy, adequate image orientation, co-registration, georeferencing and modelling of topographic distortions are of primary importance (Stumpf et al., 2014). In complement to optical images, SAR images have become a widely used source of information for measuring the topography and deformation of the Earth surface. SAR images can be used at regional scales, for basin subsidence or plate tectonics motion monitoring, and local scales, for fault, slope movement or glacier monitoring (Massonnet and Feigl, 1998). Advanced processing of SAR images has proven its ability for landslide detection and mapping (Farina et al., 2006; Cascini et al., 2009; Guzzetti et al., 2012), process monitoring (Hilley et al., 2004; Zhao et al., 2012; Raucoules et al., 2013), hazard assessment (Zhao et al., 2013; Nikolaeva et al., 2014) and risk management (Bardi et al., 2014). The choice of an optimal SAR processing technique depends on several constraints: landslide type (Dikau et al., 1996), range of expected velocity and direction of the displacement (Cruden and Varnes, 1996), areal extension of the moving mass, and land cover (e.g. presence of bare rocks, soils or dense vegetation; Jebur et al., 2014), requested accuracy, and existing catalogue of SAR data (Tofani et al., 2013). Traditional two-pass differential InSAR technique (D-InSAR) has been applied for the monitoring of slow-moving landslides on the order of cm year^{-1} (Catani et al., 2005), whereas persistent scatterers SAR interferometry (PS-InSAR; Ferretti et al., 2001; Hooper, 2004) and small baseline subset (SBAS; Berardino et al., 2002; Tolomei et al., 2013) techniques allow the monitoring of extremely slow-moving landslides on the order of mm year^{-1} (Hilley et al., 2004; Guzzetti et al., 2009). Finally, correlation of SAR amplitude images allows the monitoring of rapid landslides (on the order of m year^{-1}; Raucoules et al., 2013). As each of these techniques has its advantages and limitations, the combination of various SAR/InSAR processing techniques offers new perspectives to investigate variable displacement rates (Lauknes et al., 2010).

In this work, we focus on the analysis of two large landslides characterized by slow to moderate velocity in the order of cm day^{-1} (Cruden and Varnes, 1996). These landslides show a complex spatial pattern of displacement which is challenging to monitor with SAR images because of significant changes in the local morphology, the soil surface state and the vegetation inducing changes of the ground scattering properties between two consecutive image acquisitions. Further, the available SAR archive on these landslides is limited to ascending orbits, thus preventing a complete analysis of landslide movement over all the

* Corresponding author. Tel.: +33 3 68850036; fax: +33 3 68850125.
E-mail address: romy.schlogel@unistra.fr (R. Schlögel).

http://dx.doi.org/10.1016/j.geomorph.2014.11.031
0169-555X/

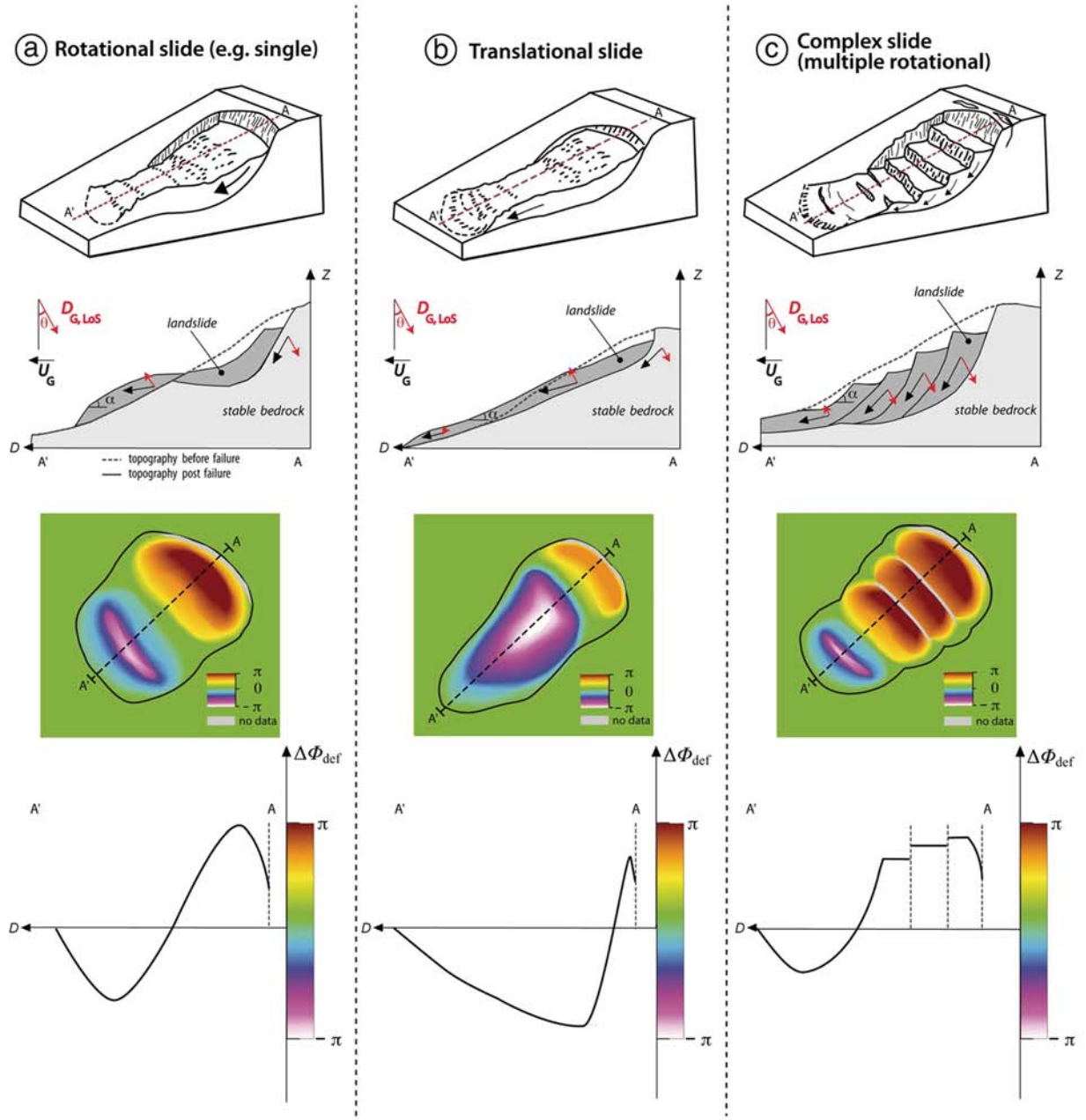

Fig. 1. Displacement pattern, morpho-structures and associated interferometric phase for three landslide types. (a) Rotational slide with a single circular slip surface; (b) translational slide with a nearly planar slip surface parallel to the slope topography; and (c) complex slide with a series of embedded circular slip surfaces. From top to bottom: Three-dimensional view with a longitudinal cross-section of the slope morphology; synthetic spatial distribution of InSAR phase values; and along a longitudinal cross-section. The distribution of phase values (Φ) is based on the following assumptions: (i) the SAR Line-of-Sight (LoS) and the landslide displacement directions are in the same vertical plane, (ii) the slope angle α is smaller than the SAR look angle θ (which is equivalent to a local incidence angle smaller than θ), and (iii) the amplitude of the displacements is small enough to produce a phase variations in the interval $[-\pi, \pi]$. D: horizontal distance along the cross-section profile, Z: elevation; $D_{G,LoS}$: displacement vector along the LoS direction, U_G: displacement vector at the ground. $\Delta\Phi_{def}$: variation of phase values.

affected slope orientations and a measurement of the displacements along the three components (Nikolaeva et al., 2014).

Therefore, we propose a geomorphologically-guided InSAR interpretation method in order to overcome some of the above mentioned constraints of the SAR images and the InSAR technique. The method, developed for L-band ALOS/PALSAR images, is based on the analysis of the spatial distribution of both surface geomorphological features and SAR phase values (Fig. 1). We assume that the direction of the landslide

Table 1
Reference case studies, defined in terms of displacement rate (v) and movement type (m), used to test the applicability of the interpretation method.

	v	m	Landslide type and morphological unit
Case 1	<0.4 cm day^{-1}	Mainly vertical	Rotational slide, ablation zone (Poche landslide)
Case 2	<0.4 cm day^{-1}	Mainly along slope	Translational slide, accumulation zone (Poche landslide)
Case 3	>0.4 cm day^{-1}	Mainly along slope	Translational slide, accumulation zone (La Valette landslide)
Case 4	>0.4 cm day^{-1}	Mainly vertical	Complex slide, ablation zone (La Valette landslide)

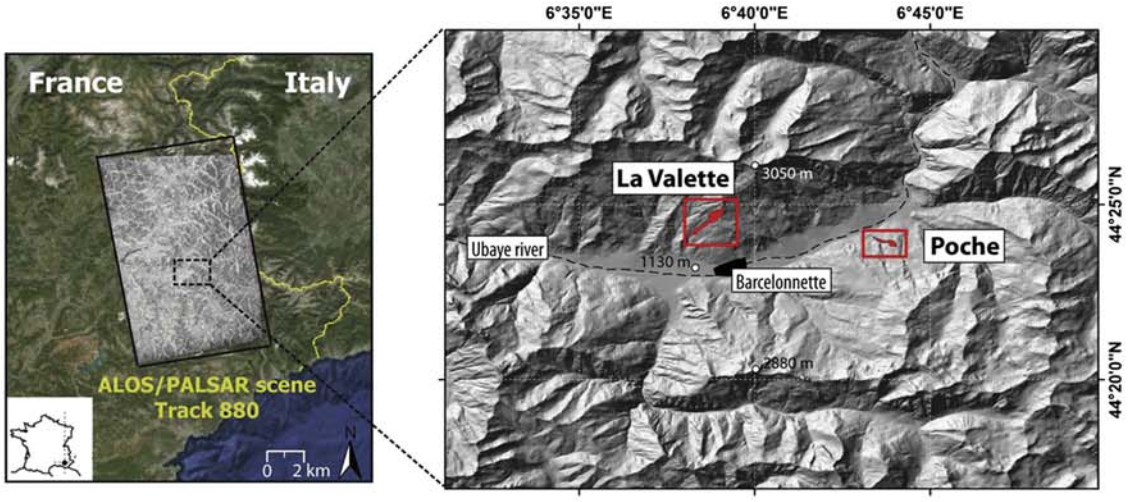

Fig. 2. Location and characteristics of the Poche and La Valette landslides in the Ubaye Valley (South East France) and extension of ALOS/PALSAR SAR scenes.

movement is controlled at depth by the geometry of the slip surfaces, and laterally by the geometry of the stable bedrock slopes confining the landslide mass (Okada, 1985; Muller and Martel, 2000; Petley et al., 2002). The geometry and spatial distribution of discontinuities, such as scarps and grabens upslope, sets of strike-slip and normal fissures on the lateral sides, and compression lobes downslope, are used to infer the movement direction (Travelletti et al., 2012; Stumpf et al., 2013). Large landslides are characterized by rotational, translational or complex style of movement (Fig. 1). Single rotational slides are confined by a circular basal slip surface and are affected by retrogression upslope (Fig. 1a). Translational slides are confined by planar basal slip surfaces and show a surface movement mainly parallel to the hillslope (Fig. 1b). Most landslides are complex and thus involve a combination of rotational and translational movement features with multiple small circular slip surfaces (Fig. 1c).

Fig. 1 also depicts the synthetic spatial distribution of interferometric phase values for these three types of movement. In the landslide upper parts (ablation zone), the vertical displacements (subsidence) are larger than the horizontal (downslope) displacements; this kinematic pattern is represented by positive phase values in the interferograms corresponding to a motion away from the satellite. In the landslide lower parts, vertical displacements (e.g. accumulation) are, most of the time, smaller than horizontal (downhill) displacements; this kinematic pattern is represented by negative phase values in the interferograms corresponding to a motion towards the satellite. Fig. 1 also presents theoretical profiles of the slope topography and of the InSAR phase values for rotational, translational and complex slides. The shape of the phase along the profile, is further used to analyse the direction and amplitude of the movement.

The method is tested on four case studies defined in terms of average landslide displacement rate and style of movement (Table 1). The four case studies represent typical motion and sliding mechanisms observed in the ablation and accumulation zones of the Poche and La Valette landslides (South French Alps, Fig. 2). After presenting the study areas and the InSAR processing technique, we analyse the InSAR data to estimate the displacement field and compare it to *in-situ* displacement measurements. Finally, we focus on the time evolution of the displacement field to analyse the non-steady state behaviour of the landslides.

2. Study areas

The Poche and La Valette landslides are located in the Ubaye Valley (South East France; Fig. 2) and have developed in clay-shale material (Callovo–Oxfordian black marls). The dynamics of these two landslides corresponds to a complex slide with various motion patterns in the ablation and accumulation zones. At first order, the kinematics is controlled by the local geometry of the bedrock and the presence of faults (Le Mignon and Cojean, 2002; Travelletti et al., 2013). The geomorphological characteristics of the landslides are detailed in Fig. 2 and Table 2.

2.1. Poche landslide: geology and kinematics

The Poche landslide is located on the north-facing slope of the Ubaye Valley, 5 km to the East of the town of Barcelonnette (Figs. 2 and 3). The triggering date is not precisely known, but is estimated in the middle of the 19th century. Currently, the landslide extends over a length of 1200 m along the EW to NW direction, and a width of 100 and 300 m in the lower and upper parts, respectively. The maximum landslide depth, estimated by seismic tomography and geotechnical boreholes, ranges from 10 to 25 m (Schmutz, 2000). The mean slope angle is ~15° in the ablation zone and ~20° in the accumulation zone. The volume of the landslide is estimated at ca. 5.0×10^5 m^3 (Schmutz, 2000; Malet and Maquaire, 2003).

For the period 1993–2013, the displacement rates measured by total station on 10 benchmarks are ~1 cm day^{-1} (Malet and Maquaire, 2003). Higher displacement rates, up to 8 cm day^{-1}, have been observed in Spring 2001 and 2008.

The landslide ablation zone consists of a combination of structural rock block slides to the South-East and a large rotational slide to the North-East (Fig. 3a; case 1). The 20°-dipping main scarp limits the

Table 2
Characteristics of the Poche and La Valette landslides in the Ubaye Valley (South East France).

	Location	Triggering date	Elevation (m)	Dimension (L, l; m)	Slope angle (α; °)	Slope direction (β; °)	Lithology
Poche	N Ubaye	>1855	1200–1500	L: 1200; l: 150–300	20 (scarp)–11 (tongue)	305 (scarp)–270 (tongue)	Black marls, moraine
La Valette	S Ubaye	1982	1240–2070	L: 2000; l: 200–500	35 (scarp)–20 (tongue)	230 (scarp)–230 (tongue)	Black marls, limestone, moraine

L: length; l: width.

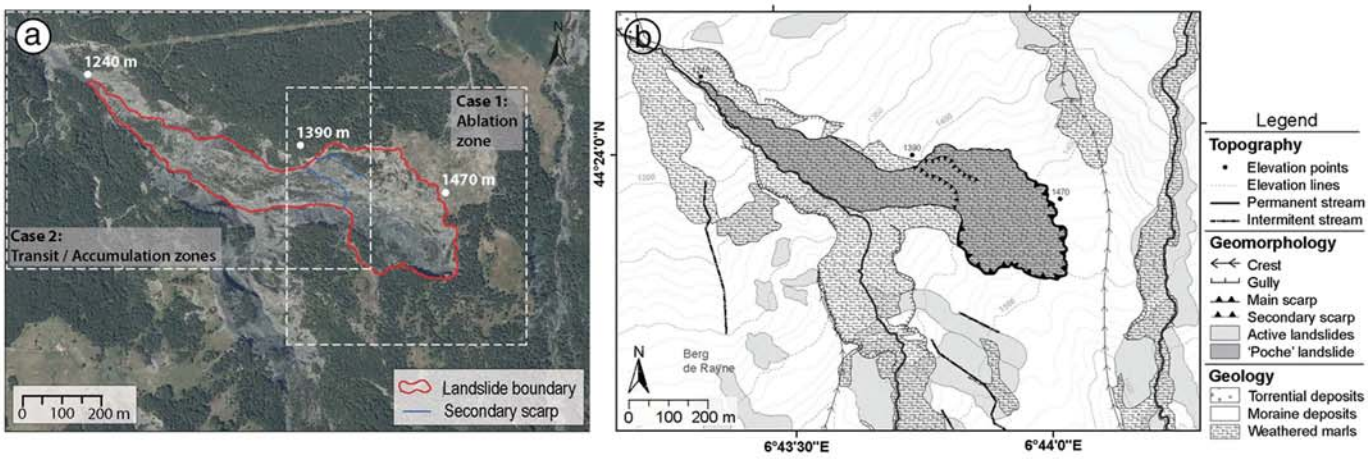

Fig. 3. Morphology of the Poche landslide. (a) Orthophotograph of the landslide in 2009 and location of ablation (case 1) and transit-accumulation zones (case 2); (b) morpho-structural map of the landslide.

~10-m-thick moraine deposits and the Callovo–Oxfordian black marls (Le Mignon and Cojean, 2002). The morphology of the ablation zone is very bumpy with the presence of numerous blocks of marls, secondary scarps and counterslopes.

The transit and accumulation zones present a flow-type morphology with the progressive burial of the thalweg of the Poche torrent (Fig. 3a, case 2). The slope angle of the accumulation zone is, at first order, constant but locally presents a series of small secondary scarps and lobes where ponds are located. The displacement pattern of this zone can be considered as translational.

2.2. La Valette landslide: geology and kinematics

The La Valette landslide is located on the south-facing slope of the Ubaye Valley to the NW of the town of Barcelonnette (Fig. 4a). The landslide, triggered in March 1982, currently extends over a length of

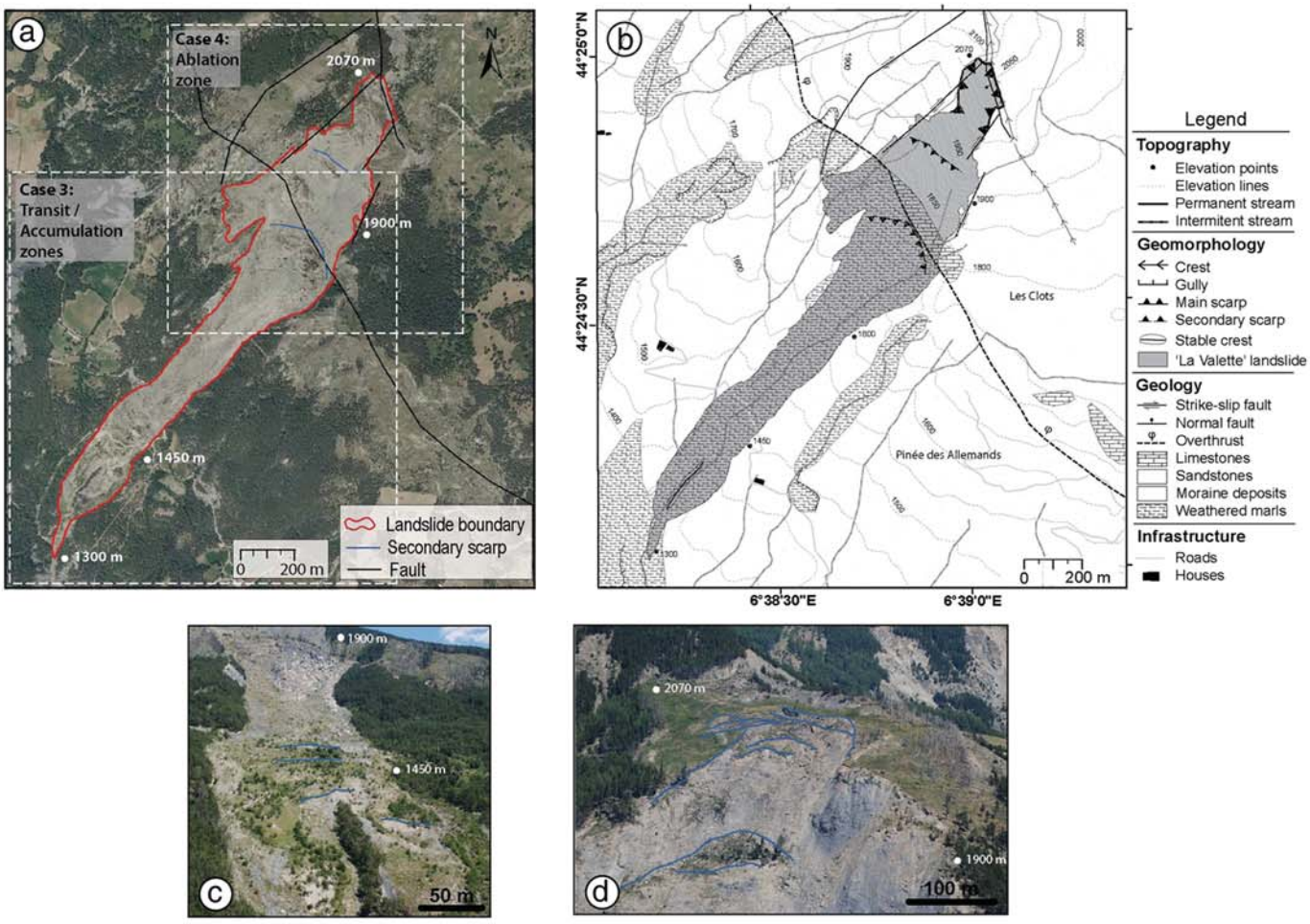

Fig. 4. Morphology of the La Valette landslide. (a) Orthophotograph of the landslide in 2009 and location of ablation (case 4) and transit-accumulation zones (case 3), (b) morpho-structural map of the landslide. (c) Photograph of the transit and accumulation zones in 2009. (d) Photograph of the ablation zone in 2009 including numerous secondary scarps.

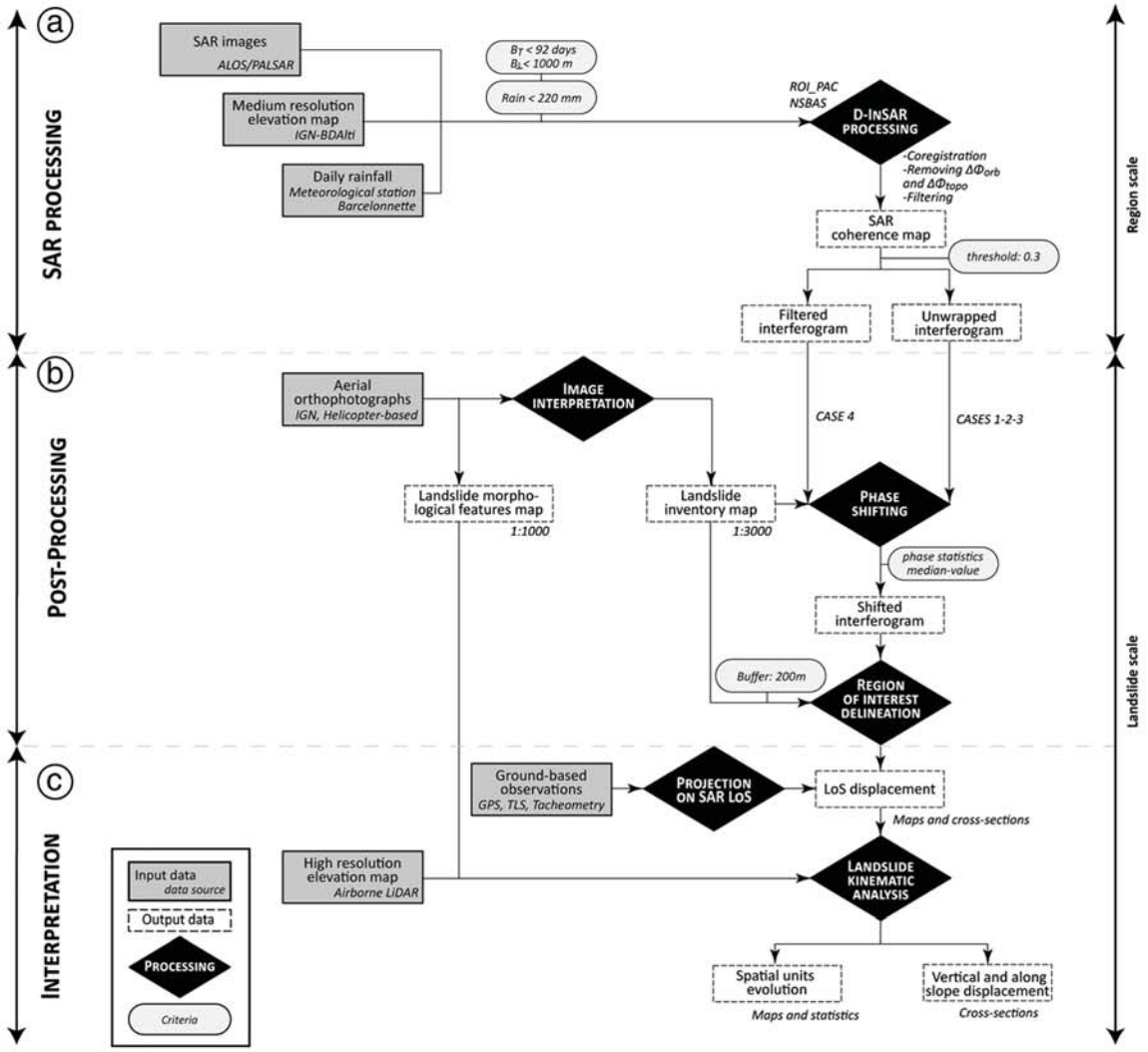

Fig. 5. Methodological flowchart and indications of the data and outputs used at each processing step. (a) SAR images selection and processing. (b) Interferograms post-processing. (c) Interferograms interpretation. The detailed characteristics of the data are presented in Table 3 and Fig. 6.

2000 m along the SW direction. It features a variable width ranging from 200 m in the transit and accumulation zones and 500 m in the ablation zone. The maximum depth, estimated by seismic and electrical resistivity tomography and geotechnical boreholes, ranges from 25 to 35 m (Travelletti et al., 2009; Hibert et al., 2012). The mean slope angle is ~30° at the main scarp and ~20° within the transit zone. The volume of the landslide is estimated at 3.5×10^6 m^3 (Le Mignon and Cojean, 2002). The landslide is located at an overthrust contact between the Callovo–Oxfordian black marls at the base and the Pelat nappe at the top (Turonian and Paleocene flysch and limestone; Fig. 4b; Travelletti et al., 2013).

The displacements are monitored with topometric benchmarks since 1991 (Squarzoni et al., 2005), differential dual-frequency GNSS (Malet et al., 2002; Malet et al., submitted for publication) and an extensometer since 2008. At regular time intervals, displacement maps are also calculated from correlation of optical satellite images (Leprince et al., 2008), satellite radar interferometry (Vietmeier et al., 1999; Squarzoni et al., 2003) and airborne and ground based laser scans (Travelletti et al., 2013). For both periods 1995–1999 and 1999–2003, the displacement rates measured from the correlation of orthophotographs are in the range of 2.5 m yr^{-1} in the accumulation zone and 20 m yr^{-1} in the ablation zone (Delacourt et al., 2007). For the period 1991–1999, Squarzoni et al. (2003) determined from the analysis of ERS-1/2 (C-band) interferograms and four kinematic subunits identified two movement types: a translational sliding with the development of a flow tongue in the transit and accumulation zones (Fig. 4c) and multiple rotational sliding with a slump type morphology in the ablation zone (Fig. 4d).

Table 3
Characteristics of the dataset used for the analysis.

	Poche	La Valette
Topographic data	2007: BD ALTI® Elevation DSM (25 m) 2007: Airborne LiDAR DSM (0.5 m)	2007: BD ALTI® Elevation DSM (25 m) 2007: Airborne LiDAR DSM (0.5 m) 2009: Airborne LiDAR DSM (0.5 m)
Orthophotograph	2007 (0.5 m), 2009 (0.5 m)	2007 (0.2 m), 2009 (0.2 m)
Ground-based displacement data	Total station campaigns on benchmarks (2007–2010)	GNSS campaigns on benchmarks (2008–2010), Permanent GNSS (>2009)

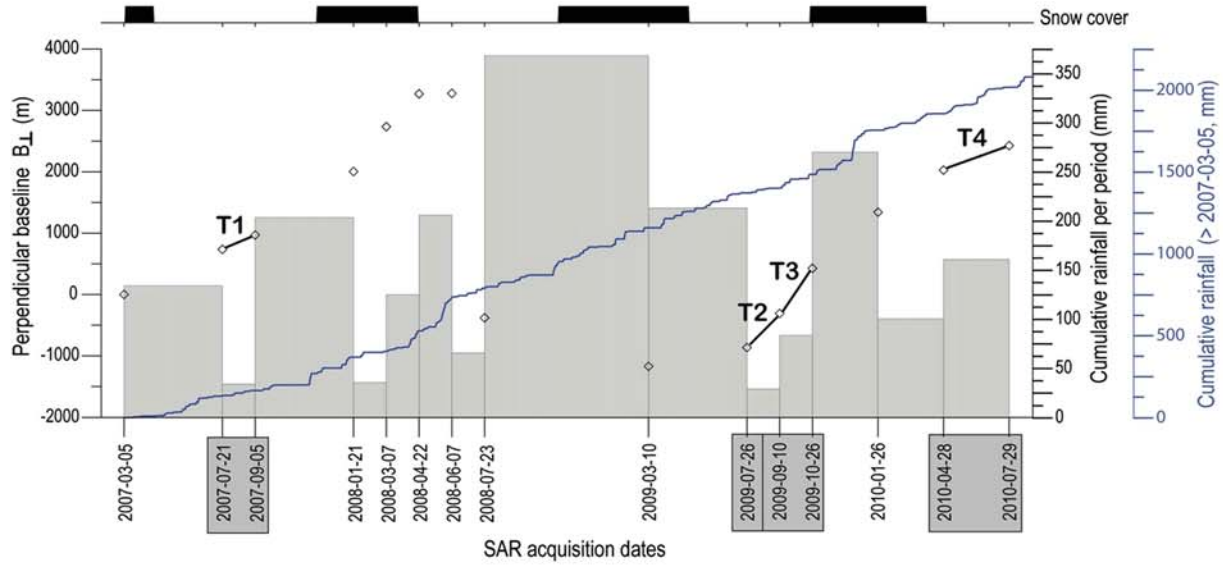

Fig. 6. Time acquisition and perpendicular baseline (white point) of the SAR images together with the cumulative net rainfall between consecutive SAR acquisitions (grey box) and for the complete time period (blue line) at the Barcelonnette meteorological station. The presence of snow cover (black box) is estimated from satellite image analysis. The interferograms T1, T2, T3 and T4, analysed in this work, are indicated.

3. Methodology

The processing and interpretation methodology is summarised in Fig. 5. It includes the selection and processing of SAR images (Fig. 5a), the post-processing of interferograms (Fig. 5b) and the calculation and interpretation of displacement (Fig. 5c). The detailed characteristics of the data are presented in Table 3 and Fig. 6.

3.1. SAR processing

An interferogram consists of the calculation of phase differences ($\Delta\Phi_{int}$) between two co-registered SAR images:

$$\Delta\Phi_{int} = \Phi(t_0) - \Phi(t_1) = \Delta\Phi_{def} + \Delta\Phi_{orb} + \Delta\Phi_{topo} + \Delta\Phi_{atm} + \Delta\Phi_{noise} \quad (1)$$

where $\Delta\Phi_{int}$ is the SAR interferometric phase, $\Delta\Phi(t_0)$ and $\Delta\Phi(t_1)$ are the SAR phase values at respectively day t_0 (reference) and day t_1, $\Delta\Phi_{def}$ is ground deformation (between two acquisition times), $\Delta\Phi_{orb}$ is orbital contribution (due to changes of the satellite orbital geometry), $\Delta\Phi_{topo}$ is topographic contribution, $\Delta\Phi_{atm}$ is atmospheric contribution (due to difference of signal propagation in the atmosphere) and $\Delta\Phi_{noise}$ is noise contribution (corresponding to changes in the scattering properties of the ground surface, changes in the thermal properties of the atmosphere or ground surface, or inaccurate image co-registration; Massonnet and Feigl, 1998).

The SAR data are coregistered using the NSBAS tools (Doin et al., 2011). The interferograms are processed using the ROI-PAC software (Fig. 6a; Rosen et al., 2004). The orbital contribution is corrected with precise satellite orbit data (<1 m) provided by the Japan Aerospace Exploration Agency (JAXA) fitted with a 2D linear offset ramp. The topographic contribution is corrected using the BDALTI® DSM (25 m) resampled at 10 m. with a bilinear interpolation. The topography-correlated phase signal due to the stratified troposphere is removed over the complete SAR scene using the wrapped phase (Beauducel and Briole, 2000;, Doin et al., 2009)

After filtering, we further interpret only the interferograms with coherence values higher than 0.30 (Fig. 5a). Two strategies are used for the interpretation. For cases 1, 2 and 3 (Table 1), the phase values are

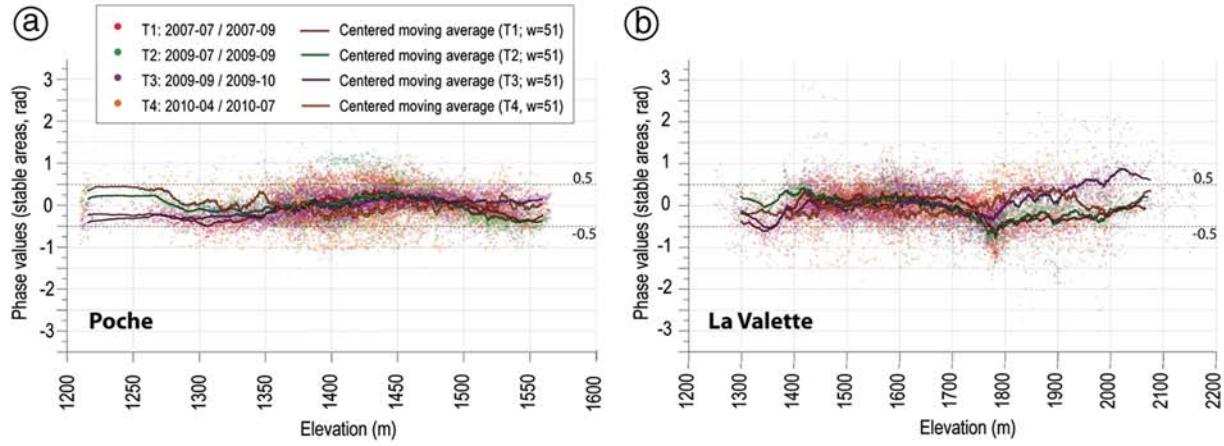

Fig. 7. Variability of phase values with elevation. (a) Phase values for the Poche landslide with respectively 83%, 85%, 96% and 64% of values in the range ±0.5 rad for the periods T1, T2, T3 and T4. (b) Phase values for the La Valette landslide with respectively 76%, 81%, 80% and 72% of values in the range ±0.5 rad for the periods T1, T2, T3 and T4. The centred moving average is calculated for each period with a season w = 51.

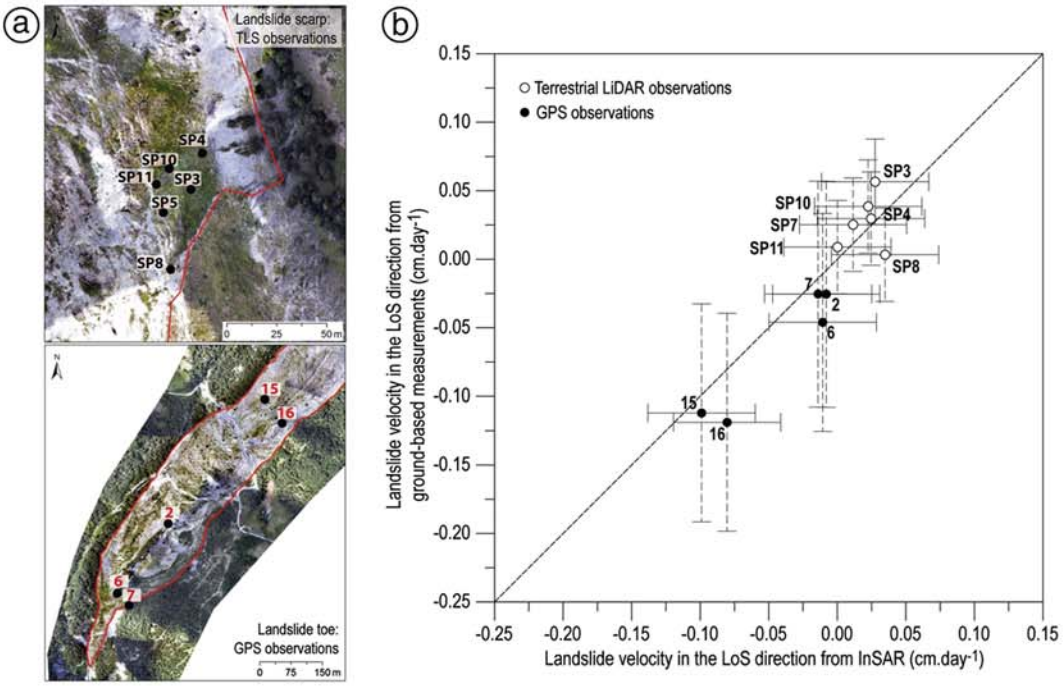

Fig. 8. Landslide velocity (vertical component and LoS direction) measured by InSAR and ground-based techniques (terrestrial LiDAR in the ablation zone and GPS in the accumulation zone) at La Valette for the period July–October 2009. The uncertainties of each measurement techniques are ±0.9 cm for InSAR, ±7 cm for GNSS, and ±3 cm for terrestrial LiDAR.

unwrapped using the branch-cut unwrapping algorithm of Goldstein et al. (1988). For case 4, unwrapping is not possible and only the wrapped phase is analysed.

3.2. Post-processing of the interferograms

All interferograms are co-registered and geocoded in cartographic coordinates (reference system Lambert 3) for comparison with other datasets. The analysis of landslide motion is then performed on small sub-scenes (2.1×1.9 km^2) of the interferograms around the two landslides (Fig. 5b).

The precise location and contours of the expected deformation area are mapped from a landslide inventory (1:3000) available for the whole region. The landslide morphological features (scarps, fractures, lobes, and gullies) observed on the aerial orthophotographs and the airborne LiDAR DSMs are used to guide the interpretation of the wrapped and unwrapped phase values.

In order to compare the interferograms, we shifted the phase values for the portions of the terrain out of the landslide limits. We subtracted the median phase values (Φ_{med}) of the area surrounding the landslide to the phase values of the sub-scene. The resulting phase values for the wrapped interferograms are thus expressed in the range $[-\pi\text{-}\Phi_{med}, \pi\text{-}\Phi_{med}]$. The shifted phase values are interpreted for zones of interest (200 m) around the landslides.

3.3. Interpretation of interferograms

To analyse the kinematics of the landslide (Fig. 6c), we convert the phase values (Φ) in displacement along the SAR LoS direction (D_{LoS}):

$$D_{LoS} = \lambda \Delta\Phi / 4\pi \quad (2)$$

where λ is the wavelength.

We further project the ground-based three-dimensional displacement vector U_G along the SAR LoS direction ($D_{G,\,LoS}$):

$$D_{G,\,LoS} = U_G \cdot n_{LoS} \quad (3)$$

where n_{LoS} is the unit vector along the LoS direction, positively orientated in the satellite-ground direction. The n_{LoS} vector can be described in the East-North-Up reference system:

$$n_{LoS} = (\sin A_v \ \sin\theta, -\cos A_v \ \sin\theta, -\cos\theta) \quad (4)$$

where A_v is the mean azimuth of the LoS and θ is the incidence angle. In our case, the unit vector is defined with $n_{LoS} = [0.61, 0.15, -0.79]$, $A_v = 75.84°$ and $\theta = 38.7°$.

Taking into account the spatial distribution of the phase values, we consider the parts of the field with absolute phase values $\Phi > 0.5$ (corresponding to a displacement of 0.9 cm in LoS) as 'moving' areas (see Fig. 7 for the areas assumed to be stable in the regions of interest). As outlined in Fig. 1, various phase values and displacement fields can be observed at the scale of a landslide due to local movements:

- At the intermediate and lower parts of the landslides, the translational sliding movement can be mainly described by along-slope displacements: in a case of a small slope, as presented in Fig. 1, this movement corresponds to negative phase values ($\Phi < -0.5$). Moreover, the accumulation of the material in this part of the landslide eventually produces an upward movement of the ground, which increases the absolute phase value.
- In the upper part of the landslides, close to the main scarps, the vertical component of the displacement is dominant with a subsidence and a

Fig. 9. Displacement (cm) and velocity (cm day^{-1}) observed in the ablation zone of the Poche landslide from L-band PALSAR InSAR data. (a) Orthophotograph (2009) and interferograms for the periods T1, T2 and T3. (b) Profiles of elevation (top), D_{LoS} (middle) and D_{vert} (bottom) for two cross-sections perpendicular to the landslide (A–A′) and along the steepest slope direction (B–B′). The location of the two profiles (of width 30 m) is indicated in (a). The colour bars indicate changes in the size of different movement type (subsidence in red, transit in yellow to orange, and stable areas in green).

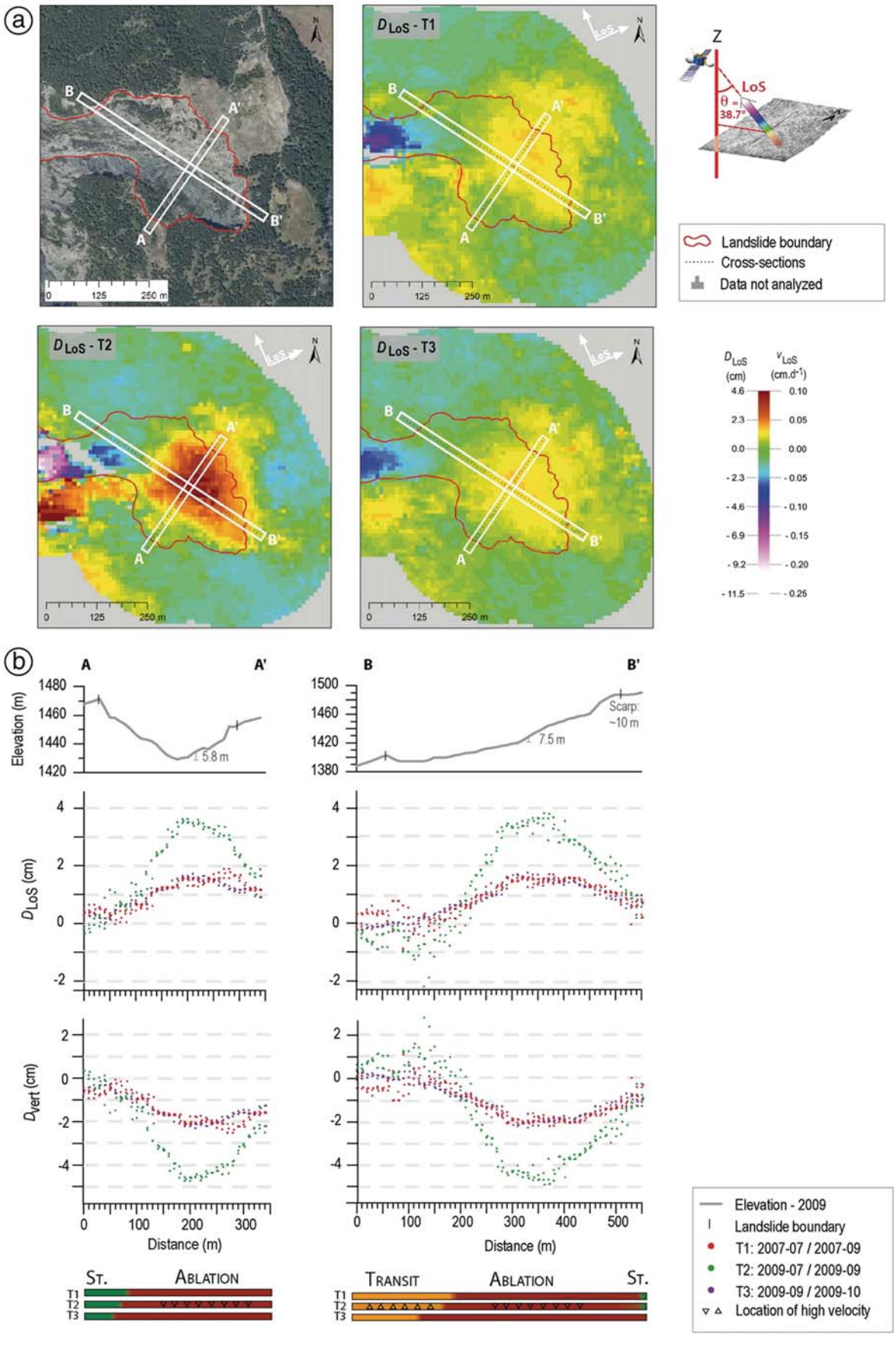
a
B
A'
A
B'
0 125 250 m
D LoS - T1
D LoS - T2
D LoS - T3
LoS
N
Z
θ = 38.7°
Landslide boundary
Cross-sections
Data not analyzed
D LoS (cm)
V LoS (cm.d-1)
4.6 2.3 0.0 -2.3 -4.6 -6.9 -9.2 -11.5
0.10 0.05 0.00 -0.05 -0.10 -0.15 -0.20 -0.25
b
A A'
B B'
Elevation (m)
1480 1460 1440 1420
1500 1460 1420 1380
5.8 m
7.5 m
Scarp: ~10 m
D LoS (cm)
D vert (cm)
Distance (m)
0 100 200 300
0 100 200 300 400 500
ST. ABLATION
TRANSIT ABLATION ST.
T1
T2
T3
Elevation - 2009
Landslide boundary
T1: 2007-07 / 2007-09
T2: 2009-07 / 2009-09
T3: 2009-09 / 2009-10
Location of high velocity

loss of material; this movement corresponds to positive phase values ($\Phi > 0.5$).

If the displacements are large (e.g. higher than half the wavelength of the radar sensor), phase jumps can be observed due to the complexity of the unwrapping method. These SAR features, in relation with the morphological features, are interpreted either as a contact among a stable slope and the landslide, or as a contact among landslide units characterized by distinct displacement rates.

Using ground-based monitoring data, we assume a main displacement direction for all sub-units. Two cases are considered. The first case corresponds to a vertical motion associated with a depletion of material (preferentially located at the top of the landslide), or with an accumulation of material (preferentially at the toe of the landslide). Therefore, we convert the LoS displacement to ground vertical displacement (D_{vert}):

$$D_{vert} = D_{LoS}/(n_z.n_{LoS}) = -D_{LoS}/\cos\theta \quad (5)$$

where n_z is the vertical unit vector (positive upward).

A positive vertical displacement ($D_{vert} \geq 0$) corresponds to a subsidence; a negative vertical displacement ($D_{vert} \leq 0$) corresponds to an uplift.

The second case corresponds to an along-slope motion, observed for a translational sliding movement. We convert the LoS displacement to ground along-slope displacement (D_{Slope}):

$$D_{Slope} = D_{LoS}/\left(n_{Slope}.n_{LoS}\right) \quad (6)$$

where n_{Slope} is the unit vector (positive downslope) which can be written in the East-North-Up reference:

$$n_{Slope} = (\sin A_d \cos\alpha,\ \cos A_d \cos\alpha, -\sin\alpha) \quad (7)$$

where A_d is the slope azimuth angle, and α is the slope angle. For this analysis, A_d and α are calculated from a high (0.5 m) resolution LiDAR DSM available for the study area over a window of 9×9 pixels.

4. Data

The dataset consists of satellite SAR images, airborne orthophotographs, airborne laser scanning digital surface models (DSMs), and displacement measurements from ground-based GNSS or total stations. We use 15 ALOS/PALSAR images (processed at Level 1.0) acquired from March 2007 to July 2010 (Fig. 6). In C-band ($\lambda = 5.6$ cm) and X-band ($\lambda = 3.1$ cm) radar sensors, the phase quality of the SAR signal degrades due to changes in the backscattering properties of the ground surface (vegetation, soil surface state, micromorphology and roughness) which is less critical in L-band ($\lambda = 23.8$ cm) sensors (Rosen et al., 1996; Strozzi et al., 2005; Wei and Sandwell, 2010). For landslide monitoring, C-band images (ERS1/2) have been mainly used in the TANDEM acquisition mode with repeat cycle of 1–3 days (Rott et al., 1999; Squarzoni et al., 2003), while X-band sensors are only suitable for the monitoring of slopes with many natural reflectors (buildings and rocky blocks; Notti et al., 2010). Therefore, for the monitoring of large displacements, large wavelengths are more suitable (García-Davalillo et al., 2014).

The ALOS archive for the study area consists of images acquired in ascending orbit (track 880). Images acquired at the high resolution Fine Beam Polarization (FBS) mode are used. For all images, the pixel dimensions are 9.78 m in the azimuth direction and 7 m in the range direction; the mean look angle θ is 38.7° over the scene; and the off-nadir azimuth α_d is 75.84°. For the InSAR processing, the criteria used to select the image pairs are: (1) a perpendicular baseline ($B_\perp$) smaller than 1000 m; (2) a temporal baseline (B_T) between both images shorter than 92 days; and (3) a net rainfall amount of less than 220 mm between consecutive dates (Fig. 6). To avoid decorrelation due to the presence of snow cover, we also excluded scenes acquired in winter.

Table 3 details the dataset used for the analysis. A medium resolution (25 m) DSM from the French National Mapping Agency (BD ALTI®, IGN), resampled at 0.000088° (9.78 m) and projected in geographic-WGS84 coordinates was used for the InSAR processing. Very high resolution (0.5 m) airborne LiDAR DSMs and aerial orthophotographs (0.5 m) were used for the morphological and kinematic analysis of the landslides.

5. Results and discussion: quality of the processing and interpretation of landslide motion

The kinematics of the landslides was analysed for the period 2007–2010 in terms of both the spatial distribution of displacement rates and the evolution of rates over time. Four periods were considered: T1 = 2007-07-21 to 2007-09-05 ($B_T = 46$ days), T2 = 2009-07-26 to 2009-09-10 (46 days), T3 = 2009-09-10 to 2009-10-26 (46 days) and T4 = 2010-04-28 to 2010-07-29 (92 days).

Here we first discuss the quality of the InSAR results and then interpret the InSAR deformation field by taking into account geomorphological and geophysical knowledge of the landslides. The LoS displacements are interpreted in terms of vertical or along-slope displacements for landslide sub-units, and compared to ground-based geodetic observations. The landslide motion is then interpreted for the complete monitoring period. The results are discussed successively for each study case.

5.1. Quality and uncertainty of the InSAR phase values and deformation

A collocation error of 1.5 pixels (e.g. ca. 15 m) in the North and East components is observed on the SAR amplitude images and is taken into account for interpreting the LoS displacements. Even with interferograms at $B_T = 46$ days and $B_\perp < 1000$ m, decorrelation is observed because of important changes of the soil surface state (variation in soil humidity, transport of sediment, fracturing) especially in the ablation zones of the two landslides. For the Poche landslide, the unwrapped interferograms T1, T2 and T3 are considered of good quality because more than 95% of the phase values are unwrapped. The interferogram T4 ($B_T = 92$ days) cannot be interpreted because the coherence is too low over the area of interest. For the La Valette landslide, the interferograms have generally a lower quality (especially in the ablation zone); consequently, the phase values for T2, T3 and T4 cannot be unwrapped and only wrapped interferograms are used for the analysis.

The uncertainty of the phase values is estimated in terms of variability of the phase values on stable terrains outside of the landslides. For the four interferograms and the two landslides, more than 70% of pixels have a phase value in the range [−0.5 rad, +0.5 rad] (Fig. 7), except for Poche at T4. Atmospheric effects remain in the phase map, mainly for the La Valette landslide partly because of the large elevation range [1200–2200 m] (Fig. 7b).

Further, at La Valette, the InSAR velocity along the LoS direction is compared to projected ground-based velocity measured for 11 benchmarks (Travelletti et al., 2009, 2013). The results are presented in Fig. 8. The InSAR velocity is consistent with the ground-based observations with maximum errors of 0.05 cm day^{-1}.

5.2. Interpretation of the InSAR slope deformation field

Figs. 9 to 12 present the interferograms. The grey colour indicates areas where the phase values are not interpreted because of low coherence values (<0.3). In the following, the InSAR displacement field is interpreted successively for each case study.

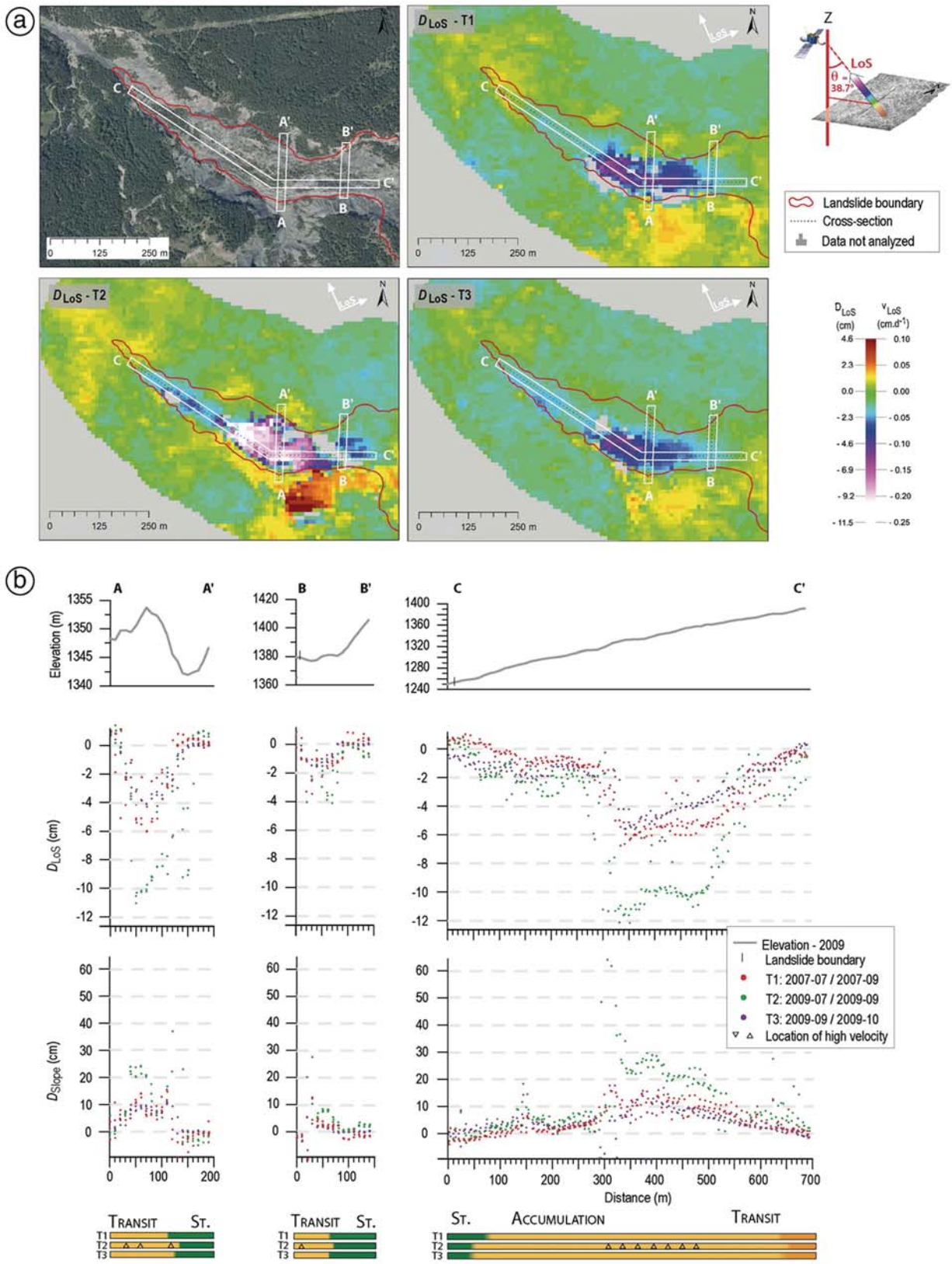

Fig. 10. Displacement (cm) and velocity (cm day^{-1}) observed in the transit-accumulation zone of the Poche landslide from L-band PALSAR InSAR data. (a) Orthophotograph (2009) and interferograms for the periods T1, T2 and T3. (b) Profiles of elevation (top), D_{LoS} (middle) and D_{slope} (bottom) for two cross-sections perpendicular to the steepest slope direction of the landslide (A–A′ and B–B′) and a cross-section along the steepest slope direction (C–C′). The location of the two profiles (of width 30 m) is indicated in (a). The colour bars indicate changes in the size of the movement type (subsidence in red, transit in yellow to orange, and stable slopes in green).

5.2.1. Case 1: InSAR deformation of the Poche ablation zone

In the ablation zone of the Poche landslide, we observe positive D_{LoS} values on the interferograms T1, T2 and T3 corresponding to a ground LoS displacement away from the satellite (Fig. 9a). A similar pattern is identified in the three interferograms. Morphological features (Figs. 1a and 3) and previous studies indicate a single rotational movement type (Le Mignon and Cojean, 2002).

For the three time periods, the subsidence is constrained within a circular area (diameter of ~300 m) with decreasing displacement rates from the centre to the edges (Fig. 9b). The amplitude of the displacement varies in time. The maximum absolute D_{LoS} values reach respectively ~2.1 ± 0.9 cm for T1, 3.8 ± 0.9 cm for T2 and 1.8 ± 0.9 cm for T3, corresponding to vertical displacements of ~2.7 ± 1.1, ~4.9 ± 1.1 and ~2.3 ± 1.1 cm, respectively. The spatial extent of the subsidence movement (e.g. $D_{LoS} \geq 0.9$ cm) is also different for the three periods (~11.2×10^4 m^2 for T1; ~9.2×10^4 m^2 for T2; and ~12.0×10^4 m^2 for T3). These observations indicate that the behaviour of the landslide is not steady-state with important changes in velocity over time.

To the South, the boundary of the subsidence corresponds to the previously mapped landslide morphological limits of 2009. To the Northeast, the subsidence signal extends far beyond the known landslide morphological limits (150 m away from the main scarp in the North-East direction; Fig. 9a) indicating a further extension of the landslide.

Two profiles clearly indicate the same deformation pattern with local sharp gradients corresponding to landslide morphological features or steep topography (Fig. 9b; A–A′, B–B′). Along the cross-section A–A′, the maximum subsidence rate occurs in the central part of a topographic depression, whereas convex slopes (e.g. secondary scarps) delimit the extension of the subsidence along the cross-section B–B′. In addition, positive centimetric D_{vert} values are observed for T2 on cross-section B–B′ (at abscissa 100 m) indicating accumulation of material, mainly to the West (Fig. 9b).

5.2.2. Case 2: InSAR deformation of the Poche transit-accumulation zone

In the transit-accumulation zone of the Poche landslide, we observe negative D_{LoS} values on the three interferograms T1, T2 and T3 corresponding to a ground LoS displacement towards the satellite (Fig. 10a). Taking into account both the azimuth and the slope of the landslide, we interpreted this movement as a translation movement type (Le Mignon and Cojean, 2002; Fig. 1b).

For the three time periods, the deformation is constrained within an ellipse (major axis length of 300 to 600 m) elongated in the E–W direction. The displacement rates are higher in the central part of the landslide, and decrease to the edges. The maximum deformation is observed close to a knick point where the sliding direction changes from N270° to N305°. Similar to the ablation zone, the amplitude of the displacement varies in time. The maximum absolute D_{LoS} values reach respectively 6.8 ± 0.9 cm for T1, 12.1 ± 0.9 cm for T2 and 6.4 ± 0.9 cm for T3, corresponding to D_{slope} values of ~18 ± 2.4, ~30 ± 2.2 and ~17 ± 2.4 cm, respectively. The spatial extent of the translational sliding (e.g. $D_{LoS} \geq 0.9$ cm in absolute values) is different for the three periods (~4.3×10^4 m^2 for T1; ~5.4×10^4 m^2 for T2; and ~5.0×10^4 m^2 for T3).

To the South and Southwest, the boundary of this deformation signal coincides with the steep scarp of the Poche torrent. To the South-East, a subsidence movement, associated with positive D_{LoS} values, corresponds to the progressive development of a shallow slump. On the contrary, no further extension of the landslide is observed to the North.

Three profiles clearly indicate the same deformation pattern with the succession of material accumulation in convex slopes and material erosion in concave slopes (Fig. 10b; A–A′, B–B′, C–C′). The spatial distribution of displacement rates suggests the occurrence of compression (convex slopes) and dilatation (concave slopes) according to the bedrock geometry.

5.2.3. Case 3: InSAR deformation of the La Valette transit-accumulation zone

Phase unwrapping is difficult for this case study because of higher displacement rates than for the Poche landslide and the related change of ground. Taking into account our criteria of analysis, the spatial extent of the zones with reliable phase values are respectively 3%, 18%, 13% and 38% for the periods T1, T2, T3 and T4 (Fig. 11a). The deformation pattern is however clearly depicted from the InSAR dataset. Similar to the case 2, the transit-accumulation zone of the La Valette landslide is characterized by negative D_{LoS} values on the interferograms T1, T2, T3 and T4 (Fig. 11a) corresponding to a ground LoS displacement towards the satellite (Fig. 11b). This movement is interpreted as a translation movement type (Hibert et al., 2012; Fig. 1b).

The maximum absolute D_{LoS} values reach respectively 8.9 ± 0.9 cm for T1, 14.7 ± 0.9 cm for T2 and 14.1 ± 0.9 cm for T3. For the three time periods, the deformation pattern has a clear flow-like shape (with a main sliding direction to the Southwest). The maximum deformation is located at the South, between the elevations 1650–1750 m, corresponding to a sharp gradient in the local topography. For the period T1, the InSAR depicts accumulation of material in the upper part of the transit zone (NW) and subsidence to the NE at the Rocher Blanc outcrop (Fig. 4b). For all periods, a decrease in displacement rates is observed from uphill to downhill; the distribution of displacement rates along the transverse cross-sections A–A′ and B–B′ suggests a laminar flow with higher velocity in the central part, and lower velocity along the edges.

5.2.4. Case 4: InSAR deformation of the La Valette ablation zone

The series of counterslopes, secondary scarps and grabens suggest that the type of movement consists of multiple rotational slides (Squarzoni et al., 2003; Travelletti et al., 2013; Fig. 1c). Numerous phase jumps are observed in the wrapped interferograms (Fig. 12a) especially for T3 and T4.

For the four time periods, the deformation is broadly constrained within the geomorphological boundaries of the landslide though some local enlargements are identified. To the SW, a new landslide tongue is progressively developing; to the East and Southeast, retrogression of the main scarp and a subsidence are observed.

The cross-sections A–A′ and B–B′, which show a large dispersion particularly along the section A–A′, indicate the same deformation pattern (Fig. 12b). The D_{LoS} values vary spatially along the landslide body confirming the complexity of the sliding motion. Changes in D_{LoS} trends are analysed along the cross-section A–A′ and B–B′ in order to map sub-units with different kinematics (Fig. 12b). Four sub-units, limited by morphological features, are identified from the wrapped phase values and are consistent with a graben structure.

5.3. Interpretation of landslide motion

The objective of this sub-section is to interpret the spatial and temporal variations in the amplitudes of displacement for the two landslides in relation with possible triggering factors.

Fig. 11. Displacement (cm) and velocity (cm day^{-1}) observed in the transit-accumulation zone of the La Valette landslide from L-band PALSAR InSAR data. (a) Orthophotograph (2009) and interferograms for the periods T1, T2, T3 and T4. The landslide boundary is represented in red. (b) Profiles of elevation (top), D_{LoS} (middle) and D_{vert} (bottom) for two cross-sections perpendicular to the landslide (A–A′ and B–B′) and a cross-section along the steepest slope direction (C–C′). The location of the two profiles (of width 30 m) is indicated in (a). The colour bars indicate changes in the size of the movement type (subsidence in red, transit in yellow to orange, and stable slopes in green).

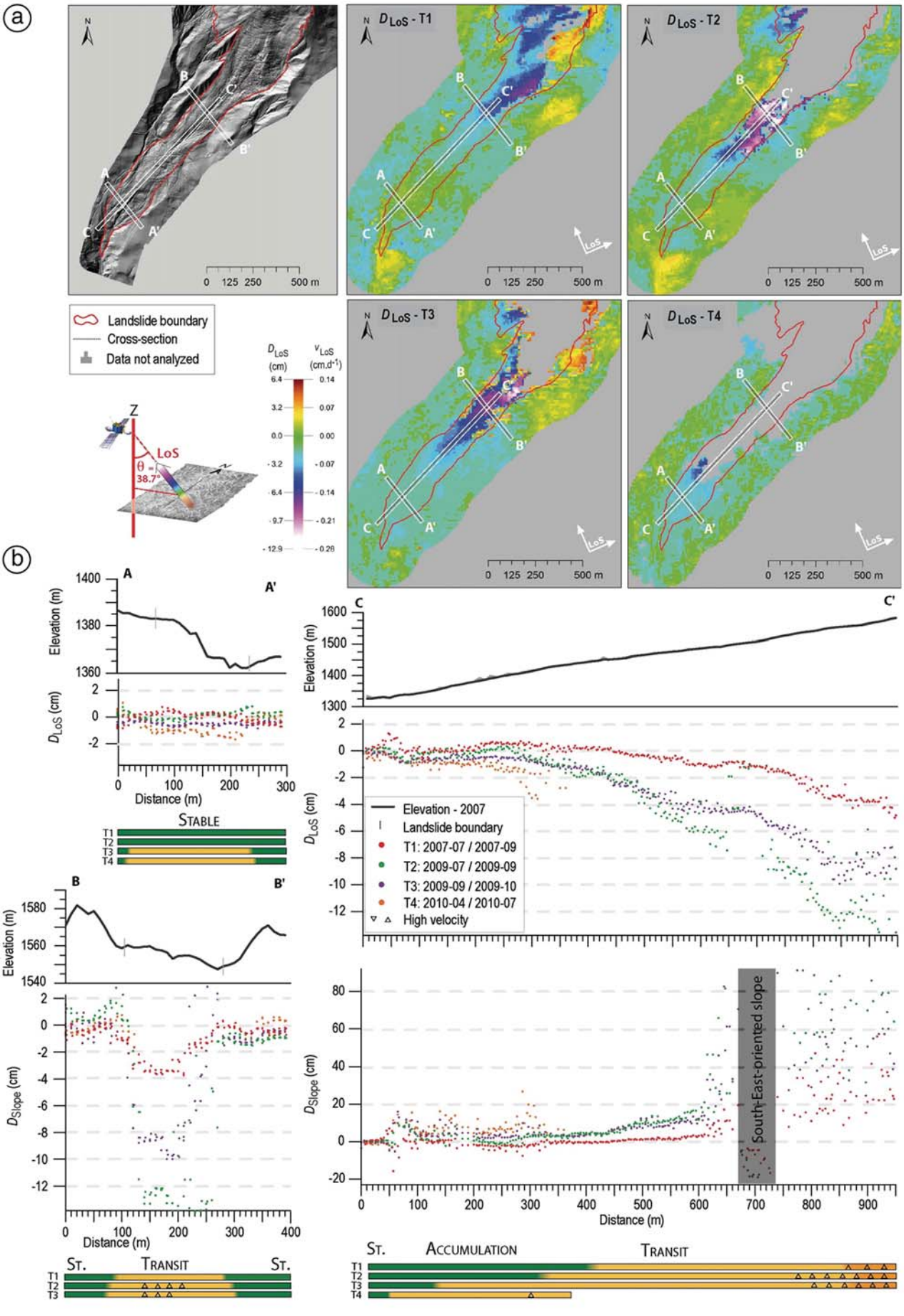
a
b
N
A
A'
B
B'
C
C'
0 125 250 500 m
D_{LoS} - T1
D_{LoS} - T2
D_{LoS} - T3
D_{LoS} - T4
LoS
Landslide boundary
Cross-section
Data not analyzed
D_{LoS} (cm)
v_{LoS} (cm.d^{-1})
6.4
3.2
0.0
-3.2
-6.4
-9.7
-12.9
0.14
0.07
0.00
-0.07
-0.14
-0.21
-0.28
Z
LoS
θ = 38.7°
Elevation (m)
D_{LoS} (cm)
Distance (m)
STABLE
T1
T2
T3
T4
Elevation - 2007
Landslide boundary
T1: 2007-07 / 2007-09
T2: 2009-07 / 2009-09
T3: 2009-09 / 2009-10
T4: 2010-04 / 2010-07
High velocity
D_{Slope} (cm)
South-East-oriented slope
ST.
TRANSIT
ACCUMULATION

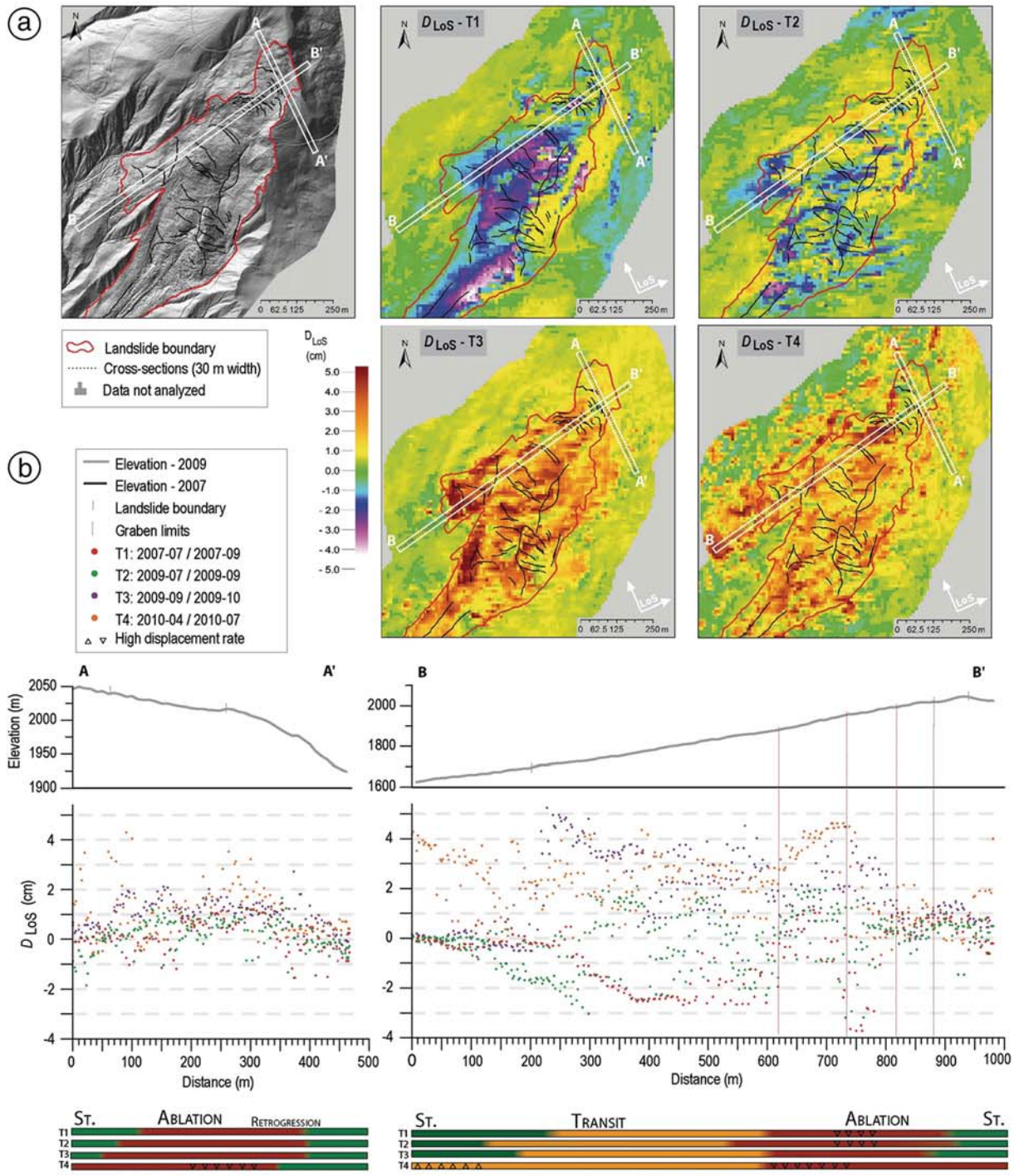

Fig. 12. Displacement (cm) and velocity (cm day^{-1}) observed in the ablation zone of the La Valette landslide from L-band PALSAR InSAR data. (a) Orthophotograph (2009) and interferograms for the periods T1, T2, T3 and T4. The landslide boundary is represented in red. (b) Profiles of elevation (top), D_{LoS} (middle) and D_{vert} (bottom) for two cross-section perpendicular to the landslide (A–A′) and along the steepest slope direction (B–B′). The location of the two profiles (of width 30 m) is indicated in (a). The colour bars indicate changes in the size of different movement type (subsidence in red, transit in yellow to orange, and stable slopes in green).

5.3.1. Kinematics of the Poche landslide

Fig. 13a shows the evolution of the D_{LoS} displacement rate of the Poche landslide for the periods T1, T2 and T3. In the ablation zone, the largest amplitudes of displacement are observed for T2 (summer 2009) and the lowest displacements are observed for T3 (autumn 2009). The subsidence rate is higher in summer 2009 (T2) than in summer 2007 (T1). At the opposite, in the transit zone, the displacements are in the same range for the three periods.

In comparison to the average velocity observed in the whole ablation and transit zones, a possible relation is observed between the surface velocity and the slope angle. The parts of the landslide with the highest velocity correspond to slopes around 20° for the ablation zone and 12° for the transit zone (Fig. 13b). The high displacement rates observed to the North and East of the ablation zone are confirmed by field observations which evidenced a retrogression of the main scarp between −3 and −9 m over the period 2007–2009. On-site EDM measurements on a

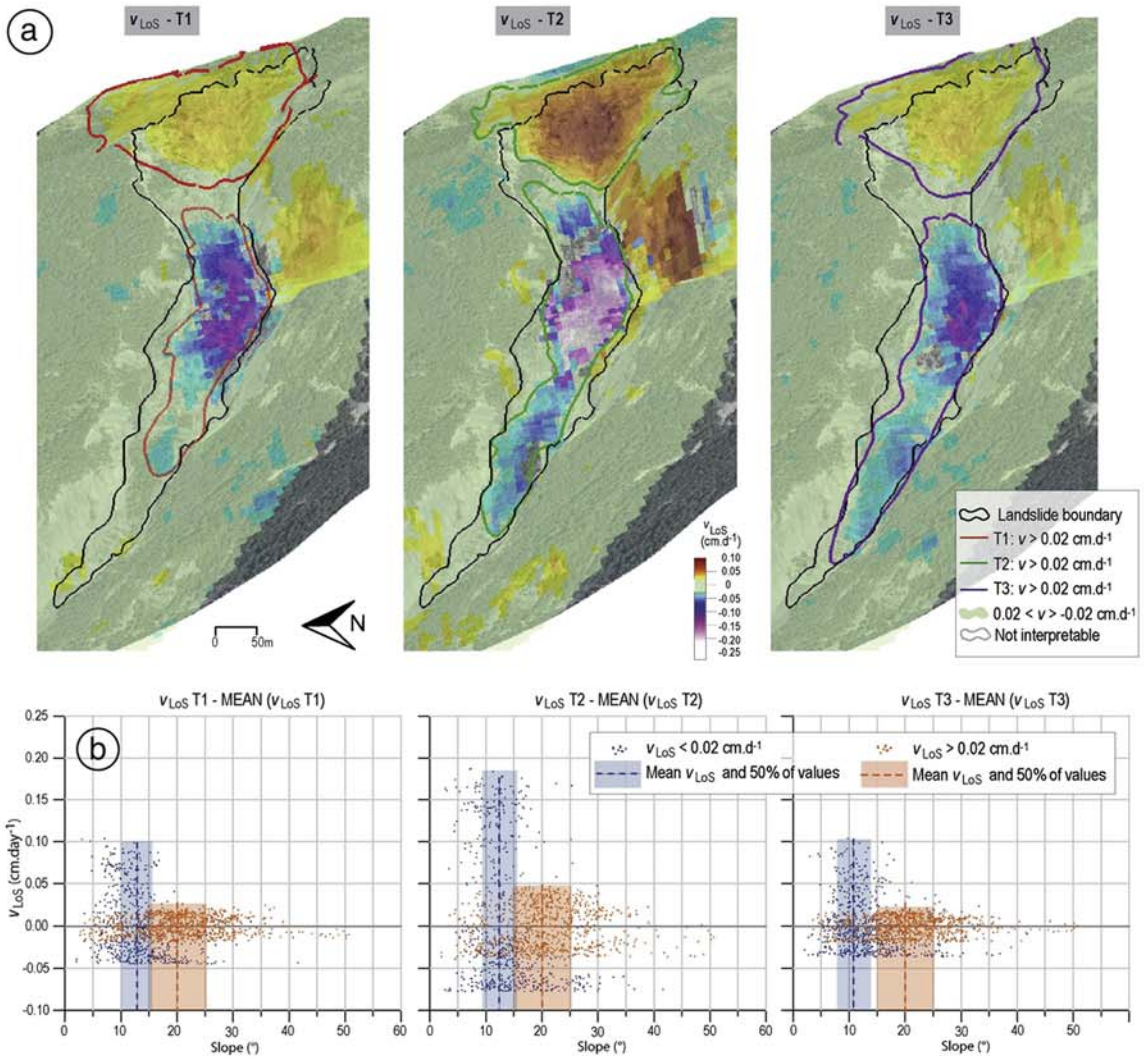

Fig. 13. InSAR displacement rates of the Poche landslide for three periods in 2007 and 2009. (a) Maps of v_{LoS} values (cm day^{-1}) at T1, T2 and T3. (b) Plots of v_{LoS} values as a function of slope angle (°). The velocity estimated at one pixel location is represented in relation to the average velocity observed in the subsidence zone (v_{LoS} > 0.02 cm d^{-1}, in orange) and in the transit zone (v_{LoS} < 0.02 cm d^{-1}, in blue).

series of benchmarks located along cross-section B–B′ (Fig. 9b) indicate an increase in the cumulative horizontal displacements from a total of 0.38 m in 2007 to a 0.60 m in 2009. Airborne orthophotographs for the same period show a similar pattern and amplitude of displacements. The highest displacement rates are observed at the point where the landslide changes its direction (from N270° to N300°) in relation with higher groundwater levels than at the terminal lobe.

5.3.2. Kinematics of the La Valette landslide

For the period 2007–2009, the evolution of the La Valette landslide (Fig. 14a) consists of a downslope progression of the main tongue and of a secondary tongue to the Northwest, of a retrogression of the main scarp and of a progressive increase of velocity in the lower parts.

The highest velocity (>0.02 cm day^{-1}) is observed in T2 (Fig. 15a). In comparison to the average velocity observed in the transit zones (Fig. 15b), the parts of the landslide with the highest velocity correspond to slope of around 17°. In the ablation zone, only wrapped phase values can be analysed. The retrogression and enlargement of the subsiding zone uphill occur at elevations higher than 1950 m. From the analysis of terrestrial LiDAR datasets for the period 2007–2009, Travelletti et al. (2013) estimate horizontal displacements of ca. 8 cm day^{-1} at 1950 m in elevation at the contact between the ablation and transit zones. Further downslope, the maximum D_{Slope} values estimated by InSAR decrease from 2 cm day^{-1} at 1600 m in elevation to 0.1 cm day^{-1} (T1) and 0.4 cm day^{-1} (T2, T3) at 1450 m in elevation, and further decrease towards the toe. Our results are consistent with the previous studies even considering different observation periods.

With C-band ERS images, Squarzoni et al. (2005) estimate displacement rates in the same order of magnitude than our results, and comprised between ~0.5 cm day^{-1} in 1999 to ~2 cm day^{-1} in 1996. With X-band TerraSAR-X images, Raucoules et al. (2013) are able to map the 3D landslide deformation pattern for the period 2010–2011 using amplitude offsets. They estimate maximum rates in the order of $D_{horiz} \approx 3.8$ cm day^{-1} and $D_{vert} \approx 3$ cm day^{-1} in the ablation area, which are higher than the displacements estimated for 2007 and 2009. They also notice the highest displacement rates in the months April to July (e.g. with velocity up to 5.5 cm day^{-1}). The same temporal pattern is observed in our dataset for the year 2009, with higher velocities in late spring/early summer than in autumn.

5.3.3. Triggering factors

For the two landslides, higher displacement rates are observed for the periods T2 and T4 in relation with larger amounts of net and effective (precipitation minus evapotranspiration) cumulated rainfall over 120 days (Fig. 15a). The evapotranspiration rate is calculated with the Penman–Monteith method. The effective cumulative rainfalls for the 30 days before the first SAR image acquisition are higher for T2

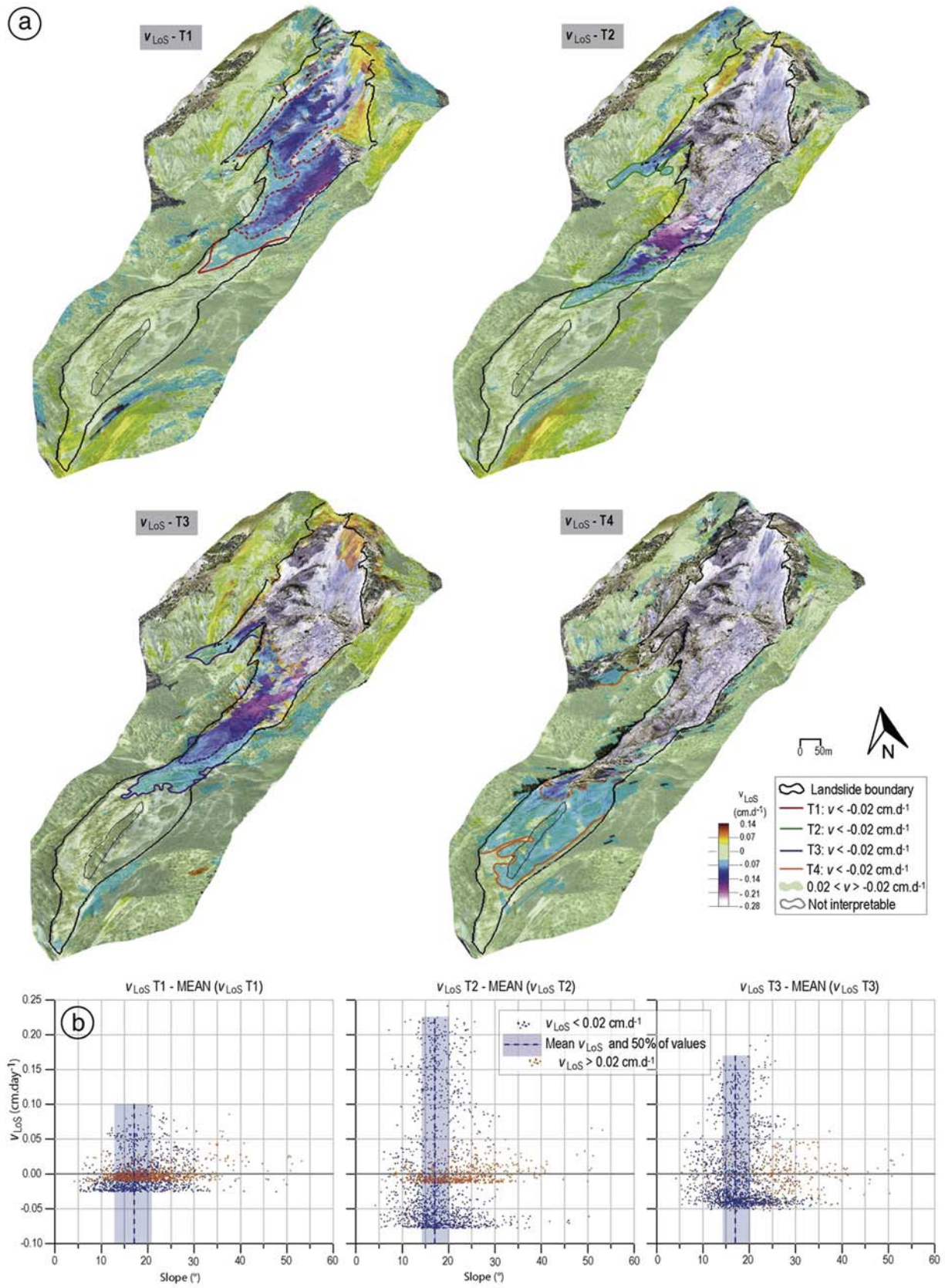

Fig. 14. InSAR displacement rates of the La Valette landslide for three periods in 2007 and 2009. (a) Maps of v_{LoS} values (cm day^{-1}) at T1, T2, T3 and T4; (b) plots of v_{LoS} values as a function of slope angle (°). The velocity estimated at one pixel location is represented in relation to the average velocity observed in the subsidence zone (v_{LoS} > 0.02 cm d^{-1}, in orange) and in the transit zone (v_{LoS} < 0.02 cm d^{-1}, in blue).

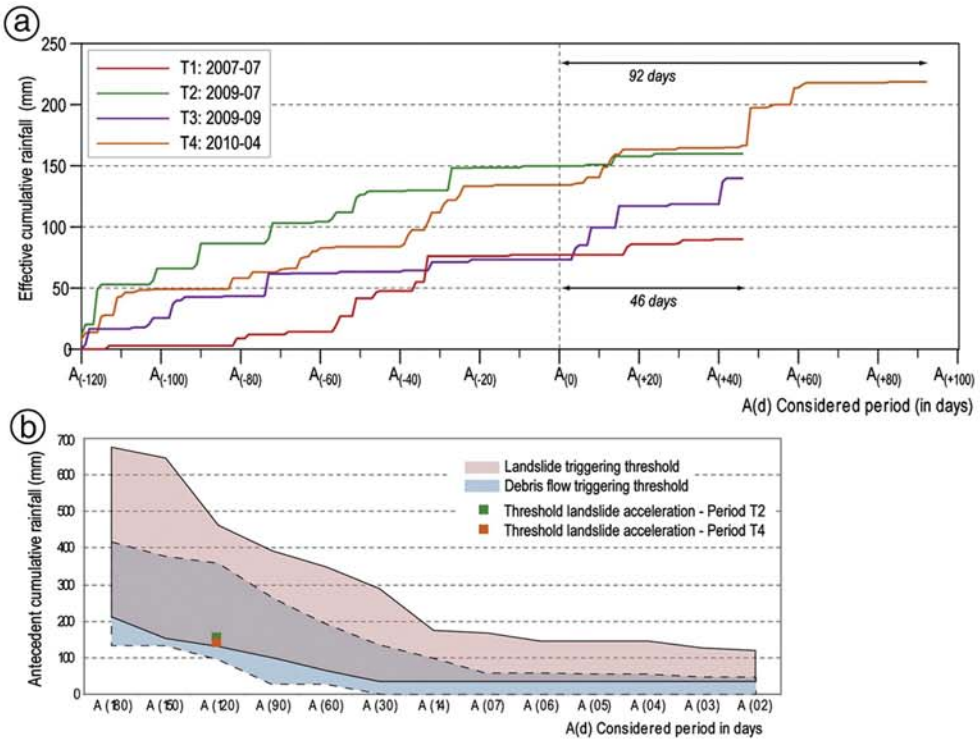

Fig. 15. Effect of rainfall amount on landslide motion. Cumulative effective rainfall observed before and during the four InSAR monitoring periods T1 to T4. The rainfall amounts are sampled at the Barcelonnette meteorological station; (b) landslide triggering rainfall thresholds estimated for the Barcelonnette region and threshold for landslide acceleration identified for two InSAR monitoring periods (T2, T4).

(20 mm) and T4 (22.5 mm) than for T1 (1.0 mm) and T3 (2.0 mm). These rainfall amounts (corresponding to landslide acceleration) are consistent with the antecedent cumulative rainfall thresholds proposed by Remaître and Malet (submitted for publication) from the analysis of the triggering conditions of 150 dated landslide and debris flow events in the Barcelonnette Basin over the period 1920–2010 (Fig. 15b).

6. Conclusion

This work demonstrates the potential of L-band ALOS/PALSAR archive images to analyse the deformation pattern of large and rapid landslides. For such case studies, the longer wavelength of L-band SAR sensors are suitable to preserve high spatial and temporal correlations and to cover vegetated landslides or ground affected by important soil surface changes. In order to overcome some limitations of InSAR processing in complex mountainous terrains, the different contributions to the SAR interferometric phase are estimated: the topography and the atmospheric delay are corrected, and a power spectrum filtering is applied on each interferogram.

A geomorphological-guided interpretation method is proposed to interpret the wrapped or unwrapped phase values for the location where the coherence value is higher than 0.3. The method integrates information on the location of specific morphological (scarps, grabens, and lobes) or topographic (steep slopes and convexity–concavity) features to analyse the spatial distribution of phase values. An *a priori* knowledge on the landslide deformation pattern (morphology and ground-based surface displacement monitoring) is used to convert and project the phase values into ground displacement. The processing is finely tuned for case studies corresponding to rotational movement, translational movement or complex movement and for two ranges of displacement rates (≤ 0.4 and >0.4 cm day^{-1}).

The results indicate that the deformation of two landslides can be monitored with ALOS/PALSAR imagery even with limited available SAR data. However, a larger and complete set of data would allow us to monitor the landslide evolution over several years using time series analysis and then estimate the relationships with the meteorological controlling factors with higher accuracy. The estimated displacement rates are in the range of the ground-based observations (GNSS and EDM) and consistent with C-band and X-band InSAR displacement rates estimated for other time periods. Highly variable displacement in space and time is identified for the two landslides in relation with rainfalls; enlargements and retrogression of the landslides scarps are also detectable for both landslides.

The proposed interpretation method is of interest for both 1) the detection and mapping of landslides in mountainous and vegetated terrains, and 2) the analysis of landslide mechanisms. ALOS/PALSAR imagery, even if only limited archive data are available, allows complementing information from other satellite SAR sensors to construct long time series of surface deformation. Further developments are the use of the spatial distribution of the deformation to infer the geometry and volume of the displaced material, and to characterize the rheology of the moving mass.

Acknowledgements

This work has been supported by the Marie Curie Research and Initial Training Network "CHANGES: Changing Hydro-meteorological Risks as Analyzed by a New Generation of European Scientists", funded by the European Community's 7th Framework Programme FP7/2007–2013 under Grant Agreement No. 263953. ALOS/PALSAR images were provided by the Japan Aerospace Exploration Agency (JAXA) and the European Space Agency (ESA) under the contract C1P.8859. The GNSS data were provided by the French Landslide Observatory (OMIV: Observatoire Multidisciplinaire des Instabilités de Versants: http://omiv.unistra.fr). The EDM measurements were acquired by the RTM-04 (Restauration des Terrains en Montagne) service of Département des Alpes-de-Haute-Provence.

References

Bardi, F., Frodella, W., Ciampalini, A., Bianchini, S., Del Ventisette, C., Gigli, G., Fanti, R., Moretti, S., Basile, G., Casagli, N., 2014. Integration between ground based and satellite SAR data in landslide mapping: the San Fratello case study. Geomorphology 223, 45–60.

Beauducel, F., Briole, P., 2000. Volcano-wide fringes in ERS synthetic aperture radar interferograms of Etna (1992–1998): deformation or tropospheric effect? J. Geophys. Res. 105 (B7), 16391–16402.

Berardino, P., Fornaro, G., Lanari, R., Sansosti, E., 2002. A new algorithm for surface deformation monitoring based on small baseline differential SAR interferograms. IEEE Trans. Geosci. Remote Sens. 40 (11), 2375–2383.

Booth, A.M., Lamb, M.P., Avouac, J.-P., Delacourt, C., 2013. Landslide velocity, thickness, and rheology from remote sensing: La Clapière landslide, France. Geophys. Res. Lett. 40, 4299–4304.

Cascini, L., Fornaro, G., Peduto, D., 2009. Analysis at medium scale of low-resolution DInSAR data in slow-moving landslide-affected areas. ISPRS J. Photogramm. Remote Sens. 64, 598–611.

Catani, F., Farina, P., Moretti, S., Nico, G., Strozzi, T., 2005. On the application of SAR interferometry to geomorphological studies: estimation of landform attributes and mass movements. Geomorphology 66, 119–131.

Cruden, D.M., Varnes, D.J., 1996. Landslide types and processes. In: Turner, R.L., Schuster, A.K. (Eds.), Landslide Investigations and Mitigation. Transportation Research Board, Washington D.C., pp. 36–75.

Delacourt, C., Allemand, P., Berthier, E., Raucoules, D., Casson, B., Grandjean, P., Pambrun, C., Varel, E., 2007. Remote-sensing techniques for analysing landslide kinematics: a review. Bull. Soc. Geol. Fr. 178, 89–100.

Dikau, R., Brunsden, D., Schrott, L., Ibsen, M.-L., 1996. Landslide Recognition: Identification, Movement and Causes. Wiley, Chichester.

Doin, M.P., Lasserre, C., Peltzer, G., Cavalie, O., 2009. Corrections of stratified tropospheric delays in SAR interferometry: validation with global atmospheric models. J. Appl. Geophys. 69, 35–50.

Doin, M., Lodge, F., Guillaso, S., Jolivet, R., Lasserre, C., Ducret, G., Grandin, R., Pathier, E., Pinel, V., 2011. Presentation of the small baseline processing chain on a case example: the Etna deformation monitoring from 2003 to 2010 using ENVISAT data. Proceeding Fringe 2011, ESA, Frascati, Italy, 19–23 September 2011, pp. 1–7.

Farina, P., Colombo, D., Fumagalli, A., Marks, F., Moretti, S., 2006. Permanent scatterers for landslide investigations: outcomes from the ESA-SLAM project. Eng. Geol. 88, 200–217.

Ferretti, A., Prati, C., Rocca, C., 2001. Permanent scatterers in SAR interferometry. IEEE Trans. Geosci. Remote Sens. 39 (1), 8–20.

García-Davalillo, J.-C., Herrera, G., Notti, D., Strozzi, T., Álvarez-Fernández, I., 2014. DInSAR analysis of ALOS PALSAR images for the assessment of very slow landslides: the Tena Valley case study. Landslides 11, 225–246.

Goldstein, R.M.M., Zebker, H.A., Werner, C.L., 1988. Satellite radar interferometry: two-dimensional phase unwrapping. Radio Sci. 23, 713–720.

Guzzetti, F., Manunta, M., Ardizzone, F., Pepe, A., Cardinali, M., Zeni, G., Reichenbach, P., Lanari, R., 2009. Analysis of ground deformation detected using the SBAS-DInSAR technique in Umbria, Central Italy. Pure Appl. Geophys. 166, 1425–1459.

Guzzetti, F., Mondini, A.C., Cardinali, M., Fiorucci, F., Santangelo, M., Chang, K.-T., 2012. Landslide inventory maps: new tools for an old problem. Earth Sci. Rev. 112, 42–66.

Hibert, C., Grandjean, G., Bitri, A., Travelletti, J., Malet, J.-P., 2012. Characterizing landslides through geophysical data fusion: example of the La Valette landslide (France). Eng. Geol. 128, 23–29.

Hilley, G.E., Bu, R., Ferretti, A., Novali, F., Rocca, F., 2004. Dynamics of slow-moving landslides from permanent scatterer analysis. Science 304, 1952–1955.

Hooper, A., 2004. A new method for measuring deformation on volcanoes and other natural terrains using InSAR persistent scatterers. Geophys. Res. Lett. 31, L23611. http://dx.doi.org/10.1029/2004GL021737.

Jebur, M.N., Pradhan, B., Tehrany, M.S., 2014. Detection of vertical slope movement in highly vegetated tropical area of Gunung pass landslide, Malaysia, using L-band InSAR technique. Geosci. J. 18, 61–68.

Lauknes, T.R., Shanker, A.P., Dehls, J.F., Zebker, H.A., Henderson, I.H.C., Larsen, Y., 2010. Remote sensing of environment detailed rockslide mapping in northern Norway with small baseline and persistent scatterer interferometric SAR time series methods. Remote Sens. Environ. 114, 2097–2109.

Le Mignon, G., Cojean, R., 2002. Rôle de l'eau dans la remobilisation de glissements–coulées (Barcelonnette, France). In: Rybar, J., Stemberk, J., Wagner, P. (Eds.), Proceedings of the 1st European Conference on Landslides, Prague, Czech Republik, Swets & Zeiltinger, Lisse, pp. 239–244.

Leprince, S., Berthier, E., Ayoub, F., Delacourt, C., Avouac, J.-P., 2008. Monitoring earth surface dynamics with optical imagery. Eos 89, 1–4.

Malet, J.-P., Maquaire, O., 2003. Black marl earthflows mobility and long-term seasonal dynamic in southeastern France. In: Picarelli, L. (Ed.), Fast Slope Movements: Prediction and Prevention for Risk Mitigation. Patron Editore, Bologna, pp. 333–340.

Malet, J.-P., Maquaire, O., Calais, E., 2002. The use of Global Positioning System techniques for the continuous monitoring of landslides: application to the Super-Sauze earthflow (Alpes-de-Haute-Provence, France). Geomorphology 43, 33–54.

Malet, J.P., Ulrich, P., Déprez, A., Masson, F., Lissak, C., Maquaire, O., 2013. Continuous monitoring and near-real time processing of GPS observations for landslide analysis: a methodological framework. In: Margottini, C., Canuti, P. Sassa (Eds.), Landslide Science and Practice. Proceedings of the Second World Landslide Forum Vol. 2. Springer, Rome, Italy, pp. 201–209. http://dx.doi.org/10.1007/978-3-642-31445-2_26.

Massonnet, D., Feigl, K.L., 1998. Radar interferometry and its application to changes in the Earth's surface. Rev. Geophys. 36, 441–500.

Muller, J.R., Martel, S.J., 2000. Numerical models of translational landslide rupture surface growth. Pure Appl. Geophys. 157, 1009–1038.

Nikolaeva, E., Walter, T.R., Shirzaei, M., Zschau, J., 2014. Landslide observation and volume estimation in central Georgia based on L-band InSAR. Nat. Hazards Earth Syst. Sci. 14, 675–688.

Notti, D., Davalillo, J.C., Herrera, G., Mora, O., Ferrata, V., 2010. Assessment of the performance of X-band satellite radar data for landslide mapping and monitoring: upper Tena Valley case study. Nat. Hazards Earth Syst. Sci. 10, 1865–1875.

Okada, Y., 1985. Surface deformation due to shear and tensile faults in a half-space. Int. J. Rock Mech. Min. Sci. Geomech. Abstr. 75, 1135–1154.

Petley, D.N., Bulmer, M.H., Murphy, W., 2002. Patterns of movement in rotational and translational landslides. Geology 30, 719–722.

Raucoules, D., De Michele, M., Malet, J., Ulrich, P., 2013. Remote sensing of environment time-variable 3D ground displacements from high-resolution synthetic aperture radar (SAR). Application to La Valette landslide (South French Alps). Remote Sens. Environ. 139, 198–204.

Remaître, A., Malet, J.-P., 2014. Rainfall patterns and climatic conditions associated to the triggering of fast- and slow-moving landslides at different time scales. A case study in the South French Alps. Landslides (submitted for publication).

Rosen, P.A., Hensley, S., Zebker, H.A., Webb, F.H., Fielding, E.J., 1996. Surface deformation and coherence measurements of Kilauea Volcano, Hawaii, from SIR-C radar interferometry. J. Geophys. Res. 101 (E10), 23109–23125.

Rosen, P.A., Hensley, S., Peltzer, G., Simons, M., 2004. Updated repeat orbit interferometry package released. EOS Trans. Am. Geophys. Union 85, 47–48.

Rott, H., Scheuchl, B., Siegel, A., 1999. Monitoring very slow slope movements by means of SAR interferometry: a case study from a mass waste above a reservoir in the Ötztal Alps, Austria. Geophys. Res. Lett. 26, 1629–1632.

Schmutz, M., 2000. Apport des méthodes géophysiques à la connaissance des glissements-coulées développés dans les marnes noires. (Thèse de doctorat). Application à Super Sauze (Alpes-de-Haute-Provence, France). Université Louis Pasteur, Strasbourg, France.

Squarzoni, C., Delacourt, C., Allemand, P., 2003. Nine years of spatial and temporal evolution of the La Valette landslide observed by SAR interferometry. Eng. Geol. 68, 53–66.

Squarzoni, C., Delacourt, C., Allemand, P., 2005. Differential single-frequency GPS monitoring of the La Valette landslide (French Alps). Eng. Geol. 79, 215–229.

Strozzi, T., Farina, P., Corsini, A., Ambrosi, C., Thüring, M., Zilger, J., Wiesmann, A., Wegmüller, U., Werner, C., 2005. Survey and monitoring of landslide displacements by means of L-band satellite SAR interferometry. Landslides 2, 193–201.

Stumpf, A., Malet, J.-P., Kerle, N., Niethammer, U., Rothmund, S., 2013. Image-based mapping of surface fissures for the investigation of landslide dynamics. Geomorphology 186, 12–27.

Stumpf, A., Malet, J.-P., Allemand, P., Ulrich, P., 2014. Surface reconstruction and landslide displacement measurements with Pléiades satellite images. ISPRS J. Photogramm. Remote Sens. 95, 1–12.

Tofani, V., Segoni, S., Agostini, A., Catani, F., Casagli, N., 2013. Use of remote sensing for landslide studies in Europe. Nat. Hazards Earth Syst. Sci. 13, 299–309.

Tolomei, C., Taramelli, A., Moro, M., Saroli, M., Aringoli, D., Salvi, S., 2013. Analysis of the deep-seated gravitational slope deformations over Mt. Frascare (Central Italy) with geomorphological assessment and DInSAR approaches. Geomorphology 201, 281–292.

Travelletti, J., Malet, J., Hibert, C., Grandjean, G., 2009. Integration of geomorphological, geophysical and geotechnical data to define the 3D morpho-structure of the La Valette mudslide, Ubaye Valley, French Alps. In: Malet, J.-P., Remaître, A., Boogard, T.A. (Eds.), Proceedings of the International Conference: Landslide Processes: From Geomorphologic Mapping to Dynamic Modelling. CERG Editions, Strasbourg, pp. 203–208.

Travelletti, J., Delacourt, C., Allemand, P., Malet, J.-P., Schmittbuhl, J., Toussaint, R., Bastard, M., 2012. Correlation of multi-temporal ground-based optical images for landslide monitoring: application, potential and limitations. ISPRS J. Photogramm. Remote Sens. 70, 39–55.

Travelletti, J., Malet, J.-P., Samyn, K., Grandjean, G., Jaboyedoff, M., 2013. Control of landslide retrogression by discontinuities: evidence by the integration of airborne- and ground-based geophysical information. Landslides 10, 37–54.

Vietmeier, J., Wagner, W., Dikau, R., 1999. Monitoring moderate slope movements (landslides) in the southern French Alps using differential SAR interferometry. Proc. 2nd International Workshop on ERS SAR Interferometry, FRINGE99, 10–12 November 1999. Liège, Belgium, pp. 31–40.

Wei, M., Sandwell, D.T., 2010. Decorrelation of L-Band and C-Band interferometry over vegetated areas in California. IEEE Trans. Geosci. Remote Sens. 48, 2942–2952.

Zhao, C., Lu, Z., Zhang, Q., De, J., 2012. Large-area landslide detection and monitoring with ALOS / PALSAR imagery data over Northern California and Southern Oregon, USA. Remote Sens. Environ. 124, 348–359.

Zhao, C., Zhang, Q., Yin, Y., Lu, Z., Yang, C., Zhu, W., Li, B., 2013. Pre-, co-, and post-rockslide analysis with ALOS/PALSAR imagery: a case study of the Jiweishan rockslide, China. Nat. Hazards Earth Syst. Sci. 13, 2851–2861.

3.2.2. Application of the interpretation methodology to a deep-seated landslide: the La Clapière case study

This section presents the application of the interpretation methodology to the analysis of the complex deep-seated La Clapière landslide (Fig. 3-3). The limitations of the method are underlined in terms of surveyable displacement rates as the upper part of La Clapière landslide is affected by very high displacement rates in the range of $cm.day^{-1}$ which do not allow phase unwrapping. Moreover, the combination of the slope morphology (slope orientation and gradient) and SAR properties (ascending track with particular incidence and azimuth angles) makes a quantitative analysis difficult. However, the analysis of the wrapped phase highlights the different sub-units of the landslide which kinematics is controlled by morpho-structures. The spatial distribution of the displacement rates is in agreement with ground-based total station measurements. This work is submitted to the peer-reviewed journal *Landslides*.

Landslides
DOI 10.1007/s10346-015-0623-0
Received: 10 January 2015
Accepted: 30 July 2015

R. Schlögel · J.-P. Malet · C. Doubre · T. Lebourg

Structural control on the kinematics of the deep-seated La Clapière landslide revealed by L-band InSAR observations

Abstract The objective of this work is to document the deformation pattern of the deep-seated La Clapière landslide for the period 2007–2010 from the combination of L-band synthetic aperture radar (SAR) interferograms, ground-based total station measurements and identification of the slope geomorphological structures. The interferograms are calculated for pairs of ALOS/PALSAR images at a time interval of 46 days. The displacement field derived from the interferograms reveals a non-uniform displacement gradient from the top (subsidence) to the bottom (accumulation). Vertical velocities are calculated from the unwrapped phase values and are in good agreement with ground-based measurements. The results demonstrate the potential of L-band ALOS/PALSAR imagery for the monitoring of active landslides characterized by complex kinematic patterns and by important changes in the soil surface backscattering in time.

Keywords Landslide · InSAR · ALOS/PALSAR · Displacement monitoring

Introduction

Knowledge on slope surface kinematics is a basic requirement for understanding the controlling mechanisms of landslide deformation. Traditional ground-based approaches (tacheometry, extensometry, GNSS) require a movement velocity above a certain threshold (e.g. centimeters per day) to detect a displacement signal; further, these techniques are time-consuming and costly (mainly in terms of field operations) and give access only to a discrete (e.g. point) information on the movement. As a complement to ground-based measurements, space-borne remote-sensing techniques allow obtaining spatially distributed information on the kinematics of slope movements (Casson et al. 2005).

Techniques using high resolution (HR) to very high resolution (VHR) space-borne optical and radar (SAR) images are able to measure 1D Line-of-Sight (LoS), 2D horizontal and sometimes fully 3D surface displacements. For instance, digital image correlation (DIC) of VHR optical satellite images has been used to estimate the horizontal component of the displacement with a centimetric accuracy (Booth et al. 2013; Stumpf et al. 2014). Over the last decade, in complement to optical images, synthetic aperture radar (SAR) images have become a widely used source of information for landslide detection (Cascini et al. 2009; Lu et al. 2012) and monitoring (Zhao et al. 2012; Raucoules et al. 2013). Comprehensive overviews of SAR observations for landslide investigations have been presented by Colesanti and Wasowski (2006) and Rott and Nagler (2006). However, these reviews predate the launch of the most recent commercial SAR sensors. Rott (2009) provides an updated summary with reference to the TerraSAR-X and COSMO-SkyMed satellites before the availability of the Sentinel constellation (Berger et al. 2012). This recent generation of SAR satellite sensors can acquire, through dedicated acquisition planning, high-frequency observations (up to every 6 days) over regional areas (e.g. 10–1000 km^2) with high resolution (up to 1-m ground resolution).

Two-pass differential InSAR technique (D-InSAR) has been applied for the monitoring of slow-moving landslides (on the order of cm year^{-1}; Massonnet and Feigl 1998; Squarzoni et al. 2003; Schlögel et al. 2015). However, InSAR methods have important limitations associated with geometric and temporal decorrelation, atmospheric artifacts, scale constraints, geometric distortions, a measurement sensitivity limited to a 1D Line-of-Sight (LoS) and average value of measurements for the time window of observation (Colesanti and Wasowski, 2006). A range of techniques has been developed to help minimizing some of these limitations such as time-series analysis (Ferretti et al. 2001; Berardino et al. 2002) or the use of external data to reduce atmospheric path delays (Li et al. 2006; Foster et al. 2013). Analyzing the deformation patterns of large landslides with InSAR is therefore still challenging.

Deep-seated landslides usually involve weathered rock and/or bedrock and consist of large slope failures associated with translational, rotational or complex movement. This type of landslides potentially occurs in tectonic active regions, and the kinematics is controlled by the structures (faults, bedding planes) of the slopes (Dramis and Sorriso-Valvo 1994; Agliardi et al. 2001; Travelletti et al. 2013). They typically move slowly, with displacement rates of a few mm year^{-1} to cm year^{-1} but can occasionally move faster and thus become potentially damaging (Hradecký and Pánek 2008). Specific morpho-structural features such as double ridges, ridge top grabens, concave counterscarps, trenches and steep slopes at the toe characterize this type of landslide (Agliardi et al. 2001).

In the South French Alps, the Argentera-Mercantour mountain range is affected by several deep-seated slope movements. At the mountain range scale, their spatial distribution has been studied through geological field surveys and interpretation of multi-date orthophotographs (Jomard 2006). These investigations concluded on the control of the landslide locations by pre-existing tectonic faults (Guglielmi et al. 2005; Jomard et al. 2007; Bois et al. 2008). At the slope scale, most of the investigations and monitoring were conducted at the La Clapière slope, which is intensively weathered and affected by various sets of discontinuities (Follacci et al. 1988; Follacci, 1999; Gunzburger and Laumonier 2002; Guglielmi et al. 2005). The conclusion of nearly 30 years of displacement monitoring is that there is still limited knowledge on the influence of the fault geometry at depth on the spatial distribution of slope kinematics (Girault and Terrier, 1994; Helmstetter et al. 2004; Delacourt et al. 2004; Delacourt et al. 2007).

In this work, we focus on the kinematic analysis of the deep-seated La Clapière landslide, characterized by a velocity in the order of cm day^{-1} and a complex spatial pattern of displacement. The work is complementary to previous investigations of the slope

kinematics using several techniques (photogrammetry of terrestrial, aerial and satellite optical images, short-wavelength C-band InSAR and on-site total station and GPS periodic measurements) covering various time periods (Girault and Terrier 1994; Fruneau et al. 1996; Casson et al. 2005; Serratrice, 2006).

After presenting the study area, the evolution of the slope surface deformation over the last 30 years and the InSAR processing technique, we analyze L-band SAR images to estimate the displacement field for the period 2007–2010 and compare it to ground-based total station measurements. We focus on the time evolution of the displacement field and identify kinematic and structural sub-units within the landslide body. L-band SAR images proved their usefulness for monitoring such type of active landslides affected by significant changes in the local morphology and the soil surface state modifying the ground scattering properties between two consecutive SAR images.

Geological and geomorphological characteristics of the La Clapière slope

The La Clapière landslide is located in the Tinée valley in the Southeast French Alps, approximately 80 km north of Nizza (Fig. 1a). The active landslide, which is part of a large unstable slope deforming since 3.6 ka (Guglielmi et al. 2005; Lebourg et al. 2010), has been triggered in the early twentieth century (Fig. 1a). In 2014, the landslide has a relative elevation of 750 m (between 1100 and 1850 m a.s.l.) and a volume estimated at 60 million cubic meters (Jomard et al. 2007). The slope is facing the South-West direction (Fig. 1b, c).

The top of the La Clapière landslide corresponds to a 120-m scarp which consists of two lobes (Fig. 1) extending over a width of 800 m at the elevation of 1600 m. The steepest slopes, as well as secondary scarps, are observed at elevation between 1400 and 1500 m corresponding to an outcrop of hard rocks (migmatite and metadiorite) at the 'Barre d'Iglière' (Follacci, 1987). The landslide body is developed in Hercynian rocks composed mainly of weathered and fractured migmatic gneiss (Follacci 1999; Fig. 1c) and overlaps at its base Quaternary alluvial sediments of the Tinée river. The Hercynian-foliated material is dipping sub-horizontally at 5° outside of the landslide body while it is dipping at 10° to 30° within the landslide body (Ivaldi et al. 1991; Gunzburger and Laumonier 2002; Delteil et al. 2003). At the top of the slope, above 1800 m, the metamorphic rocks are weathered over a thickness ranging from 50 to 200 m. In the middle part of the slope and at the toe, the gneiss is fractured (Corsini et al. 1994). Compressive features are observed at the Cascaï thrust that has a N 130° E orientation and dips to the North-East. Extensive features are observed along two main directions:

- a N 110–140° E set of discontinuities/normal faults dipping 60° to the South-West, with a 150-m average spacing. These structures form the landslide main and secondary scarps (Jomard 2006).
- a N010-30°E set of discontinuities/strike-slip dipping 70° to 80° to the South-East and the North-West, sometimes containing a thick filling of tectonic breccia. These structures limit the extension of the landslide to the North-East and the South-West.

The active landslide body can be schematically divided into three zones according to the rock fracturing and the spatial distribution of surface displacement rates (Cappa et al. 2004):

1. The main unit separated in two parts by a major scarp, is located at an elevation between 1100 and 1600 m (Fig. 1b, c). The scarp is oriented N 090° E and is dipping 50° towards the valley. These two parts consist of fractured rocks moving downslope at a velocity varying from 45 to 90 cm year^{-1} (Fig. 2)
2. The upper North-East unit (Fig. 1b, c) which behaves as an isolated block sliding along its own failure surface and overlapping the main central unit at a velocity varying from 100 and 380 cm year^{-1} (Fig. 2)
3. The upper North-West unit (Fig. 1b, c) which behaves as a fractured rock mass with active tension cracks and moves at a velocity varying from 20 to 70 cm year^{-1} (Fig. 2)

Recent evolution of the landslide kinematics

The onset of the La Clapière movement is dated around the years 1950–1955 (even if a main scarp was already visible in 1937; Follacci 1987), possibly as a consequence of the major flood events of the Tinée river in 1951–1957 and a destabilization of the lower parts of the slope (Guglielmi et al. 2005). For the period 1951–1983, the landslide velocity is estimated from the correlation of aerial orthophotographs acquired in 1951, 1964, 1974 and 1983 (e.g. mean velocity values in green in Fig. 2). The velocity increased from 50 cm year^{-1} for the period 1951–1966 period to 150 cm year^{-1} for the period 1974–1983 (Follacci et al. 1988).

Since 1982, the landslide surface displacements are monitored by total station on a series of 43 targets (Fig. 2) at a monthly frequency (Follacci et al. 1988; 1993). According to Follacci (1987), the parallelism of the directions of motion of the benchmarks and the synchronism of the seasonal accelerations support the hypothesis of a deep failure. The grey line (Fig. 2) represents the monthly velocity of benchmark 10 which is located in the central part of the landslide and which can be considered as representative of the landslide kinematics for the period 1982–1995 (Helmstetter et al. 2004). An increase of this benchmark velocity occurs between January 1986 and January 1988, up to 8 cm day^{-1} during summer 1987 and 9 cm day^{-1} in October 1987. From 2000, the monthly velocity is calculated for ten targets (five historical targets numbered 6, 10, 16, 17, 24 and five new targets numbered 32, 34, 44, 43, 54; Fig. 2). For this period, the velocity varies from 1 cm day^{-1} (ca. 3.5 m year^{-1}) in 2000 to 2.5 cm day^{-1} (9 m year^{-1}) in 2001 which is the maximal annual velocity recorded (Fig. 2b). From 2002 to 2007, the landslide velocity decreases to less than 0.2 cm day^{-1}. In spring, a small acceleration phase is observed before the stop of the total station measurements in June 2009. No ground-based surface displacement observations are available for the period 2009–2011. In 2011, GPS receivers were installed on the landslide at location CLP1 and CLP2 (Fig. 2). The French National Landslide Observatory (OMIV) is now in charge of the continuous monitoring of the landslide. A short acceleration has been observed in the spring of 2013 (ca. 1 cm day^{-1}) but not comparable to those of 1987 and 2001.

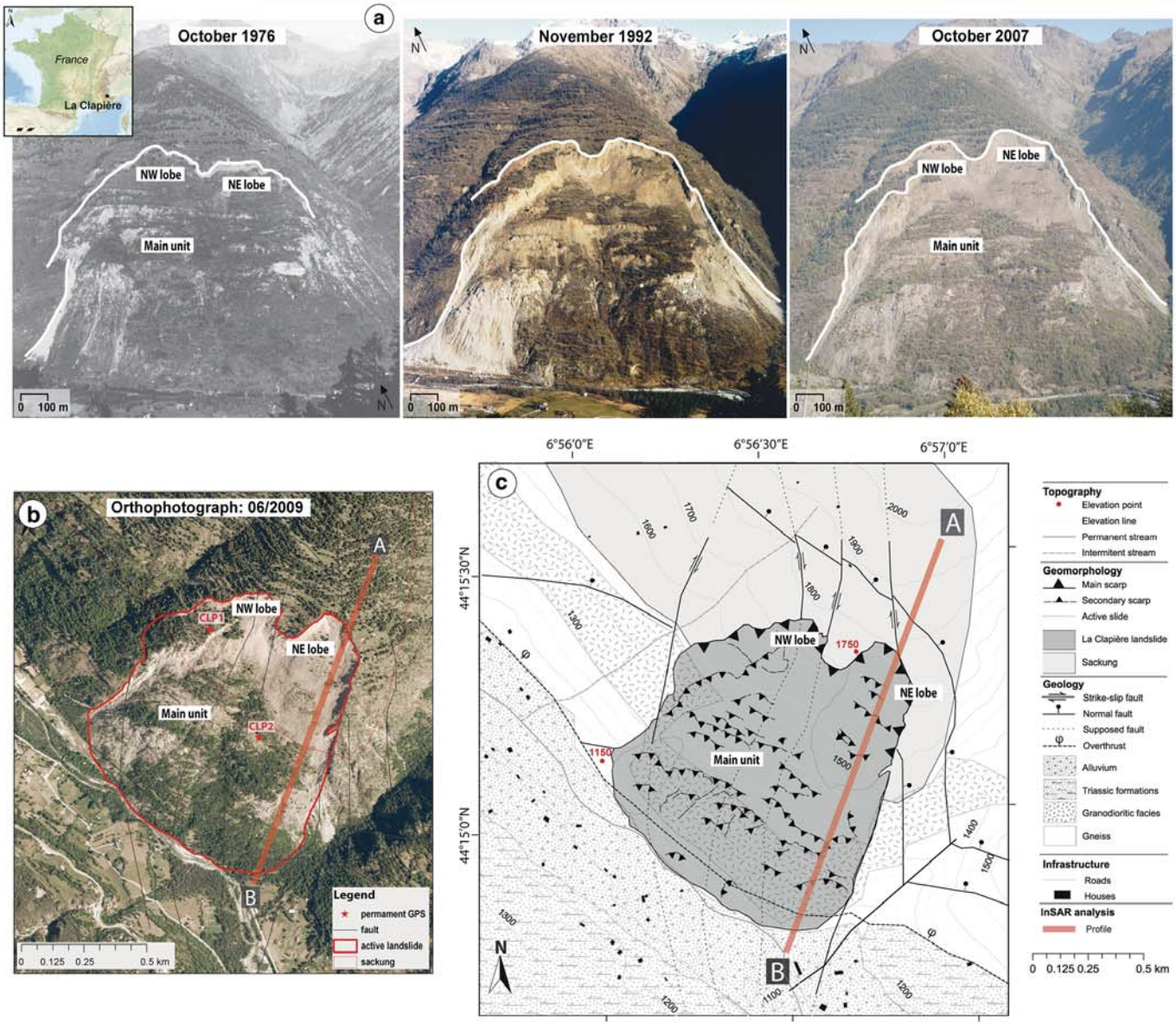

Fig. 1 Geomorphology of the La Clapière landslide. **a** Photographs of the La Clapière landslide in 1976, 1992 and 2007. **b** Orthophotograph of the landslide in 2009. **c** Morpho-structural map of the landslide.

Methods

Dataset: SAR images and ground-based total station measurements

The dataset (Fig. 3) consists of satellite SAR images, airborne orthophotographs, a high resolution digital surface models (DSMs) and displacement measurements from a ground-based total station. We use 15 ALOS/PALSAR images (processed at Level 1.0) acquired from March 2007 to July 2010 (Fig. 3). This large wavelength L-band radar sensor (λ=23.8 cm) is more suitable for landslide monitoring than shorter C-band and X-band radar sensors as it allows higher quality of the backscattered phase signal on rapidly evolving ground surfaces (vegetation, soil surface state, micromorphology and roughness; Wei and Sandwell 2010).

The ALOS/PALSAR catalogue consists of SAR images acquired along ascending orbit (track 880) and with a high-resolution Fine Beam Polarization (FBS) mode. For all images, the pixel dimensions are 9.78 m and 7 m along the azimuth and range direction, respectively. The mean look angle θ is 38.7° over the scene, and the off-nadir azimuth α_d is 75.8°. For the InSAR processing, the criteria used to select the image pairs are as follows: (1) a perpendicular baseline ($B_\perp$) smaller than 1000 m; (2) a temporal baseline (B_T) between both images of 46 days; and (3) a net rainfall amount of less than 200 mm between consecutive dates (Fig. 3). To avoid decorrelation due to the presence of snow cover, we also excluded scenes acquired in winter. The four interferograms analyzed in this work are named T1, T2, T3 and T4 (Fig. 3).

A medium resolution (25 m) DSM from the French National Mapping Agency (BD ALTI®, IGN), resampled at 0.000088° (9.78 m) and projected in geographic-WGS84 coordinates was used for the InSAR processing. A high resolution (0.000052°) airborne LiDAR DSM, resampled at a pixel size of 5 m, is used for calculation of the ground displacements. Three aerial

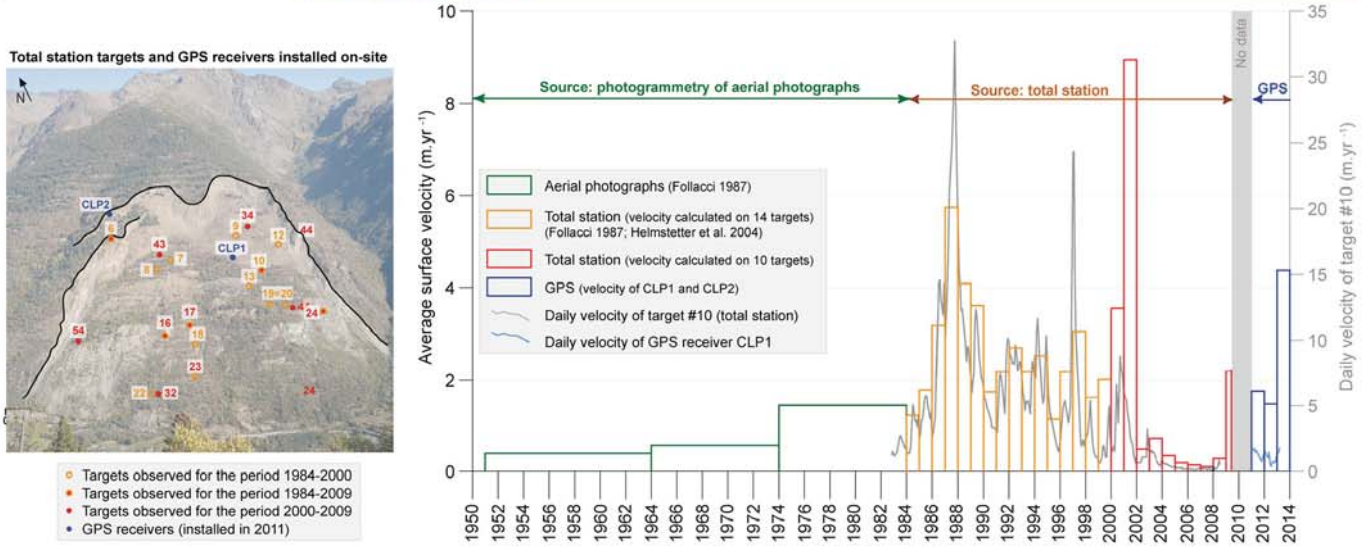

Fig. 2 Evolution of the mean velocity of the landslide body from 1950 to 2013 measured by photogrammetry of airborne photographs (1951–1984), by ground-based total station measurements on benchmarks (1984–2009) and by continuous GPS measurements (2011–2013). The velocity time series is constructed from previous studies (Follacci 1987; Helmstetter et al. 2004) and calculated from total station observations provided by the Centre d'Etudes Techniques de l'Equipement (CETE-06).

orthophotographs (0.5 m) of 2004, 2009 and 2012 were used for the morphological analysis and the interpretation of the results.

Total station measurements were provided by the public authority Centre d'Etudes et d'Expertise sur les Risques, l'Environnement, la Mobilité et l'Aménagement (CEREMA in charge of the slope risk management. The automated total station measures distances and horizontal/vertical angles on 1 to 2-km distant targets in line-of-sight. Two to five of the targets used for total station measurements were acquired daily over the period 2000–2009.

D-InSAR processing and interpretation

The processing of the SAR images and interpretation methodology of the interferograms are summarized in Fig. 4. Each interferogram consists of the calculation of phase differences ($\Delta\Phi_{int}$) between two co-registered SAR images (Eq. 1):

$$\Delta\Phi_{int} = \Phi(t_o) - \Phi(t_1) + \Delta\Phi_{def} + \Delta\Phi_{orb} + \Delta\Phi_{topo} + \Delta\Phi_{atm} + \Delta\Phi_{noise} \quad (1)$$

where $\Delta\Phi_{int}$ is the SAR interferometric phase, $\Delta\Phi(t_o)$ and $\Delta\Phi(t_1)$ are the SAR phase values at, respectively, day t_o (reference) and day t_1, $\Delta\Phi_{def}$ is ground deformation (between two acquisition times), $\Delta\Phi_{orb}$ is orbital contribution (due to changes of the satellite orbital geometry), $\Delta\Phi_{topo}$ is topographic contribution, $\Delta\Phi_{atm}$ is atmospheric contribution (due to difference of signal propagation in the atmosphere) and $\Delta\Phi_{noise}$ is noise contribution (corresponding to changes in the scattering properties of the ground surface,

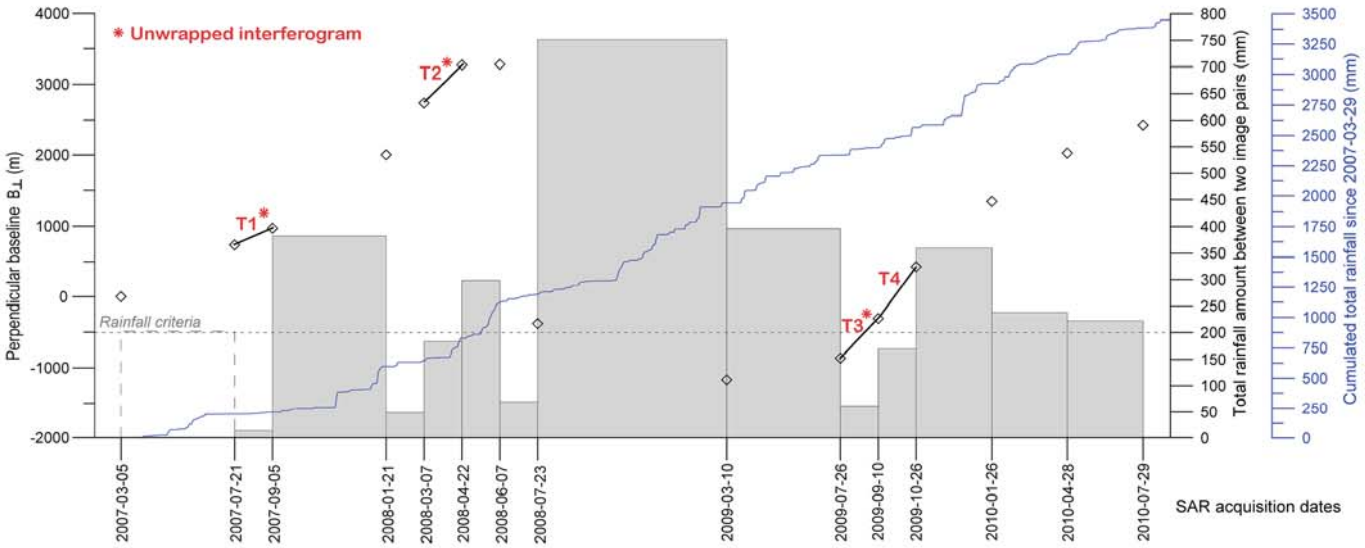

Fig. 3 Time acquisition and perpendicular baseline (*white point*) of the SAR images together with the cumulative net rainfall between consecutive SAR acquisitions (*grey box*) and for the complete time period (*blue line*) at the St-Etienne de Tinée meteorological station. The interferograms T1, T2, T3 (*unwrapped*) and T4 (*wrapped*) are indicated. A *dotted grey line* indicates the 200 mm of cumulated rainfall used as selection criterion for the SAR images

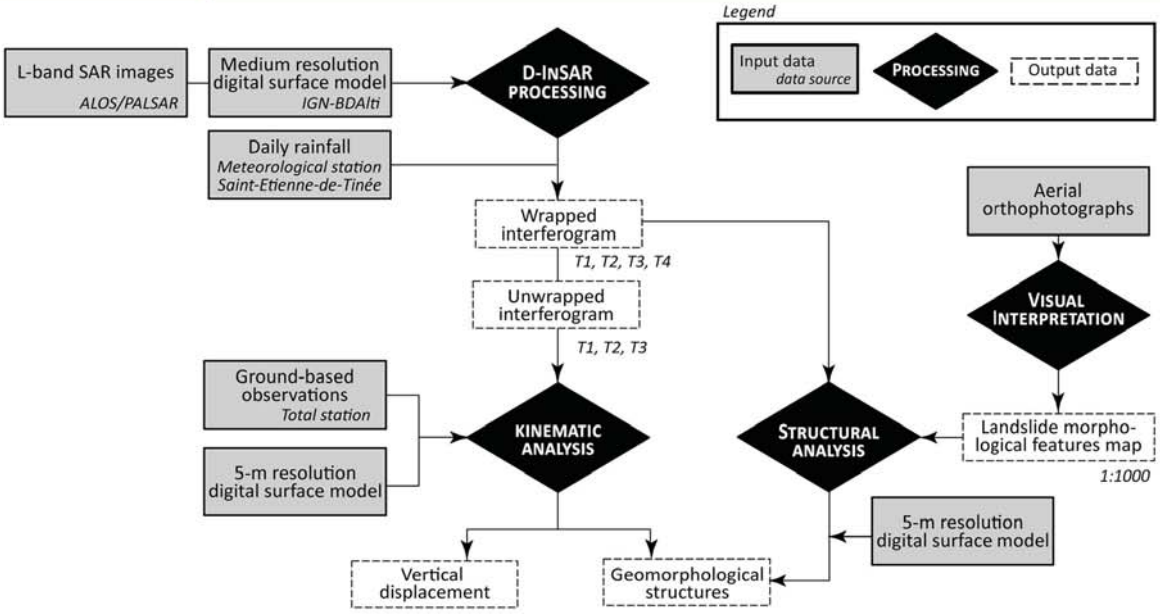

Fig. 4 Flowchart of the methodology and indications of the data and outputs used at each processing step (modified from Schlögel et al. 2015)

changes in the thermal properties of the atmosphere or ground surface or inaccurate image co-registration; Massonnet and Feigl 1998).

The co-registration between SAR images is performed using a quadratic fit with the software package NSBAS (Doin et al. 2011) to take into account orbital parameter and the topography. Then, the interferograms are processed with the software package ROI_PAC (Fig. 4; Rosen et al. 2004). The topographic contribution is corrected using the BDALTI® DSM (25 m) resampled at 10 m. The orbital contribution is corrected with precise satellite orbit data (<1 m) provided by the Japan Aerospace Exploration Agency (JAXA) fitted with a 2D linear offset ramp. Further, a range-dependent spectral filtering is applied to improve coherence of the interferograms with long spatial baselines with NSBAS.

After filtering, we interpret only the interferograms with coherence values higher than 0.30 (e.g. T1, T2, T3 and T4; Fig. 3). The phase values are unwrapped using the branch-cut unwrapping algorithm of Goldstein et al. (1988) and geocoded.

The interpretation of the interferograms is performed at the slope scale in a Geographical Information System (GIS). First, the interferograms are converted in the local reference system Lambert NTF Zone III and resampled at a pixel size of 9.78 m. The precise location and contours of the expected deformation area are mapped from the interpretation of the series of orthophotographs. Second, in order to compare the interferograms, we shifted the phase values taking as reference the portions of the terrain out of the landslide body. We subtracted the median phase values (Φ_{med}) of the area surrounding the landslide to the phase values of the sub-scene. The resulting phase values for the wrapped interferograms are thus expressed in the range $[-\pi-\Phi_{med}, \pi-\Phi_{med}]$.

The landslide morphological features (scarps, fractures, lobes, gullies) observed on the aerial orthophotographs and the DSM are used to guide the interpretation of the wrapped and unwrapped phase values. For the analysis of the unwrapped phase values, we converted the phase values in displacement along the SAR LoS direction (D_{LoS}) using Eq. 2:

$$D_{LoS} = \lambda \Delta\Phi / 4\pi \quad (2)$$

where λ is the wavelength, and Φ is the phase value.

Taking into account the spatial distribution of the phase values, we consider the portions of the terrain with absolute phase values Φ>0.5 (corresponding to a LoS displacement of 0.9 cm) as 'moving' areas. According to Schlögel et al. (2015), various phase values and displacement fields can be observed at the scale of a landslide due to heterogeneous local movements:

- In the lower part of the landslide, the horizontal component of the displacement (expressed along the downslope direction) is dominant with an accumulation of the displaced material; this movement corresponds to negative phase values (Φ<−0.5).
- In the upper part of the landslide, close to the main and secondary scarps, the vertical component of the displacement is dominant with a subsidence and a transport of material downslope; this movement corresponds to positive phase values (Φ>0.5).

Using ground-based monitoring data, we assumed a main displacement direction for all the kinematical units of the landslides. Two cases are considered. The first case corresponds to a vertical motion associated with a depletion of material (preferentially located in the upper part of the landslide) or with an accumulation of material (preferentially at the toe of the landslide). Therefore, we convert the LoS

displacement into ground vertical displacement (D_{vert}) with Eq. 3:

$$D_{vert} = D_{LoS}/(n_z.n_{LoS}) = -D_{LoS}/\cos\theta \quad (3)$$

where n_z is the vertical unit vector (positive upward), n_{LoS} is the unit vector in the LoS direction and θ is the mean incidence angle (equal to 39.7° in this region). A positive vertical displacement ($D_{vert} \geq 0$) corresponds to a subsidence; a negative vertical displacement ($D_{vert} \leq 0$) corresponds to an uplift or an accumulation of material.

The second case corresponds to an along-slope motion, observed in the case of a predominant translational sliding. According to the orientation of the displacement field of the landslide (ca. N210°E) and the mean slope gradient (ca. 33°) close to the incidence angle (θ), we decided to project the displacement only in the vertical direction. SAR images acquired in ascending orbits would have been a source of information to calculate the 'along-slope' displacement vectors, but unfortunately, no images are available in the satellite archives.

Results: analysis of the landslide kinematics

The landslide kinematics was analyzed for the period 2007–2010 in terms of the spatial distribution of velocity and the evolution of velocity over time by combining the ground-based total station measurements and the InSAR-derived displacement fields.

Landslide velocity fields from the ground-based total station measurements

The total station installed in front of the landslide is the only source of ground-based surface displacement measurements for the period 2000–2009 (Fig. 5a). Trends in the surface displacements can be identified for a series of six targets located along a cross section from the scarp to the toe of the landslide. According to their position within the landslide body, the targets have different kinematic behaviour. The target #40 located at the crown is stable; in the landslide body, the displacements are higher for the targets #34 and #10 located in the upper part than for the targets #44 and #24 located in the middle and lower parts. The cumulated displacements are in a range of factor 5 for the period 2000–2009, from 10 m at the toe (#24) to nearly 50 m at the base of the main scarp (#34).

Figure 5b also highlights the important acceleration observed in 2000–2001. The acceleration started at different times according to the landslide units, in June 2000 for target #34 at the base of the scarp to December 2000 for the targets #44 and #24 in the lower parts. The peaks of velocity are observed from April to August 2001; the deceleration occurred in November 2001. A small rise in velocity is again observed for all targets between November 2002 and July 2003. Then, for almost 5 years, the landslide exhibits constant velocity for all units. The onset of a new acceleration is observed in February 2009 at targets #6, #44 and #34. Unfortunately, the total station measurements have ceased in July 2009 due to malfunctioning of the instrument and expensive maintenance costs.

The evolution of the displacements per component (E, N, Z) is presented in Fig. 6. The daily position of the targets at midday (12.00) and the error bars are plotted for four targets for the period 2007 to 2009.

The variability of measurements is more important for the targets located in the upper part of the landslide where the distances total station-target are longer. Considering this variability, we still consider the target #40 as stable even if a tilt is observed (with the succession of positive and negative variations) due to its position at the crown. In the upper part of the landslide body, the benchmark #34 is the most rapid, especially in the North component; from April 2008, the velocity increases from 0.1 to 1.6 cm day^{-1}. Best-fit (R^2 values>0.80) linear regression lines are

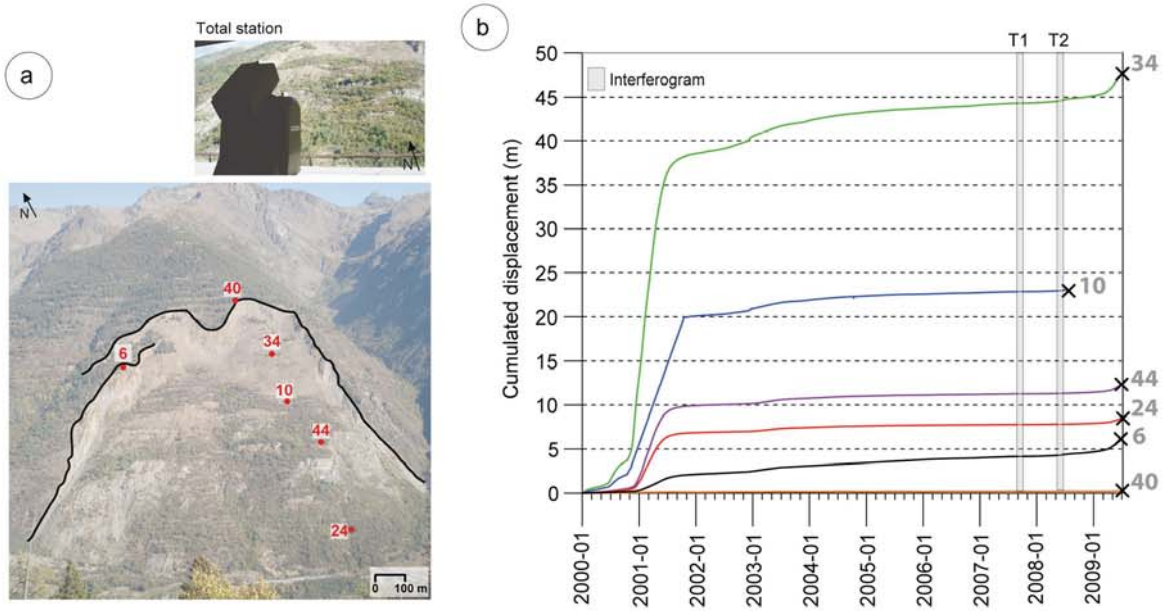

Fig. 5 Landslide surface displacement measured by total station on a series of targets. **a** Photograph of the total station and location of the targets used in the analysis. The targets are located along a cross section in the South part of the landslide. **b** Evolution of the distance tacheometer-target for six benchmarks from 2000 to 2009. The black cross indicates the stop of the measurement. The *grey lines* indicate the interferograms available during the monitoring period (T1, T2)

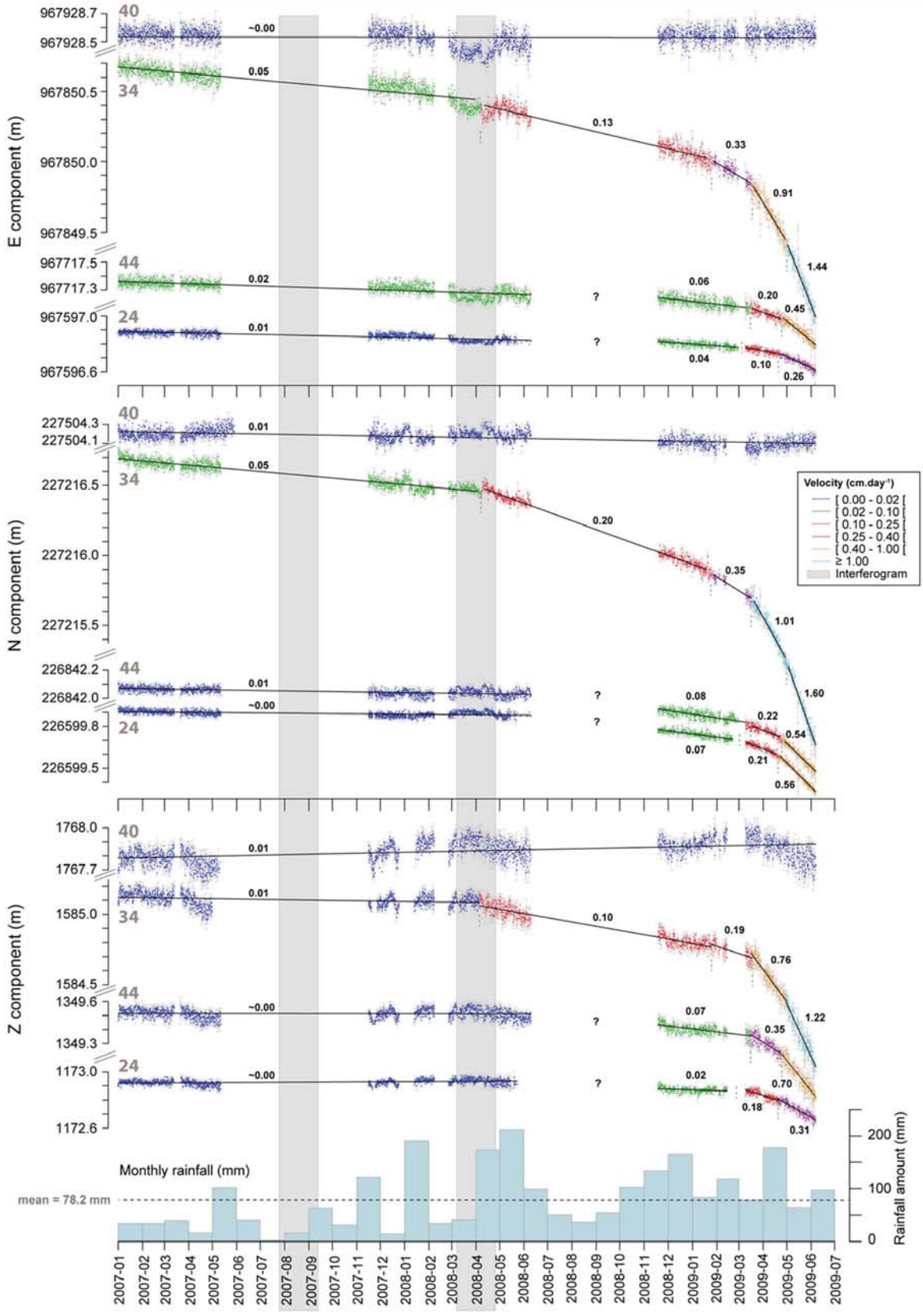

Fig. 6 Evolution of the E, N and Z components of four targets for the period 2007–2009. The velocity is calculated by fitting a regression line per sub-periods of velocity assumed constant and to a R^2 values higher than 0.80. The value of the velocity (in cm day^{-1}) is indicated above the regression line. Six classes of velocity are identified. The monthly rainfall is indicated for the monitoring period; the average monthly cumulated rainfall is 78.2 mm for the period

plotted on the displacement time series to estimate the velocity (Fig. 6).

In the lower parts, the velocity decreases and the type of deformation changes; the maximal velocity is observed for target #44 with a value of 0.7 cm day^{-1} in the Z component. The target #24 presents lower velocity than the target #44 but the trend is similar; the maximal velocity reaches 0.5 cm day^{-1} in the N component and only 0.3 cm day^{-1} in the Z component.

The analysis of the target displacements indicates that the acceleration of the landslide does not occur at the same time for all targets and that the periods of high velocity do not have the same duration. It suggests that the geological structures of the landslide control the spatial distribution of velocity and that the North-East lobe has a completely different kinematic behaviour.

On the basis of the analysis, two kinematic regimes are identified for the years 2007–2009 consisting in periods of slow displacement (velocity <0.2 cm day^{-1}) and periods of high displacement (velocity >0.2 cm day^{-1}). Figure 8 presents the geometry of the 3D vectors for the same targets for respectively the slow-moving period (Fig. 7a) and the fast-moving period (Fig. 7b). The ratios of horizontal (E-N) to vertical (Z) displacements are presented for each target respectively in blue (slow-moving period) and red (fast-moving period) colours. For the slow-moving period (Fig. 8a), the horizontal displacements are generally larger than the than vertical displacement testifying of a predominant translational sliding of the slope. For the fast-moving period (Fig. 7b), larger vertical displacements are observed than for the slow-moving period indicating that the deformation combines translational and rotational sliding. The directions of the displacement are also analyzed in relation to the local topographic slope gradient computed on a 5-m resolution digital surface model. Figure 7 indicates that the displacement vector is generally parallel to the local slope gradient for the period of low velocity (Fig. 7a) while it is oriented downward of the local slope gradient for the period of high velocity (Fig. 7b).

Landslide deformation fields from InSAR

Figure 8 presents the interferograms T1, T3 and T4. Areas with coherence below the threshold of 0.3 are in grey. At T1, the active area is limited to the lower part of the landslide while ground displacements outside of the landslide, east of its upper geomorphological boundary occur. The landslide can be divided in three units delimited by yellow-orange colours at the top, blue-purple colours at the toe and green colours at the Northern part of the lateral scarp. The distribution of phase values is oriented NW-SE, i.e. perpendicular to the slope direction and parallel to the main and secondary scarps. The North-East lobe is clearly identified along the main scarp. The deformation fields for these three 46-day periods (T1, T2, T4) can be explained by high velocities and depict the geometry of the multiple rotational slides (secondary scarps and counter slopes) observed in the upper part of the landslide.

Figure 9 presents the unwrapped phase values in the three interferograms. Phase unwrapping is complex within the landslide contours due to important changes of the ground properties.

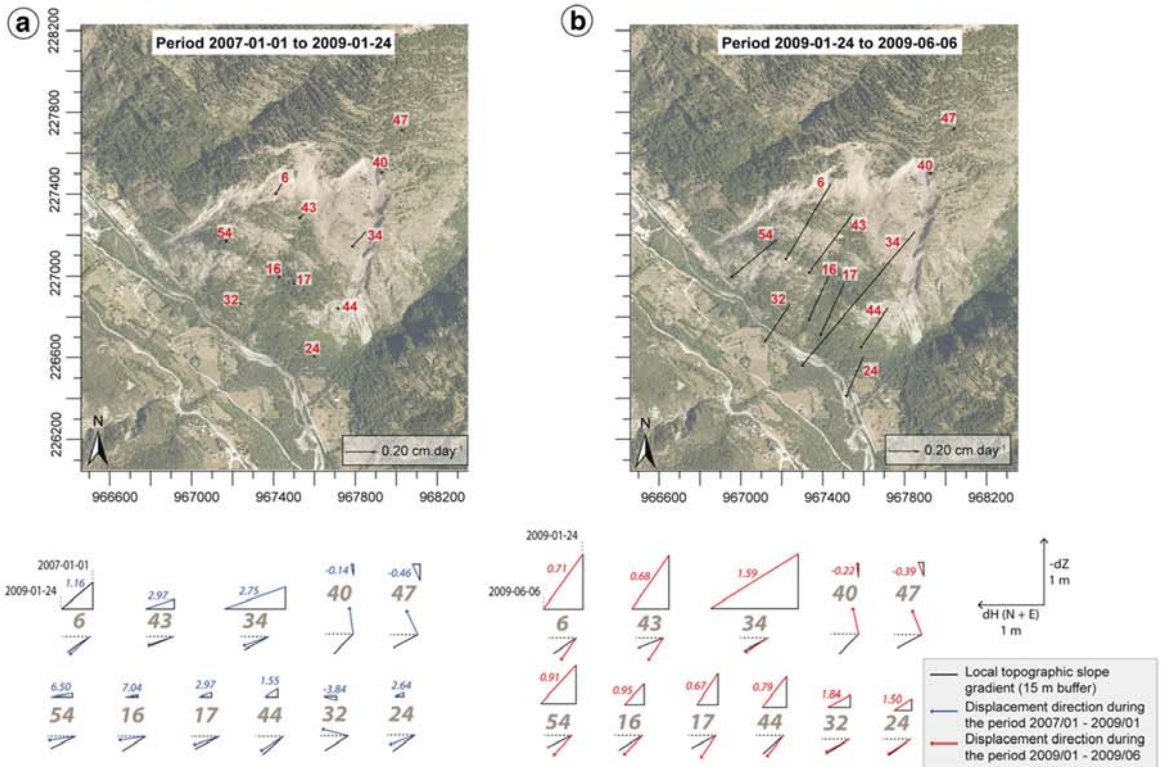

Fig. 7 Analysis of the geometry of the 3D displacement vectors for a period of low velocity (<0.2 cm day^{-1}; <2009/01/24) and a period of high velocity (>0.2 cm day^{-1}; >2009/01/24). **a** Map of 3D vectors for several targets for a period of low velocity. The ratio of vertical to horizontal displacement is indicated in *blue* for the period from 2007/01/01 to 2009/01/24. **b** Map of 3D vectors for several targets for a period of high velocity. The ratio of vertical to horizontal displacement is indicated in *red* for the period from 2009/01/24 to 2009/06/06. The horizontal displacement corresponds to the sum of the North (N) and East (E) components. The directions of displacement are compared to the local slope gradient

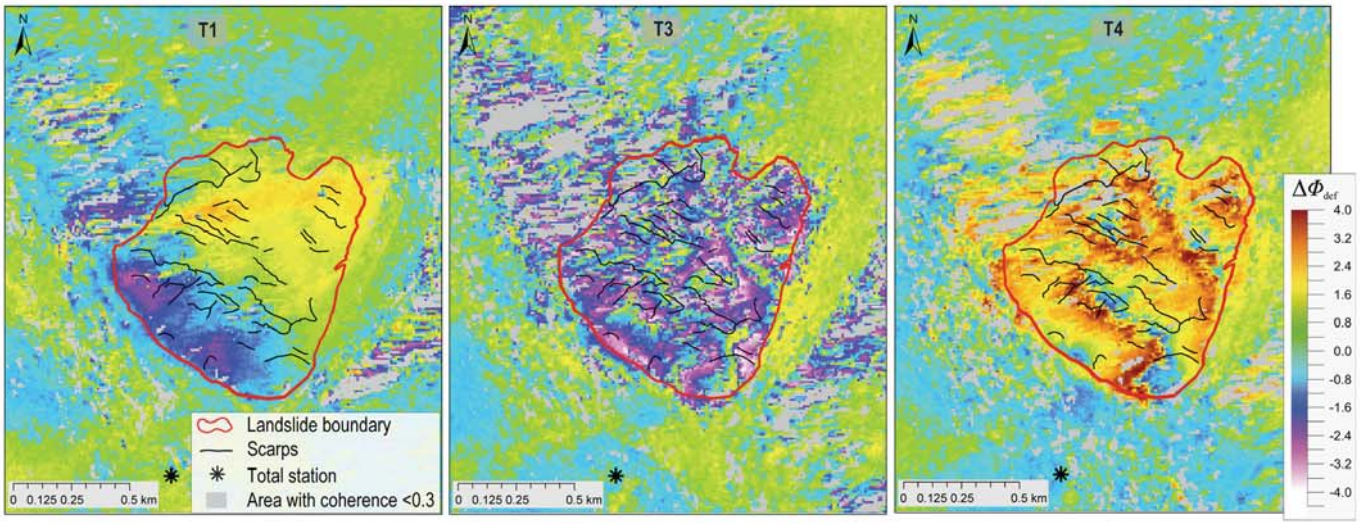

Fig. 8 Wrapped interferograms for the periods T1, T3 and T4. The phase values in the assumed stable areas outside of the landslide limits have been shifted to zero. The landslide boundary is indicated in *red* and the scarps are plotted in *black*. Areas of the interferograms with coherence value lower than 0.3 are in *grey*

Unwrapping was particularly difficult for the interferogram T3 probably due to higher velocities.

In the upper part, we observe positive D_{LoS} values on the interferograms T1, T2 and T3 corresponding to a ground LoS displacement away from the satellite, consistent with the subsidence of material in the ablation zone due to sliding of material at depth. In the lower part, we observe negative D_{LoS} values on the three interferograms corresponding to a ground LoS displacement towards the satellite consistent with the uplift at the toe due to material accumulation at depth. This non-uniform displacement gradient from the top to the bottom of the landslide is identified for the three interferograms.

The amplitude of the vertical displacements varies in time (Fig. 9). The maximum absolute D_{LoS} values reach respectively 4.6±0.9 cm for T1, 12.6±0.9 cm for T2 and 11.4±0.9 cm for T3, corresponding to vertical displacements of 6.0±1.1 cm (T1), 16.4 ±1.1 cm (T2) and 14.8±1.1 cm (T3). For T4, statistics are not computed because phase unwrapping was only possible on a very limited portion of the landslide (less than 10 % in surface) due to decorrelation and probably high displacement gradients. These observations indicate that the displacements are not steady-state with significant variations in space and time.

Spatial variations in D_{LoS} and V_{LoS} values along the profile A–B (Fig. 10) allow distinguishing several kinematic units. Three kinematic units, limited by morphological structures, are identified from the unwrapped phase values, in agreement with the wrapped phase field in Fig. 8, and displacement observed in the vertical and horizontal components by total station measurements (Fig. 7), the multiple rotational slides observed by Jomard et al. (2007), and the inferred geometry of the slip surface of Cappa et al. (2004).

Discussion

The space and time variations of the 3D displacement field is interpreted in relation to the geological structure of the slope, the geometry of the slip surface and geomorphological features at the surface with the presence of several scarps and counterslopes at the top and accumulation lobes at the bottom (Fig. 10). On average, the vertical velocities are in the range −0.05 and −0.10 cm day^{-1} in the upper part of the slope, decrease to less than −0.05 cm day^{-1} in the middle part of the slope and to 0.02 to 0.05 cm day^{-1} in the lower part of the slope. The movement, interpreted from both ground-based and satellite InSAR observations, corresponds mainly to subsidence at the top, to translation (along the slope of the slip surface) in the middle part and to uplift at the bottom (Fig. 10). From the elevations 1300 to 1750 m, the landslide material is characterized by extensional features; from the elevations 1225 m to 1300 m, the landslide material is characterized by compressional features.

For the period 2007–2009, an increase in landslide velocity is observed for all units, even though the quantification if this acceleration is difficult as phase unwrapping was not possible throughout the whole landslide for the three interferograms. In the subsiding area, the vertical velocities V_{vert} are in the range 0.25 to 0.30 cm day^{-1} at T3 while the maximal vertical velocities are in the range from 0.10 to 0.15 cm day^{-1} at T2 and T1. In the accumulation area at the toe, the vertical velocities are in the range from 0.05 to 0.10 cm day^{-1} for T1, T2 and T3, though locally a slightly higher at T2 (>0.10 cm day^{-1}) according to the values along this profile.

The spatial pattern of the velocity field in the period 2007–2009 is similar to the pattern measured by Girault and Terrier (1994) by terrestrial photogrammetry for the period 1970–1989, with mainly accumulation of material at the toe (expressed by a progression of material downslope) and a subsidence movement at the top (expressed by a retrogression of material upslope in the horizontal component; Fig. 11b). Elevation of the boundary between subsidence and accumulation is estimated at 1375 m in 1989 (Girault and Terrier, 1994) while it is located at 1300 m in 2009 (Fig. 10). The vertical velocities measured by InSAR are lower for the period 2007–2009 than for the year 1991 when vertical velocities in the range from 0.20 to 0.70 cm day^{-1} were measured from the analysis of C-band ERS interferograms (Fruneau et al., 1996).

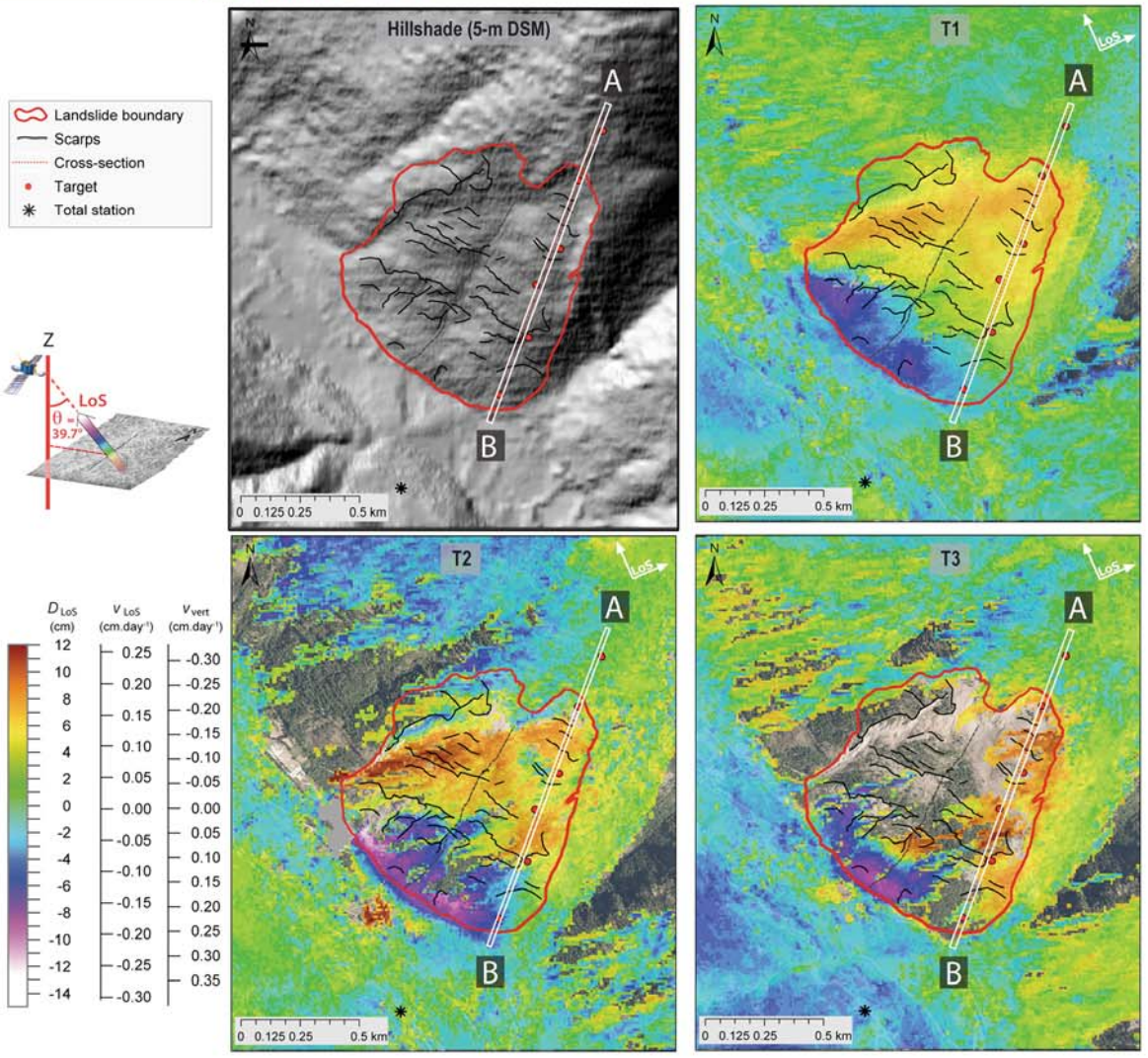

Fig. 9 Displacement (cm) and velocity (cm day^{-1}) fields observed for the La Clapière landslide. The hillshade of a 5 m resolution digital surface model (year 2009) and the unwrapped interferograms for the periods T1, T2 and T3 are presented

For the period 2007–2009, higher surface velocities are observed for the period T3 in relation with larger amounts of net and effective (precipitation minus evapotranspiration) cumulated rainfall over 120 days (Fig. 12). The evapotranspiration rate is calculated with the Penman-Monteith method. The effective cumulative rainfall amounts for the 40 days before the first SAR image acquisition are higher for T3 (~100 mm) than for T1 (~30 mm) and T2 (~50 mm) but are lower for T3 if we consider only the 25 days before the SAR acquisition of July 26th 2009. This means that short and intense meteorological events are not linked to the acceleration observed for the period T3. In addition, the 30-year-long averaged net rainfall values for the 4 months before July 26th (averaged for the past 30 years) is lower than the 4-month-long observed net rainfall for the year 2009. Thickness and duration of snow cover (2.1 m at 2100 m elevation and 129 days, respectively) were larger during the winter 2008–2009, than during the winter 2007–2008 (1.4 m at 2100 m elevation; 109 days). According to Cappa et al. (2004) and Lebourg et al. (2005), in case of abnormal rainfall events (up to 200 mm) and/or rapid snowmelt in a localized range of elevations (1800–2500 m), the water can percolate quickly within the landslide body through the network of fractures and faults and induce an acceleration of the landslide motion.

Conclusion

This work demonstrates the potential of L-band ALOS/PALSAR archive images to estimate the displacement field of large and rapid landslides with a traditional D-InSAR approach. For such case studies, the longer wavelength of L-band SAR sensors are suitable to preserve high spatial and temporal correlations and to quantify the movement of the ground affected by large changes in soil surface properties.

Even with complex field conditions (e.g. slope gradient and orientation of the landslide vs. ascending track of the satellite), an analysis of the landslide kinematics over the period 2007–2009 is proposed. The analysis of the wrapped phase values and in

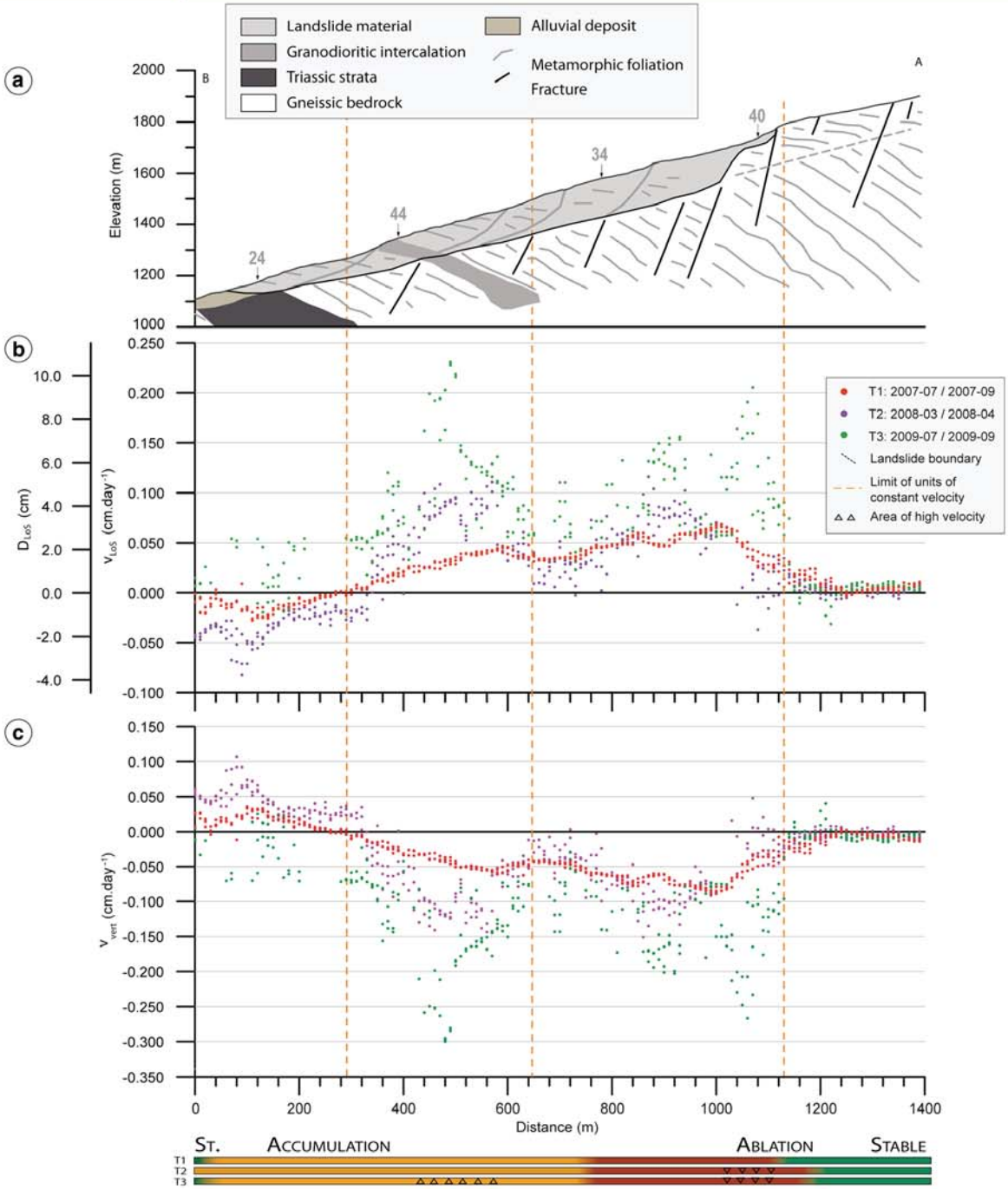

Fig. 10 Displacement (DLoS, DVert; cm), velocity (VLoS; cm day^{-1}) observed at the La Clapière landslide from L-band ALOS/PALSAR SAR data. **a** Topography, lithology and geometry of the slip surfaces along a longitudinal cross section in the Eastern part of the landslide (*A*–*B*). The location of the 30-m-width profile is indicated in Fig. 9, and the landslide geometry is from Cappa et al. (2004). The displacement pattern is indicated by the theoretical vectors for each unit. **b** LOS displacements (DLoS) and velocity along profile *A*–*B* for the unwrapped interferograms T1, T2 and T3. **c** Vertical velocity (Vvert) along profile *A*–*B* for the unwrapped interferograms T1, T2 and T3. The *colour bars* indicate changes in the movement type (subsidence in *red*, accumulation in *orange*, stable slopes in *green*)

particular the high large gradients allows detecting the active geological structures (fractures, faults) and morphological structures (scarps, grabens, gullies, steep slopes) and their role on the dynamics of the slope. The analysis indicates that the direction of the motion is (1) perpendicular to the N 140° E overthrust and to the main fractures of the massif and (2) parallel to the N010-030°E-oriented faults crossing the landslide. Several sliding units were identified from the displacement field derived from InSAR and ground-based measurements.

The analysis of the unwrapped phase values (for portions of the slope where unwrapping was possible) indicates an acceleration of the upper part of the landslide with vertical velocities V_{vert} ranging

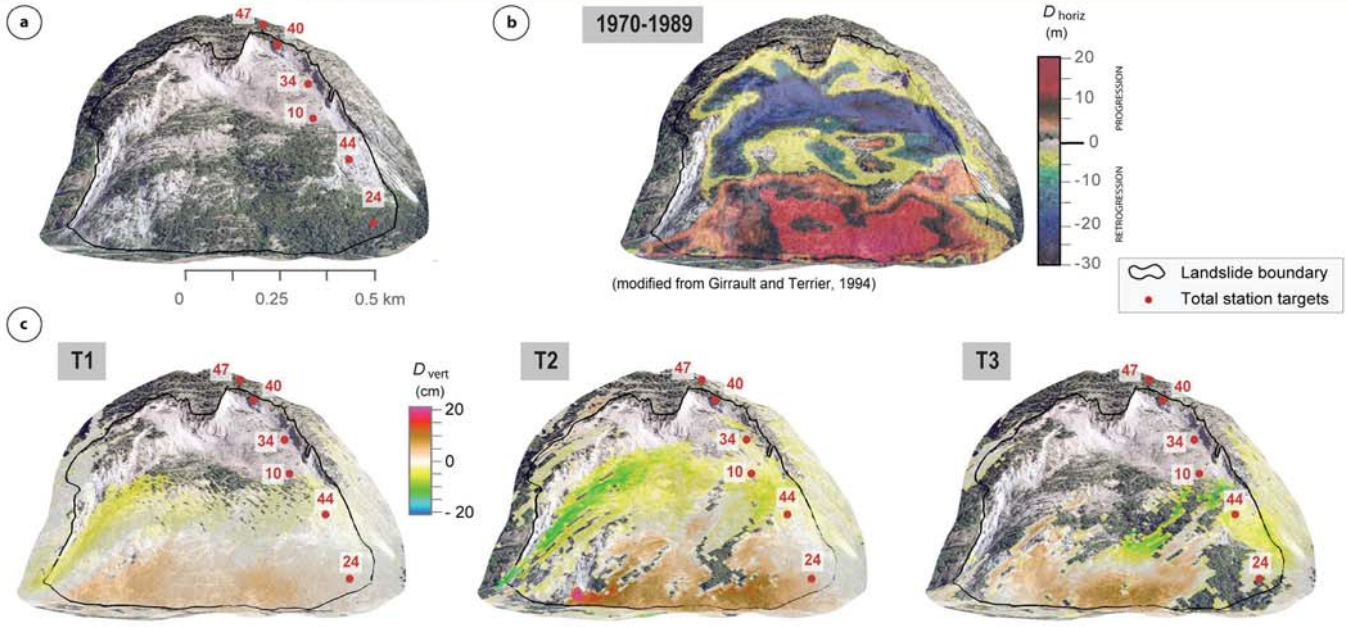

Fig. 11 Horizontal and vertical displacement fields of the La Clapière landslide. **a** Orthophotograph of the landslide in 2009. **b** Mean horizontal displacement field (dH) measured by comparison of digital surface models (DSM) between 1970 and 1989 (modified from Girault and Terrier 1994). **c** Vertical displacement field (dV) measured by InSAR at T1, T2 and T3. The landslide boundary is indicated in *black* and the targets by *red dots*

from 0.1 cm day^{-1} in 2007 to 0.15 cm day^{-1} in 2008 and to 0.25–0.30 cm day^{-1} in 2009. This acceleration identified in 2009 with InSAR is also observed on ground-based measurements. The deformation field is complex and controlled by the main structural discontinuities crossing the landslide, such as intermediate scarps in the upper part and the Barre d'Iglière in the lower part. The triggering factors of the 2009 acceleration are difficult to highlight. The combination of a thicker snow cover, a higher number of days with a snow cover and a net rainfall amount cumulated over 120 days higher than the 30-year-long averages may explain the acceleration.

ALOS/PALSAR imagery, even if only a limited archive data is available, allows complementing information from other satellite SAR sensors to construct time series of surface deformation and document the complex destabilization of the La Clapière slope. The estimated displacement rates are in the range of the ground-based total station observations and consistent with other monitoring studies.

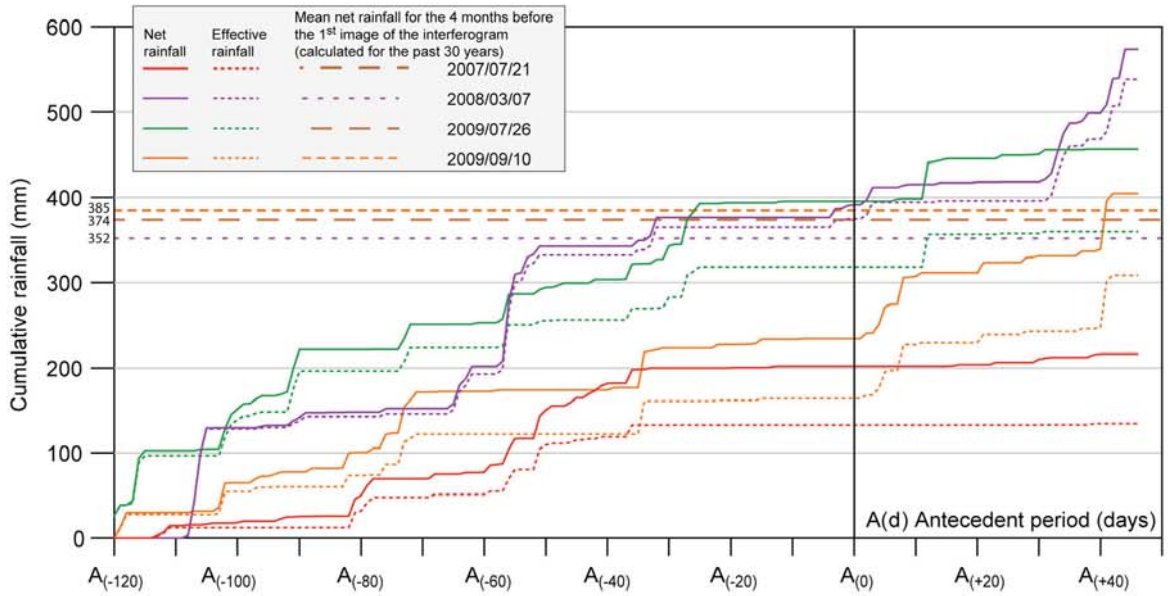

Fig. 12 Landslide movement in relation with rainfall amounts over several time spans. Antecedent net and effective (precipitation minus evapotranspiration) cumulative rainfall at the Saint-Etienne-de-Tinée rain gauge from 120 days before the first SAR image acquisition (i.e. A(0))and for temporal baseline of 46 days (T1, T2, T3, T4). Thirty-year-long averaged net rainfall values for the 4 months before the first acquisition are indicated by *coloured dotted lines*

Acknowledgments

This work was supported by the EU 7th framework Marie Curie ITN project 'CHANGES: Changing Hydro-meteorological Risks as Analyzed by a New Generation of European Scientists' under Grant Agreement No. 263953. ALOS/PALSAR images are provided by the Japan Aerospace Exploration Agency (JAXA) and the European Space Agency (ESA) under the contract C1P.8859. The total station measurements were provided by Centre d'Etudes et d'Expertise sur les Risques, l'Environnement, la Mobilité et l'Aménagement (CEREMA) in agreement with the Direction Départementale des Territoires et de la Mer (DDTM-06). We thank E. Palis (University of Nice) for fruitful discussion on the geomorphology of the landslide.

References

Agliardi F, Crosta G, Zanchi A (2001) Structural constraints on deep-seated slope deformation kinematics. Eng Geol 59:83–102

Berardino P, Fornaro G, Lanari R, Member S, Sansosti E (2002) A new algorithm for surface deformation monitoring based on small baseline differential SAR interferograms. IEEE Trans Geosci Remote Sens 40:2375–2383

Berger M, Moreno J, Johannessen JA, Levelt PF, Hanssen RF (2012) ESA's sentinel missions in support of Earth system science. Remote Sens Environ 120:84–90

Bois T, Bouissou S, Guglielmi Y (2008) Influence of major inherited faults zones on gravitational slope deformation: a two-dimensional physical modelling of the La Clapière area (Southern French Alps). Earth Planet Sci Lett 272:709–719

Booth AM, Lamb MP, Avouac J-P, Delacourt C (2013) Landslide velocity, thickness, and rheology from remote sensing: La Clapière landslide, France. Geophys Res Lett 40:4299–4304

Cappa F, Guglielmi Y, Soukatchoff V, Mudry J, Bertrand C, Charmoille A (2004) Hydromechanical modeling of a large moving rock slope inferred from slope levelling coupled to spring long-term hydrochemical monitoring: example of the La Clapière landslide (Southern Alps, France). J Hydrol 291:67–90

Cascini L, Fornaro G, Peduto D (2009) Analysis at medium scale of low-resolution DInSAR data in slow-moving landslide-affected areas. ISPRS J Photogramm Remote Sens 64:598–611

Casson B, Delacourt C, Allemand P (2005) Contribution of multi-temporal sensing images to characterize landslide slip surface—application to the La Clapière landslide (France). Nat Hazards Earth Syst Sci 5:425–437

Colesanti C, Wasowski J (2006) Investigating landslides with space-borne synthetic aperture radar (SAR) interferometry. Eng Geol 88:173–199

Corsini M, Ruffet G, Caby R (1994) Alpine and late Hercynian geomorphologic constraints in the Argentera Massif (Western Alps). Eclogae Geol Helv 97:3–15

Delacourt C, Allemand P, Casson B, Vadon H (2004) Velocity field of the "La Clapière" landslide measured by the correlation of aerial and QuickBird satellite images. Geophys Res Lett 31:1–5

Delacourt C, Allemand P, Berthier E, Raucoules D, Casson B, Grandjean P, Pambrun C, Varel E (2007) Remote-sensing techniques for analysing landslide kinematics: a review. Bull Soc Geol Fr 178:89–100

Delteil J, Stephan J-F, Attal M (2003) Control of Permian and Triassic faults on Alpine basement deformation in the Argentera massif (external southern French Alps). Bull Soc Geol Fr 174:55–70

Doin M-P, Lodge F, Guillaso S, Jolivet R, Lasserre C, Ducret G, Grandin R, Pathier E, Pinel V (2011) Presentation of the small baseline processing chain on a case example: The Etna deformation monitoring from 2003 to 2010 using ENVISAT data. Proc. Fringe 2011, ESA, Frascati, Italy. pp. 1–7.

Dramis F, Sorriso-Valvo M (1994) Deep-seated gravitational slope deformations, related landslides and tectonics. Eng Geol 38(3–4):231–243

Ferretti A, Prati C, Rocca F (2001) Permanent scatterers in SAR interferometry. IEEE Trans Geosci Remote Sens 39:8–20

Follacci J-P (1987) Les mouvements du versant de la Clapière à Saint-Etienne-de-Tinée. Bull Liaison Lab Ponts Chaussées 150–151:39–54

Follacci J-P (1999) Seize ans de surveillance du glissement de La Clapière (Alpes Maritimes). Bull Liaison Lab Ponts Chaussées 220:35–51

Follacci J-P, Guardia P, Ivaldi J-P (1988) La Clapière landslide in its geodynamical setting. In: Bonnard C (ed) Proc. 5th Int. Symp. Landslides, vol. 3. Balkema, Brookfield, pp 1323–1327

Follacci J-P, Rochet L, Serratrice J-F (1993) Glissement de La Clapière, St. Etienne de Tinée, Synthèse des connaissances et actualisation des risques, Rapport CETE, Nice, 76pp.

Foster J, Kealy J, Cherubini T, Businger S, Lu Z, Murphy M (2013) The utility of atmospheric analyses for the mitigation of artifacts in InSAR. J Geophys Res Solid Earth 118:748–758

Fruneau B, Achache J, Delacourt C (1996) Observation and modelling of the Saint-Étienne-de-Tinée landslide using SAR interferometry. Tectonophysics 265:181–190

Girault F, Terrier M (1994) Analyse par photogrammétrie des mouvements de terrain : application aux sites de la Clapière, du Friolin, de Boulc et de l'Harmalière. Rapport BRGM, Marseille, **96pp**

Goldstein RMM, Zebker HA, Werner CL (1988) Satellite radar interferometry: two-dimensional phase unwrapping. Radio Sci 23:713–720

Guglielmi Y, Cappa F, Binet S (2005) Coupling between hydrogeology and deformation of mountainous rock slopes: insights from La Clapière area (southern Alps, France). C R Geosci 337:1154–1163

Gunzburger Y, Laumonier B (2002) Origine tectonique du pli supportant le glissement de terrain de la Clapière (Nord-Ouest du massif de l'Argentera–Mercantour, Alpes du Sud, France) d'après l'analyse de la fracturation. C. R Geosci 334:415–422

Helmstetter A, Sornette D, Grasso J-R, Andersen J, Gluzman S, Pisarenko V (2004) Slider block friction model for landslides: application to Vaiont and La Clapière landslides. J Geophys Res 109, B02409

Hradecký J, Pánek T (2008) Deep-seated gravitational slope deformations and their influence on consequent mass movements (case studies from the highest part of the Czech Carpathians). Nat Haz 45(2):235–253

Ivaldi J-P, Guardia P, Follacci J-P, Terramorsi S (1991) Plis de couverture en échelon et failles de second ordre associés à un décrochement dextre de socle sur le bord nord-ouest de l'Argentera (Alpes-Maritimes, France). C R Acad Sci II 313:61–368

Jomard H (2006) Analyse multi-échelles des déformations gravitaires du Massif de l'Argentera Mercantour. PhD Thesis, University of Nice, 268pp.

Jomard H, Lebourg T, Tric E (2007) Identification of the gravitational boundary in weathered gneiss by geophysical survey: La Clapière landslide (France). J Appl Geophys 62:47–57

Lebourg T, Binet S, Tric E, Jomard H, El Bedoui S (2005) Geophysical survey to estimate the 3D sliding surface and the 4D evolution of the water pressure on part of a deep seated landslide. Terra Nov 17:399–406

Lebourg T, Hernandez M, Zerathe S, El Bedoui S, Jomard H, Fresia B (2010) Landslides triggered factors analysed by time lapse electrical survey and multidimensional statistical approach. Eng Geol 114:238–250

Li Z, Fielding EJ, Cross P, Muller J-P (2006) Interferometric synthetic aperture radar atmospheric correction: GPS topography-dependent turbulence model. J Geophys Res Solid Earth 111, B02404

Lu P, Casagli N, Catani F, Tofani V (2012) Persistent scatterers interferometry hotspot and cluster analysis (PSI-HCA) for detection of extremely slow-moving landslides. Int J Remote Sens 33(2):466–489

Massonnet D, Feigl KL (1998) Radar interferometry and its application to changes in the Earth's surface. Rev Geophys 36:441–500

Raucoules D, De Michele M, Malet J-P, Ulrich P (2013) Time-variable 3D ground displacements from high-resolution synthetic aperture radar (SAR). Application to La Valette landslide (South French Alps). Remote Sens Environ 139:198–204

Rosen PA, Hensley S, Peltzer G, Simons M (2004) Updated repeat orbit interferometry package released. EOS Trans Am Geophys Union 85:47–47

Rott H (2009) Advances in interferometric synthetic aperture radar (InSAR). Prog Phys Geogr 33:769–791

Rott H, Nagler T (2006) The contribution of radar interferometry to the assessment of landslide hazards. Adv Sp Res 37:710–719

Schlögel R, Doubre C, Malet J-P, Masson F (2015) Landslide deformation monitoring with ALOS/PALSAR imagery: a D-InSAR geomorphological interpretation method. Geomorphology 231:314–330

Serratrice J-F (2006) Modeling of major rockfalls by spreading: application to the "La Clapière" and "Séchilienne" sites (French Alps). Bull Liaison Lab Ponts Chaussées 263–264:53–70

Squarzoni C, Delacourt C, Allemand P (2003) Nine years of spatial and temporal evolution of the La Valette landslide observed by SAR interferometry. Eng Geol 68:53–66

Stumpf A, Malet J-P, Allemand P, Ulrich P (2014) Surface reconstruction and landslide displacement measurements with Pléiades satellite images. ISPRS J Photogramm Remote Sens 95:1–12

Travelletti J, Malet J-P, Samyn K, Grandjean G, Jaboyedoff M (2013) Control of landslide retrogression by discontinuities: evidence by the integration of airborne- and ground-based geophysical information. Landslides 10:37–54

Wei M, Sandwell DT (2010) Decorrelation of L-band and C-band interferometry over vegetated areas in California. IEEE Trans Geos Remote Sens 48:2942–2952

Zhao C, Lu Z, Zhang Q, de la Fuente J (2012) Remote sensing of environment large-area landslide detection and monitoring with ALOS/PALSAR imagery data over Northern California and Southern Oregon, USA. Remote Sens Environ 124:348–359

R. Schlögel · J.-P. Malet (✉) · C. Doubre
Institut de Physique du Globe de Strasbourg, UMR7516,
Université de Strasbourg/EOST, CNRS,
5 rue René Descartes, 67084, Strasbourg, Cedex, France
e-mail: jeanphilippe.malet@unistra.fr

T. Lebourg
Géosciences Azur, CNRS UMR 6526,
Université de Nice-Sophia Antipolis,
250 Avenue A. Einstein, Valbonne, France

3.3. Creation of a multi-date landslide inventory at the regional scale by the combination of multi-source data

The joint interpretation of various datasets is not straightforward. As already mentioned, it depends on the quality and resolution of the data, the experience of the expert, the geomorphology of the region and the purpose of the analysis. In the framework of our research, the aim is to provide a multi-date landslide inventory for the mid part of the Ubaye valley (e.g. Barcelonnette Basin) by combining several sources of information and field mapping. Descriptors of landslide kinematics at different time intervals (e.g. displacement rates for short time intervals of 5 years, changes in landslide geometry and morphology for time interval of 50 years, and stages of landslide activity for long time intervals of > 100 years) are proposed from the analysis and integrated into the inventory.

The data sources consist of series of images (orthophotographs, geomorphological maps, elevation datasets, InSAR deformation maps) combined to historical reports from the local risk managers (RTM – Service de Restauration des Terrains de Montagne), dendrogeomorphologic information (Lopez-Saez et al., 2012) and field surveys. The methodology for the creation of the inventory, the definition of the descriptors and the statistical analysis of the inventory is submitted to the peer-reviewed journal *Natural Hazards and Earth System Science.* The detailed methodology to interpret interferometric phases of the L-band SAR images over large areas and complement the landslide inventory (detection of unstable slopes not previously mapped, mapping of the extension of large landslides, characterization of landslide displacement rates) is detailed in Appendix 3.

Nat. Hazards Earth Syst. Sci., 15, 2369–2389, 2015
www.nat-hazards-earth-syst-sci.net/15/2369/2015/
doi:10.5194/nhess-15-2369-2015

Natural Hazards and Earth System Sciences
Open Access
EGU

Analysis of a landslide multi-date inventory in a complex mountain landscape: the Ubaye valley case study

R. Schlögel[1,a], J.-P. Malet[1], P. Reichenbach[2], A. Remaître[1], and C. Doubre[1]

[1]Institut de Physique du Globe de Strasbourg, UMR7516, Université de Strasbourg/EOST, CNRS, 5 rue René Descartes, 67084 Strasbourg, CEDEX, France
[2]CNR-IRPI, via Madonna Alta 126, 06128 Perugia, Italy
[a]now at: Institute for Applied Remote Sensing, EURAC, Viale Druso 1, 39100 Bolzano, Italy

Correspondence to: R. Schlögel (romy.schloegel@eurac.edu)

Received: 9 March 2015 – Published in Nat. Hazards Earth Syst. Sci. Discuss.: 30 March 2015
Accepted: 16 September 2015 – Published: 22 October 2015

Abstract. In the paper we analyse a multi-date landslide inventory prepared for a mountainous area affected by several landslide types with different degrees of activity, we attempt to quantify the uncertainties associated to the mapping, we measure the evolution of morphological indicators and estimate landslide activity and temporal occurrence. The inventory, covering the period 1956–2010, is prepared for the middle section of the Ubaye valley (southern French Alps) based on the analysis of multi-source documents (geomorphological maps, historical reports of landslide events, field surveys, orthophotographs and SAR (synthetic aperture radar) satellite images). The uncertainties derived from the expert interpretation of different sources of information, the landslide morphological features and the affected land covers are taken into account in relation to the source documents.

Morphological indicators are calculated to describe quantitatively the evolution of the landslides (length, area, relative elevation, runout distance). Frequency–area density functions are computed to estimate the changes in the landslide distributions and a Poisson model is used to estimate the probability of reactivation of the observed landslides and the occurrence of new failures. The proposed multi-date inventory and the associated statistics provide additional information to the event catalogue managed by the local policy makers.

1 Introduction

Landslide inventory maps are important documents to describe mass movement spatial distribution in a region and to prepare susceptibility, hazard and risk maps (Guzzetti et al., 2012). They are also useful to investigate the distribution, types and patterns of landslides in relation to geomorphology, lithology, land cover, tectonic settings and hydrogeological conditions (Guzzetti et al., 1996; Corominas et al., 2014; Günther et al., 2013).

Inventory maps are either archive or geomorphological inventories (Guzzetti et al., 2000; Malamud et al., 2004). Archive inventories include landslides information obtained from the literature, or other archive sources (Reichenbach et al., 1998; Salvati et al., 2003). Geomorphological landslide inventories, classified as historical, event, seasonal or multi-temporal inventories cluster different information: the movement type, the estimated age, the degree of activity, the depth, and the velocity (Guzzetti et al., 2012). Geomorphological features, such as fissures, grabens, ponds, vegetation removal and other morphological changes, may provide information on landslide activity. Geomorphological landslide inventory maps prepared for different periods associated with event landslide maps can be useful to evaluate the temporal and the spatial evolution of multiple failures over long periods of time (e.g., years to decades; Galli et al., 2008). The event-based or multi-date landslide inventories preparation is hindered by uncertainties linked to the specificity of the source documents (scale, spatial resolution, time period), the type and size of the landslides as well as by the skills of the

expert. Preparing multi-temporal landslide inventories at regional scale requires investigating relationships among variables over different time resolutions. In these inventory maps, the date (or periods) of the landslides is attributed either on the basis of the date (or periods) of the triggers, the date of the source document (photographs, reports) or the date of field surveys (Guzzetti et al., 2012).

In this work, we propose a multi-date landslide inventory showing the evolution of landslide boundaries for more than two periods prepared from the interpretation of various types of documents. Despite modern technological advances, and the availability of new satellite products, the visual interpretation of airborne photographs is still the most common method to obtain landslide information (Guzzetti et al., 2012) though several other sources of information that may be used such as optical remote sensing images and LiDAR-derived topographic information (Ardizzone et al., 2007; van den Eeckhaut et al., 2007; Haneberg et al., 2009; Razak et al., 2013; Martha et al., 2010; van den Eeckhaut et al., 2012). Images acquired by synthetic aperture radar (SAR) satellite sensors are also considered as a powerful source of information, mainly for the recognition of slow-moving landslides (Singhroy and Molch, 2004; Zhao et al., 2012).

Preparing an inventory map is a time-consuming and not straightforward procedure which requires experienced geomorphologists trained in the recognition of slope features and processes (Wills and McCrink, 2002; van den Eeckhaut et al., 2005; Guzzetti et al., 2012). In addition, the quality of the final map depends on the spatial resolution of the airborne photographs, the scale of the topographic maps, and the complexity of the landscape (Carrara et al., 1992; Ardizzone et al., 2002; Galli et al., 2008). The interpretation of the airborne photographs to produce the landslide inventory map may also induce some mapping errors (Marchesini et al., 2013; Santangelo et al., 2015). According to Brardinoni et al. (2003), forest canopy (notably in old-growth forest) increases the population of "not visible" landslides which can represent up to 85 % of the total number of failures. As mentioned by Bell et al. (2012), one challenge is to quantify the effect of event or continuous reactivations which leave their footprint in the landscape.

The magnitude (or intensity) of landslides depends on the landslide type and several proxies can be used for its quantification such as the landslide dimensions (area, volume, travel distance) or velocity (Corominas et al., 2014). Frequency–magnitude relationships for different locations and landslide types are frequently considered as a proxy for landslide magnitude (van den Eeckhaut et al., 2007; Florsheim and Nichols, 2013; Malamud et al., 2004; Schlögel et al., 2011; Guzzetti et al., 2006). In order to complete the quantitative analysis of the multi-date inventory, landslide temporal probability can also be assessed using a Poisson model.

The objectives of this work are the following: (i) to prepare a multi-date landslide inventory map from multi-source data, (ii) to identify and quantify uncertainties and interpretation errors associated to the mapping, (iii) to propose indicators to estimate the interpretation errors in order to improve the reliability of the landslide inventory maps and (iv) to analyse quantitatively the multi-date inventory. The study area is located in the middle part of the Ubaye valley (south-eastern France) severely affected by different landslides types (Maquaire et al., 2003), and the investigated time period extends from 1956 to 2010.

2 Study area

The Ubaye valley is located in the southern French Alps (Fig. 1a). In the middle section of the valley (e.g. the Barcelonnette Basin), several communities developed throughout the last millennia and the number of inhabitants was around 6000 people in 2012.

The Barcelonnette Basin is a geological window between two Eocene crystalline sheet thrusts (Parpaillon and Autapie) overlaying autochthonous black marls (Fig. 1b). Limestone, sandstone, flysch and gypsum constitute most of the rocks within the thrusts; they constitute the steepest slopes and crests, ranging from 2500 to 3000 m in elevation. The slopes, with angles ranging from 5 to 45°, present an irregular geometry with steep convex planar and hummocky surfaces/profiles. Below the sheet thrusts, the steepest convex slopes (> 35°) are carved in black marl outcrops. The gentle slopes (5–15°) correspond to moraine deposits of about 10–20 m thickness which are overlaying the black marls. Scree slopes also cover large areas, especially below the sheet thrust crests with a thickness ranging from 2 to 10 m. The lower parts of the slopes and the valley bottom are formed of torrential deposits whose thickness varies from 50 to 200 m.

The climate is controlled by both Mediterranean and mountain influences (Malet et al., 2005a), with a clear monthly rainfall variability (734 ± 400 mm for the period 1928–2013), significant daily temperature range (> 20 °C), more than 120 days of freezing per year (on average), long dry periods (from May to October) and the occurrence of summer rainstorms (with rainfall intensity up to 60 mm h^{-1}).

Forests cover around 40 % of the area, while grasslands and arable lands are present for about 25 and 5 %, respectively; the rest of the area (30 %) is covered by bare soils and urbanized areas.

Numerous studies were conducted for the analysis of mass movements (Flageollet et al., 1999; Malet et al., 2005a; Maquaire et al., 2003; Razak et al., 2011; Remaître et al., 2005; Thiery, 2007; Thiery et al., 2014) and several landslide types were mapped and analysed along the slopes (Fig. 1a). Typologies of slides (Cruden and Varnes, 1996) mainly constituted by rocks and debris are the following:

– shallow translational landslides (e.g. the Riou Chanal landslides, south of Uvernet; Fig. 1d);

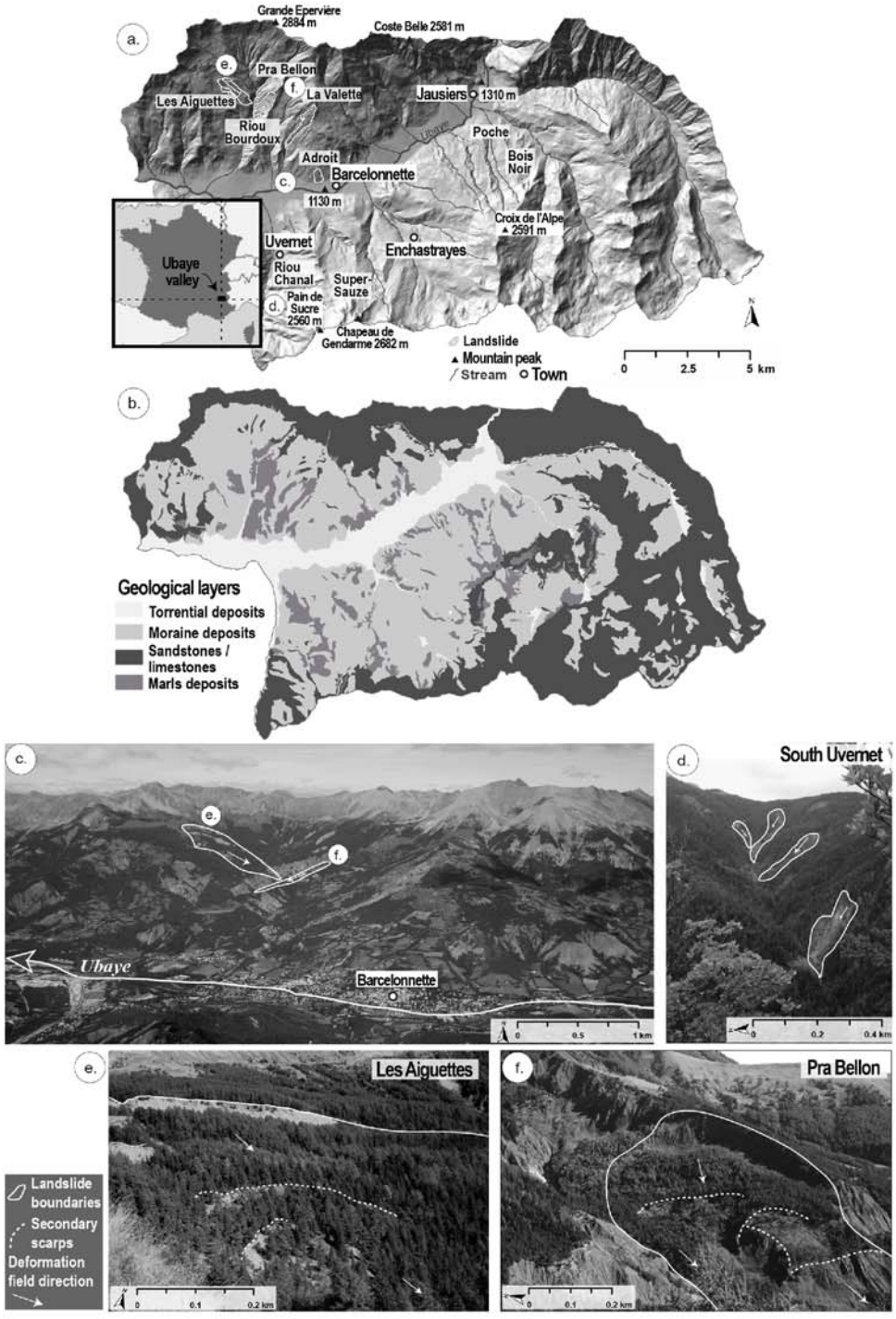

Figure 1. The Ubaye valley (southern French Alps) study area. **(a)** Shaded relief image of the area and location of the main monitored landslides. **(b)** Simplified geological map. **(c)** Typical landscape of the south-facing slopes located on the right riverbank of the Ubaye River. **(d)** Shallow translational landslides situated south of Uvernet in the Riou Chanal catchment. **(e)** Crown area of the Les Aiguettes deep-seated translational landslide. **(f)** Crown area of the Pra Bellon deep-seated rotational landslide.

Table 1. List of the data available for the Ubaye valley used for landslide recognition and mapping.

	Type of data	Source	Resolution	Scale	Date	Landslide information
1.	Orthophotograph	IGN	1.5 m	1 : 35 000	31/07/1956	Location/Type
2.	Orthophotograph	IGN	1.0 m	1 : 15 000	10/07/1974	Location/Type
3.	Orthophotograph	IGN	1.0 m	1 : 20 000	01/07/1982	Location/Type
4.	Orthophotograph	IGN	0.7 m	1 : 25 000	25/07/1995	Location/Type
5.	Orthophotograph	IGN	0.5 m	1 : 25 000	24/06/2000	Location/Type
6.	Orthophotograph	IGN	0.5 m	1 : 25 000	03/07/2004	Location/Type
7.	Orthophotograph	IGN	0.5 m	1 : 25 000	19/07/2009	Location/Type
8.	Airborne SAR DSM	IfSAR-Fugro	5.0 m	–	2009	Location
9.	Elevation-line DSM	EOST[a]	10 m	–	2004	Location
10.	Geological map	BRGM	–	1 : 25 000	1974	Location/Type
11.	Geomorphological map	ZERMOS	–	1 : 25 000	1975	Location
12.	Geomorphological map	Utrecht Univ.[b]	–	1 : 25 000	1989	Location/Type
13.	Geomorphological map	RTM[c]	–	1 : 10 000	2001	Location/Type
14.	Geomorphological inventory	EOST[a]	–	1 : 5000	2004	Location/Time/Intensity
15.	Historical catalogue	RTM/BRGM	–	–	1850–2012	Location/Time
16.	Historical reports	RTM[c]	–	–	1990–2012	Location/Time
17.	Dendrogeomorphic data	Irstea[d]	–	1 : 3000	1850–2004	Location/Time
18.	L-band SAR images	EOST[e]	10 m	–	2007–2010	Location/Time/Intensity

[a] Thiery (2007); [b] Salomé and Beukenkamp (1989); [c] Stien (2001); [d] Lopez-Saez et al. (2012, 2013); [e] Schlögel et al. (2015).
IGN: French National Geographic Institute; IfSAR-Fugro: Fugro EarthData GeoSAR airborne Interferometric Synthetic Aperture Radar; EOST: Ecole et Observatoire des Sciences de la Terre, University of Strasbourg; BRGM: Bureau de Recherches Géologiques et Minières; ZERMOS: Zones Exposées à des Risques liés aux MOuvements du Sol ; RTM: Restauration des Terrains en Montagne; Irstea: Institut national de Recherche en Sciences et Technologies pour l'Environnement et l'Agriculture.

- deep-seated translational landslides (e.g. the Aiguettes landslide, Fig. 1e; Lopez-Saez et al., 2013);
- deep-seated rotational landslides (e.g. the Pra Bellon landslide, Fig. 1f; Lopez-Saez et al., 2012);
- mudslides (e.g. the La Valette and Super-Sauze mudslides, Malet et al., 2005b; Travelletti et al., 2014).

To be consistent with the results of Thiery et al. (2007, 2014), the descriptive terms deep-seated and shallow define landslides with sliding depth of, respectively, more and less than 6 m (estimated from field observations).

3 Data

Several sources of information are available for the Ubaye valley, namely: (i) orthophotographs, (ii) hillshades and contour lines maps, (iii) geological and geomorphological maps, (iv) dendrogeomorphic data, (v) interferograms of L-band SAR images (Schlögel et al., 2015) and (vi) reports of historical landslides (Table 1).

Orthophotographs, geomorphological maps, historical catalogues and reports provide information on landslide types, locations and sometimes, activity. Seven sets of airborne orthophotographs at different scales with spatial resolution ranging from 0.5 to 1.5 m acquired by the French National Geographic Institute (IGN) are available for the period 1956–2009. Available geological and geomorphological maps provide local information on ancient and active unstable slopes. Reports (Stien, 2001) and historical landslide catalogues are organized in a GIS point-based database as provided by the local risk managers (RTM – Restauration des Terrains en Montagne). Several people have recorded landslide events covering different portions of the territory since the 1850s and the completeness of the catalogue is not guaranteed for the oldest years. Hillshade map may help for precise location of recent mass failures but hardly highlights the type of the movement. A hillshade map and contour lines were obtained automatically from an airborne SAR DSM (2009) with 5 m resolution, while another set of contour lines was generated manually at 10 m resolution from an IGN topographical map (Thiery, 2007). In addition, dendrogeomorphological data provide information on landslide activity at local scale. Data were collected for the Pra Bellon and the Bois Noir landslides (Lopez-Saez et al., 2012, 2013) and compared at the regional scale.

Since 10 years, SAR interferograms are used for landslide detection, mapping and monitoring (Canuti et al., 2004; Colesanti and Wasowski, 2006; Lu et al., 2012; Metternicht et al., 2005). For the Ubaye valley, only ascending ALOS/PALSAR images are available, limiting the coverage of the territory to 60 % because of layover and slope portions hidden by the relief (Fig. 2; Cascini et al., 2009). The interpretable slope portions are oriented to the N, NW, W, SW and S including all those with topographic angles lower than 10°. Further, according to our time series of SAR images, the ambiguity of phase measurements limits the track-

ing to displacement rates lower than 5.9 cm for periods of 46 days. Interferograms obtained from SAR images were used to update geomorphological inventory, to detect features activated during recent periods and to identify unknown landslides. In this work, we use a traditional Differential Interferometric Synthetic Aperture Radar (D-InSAR) technique adapted to mountainous areas without the presence of corner reflectors. In the area, pairs of co-registered SAR images allowed to generate deformation maps helpful for the detection and mapping of ground surface changes (Hanssen, 2001). The methodology of SAR images processing with the ROI_PAC (Repeat Orbit Interferometry PACkage) and NSBAS (New Small BAseline Subsets) algorithms (Doin et al., 2011; Rosen et al., 2004) is described in Schlögel et al. (2015).

Geomorphological landslide inventories compiled for parts of the study area were organized in a GIS polygon-based database (Thiery, 2007). The inventory map provided for the year 2004 gives precise information on landslide location, type, and activity as well as some morphological indicators. As the available maps and images have different scales, spatial resolutions and formats, they were first georeferenced and orthorectified in the system NTF (New French Triangulation) Lambert zone III. Spatial extension of the main data sets used for multi-date mapping varies over the scene affecting the coverage completeness (Fig. 2).

4 Methods

The available maps and images were organized in a GIS according to their acquisition dates, spatial coverage (Fig. 2) and level of importance for preparing the multi-date inventory. The following sections describe the multi-steps approach used to (i) recognise and map the landslides at different periods of time, (ii) estimate the uncertainty associated to each source of information, (iii) evaluate landslide activity and (iv) analyse density maps, descriptive statistics, size-frequency distributions and temporal probability.

4.1 The multi-date landslide inventory

The multi-date landslide inventory was prepared at 1 : 5000 scale for the period 1956–2010 by combining 2-D visual interpretation of maps (airborne orthophotographs, hillshade maps, elevation data) and Google Earth 3-D views, analysis of geomorphological maps, processing of SAR data, consulting of reports and landslide catalogues provided by authorities and field recognition. The landslide inventory for the year 2004, published by Thiery et al. (2007), was prepared at 1 : 10 000 scale through air-photo interpretation, field surveys and analysis of literature in years 2002 and 2003. After being updated and extended to a larger area at the appropriate scale according to the same mapping technique, it constituted the base document to prepare a multi-date inventory at a finer resolution. The landscape interpretation was performed mainly using georeferenced orthophotographs, while the geomorphological maps available for intermediate dates (1975, 1989 and 2001) were considered as ancillary data. For some landslides, historical reports were available and used to confirm the landslide evolution (Stien, 2001). An example of the maps and base inventory is presented in Fig. 3 for the Pra Bellon site, corresponding to either one large slide or multiple slides according to experts' interpretation. Qualitative comparison of different geomorphological maps (Fig. 3a–c) with the base inventory and the most recent orthophotograph (Fig. 3d) allows the interpretation of the landslide evolution over time to prepare the multi-date inventory.

Information of landslide boundaries provided by the base document was crossed and compared with the past years (i.e. 1956, 1974, 1982, 1995, 2000) and the recent year (2009) to detect landslides size and their shape evolutions. Orthophotographs were used to prepare the geomorphological inventories for different years, as for instance 1956 and 2009 years corresponding to G_{56} and G_{09}, respectively. G_{56} is an inventory of the landslides observed in 1956 where the relict and dormant landslides were removed; the G_{09} inventory shows landslides which were (re)activated at least once in the period from 1956 to 2009, and therefore considered as active. The inventories include a qualitative estimation of the landslide changes integrated as the vegetation indicator. This indicator is able to record some landslide reactivation(s) when precise boundaries of new landslides cannot be distinguished due to the vegetation. Uncertainty of landslide interpretation depending on the ability of the expert to recognise precisely the landslides boundaries and orthophotograph quality and scale is detailed in Sect. 4.2. The relict and dormant landslides were also mapped and are shown in two different inventory maps (see definitions in Sect. 4.3). In the attribute table, each landslide polygon is coded with several descriptors (Table 2):

- landslide typology, defined according to the style of movement and/or material (shallow translational slide, deep-seated translational slide, rotational slide and mudslide);
- landslide morphology defined in terms of size (area and perimeter), elevation difference between the lowest and the highest point of the landslide body, runout distance and angle of reach (Corominas, 1996);
- landslide kinematics, defined in terms of degree of activity, average displacement rate of evaluated from the spatial evolution of the landslide boundaries, and changes of the vegetation coverage (vegetation indicator).
- landslide interpretation uncertainty index, qualifying the detectability of the landslide (re)activation by evaluating shape and activity between each date.

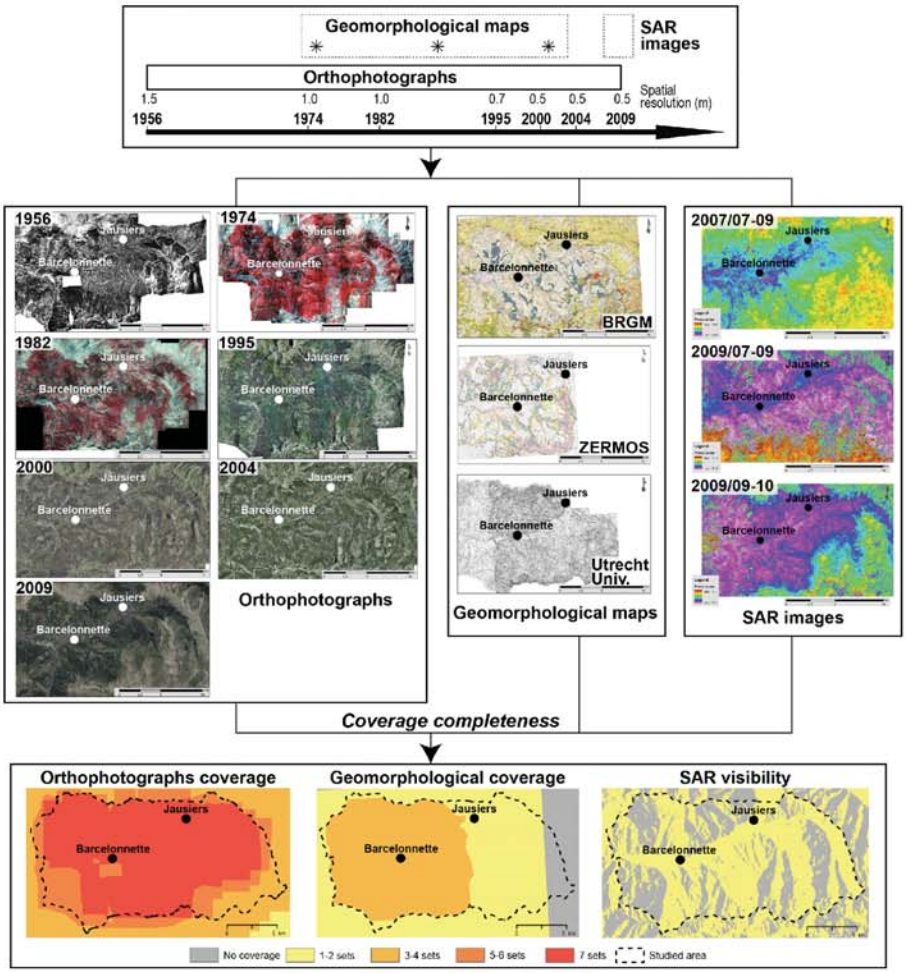

Figure 2. The figure shows available document types (orthophotographs, geomorphological maps, SAR images), their temporal coverage and spatial completeness.

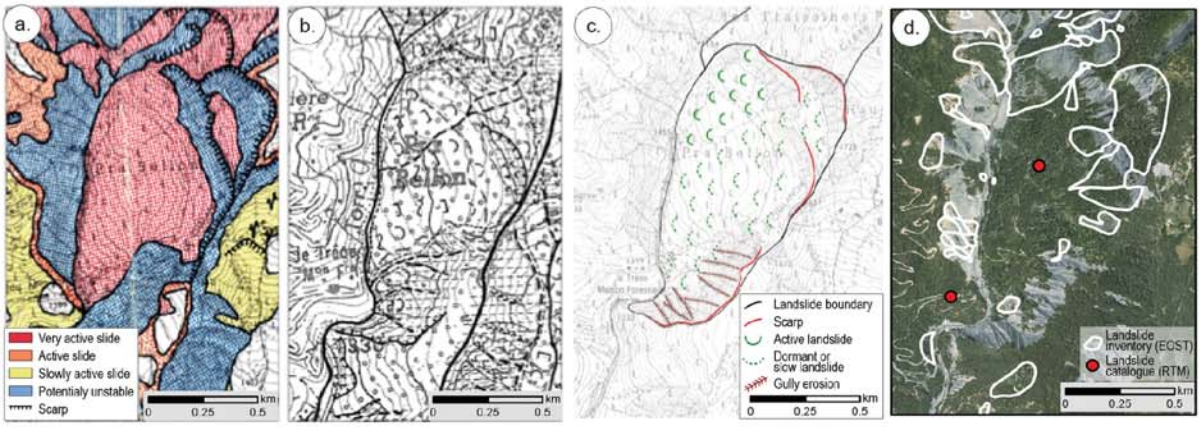

Figure 3. Different sources of information available for the Pra Bellon landslide. **(a)** Geomorphological map from 1975 (ZERMOS, 1975). **(b)** Geomorphological map from 1989 (Utrecht University; Salomé and Beukenkamp, 1989). **(c)** Geomorphological map from 2001 (Stien, 2001). **(d)** Landslide geomorphological inventory map from 2007 (Thiery, 2007).

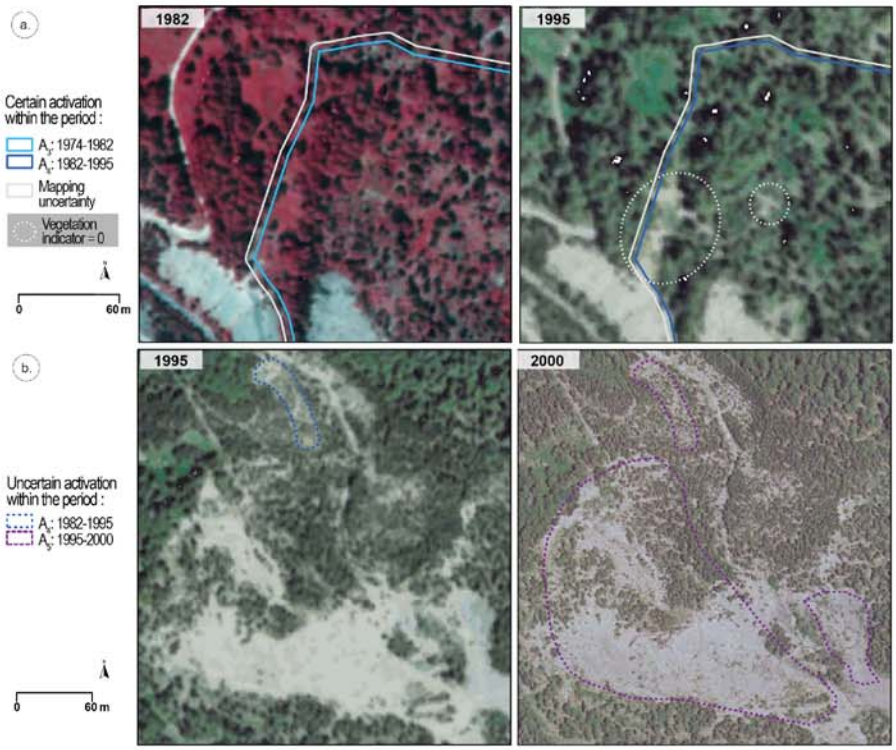

Figure 4. Examples of landslide classification according to the vegetation and uncertainty type. **(a)** A certain landslide reactivation with a vegetation indicator of 0 and a landslide interpretation uncertainty index of 1. While the landslide is more than 50 % under forest, the buffer areas corresponding to the quantitative mapping uncertainty extend the boundaries for 5 and 3.5 m, respectively in 1982 and 1995. **(b)** A supposed reactivation with a vegetation indicator of 0 and a landslide interpretation uncertainty index of 2.

Information on the affected lithology, the surficial formations and the land cover of the source and deposition areas are also indicated in the attribute table.

4.2 Uncertainty estimation

The precision of landslide maps is defined as the ability of the expert to locate landslide features with exactness and give a good description in a GIS database, which is related to the quality of the airborne photographs and topographic maps used (Ardizzone et al., 2002). On the other hand, the accuracy is the degree to which information in the spatial database matches absolute $x - y - z$ coordinates and true attribute values, highly dependent to the orthorectification and co-registration processes (Baynes et al., 2002). Following these definitions, we identified two approaches to estimate the uncertainty: (i) the indexation of the expert skills to recognise the landslide shape and activity and (ii) the estimation of mapping uncertainty by calculating buffer zones around the landslide boundaries to consider the diversity of the data source and the vegetation cover. The landslide interpretation uncertainty index is coded into two classes (1 or 2) included in the attribute table of the geomorphological landslide inventories (Table 2). A value of 1 represents landslide (re)-activations which are clearly visible by the expert (i.e. certain), while a value of 2 indicates a questionable interpretation (i.e. uncertain). This qualitative uncertainty index documents the reliability of the expert's observation and interpretation to recognise a landslide (re)-activation between two periods of time. This index also depends on the source documents (quality, spatial resolution), the landslide type (e.g. deep-seated or shallow) and the terrain conditions (e.g. forested area, grassland...). Indeed, forest harvesting, ploughed lands or new infrastructures may confuse the visual interpretation of the expert. Examples of reliable landslide reactivations and supposed ones are presented in Fig. 4a and b, respectively. Certain landslide (re)-activations with index equal to 1 are analysed statistically according to their evolution in time, while the uncertain ones indicate the visual interpretation uncertainty to detect potential reactivations.

The mapping uncertainty are coded according to two values; the percentage of forest covering the active landslide and the orthophotograph properties. This uncertainty may be related to spatial shifts between images due to the georeferencing procedure or to potential graphical mistakes. While we assume that all orthophotographs are well geocoded, the orthophotograph of 2000 provided by IGN has been wrapped to the other images but a shift of 1.5 m on average remains.

Table 2. List of the attributes associated to landslide polygons stored in the database.

Attributes	Definition	Descriptors/Units
Type (and sub-type)	Typology of Cruden and Varnes (1996)	Deep-seated rotational slide, deep-seated translational slide, shallow translational slide, complex mudslide
Degree of activity	Definition adapted after McCalpin (1984) and Varnes (1978)	relict, dormant, active
Size	Area/perimeter	m^2/m
Elevation range	Difference between the highest and the lowest elevation points measured along the slide perimeter	m
Longest distance (runout)	Horizontal distance between the highest and lowest points located along the slide perimeter	m
Angle of reach	Angle of the line joining the scarp and the landslide toe	°
Average displacement rate	Landslide evolution calculated from the spatial evolution of its spatial boundaries over time	$m\,yr^{-1}$
Vegetation indicator	Qualitative estimation of the degree of activity	0 (reactivation) 1 (no change)
Landslide interpretation uncertainty index	Estimation of the visual interpretation	1 (certain) 2 (uncertain)

This shift has been estimated by comparing ground control points over the whole area. Therefore, in this uncertainty factor, we consider the mapping errors by computing a buffer area corresponding to the spatial shift, or if none is observed, to the spatial resolution associated to the orthophotograph. In optimal conditions, meaning good detectability of the whole landslide body (with no or a few forest coverage), we assume that the landslide boundaries can be mapped with an uncertainty corresponding to the spatial resolution. The whole set of orthophotographs is of good quality with scales varying between 1 : 15 000 and 1 : 35 000. We assume minimal mapping uncertainties corresponding to an area extended of 1.5, 1.0, 1.0, 0.7, 1.5, 0.5 and 0.5 m for 1956, 1974, 1982, 1995, 2000, 2004 and 2009, respectively around the original digitized features. For the geomorphological inventories of 2009, SAR images are used as complement of information for the landslide mapping. The SAR images have a spatial resolution of 10 m and deformation field measured by D-InSAR is around 1 cm (Schlögel et al., 2015). In this quantitative mapping uncertainty, we only consider the orthophotograph properties to calculate the uncertainty associated to the data source. This uncertainty type can vary depending on the difficulties to recognize landslide boundaries under forest. To consider the latter in the uncertainty mapping, we propose to extend the buffer area if the landslide is covered by more than 50 % of forest. Thus, the buffer area of landslide boundaries is the value corresponding to the data resolution (or shift) if the landslide is covered by less than 50 % of forest, while it is the data resolution multiplied by a factor of 5 if the landslide is more than 50 % under forest (see Fig. 4a). These thresholds correspond in the first case to the Nyquist–Shannon sampling theorem stating that an object is perfectly detected on pixel-based images when its size is twice the resolution of the data (Shannon, 1949). Detailed information on the underestimation of the landslide areas and the uncertainty of the boundary location under forest cover are not clearly available in the literature (Wolfe and Williams, 1987). In the case of dense forest coverage, based on several test cases in our data set, we assume that the width of tree's canopy generates an uncertainty on the detection of the underlying features which is approximately equal to five times the resolution. Consequently, the width of the buffer is 7.5, 5.0, 5.0, 3.5, 2.5, 2.5 and 2.5 m for 1956, 1974, 1982, 1995, 2000, 2004 and 2009, respectively. For the second uncertainty indicator, we assume that this buffer area corresponds to minimal but relevant extended landslide boundaries. Therefore, we consider that the mostly extended buffer indicates a mapping uncertainty of 7.5 m when the boundaries are not clearly identified. To sum up, the buffer area (i.e. the uncertainty mapping) varies between 0.5 to 1.5 m if the forest coverage is below 50 %, while it varies between 2.5 to 7.5 m if more than half of the landslide is under forest. Example of reliable landslide reactiva-

tions (uncertainty index of 1) with their associated quantitative mapping uncertainty are presented in Fig. 4a for the period 1974–1982 and 1982–1995 with buffer zone of 5 and 3.5 m, respectively.

4.3 Landslide activity

The degree of activity of the landslides was evaluated and classified in three categories using the terminology proposed by McCalpin (1984): (i) relict when the landslide which occurred 10 000 years BP is still visible in the landscape but does not show morphological evidences of deformation (oldest and largest failures dated from the Holocene period; Jorda, 1980); (ii) dormant when slope evidence of landslide movement can be estimated for a period of 100–10 000 years, and (iii) active when the displacement rates are in the range of few centimetres per year or when significant changes of the sub-surface morphology are observed during the last 100 years. In this study, the active landslides consist in slope movements represented either by a change in landslide size (retrogression of the main scarp, enlargement, downhill progression of the material) or by internal deformation (development of secondary scarps and lobes, changes in the soil surface state) between 1956 and 2009.

The inventories of active landslides (A_1 to A_7) are prepared with the visual orthophotos interpretation, evaluating the landslide differences observed for the studied intervals (Fig. 5a). The A_1 inventory provides information on landslides pre-1956; the A_2, A_3, A_4, A_5, A_6 and A_7 inventories provide information on the new and reactivated landslides, respectively for the period between 1956 and 1974, between 1974 and 1982, between 1982 and 1995, between 1995 and 2000, between 2000 and 2004 and between 2004 and 2009.

The analysis of nine L-band SAR interferograms covering the period 2007–2010 is used to complement the database on the recent landslide activity. The boundaries of the landslides detected by SAR interferograms were adjusted according to the morphology of the slope and the interpretation of the orthophotographs (Fig. 5b). Specific spatial arrangements of wrapped phase values (e.g. decametric to hectometric circular footprints with a continuous value change higher than a phase difference of ± 0.9 rad period^{-1} or 0.02 cm day^{-1}; Schlögel et al., 2015) are considered as landslide signals. For slow-moving landslides, fringes can be determined in these footprints (Fig. 5b) and displacement rates are estimated (Fig. 5c). For fast-moving landslides, displacement rates cannot be estimated and only the presence of a deforming slope is determined on the basis of speckles looking like noise (see Fig. 5b with the example of the landslide located at the NE).

In 2012, field surveys aiming to verify the InSAR signals concluded that 110 signals corresponded to landslide events (Fig. 6b) and were integrated in the G_{09} geomorphological inventory and in the A_7 inventory (Fig. 6a). The other 230 verified InSAR signals were not considered as landslide events as they corresponded either to changes in the soil surface properties (new infrastructures, cultivated crops or harvested forests) or to other types of ground deformation (such as rockfall, sackung and gully erosion).

4.4 Statistical analyses of the landslide inventory maps

Several statistical indicators are calculated to evaluate the density, mobility and size evolution, size-frequency distributions and return periods to calculate temporal probability of landslide events.

4.5 Landslide density maps

Landslide density maps are prepared to quantify the spatial abundance of landslides (Campbell, 1973; DeGraff and Canuti, 1988; Wright et al., 1974). Landslide density is the proportion of landslide surfaces per mapping units and is computed with Eq. 1:

$$D_{\mathrm{L}} = \frac{A_{\mathrm{L}}}{A_{\mathrm{M}}}, 0 \leq D_{\mathrm{L}} \leq 1, \quad (1)$$

where A_{M} is the area of the mapping unit and A_{L} is the landslide cumulated surface in the mapping unit. Density is calculated by counting the slope portion affected by active and new landslides for the period 1956–2009. In our case, the analysis is performed using a 250 m grid (corresponding to an area of 62 500 m^2). The threshold used to consider a landslide grid cell is the presence of a landslide for a surface larger than 250 m^2 (e.g 0.04 %). The landslide density is classified into four classes: [0–0.3[; [0.3–0.5[; [0.5–0.7[; [0.7–1.0]. The 2009 (G_{09}) geomorphological inventory is used to prepare the density maps. Criteria were chosen according to the high variability of the landslide sizes in this area: mean landslide area around 27 000 m^2 with standard deviation of ca. 80 000 m^2).

4.5.1 Landslide mobility and evolution

Descriptive statistics on landslide mobility and activity evolution are calculated combining the different geomorphological inventories (R, D, G_{56} and G_{09}; Table 3). The age of relict (R) and dormant (D) landslides is unknown and no reactivation of these landslides has been recorded over the last 60 years. For the active landslides over the last 60 years, the evolution of morphological descriptors used as proxies of landslide mobility between 1956 and 2009 is presented for the inventories G_{56} and G_{09}. For the G_{56} inventory, landslide features are well distinguished but the date of the triggering event is unknown. However, we decided to only keep landslides showing an indication of activity at least one time between 1956 and 2009 in this geomorphological inventory. For the G_{09} inventory, both the new and reactivated landslides between 1956 and 2009 are considered (Table 3). A landslide activation corresponds either to an internal morphological change within the landslide boundary, or an en-

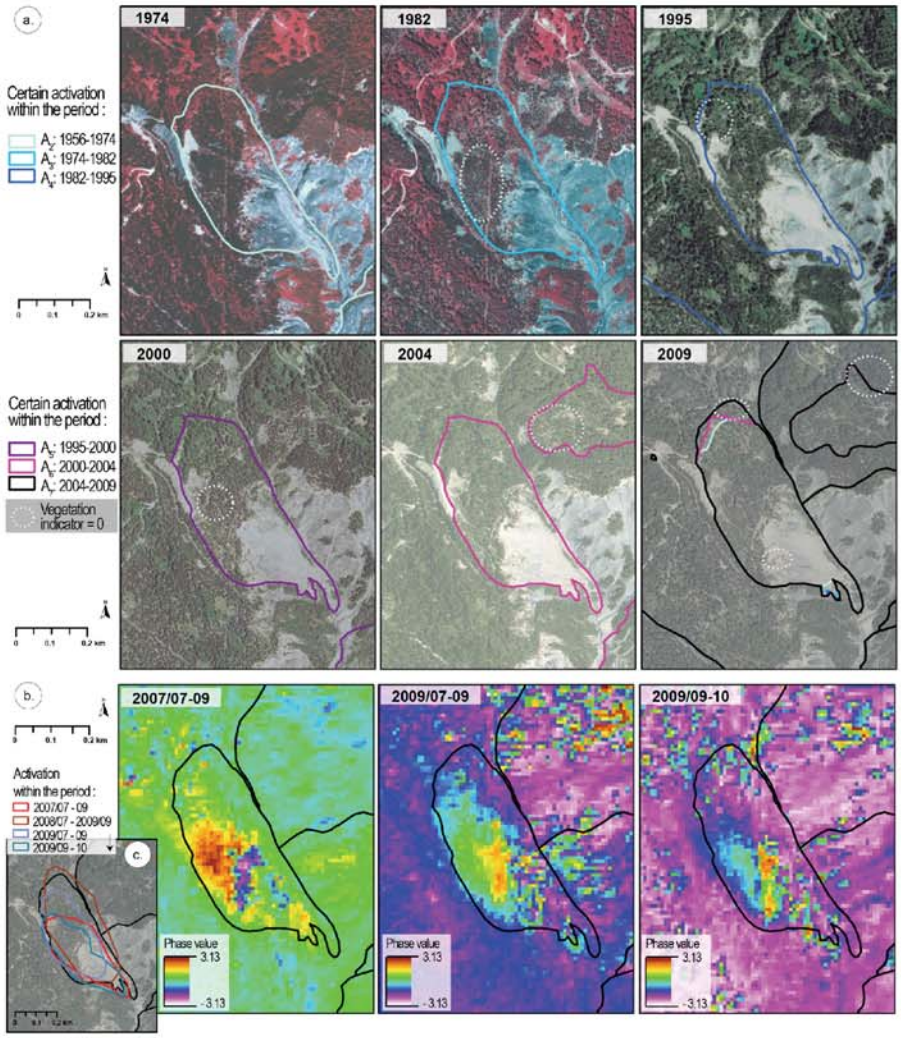

Figure 5. Combination of orthophotographs and SAR interferograms for the creation of the landslide geomorphological inventories. **(a)** Extension of active landslides in 1974, 1982, 1995, 2000, 2004, 2009 on the orthophotograph on a slope located in the Riou Bourdoux catchment. **(b)** SAR interferograms of the same slope with several landslide signals corresponding to specific spatial arrangement of phase values (in radians) for three periods of 46 days (July–September 2007, July–September 2009, and September–October 2009). The extension of the landslides interpreted by visual interpretation of the series of orthophotographs and from field recognitions is indicated with the black line. Sub-units within the landslides of various surface displacement rates are identified. **(c)** Interpreted extension of the landslide sub-units from the SAR interferograms for three time periods of 46 days.

largement of the landslide size (Fig. 5a). The average number of landslides and areas in the study area per year is listed in Table 4. Comparison of G_{09} and G_{56} allows us to estimate the size evolution and the mobility of active landslides in comparison to R and D landslides. The angle of reach (as a proxy of landslide mobility) is calculated for different landslide types mapped in G_{09}.

4.5.2 Landslide size-frequency distributions

Landslide area-frequency distributions are calculated to compare the landslide distributions for several time periods and morphological sub-units. Two size distribution models were proposed in the literature: (1) the Double Pareto distribution (Stark and Hovius, 2001) defined by a positive and a negative power scaling, and (2) the Inverse Gamma distribution (Malamud et al., 2004) defined by a power-law decay for medium and large landslides and an exponential rollover for small landslides. According to best-fit criteria on our data, we choose a maximum-likelihood fit of the simplified version of the double Pareto (DPS) distribution defined by Eq. (2):

$$\mathrm{pdf}\,(x\,|\alpha,\beta,t) = \frac{\beta(t/\alpha)}{\left(1+(x/t)^{-\alpha}\right)^{(1+(\beta/\alpha))}\left(x^{(\alpha+1)}\right)}, \qquad (2)$$

where α controls the slope of the distribution for high values tail, β controls the slope for low values, and t con-

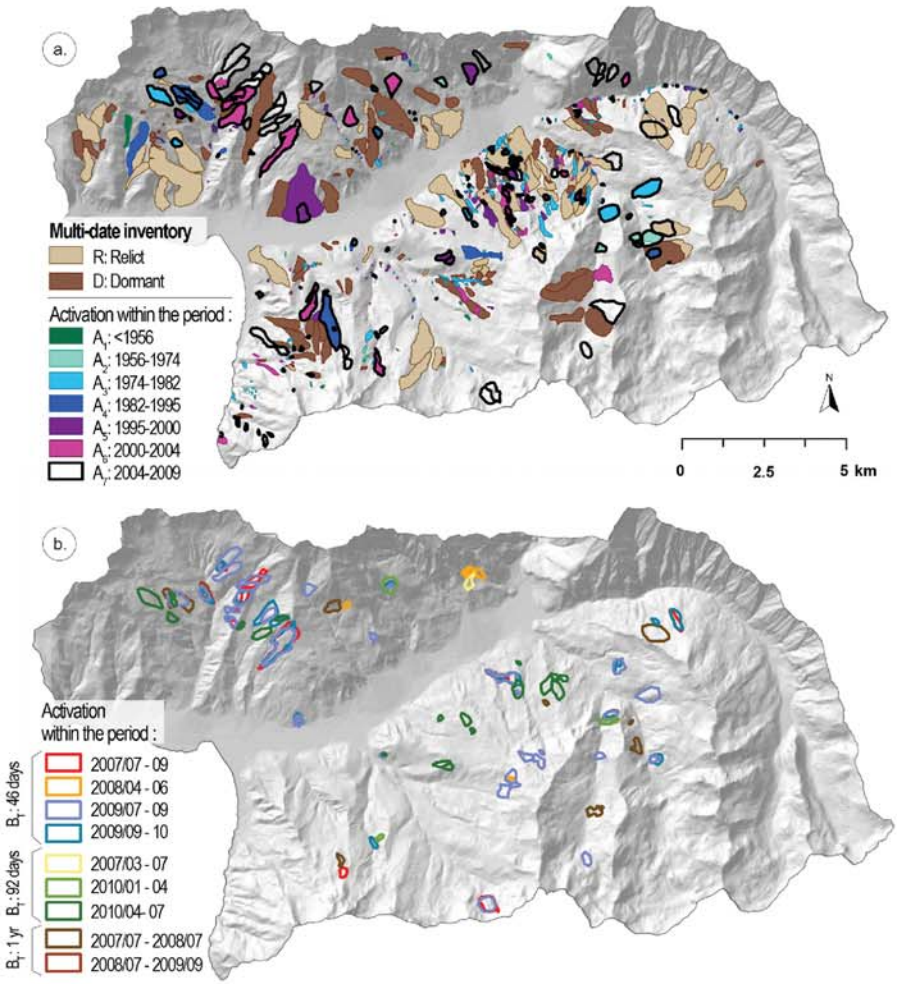

Figure 6. Multi-date landslide geomorphological inventory maps. **(a)** In the map landslides are classified according to the degree of activity (R: relict; D: dormant; A_1–A_7: active). **(b)** Map showing landslide activations for the period 2007–2010 detected by D-InSAR with different temporal baselines (B_T = 46 days, 92 days and 1 year).

Table 3. Descriptive statistics of the geomorphological inventories for different landslide types and degrees of activity. Inventories are divided according to the degree of activity: R (relict, i.e. inactive landslides), D (dormant, i.e. inactive-mature landslides), G_{56} (landslide triggered before 1956 and still active between 1956 and 2009) and G_{09} (active and new landslides from 1956 to 2009). The abbreviations "rot." and "transl." stand for "rotational" and "translational", respectively.

	Date	Type	Activity	Number	Area (km^2)	Density
R	Very old	Deep-seated rot./transl.	Relict	59	16.7	7.1 %
D	Old	Deep-seated rot./transl.	Dormant	115	11.5	4.9 %
G_{56}	$\leq$ 1956	all	New, active	512	13.7	5.8 %
		Deep-seated rot.	New, active	174	9.3	3.9 %
		Deep-seated transl.	New, active	287	4.1	1.7 %
		Shallow transl.	New, active	46	0.2	0.1 %
		Mudslide	New, active	5	0.2	0.1 %
G_{09}	$\leq$ 2009	all	New, active	614	16.6	7.1 %
		Deep-seated rot.	New, active	208	10.7	4.5 %
		Deep-seated transl.	New, active	345	4.9	2.1 %
		Shallow transl.	New, active	55	0.4	0.2 %
		Mudslide	New, active	6	0.7	0.3 %

Table 4. Number and size of new and active landslides for different time periods: A_1 (before 1956), A_2 (from 1956 to 1974), A_3 (from 1974 to 1982), A_4 (from 1982 to 1995), A_5 (from 1995 to 2000), A_6 (from 2000 to 2004) and A_7 (from 2004 to 2009).

	Date	Activity	Number	Number yr^{-1}	Area yr^{-1}	Density
A_1	$^{(*)} \leq 1956$	Active	74	–	–	–
A_2	1956 [to 1974]	Active	131	7.3	$1.8 \times ^{5}$	1.4 %
		New	28	1.6	$1.9 \times ^{4}$	0.1 %
A_3	1974 [to 1982]	Active	265	33.1	$7.9 \times ^{5}$	2.7 %
		New	35	4.4	$2.0 \times ^{4}$	0.1 %
A_4	1982 [to 1995]	Active	148	11.4	$4.3 \times ^{5}$	2.4 %
		New	13	1.0	$4.8 \times ^{3}$	0.1 %
A_5	1995 [to 2000]	Active	103	20.6	$8.0 \times ^{5}$	1.7 %
		New	13	2.6	$4.3 \times ^{4}$	0.1 %
A_6	2000 [to 2004]	Active	111	27.8	$9.4 \times ^{5}$	1.6 %
		New	4	1.0	$8.3 \times ^{3}$	0.1 %
A_7	2004 [to 2009]	Active	116	23.2	$1.4 \times ^{6}$	3.0 %
		New	11	2.2	$1.6 \times ^{5}$	0.3 %

$^{(*)}$: the precise date is unknown.

trols the maximum position of the distribution function (rollover). The web tool developed by Rossi et al. (2012) was used to estimate the DPS distributions of the landslide area directly from the landslide inventory maps. Different frequency density functions were calculated considering the lithology of the landslide source areas (marls, moraine, limestones/sandstones/screes), two morphological sub-units (northern zone, southern zone combined with eastern zone in order to take into account enough landslides in the statistical analysis) and the degree of activity (D, G_{56} and G_{09}, respectively in Table 3). These partitions were constituted in order to count enough elements per data set to compare.

4.5.3 Landslide temporal probability

The Poisson distribution is a discrete distribution function used for characterizing the temporal occurrence of landslides. The probability of experiencing n landslides during time t is calculated with Eq. (3):

$$P\left[N_{\mathrm{L}}(t) = n\right] = P_t = e^{(-\lambda t)} \frac{(\lambda t)^n}{n!} \qquad \text{with } n = 0, 1, 2\ldots, \quad (3)$$

where λ is the estimated average rate of landslide occurrence, which corresponds to $1/\mu$, with μ the estimated mean recurrence interval between successive failure events. The model parameters λ and μ are usually obtained from a historical catalogue of landslide events or from a multi-date landslide inventory map. In our multi-date inventory, λ corresponds to the number of landslides recorded in the study area divided by the period considered (e.g. 10 landslides in 53 years = 0.189 landslides yr^{-1}), while μ is the mean time between two successive landslides (53 years with 10 landslides = 5.3 years). A simple approach is therefore used to estimate the temporal probability of landslide reactivation by calculating how many times a portion of the territory is affected by landslides for a given period of time. The exceedance probability of having one or more landslides in each grid-cell (250 × 250 m) is computed by (i) ascertaining the mean recurrence interval of landslides in each mapping unit (from 1956 to 2009), (ii) assuming that the rate of slope failures remains the same for the future, and (iii) using a Poisson probability model (Crovelli, 2000; Guzzetti et al., 2003, 2005). The landslide recurrence is calculated per grid-cell on the basis of the observed rate of landslide occurrence for the period 1956–2009, knowing the interval of (re)-activations (e.g. A_2, A_3, A_4, A_5, A_6 and A_7).

5 Results

5.1 Analysis of landslide density

In this section we compare the location and extension of slope failures reported in the geomorphological inventory of active landslides observed in 2009 (G_{09}) with the 1956 geomorphological inventory (G_{56}) (Table 3).

The density of active landslides in Ubaye is ca. 2.6 landslides km^{-2} (for a total area of 235 km^2). The density of deep-seated rotational and deep-seated/shallow translational slides (Table 3) affecting the test area is computed using a grid cell of 250 m × 250 m (Fig. 7a, b). The density is computed for three different morphological units (Fig. 7) delimited by the E/W-oriented Ubaye River (northern and southern areas, zone 1 and zone 2, respectively) and by the "Montagne de l'Alpe" passing by the "Croix de l'Alpe" crest N/S-oriented (eastern area or zone 3). High density of translational slides is observed in zone 2 where they are distributed homogeneously (Fig. 7a and b), while they are more concentrated in the north of zone 3. Their average size is 20 755 m^2 in zone 1 (3 landslides km^{-2}),

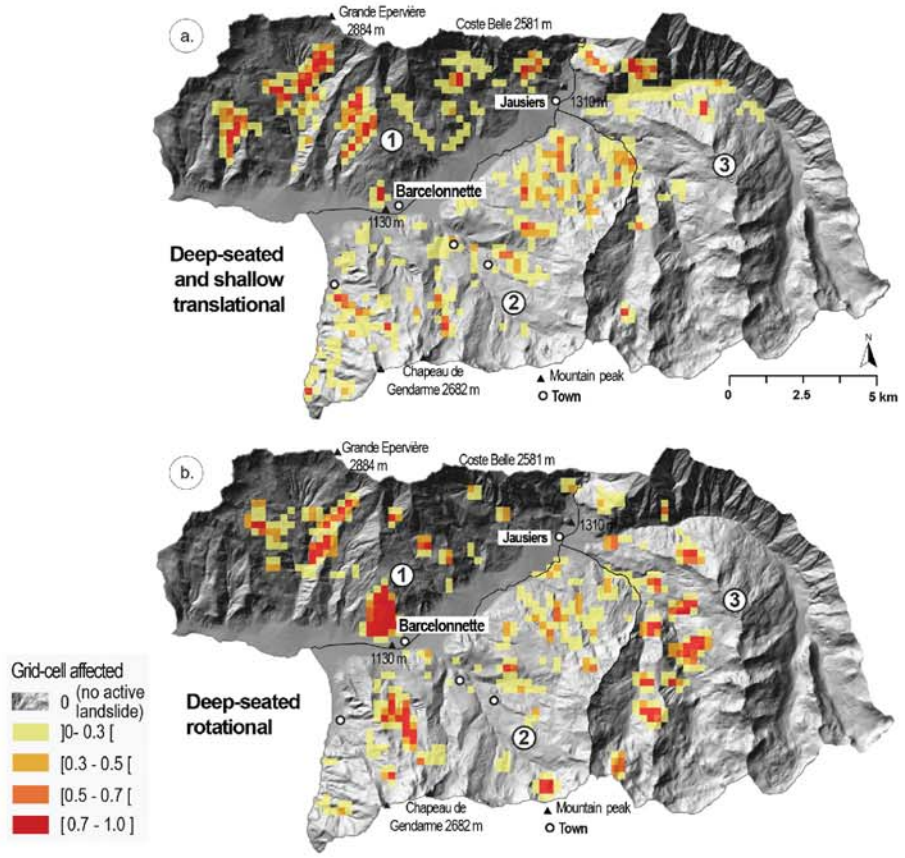

Figure 7. Landslide density maps. **(a)** Percentage of grid-cell affected by active deep-seated and shallow translational slides. **(b)** Percentage of grid-cell affected by active deep-seated rotational slides. The grid-cell dimension is 250 m × 250 m.

12 855 m^2 in zone 2 (1.6 landslides km^{-2}) and 10 975 m^2 in zone 3 (0.9 landslides km^{-2}). Deep-seated rotational slides are less present in zone 1 and rarely observed to the east of the Riou Versant (Fig. 7b). Their average size is 85 700 m^2 in zone 1 (0.6 landslides km^{-2}), 25 420 m^2 in zone 2 (1.8 landslides km^{-2}), and 109 500 m^2 in zone 3 (0.3 landslides km^{-2}). In zone 3, the landslide average area is almost 10 times larger for rotational slides than for translational slides. The slopes oriented to the west are more affected by landslides (i.e. mean slope orientations of 220 and 226°; Figs. 7a, b and 8a). The average value of the mean landslide slope angles reaches 25° with a standard deviation of 4°. The deep-seated landslides and the three complex mudslides have been mostly reactivated in regolith deposits (i.e. moraine and weathered marls) constituting most of the territory. The few shallow translational landslides are almost equally observed in bedrocks and regolith deposits.

Figure 8a indicates that slopes oriented to the N, NW and W are mostly affected by active landslides. This observation might be explained by a longer persistence of snow cover on these slopes in winter and early spring but the inventory completeness is also influenced by the SAR coverage. In addition, slopes oriented to the NW and W are more represented over the area, while it is the opposite for those oriented to the NE. Percentage of forested area is also higher to the NW and lower to the NE and E. Correlation between the landslide occurrences and the land cover highlights that around 65 % of the active landslides are more than 50 % under forest.

5.2 Analysis of landslide mobility and evolution

This section describes the landslide geometrical parameters for relict, dormant and active landslides (R, D, and G_{09}; Table 3) in terms of mobility as well as spatial and temporal evolution. According to the complete landslide inventory (R, D, and G_{09}), the area is affected by 788 mass movements corresponding to an average density of ca. 3.4 landslides km^{-2}. 59 slides are relict, 115 are dormant and 614 slides are classified as active (i.e. 2.6 landslides km^{-2}). In terms of affected surfaces, the relict, dormant and active slides correspond respectively to 7.1 %, 5.8 % and 7.1 % of the surface of the area (Table 3). The dormant landslides are less represented in surface but more numerous than the relict landslides (Fig. 8b). The active landslides (more than three-quarters of the total number of

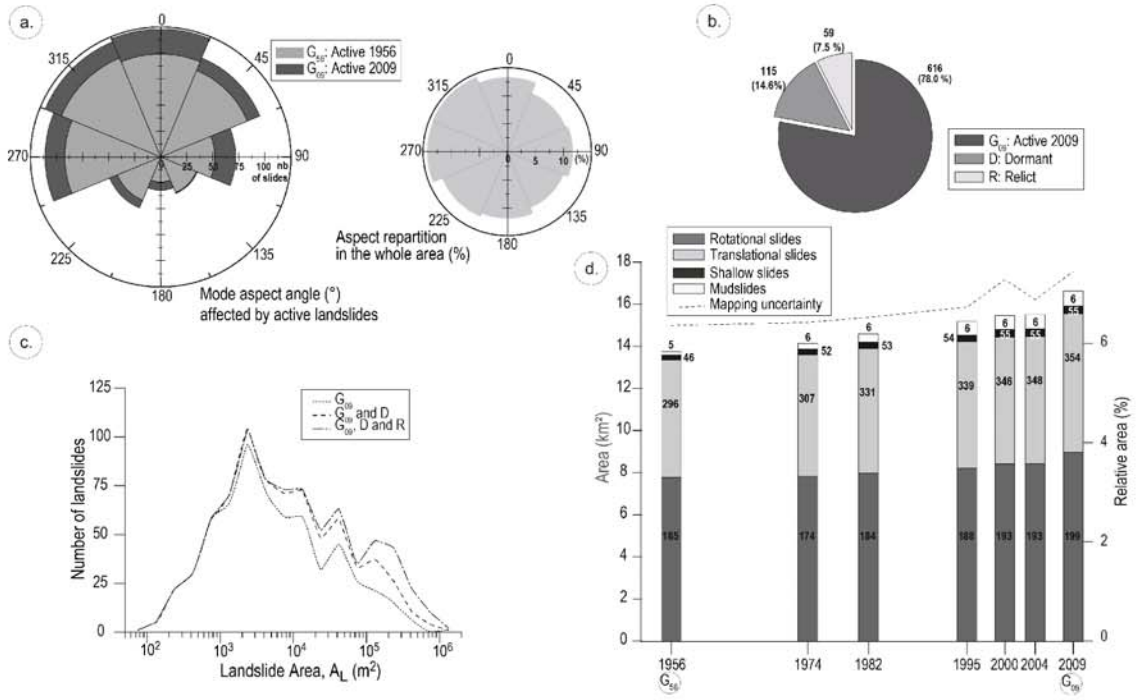

Figure 8. Statistics of the landslides observed in the Ubaye valley according to **(a)** the distribution of slope aspects; **(b)** the landslide degree of activity (relict, dormant and active), **(c)** the landslide distribution in terms of number and area, and **(d)** the area affected by different landslide types from 1956 to 2009. The number of landslide per type is indicated on the graph. Dotted line represents the total area affected by landslide considering the quantitative mapping uncertainty.

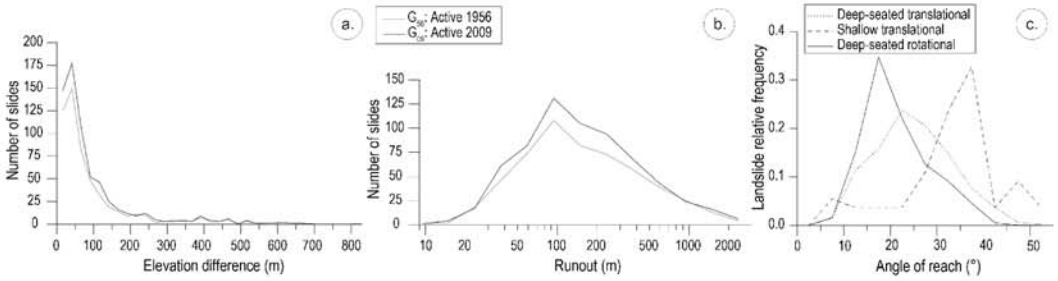

Figure 9. Analysis of the landslide geomorphological parameters: **(a)** Elevation difference and **(b)** runout distance of the new and (re)-activated landslides observed in 1956 and 2009. **(c)** Angle of reach for the different landslide types in 2009.

landslides; Fig. 8b) cover an area of around $16.6 \pm 0.9\,km^2$ in 2009 (Fig. 8d). According to the uncertainty index, the uncertain active landslides cover almost $1\,km^2$ of the territory in G_{09}. The active landslides range in size from 100 to $140\,000\,m^2$; the average size of the active landslides is equal to $28\,500\,m^2$ (Fig. 8c). Among the active landslides, the rotational slides are more represented in surface than in number, meaning that they are, on average, larger than the shallow and deep translational landslides (Fig. 8d). Total of landslide areas with their mapping uncertainty (i.e. buffer zones) represented $16.6 \pm 0.5\,km^2$ of the territory in G_{09}. Around 6 and 4 % of the landslides reactivated in 1974 and 1982, respectively, might correspond to an uncertainty of mapping. This quantitative mapping uncertainty is higher in the 2000 inventory due to the geometrical correction of the corresponding orthophotograph (dotted line in Fig. 8c).

The sizes of the active landslides in 2009 and 1956 (G_{09}; G_{56}; Table 3) are compared. From 1956 to 2009, 102 new landslides are observed corresponding to a surface increase of $2.9\,km^2$ (1.3 % of the area). The analysis of the elevation differences (Table 2) for the landslides boundaries mapped in G_{56} comparing to the ones mapped in G_{09} indicates small differences, in the range between 20 and 100 m, with an average of ca. 50 m (Fig. 9a). The runout distance ranges between 10 and more than 2000 m but most of the values range between 50 and 200 m (Fig. 9b). Figure 9c indicates that the

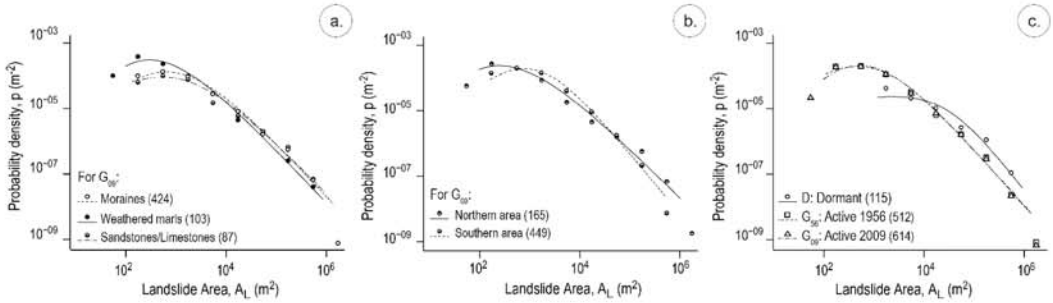

Figure 10. Landslide frequency–area distributions and maximum-likelihood fit of a Double-Pareto Simplified model. **(a)** Frequency–area distributions for three categories of lithology of the landslide bodies. **(b)** Frequency–area distributions for two morphological units of the Ubaye valley (right and left riverbanks of the Ubaye River corresponding, respectively, to the northern and southern areas). **(c)** Frequency–area distributions for three categories of degrees of activity.

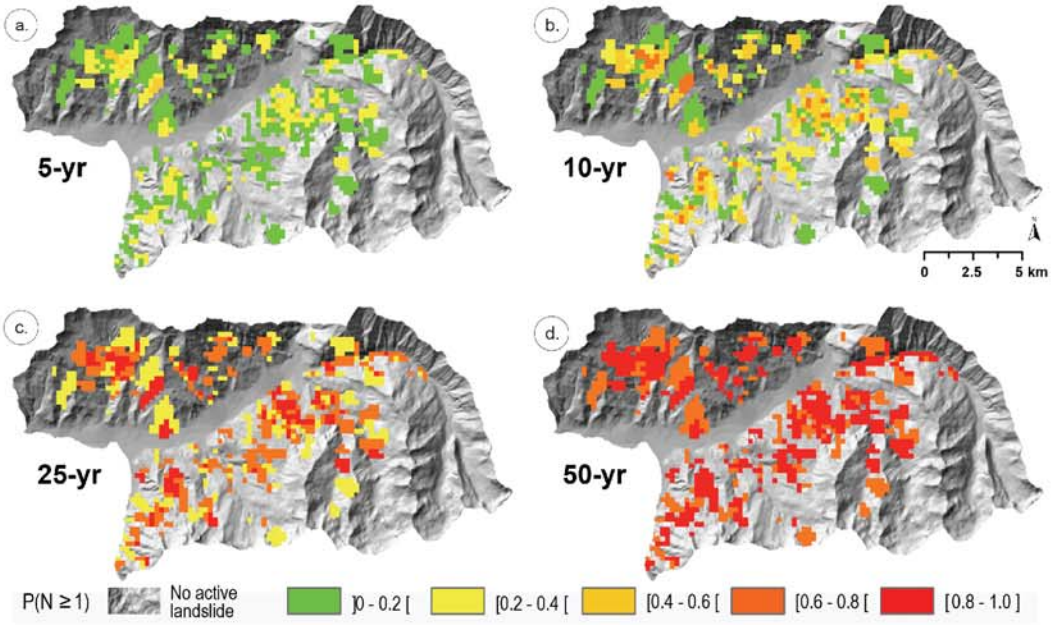

Figure 11. Exceedance probability of temporal occurrence of landslide (re)-activation calculated from the mean recurrence interval of past landslides (Fig. 6a) with a Poisson probability model. Exceedance probability is calculated for four return periods (5, 10, 25 and 50 years). A probability of zero is obtained in the areas where no active landslides are observed.

angles of reach are in the range 15-25° for the rotational slides, in the range 12–35° (with a scattered distribution) for the deep translational slides and in the range 30–40° for the shallow translational slides. These values are consistent with the geomorphological features associated to these landslide types.

5.3 Analysis of size-frequency distribution

The multi-date landslide inventory was prepared with heterogeneous multi-source data at different spatial resolutions and scales. The landslide inventories are compared with the assumption that the heterogeneity of the data set and the interpretation rules used for mapping the landslide do not impact the landslide frequency–area distribution. Frequency–area density functions were calculated by taking into account different landslides subsets (Fig. 10): (i) the geomorphological inventory of 2009 (G_{09}; Table 3) classified according to the lithology and, (ii) the geomorphological inventory of 2009 (G_{09}; Table 3) classified according to the morphology; and (iii) the multi-date inventory classified according to landslide activity (D, G_{56} and G_{09}; Table 3).

The frequency–area distributions indicate the presence of few small landslides, meaning that some of the landslides are missing in the database because of their size. The frequency density for medium and large landslides follows a negative power law trend. The α values are 0.62 ± 0.04 (for weathered marls) and 0.57 ± 0.01 (for limestones, sand-

stones and screes; Fig. 10a), meaning that large events can occur in both lithologies but are expected to be smaller in the weathered marls. The α values are different for the northern area (0.51 ± 0.03) than for the southern area (0.86 ± 0.03; Fig. 10b). It indicates that the landslides are larger in the northern area explained by specific geomorphological conditions (higher number of steep slopes, presence of the thrust sheets). However, the frequency–area distribution is dependent on the number of events, and three very large landslides (Pra Bellon, Les Aiguettes and La Valette) are observed in this unit, biasing the calculation. In the southern area, the β values are higher according to the frequency of the small landslides but the distribution is scattered with high values of standard deviation up to $\pm$ 0.73. Finally, the frequency–area distribution of the dormant landslides shows a completely different distribution without a rollover with respect to the active landslide because of their large size (Fig. 10c). The high variation of β values (1.17 ± 0.12 to 4.49 ± 0.73) can be related to the difficulty to map small events, especially in the past years, and thus their underestimation (Guzzetti et al., 2002). Despite these limitations, a rollover is observed for the smallest landslides, which are more frequent around 480 m^2 in 1956 (G_{56}) and around 520 m^2 in 2009 (G_{09}).

5.4 Analysis of landslide temporal probability

Knowing the recurrence time between successive failures for the period 1956–2009, the exceedance probability of landslide reactivation is estimated for four return periods from 5 to 50 years (Fig. 11). For a return period of 10 years, high probability of landslide reactivation is expected to the NW of the area, in relation to the numerous reactivations of the Pra Bellon, Les Aiguettes and La Valette landslides over the last 60 years. Table 5 indicates the number, area and percentage of cells for different temporal probabilities and return periods. Five probability classes are considered to highlight the evolution of landslide reactivation over time. Within 10 years, the probability that territory already affected by landslides is going to be reactivated is low for 66 % of the whole area, while it was of 97 % after 5 years (Table 5). Only 3 % of the whole catchment has a high probability of activity considering a return period of 10 years (e.g. La Valette, Les Aiguettes and Pra Bellon landslides). Within 25 years, 30 % of the territory has a probability higher than 0.8 to be reactivated, while in the next 50 years, it reaches almost 60 %. The computation is based on the temporal sequence analysed and therefore, less reliable for a return period of 50 years as it is close to the period considered in this study.

6 Discussion: evolution of landslide activity

This section discusses the evolution of landslide activity comparing inventories of different sources and temporal coverage: (i) the activity estimated from the multi-date inventory (Fig. 12), (ii) the punctual catalogue of events over the period from 1850 to 2010 (Fig. 13) and (iii) all the inventories combined together for the common period (Fig. 14).

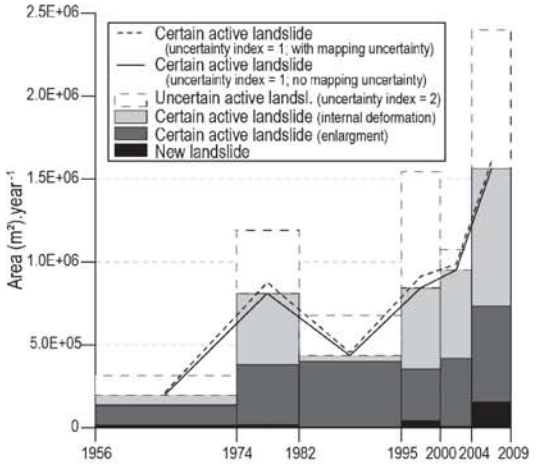

Figure 12. Areal extension of new and reactivated landslides per year. The dotted boxes indicate supposed active landslides according to the landslide interpretation uncertainty index (i.e. equal to 2) added in the attribute table and the dotted trend compares the total areas with buffers according to the qualitative uncertainty.

The analysis of landslide activity shows that 1.3 % of the territory was affected by new landslides between 1956 and 2009 (Table 3). Deep-seated rotational landslides mainly affect the slopes in area, while translational landslides are more numerous in number. Table 4 indicates the evolution of landslide activity over the period 1956–2009 considering the number, area and density properties of the new and the reactivated landslides. On the whole territory, only a few new landslides (from 1.0 to 4.4 landslides yr^{-1}) occurred, while landslide reactivations are numerous (from 7.3 to 33.1 landslides yr^{-1}). The evolution of the active landslide area from 1956 to 2009 (A_2, A_3, A_4, A_5, A_6 and A_7; Table 4) is presented in Fig. 12. For the entire period ($A_2 - A_7$), the new landslides are represented in black, the reactivated landslides defined by changes in size are in dark grey and the reactivated landslides defined by internal deformation are in grey; the uncertain active landslides (landslide interpretation uncertainty index equal to 2) are shown in dotted boxes. The certain active landslide areas including buffer zones corresponding to the resolution and land cover (represented by dotted lines in Fig. 12) indicate a higher uncertainty for the period 1995–2000. Visual analysis shows that areas affected by active landslides are similar between the periods 1974–1982 and 1995–2000 and then, they increase to 2009.

The periods of landslide activity covering the years 1850–2010 identified from dendrogeomorphological observations (Lopez-Saez et al., 2011, 2012, 2013; Fig. 13a–c) are compared to the landslide catalogue collected by the local risk managers (RTM and BRGM; Fig. 13d) since 1850. The dendrogeomorphological information was collected only at

Table 5. Temporal probability of landslide reactivation for 5-, 10-, 25- and 50-year return periods. For each period the table indicates the number of cells, the landslide area in square kilometres and in percentage for five probability classes (see Fig. 11).

$P(N \geq 1)$	0–0.2			0.2–0.4			0.4–0.6			0.6–0.8			0.8–1.0		
years	# cells	area (km^2)	%	# cells	area (km^2)	%	# cells	area (km^2)	%	# cells	area (km^2)	%	# cells	area (km^2)	%
5	540	33.8	65.7	261	16.3	31.8	21	1.3	2.6	0	0	0	0	0	0
10	334	20.9	40.6	206	12.9	25.1	235	14.7	28.6	47	2.9	5.7	0	0	0
25	0	0	0	334	20.9	40.6	0	0	0	337	21.1	41.0	151	9.4	8.4
50	0	0	0	0	0	0	0	0	0	334	20.9	40.6	488	30.5	9.4

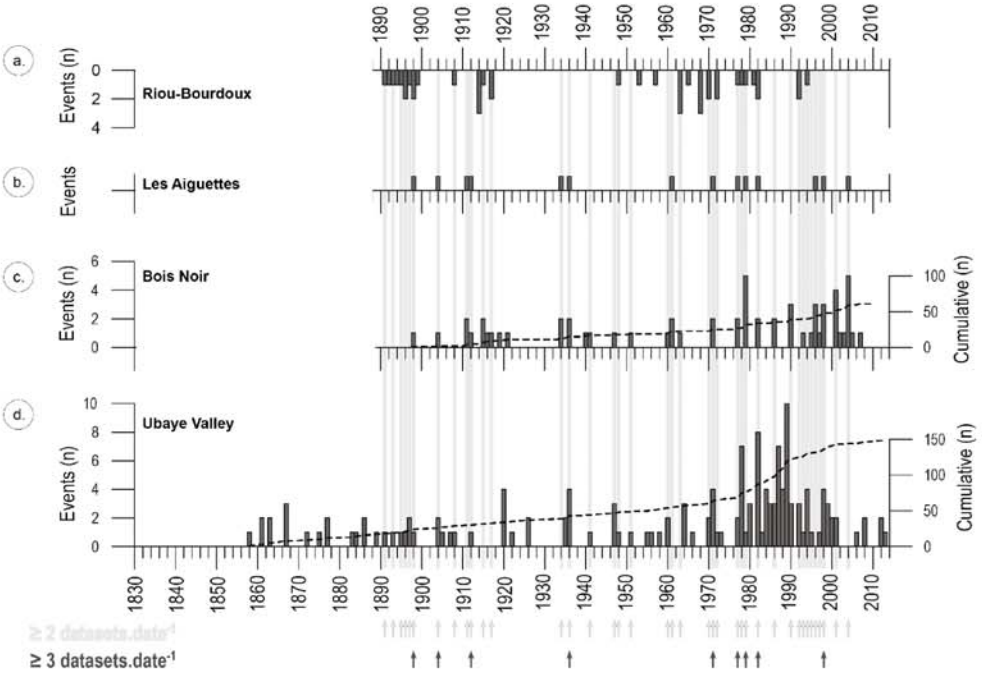

Figure 13. Comparative analysis of periods of landslide activity recorded in several data sets. **(a)** Landslide dendrogeomorphological observations for the Riou Bourdoux catchment (Lopez-Saez et al., 2013); **(b)** Dendrogeomorphological observations for the Pra Bellon landslide (Lopez-Saez et al., 2012); **(c)** Dendrogeomorphological observations for the Les Aiguettes landslide (Lopez-Saez et al., 2011) and **(d)** RTM and BRGM landslide catalogues for the Ubaye valley. Below, arrows point out the most active years considering at least 2 or 3 of the data sets presented.

some unstable slopes (Aiguettes, Pra Bellon and Bois Noir landslides; Fig. 1e–f), while the event catalogue covers the whole study area. Periods (years) of landslide activity are identified from the comparison of the landslide catalogues. A total of 31 and 10 periods with increased landslide activity are, respectively, identified in two and three data sets (arrows in Fig. 13). From the dendrogeomorphological analysis, Lopez-Saez et al. (2013) identified 12 major reactivations for the Aiguettes landslide (i.e. in 1898, 1904, 1911, 1916, 1936, 1961, 1971, 1977, 1979, 1996, 1998, and 2004). Considering the timing of annual tree ring formation at Bois Noir, landsliding is likely to have occurred in 1874–1875, 1896–1897, 1946–1947, 1992–1993, and 2003–2004 (Lopez-Saez et al., 2011). According to Lopez-Saez et al. (2012), the Pra Bellon landslide had no relevant reactivation for the period 1980–1990, while the La Valette landslide has been triggered in 1982 and major failures were observed at Super-Sauze between 1978 and 1982 (Flageollet et al., 1999; Malet, 2003). Figure 13 indicates that many reactivations were recorded at the Bois Noir landslide for the year 2004, but only a few landslides are recorded elsewhere in the region. The period between 1992 and 2000 is considered as active with at least more than two large events recorded in dendrogeomorphological archives. However, it is extremely difficult to extrapolate local information from specific slopes of different landslide types to the entire valley.

Figure 14a points out that the period between 1974 and 1982 recorded more new and reactivated landslides than the other periods with, respectively, 33 and 4 events yr^{-1}. In comparison, less than 2 new landslides or

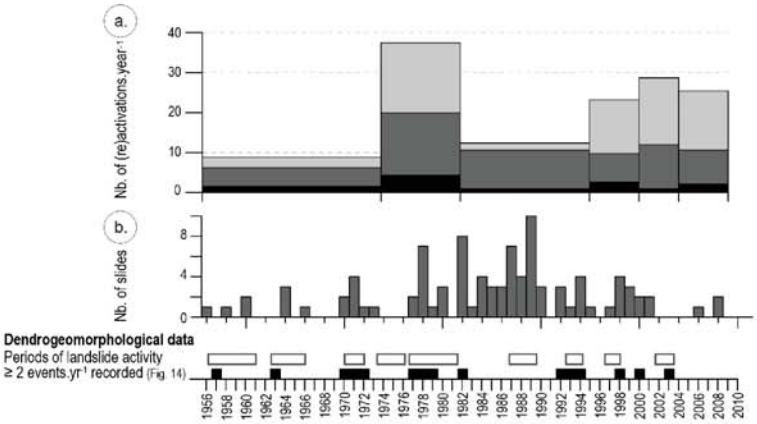

Figure 14. Comparison of landslide activity given by different landslide inventories available for the Ubaye valley. **(a)** Number of new landslides or landslide (re)-activations from the multi-date inventory. **(b)** Number of landslides from the historical landslide catalogue of RTM/BRGM and below, periods of landslide activity recorded by dendrogeomophological observations of two sites in the valley (Thiery, 2007).

12 reactivations yr^{-1} have been recorded in the first and third periods (1956–1974 and 1982–1995). After 1995, more landslides were registered. A peak of landslide activity (Fig. 13d) is observed in terms of number of events in 1989, but this is not observed considering the multi-date inventory and the evolution of landslide sizes and areas (Figs. 12 and 14a). For the period 1995–2009, the number of active landslides is roughly the same, while an increase of areas affected by landslides from 2004 to 2009 is recorded. Comparison with dendrogeomorphological archives are not steady-state however some periods of activity can be correlated over the whole data set of results, such as between 1956–1960, 1964–1966, 1970–1972, 1977–1980, 1982, 1987–1989, 1993–1994, 2000 and 2002–2003. For the most recent years, the catalogue of events recorded by the policy makers seems incomplete and dendrogeomorphological observations are missing (Fig. 14b).

7 Conclusion

The interpretation of aerial photographs and SAR images allowed us to increase the number of detected landslide events (new landslide or landslide reactivations) than those indicated in historical catalogues, and to prepare a multi-date inventory. However, the interpretation is difficult and depends on: (i) the skill of the geoscientist, (ii) the knowledge of the field conditions and (iii) the data considered to recognize landslide features. The empirical results given by the multi-date inventory statistical analysis are interpreted considering the inventory completeness and reliability due to limitations and biases. A qualitative landslide interpretation index is proposed in addition to a mapping uncertainty measurement taking into account the data properties and the land cover affecting each landslide. The computed buffer areas showed that at least 85 % of the landslides evolving with a size enlargement over time are not comprised into the mapping uncertainty (except considering the 2000 period with at least 60 % of the landslides). A few enlargements of landslides (e.g. 6 and 4 % of the landslides reactivated in 1974 and 1982, respectively) are either due to the uncertainty of mapping in forested area and/or influence of data quality, or correspond to a real reactivation in size. In addition, in optimal conditions (landslides with less than 50 % under vegetal cover), we assume that our data set allows us to detect most of the landslides having a displacement larger than a distance of twice the data resolution. For instance, between 2004 and 2009, the displacement rate of the active landslide should be at least 0.2 m yr^{-1} to be certainly detected following the approach described in this study.

Differences in area-frequency distributions are observed according to the geomorphological settings of the landslides and their degree of activity. It also reveals the difficulty to map the small size events. We assume that the inventory is complete for landslides with areas over 500 m^2 (rollover of 480 and 520 m^2 for G_{56} and G_{09}, respectively) even if well-trained eyes are able to recognize landslides with areas of at least 100 m^2.

L-band D-InSAR allowed the detection of slow-moving landslides on a portion of the territory (around 60 %) according to the SAR properties. It provided additional information on the active landslides (sometimes unknown or under forest) for the period 2007–2010 and allowed us to integrate new events in the last geomorphological inventory.

As multi-temporal inventories are time-consuming to prepare, only few works have been published on the temporal probability of occurrence of future landslides (Coe et al., 2000; Guzzetti et al., 2005; Lopez-Saez et al., 2012). The approach presented in this paper allows determination of quantitative probabilities of reactivation estimated directly from the frequency of past events combining recent very

slow-moving landslides by SAR results interpretation and landslide (re)activations over the last 60 years by orthophotographs interpretation. The approach uses a Poisson probability model based on some assumptions even if most hazardous events, and especially landslides, are probably not independent and do not occur randomly (Coe et al., 2000). Indeed, a landslide reactivation can increase or decrease the slope susceptibility to future landslides, thus creating a low-to-high instability in the future. Changes in land use or climatic conditions also affect the future occurrence of landslides.

In addition, the preparation of a multi-date inventory as explained in this study induces underestimation of small events due to the limitations in the visual analysis because of the terrain conditions and the data sources. However, the vegetation indicator is useful to record reactivations when the precise landslide boundaries are not visible due to the forest coverage. The comparison of landslide activity measured by the multi-date inventory and by the landslide historical catalogue pointed out the incompleteness of the historical catalogue for the recent years. Even if they are definitively more complicated to interpret, construction of large multi-source data sets for multi-date inventory preparation is required for the analysis of landslide occurrences. Preliminary statistical analyses of landslide inventories are relevant to explore the spatial and temporal distribution of landslides events and assess the landslide hazard for different landslide types.

Acknowledgements. This work was supported by the Marie Curie Research and Initial Training Network "CHANGES: Changing Hydro-meteorological Risks as Analyzed by a New Generation of European Scientists", funded by the European Community's 7th Framework Programme FP7/2007–2013 under Grant Agreement No. 263953. The orthophotographs and elevation data were provided by IGN (Institut Géographique National) and other public partners. The access to ALOS/PALSAR images was given by the Japan Aerospace eXploration Agency (JAXA) and the European Space Agency (ESA) under the contract C1P.8859. The historical catalogue of landslide events was provided by the RTM-04 (Restauration des Terrains en Montagne) service of Département des Alpes-de-Haute-Provence. The authors would like to thank M. Rossi and M. Santangelo (CNR-IRPI, Italy) for their advices.

Edited by: T. Glade
Reviewed by: two anonymous referees

References

Ardizzone, F., Cardinali, M., Carrara, A., Guzzetti, F., and Reichenbach, P.: Impact of mapping errors on the reliability of landslide hazard maps, Nat. Hazards Earth Syst. Sci., 2, 3–14, doi:10.5194/nhess-2-3-2002, 2002.

Ardizzone, F., Cardinali, M., Galli, M., Guzzetti, F., and Reichenbach, P.: Identification and mapping of recent rainfall-induced landslides using elevation data collected by airborne Lidar, Nat. Hazards Earth Syst. Sci., 7, 637–650, doi:10.5194/nhess-7-637-2007, 2007.

Baynes, F. J., Lee, I. K., and Stewart, I. E.: A study of the accuracy and precision of some landslide risk analyses, Aust. Geomech., 37, 149–156, 2002.

Bell, R., Petschko, H., Röhrs, M., and Dix, A.: Assessment of landslide age, landslide persistence and human impact using airborne laser scanning digital terrain models, Geogr. Anna. A, 94, 135–156, 2012.

Brardinoni, F., Slaymaker, O., and Hassan, M. A.: Landslide inventory in a rugged forested watershed: a comparison between air-photo and field survey data, Geomorphology, 54, 179–196, 2003.

Campbell, R. H.: Isopleth map of landslide deposits, Point Dume quadrangle, Los Angeles County, California, an experiment in generalizing and quantifying areal distribution of landslides: U.S. Geological Survey Miscellaneous Field Studies Map MF-535, scale 1 : 24 000, 1973.

Canuti, P., Casagli, N., Ermini, L., Fanti, R. and Farina, P.: Landslide activity as a geoindicator in Italy: significance and new perspectives from remote sensing, Environ. Geol., 45, 907–919, 2004.

Carrara, A., Cardinali, M., and Guzzetti, F.: Uncertainty in assessing landslide hazard and risk, ITC J., 2, 172–183, 1992.

Cascini, L., Fornaro, G., and Peduto, D.: Analysis at medium scale of low-resolution DInSAR data in slow-moving landslide-affected areas, ISPRS J. Photogramm., 64, 598–611, 2009.

Coe, J. A., Michael, J. A., Crovelli, R. A., and Savage, W. Z.: Preliminary map showing landslide densities, mean recurrence intervals, and exceedance probabilities as determined from historic records, Seattle, Washington, USA. USGS Open-File Report 00-0303, 2000.

Colesanti, C. and Wasowski, J.: Investigating landslides with space-borne Synthetic Aperture Radar (SAR) interferometry, Eng. Geol., 88, 173–199, 2006.

Corominas, J.: The angle of reach as a mobility index for small and large landslides, Can. Geotech. J., 33, 260–271, 1996.

Corominas, J., van Westen, C. J., Frattini, P., Cascini, L., Malet, J.-P., Fotopoulou, S., Catani, F., Eeckhaut, M., Mavrouli, O., Agliardi, F., Pitilakis, K., Winter, M. G., Pastor, M., Ferlisi, S., Tofani, V., Hervás, J., and Smith, J. T.: Recommendations for the quantitative analysis of landslide risk, B. Eng. Geol. Environ., 73, 209–263, 2014.

Crovelli, R. A.: Probability models for estimation of number and costs of landslides. U.S. Geological Survey Open File Report 00-249, 2000.

Cruden, D. M. and Varnes, D. J.: Landslide types and processes, in: Landslides-investigations and mitigation, edited by: Turner, R. L. and Schuster, A. K., 36–75, Washington D.C., USA, 1996.

DeGraff, J. V and Canuti, P.: Using isopleth mapping to evaluate landslide activity in relation to agricultural practices, Bull. Int. Assoc. Eng. Geol., 38, 61–71, 1988.

Doin, M.-P., Lodge, F., Guillaso, S., Jolivet, R., Lasserre, C., Ducret, G., Grandin, R., Pathier, E., and Pinel, V.: Presentation of the small baseline processing chain on a case example: the Etna deformation monitoring from 2003 to 2010 using ENVISAT data, in Proc. "Fringe 2011 Workshop", Frascati, Italy, 19–23 September 2011, p. 7., 2011.

Flageollet, J.-C., Maquaire, O., Martin, B., and Weber, D.: Landslides and climatic conditions in the Barcelonnette and Vars basins (Southern French Alps, France), Geomorphology, 30, 65–78, 1999.

Florsheim, J. L. and Nichols, A.: Landslide area probability density function statistics to assess historical landslide magnitude and frequency in coastal California, Catena, 109, 129–138, 2013.

Galli, M., Ardizzone, F., Cardinali, M., Guzzetti, F. and Reichenbach, P.: Comparing landslide inventory maps, Geomorphology, 94, 268–289, 2008.

Günther, A., Reichenbach, P., Malet, J.-P., Eeckhaut, M., Hervás, J., Dashwood, C., and Guzzetti, F.: Tier-based approaches for landslide susceptibility assessment in Europe, Landslides, 10, 529–546, 2013.

Guzzetti, F., Cardinali, M., and Reichenbach, P.: Map of sites historically affected by landslides and floods, The AVI Project, CNR Gruppo Nazionale per la Difesa dalle Catastrofi Idrogeologiche Publication number 1356, scale 1 : 1 200 000, 1996.

Guzzetti, F., Cardinali, M., Reichenbach, P., and Carrara, A.: Comparing landslide maps: a case study in the upper Tiber River Basin, Central Italy, Environ. Manage., 25, 247–363, 2000.

Guzzetti, F., Malamud, B. D., Turcotte, D. L., and Reichenbach, P.: Power-law correlations of landslide areas in central Italy, Earth Planet. Sc. Lett., 195, 169–183, 2002.

Guzzetti, F., Reichenbach, P., Cardinali, M., Ardizzone, F., and Galli, M.: The impact of landslides in the Umbria region, central Italy, Nat. Hazards Earth Syst. Sci., 3, 469–486, doi:10.5194/nhess-3-469-2003, 2003.

Guzzetti, F., Reichenbach, P., Cardinali, M., Galli, M., and Ardizzone, F.: Probabilistic landslide hazard assessment at the basin scale, Geomorphology, 72, 272–299, 2005.

Guzzetti, F., Galli, M., Reichenbach, P., Ardizzone, F., and Cardinali, M.: Landslide hazard assessment in the Collazzone area, Umbria, Central Italy, Nat. Hazards Earth Syst. Sci., 6, 115–131, doi:10.5194/nhess-6-115-2006, 2006.

Guzzetti, F., Mondini, A. C., Cardinali, M., Fiorucci, F., Santangelo, M., and Chang, K.-T.: Landslide inventory maps: new tools for an old problem, Earth-Science Rev., 112, 42–66, 2012.

Haneberg, W. C., Cole, W. F., and Kasali, G.: High-resolution lidar-based landslide hazard mapping and modeling, UCSF Parnassus Campus, San Francisco, USA, B. Eng. Geol. Environ., 68, 263–276, 2009.

Hanssen, R. F.: Radar interferometry: data interpretation and error analysis, Kluwer, Academic Publishers, Dordrecht, the Netherlands, 308 pp., 2001.

Jorda, M.: Morphogenèse et évolution des paysages des Alpes de Haute-Provence depuis le Tardiglaciaire. Facteurs naturels et facteurs anthropiques, Bull. de l'Association des Géographes Français, 472, 295–304, 1980.

Lopez-Saez, J., Corona, C., Stöffel, M., Astrade, L., Berger, F., and Malet, J.-P.: Dendrogeomorphic reconstruction of past landslide reactivation with seasonal precision: the Bois Noir landslide, southeast French Alps, Landslides, 9, 189–203, 2011.

Lopez-Saez, J., Corona, C., Stöffel, M., Schoeneich, P., and Berger, F.: Probability maps of landslide reactivation derived from tree-ring records: Pra Bellon landslide, Southern French Alps, Geomorphology, 138, 189–202, 2012.

Lopez-Saez, J., Corona, C., Stöffel, M., and Berger, F.: High-resolution fingerprints of past landsliding and spatially explicit, probabilistic assessment of future reactivations: Aiguettes landslide, southeastern French Alps, Tectonophysics, 602, 355–369, 2013.

Lu, P., Casagli, N., Catani, F., and Tofani, V.: Persistent Scatterers Interferometry Hotspot and Cluster Analysis (PSI-HCA) for detection of extremely slow-moving landslides, Int. J. Remote Sens., 33, 466–489, 2012.

Malamud, B. D., Turcotte, D. L., Guzzetti, F., and Reichenbach, P.: Landslide inventories and their statistical properties, Earth Surf. Processes, 29, 687–711, 2004.

Malet, J.-P.: Les "glissements de type écoulement" dans les marnes noires des Alpes du Sud. Morphologie, fonctionnement et modélisation hydro-mécanique, PhD Thesis, University Louis Pasteur, Strasbourg, France, 2003.

Malet, J.-P., van Asch, T. W. J., van Beek, R., and Maquaire, O.: Forecasting the behaviour of complex landslides with a spatially distributed hydrological model, Nat. Hazards Earth Syst. Sci., 5, 71–85, doi:10.5194/nhess-5-71-2005, 2005a.

Malet, J.-P., Laigle, D., Remaître, A., and Maquaire, O.: Triggering conditions and mobility of debris flows associated to complex earthflows, Geomorphology, 66, 215–235, 2005b.

Marchesini, I., Santangelo, M., Fiorucci, F., Cardinali, M., Rossi, M., and Guzzetti, F.: A GIS method for obtaining geologic bedding attitude, in: Landslide Science and Practice, edited by: Margottini, C., Canuti, P., and Sassa, K., Springer, Berlin, Heidelberg, Germany, 243–247, 2013.

Martha, T. R., Kerle, N., Jetten, V., van Westen, C. J., and Kumar, K. V.: Characterising spectral, spatial and morphometric properties of landslides for semi-automatic detection using object-oriented methods, Geomorphology, 116, 24–36, 2010.

Maquaire, O., Malet, J.-P., Remaître, A., Locat, J., Klotz, S., and Guillon, J.: Instability conditions of marly hillslopes: towards landsliding or gullying? The case of the Barcelonnette Basin, South East France, Eng. Geol., 70, 109–130, 2003.

McCalpin, J.: Preliminary age classification of landslides for inventory mapping, Proc. Annu. Symp. Eng. Geol. Soil Eng., 21, 99–111, 1984.

Metternicht, G., Hurni, L., and Gogu, R.: Remote sensing of landslides: an analysis of the potential contribution to geo-spatial systems for hazard assessment in mountainous environments, Remote Sens. Environ., 98, 284–303, 2005.

Razak, K. A., Straatsma, M. W., van Westen, C. J., Malet, J.-P., and de Jong, S. M.: Airborne laser scanning of forested landslides characterization: terrain model quality and visualization, Geomorphology, 126, 186–200, 2011.

Razak, K. A., Santangelo, M., van Westen, C. J., Straatsma, M. W., and de Jong, S. M.: Generating an optimal DTM from airborne laser scanning data for landslide mapping in a tropical forest environment, Geomorphology, 190, 112–125, 2013.

Reichenbach, P., Guzzetti, F., and Cardinali, M.: Map of sites historically affected by landslides and floods in Italy, 2nd edition, CNR GNDCI publication n. 1786, Rome, Italy, scale 1 : 1 200 000, 1998.

Remaître, A., Malet, J., Maquaire, O., Ancey, C., and Locat, J.: Flow behaviour and runout modelling of a complex debris flow in a clay-shale basin, Earth Sci. Rev., 30, 479–488, 2005.

Rosen, P. A., Hensley, S., Peltzer, G., and Simons, M.: Updated repeat orbit interferometry package released, Eos, Trans. Am. Geophys. Union, 85, 47–47, 2004.

Rossi, M., Ardizzone, F., Cardinali, M., Fiorucci, F., Marchesini, I., Mondini, A. C., Santangelo, M., Ghosh, S., Riguer, D. E. L., Lahousse, T., Chang, K. T., and Guzzetti, F.: A tool for the estimation of the distribution of landslide area in R, Geophys. Res. Abstr., 14, EGU2012–9438–1, 2012.

Salomé, A. I. and Beukenkamp, P.: Geomorphological mapping of a high-mountain area in black and white, Z. Geomorphol., 33, 19–23, 1989.

Salvati, P., Guzzetti, F., Reichenbach, P., Cardinali, M., and Stark, C. P.: Map of landslides and floods with human consequences in Italy. CNR GNDCI publication n. 2822, Rome, Italy, scale 1 : 1 200 000, 2003.

Santangelo, M., Marchesini, I., Bucci, F., Cardinali, M., Fiorucci, F., and Guzzetti, F.: An approach to reduce mapping errors in the production of landslide inventory maps, Nat. Hazards Earth Syst. Sci., 15, 2111–2126, doi:10.5194/nhess-15-2111-2015, 2015.

Schlögel, R., Torgoev, I., De Marneffe, C., and Havenith, H.-B.: Evidence of a changing size-frequency distribution of landslides in the Kyrgyz Tien Shan, Central Asia, Earth Surf. Processes, 36, 1658–1669, 2011.

Schlögel, R., Doubre, C., Malet, J.-P., and Masson, F.: Landslide deformation monitoring with ALOS/PALSAR imagery: a D-InSAR geomorphological interpretation method, Geomorphology, 231, 314–330, 2015.

Shannon, C. E.: Communication in the presence of noise, P. I.R.E., 37, 10–21, 1949.

Singhroy, V. and Molch, K.: Characterizing and monitoring rockslides from SAR techniques, Adv. Space. Res., 33, 290–295, 2004.

Stark, C. P. and Hovius, N.: The characterization of landslide size distributions, Geophys. Res. Lett., 28, 1091–1094, 2001.

Stien, D.: Glissements de terrains et enjeux dans la vallée de l'Ubaye et le pays de Seyne. Rapport ONF-RTM, Division de Barcelonnette, France, 2001.

Thiery, Y.: Susceptibilité du Bassin de Barcelonnette (Alpes du sud, France) aux mouvements de versant?: cartographie morphodynamique, analyse spatiale et modélisation probabiliste, Thèse de Doctorat, Université de Caen Basse-Normandie, France, 2007.

Thiery, Y., Malet, J.-P., Sterlacchini, S., Puissant, A., and Maquaire, O.: Landslide susceptibility assessment by bivariate methods at large scales: application to a complex mountainous environment, Geomorphology, 92, 38–59, 2007.

Thiery, Y., Maquaire, O., and Fressard, M.: Application of expert rules in indirect approaches for landslide susceptibility assessment, Landslides, 11, 411–424, 2014.

Travelletti, J., Malet, J.-P., and Delacourt, C.: Image-based correlation of Laser Scanning point cloud time series for landslide monitoring, Int. J. Appl. Earth Obs., 32, 1–18, 2014.

van den Eeckhaut, M., Poesen, J., Verstraeten, G., Vanacker, V., Moeyersons, J., Nyssen, J., and van Beek, L. P. H.: The effectiveness of hillshade maps and expert knowledge in mapping old deep-seated landslides, Geomorphology, 67, 351–363, 2005.

van den Eeckhaut, M., Poesen, J., Govers, G., Verstraeten, G., and Demoulin, A.: Characteristics of the size distribution of recent and historical landslides in a populated hilly region, Earth Planet. Sc. Lett., 256, 588–603, 2007.

van den Eeckhaut, M., Hervás, J., Jaedicke, C., Malet, J.-P., Montanarella, L., and Nadim, F.: Statistical modelling of Europe-wide landslide susceptibility using limited landslide inventory data, Landslides, 9, 357–369, 2012.

Varnes, D. J.: Slope movement types and processes, in: Special Report 176: Landslides: Analysis and Control, edited by: Schuster, R. L. and Krizek, R. J., 11–33, Transportation and Road Research Board, National Academy of Science, Washington, D.C., USA, 1978.

Wills, C. J. and McCrink, T. P.: Comparing landslide inventories: the map depends on the method, Environ. Eng. Geosci., 8, 279–293, 2002.

Wolfe, M. D. and Williams, J. W.: Rates of landsliding as impacted by timber management activities in Northwestern California, Discussion Bull. Of Assoc. Eng. Geol., 24, 429–431, 1987.

Wright, R. H., Campbell, R. H. and Nilsen, T. H.: Preparation and use of isopleth maps of landslide deposits, Geology, 483–486, 1974.

ZERMOS: Carte des Zones Exposées à des Risques liés aux MOuvements du Sol et du sous-sol, Barcelonnette, 1/25 000, 1975.

Zhao, C., Lu, Z., Zhang, Q. and de la Fuente, J.: Large-area landslide detection and monitoring with ALOS / PALSAR imagery data over Northern California and Southern Oregon, USA, Remote Sens. Environ., 124, 348–359, 2012.

3.4. Synthesis of the research findings on the interpretation of the multi-date inventory at different scales

3.4.1. Results of landslides mapping and kinematics analysis with DInSAR at slope scale

Section 3.2. presents interesting information about the real deformation field, the particular kinematic and the velocity of some landslide types. This study proves that the methodology is applicable to analyse complex and active landslides. Deformation maps created by DInSAR allow us to detect specific sliding compartments of the landslides as well as deep structures that play a role in the destabilization of the slopes. Both wrapped and unwrapped interferograms are able to detect ground deformation and particular structures. Landslide velocity is also estimated according to an *a priori* knowledge of the field to guide the unwrapping processing.

These results constitute relevant information about landslide activity and intensity for the period 2007-2010. This sub-inventory of active landslides gives precious information about intensity (velocity) to be included in the regional multi-date inventory.

3.4.2. Results of landslides mapping by multi-source data at regional scale

Section 3.3. provides a complete multi-date inventory prepared by visual analysis of multi-source data. By a simple comparison of datasets, it reveals the new and active landslides for different periods between 1956 and 2009. General statistics and attribute parameters on mobility were calculated in order to characterized the phenomena. The evolution of landslide activity in the Ubaye valley is evaluated and compared to archives constituted by other techniques of analysis (i.e. landslide event catalogue, dendrochronology). Frequency-area density functions show distinct distributions according to the location of the landslides in different geological layers, in the northern or southern zones and considering the different inventories (function of the activity degree). The recurrence of the phenomena has also been estimated for different return periods on the basis of active areas over the 53-years.

The comparison of the events recorded between 1956 and 2009 with the historical database (1850-2012) shows incompleteness of the available archive. Indeed, our visual analysis of the reactivated or new landslides allows detecting more (re)activations than the historical catalogue. This indication proves that, even if tedious and time-consuming, the visual interpretation of remote sensing data is still mandatory for a landslide hazard assessment. Particular meteorological events could have been correlated to periods of high landslide activity. Exceedance probability analysis shows that over a return period of 50 years, there is more than 60% chance to have a new landslide event on all the territory already unstable. This statistical observation based on the visual analysis demonstrates again that the Ubaye valley is high frequency landslide-prone.

3.4.3. Limitations and conclusions

Limitations of the methodologies applied in this chapter depend on the working scale. DInSAR technique for landslide investigation has limitations due to several factors inducing high decorrelation of the signal, such as:

- The high velocity rates of sliding slopes (e.g. ablation zone of La Valette landslide);
- The combination of SAR and field properties, inducing deformation of the signal (layover) according to the orientation and angle of some slopes (see Fig. 3-3a);
- The presence of dense vegetation (even with L-band sensor);
- The changing climatic conditions (e.g. presence of snow, intense rainfall);
- The temporal baseline which cannot overpass 46 days for quantitative kinematic analyses;
- The perpendicular baseline between some acquisitions (Fig. 3-3a) that we prefer below 1200 m.

In addition, InSAR allows us to detect only active landslides. Therefore, it cannot be used to create landslide event inventories. In this study, InSAR signals corresponding to active portion of landslides are remapped at higher resolution (i.e. 1:3,000) according to the geomorphology of the terrain. These new polygons, which reflect active landslides, are introduced in the 2009 geomorphological inventory. Unfortunately, due to SAR geometrical properties (layover, hidden slopes), they do not constitute a full inventory of active movements of the region for one period.

After these activity, intensity and temporal occurrence analyses, the spatial occurrence has to be evaluated at regional scale. In Chapter 4, different mapping units of analysis were delineated on the basis of different DTMs. Then, landslide susceptibility models were computed according to the mapping units in order to assess the relative landslide hazard for the Ubaye valley. Calculated at a grid-cell base in this chapter, the temporal exceedance probability can also be computed according to the terrain units. Then, landslide intensity is calculated on the basis of the landslides with a size evolution as measured in the attribute table of the multi-date inventory. Three components of hazard are therefore analysed at local scale and compared to the observed landslides.

CHAPTER 4: Susceptibility zonation and quantitative hazard forecast

The objectives of this chapter are (1) to evaluate the effect of terrain unit delineation using different DTMs resolution, (2) to analyse the effects of terrain units on landslide susceptibility zonation and (3) to discuss the landslide hazard at local scale. The chapter is divided into six sections.

Section 4.1 focuses on the effects of DTMs resolution on the delineation of terrain units. It presents the different elevation products available and the methodology of terrain partitioning. Two different units of analysis are considered for hazard assessment: (i) a terrain unit delineation with size constrains still representative of the landscape and (ii) a slope unit delineation created by considering drainage lines and slope aspect.

In section 4.2, the susceptibility models, applied to the different mapping units (§ 4.1.2), are computed using logistic regression.

In section 4.3, temporal exceedance probabilities are computed for the mapping units (§ 4.1.2) exploiting a Poisson law. It evaluates the probability of landslide failures (from the multi-date inventory presented in § 3.3) for different return periods.

In Section 4.4, we present a methodology to evaluate landslide intensity at regional scale. Landslide mobility is calculated, and temporal probabilities higher than a landslide size threshold are estimated for different return periods.

Landslide hazard is analysed at local scale on the basis of four hotspots in section 4.5. Landslide occurrence probabilities are examined and discussed for Riou-Bourdoux, Super-Sauze, Poche and Sanières catchments (i.e. see description in § 2.3.4).

Finally, the section 4.6 discusses the hazard assessment and possibilities of improvement.

This chapter presents preliminary results of a collaborative work carried out with the CNR-IRPI (Perugia, Italy) that will be submitted for publication in the next months.

4.1. Selection of mapping units

This first section is dedicated to the partitioning of the landscape into terrain units, representing slope facets, or individual landforms, mapped as individual polygons. First, the different DTMs products and their comparison in terms of metadata, spatial resolution and elevation difference are presented. Second, the method of terrain unit delineation considering a size constrain is explained and applied to the three DTMs. A comparison of the results is completed and finally, the choice of the most relevant mapping unit delineation for susceptibility zonation is discussed.

4.1.1. Effect of DTM resolution on terrain unit delineation

The study area is covered by Digital Terrain Models (DTMs) created at different scales and different periods, by several data producers with distinct methodologies and technologies. This section aimed to apprehend the effect of the elevation data source on the mapping units delineation, which is function of the resolution and the accuracy of the topographic surface model.

4.1.1.1. Description of the DTMs metadata

Three Digital Terrain Models of different spatial resolutions have been used: a 5-m airborne DTM (IfSAR[1]), a 10-m DTM (Airborne Laser Scanning and 5-m DSM contour interpolation) and a 25-m DTM from BD Alti® IGN[2]. The methodology used to generate each elevation model by the producer is described thereafter.

A. 5-m airborne DTM

Airborne Interferometric Synthetic Aperture Radar (IfSAR) data provides digital terrain and surface models using airborne radar antennas with a better spatial resolution than spaceborne sensors. Vegetation, buildings and man-made features were removed from the raw data. The IFSAR Type II offers a 5-m spatial resolution with a vertical RMSE of 1 m. The study area was covered with this mean in 2009 by Intermap.

B. 10-m DTM (interpolation of IGN contours integrated in the 5-m DSM)

A hybrid Digital Terrain Model was created at 10-m resolution from multiple sources including contours lines from IGN 1:25,000 maps, enlarged at 1:10,000 scale by IGN (created through photogrammetric methods and elevation points from geodetic triangulation network, as the 25-m DTM described below) that were scanned and georeferenced and the 5-m airborne IfSAR DTM described hereinabove. The digitisation of supplementary contour lines was made at 1:5,000 scale in flat areas and at 1:2,000 or even 1:1,000 in mountainous regions with an equidistance of 10 m, in order to guide the further interpolation in complex areas. Contour lines were even added in some cases according to photointerpretation and expert knowledge to obtain the best representation of the topographic surface (Thiery, 2007). Both data sets were combined using Best-Fit alignment in Polyworks software, with ordinary kriging interpolation method with semi-variogram (Krige, 1966; Baillargeon, 2005), that has shown the best results in terms of accuracy (Thiery, 2007). As the technique was not applied to the whole area, we decided to keep the IfSAR data in the south-eastern part of the study area.

C. 25-m DTM from BD Alti® IGN

BD ALTI is an elevation reference description of the French territory obtained by IGN from contour vector files and photogrammetric points derived from stereo pairs of aerial photographs (1:20,000 to 1:60,000). ASCII grids covering the entire study area are delivered in Lambert-93 projection using the RGF93 geoid. The reprojection to NTF_Lambert_zone_III was performed in Global Mapper, preserving the original 25-m grid.

4.1.1.2. Comparison of the DTMs

Looking at the distribution of histograms, the 5-m DTM appears smoothed comparing to the other between 1400 and 2000 m (Fig. 4-1). It seems that 5-m DTM has more values around 1200 m than the other two products.

[1] http://gis.icao.int/icaoetod/INTERMAP_IFSAR_Data_Collection_English.pdf

[2] http://professionnels.ign.fr/bdalti

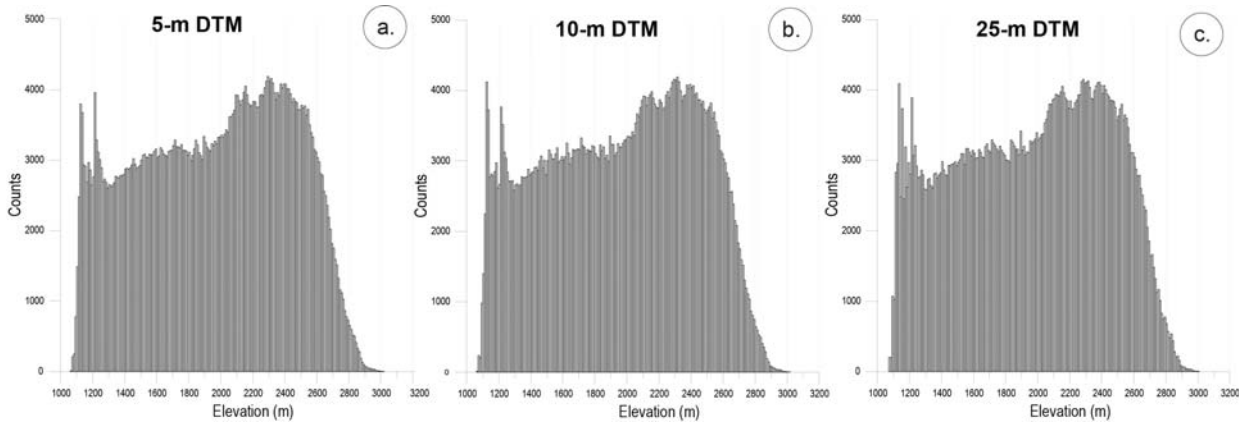

Figure 4-1: Histograms of elevation per elevation class for the DTMs at 5-m (a), 10-m (b) and 25-m (c) resolution

Absolute uncertainty was verified on the basis of 24 planimetric and altimetric Ground Control Points (GCPs) from the IGN database[3] (Table 4-1). Accuracies of those field measurements are 0.1 m in XY-direction, 0.5 m in Z-direction for planimetric GCPs and 2.0 m in XY-direction, 0.001 m in Z-direction for altimetric GCPs. In Table 4-1, results show a standard deviation of absolute accuracy lower for the 25-m DTM. In addition, the absolution accuracy is of less than 3 m when slope is below 10° but an absolute accuracy for the 5-m DTM at slopes between 10-20° (i.e. 15.1 m) and more higher for the 10-m DTM at slopes below 20° (i.e. 20.5 m).

Table 4-1: Absolute uncertainty calculated on the basis of IGN planimetric and altimetric GCPs.

Absolute uncertainty	5-m DTM	10-m DTM	25-m DTM
Standard deviation (m)	14.2	14.8	11.6
Maximum (m)	28.4	28	33.1
Minimum (m)	-26.3	-28.3	-13.4
Difference for slope 0-10°	2.4	2.7	10.4
Difference for slope 10-20°	15.1	12.8	9.8
Difference for slope >20°	16.9	20.6	11.5

Figure 4-2 represents the subtractions between the different DTMs and locates the high elevation differences between them. Statistics of the relative difference between the DTMs on the whole Ubaye valley are presented in Table 4-2. It shows a standard deviation clearly lower between the 5-m and 10-m DTMs (i.e. 6.7 m) while the lower mean difference (i.e. 0.2 m) is estimated between the 10-m and the 25-m meaning that the 10-m is closer to the 25-m one having a higher absolute uncertainty.

[3] http://geodesie.ign.fr/fiches/index.php?module=e&action=visugeod

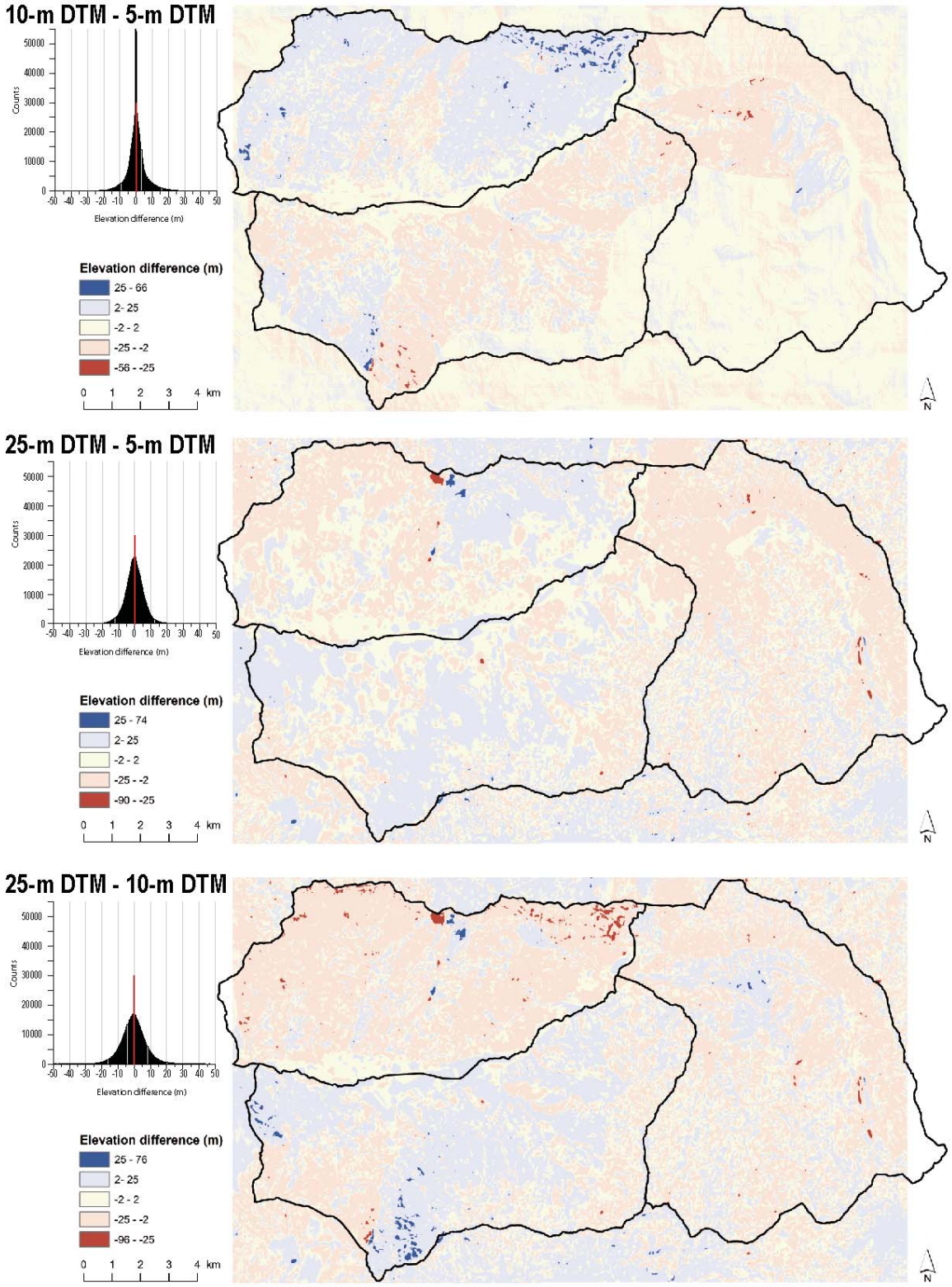

Figure 4-2: Relative comparison of the DTMs. Values are extracted each 25 m. Histograms represent the distribution of their values and maps show where highest discordances are observed.

Table 4-2. Relative difference of DTMs based on the extraction of elevation values each 25 m along all the area (i.e. 541,365 counts in total).

DTM comparison statistics	10-m DTM –5-m DTM	25-m DTM – 5-m DTM	25-m DTM -10-m DTM
Standard deviation (m)	4.8	10	10.7
Maximum (m)	14.5	13.9	11.8
Minimum (m)	-9.7	-22.4	-30.8
Mean (m)	0.5	0.7	0.2
Difference for slope: 0-10°	3	9.9	8.9
Difference for slope 10-20°	5.9	7.9	9.1
For slope: >20 (°)	5.8	12.2	14.4

4.1.1.3. Partitioning of the landscape and delineation of mapping units

Different mapping units can be used to partition the landscape for landslide hazard assessment (see § 1.3.2). Slope-units are homogeneous portions of the landforms (e.g. slope-facets), they are delineated according to common slope aspect and hydrological properties of the half-catchments. For this study, we have decided to develop a tool to apply a size constrain for the delineation in order to satisfy the needs of the local risk managers and stakeholders of the valley. This section describes the procedure to partition the landscape according to terrain units (TUs) derived from slope-units (SLUs) while the next section compare its application to different DTMs.

The first step before partitioning the landscape into mapping units (e.g. TUs) is the preparation of the DTMs. Flood plains with slope angles <5° have been mapped according to the interpretation of the orthophotographs and removed from the DTMs in order to avoid wrong delineation where slope angle variability is low.

The second step is the choice of the appropriate delineation method to partition the landscape. By definition, the size of a slope unit depends on the morphological and hydrological properties of the terrain. In this study, the purpose is to custom a partitioning method based on watershed in order to subdivide the territory in small homogeneous terrain units. We have used the method proposed by Alvioli et al. (2014) and then develop a tool to constrain the mapping units in the area range $50{,}000 \leq A \leq 80{,}000$ m^2. This choice was made to be consistent with scale of the risk regulation documents (e.g. 1:10,000 to 1:25,000 scale) in France (MATE/METL, 1999) and because 90% of the landslide sizes observed in the study area are lower than 80,000 m^2.

We used a hydrologic partition model (r.watershed module of GRASS GIS; Ehlschlaeger, 1989) whose main controlling parameter is an accumulation area that defines a threshold for the minimum size of the output half-basins according to the method developed by Alvioli et al. (2014). The tool has been run with different threshold values (i.e. 5,000, 10,000, 20,000 and 40,000 m^2). Among the results, an accumulation area of 20000 m^2 was chosen in order to avoid small areas created by artefacts of the DTMs on gentle slopes. Then, by an iterative processing, the TUs is either reduced (by slitting the large units) or merged to others in order to fit to the size constrain ($50{,}000 \leq A \leq 80{,}000$ m^2).

4.1.1.4. Comparison of mapping unit delineations according to the DTMs resolution

This section describe the application of a TUs delineation procedure to different DTMs. The results of the method developed by Alvioli et al. (2014) before its combination to an iterative process for constraining the size threshold (as described in § 4.1.1.3) are presented in Figure 4-3. The distributions obtained are different according to the different DTM resolutions. We take the corresponding half-basins as a starting point to build our optimal terrain units set for the 5-m, 10-m and 25-m DTMs (see Fig. 4-3 a, b and c). At this stage of the procedure, we can notice that the frequency distributions of half-

basins are similar for the 5-m and 10-m DTMs with a lot of small units; they are more scattered for the 25-m DTM. Indeed, coarser the resolution, lower the number of half-basins and small ones in particular.

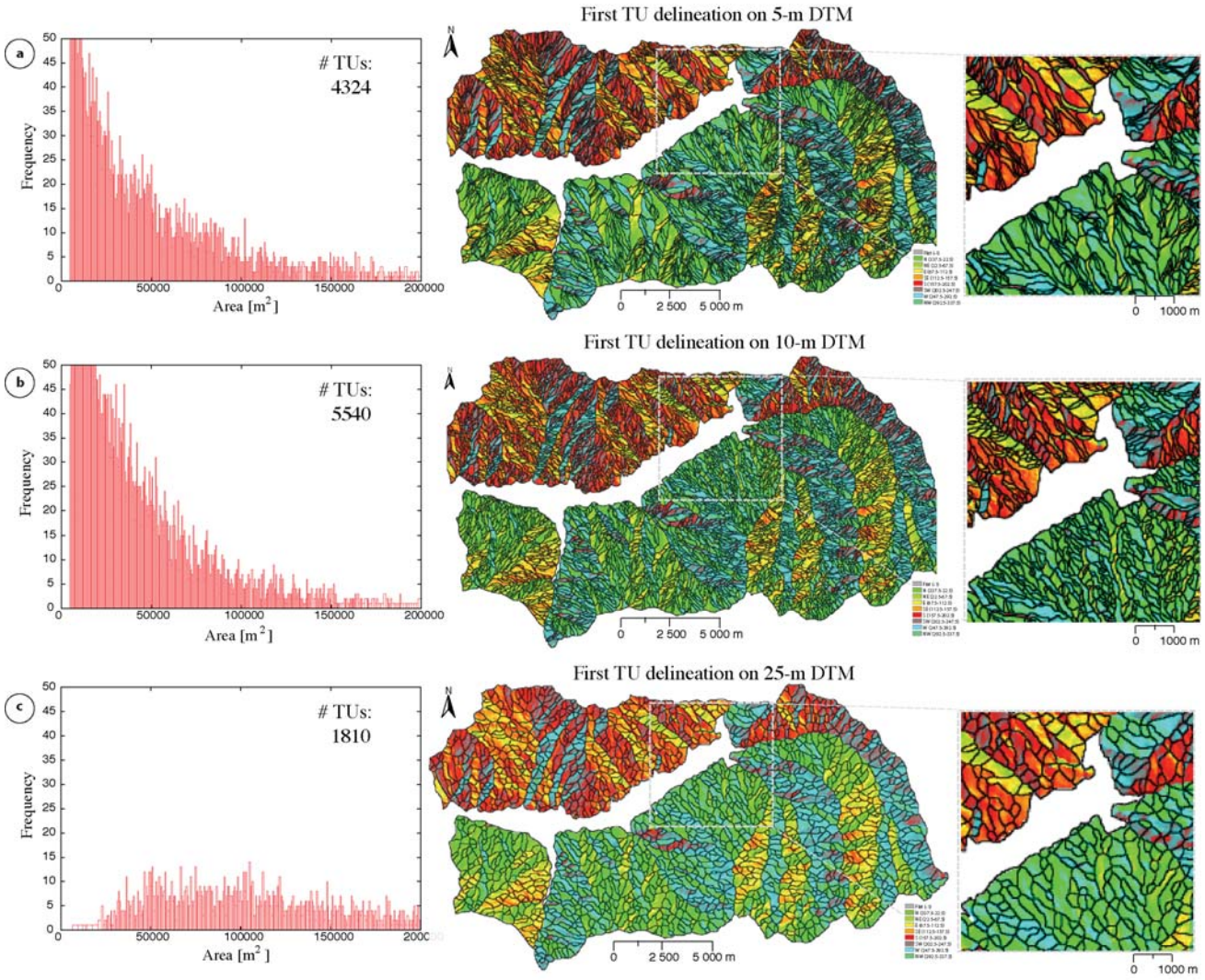

Figure 4-3: Comparison of TU delineation for three DTMs according to the procedure proposed by Alvioli et al. (2014). (a) Distribution of TU frequency vs. area, map of TUs and zoom on TU delineation for the 5-m DTM. (b) Distribution of TU frequency vs. area, map of TUs and zoom on TU delineation for the 10-m DTM. (c) Distribution of TU frequency vs. area, map of TUs and zoom on TU delineation for the 25-m DTM.

Then, the distribution of the areas was narrowed to the defined size threshold ($50{,}000 \leq A \leq 80{,}000$ m^2) by an iterative way: (1) by removing areas smaller than 20,000 m^2, (2) by partitioning areas larger than 80,000 m^2. The procedure is repeated until getting a satisfactory distribution (i.e. high TU frequency into the threshold). The removal of very small areas ($A \leq 20{,}000$ m^2) is performed using a tool designed to work respecting to an aspect constraint and the surrounded TUs. The aspect constraint consists in merging a small area with a larger one only if their average aspect is similar. In addition, TUs are merged if they share a boundary whose length is at least 30% of the perimeter of the smaller area. These values were decided heuristically. At each run of the small area removal procedure, we can specify an area threshold to choose small half-basins from the whole set, and operate only on those ones. The partition of large areas ($A \geq 80{,}000$ m^2) is performed by running the hydrologic model (i.e. the r.watershed module) with a threshold accumulation area smaller than the starting one, only on those TUs whose size is larger than the specified value. At each step of the procedure, we plot the distribution of the areas, and decide the parameters for the next iteration. The plots corresponding to the 12th iteration step of the procedure are shown in Fig. 4-4.

Even if the results are satisfying for the first two DTMs (Fig. 4-4 a and b), the tool does not always find the suitable neighbouring polygon to remove the small TUs. Therefore, not all the areas are removed below the required threshold. The solution could be (1) to remove small areas at once, and (2) to merge them with the neighbouring polygon if its longer boundary is shared with the small area. In addition, the hydrologic model cannot generate suitable half-basin when partitioning the large areas. For instance, decreasing the threshold generates very small half-basins, which have to be rejected because they would fall below the lower area requirement. Finally, the result of TU partitioning can contain small mistakes due to the random merging of very small areas in regions where the aspect variability is not enough to define a clear cut which is meaningful for the merging. In addition, a few large areas have not been split mainly due to the homogeneity in terms of aspect angle.

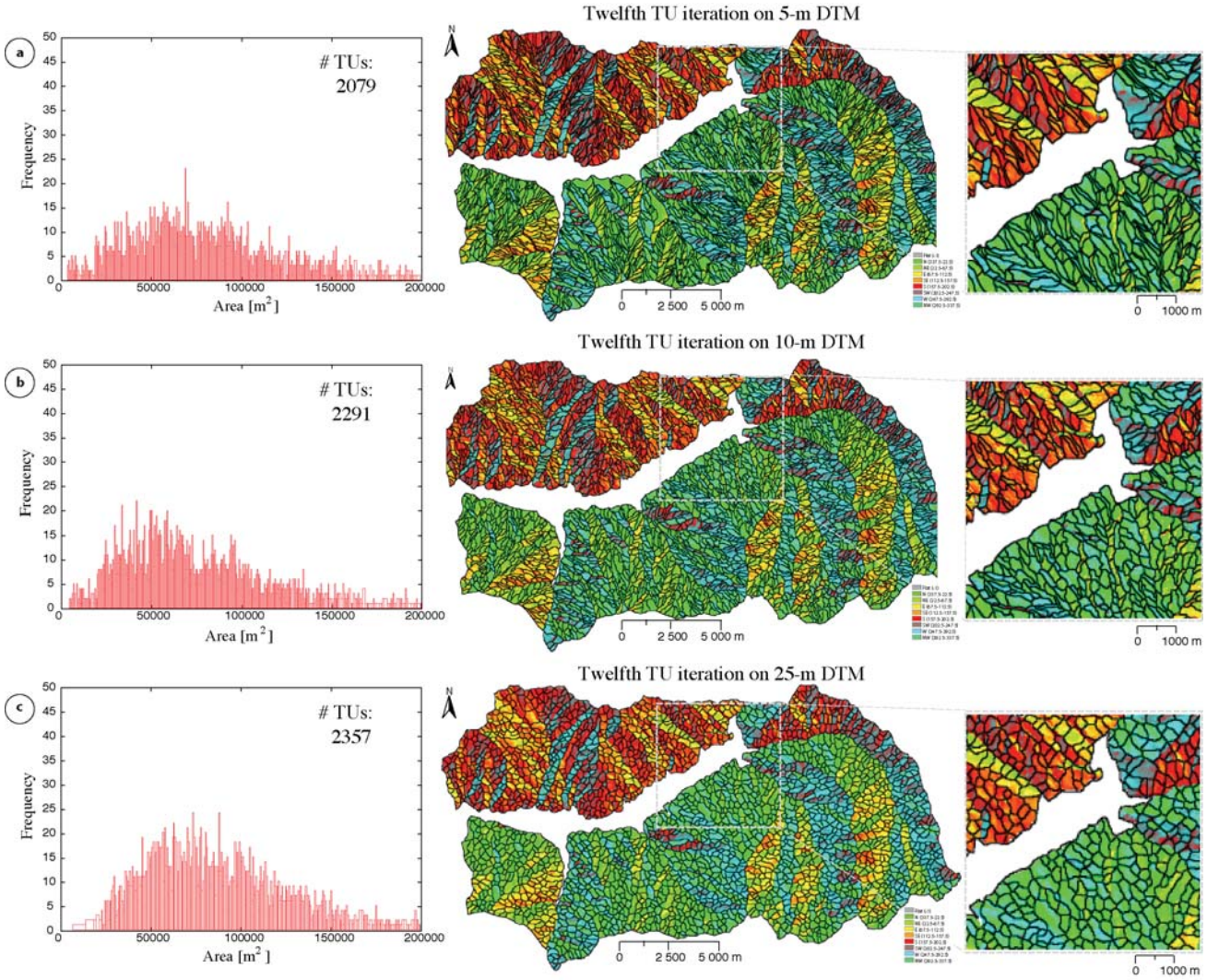

Figure 4-4: Comparison of TU delineation for three DTMs at the 12th iteration. (a) Distribution of TU frequency vs. area, map of TUs and zoom on TU delineation for the 5-m DTM. (b) Distribution of TU frequency vs. area, map of TUs and zoom on TU delineation for the 10-m DTM. (c) Distribution of TU frequency vs. area, map of TUs and zoom on TU delineation for the 25-m DTM.

The final results of the partitioning procedure applied to the three DTMs are presented in Figure 4-5 (a, b and c) and their statistical analysis is depicted in Table 4-2. After 27 iterations, the procedure allowed us to obtain a normal distribution of maximum TU frequency around 50,000-80,000 m², following 2,720, 2,968 and 2,796 TUs for 5-m, 10-m and 25-m DTM, respectively. We are also able to say that 36.7%, 36.9% and 34.4% of the TUs for 5-m, 10-m and 25-m DTM, respectively have a size in this threshold. In addition, the evolution of TUs counts according to the iteration steps (see Fig. 4-5d) shows us that the processing tends to the stabilization of TU numbers starting from the 22nd iteration.

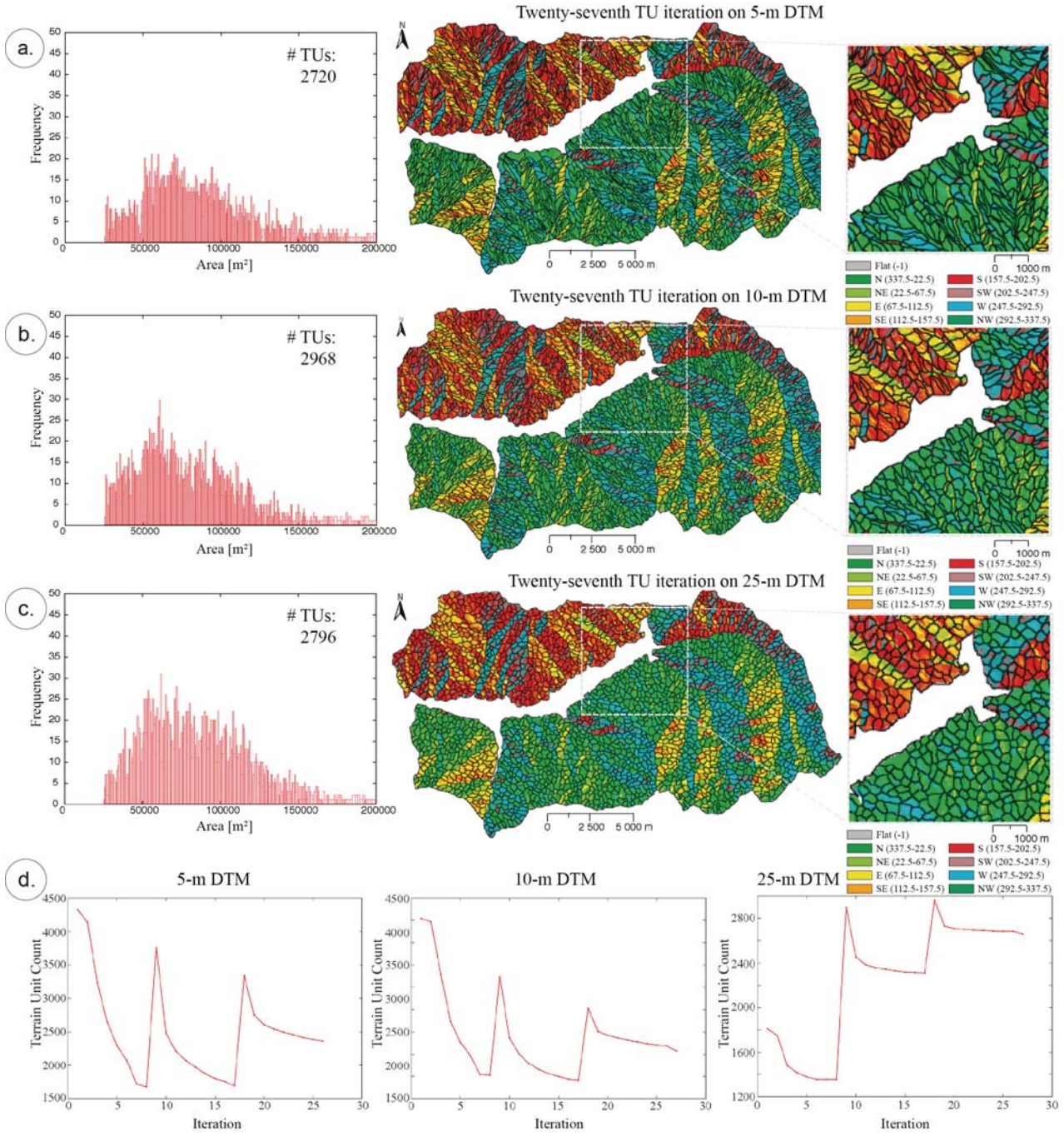

Figure 4-5: Comparison of TU delineation for three DTMs at the 27th iteration. (a) Distribution of TU frequency vs. area, map of TUs and zoom on TU delineation for the 5-m DTM. (b) Distribution of TU frequency vs. area, map of TUs and zoom on TU delineation for the 10-m DTM. (c) Distribution of TU frequency vs. area, map of TUs and zoom on TU delineation for the 25-m DTM. (d) Evolution of TU counts in function of the number of iteration.

On Figure 4-5, we see that the 5-m DTM gives more elongated TUs and sometimes very large ones (frequency distribution shifted to the large sizes) while those from 10-m DTM are more circular and the frequency distribution peak is localised into the size threshold. Although for 25-m DTM (Fig. 4-5c), even if the distribution correspond to our objective, the TUs do not represent anymore the terrain reality as they are all rounded and not meaningful from a hydrological point of view. According to the statistical analysis of TUs presented in Table 4-3, the standard deviation of slope angle in the TUs created with the 25-m DTM is lower than for the others (i.e. 5.4 comparing to 7.0 or 7.2 for 5-m and 10-m DTMs, respectively). The mean surface ratio (indicating the ruggedness of the slope) in TUs is lower for the TUs created with 25-m resolution DTM. These observations show that with a coarse DTM resolution, a relevant and sharpened delineation with TUs areas mainly lower than 100,000 m² is not possible as

drainage lines and crests are not anymore the predominant morphological features. Moreover, the statistical analysis of TUs parameters proved that DTM-derived properties of them are all smoothed for TUs created with 25-m DTM.

The heuristic analysis of the delineation for the whole area shows us that the 10-m DTM-based delineation is more homogeneous while the 5-m DTM-based can have really sharp changes between detailed or coarse partitioning. In addition to the resolution effect on delineation, it seems that TUs shape and size also depend on the quality variability of the DTMs (described in § 4.1.1.3). According to our knowledge of the metadata, we can say that the TU delineation from the 10-m seems is better considering the DTMs properties in term of quality and accuracy in absolute and relative positions.

4.1.2. Mapping units for landslide spatial and temporal occurrence evaluation

4.1.2.1. Terrain Unit (TU) approach

According to the aforementioned section, we have decided to use the TU delineation considering the 10-m DTM which seems to be a good compromise between the needs of the policy makers and in agreement to the topographic properties of the landscape and the landslide size. In addition, the source areas of the landslides cross in a few cases different TUs. As the landslides are really large in this area (i.e. mean size = 31,835 m^2 and maximum size ≤ 1,368,400 m^2; Tab. 4-2), they generally cross several TUs which might influence the results of susceptibility zonation.

In order to integrate landslide (or source area) size larger than the TUs (mean size ≈ 80,000 m^2; Tab. 4-3), a delineation based on larger mapping units outlining the hydro-geomorphological properties of the sub-basins is depicted in the next section.

Table 4-3: Statistical analysis for three TUs and one SLU (see § 4.2) delineations as well as for the observed landslides and their source areas.

Objects	Nb	Mean area (m^2)	Std dev. area (m^2)	Min area (m^2)	Max area (m^2)	Mean slope (°)	Std dev. slope (°)	Mean surface ratio
TU with 5-m DEM	2,720	87,238	42,296	25,252	537,637	24.5	7.0	1.133
TU with 10-m DEM	2,968	79,942	36,395	25,036	319,803	25.0	7.2	1.140
TU with 25-m DEM	2,796	85,902	36,452	23,264	341,883	23.5	5.4	1.120
SLU with 10-m DEM	952	249,269	203,876	50,271	1,781,051	24.5	8.1	1.136
Landslide bodies	662	31,835	88,935	97	1,368,391	24.9	4.1	1.129
Source areas	662	6,525	17,032	43	206,464	25.5	2.4	1.134

4.1.2.2. Slope Unit (SU) approach

Considered that the small size of mapping units might influence the performance of the susceptibility model, another automatic delineation of mapping units was tested. The Web Processing Service for SLU delineation (Alvioli et al., 2014) allowed us to incrementally achieve a satisfactory definition of slope units (see § 1.3.2) on the basis of the 10-m DTM. Additional data are required in order to specify parameters constraining the size and aspect of slope units. The calculation is performed using a parallel algorithm, resulting in a processing time short enough to allow the user to tune the input parameters, repeating the process for a sufficient number of times in order to obtain a satisfactory result. The algorithm starts from a hydrologically-consistent partition of the study area into half-basins with a large number of contributing DTM cells. Each of the half-basins is then checked against the following

requirements: maximum area required by the user and maximum standard deviation of the aspect on two orthogonal directions (Alvioli et al., 2014). The specific half-basins that do not meet the requirements are partitioned further, requiring a lower number of contributing cells. The process is iterated until no half-basin exceeds the user-specified thresholds.

The slope units are defined according to our knowledge of the landscape and in agreement with the properties of the DTM. We chose heuristically the input parameters giving us the results that we consider to fit the best our data of analysis: a minimum area = 75,000 m^2; a circular variance = 0.175; a reduction factor = 100 and a threshold = 200,000 m^2. We noticed that a change in the minimum and threshold sizes may affect a lot the delineation. For example, a lower minimum size gives nonsense results as it subdivide the half-basins into thin and long units because the procedure is mainly based on the hydrologic properties of the terrain.

4.2. Susceptibility zonation with logistic regression

For this study area, a direct landslide susceptibility map has been elaborated with the French legal procedure (PPRN) for landslide hazard and risk at 1:10,000 scale (MATE/METL, 1999; Leroi et al., 2005). In addition, a knowledge-driven approach using bivariate statistics (weights of evidence) has already been applied for a portion of the valley (Thiery et al., 2007). This susceptibility map has been combined to an indirect approach (fuzzy sets) guided by expert rules to identify the best classes with a sensitivity analysis on weights (Thiery et al., 2014). In the framework of this study, we have decided to apply multivariate statistics (i.e. a logistic regression) as the method shows good results for susceptibility mapping (e.g. Cox, 1958; Bernknopf et al., 1988; Wieczorek et al., 1996; Gorsevski et al., 2000; Dai et al., 2001; Lee and Min, 2001; Ohlmacher and Davis, 2003; Lee, 2004; Ayalew et al., 2005; Guzzetti et al., 2005; Rossi et al., 2010). Moreover, it has the advantage of requiring only a few theoretical assumptions.

4.2.1. Data and model

Landslide susceptibility is calculated using a logistic regression (LR) statistical model with the R-script developed by Rossi et al. (2012). Susceptibility zonation was processed at CNR-IRPI (Perugia) during a research stay in late 2014. The results are exploratory, and an improvement is expected in the coming weeks.

4.2.1.1. Dependent variables

Over an area of around 260 km^2, 662 landslides have been mapped. They have several types with a predominant component (e.g. translational, rotational or rock-block-slides; see § 3.3). For the susceptibility zonation, we have decided not to create different susceptibility zonation maps according to the different landslide type. Indeed, the landslide observed all over the valley are mainly complex and deep-seated and a few landslides defined as shallow landslides are observed. The ideal configuration would have be to process different susceptibility zonation maps according to deep-seated translational slides, deep-seated rotational slides and shallow translational slides (Thiery et al., 2007). However, as preliminary study, we wanted to concentrate the investment by understanding the procedure and by choosing the appropriated variables. In addition, the underestimation of the shallow landslidesover the whole area would induce a small proportion of SLUs affected by landslides the training set which is not the best configuration for processing linear regression.

Based on previous experiences in the Collazzone area (F Guzzetti et al., 2006; Galli et al., 2008) and in Umbria (Carrara et al., 1991, 1995, 1999; Guzzetti et al., 1999), SLUs having less than 2% of the area covered by slope failures were considered free of landslides, and SLUs having 2% or more of their area covered by slope failures were considered as containing landslides. For the smaller TUs, a threshold of

one pixel (i.e. 100 m^2) for TUs (Table 4-3) has been considered. Presence or absence of phenomena into the mapping unit is represented by 1 or 0 value, respectively (#2 at Table 4-4). On the contrary, if there is no landslide or less than one pixel or 2%, a 0-value is attributed to the unit.

According to the *stricto sensu* definition, landslide susceptibility refers to the identification of the initiation areas (e.g. source areas) of the landslides. Notwithstanding, approaches considering both the whole landslides or just the source areas are found in the literature. Thus, we decided to calculate susceptibility zonation considering the mapped source areas and the whole landslide bodies. Presence of the dependant variables according to the mapping unit delineation is represented in Figure 4-6. As source areas may be small (e.g. 47 m^2 as minimum), we decided to not use threshold for considering them in the input data file (#2; Table 4-4).

Table 4-4: Comparison of mapping units with considered dependant variables.

	Thresholds		Ratio #/total		Ratio presence/absence	
	TU	SLU ratio	TU ratio	SLU ratio	TU ratio	SLU ratio
Landslide bodies	100 m^2	2%	30%	34%	44%	52%
Source areas	0	0%	23%	41%	30%	68%

The logistic regression analysis is performing well for datasets that are more or less equal in size (Garcia-Ruiz et al., 2003; Nefeslioglu et al., 2008) but there are many studies where the ratio of landslide presence (1) vs. landslide absence (0) is taken as unequal proportions (e.g. Atkinson and Massari, 1998; Guzzetti et al., 1999; Dai and Lee, 2002; Ohlmacher and Davis, 2003; Ayalew and Yamagishi, 2005). Since the susceptibility map produced by a logistic regression technique is directly controlled by this ratio in the mapping units, any increase of mapping units free of landslides tends to decrease the areas susceptible to landslides in the susceptibility map. Contrary to this, the susceptible areas to landslides increase with a decrease in the ratio of absence/presence of landslides (Can et al., 2005). In our case study, the dependant variables (i.e. landslide or source area) are not considered as rare event as 30-34% of the mapping units are affected by landslides or 23-41% by a portion of their defined source areas according to the thresholds (see Table 4-3).

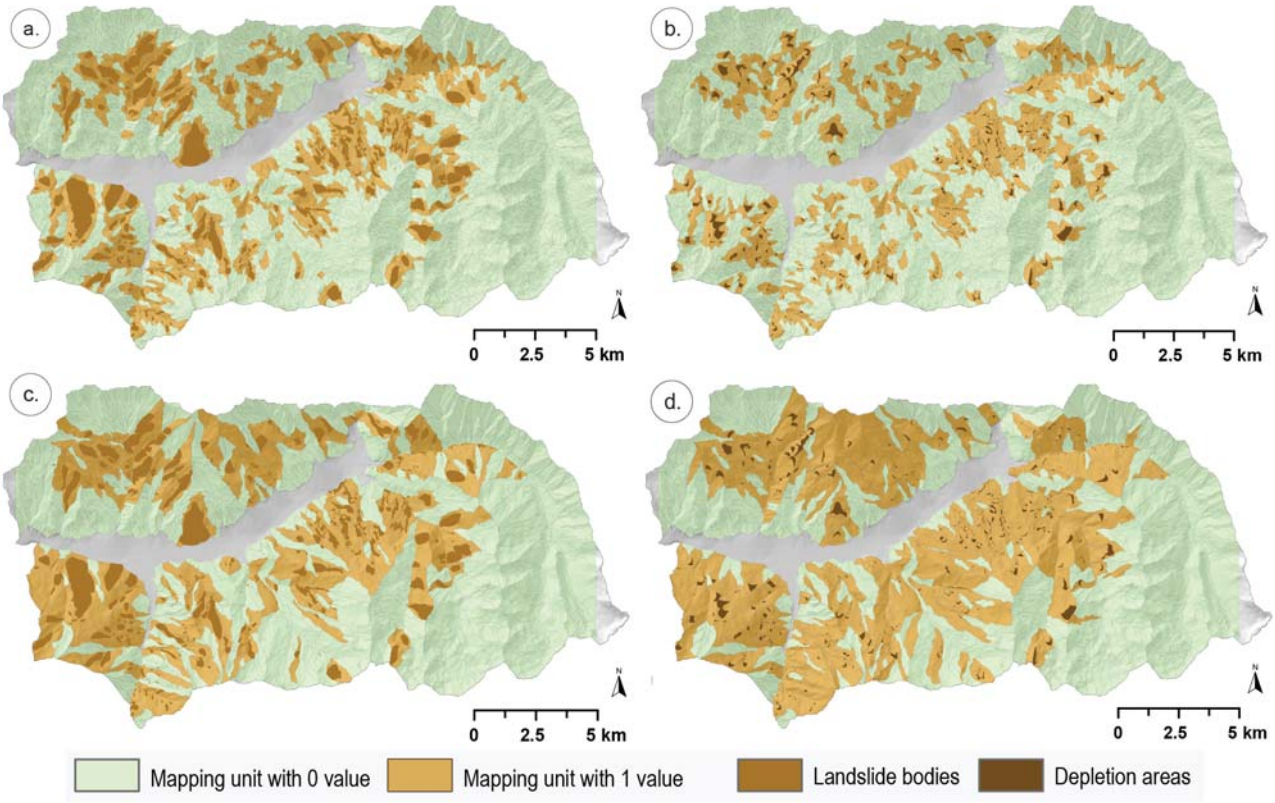

Figure 4-6: Mapping units with and without dependant variable(s). (a) Terrain units with(out) landslide bodies. (b) Terrain units with(out) source areas. (c) Slope units with(out) landslide bodies. (d) Slope units with(out) source areas. Threshold of 100m² and 2% are used for landslide bodies into terrain units and slope units, respectively. All the terrain/slope units are considered for presence of source areas.

4.2.1.2. Explanatory variables

A set of 19 independent (explanatory) variables (Table 4-4) is used for the multivariate terrain classification, including eight morphological, six lithological, four land use variables (see Fig. 4-7), and one variable describing the presence of old, stabilized and partially eroded landslides (relict and dormant landslides in § 3.3). Calculated on the basis of the mapping units, the DTM-derived explanatory variables are continuous values while others are expressed in percentages. The mean and the standard deviation are computed for each terrain or slope units for the following parameters: slope inclination, longitudinal and cross-sectional curvature and elevation (#3-10 in Table 4-4).

A detailed description of the explanatory variables derived from 10-m DTM is presented below:

(i) Slope inclination (Fig. 4-7a) - the slope gradient greatly influences the susceptibility of a slope to landsliding. In general landslide frequency increases with the slope gradient until the maximum frequency is reached around 35–40° classes, followed by a decrease (Lee and Min, 2001; Dai and Lee, 2002). The high frequency of failures with increasing slopes may be attributed to reduce the shear strength in particular lithological layers. In our study, the landslide distribution indicates that landslide frequency increases with the mean slope angle until the maximum is reached in the 20–30° interval, followed by a decrease. About 80% of the landslides are distributed between mean slope inclinations from 15 to 35°. The areas of steep slopes (i.e. close to the vertical) with outcropping bedrock are generally more stable and less susceptible to landslides.

(ii) Elevation (Fig. 4-7b) comes directly from the contour lines drawn each 10-m and interpolated for the DTM creation. The majority of the landslides (i.e. 87.6%) are distributed between ca. 1200-2000 m, with a peak between 1500-2000 m (i.e 42.1%). Landslide

frequency decreases above 2000 m. Due to the geological history, some elevation levels are linked to some particular lithologies (e.g. flysch deposits mainly observed at elevations above 2000 m).

(iii) Longitudinal (or profile) curvature - the curvature of the corresponding normal section, which is tangential to a flow-line. Positive profile curvature indicates convex and negative concave profiles (Fig. 4-7c). Mean values tend to be positive where the landslides are observed. 63.3% of the landslides show positives longitudinal curvature values.

(iv) Plan (or cross-sectional) curvature - the curvature corresponds to the normal section, which is tangential to a contour. Positive plan curvature indicates divergence and negative concentration of flow (Fig. 4-7e). Mean values tend to be negative where the landslides are observed (57.3% of negative mean values) confirming that landslides occur in areas where flows are concentrated by the topographic features.

Table 4-5: Input data inserted for susceptibility zonation

#	Input data	Value/unit
1	Mapping Unit number	Number
2	Landslide or source area variable	0 or 1
3	Mean slope inclination	(°)
4	Standard deviation of slope inclination	(°)
5	Mean longitudinal terrain curvature	1/100 (z units)
6	Standard deviation of longitudinal terrain curvature	1/100 (z units)
7	Mean cross-sectional terrain curvature	1/100 (z units)
8	Standard deviation of cross-sectional terrain curvature	1/100 (z units)
9	Mean terrain elevation	(m)
10	Standard deviation of terrain elevation	(m)
11-16	Areas of particular lithology(ies)	(%)
17-20	Areas of particular land use(s)	(%)
21	Dormant and relict landslides	(%)

The predisposing factors layers were updated to cover the whole area and corrected in terms of accuracy of mapping and coregistration. Lithology initially divided into 11 classes was reclassified into 6 classes (see Fig. 4-7d; #11-16 in Table 4-4), such as: torrential and lacustrine deposits (#11), blocks and screes (#12), weathered marls (#13), moraine deposits (#14), marly-limestone or limestone (#15), gypsum, sandstone and quartzite (#16). The map of land use is divided into 7 classes (see Fig. 4-7f): but only 4 of them are considered in the analysis, i.e. forest (#17), arable land (#18), grassland (#19) and bare rocks (#20) while built area, water surface and alluvial deposits are under-represented (i.e. < 1%) over the whole area.

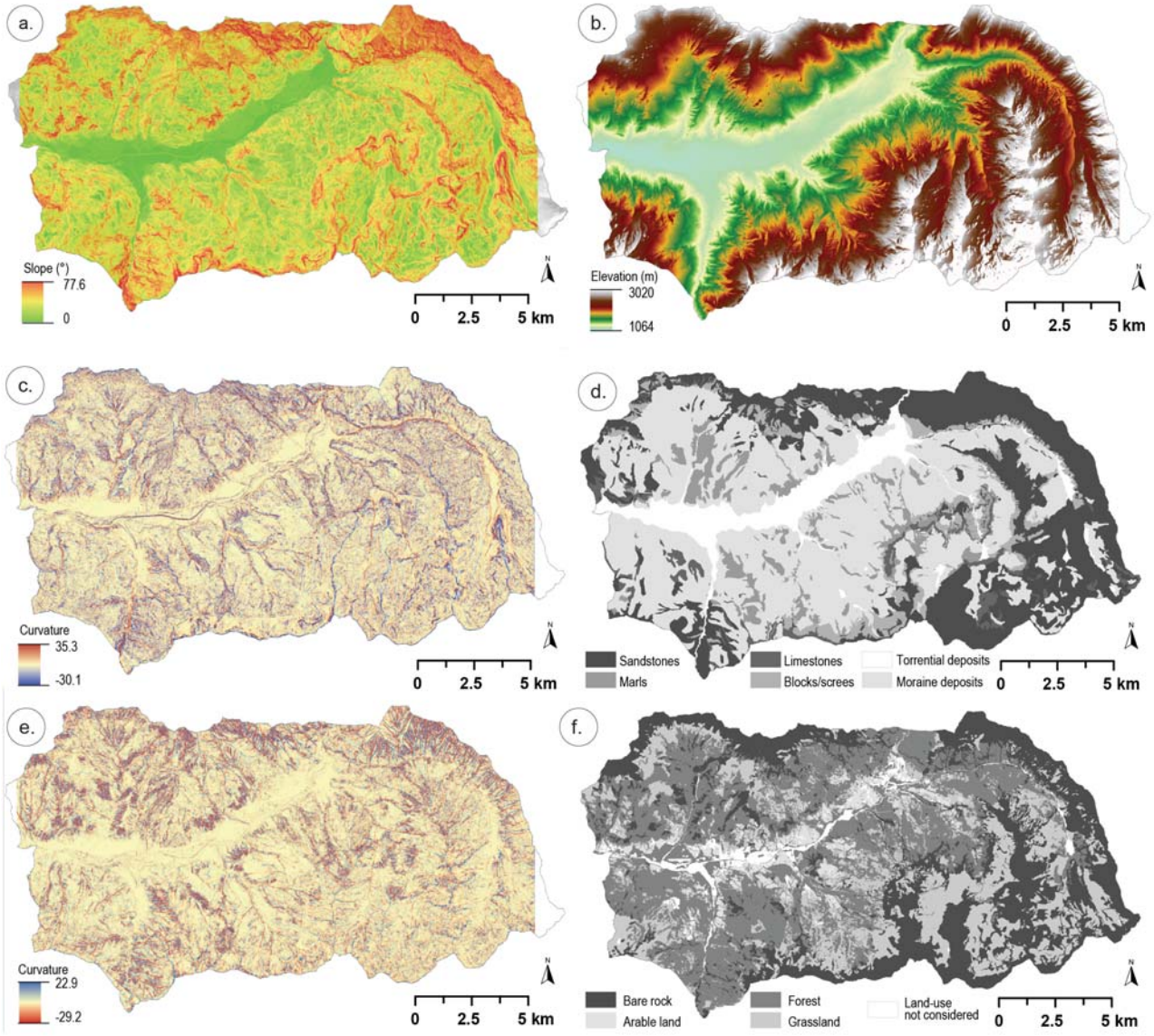

Figure 4-7: Explanatory variables used for susceptibility zonation. (a) Slope angle. (b) Elevation. (c) Longitudinal curvature. (d) Lithological layers. (e) Cross-sectional curvature. (f) Land use layers.

4.2.1.3. Logistic regression model

The aim of logistic regression in landslide susceptibility (LS) is to find the best fitting function to describe the relationship between the presence or absence of landslides (dependent variable) and a set of independent parameters, which are the preparatory factors for landslides. In the LR model, the dependent variable (z) is dichotomous, which is a binary value and it is TRUE if a landslide is present and FALSE if it is absent, and independent variables are either categorical or continuous. The model aims to establish the probability that a mapping unit contains a landslide (z=TRUE) given the set of independent variables (Atkinson and Massari, 1998). The coefficients in the LR model are estimated using the maximum-likelihood method or in other words, the coefficients that make the observed results most 'likely' are selected (Jaiswal et al., 2010). In the R-software, the regression model is fitted using iteratively reweighted least squares method under the link function (link=logit).

In logistic regression, the more independent variables are included, the more complete the model will be, but only when they play a major role in determining the dependent variable (Ayalew et al., 2005). Selecting those independent variables with a major role is a hard task; there are neither universal

criteria nor guidelines. According to the available data for this region, we decided to keep classical parameters (see Table 4-4) to analyse preliminary results and then, open up prospects for their improvement.

Other studies have shown that selecting different training sets, randomly chosen from the landslide free areas, do not have much effect on the performance of the model (Yesilnacar and Topal, 2005; Jaiswal et al., 2010). Preliminary modelling attempts have constrained us to use 100% of the territory to train the model and simplify the interpretation of the results. Further improvements of the input files are required to split the dataset into training and validation sets and allow the validation of the model. Indeed, as several landslides can be located in the same mapping unit, the partition is arduous and should take place at the scale of the mapping unit to avoid duplicates landslides in both training and validation sets. In the absence of a strict validation of the model, its efficiency will be assessed through its capacity to predict landslides on a limited set of hotspots.

4.2.2. Preliminary results of landslide susceptibility mapping

Only the results considering the slope-unit delineation are presented in this section, as the first analyses show high false positive values when using terrain unit delineation. Further investigation is necessary to provide relevant susceptibility zonation with small mapping units.

Figure 4-8 portrays results of the LR classification method: (a, d) maps showing the predicted LS, in five unequally-extended classes ([0.0–0.2[; [0.2–0.45[; [0.45–0.55[; [0.55–0.8[; [0.8– 1.0]), (b, e) histograms showing the number of slope units in the same five susceptibility classes, (c, f) a four-fold plot summarizing the number of true positives[4] (TP), true negatives[5] (TN), false positives[6] (FP), and false negatives[7] (FN); the 0.4 probability threshold was empirically used to separate positive and negative contingency classes. The four-fold plots (Fig. 4-8c and f) are equivalent to contingency tables (Table 4-5) that summarize the cases (slope units) correctly and incorrectly classified by the individual models (Jollifee and Stephenson, 2003).

Performance assessment of the training dataset is based on the Receiver Operating Characteristics (ROC) curve (Zweig and Campbell, 1993). The ROC curve is a plot of the sensitivity (proportion of true positives) of the model prediction against the complement of its specificity (proportion of false positives), at a series of thresholds for a positive outcome. Sensitivity is the probability that a mapping unit with landslide is correctly classified, and is plotted on the y-axis in an ROC curve; sensitivity is the false negative rate. Specificity is the probability that a mapping unit with no-landslide (or no-scarp) is correctly classified; 1 — specificity is the false positive rate and is taken along the x-axis of the curve.

[4] True positive: mapping units showing predicted landslides where observed landslides occurred.

[5] True negative: mapping units without predicted landslides as no landslide occurred.

[6] False positive: mapping units showing predicted landslides where no landslide occurred.

[7] False negative: mapping units without predicted landslides whereas observed landslides occurred.

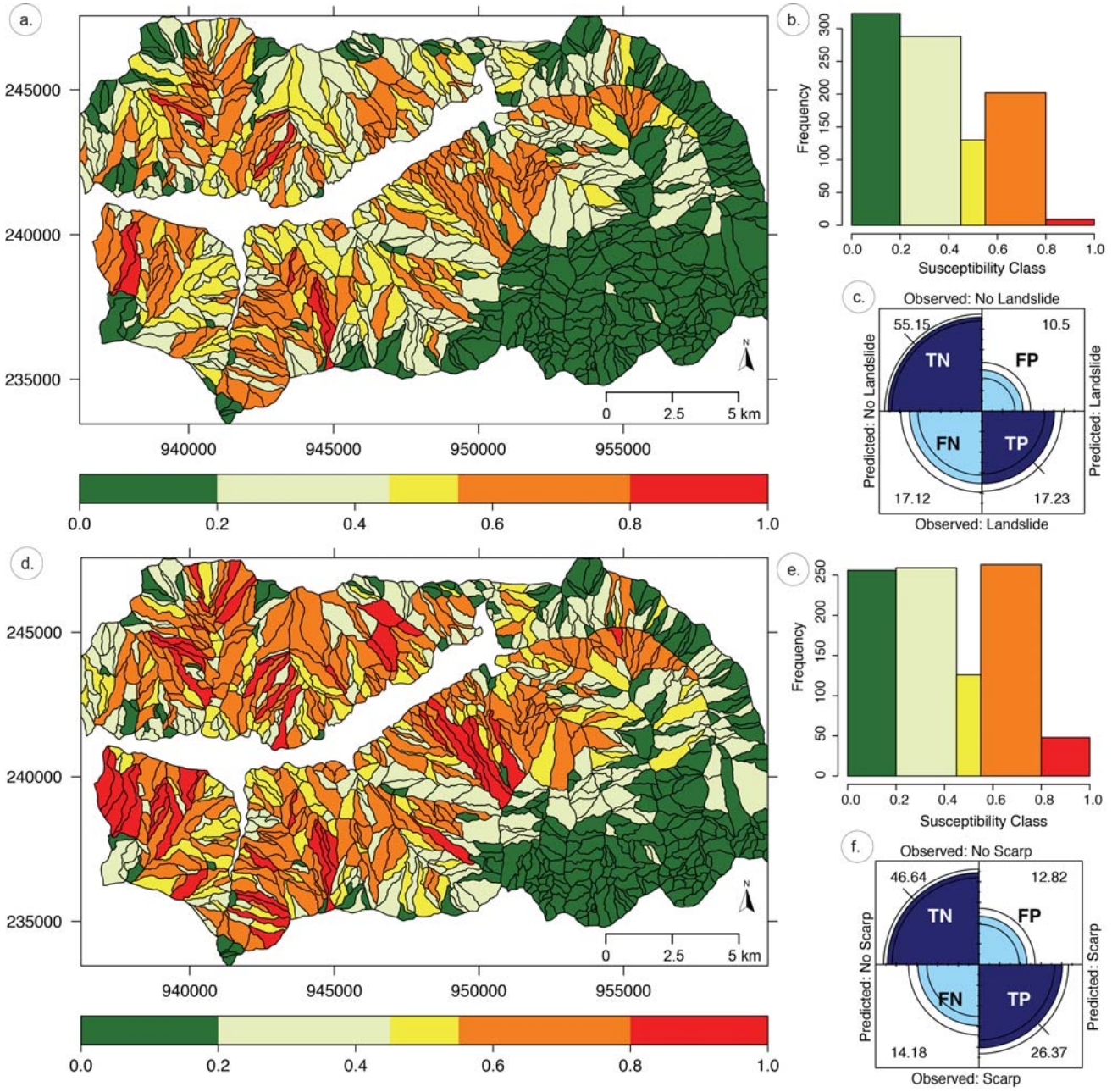

Figure 4-8: Results of landslide susceptibility (LS) models. (a) Maps portraying the LS zonations using landslide bodies (a) and source areas (d) dependent variable; (b, e) count of slope units in five unequally spaced susceptibility classes; (c, f) four-fold plots summarizing the number of true positives (TP), true negatives (TN), false positives (FP), and false negatives (FN).

Table 4-5 shows the coefficients of different factors derived from the logistic regression model. The positive and negative coefficients respectively indicate the contribution of the variable towards increasing and reducing the likelihood of landslides in the mapping unit. The estimated coefficients from the model output were used to compute the spatial probability value of each slope unit. Fig. 4-8a shows the susceptibility map expressing the spatial probability of a landslide occurring in a slope unit under the given geo-environmental conditions of the Ubaye valley. It highlights very high susceptible zones at La Valette, Les Aiguettes and Super-Sauze sub-basins and low susceptible zones to the SE. in However, 17% of FN and 10.5% of FP are recorded (Fig. 4-8c). Fig. 4-8d presents the susceptibility map obtained considering the source areas but very low and low susceptible classes and high susceptible class have the same frequency what seems abnormal (see Fig. 4-8e). Indeed, many slope-units were not well identified with almost 13% of FP and 14% of FN (Fig. 4-8f). A spatial analysis of the hazard assessment at local scale is presented in § 4.5.

Table 4-6: Logistic regression coefficients model output for model considering landslide bodies and source areas as dependant variables.

	Logistic Regression coefficients	
	Landslide bodies	*Source areas*
(Intercept)	0.7588	1.4427
Mean slope inclination	-0.0408	-0.0213
Standard deviation of slope inclination	-0.0580	-0.0455
Mean longitudinal terrain curvature	-0.0385	0.0642
Standard deviation of longitudinal terrain curvature	0.9779	1.1500
Mean cross-sectional terrain curvature	-1.7151	-2.6341
Standard deviation of cross-sectional terrain curvature	-0.1546	-0.3025
Mean terrain elevation	0.0004	0.0005
Standard deviation of terrain elevation	0.0085	0.0119
LITHO1: lacustrine and torrential deposits	-0.0203	-0.0210
LITHO2: screes and blocks	-0.0257	-0.0294
LITHO3: weathered marls	-0.0127	-0.0197
LITHO4: moraine	-0.0144	-0.0186
LITHO56: (marly-)limestone	-0.0297	-0.0411
LITHO78: sandstone/gypsum/quartzite	-0.0300	-0.0422
LANDUSE1: forest	0.0097	0.0009
LANDUSE2: arable land	-0.0102	-0.0156
LANDUSE3: grass land	-0.0179	-0.0236
LANDUSE4: bare rock	-0.0166	-0.0246
Dormant and relict landslides	-0.0030	-0.0027

Table 4-7: Contingency table LS zonation results. Counts are expressed in events. The ROC area curve shows the model performance.

Landslide bodies - SLU	No Landslide Predicted	Landslide Predicted	Total	A_{ROC}
No Landslide Observed	525	100	625	0.778
Landslide Observed	163	164	327	
Total	688	264	952	
Source areas - SLU	No Scarp Predicted	Scarp Predicted	Total	A_{ROC}
No Scarp Observed	444	122	566	0.796
Scarp Observed	135	251	386	
Total	579	373	952	

In Figure 4-9, the ROC curves show the "hit rate[8]" (y-axis) which is TP/(TP+FN) vs. the "false alarm rate[9]" (x-axis) which is FP/(FP+TN), equivalent to 1−TN/(FP+TN), or 1 — specificity (Fawcett, 2006). The area under the ROC curve, A_{ROC}, is a quantitative measure of the model performance (Mason and

[8] Hit rate: proportion of mapping units where observed landslides occurrence matches the predicted probabilities (i.e. true positive).

[9] False alarm rate: proportion of mapping units where high failure probabilities are predicted whereas no landslide occurred.

Graham, 2002; Jollifee and Stephenson, 2003). Indeed, this area under the curve represents the probability that the landslide susceptibility value for a landslide (or scarp) mapping unit calculated by the model will exceed the result for a randomly chosen no-landslide (or no-scarp) mapping unit. The areas under the curve obtained are 0.778 (i.e. an accuracy of ~78% for the training model; Fig. 4-9a) and 0.796 (i.e. an accuracy of ~79% for the training mode; Fig. 4-9b) when the landslide body and the source area, respectively constitutes the dependent variable.

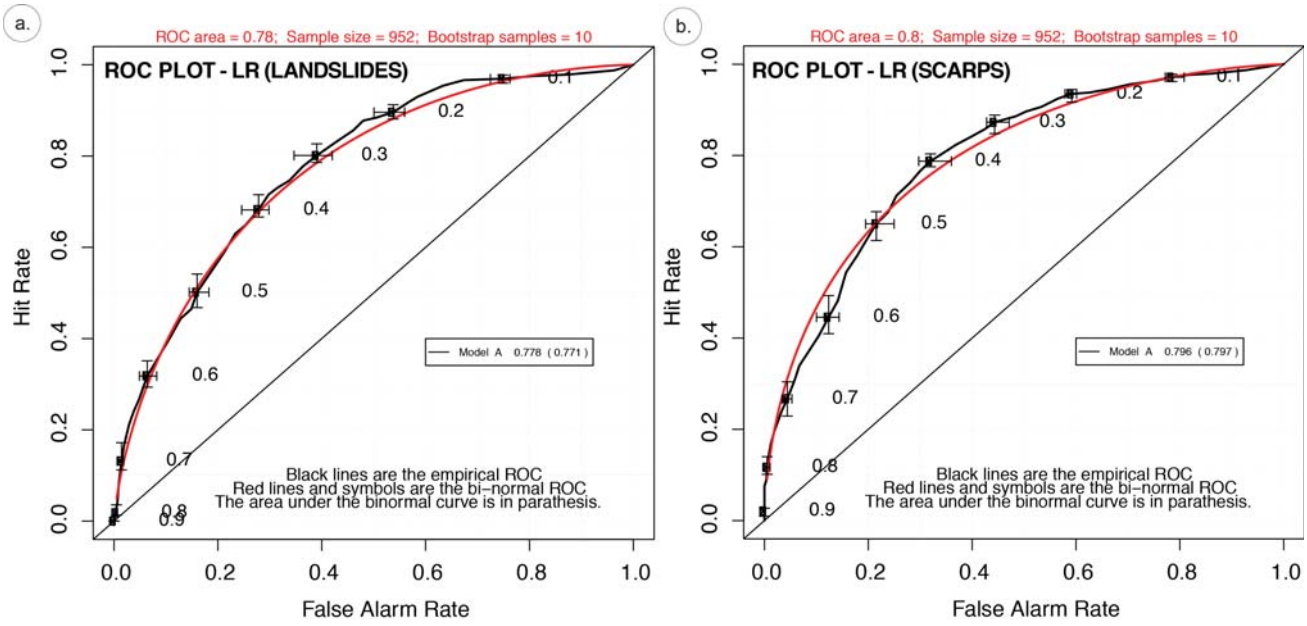

Figure 4-9: ROC curves for LR considering (a) landslide body or (b) source areas as dependant variable.

4.2.3. Discussion and perspectives

The results clearly show that the threshold of considering the dependant variable in the mapping unit (i.e. 1 or 0 value) play an important role in the model. Indeed, we would expect lower high (and very high) susceptible classes by considering the source areas but we obtained the opposite. The model shows a high overestimation of the high susceptible classes meaning an exaggeration of the area of actual landslide hazard. Indeed, in some cases, SLUs are only affected by a portion (few square metres) of the source area and a presence value is attributed. Moreover, when the area of individual landslide sources is small, slope units covering relatively large surface area often do not match with the local geo-environmental setting bearing on slope instability (Jaiswal et al., 2010). One way to overcome this is to resize the slope units according to the present landslide size by partitioning a river basin into nested subdivisions, coarser for larger landslides and finer for smaller failures (Guzzetti et al., 1999).

In addition, the relative importance of the independent variables can be assessed using the corresponding coefficients in the LR model. In this study, a few coefficients are positive (Table 4-6), indicating that they are not positively related to the probability of landslide formation through the log transformation. Another possibility to improve the results would be to investigate the independent variables and see if they can be correlated together which may induce redundancy into the model (e.g. geology correlated to elevation above 2000 m). An additional principal component analysis (PCA) could also reveal the influence of each parameter on the presence of landslide guiding the choice of the best fitting parameters to consider.

4.3. Landslide temporal exceedance probability estimation

4.3.1. Method of temporal exceedance probability calculation

The temporal probability of slope failures is estimated by the frequency of landslide occurrence which is usually calculated on the basis of a multi-temporal inventory (Guzzetti et al., 2005; F Guzzetti et al., 2006). In the framework of this research, we counted the number of landslides in the multi-date inventory in each terrain or slope unit, taking into account a specified area threshold to avoid overestimation due to tiny portions of landslides falling into large terrain or slope unit. For each mapping unit, we estimate the landslide recurrence based on the past rate of landslide occurrence, i.e. the expected time between successive failures. Knowing the mean recurrence interval of landslides in each mapping unit (from 1956 to 2009; see § 3.3), assuming that the rate of slope failures will remain the same for the future, and adopting a Poisson probability model (Crovelli, 2000; Guzzetti et al., 2003, 2005), we then computed the exceedance probability of having one or more landslides in each unit for four return periods: 5, 10, 25, 50 years.

4.3.2. Results

4.3.2.1. Landslide temporal evolution

The landslide temporal evolution was computed from the total frequency of landslides affecting each mapping unit, provided that the sliding portions included in the considered unit have a size greater than the defined threshold (2% for slope units and 100 m^2 for terrain unit). The map shows the number of active landslides in each mapping unit over the 53-year period (Fig 4-10). Class limits were chosen according to the frequency distribution. The maximum frequency reaches 18 events per terrain unit and 27 events per slope unit. 22.3 % of the terrain units and 35.5% of the slope units contain at least one event. 31 slope units (3.3%) and 18 terrain units (0.6%) are affected by more than 10 events (3.3%). The most densely affected mapping units are located around Poche, the downstream left bank of the Aubriès watercourse and the upper part of the Sanières watershed.

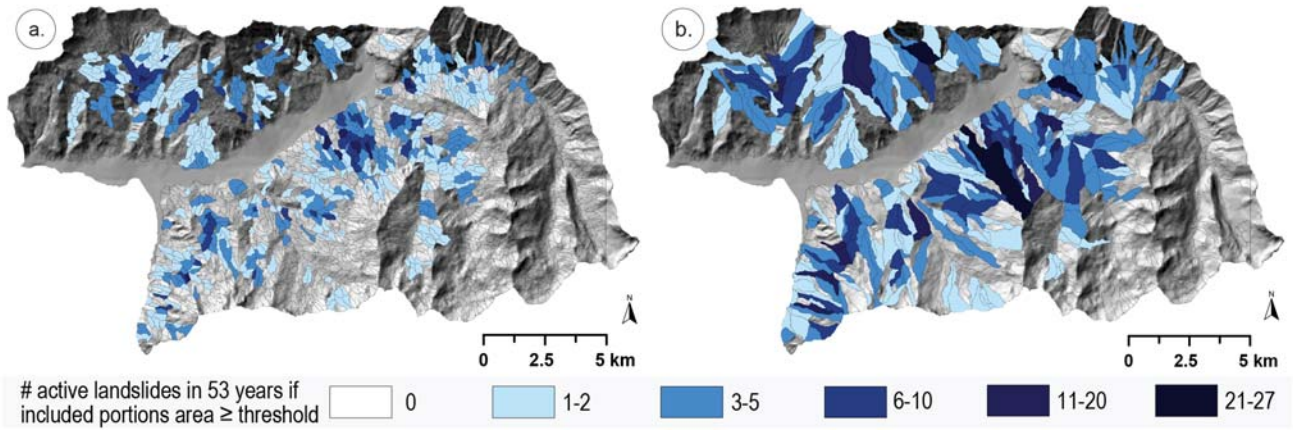

Figure 4-10. Number of active landslides in mapping unit with at least one new landslide or reactivation recorded over the time considered (i.e. 53 years) if their included portion exceeded specified threshold (2% for slope units and 100 m^2 for terrain unit).

4.3.2.2. Exceedance probability of landslides

Exceedance probability maps based on the frequency of landslides in each mapping unit were built from the mean recurrence interval of past landslide events recorded in the multi-date inventory (as shown in Fig. 4-10), assuming it will remain the same for the future, and adopting a Poisson probability model. The map showing the exceedance probability according to the terrain units delineation for four

return periods (5, 10, 25, 50 years) is presented in Figure 4-11 (considering the number of events shown in Fig. 4-10a), and the one that refers to the slope units delineation in Fig. 4-12 (based on Fig. 4-10b).

Information about the number and area of slope and terrain units belonging to each probability class (with a 0.2 step) is given in Table 4-7. The gap identified for the 0.4-0.6 class of the 25-year return period maps is due to the use of integer numbers as frequency indicator, leading to a discontinuous representation of the exceedance probability with this classification method. The 5-year return period map (Fig. 4-11a) shows essentially terrain units with low exceedance probability; 56% of the area is linked with a probability comprised between 0 and 0.2, only 2.8% of the valley area exceed the 0.6 value. Poche, La Valette, Sanières and Abriès watersheds present exceedance probability above 0.4. From the 50-year map (Fig. 4-11d), each terrain unit reaches an exceedance probability of minimum 0.6 in the whole valley.

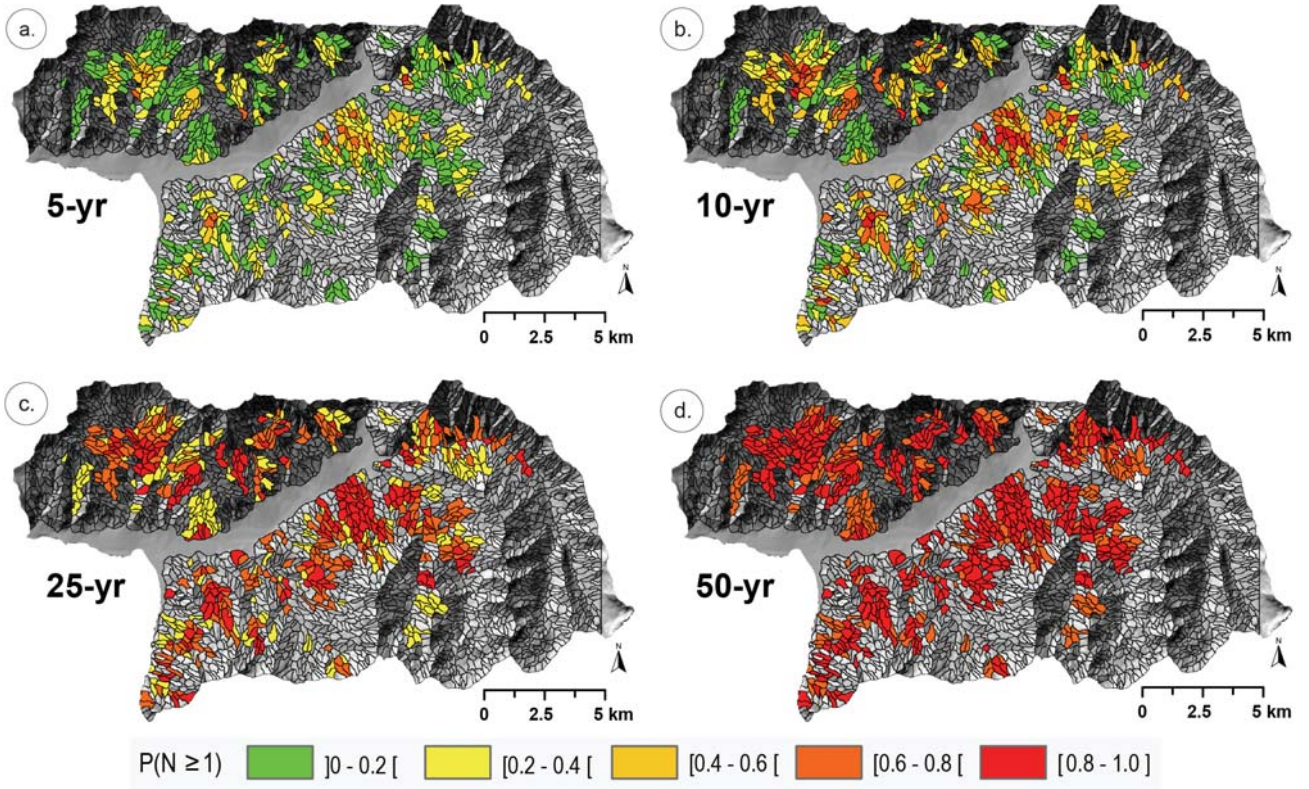

Figure 4-11: Exceedance probability of landslide temporal occurrence calculated for each terrain units. Maps compute the mean recurrence interval of past landslide events from the multi-date inventory map, assuming it will remain the same for the future, and adopting a Poisson probability model. Exceedance probability is represented for four return periods: (a) 5 years, (b) 10 years, (c) 25 years and (d) 50 years.

A similar analysis can be provided for the slope units delineation exceedance probability map (Fig 4-12). The larger area of the slope units increases artificially the probability by integrating more events in each mapping unit, but it does not modify significantly the relative spatial distribution of the exceedance probability in the valley. The 5-year return period map (Fig. 4-12a) shows that 40.8% of the whole area present an exceedance probability between 0 and 0.2, which is slightly lower than the result of the terrain units delineation. From the 50-year map (Fig. 4-12d), 76.3% of the area split in slope units shows probabilities between 0.8 and 1, against 66.4% in the terrain units case.

Table 4-8: Number, total area and percentage of mapping units in five classes of the probability of temporal landslide occurrence (see Fig. 4-8 and 4-9). Temporal probability of landslide occurrence obtained exploiting the new and reactivated landslides recorded in the multi-date inventory map and adopting a Poisson probability model.

P(N ≥1)	0.0 - 0.2			0.2 - 0.4			0.4 - 0.6			0.6 - 0.8			0.8 - 1.0		
yrs	# TU	area km^2	%	# TU	area km^2	%	# TU	area km^2	%	# TU	area km^2	%	# TU	area km^2	%
5	368	31.2	55.7	214	19.0	32.4	61	5.2	9.2	17	1.4	2.6	1	0.1	0.2
10	222	18.2	33.6	146	13.0	22.1	182	16.0	27.5	83	7.4	12.6	28	2.3	4.2
25	0	0	0	222	18.2	33.6	0	0	0	247	21.7	37.4	192	17.1	29.0
50	0	0	0	0	0	0	0	0	0	222	18.2	33.6	439	38.8	66.4
	# SLU			# SLU			# SLU			# SLU			# SLU		
5	138	35.3	40.8	121	34.5	35.8	48	13.0	14.2	23	10.9	6.8	8	4.7	2.4
10	80	19.7	23.7	58	15.5	17.2	100	27.4	29.6	62	18.1	18.3	38	17.6	11.2
25	0	0	0	80	19.7	23.7	0	0	0	110	31.4	32.5	148	47.3	43.8
50	0	0	0	0	0	0	0	0	0	80	19.7	23.7	258	78.7	76.3

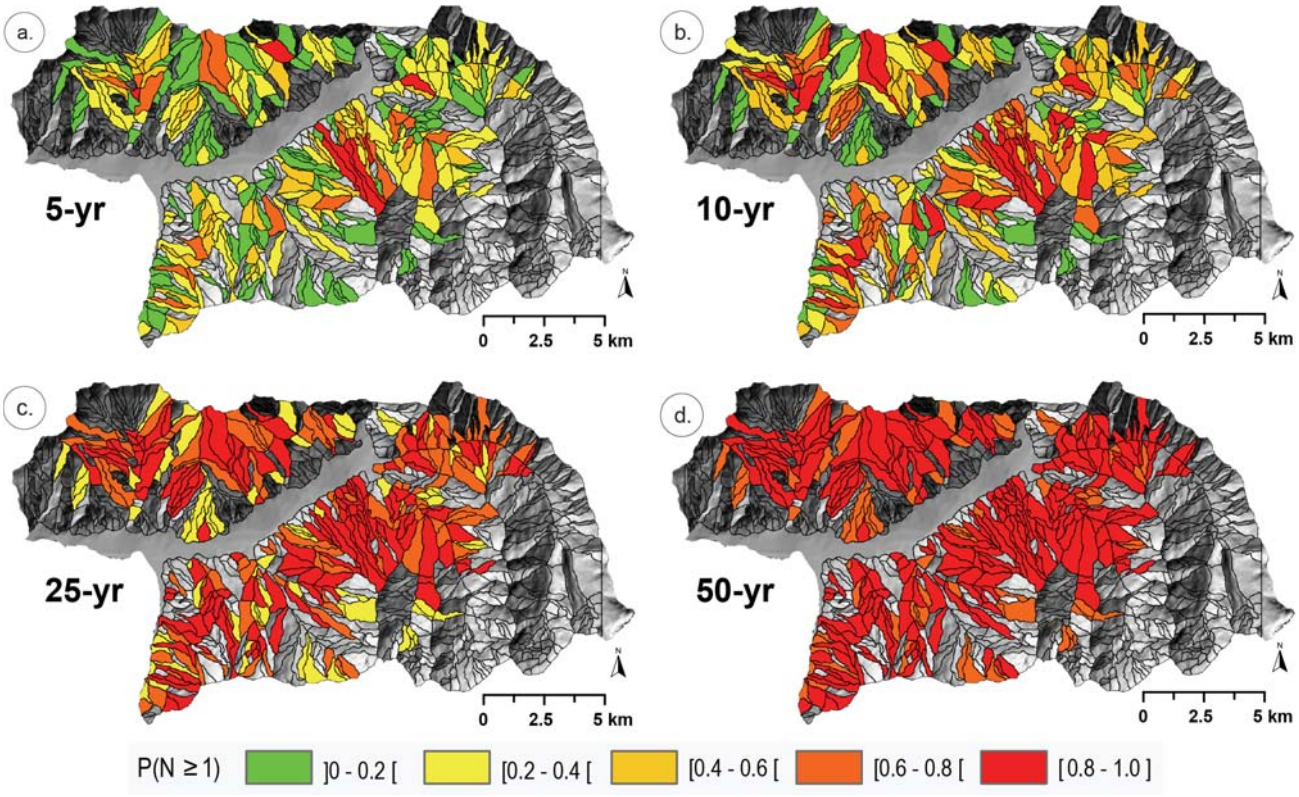

Figure 4-12: Exceedance probability of landslide temporal occurrence calculated for each slope units. Maps compute the mean recurrence interval of past landslide events from the multi-date inventory map, assuming it will remain the same for the future, and adopting a Poisson probability model. Exceedance probability is represented for four return periods: (a) 5 years, (b) 10 years, (c) 25 years and (d) 50 years.

4.4. Landslide intensity

4.4.1. Method of calculation of landslide areal evolution

The landslide areal evolution has been computed at the terrain unit scale. For each period of analysis between two successive inventories, the new area of each active landslide was delimited in each terrain unit. The sum of new areas of the different parts of landslides contained in each terrain unit was calculated. The duration of the active period was obtained from the inception of the activity to its completion, subtracting the possible time gaps during which no activity was recorded among the different landslides present in the terrain unit. A mean areal evolution, expressed in $m^2.yr^{-1}$, was then computed from this total area and the number of active years as defined above.

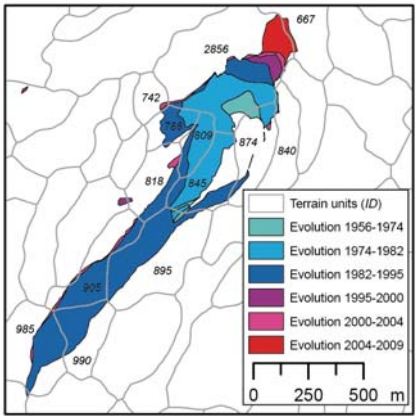

TU #	Evolution (m²) 1956-1974	1974-1982	1982-1995	1995-2000	2000-2004	2004-2009	Areal evolution (m²)	Active duration (yr)	Mean areal evolution (m².yr⁻¹)
667						2697	2697	5	539
742			298		714		1011	17	59
788		5275	14044				19319	21	920
809		20543	6710				27253	21	1298
818			12283	325	1585		14192	22	645
840		1122	81		38		1241	25	50
845	1552	32580	16104				50236	39	1288
874	2167	5690	2381		433		10671	43	248
895	1027	1095	52084				54206	39	1390
905			37396		3579		40975	17	2410
985			29033		1153		30186	17	1776
990			26051		2		26053	17	1533
2856	10629	48763	19610	8228	5133	17799	110163	53	2079

Figure 4-13: Method for landslide evolution calculation (example of La Valette case study). Map of portions of landslide area evolution over time periods considering the mapping unit (e.g. TU). Table of periodic, total and mean areal evolution.

4.4.2. Results

4.4.2.1.Size-frequency relation

The method described to calculate size-evolution of active landslides was applied to the Ubaye valley in order to see the regions where (i.e. in which terrain units) they are observed (Fig. 4-14). A threshold of 500 m^2 was chosen after an analysis of the size distribution of the mobile portions. In total, 377 TUs contains landslides with an evolution in size ≥500 m^2 whereas 2314 TUs do not (Fig. 4-14a). For SLUs, 220 of them are affected while 658 are not (Fig. 4-14b). A maximum of seven landslides with size evolution ≥500 m^2 were counted per mapping unit. No more than 5 landslides exist in the smaller TUs. Only 9 of these ones have 4 or more landslides included while 22 are counted in SLUs. The most active landslides affect SLUs located around the Riou-Bourdoux and Poche catchments, the South of Uvernet (e.g. Riou Chanal), and the upper part of the Sanières watershed (Fig. 4-14b).

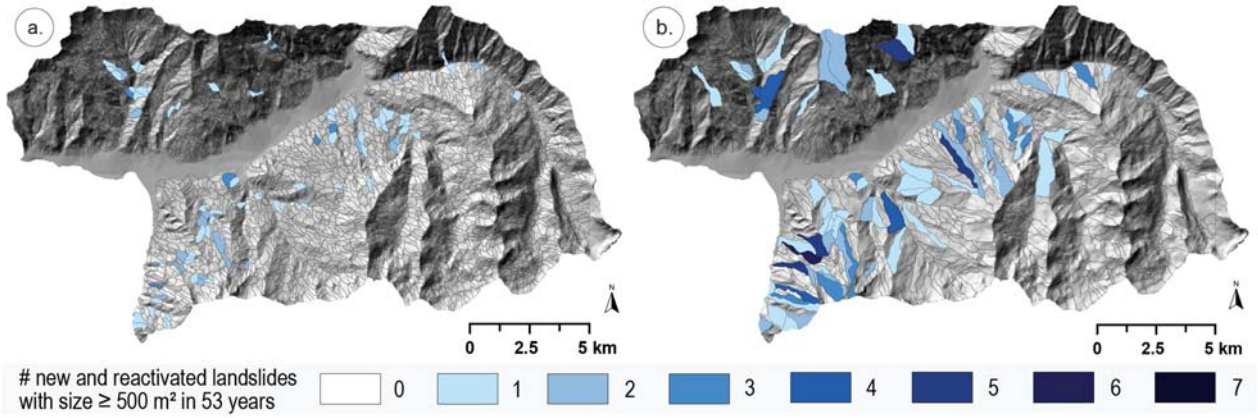

Figure 4-14: Number of new and reactivated landslides with a size evolution greater than 500 m² over the time considered (i.e. 53 years). Calculation realised on mapping units affected by at least one new landslide or an old one with a size enlargement.

4.4.2.2. Exceedance probability of areal evolution

Figure 4-15 portrays landslide temporal occurrence considering the terrain units delineation in the Ubaye valley for four return periods (5, 10, 25 and 50 years), and for a specific increase in landslide size (>500 m², as defined in Fig. 4-14). This joint probability (i.e. temporal and size) indicates that a slope unit will be affected by future landslides or reactivations that exceed a given area, in a given time, considering the environmental setting.

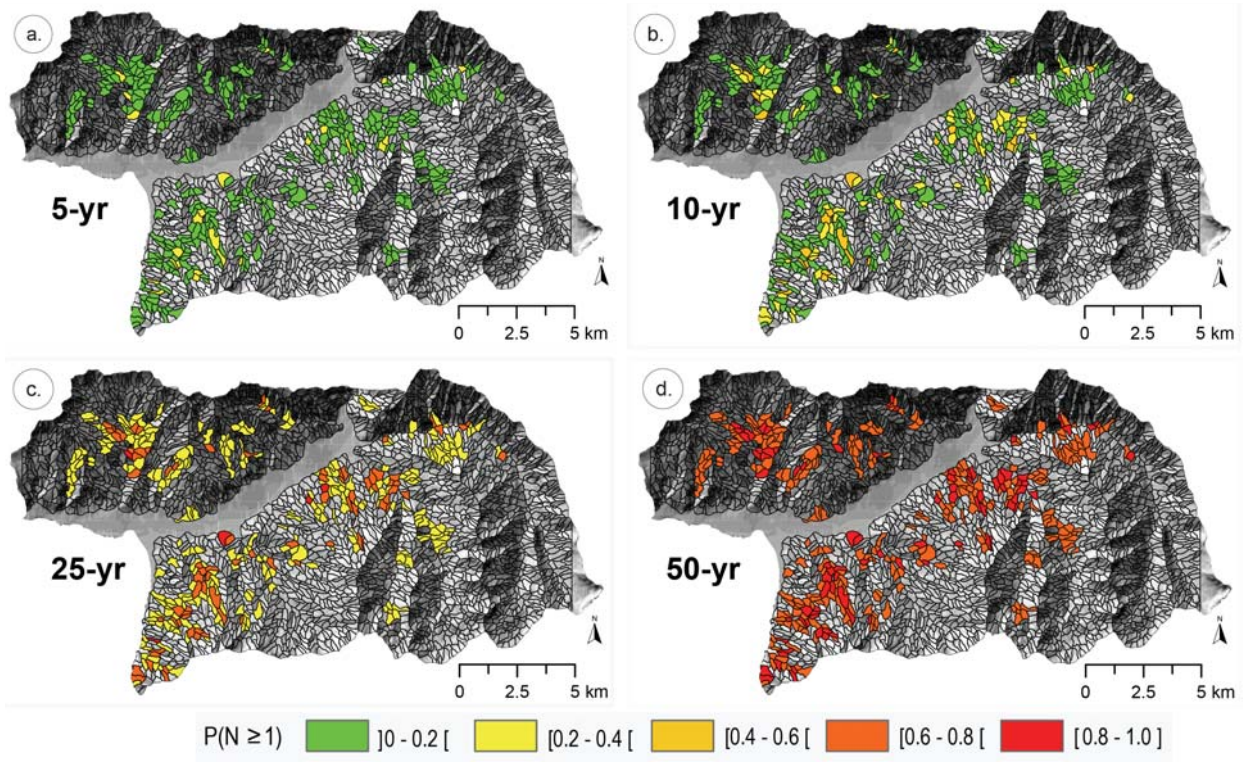

Figure 4-15: Exceedance probability of landslide areal evolution calculated on the basis of a Poisson law for each TU affected by at least one landslide. Maps compute the mean recurrence interval of past landslide evolutions greater than 500 m² events from the new landslide portions registered over time periods. Exceedance probability is represented for four return periods: (a) 5 years, (b) 10 years, (c) 25 years and (d) 50 years.

The 5-year return period exceedance probability map shows probabilities lower than 0.4 in the whole valley (Fig. 4-15a). 93.7% of the area show probabilities below 0.2. Table 4-8 gives statistics on the frequency of mapping units in each probability class. Compared to the temporal evolution occurrence maps (Fig. 4-11), this joint temporal and size evolution show a significantly different spatial distribution of the calculated values. The most active landslides, in terms of temporal and size activity, are located in the Riou-Bourdoux watershed, around Pra Loup village and in the area of Poche. The 25-year return period map (Fig. 4-15c) shows in these mentioned preferential locations probabilities above 0.6. In the 50-year map (Fig. 4-15d), each terrain unit reaches a minimum exceedance probability of 0.6 (Table 4-7). 22.7% of the valley area is affected by a probability exceeding 0.8.

The same analysis was performed with the slope unit delineation (Fig. 4-16). The spatial distribution shows differences from the terrain unit delineation. The main active areas in terms of temporal and size activity are visible in the western parts of the Sanières watershed and the Riou des Ribes watershed, in the Pra Loup vicinity and finally in the eastern side of the Riou-Bourdoux watershed. Fig. 4-16a shows the 5-year return period exceedance probability map; 15.7% of the whole valley area present probabilities ranging from 0.2 and 0.4 while 1.9% of the valley shows values above 0.6. This latter class was absent from the terrain unit delineation due to the smaller aggregation scale. 25- and 50-year return period exceedance probability maps present a large proportion of slope units with values above 0.8, with respectively 8.4 and 36.8% of the area of the valley.

Table 4-9: Number, total area and percentage of mapping units in five classes of the probability of temporal landslide occurrence (see Fig. 4-15 and 4-16). Temporal probability of landslide occurrence obtained exploiting landslide evolutions greater than 500 m² events recorded into the multi-date inventory map and adopting a Poisson probability model.

P(N ≥1)	0.0 - 0.2			0.2 - 0.4			0.4 - 0.6			0.6 - 0.8			0.8 - 1.0		
yrs	# TU	area km^2	%	# TU	area km^2	%	# TU	area km^2	%	# TU	area km^2	%	# TU	area km^2	%
5	449	37.6	93.7	30	3.1	6.3	0	0	0	0	0	0	0	0	0
10	373	30.7	77.9	76	6.9	15.9	30	3.1	6.3	0	0	0	0	0	0
25	0	0	0	373	30.7	77.9	0	0	0	97	9.1	20.3	9	0.9	1.9
50	0	0	0	0	0	0	0	0	0	373	30.7	77.9	106	10.0	22.1
	# SLU			# SLU			# SLU			# SLU			# SLU		
5	215	57.9	82.4	41	16.9	15.7	5	2.7	1.9	0	0	0	0	0	0
10	165	40.6	63.2	50	17.3	19.2	36	14.3	13.8	10	5.3	3.8	0	0	0
25	0	0	0	165	40.6	63.2	0	0	0	74	27.6	28.4	22	9.3	8.4
50	0	0	0	0	0	0	0	0	0	165	40.6	63.2	96	36.9	36.8

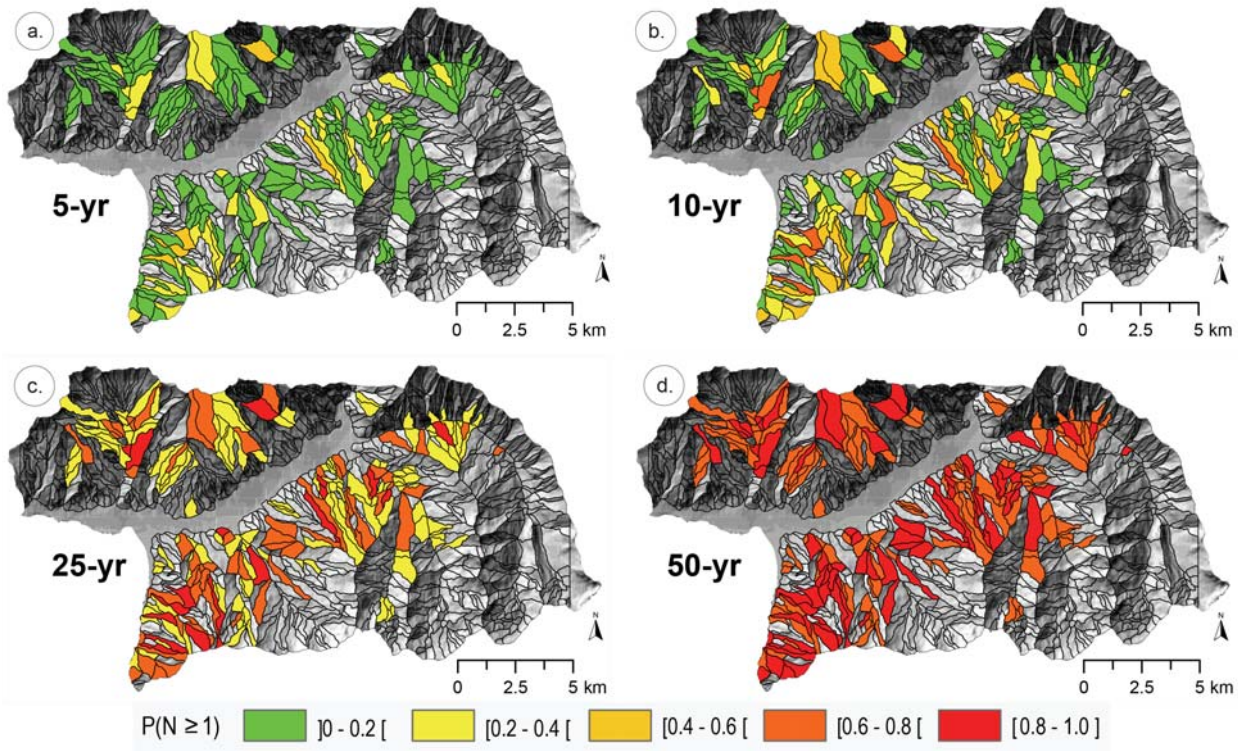

Figure 4-16: Exceedance probability of landslide areal evolution calculated on the basis of a Poisson law for each SLU affected by at least one landslide. Maps compute the mean recurrence interval of past landslide evolutions greater than 500 m² events from the new landslide portions registered over time periods. Exceedance probability is represented for four return periods: (a) 5 years, (b) 10 years, (c) 25 years and (d) 50 years.

4.5. Landslide hazard assessment in the Ubaye valley

A quantitative landslide hazard assessment on natural slopes requires the estimation of three basic parameters (as evaluated in the former sections; Fig. 4-14): (1) the spatial probability (*S*): indicating the relative spatial probability of occurrence of landslides (all types considered); (2) the temporal probability ($P(N_L)$): indicating the annual probability of occurrence of triggering events that generate landslides, and (3) the magnitude probability ($P(A_L)$): indicating the probability that the landslide might be of a given size. Using the above probabilities, the landslide hazard on natural slopes can be estimated as the joint probability of the landslide size, of the landslide occurrence in an established time period and of the landslide spatial occurrence (Guzzetti et al., 2005).

4.5.1. Probabilities for landslide hazard estimation

In order to analyse and interpret properly the hazard in function of the calculated probabilities, we have to cope with (i) the limited performances of the models and their assumptions, (ii) the limits of the dataset used to assess the probabilities, and (iii) the heterogeneity in landslide types and complex environmental conditions. Depicted in the former sections, (i) depends on the definition attributed to each probability. As magnitude-frequency relationships are not conceived for assessing landslide reactivation events (that we have mostly in this region), the hazard assessment considering intensity will tend to overestimate areas where numerous small landslides have been occurred and underestimate areas where a large landslide (reactivated many times over the considered period) is continuously moving. Moreover, the results are inventory-dependant (ii) with consider a period of 53 years and only 6 states during that time (i.e. between 1956-1972; 1972-1984; 1984-1995; 1995-2000; 2000-2004; 2004-2009). To be consistent with the definitions to calculate the probabilities, we

based our calculations on the number of landslides which as been changed within the time span and not on the number of reactivations (or changes). Indeed, the latter would have the effect to wrongly overestimate the probability. As described in the previous section, the minimal landslide size to count an event is 500 m² and the threshold of considering it into a specific mapping unit is 100 m². In addition, as the landslides are observed in different geological conditions and are heterogeneous in terms of size and type (iii), the triggering factors are numerous and in interactions to each other. The probability of failure cannot be obtained considering the annual exceedance probability of a critical meteorological event. Therefore, hazard calculated from the frequency of landslide triggers should have required a particular analysis, for each landslide type, in order to determine a reliable relation between the trigger, its magnitude and the occurrence of landslide (Corominas et al., 2014).

The probabilities estimations are based on the delineation in SLUs which consider the hydro-morphological properties of the half-basins. *S* has been calculated by LR on the basis of the whole landslide bodies (as dependant variable) with a 2% threshold of SLU size for considering it (see results in Fig. 4-8a). $P(N_L)$ has been computed by counting the number of events occurring into a SLU (threshold: 100 m²) for the 53-year period. The exceedance probability of having at least one landslide is calculated for a 10-year return period. In order to know the probability to have a landslide of a given magnitude, a size threshold (A_L) of 500 m² is chosen. This threshold was chosen consistently from the visual detection evolution threshold on orthophotographs, which differs with the document quality. We considered that the areal evolution from one inventory to another of about 80 m² per interval (leading to 500 m² over the 53-year period) was the minimum value to take evolving landslides into account in the probability map. Out of 312 evolving landslides, 67 records with small evolutions were removed. Then, $P(N_L) * P(A_L)$ gives us the probability of landslide larger than a given magnitude (i.e. ≥500 m²). This probability is calculated by counting the sum of activated area for the landslides presented in a SLU for our time span (i.e. 53 years). The number of evolutions is not taken into account because the magnitude-frequency relationships cannot assess landslide reactivation events.

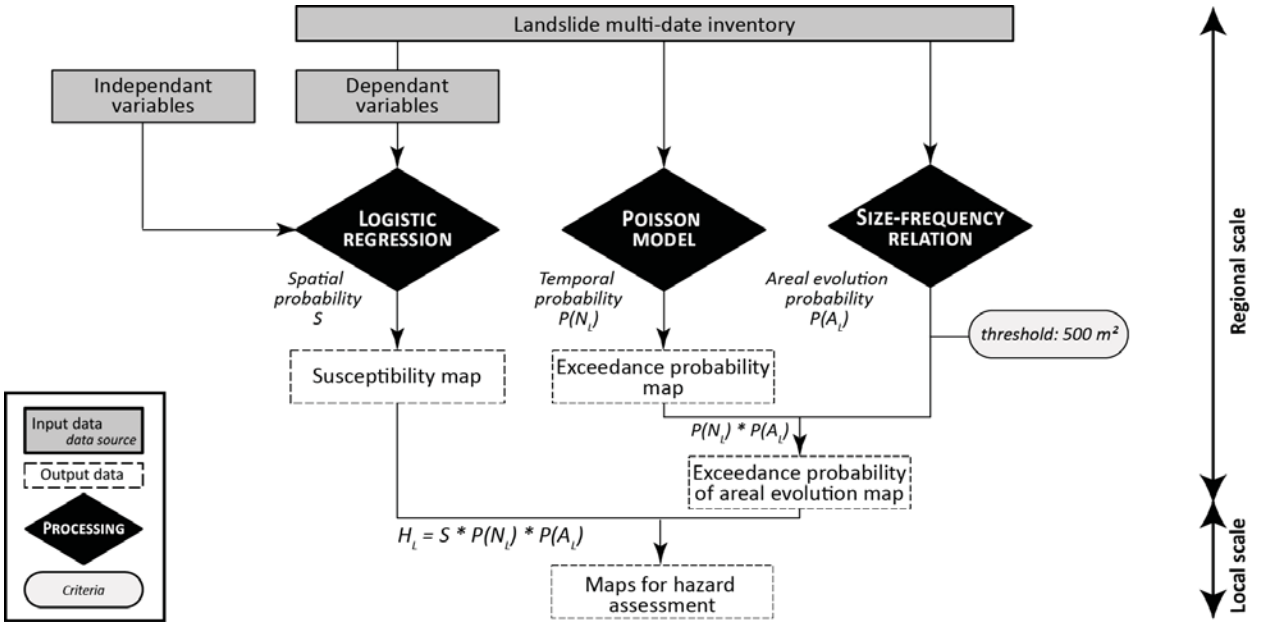

Figure 4-17: Flowchart of landslide hazard assessment

The literature shows that authors use different probability classes to represent the results considered in the same kind of frameworks. Some studies use four classes of susceptibility using quantiles can be chosen, for low, moderate, high and very high susceptible classes such as 0-0.25, 0.25-0.5, 0.5-0.75 and 0.75-1, respectively (Ayalew and Yamagishi, 2005; Das et al., 2010). Other authors prefer the division into five classes to represent very low (0-0.2), low (0.2-0.4), uncertain (0.4-0.6), high (0.6-0.8) and very high (0.8-1) susceptibility (e.g. Guzzetti et al., 2006). Unequally spaced classes are also used as for the results presented in § 4.3 (e.g. Rossi et al., 2010). Temporal probability classes depend on the available

datasets as well as the purpose of the analysis, thus five to ten classes can be used. In order to be homogeneous with all the calculated probabilities (Fig. 4-17), we have decided to classify the maps into five equally spaced classes, such as: very low (0-0.2), low (0.2-0.4), moderate (0.4-0.6), high (0.6-0.8) and very high (0.8-1).

Comparison of slope-unit frequency obtain per probability class is shown in Fig. 4-18. Susceptibility zonation (a1) shows a good homogeneity of SLU counts in the very low, low, moderate and high classes. However, the LR does not attribute very high probability values to a large number of slope-units (2.1%). In terms of source areas (a2), the most represented probability interval is the [0.6-0.8[class. 43.5% of the source areas have their centroid that falls into it, closely followed by the [0.4-0.6[class which counts 38.3% of the studied source areas. True positive and false positive were characterized respectively by probability classes in the range [0-0.4[and [0.4-1.0]. Each SLU is linked with a non-null value of probability with the susceptibility zonation. The fraction of false positive is then limited to only 16.1% of the SLUs (a3).

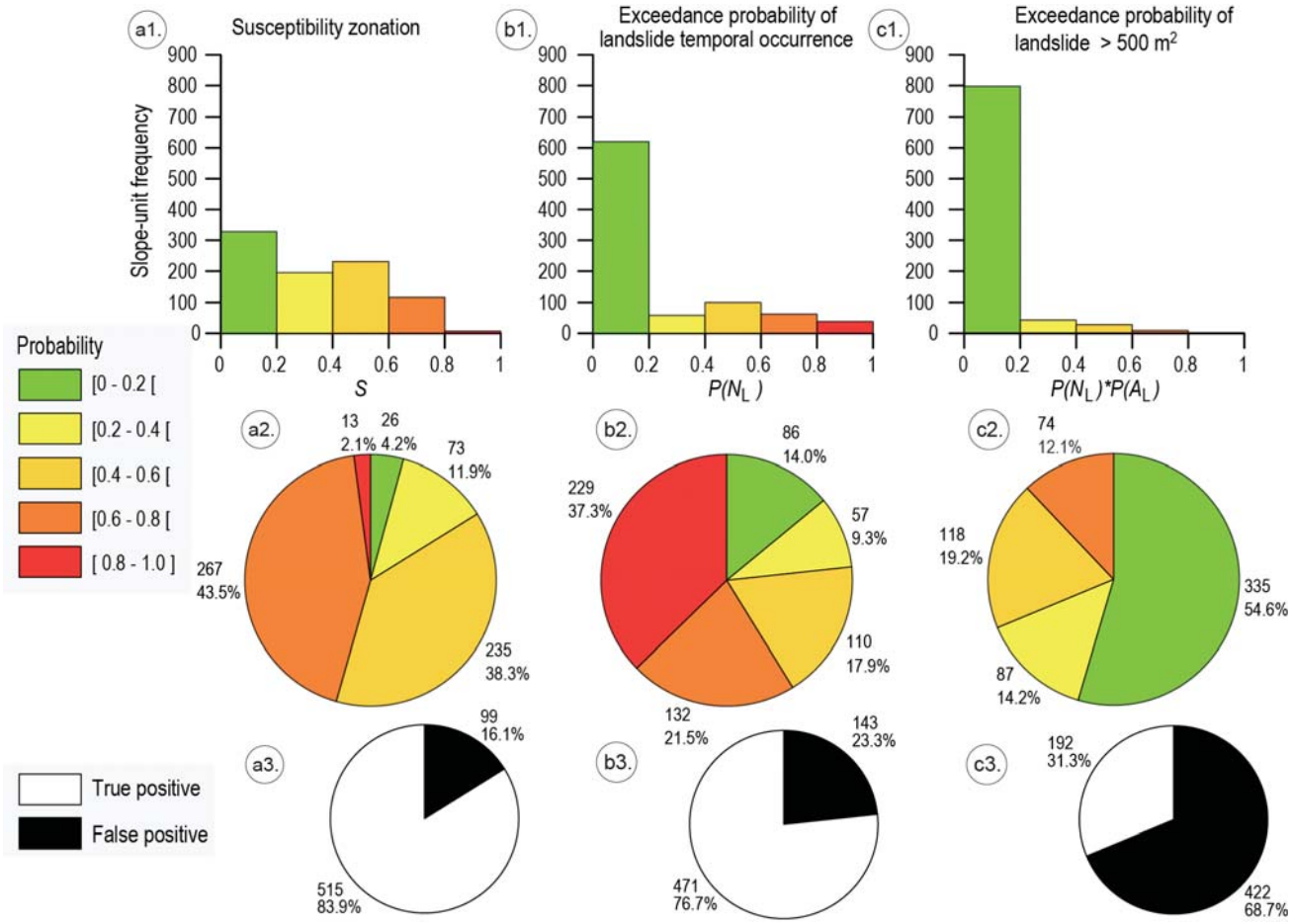

Figure 4-18: Probability class comparison between the three models. (a1) Slope-unit frequency per spatial probability class given by the LR. (b1) Slope-unit frequency per exceedance probability classes of temporal occurrence. (c1) Slope-unit frequency per exceedance probability classes according to a size threshold (i.e. ≥ 500 m²). (a2) Active landslides scarps frequency associated with the spatial probability class in which their centroid is located (b2) Active landslides scarps frequency with their associated temporal probability class (c2) Active source areas frequency with their associated temporal probability classes linked with a size threshold (i.e. ≥ 500 m²). True and false positives considering source area presence in slope units of undetermined, high and very high probability classes, represented in white and black, respectively (a3, b3, c3).

The exceedance probability of landslide temporal occurrence (b1) has a dissymmetric distribution because a large part of the valley was not affected in the past by landslides (61.5 % of the number of SLUs), and thus receives a null exceedance probability. Setting aside this methodological bias, the most represented class in terms of slope-units is the [0.4-0.6[intervals. In terms of source areas, their

centroids are preferentially located in the most likely class (b2). The number of false positives is higher due to the number of slope-units associated with the null class (b3).

The same effect on the null class is observed in the third map showing the combination of temporal exceedance probability with a size threshold (i.e. ≥ 500 m^2). Due to the two thresholds taken into consideration during the creation of the map (the 100-m^2 threshold avoiding the small parts of landslides located in large SLUs and the 500-m^2 threshold highlighting robust cartographic evolutions), the number of SLUs associated with null or low probability is higher, giving 68.7% of false positive (c3). The second most represented class in terms of SLUs is the [0.2-0.4[class, in relation with the impossibility to take the number of reactivations into account (c1). Only the number of evolving landslides above the multiple thresholds is counted. In terms of scarps, most of them have their centroid falling into low probability SLUs. The second most represented class is the [0.4-0.6[intervals, with 19.2% of active landslides. The high probability class includes 12.1% of source areas, while the low probability class groups 14.2% of them.

4.5.2. Hazard analysis on particular hotspots

Landslide hazard assessment of hotspot catchments (see their description in § 2.3.4 on the basis of their active landslides), are presented here: the Riou-Bourdoux catchment (Pra Bellon landslide), the Sauze catchment, the Poche catchment and the Sanières catchment.

4.5.2.1. Riou-Bourdoux catchment

Located in the Riou-Bourdoux catchment, the Pra-Bellon slope (see pictures in Fig. 2-14a; § 2.3.4) represents a threat for the Saint-Pons village, 3-km downhill. Indeed, north- and south- facing slopes bordering the Riou-Bourdoux torrent are hilly affected by landslides (Fig. 4-17a). The Pra-Bellon complex landslide (see red contour line in Fig. 4-17a) is a part of slope almost entirely affected by embedded landslides. Susceptibility model presents the area affected by the Pra-Bellon landslide as moderately susceptible while the downstream part is highly susceptible (Fig. 4-17b). High to very high exceedance probabilities (Fig. 4-17c) of the Pra-Bellon slope indicated that a lot of events where recorded during the considered time span of 53 years. This affirmation is based on both the observed internal reactivations of the large sliding units (information given by the vegetation index; see definition in § 3.3) and additional small internal reactivations. Small active landslides also affect east and southeast-facing slopes (right riverbank) what gives to the SLUs very high to high probabilities, respectively. On the contrary, on the east-facing slope to the east of the Chalanche crest (elevations from 2000-1600 m), the probability to have a landslide is very low as this catchment is not active, mainly dormant landslides are observed. The combination of temporal exceedance probability with a size threshold (Fig. 4-17d) show high probability of the main SLU to be affected by a landslide ≥ 500 m^2 over the next 10 years.

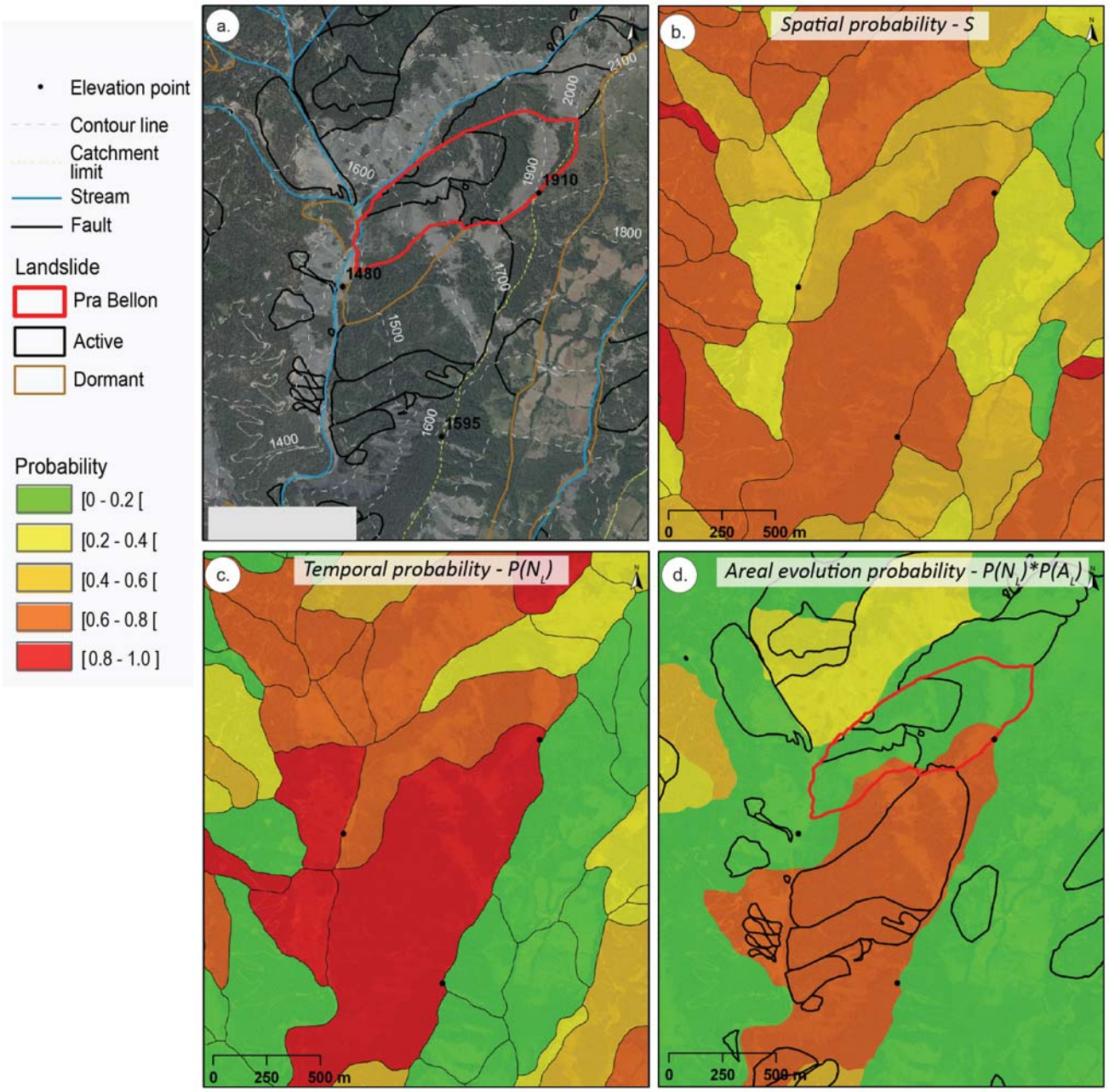

Figure 4-19: Landslide hazard assessment at Riou-Bourdoux catchment. (a) Morpho-structural map. (b) Susceptibility zonation results. (c) Exceedance probability P(N≥1) for 10-year return period (d) Exceedance probability of landslide areal evolution for 10-year return period.

4.5.2.2. Sauze catchment

Located in the headwater catchment of the Sauze torrent between 2105 m and 1740 m (Fig. 4-20a), the complex Super-Sauze mudslide is considered as active (see Fig. 2-19 and 2-20; § 2.3.4). To the West and North, it is surrounded by small active landslides mainly developed in black marls (Fig. 4-20a). The susceptibility map of this area shows moderate to low probabilities in this area (Fig. 4-20b). However, a highly susceptible east-facing SLU is observed (i.e. on the slope going to the ski resort). As some reactivations of the small landslides where observed, a high exceedance probability is calculated for two north-facing and SW-facing SLUs while it is only moderated for SLUs where the Super-Sauze landslide has been occurred (Fig. 4-20c). Since its triggering in the 1960s, the Super-Sauze landslide have had three major reactivations with size enlargement. The combination of temporal exceedance probability with a size threshold (Fig. 4-17d) show only one SLU of moderate probability to be affected

by a landslide ≥ 500 m^2 over the next 10 years. The very low probability of SLUs is due to the fact that the number of reactivations is not considered in the calculation and that only SLUs affected by many landslides which had size evolutions, can get a high exceedance probability.

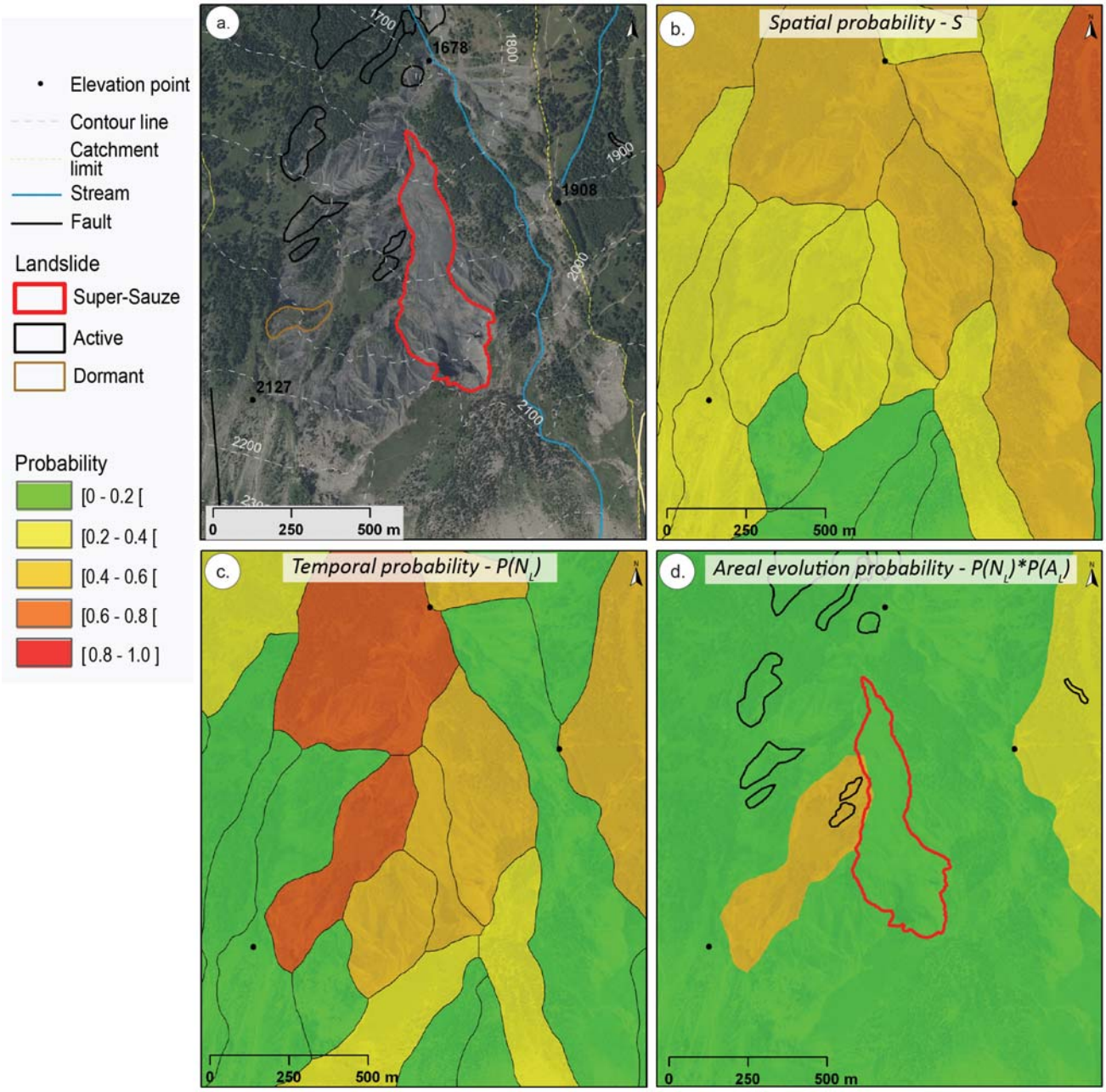

Figure 4-20: Landslide hazard assessment at Super-Sauze catchment. (a) Morpho-structural map. (b) Susceptibility zonation results. (c) Exceedance probability P(N≥1) for 10-year return period (d) Exceedance probability of landslide areal evolution for 10-year return period.

4.5.2.3. Poche catchment

The complex and active Poche mudslide (see Fig. 2-17 and 2-18; § 2.3.4) is located in the catchment of the Poche torrent between 1500 m and 1250 m (Fig. 4-21a). Several active, dormant and relict landslides surround it. They are often observed in marl deposits covered by a morainic layer. The susceptibility map surprisingly shows low probability to the ablation and accumulation areas of the Poche landslide (yellow SLUs; Fig. 4-21b) while the probability is moderated outside the landslide boundaries. Uphill, some high susceptible SLUs are observed where active (e.g. elevations: 1550-

1600 m) and relict landslides are located. It is interesting to see that almost all the SLUs with high susceptibility have a very high exceedance probability in this area (Fig. 4-21c). In the ablation and accumulation areas of the Poche landslide, the exceedance probability is also moderate while outside it might be high to very high. The Poche landslide has had three major reactivations with size enlargement, and the last one between 1982 and 1995, was more than 22,000 m^2 large. The combination of temporal exceedance probability with a size threshold (Fig. 4-21d) shows some SLUs of moderate probability to be affected by a landslide ≥ 500 m^2 over the next 10 years at higher and lower altitudes. The small SLUs size (e.g. ablation and accumulation zones) has definitely a huge effect on the calculation of exceedance probability according to a size threshold.

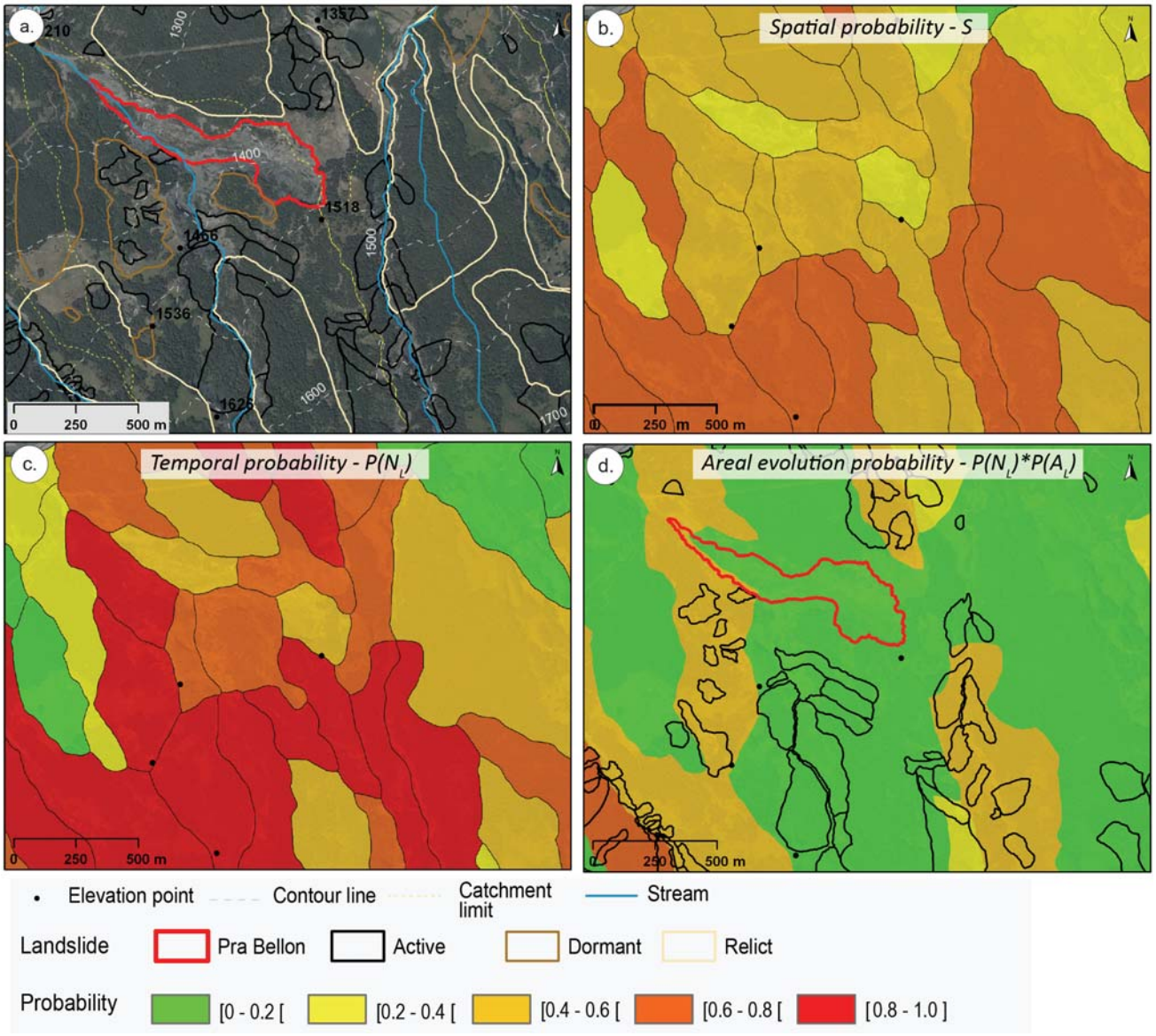

Figure 4-21: Landslide hazard assessment at Poche catchment. (a) Morpho-structural map. (b) Susceptibility zonation results. (c) Exceedance probability P(N≥1) for 10-year return period (d) Exceedance probability of landslide areal evolution for 10-year return period.

4.5.2.4. Sanières catchment

Located in the lower part of the Sanières catchment, between 1500 m and 1650 m (Fig. 4-22a), the Sanières rockslide has been triggered in August 2014 (see Fig. 2-10; § 2.3.4). As shown in the morpho-structural map, this area is intensively affected by faults which can be one predisposing factor to this

type of landslides. Some small landslides are observed at the right side of the torrential channel as well as some dormant landslides.

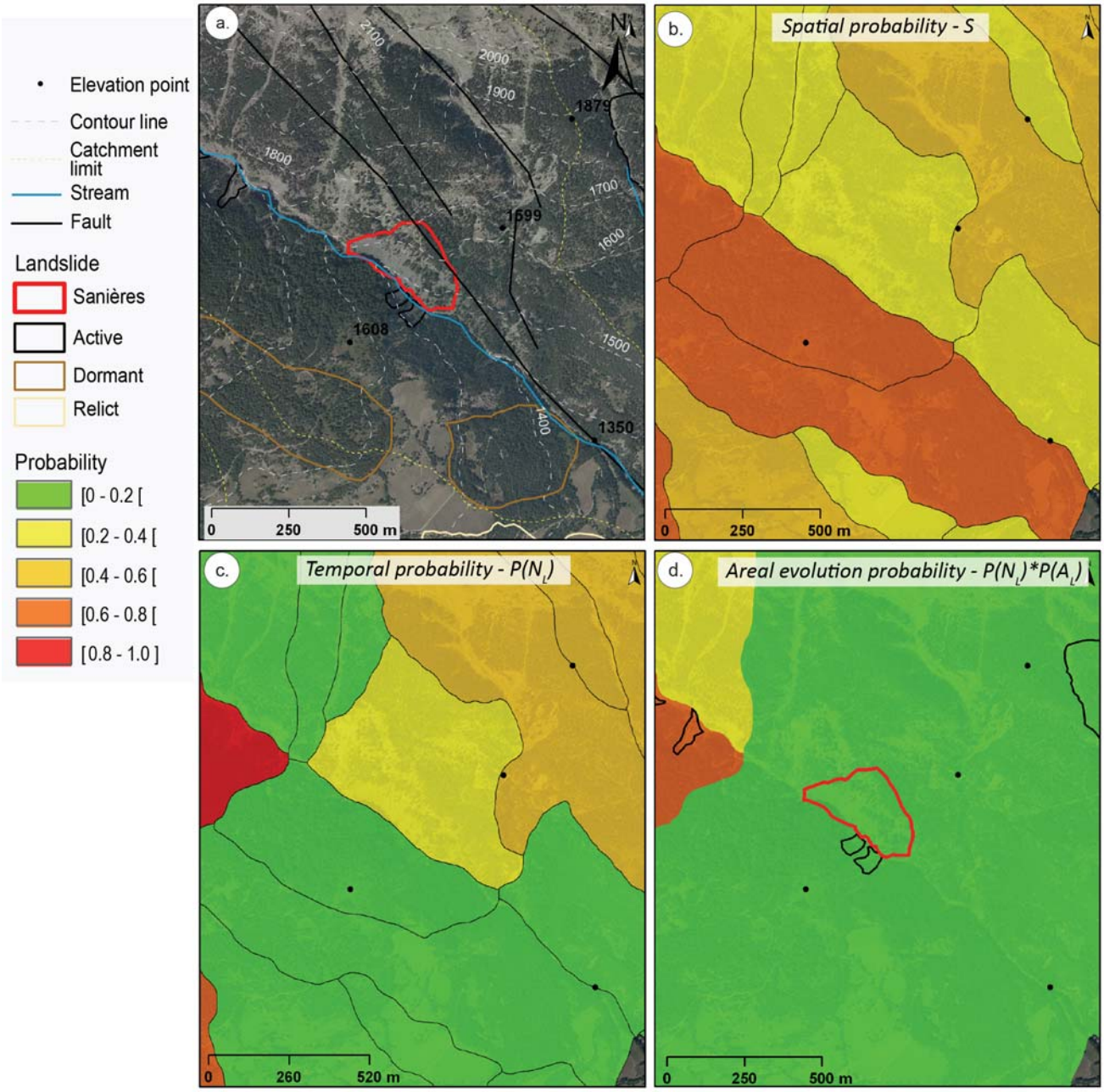

Figure 4-22: Landslide hazard assessment at Sanières catchment. (a) Morpho-structural map. (b) Susceptibility zonation results. (c) Exceedance probability P(N≥1) for 10-year return period (d) Exceedance probability of landslide areal evolution for 10-year return period.

In Figure 4-22b, we see that the landslide susceptible map presents surprisingly high susceptible class to the right side while the left side (where the Sanières landslide has been occurred) has a low susceptible class. This means that the predisposing conditions were not optimal for landslide triggering and also that an important meteorological or seismic event have been the cause of this landslide.

The combination of temporal exceedance probability with a size threshold shows upstream only one SLU of high probability to be affected by a landslide larger than 500 m^2 over the next 10 years (Fig. 4-22d). This is mainly due to its large size and the numerous shallow landslides occurring along the riverbank. As for the Super-Sauze landslide, the very low probability of SLUs is due to the fact that the

number of reactivations is not considered in the calculation while SLUs affected by many landslides has a real impact on exceedance probability.

4.6. Discussion

A comprehensive landslide susceptibility mapping can help stakeholders to assess the slope stability for hazard management and land-use planning. Despite the substantial research done on landslide susceptibility mapping using statistical methods during last two decades, geotechnical and physically-based susceptibility models still represent better the actual field conditions. The generalisations commonly adopted in the statistical landslide susceptibility method and the underlying assumptions make the output less reliable mainly due to the complexities of landslide controlling factors. However, the preliminary results of the LR used in this study as multivariate statistical analysis tool gave satisfactory results. Although an optimization of the considered parameters and additional data (e.g. soil thickness) would increase the performance of the model, an accuracy of ~78-79% has been estimated. As suggested before, another possibility would have been to test a LR at a pixel-based and analyse if the results are more relevant.

According to the environmental conditions and the landslide properties, temporal probability function of size threshold is difficult to assess statistically. The effect of SLU size is a major factor to consider as well as the really few new landslide events over the last 50 years. In this research study a size threshold of 500 m^2 was considered. Another possibility to analyse the hazard would have been to consider a larger threshold. For instance, it can be chosen in function of the lower size evolution of the three active landslides depicted in Table 4-9 (e.g. 5,000 m^2). The exceedance probability for a given landslide magnitude has to be analysed according to the size threshold but in our study area, as the number of active landslide is low, the temporal probability (of landslide reactivation) will always be underestimated. Unfortunately, this statistical law does not allow us to study large reactivations. Indeed, area evolution upper 20,000 m^2 (e.g. for Sauze and Poche landslides; Table 4.9) are contained with difficulty in the same mapping unit than the landslide according to the small SLU sizes.

Table 4-10: Landslide area evolution

Landslide area evolution (m^2)	1956-1974	1974-1982	1982-1995	1995-2000	2000-2004	2004-2009
Sauze	85,346	14,477	20,156	0	1,379	4,177
Poche	9,320	6,103	22,233	0	0	0
Sanières	650	0	2,785	0	0	4,129

At this stage, we imagine three possibilities to improve the reliability of the results making them more consistent to the field conditions. The first option could be to enlarge the size of the mapping units. The effect will be to increase the number of small active landslides inside and thus, the exceedance probability considering a particular threshold. However, a coarser spatial resolution of the mapping unit may not be justified for risk mapping according to the PPRN approach. Another option to consider the intensity in hazard assessment is to estimate exceedance probability based on square metres (corresponding to landslide) per year. However, this velocity parameter has never been used in statistical analysis of (slow-moving) slides and thus, we cannot predict a good accuracy of the results. Finally, the combination of probability of occurrence with physically based run out models (with debris volumes and/or velocity) is a non-negligible option. However, this kind of analysis is scale-dependant and we have proved in this analysis that getting precise information at regional scale is a tedious and time-consuming task.

General Conclusion

This research demonstrated the interest of combining multi-source data and techniques for landslide analysis at different spatial and temporal scales. Ground-based and remote sensing techniques were applied to detect and monitor various landslide types. Statistical analyses were used to characterize the observed events and estimate landslide hazard for different time periods. According to their types and the environmental conditions, landslide can be active for very short- to very long periods. This work investigated how a combination of methods is relevant for the creation of multi-date landslide inventories. The main objectives of the research were:

- to update existing landslide inventory maps of the Ubaye valley and create a **multi-date landslide database** from the visual interpretation of time series of aerial photographs, geomorphological maps, historical reports, field surveys and SAR images;
- to characterize the **spatial and temporal occurrences** (displacement pattern, geomorphological evolution) and the **intensity** of the phenomena;
- to identify relations among landslide predisposing factors and landslide locations using statistical multivariate models, and propose a quantitative hazard assessment in a probabilistic framework.

The methods have been developed at the **slope (1:5,000-1:2,000)** and the **regional (1:25,000-1:10,000) scales,** and the analysis covers the period from 1850 to 2010 but most of the geospatial data used are for the period 1950-2010. The main study site if the middle section of the Ubaye valley (Barcelonnette Basin), and includes one case study in the Tinée valley.

Considering the diversity of modern remote sensing systems and image processing techniques as well as the different hazard assessment approaches, a review of the State-of-the-Art for landslide analysis is proposed in **Chapter 1**. The review provides key definitions and concepts used for the recognition of landslides and the methodology for hazard assessment.

The **Chapter 2** aims at presenting the geographical, geomorphological and geological characteristics of the study area. The natural hazards observed in the region are presented with a focus on some local hotspots affected by active landslides.

Landslide inventories are the basis of hazard and risk assessment. In the framework of this research, advanced remote sensing techniques (e.g. InSAR) and traditional mapping techniques (e.g. image interpretation, field surveys) have been used. Despite some limitations, InSAR is a cost-efficient and adaptable remote sensing technology able to complement standards methods. The creation of a multi-date landslide inventory from the analysis of multi-source, multi-scalar and multi-temporal data are presented in **Chapter 3**. The kinematics and spatio-temporal distribution of the landslides were analysed at different scales.

In the first section of Chapter 3, L-band **SAR images** (from 2007 to 2010) are used in order to **monitor the displacement patterns of large landslides** at the **slope-scale**. A classical D-InSAR processing chain was used for the creation of the interferograms, phase filtering and phase unwrapping. The wrapped and unwrapped phase values allowed us to detect displacement patterns of complex and active landslides (La Valette, Poche and La Clapière landslides). The **geomorphologically-guided methodology** proposed an interpretation of the InSAR signatures according to different deformation modes. Indeed, positive phase values (displacement away from the satellite) indicate the ablation zones characterised by a predominant vertical displacement (subsidence) while negative phase values (displacement towards the satellite) identify the transit and accumulation zones with displacement mainly along the slope and thus, with a predominant horizontal component. Even at slope-scale the phase unwrapping processing was a difficult task for analysing important deformation (i.e. > 0.4 $cm.day^{-1}$) in mountainous environment with dense vegetation cover and changing meteorological conditions. However, **changes in velocity fields** have been estimated and validated in comparison to ground-based measurements. The development of a geomorphologically-guided methodology for analysing unwrapped interferometric phase has proved its effectiveness but also showed limitations in terms of maximum detected velocity (depending of sensor wavelength). When relevant unwrapping was not possible, the wrapped phase gave us interesting information about the influence of geological structures on the deformation patterns.

The second section of Chapter 3 details the methodology to **prepare a multi-date inventory at regional-scale from the interpretation of various datasets**. Several **landslide descriptors** have been used to document the landslide location and evolution in space and time. Comparative analysis of various datasets is mandatory to create a complete multi-date inventory map. Assuming that all **relict, dormant and active landslides** were mapped, the multi-date inventory is analysed statistically on the several sub-periods and sub-regions of the study area. The comparison of (re)activations counts recorded in the multi-date inventory with punctual events recorded in the field by local risk managers (RTM) and other geoscientists (e.g. by dendrochronology) shows some discrepancies due to the spatial and temporal scales of analysis. For instance, **periods of landslide activity** were not determined at the same dates with the different techniques. Determining the landslide triggers depends on the landslide properties and the meteorological conditions (either short and intense or continuous). **Frequency-area density functions** indicate different distributions according to the location, geology and level of activity of the landslides. The estimation of **temporal occurrence of landslide** re**activations** with a Poisson probability model allowed us to compute exceedance probabilities of having at least one event over different return periods.

The **Chapter 4** forecasts the landslide susceptibility and hazard for the Ubaye valley using several spatial units of calculation. A methodology to delineate the regions of interest into appropriate terrain units was proposed and tested. The partitioning method aims to **divide the half-basins into units according to a size threshold** (threshold between 50,000 m^2 and 80,000 m^2) **and identical geomorphological properties**. The purpose was to provide small slope and terrain units in order to test the impact of several DTM resolutions on the statistics of the terrain units. Spatial and temporal probabilities of landslide occurrence are then computed using statistical models. A **logistic regression model** was used to evaluate susceptibility zonation (S) for both the landslide source areas and the whole landslide bodies. The results obtained with terrain units gave not relevant results (many false negative) and a strong influence of the elevation variable (which is possibly redundant with some geotypes). The **landslide susceptibility zonation gives good landslide prediction** and less false negative with slope-units using an area threshold of 2% to eliminate small parts of landslides falling in the large mapping units and considering the entirety of the landslides body instead of only the depletion area as dependant variable. However, the logistic regression attributes very high probability values to a very small number of slope-units (2.1%), contrary to what might have been expected. An accuracy of ~78-79% was estimated but an optimization of the input parameters (removing of elevation variable) and additional data (such as soil thickness) would increase the performance of the model. $P(N_L)$ was computed by counting the **number of events occurring into a mapping unit for the period of analysis**. It shows a dissymmetric distribution due to the fact that large parts of the valley

were not affected by landslides during this period. On the basis of the multi-date inventory giving us information on landslide evolution (increase in size), the new size of each active landslide was delimited in each terrain unit for each period of analysis. In order to estimate the **probability of having a landslide of a given magnitude**, a size threshold *(A_L)* of 500 m^2 is chosen. This areal evolution threshold was chosen consistently from the visual detection of evolution threshold on the orthophotographs. Finally, a landslide hazard analysis is proposed for particular hotspots characterized by active landslides (Pra-Bellon, Sauze, Poche and Sanières). According to the susceptibility zonation, only the Pra-Bellon landslide was located in high susceptibility class while the others are in slope-units of moderate or low hazard, partially due to the **effect of small slope-unit size** (leading to an artificially small number of events falling inside them).

Perspectives of improvement are proposed to modify the mapping unit into another delineation of slope units (larger size) or grid-cells. As multivariate analysis performances are limited, physically-based susceptibility models could be used because they are more suitable to explain the sliding response to the actual field conditions at slope-scale. However, they need lots of data to characterize the mechanical and environmental slope parameters and are not easily applicable at regional scale. Another improvement could assess the hazard by considering the landslide magnitude in terms of yearly relative evolution of the total sliding area (exceedance probability of having a given portion of the mapping unit hit by landslides) or the yearly evolution of the run out length.

Bibliography

Ai, N.S., Miao, T.D., 1987. A model of progressive slope failure under the effect of the neotectonic stress field. Catena Supplement 10, 21–29.

Aleotti, P., Chowdhury, R.N., 1999. Landslide hazard assessment: summary review and new perspectives. Bulletin of Engineering Geology and the Environment 58, 21–44. doi:10.1007/s100640050066

Alvioli, M., Ardizzone, F., Guzzetti, F., Marchesini, I., Rossi, M., 2014. Non-susceptible landslide areas in Italy and in the Mediterranean Region, in: Geophysical Research Abstracts. Vienna, Austria, 27 April - 2 May 2014, pp. EGU2014–6846.

Amadesi, E., Vianello, G., 1978. Nuova guida alla realizzazione di una carta di stabilità dei versanti. Memorie della Societa Geologica Italiana 19, 53–60.

Antoine, P., 1977. Réflexions sur la cartographie ZERMOS et bilan des expériences en cours. Bulletin du Bureau des Recherches Géologiques et Minières 3, 9–20.

Antoine, P., Giraud, A., Meunier, M., van Asch, T.W.J., 1995. Geological and geotechnical properties of the "Terres Noires" in southeastern France: weathering, erosion, solid transport and instability. Engineering Geology 40, 223–234. doi:10.1016/0013-7952(95)00053-4

Ardizzone, F., Cardinali, M., Carrara, A., Guzzetti, F., Reichenbach, P., 2002. Uncertainty and errors in landslide mapping and landslide. Natural Hazards and Earth System Sciences 2, 3–14. doi:10.5194/nhess-2-3-2002

Atkinson, P.M., Massari, R., 1998. Generalised linear modelling of susceptibility to landsliding in the Central Apennines, Italy. Computers & Geosciences 24, 373–385. doi:10.1016/S0098-3004(97)00117-9

Ayalew, L., Yamagishi, H., 2005. The application of GIS-based logistic regression for landslide susceptibility mapping in the Kakuda-Yahiko Mountains, Central Japan. Geomorphology 65, 15–31. doi:10.1016/j.geomorph.2004.06.010

Ayalew, L., Yamagishi, H., Marui, H., Kanno, T., 2005. Landslides in Sado Island of Japan: part II. GIS-based susceptibility mapping with comparisons of results from two methods and verifications. Engineering Geology 81, 432–445. doi:10.1016/j.enggeo.2005.08.004

Baillargeon, S., 2005. Le krigeage : revue de la théorie et application à l'interpolation spatiale de données de précipitations. Mémoire de Maîtrise es Sciences de la Facultré des Etudes Supérieures de l'Université de Laval.

Baldi, P., Cenni, N., Fabris, M., Zanutta, A., 2008. Kinematics of a landslide derived from archival photogrammetry and GPS data. Geomorphology 102, 435–444. doi:10.1016/j.geomorph.2008.04.027

Baldo, M., Bicocchi, C., Chiocchini, U., Giordan, D., Lollino, G., 2009. Geomorphology LIDAR monitoring of mass wasting processes: the Radicofani landslide, Province of Siena, Central Italy. Geomorphology 105, 193–201. doi:10.1016/j.geomorph.2008.09.015

Bălteanu, D., Chendeș, V., Sima, M., Enciu, P., 2010. A country-wide spatial assessment of landslide susceptibility in Romania. Geomorphology 124, 102–112. doi:10.1016/j.geomorph.2010.03.005

Banai, R., 1993. Fuzziness in geographical information systems: contributions from the analytic hierarchy process. International Journal of Geographical Information Systems 7, 315–329. doi:10.1080/02693799308901964

Barredo, J.I., Benavides, A., Hervás, J., van Westen, C.J., 2000. Comparing heuristic landslide hazard assessment techniques using GIS in the Tirajana basin, Gran Canaria Island, Spain. International Journal of Applied Earth Observation and Geoinformation 2, 9–23. doi:10.1016/S0303-2434(00)85022-9

Baum, R.L., Schuster, R.L., Godt, J.W., 1999. Map showing locations of damaging landslides in Santa Cruz County, California, resulting from 1997 to 98 El Nino rainstorms. U.S. Geological Survey Miscellaneous Field Studies Map, MF-2325-D, scale 1:125,000.

Baynes, F.J., Lee, E.M., 1998. Geomorphology in landslide risk analysis, an interim report, in: Moore, P., Hungr, O. (Eds.), Proc.8th Congress of the Int. Assoc. Eng. Geologists. Balkema, pp. 1129–1136.

Berardino, P., Fornaro, G., Lanari, R., Member, S., Sansosti, E., 2002. A new algorithm for surface deformation monitoring based on small baseline differential SAR interferograms. IEEE Transactions on Geoscience and Remote Sensing 40, 2375–2383. doi:10.1109/TGRS.2002.803792

Bernknopf, R.L., Cambell, R.H., Brookshire, D.S., Shapiro, C.D., 1988. A probabilistic approach to landslide hazard mapping in Cincinnati, Ohio, with applications for economic evaluation. Bulletin of the International Association of Engineering Geology 25, 39–56.

Blahut, J., van Westen, C.J., Sterlacchini, S., 2010. Analysis of landslide inventories for accurate prediction of debris-flow source areas. Geomorphology 119, 36–51. doi:10.1016/j.geomorph.2010.02.017

Blanchard, R., 1950. Les grandes Alpes françaises du Sud. Tome V : les Alpes Occidentales, Arthaud. ed. Grenoble.

Booth, A.M., Lamb, M.P., Avouac, J.-P., Delacourt, C., 2013. Landslide velocity, thickness, and rheology from remote sensing: La Clapière landslide, France. Geophysical Research Letters 40, 4299–4304. doi:10.1002/grl.50828

Bovenga, F., Wasowski, J., Nitti, D.O., Nutricato, R., Chiaradia, M.T., 2012. Using COSMO / SkyMed X-band and ENVISAT C-band SAR interferometry for landslides analysis. Remote Sensing of Environment 119, 272–285. doi:10.1016/j.rse.2011.12.013

Braam, R.R., Weiss, E.E.J., Burrough, P.A., 1987. Spatial and temporal analysis of mass movement using dendrochronology. Catena 14, 573–584. doi:10.1016/0341-8162(87)90007-5

Brabb, E.E., Wieczorek, G.F., Harp, E.L., 1989. Map showing 1983 landslides in Utah. U.S. Geological Survey Miscellaneous Field Studies Map MF-1867.

Brand, E.W., 1988. Special lecture: landslide risk assessment in Hong Kong, in: Proceedings 5th International Symposium on Landslides, Vol. 2. Lausanne, pp. 1059–1074.

Breinl, K., Turkington, T., Stowasser, M., 2013. Stochastic generation of multi-site daily precipitation for applications in risk management. Journal of Hydrology 498, 23–35. doi:10.1016/j.jhydrol.2013.06.015

Brunetti, M.T., Guzzetti, F., Rossi, M., 2009. Probability distributions of landslide volumes. Nonlinear Processes in Geophysics 16, 179–188. doi:10.5194/npg-16-179-2009

Brunsden, D., 1985. Landslide types, mechanisms, recognition, identification, in: Morgan, C.S. (Ed.), Landslides in the South Wales Coalfield. Proceedings Symposium, April 1–3, The Polytechnic of Wales, pp. 19–28.

Brunsden, D., 1993. Mass movement; the research frontier and beyond: a geomorphological approach. Geomorphology 7, 85–128. doi:10.1016/0169-555X(93)90013-R

Buma, J., 2000. Finding the most suitable slope stability model for the assessment of the impact of climate change on a landslide in Southeast France. Earth Surface Processes and Landforms 25, 565–582.

Calò, F., Ardizzone, F., Castaldo, R., Lollino, P., Tizzani, P., Guzzetti, F., Lanari, R., Angeli, M.-G., Pontoni, F., Manunta, M., 2014. Enhanced landslide investigations through advanced DInSAR techniques: the Ivancich case study, Assisi, Italy. Remote Sensing of Environment 142, 69–82. doi:10.1016/j.rse.2013.11.003

Campbell, R.H., 1973. Isopleth map of landslide deposits, Point Dume quadrangle, Los Angeles County, California, an experiment in generalizing and quantifying areal distribution of landslides: U.S. Geological Survey Miscellaneous Field Studies Map MF-535, scale 1:24,000.

Can, T., Nefeslioglu, H.A., Gokceoglu, C., Sonmez, H., Duman, T.Y., 2005. Susceptibility assessments of shallow earthflows triggered by heavy rainfall at three subcatchments by logistic regression analyses. Geomorphology 72, 250–271.

Canuti, P., Casagli, N., 1996. Considerazioni sulla valutazione del rischio dei frana. Estratto da "Fenomeni Franosi e Centri Abitati," in: Atti Del Convegno Di Bologna Del 27 Maggio 1994. CNR-GNDCI-Linea 2 "Previsione E Prevenzione Di Eventi Granosi a Grande Rischio". Pubblicazione No. 846. p. 61.

Canuti, P., Casagli, N., Ermini, L., Fanti, R., Farina, P., 2004. Landslide activity as a geoindicator in Italy: significance and new perspectives from remote sensing. Environmental Geology 45, 907–919.

Cardinali, M., Antonini, G., Reichenbach, P., Guzzetti, F., 2001. Photo geological and landslide inventory map for the Upper Tiber River basin. CNR, Gruppo Nazionale per la Difesa dalle Catastrofi Idrogeologiche, Publication n. 2116, scale 1:100,000.

Cardinali, M., Ardizzone, F., Galli, M., Guzzetti, F., Reichenbach, P., 2000. Landslides triggered by rapid snow melting: the December 1996–January 1997 event in Central Italy, in: Claps, P., Siccardi, F. (Eds.), Proceedings 1st Plinius Conference, Maratea. Bios Publisher, Cosenza, pp. 439–448.

Cardinali, M., Galli, M., Ardizzone, F., Reichenbach, P., Guzzetti, F., 2004. Analysis of landslide occurrence in the Collazzone Area, central Umbria, Italy. Geophysical Research Abstracts 6, 02792.

Cardinali, M., Galli, M., Guzzetti, F., Ardizzone, F., Reichenbach, P., Bartoccini, P., 2006. Rainfall induced landslides in December 2004 in south-western Umbria, central Italy: types, extent, damage and risk assessment. Natural Hazards and Earth System Sciences 6, 237–260. doi:10.5194/nhess-6-237-2006

Cardinali, M., Guzzetti, F., Brabb, E.E., 1990. Preliminary map showing landslide deposits and related features in New Mexico, 4 sheets, scale 1:500,000.

Cardinali, M., Reichenbach, P., Guzzetti, F., Ardizzone, F., Antonini, G., Galli, M., Cacciano, M., Castellani, M., Salvati, P., 2002. A geomorphological approach to the estimation of landslide hazards and risks in Umbria, Central Italy. Natural Hazards and Earth System Sciences 2, 57–72. doi:10.5194/nhess-2-57-2002

Cardona, O.D., Hurtado, J.E., Duque, G., Moreno, A., Chardon, A.C., Velásquez, L.S., Prieto, S.D., 2003. The notion of disaster risk. Conceptual framework for integrated risk management.

Caris, J.P.T., Van Asch, T.W.J., 1991. Geophysical, geotechnical and hydrological investigations of a small landslide in the French Alps. Engineering Geology 31, 249–276. doi:10.1016/0013-7952(1)90011-9

Carrara, A., 1983. Multivariate models for landslide hazard evaluation. Journal of the International Association for Mathematical Geology 15, 403–426. doi:10.1007/BF01031290

Carrara, A., 1993. Uncertainty in evaluating landslide hazard and risk, in: Nemec, J., Nigg, J.M., Siccardi, F. (Eds.), Prediction and Perception of Natural Hazards SE - 12, Advances in Natural and Technological Hazards Research. Springer Netherlands, pp. 101–109. doi:10.1007/978-94-015-8190-5_12

Carrara, A., Cardinali, M., Detti, R., Guzzetti, F., Pasqui, V., Reichenbach, P., 1990. Geographical information systems and multivariate models in landslide hazard evaluation, in: ALPS 90 Alpine Landslide Practical Seminar, Sixth International Conference and Field Workshop on Landslides, Aug 31–Sept 12, Milan, Italy. Università degli Studi de Milano, pp. 17–28.

Carrara, A., Cardinali, M., Detti, R., Guzzetti, F., Pasqui, V., Reichenbach, P., 1991. GIS techniques and statistical models in evaluating landslide hazard. Earth Surface Processes and Landforms 16, 427–445. doi:10.1002/esp.3290160505

Carrara, A., Cardinali, M., Guzzetti, F., 1992. Uncertainty in assessing landslide hazard and risk. ITC Journal 2, 172–183.

Carrara, A., Cardinali, M., Guzzetti, F., Reichenbach, P., 1995. GIS technology in mapping landslide hazard, in: Carrara, A., Guzzetti, F. (Eds.), Assessing Natural Hazards. Kluwer Academic Publishers, Dordrecht, pp. 135–176.

Carrara, A., Catalano, E., Soriso Valvo, M., Reali, C., Osso, I., 1978. Digital terrain analysis for land evaluation. Geol. Appl. ed Idrogeol. 13, 69–127.

Carrara, A., Crosta, G.B., Frattini, P., 2008. Comparing models of debris-flow susceptibility in the alpine environment. Geomorphology 94, 353–378. doi:10.1016/j.geomorph.2006.10.033

Carrara, A., Detti, R., Federici, G., Pasqui, V., 1988. Reticoli idrografici e parametri morfologici di bacino da modelli digitali del terreno. CNR-Linea 3, Gruppo Naz. Difesa Catastrofi Idrogeol., Genova.

Carrara, A., Guzzetti, F., Cardinali, M., Reichenbach, P., 1999. Use of GIS technology in the prediction and monitoring of landslide hazard. Natural Hazards 20, 117–135. doi:10.1023/A:1008097111310

Carrara, A., Pike, R.J., 2008. GIS technology and models for assessing landslide hazard and risk. Geomorphology 94, 257–260. doi:10.1016/j.geomorph.2006.07.042

Carrara, A., Pugliese Caratelli, E., Merenda, L., 1977. Computer-based data bank and statistical analysis of slope instability phenomena. Zeitschrift für Geomorphologie 21, 187–222.

Carver, S.J., 1991. Integrating multi-criteria evaluation with geographical information systems. International Journal of Geographical Information Systems 5, 321–339. doi:10.1080/02693799108927858

Casagli, N., Fanti, R., Nocetini, M., Righini, G., 2005. Assessing the capabilities of VHR satellite data for debris flow mapping in the Machu Picchu area, in: Sassa, K., Fukuoka, H., Wang, F., Wang, G. (Eds.), Landslides: Risk Analysis and Sustainable Disaster Management. Springer, pp. 61–70.

Cascini, L., Bonnard, C., Corominas, J., R, J., Montero-Olarte, J., 2005. Landslide hazard and risk zoning for urban planning and development, in: Hungr, O., Fell, R., Couture, R., Eberthardt, E. (Eds.), Landslide Risk Management. Taylor & Francis, London, pp. 199–235.

Casson, B., 2004. Apports de l'imagerie optique haute résolution pour l'étude 3D des glissements de terrain. Thèse de Doctorat, Université Claude Bernard - Lyon 1.

Casson, B., Delacourt, C., Allemand, P., 2005. Contribution of multi-temporal remote sensing images to characterize landslide slip surface - Application to the La Clapière landslide (France). Natural Hazards and Earth System Sciences 5, 425–437. doi:10.5194/nhess-5-425-2005

Casson, B., Delacourt, C., Baratoux, D., Allemand, P., 2003. Seventeen years of the ''La Clapière" landslide evolution analysed from ortho-rectified aerial photographs. Engineering Geology 68, 123–139. doi:10.1016/S0013-7952(02)00201-6

Castagnetti, C., Bertacchini, E., Corsini, A., Capra, A., 2013. Multi-sensors integrated system for landslide monitoring: critical issues in system setup and data management. European Journal of Remote Sensing 46, 104–124. doi:10.5721/EuJRS20134607

Chacón, J., Corominas, J., 2003. Special issue on landslides and GIS. Natural Hazards 30, 263–499. doi:10.1023/B:NHAZ.0000007387.21450.3c

Champatiray, P., 2000. Perationalization of cost-effective methodology for landslide hazard zonation using RS and GIS: IIRS initiative, in: Roy, P., van Westen, C.J., Jha, V., Lakhera, R. (Eds.), Natural Disasters and Their Mitigation; Remote Sensing and Geographical Information System Perspectives. Indian Institute of Remote Sensing, Dehradun, India, pp. 95–101.

Charlier, C., Decrop, G., 1997. De l'expertise scientifique au risque négocié : le cas du risque en montagne, Cemagref. ed.

Cheng, K.S., Wei, C., Chang, S.C., 2004. Locating landslides using multi-temporal satellite images. Advances in Space Research 33, 296–301. doi:10.1016/S0273-1177(03)00471-X

Chowdhury, R.N., 1976. Mechanism of natural slope failures in the Greater Wollongong area of New South Wales. Search 7, 396–397.

Chung, C.F., Fabbri, A.G., van Westen, C.J., 1995. Multivariate regression analysis for landslide hazard zonation, in: Carrara, A., Guzzetti, F. (Eds.), Geographic Information Systems in Assessing Natural Hazards. Kluwer, Dordrecht, pp. 107–133. doi:10.1007/978-94-015-8404-3_7

Ciampalini, A., Bardi, F., Bianchini, S., Frodella, W., Del Ventisette, C., Moretti, S., Casagli, N., 2014. Analysis of building deformation in landslide area using multisensor PSInSAR™ technique. International Journal of Applied Earth Observation and Geoinformation 33, 166–180. doi:10.1016/j.jag.2014.05.011

Clerici, A., Perego, S., Tellini, C., Vescovi, P., 2002. A procedure for landslide susceptibility zonation by the conditional analysis method. Geomorphology 48, 349–364. doi:10.1016/S0169-555X(02)00079-X

Coe, J.A., Michael, J.A., Crovelli, R.A., Savage, W.Z., 2000. Preliminary map showing landslide densities, mean recurrence intervals, and exceedance probabilities as determined from historic records, Seattle, Washington. USGS Open-File Report 00-0303.

Colesanti, C., Ferretti, A., Prati, C., Rocca, F., 2003. Monitoring landslides and tectonic motions with the Permanent Scatterers Technique. Engineering Geology 68, 3–14. doi:10.1016/S0013-7952(02)00195-3

Colesanti, C., Wasowski, J., 2006. Investigating landslides with space-borne Synthetic Aperture Radar (SAR) interferometry. Engineering Geology 88, 173–199. doi:10.1016/j.enggeo.2006.09.013

Corominas, J., 2000. Landslides and climate, in: Bromhead, E.N., Dixon, N., Ibsen, M.-L. (Eds.), Landslides in Research, Theory and Practice; Proc. 8th Intern. Symp. on Landslides, Cardiff, 26-30th June 2000. London: Thomas Telford, London.

Corominas, J., Leroi, E., Savage, W.Z., Moya, J., 2008. A review of assessing landslide frequency for hazard zoning purposes. Engineering Geology 102, 193–213.

Corominas, J., Moya, J., 2010. Contribution of dendrochronology to the determination of magnitude–frequency relationships for landslides. Geomorphology 124, 137–149. doi:10.1016/j.geomorph.2010.09.001

Corominas, J., van Westen, C.J., Frattini, P., Cascini, L., Malet, J.-P., Fotopoulou, S., Catani, F., Eeckhaut, M., Mavrouli, O., Agliardi, F., Pitilakis, K., Winter, M.G., Pastor, M., Ferlisi, S., Tofani, V., Hervás, J., Smith, J.T., 2014. Recommendations for the quantitative analysis of landslide risk. Bulletin of Engineering Geology and the Environment 73, 209–263. doi:10.1007/s10064-013-0538-8

Corona, C., Lopez-Saez, J., Stöffel, M., 2014. Defining optimal sample size, sampling design and thresholds for dendrogeomorphic landslide reconstructions. Quaternary Geochronology 22, 72–84. doi:10.1016/j.quageo.2014.02.006

Cox, D.R., 1958. The regression analysis of binary sequences. Journal of the Royal Statistical Society. Series B (Methodological) 20, 215–242. doi:10.2307/2983890

Crovelli, R.A., 2000. Probability models for estimation of number and costs of landslides. U.S. Geological Survey Open File Report 00-249.

Crozier, M.J., 1986. Landslides: causes, consequences and environment. Croom Helm.

Crozier, M.J., 1996. Magnitude/frequency issues in landslide hazard assessment, in: R, M., Schulte, A. (Eds.), Beitrage Zur Physiogeographie. Barsch Festschrift, Heidelberger Geographische Arbeiten. Heft 104. pp. 221–236.

Crozier, M.J., Glade, T., 2005. Landslide hazard and risk: issues, concepts and approach, in: Glade, T., Anderson, M.G., Crozier, M.J. (Eds.), Landslide Hazard and Risk. Chichester, pp. 1–40.

Cruden, D.M., 2003. Landslide in the thick loess terrain of North-West China. Geomorphology 49, 172–173. doi:10.1016/S0169-555X(02)00162-9

Cruden, D.M., Varnes, D.J., 1996. Landslide types and processes, in: Turner, A.K., Schuster, R.L. (Ed.), Landslides-Investigations and Mitigation. Washington D.C, pp. 36–75.

Czuchlewski, K.R., Weissel, J.K., Kim, Y., 2003. Polarimetric synthetic aperture radar study of the Tsaoling landslide generated by the 1999 Chi-Chi earthquake, Taiwan. Journal of Geophysical Research: Earth Surface 108, 6006. doi:10.1029/2003JF000037

Dai, F.., Lee, C.., 2002. Landslide characteristics and slope instability modeling using GIS, Lantau Island, Hong Kong. Geomorphology 42, 213–228. doi:10.1016/S0169-555X(01)00087-3

Dai, F.C., Lee, C.F., Li, J., Xu, Z.W., 2001. Assessment of landslide susceptibility on the natural terrain of Lantau Island, Hong Kong. Environmental Geology 40, 381–391. doi:10.1007/s002540000163

Dai, F.C., Lee, C.F., Ngai, Y.Y., 2002. Landslide risk assessment and management: an overview, Engineering Geology. doi:10.1016/S0013-7952(01)00093-X

Daniel, G., Prono, E., Renard, F., Thouvenot, F., Hainzl, S., Marsan, D., Helmstetter, A., Traversa, P., Got, J.L., Jenatton, L., Guiguet, R., 2011. Changes in effective stress during the 2003–2004 Ubaye seismic swarm, France. Journal of Geophysical Research 116, B01309. doi:10.1029/2010JB007551

Das, I., Sahoo, S., van Westen, C.J., Stein, A., Hack, R., 2010. Landslide susceptibility assessment using logistic regression and its comparison with a rock mass classification system, along a road section in the northern Himalayas (India). Geomorphology 114, 627–637. doi:10.1016/j.geomorph.2009.09.023

Davis, W.M., 1899. The geographic cycle. The Geographical Journal 14, 481–504. doi:10.2307/1774538

De Vita, P., Reichenbach, P., Bathurst, J.C., Borga, M., Crozier, G.M., Glade, T., Guzzetti, F., Hansen, A., Wasowski, J., 1998. Rainfall-triggered landslides: a reference list. Environmental Geology 35, 219–233. doi:10.1007/s002540050308

Debella-Gilo, M., Kääb, A., 2012. Measurement of surface displacement and deformation of mass movements using least squares matching of repeat high resolution satellite and aerial images. Remote Sensing 4, 43–67. doi:10.3390/rs4010043

Debelmas, J., Escher, A., Trumpy, R., 1983. Profiles through the western Alps, in: Profile of Orogenic Belts, Geodyn. Ser. AGU, Washington, DC, pp. 83–96. doi:10.1029/GD010p0083

DeGraff, J. V, 1985. Using isopleth maps of landslide deposits as a tool in timber sale planning. Bulletin Association of Engineering Geologists 22, 445–453.

DeGraff, J. V, Canuti, P., 1988. Using isopleth mapping to evaluate landslide activity in relation to agricultural practices. Bulletin of the International Association of Engineering Geology 38, 61–71. doi:10.1007/BF02590449

Dehn, M., Buma, J., 1999. Modelling future landslide activity based on general circulation models. Geomorphology 30, 175–187. doi:10.1016/S0169-555X(99)00053-7

Delacourt, C., Allemand, P., Berthier, E., Raucoules, D., Casson, B., Grandjean, P., Pambrun, C., Varel, E., 2007. Remote-sensing techniques for analysing landslide kinematics: a review. Bulletin de la Société Géologique de France 178, 89–100. doi:10.2113/gssgfbull.178.2.89

Delacourt, C., Allemand, P., Casson, B., Vadon, H., 2004. Velocity field of the "La Clapière" landslide measured by the correlation of aerial and QuickBird satellite images. Geophysical Research Letters 31, L15619. doi:10.1029/2004GL020193

Delacourt, C., Raucoules, D., Le Mouélic, S., Carnec, C., Feurer, D., Allemand, P., Cruchet, M., 2009. Observation of a large landslide on La Reunion Island using differential SAR interferometry (JERS and Radarsat) and correlation of optical (Spot5 and aerial) images. Sensors 9, 616–630. doi:10.3390/s90100616

Delsigne, F., Lahousse, P., Flez, C., Guiter, G., 2001. Le Riou-Bourdoux : un "monstre" alpin sous haute surveillance. Revue Forestière Française 53, 527–541. doi:10.4267/2042/5269

Dewitte, O., Jasselette, J.-C., Cornet, Y., van den Eeckhaut, M., Collignon, A., Poesen, J., Demoulin, A., 2008. Tracking landslide displacements by multi-temporal DTMs: a combined aerial stereophotogrammetric and LIDAR approach in western Belgium. Engineering Geology 99, 11–22. doi:10.1016/j.enggeo.2008.02.006

Dietrich, W.E., Bellugi, D., Real de Asua, R., 2001. Validation of the shallow landslide model, SHALSTAB, for forest management, in: Wigmosta, M.S., Burges, S.J. (Eds.), Land Use and Watersheds: Human Influence on Hydrology and Geomorphology in Urban and Forest Areas: American Geophysical Union, Water Science and Applications, 2. pp. 195–227.

Dietrich, W.E., Reiss, R., Hsu, M.-L., Montgomery, D.R., 1995. A process-based model for colluvial soil depth and shallow landsliding using digital elevation data. Hydrological Processes 9, 383–400. doi:10.1002/hyp.3360090311

Dikau, R., Brunsden, D., Schrott, L., Ibsen, M.-L., 1996. Landslide recognition: identification, movement and causes, Wiley. ed. Chichester.

Ducret, G., Doin, M.-P., Grandin, R., Lasserre, C., Guillaso, S., 2011. DEM corrections before unwrapping in a small baseline strategy for InSAR time series analysis, in: Geoscience and Remote Sensing Symposium (IGARSS). IEEE, pp. 1353–1356. doi:10.1109/IGARSS.2011.6049316

Eastman, J.R., 1997. IDRISI for Windows, version 2.0: tutorial exercises. Clark University, Worcester.

Ehlschlaeger, C., 1989. Using the AT search algorithm to develop hydrologic models from digital elevation data, in: Proceedings of International Geographic Information Systems (IGIS) Symposium '89. Batimore, MD, 18-19 March 1989, pp. 275–281.

Ercanoglu, M., 2005. Landslide susceptibility assessment of SE Bartin (West Black Sea region, Turkey) by artificial neural networks. Natural Hazards and Earth System Sciences 5, 979–992. doi:10.5194/nhess-5-979-2005

Evin, M., 1997. Géologie de l'Ubaye. Sapença de la Valeia, Barcelonnette.

Fall, M., Azzam, R., Noubactep, C., 2006. A multi-method approach to study the stability of natural slopes and landslide susceptibility mapping. Engineering Geology 82, 241–263. doi:10.1016/j.enggeo.2005.11.007

Fawcett, T., 2006. An introduction to ROC analysis. Pattern Recognition Letters 27, 861–874. doi:10.1016/j.patrec.2005.10.010

Feizizadeh, B., Blaschke, T., 2012. GIS-multicriteria decision analysis for landslide susceptibility mapping: comparing three methods for the Urmia lake basin, Iran. Natural Hazards 65, 2105–2128. doi:10.1007/s11069-012-0463-3

Fell, R., Corominas, J., Bonnard, C., Cascini, L., Leroi, E., Savage, W.Z., 2008a. Guidelines for landslide susceptibility, hazard and risk zoning for land use planning. Engineering Geology 102, 99–111. doi:10.1016/j.enggeo.2008.03.014

Fell, R., Corominas, J., Bonnard, C., Cascini, L., Leroi, E., Savage, W.Z., 2008b. Guidelines for landslide susceptibility, hazard and risk zoning for land use planning. Engineering Geology 102, 85–98.

Fell, R., Ho, K.K.S., Lacasse, S., Leroi, E., 2005. State of the art paper: a framework for landslide risk assessment and management, in: International Conference on Landslide Risk Management. Vancouver, Canada, p. 23.

Ferretti, A., Fumagalli, A., Novali, F., Prati, C., Rocca, F., Rucci, A., 2011. A new algorithm for processing interferometric data-stacks: SqueeSAR. IEEE Transactions on Geoscience and Remote Sensing 49, 3460–3470. doi:10.1109/TGRS.2011.2124465

Ferretti, A., Monti-Guarnieri, A., Prati, C., Rocca, F., Massonnet, D., 2007. InSAR principles: guidelines for SAR interferometry processing and interpretation.

Ferretti, A., Prati, C., Rocca, F., 1999. Multibaseline InSAR DEM reconstruction: the wavelet approach. IEEE Transactions on Geoscience and Remote Sensing 37, 705–715. doi:10.1109/36.752187

Ferretti, A., Prati, C., Rocca, F., 2001. Permanent scatterers in SAR interferometry. IEEE Transactions on Geoscience and Remote Sensing 39, 8–20. doi:10.1109/36.898661

Fielding, E.J., 2010. ROI _ PAC Internals.

Finlay, P.J., Fell, R., 1997. Landslides: risk perception and acceptance. Canadian Geotechnical Journal 34, 169–188. doi:10.1139/t96-108

Finlay, P.J., Mostyn, G.R., Fell, R., 1999. Landslide risk assessment: prediction of travel distance. Canadian Geotechnical Journal 36, 556–562. doi:10.1139/t99-012

Fiorucci, F., Cardinali, M., Carlà, R., Rossi, M., Mondini, A.C., Santurri, L., Ardizzone, F., Guzzetti, F., 2011. Seasonal landslide mapping and estimation of landslide mobilization rates using aerial and satellite images. Geomorphology 129, 59–70. doi:10.1016/j.geomorph.2011.01.013

Flageollet, J.-C., Maquaire, O., Martin, B., Weber, D., 1999. Landslides and climatic conditions in the Barcelonnette and Vars basins (Southern French Alps, France). Geomorphology 30, 65–78. doi:10.1016/S0169-555X(99)00045-8

Frayssines, M., Hantz, D., 2006. Failure mechanisms and triggering factors in calcareous cliffs of the Subalpine Ranges (French Alps). Engineering Geology 86, 256–270. doi:10.1016/j.enggeo.2006.05.009

Friedl, M.A., Brodley, C.E., 1997. Decision tree classification of land cover from remotely sensed data. Remote Sensing of Environment 61, 399–409. doi:10.1016/S0034-4257(97)00049-7

Froger, J.-L., 2003. Radar remote sensing. Lecture notes. Clermont-Ferrand, France.

Fruneau, B., Achache, J., Delacourt, C., 1996. Observation and modelling of the Saint-Étienne-de-Tinée landslide using SAR interferometry. Tectonophysics 265, 181–190. doi:10.1016/S0040-1951(96)00047-9

Fuchu, D., Lee, C.F., Sijing, W., 1999. Analysis of rainstorm-induced slide-debris flows on natural terrain of Lantau Island, Hong Kong. Engineering Geology 51, 279–290. doi:10.1016/S0013-7952(98)00047-7

Fujii, Y., 1969. Frequency distribution of landslides caused by heavy rainfall. Journal Seismological Society Japan 22, 244–247.

Galli, M., Ardizzone, F., Cardinali, M., Guzzetti, F., Reichenbach, P., 2008. Comparing landslide inventory maps. Geomorphology 94, 268–289. doi:10.1016/j.geomorph.2006.09.023

Galli, P., Bosi, V., Piscitelli, S., Giocoli, A., Scionti, V., 2006. Late Holocene earthquakes in southern Apennine: paleoseismology of the Caggiano fault. International Journal of Earth Sciences 95, 855–870. doi:10.1007/s00531-005-0066-2

García-Davalillo, J.C., Herrera, G., Notti, D., Strozzi, T., Álvarez-Fernández, I., 2013. DInSAR analysis of ALOS PALSAR images for the assessment of very slow landslides: the Tena Valley case study. Landslides 11, 225–246. doi:10.1007/s10346-012-0379-8

Garcia-Ruiz, J.M., Lorente-Grima, A., Begueria-Portugues, S., Marti-Bono, C., Valero-Garces, B., Lopez-Moreno, J.I., 2003. Damocles project report. Contract No EVG1-CT-1999-00007. Instituto Pirenaico de Ecologia, CSIC, Zaragoza, Spain.

Giordan, D., Allasia, P., Manconi, A., Baldo, M., Santangelo, M., Cardinali, M., Corazza, A., Albanese, V., Lollino, G., Guzzetti, F., 2013. Geomorphology morphological and kinematic evolution of a large earthflow: the Montaguto landslide, southern Italy. Geomorphology 187, 61–79. doi:10.1016/j.geomorph.2012.12.035

Glade, T., 2003. Landslide occurrence as a response to land use change: a review of evidence from New Zealand. Catena 51, 297–314. doi:10.1016/S0341-8162(02)00170-4

Glade, T., Crozier, M., 2005. A review of scale dependency in landslide hazard and risk analysis, in: Glade, T., Anderson, M., Crozier, M.J. (Eds.), Landslide Hazard and Risk. John Wiley & Sons, Ltd, Chichester, West Sussex, England, pp. 75–138. doi:10.1002/9780470012659

Glenn, N.F., Streutker, D.R., Chadwick, D.J.J., Thackray, G.D., Dorsch, S.J., 2006. Analysis of LiDAR-derived topographic information for characterizing and differentiating landslide morphology and activity. Geomorphology 73, 131–148. doi:10.1016/j.geomorph.2005.07.006

Goldstein, R.M., Zebker, H.A., Werner, C.L., 1988. Satellite radar interferometry: two-dimensional phase unwrapping. Radio Science 23, 713–720.

Gorsevski, P. V, Gessler, P., Foltz, R.B., 2000. Spatial prediction of landslide hazard using discriminant analysis and GIS, in: Proceedings of the 4th International Conference on Integrating GIS and Environmental Modeling: Problems, Prospects and Research Needs, Banff, Alberta, 2-8 September, 2000.

Gorum, T., van Westen, C.J., Korup, O., van der Meijde, M., Fan, X., van der Meer, F.D., 2013. Complex rupture mechanism and topography control symmetry of mass-wasting pattern, 2010 Haiti earthquake. Geomorphology 184, 127–138. doi:doi:10.1016/j.geomorph.2012.11.027

Goswami, R., Mitchell, N.C., Brocklehurst, S.H., 2011. Distribution and causes of landslides in the eastern Peloritani of NE Sicily and western Aspromonte of SW Calabria, Italy. Geomorphology 132, 111–122. doi:10.1016/j.geomorph.2011.04.036

Govi, M., 1977. Photo-interpretation and mapping of the landslides triggered by the Friuli earthquake 1976. Bulletin of Engineering Geology and the Environment 15, 67–72. doi:10.1007/BF02592650

Gruner, U., 2008. Climatic and meteorological influences on rockfall and rockslides, in: 11th Interpraevent Congress 2008 Protection of Populated Territories From Floods, Debris Flows, Mass Movements and Avalanches, Vol. 2. Dornbirn, Austria, 26-30 May, pp. 147–158.

Guillon, J., 2001. Interprétation morphologique de l'évolution du glissement-coulée de Poche et caractérisation physico-mécanique des matériaux marneux (Alpes-de-Haute-Provence, France). Master Thesis, Strasbourg I University.

Guns, M., Vanacker, V., 2014. Shifts in landslide frequency-area distribution after forest conversion in the tropical Andes. Anthropocene 6, 75–85. doi:10.1016/j.ancene.2014.08.001

Günther, A., Reichenbach, P., Guzzetti, F., Richter, A., 2007. Criteria for the identification of landslide risk areas in Europe: the Tier 1 approach, in: Hervás, J. (Ed.), Guidelines for Mapping Areas at Risk of Landslides in Europe. Proc. Experts Meeting, JRC Ispra, Italy, 23-24 October 2007. JRC Scientific and Technical Report EUR 23093 EN. Office for Official Publications of the European Communities, Luxembourg, pp. 37–39.

Günther, A., Reichenbach, P., Malet, J.-P., Eeckhaut, M., Hervás, J., Dashwood, C., Guzzetti, F., 2013. Tier-based approaches for landslide susceptibility assessment in Europe. Landslides 10, 529–546. doi:10.1007/s10346-012-0349-1

Gupta, R.P., Joshi, B.C., 1990. Landslide hazard zoning using the GIS approach – A case study from the Ramganga catchment, Himalayas. Engineering Geology 28, 119–131. doi:10.1016/0013-7952(90)90037-2

Guthrie, R.H., Evans, S.G., 2004. Analysis of landslide frequencies and characteristics in a natural system, coastal British Columbia. Earth Surface Processes and Landforms 29, 1321–1339. doi:10.1002/esp.1095

Guzzetti, F., 2004. Book review of "Catastrophic landslides: effects, occurrence, and mechanisms." Natural Hazards and Earth System Sciences 4, 531–531. doi:10.5194/nhess-4-531-2004

Guzzetti, F., 2006. Landslide hazard and risk assessment. PhD Thesis, University of Bonn, Bonn, Germany.

Guzzetti, F., Ardizzone, F., Cardinali, M., Rossi, M., Valigi, D., 2009. Landslide volumes and landslide mobilization rates in Umbria, central Italy. Earth and Planetary Science Letters 279, 222–229. doi:10.1016/j.epsl.2009.01.005

Guzzetti, F., Cardinali, M., 1990. Landslide inventory map of the Umbria region, Central Italy, in: Cancelli, A. (Ed.), Proceedings ALPS 90 6th International Conference and Field Workshop on Landslides. Ricerca Scientifica Ed Educazione Permanente, Università Degli Studi Di Milano. Milano, Italy, pp. 273–284.

Guzzetti, F., Cardinali, M., Reichenbach, P., Carrara, A., 2000. Comparing landslide maps: a case study in the upper Tiber River Basin, Central Italy. Environmental Management 25, 247–363. doi:10.1007/s002679910020

Guzzetti, F., Cardinali, M., Reichenbach, P., Galli, M., Ardizzone, F., Salvati, P., 2004. Geomorphological mapping to assess landslide risk: examples from the Umbria Region, Central Italy, in: Proceedings 2004 International Conference on Slopeland Disaster Mitigation. Taipei, 5-6 October 2004, pp. 61–79.

Guzzetti, F., Carrara, A., Cardinali, M., Reichenbach, P., 1999. Landslide hazard evaluation: a review of current techniques and their application in a multi-scale study, Central Italy. Geomorphology 31, 181–216. doi:10.1016/S0169-555X(99)00078-1

Guzzetti, F., Galli, M., Reichenbach, P., Ardizzone, F., Cardinali, M., 2006. Landslide hazard assessment in the Collazzone area, Umbria, Central Italy. Natural Hazards and Earth System Sciences 6, 115–131. doi:10.5194/nhess-6-115-2006

Guzzetti, F., Malamud, B.D., Turcotte, D.L., Reichenbach, P., 2002. Power-law correlations of landslide areas in central Italy. Earth and Planetary Science Letters 195, 169–183. doi:10.1016/S0012-821X(01)00589-1

Guzzetti, F., Mondini, A.C., Cardinali, M., Fiorucci, F., Santangelo, M., Chang, K.-T., 2012. Landslide inventory maps: new tools for an old problem. Earth-Science Reviews 112, 42–66. doi:10.1016/j.earscirev.2012.02.001

Guzzetti, F., Peruccacci, S., Rossi, M., Stark, C.P., 2008. The rainfall intensity-duration control of shallow landslides and debris flows: an update. Landslides 5, 3–17. doi:10.1007/s10346-007-0112-1

Guzzetti, F., Reichenbach, P., Ardizzone, F., Cardinali, M., Galli, M., 2006. Estimating the quality of landslide susceptibility models. Geomorphology 81, 166–184. doi:10.1016/j.geomorph.2006.04.007

Guzzetti, F., Reichenbach, P., Cardinali, M., Ardizzone, F., Galli, M., 2003. Impact of landslides in the Umbria Region, Central Italy. Natural Hazards and Earth System Sciences 3, 469–486. doi:10.5194/nhess-3-469-2003

Guzzetti, F., Reichenbach, P., Cardinali, M., Galli, M., Ardizzone, F., 2005. Probabilistic landslide hazard assessment at the basin scale. Geomorphology 72, 272–299. doi:10.1016/j.geomorph.2005.06.002

Hansen, A., 1984a. Landslide hazard analysis, in: Brunsden, D., Prior, D.B. (Eds.), Slope Instability. New York, pp. 523–602.

Hansen, A., 1984b. Engineering geomorphology: the application of an evolutionary model of Hong Kong's terrain. Zeitschrift für Geomorphologie Supplement, 39–50.

Hanssen, R.F., 2001. Radar interferometry: data interpretation and error analysis. Academic Publishers, Dordrecht, The Netherlands: Kluwer.

Hanssen, R.F., Weckwerth, T.M., Zebker, H.A., Klees, R., 1999. High-resolution water vapor mapping from interferometric radar measurements.

Harp, E.L., Jibson, R.W., Dart, R.L., 2011a. The effect of complex fault rupture on the distribution of landslides triggered by the 12 January 2010, Haiti earthquake, in: Proceedings of the Second World Landslide Forum – 3-7 October 2011, Rome. p. 625.

Harp, E.L., Keefer, D.K., Sato, H.P., Yagi, H., 2011b. Landslide inventories: the essential part of seismic landslide hazard analyses. Engineering Geology 122, 9–21. doi:10.1016/j.enggeo.2010.06.013

Havenith, H.-B., Strom, A., Caceres, F., Pirard, E., 2006a. Analysis of landslide susceptibility in the Suusamyr region, Tien Shan: statistical and geotechnical approach. Landslides 3, 39–50. doi:10.1007/s10346-005-0005-0

Havenith, H.-B., Torgoev, A., Schlögel, R., Braun, A., Torgoev, I., Ischuk, A., n.d. Tien Shan geohazards database: landslide susceptibility and impacts. Geomorphology subm.

Havenith, H.-B., Torgoev, I., Meleshko, A., Alioshin, Y., Torgoev, A., Danneels, G., 2006b. Landslides in the Mailuu-Suu Valley, Kyrgyzstan – Hazards and impacts. Landslides 3, 137–147. doi:10.1007/s10346-006-0035-2

Hearn, G.J., Griffiths, J.S., 2001. Landslide hazard mapping, in: Griffiths, J.S. (Ed.), Landslide Surface Evaluation for Engineering Practice. pp. 43–52.

Helmstetter, A., Sornette, D., Grasso, J.-R., Andersen, J. V, Gluzman, S., Pisarenko, V., 2004. Slider block friction model for landslides: application to Vaiont and La Clapière landslides. Journal of Geophysical Research 109, B02409. doi:10.1029/2002JB002160

Herrera, G., Gutiérrez, F., García-Davalillo, J.C., Guerrero, J., Notti, D., Galve, J.P., 2013. Multi-sensor advanced DInSAR monitoring of very slow landslides: the Tena Valley case study (Central Spanish Pyrenees). Remote Sensing of Environment 128, 31–43. doi:10.1016/j.rse.2012.09.020

Hervás, J., Barredo, J.I., Rosin, P.L., Pasuto, A., Mantovani, F., Silvano, S., 2003. Monitoring landslides from optical remotely sensed imagery: the case history of Tessina landslide, Italy. Geomorphology 54, 63–75. doi:10.1016/S0169-555X(03)00056-4

Hibert, C., Grandjean, G., Bitri, A., Travelletti, J., Malet, J.-P., 2012. Characterizing landslides through geophysical data fusion: example of the La Valette landslide (France). Engineering Geology 128, 23–29. doi:10.1016/j.enggeo.2011.05.001

Holm, K., Bovis, M., Jakob, M., 2004. The landslide response of alpine basins to post-Little Ice Age glacial thinning and retreat in southwestern British Columbia. Geomorphology 57, 201–216. doi:10.1016/S0169-555X(03)00103-X

Hong, Y., Adler, R., Huffman, G., 2007. Use of satellite remote sensing data in the mapping of global landslide susceptibility. Natural Hazards 43, 245–256. doi:10.1007/s11069-006-9104-z

Hooper, A., 2008. A multi-temporal InSAR method incorporating both persistent scatterer and small baseline approaches. Geophysical Research Letters 35, L16302. doi:10.1029/2008GL034654

Hovius, N., Stark, C.P., Allen, P.A., 1997. Sediment flux from a mountain belt derived by landslide mapping. Geology 25, 231–234. doi:10.1130/0091-7613(1997)025<0231:SFFAMB>2.3.CO;2

Huang, S.L., Chen, B.K., 1991. Integration of Landsat and terrain information for landslide study. Proceedings of the Thematic Conference on Geologic Remote Sensing 8, 743–754.

Hungr, O., 1997. Some methods of landslide hazard intensity mapping, in: Cruden, D.M., Fell, R. (Eds.), Landslide Risk Assessment. Balkema Publisher, Rotterdam, pp. 215–226.

Hungr, O., Corominas, J., Eberhardt, E., 2005. Estimating landslide motion mechanisms, travel distance and velocity, in: Hungr, O., Fell, R., Couture, R., Eberhardt, E. (Eds.), Landslide Risk Management. Taylor and Francis, London, pp. 99–128.

Hungr, O., Evans, S.G., Hazzard, J., 1999. Magnitude and frequency of rock falls and rock slides along the main transportation corridors of southwestern British Columbia. Canadian Geotechnical Journal 36, 224–238. doi:10.1139/t98-106

Hutchinson, J.N., 1988. General report: morphological and geotechnical parameters of landslides in relation to geology and hydrology, in: Bonnard, C. (Ed.), Proc. 5th International Symposium on Landslides, Vol. 1A. Balkema, Rotterdam, Netherlands, pp. 3–35.

Iverson, R.M., Logan, M., Denlinger, R.P., 2004. Granular avalanches across irregular three-dimensional terrain: 2. Experimental tests. Journal of Geophysical Research: Earth Surface 109, F01015. doi:10.1029/2003JF000084

Ives, J.D., Messerli, B., 1981. Mountain hazards mapping in Nepal – Introduction to an applied mountain research project. Mountain Research and Development 1, 223–230. doi:10.2307/3673059

Jaiswal, P., van Westen, C.J., Jetten, V., 2010. Quantitative landslide hazard assessment along a transportation corridor in southern India. Engineering Geology 116, 236–250. doi:10.1016/j.enggeo.2010.09.005

Jibson, R.W., Harp, E.L., Michael, J.A., 1998. A method for producing digital probabilistic seismic landslide hazard maps: an example from Southern California. U.S. Geological Survey Open-File Report.

Jibson, R.W., Keefer, D.K., 1989. Statistical analysis of factors affecting landslide distribution in the New Madrid seismic zone, Tennessee and Kentucky. Engineering Geology 27, 509–542. doi:10.1016/0013-7952(89)90044-6

Joerin, F., Thériault, M., Musy, A., 2001. Using GIS and outranking multicriteria analysis for land-use suitability assessment. International Journal of Geographical Information Science 15, 153–174. doi:10.1080/13658810051030487

Jollifee, I.T., Stephenson, D.B., 2003. Forecast verification. A practitioner's guide in atmospheric science. John Wiley & Sons, Chichester, West Sussex, England.

Jongmans, D., Campillo, M., 1993. The response of the Ubaye valley (France) for incident SR and SV waves: comparison between measurements and modelling. Bulletin of seismological society of America 83, 907–924.

Jorda, M., 1980. Morphogenèse et évolution des paysages des Alpes de Haute-Provence depuis le Tardiglaciaire. Facteurs naturels et facteurs anthropiques. Bulletin de l'Association des Géographes Français 472, 295–304. doi:10.3406/bagf.1980.5196

Julian, M., Anthony, E., 1996. Aspects of landslide activity in the Mercantour Massif and the French Riviera, southeastern France. Geomorphology 15, 275–289. doi:10.1016/0169-555X(95)00075-G

Kanungo, D.P., Arora, M.K., Sarkar, S., Gupta, R.P., 2009. Landslide Susceptibility Zonation (LSZ) mapping – A review. Journal of South Asia Disaster Studies 2, 81–105.

Kappes, M.S., Malet, J.-P., Remaître, A., Horton, P., Jaboyedoff, M., Bell, R., 2011. Assessment of debris-flow susceptibility at medium-scale in the Barcelonnette Basin, France. Natural Hazards and Earth System Sciences 11, 627–641. doi:10.5194/nhess-11-627-2011

Kaufman, L., Rousseeuw, P.J., 1990. Finding groups in data: an introduction to cluster analysis. John Wiley & Sons, New York. doi:10.1002/9780470316801

Kaufmann, V., 2012. The evolution of rock glacier monitoring using terrestrial photogrammetry: the example of Äußeres Hoch-ebenkar rock glacier (Austria). Austrian Journal of Earth Sciences 105, 63–77.

Keefer, D., 2002. Investigating landslides caused by earthquakes – A historical review. Surveys in Geophysics 23, 473–510. doi:10.1023/A:1021274710840

Keefer, D.K., 1984. Rock avalanches caused by earthquakes: source characteristics. Science 223, 1288–1290. doi:10.1126/science.223.4642.1288

Keefer, D.K., 2000. Statistical analysis of an earthquake-induced landslide distribution - the 1989 Loma Prieta, California event. Engineering Geology 58, 231–249. doi:10.1016/S0013-7952(00)00037-5

Kerckhove, C., 1969. La « zone du Flysch » dans les nappes de Embrunais-Ubaye (Alpes occidentales). Géologie Alpine 45, 5–204.

Kienholz, H., 1977. Kombinierte Geomorphologische Gefahrenkarte 1:10,000 von Grindelwald. Catena 3, 265–294. doi:10.1016/0341-8162(77)90034-0

Kienholz, H., 1978. Maps of geomorphology and natural hazard of Grindelwald, Switzerland, scale 1:10,000. Arctic and Alpine Research 10, 169–184.

Korup, O., Schmidt, J., McSaveney, M.J., 2005. Regional relief characteristics and denudation pattern of the western Southern Alps, New Zealand. Geomorphology 71, 402–423. doi:10.1016/j.geomorph.2005.04.013

Koukis, G., Sabatakakis, N., Nikolau, N., Loupasakis, C., 2005. Landslide hazard zonation in Greece, in: Sassa, K., Fukuoka, H., Wang, F., Wang, G. (Eds.), Landslides SE - 37. Springer Berlin Heidelberg, pp. 291–296. doi:10.1007/3-540-28680-2_37

Krige, D.G., 1966. Two dimensional weighted moving average trend surfaces for ore-evaluation. Journal of the South African Institute of Mining and Metallurgy 66, 13–38.

Kurtz, C., Stumpf, A., Malet, J.-P., Gançarski, P., Puissant, A., Passat, N., 2014. Hierarchical extraction of landslides from multiresolution remotely sensed optical images. ISPRS Journal of Photogrammetry and Remote Sensing 87, 122–136. doi:10.1016/j.isprsjprs.2013.11.003

Lacroix, P., Zavala, B., Berthier, E., Audin, L., 2013. Supervised method of landslide inventory using panchromatic SPOT5 images and application to the earthquake-triggered landslides of Pisco (Peru, 2007, Mw8.0). Remote Sensing 5, 2590–2616. doi:10.3390/rs5062590

Larsen, I.J., Montgomery, D.R., Korup, O., 2010. Landslide erosion controlled by hillslope material. Nature Geoscience 3, 247–251. doi:10.1038/ngeo776

Latreille, M., 1961. Les nappes de l'Embrunais entre Durance et Haut-Drac. Imprimerie nationale.

Lauknes, T.R., Shanker, A.P., Dehls, J.F., Zebker, H.A., Henderson, I.H.C., Larsen, Y., 2010. Detailed rockslide mapping in northern Norway with small baseline and persistent scatterer interferometric SAR time series methods. Remote Sensing of Environment 114, 2097–2109. doi:10.1016/j.rse.2010.04.015

Le Mignon, G., Cojean, R., 2002. Rôle de l'eau dans la remobilisation de glissements–coulées (Barcelonnette, France), in: Rybar, J., Stemberk, J., Wagner, P. (Eds.), Proceedings of the 1st European Conference on Landslides, Prague, Czech Republik, Swets & Zeiltinger, Lisse. pp. 239–244.

Lee, C.T., Huang, C.C., Lee, J.F., Pan, K.L., Lin, M.L., Dong, J.J., 2008. Statistical approach to earthquake-induced landslide susceptibility. Engineering Geology 100, 43–58. doi:10.1016/j.enggeo.2008.03.004

Lee, S., 2004. Application of likelihood ratio and logistic regression models to landslide susceptibility mapping using GIS. Environmental Management 34, 223–232. doi:10.1007/s00267-003-0077-3

Lee, S., 2005. Application of logistic regression model and its validation for landslide susceptibility mapping using GIS and remote sensing data. International Journal of Remote Sensing 26, 1477–1491. doi:10.1080/01431160412331331012

Lee, S., Lee, M.-J., 2006. Detecting landslide location using KOMPSAT 1 and its application to landslide-susceptibility mapping at the Gangneung area, Korea. Advances in Space Research 38, 2261–2271. doi:10.1016/j.asr.2006.03.036

Lee, S., Min, K., 2001. Statistical analysis of landslide susceptibility at Yongin, Korea. Environmental Geology 40, 1095–1113. doi:10.1007/s002540100310

Lee, S., Ryu, J.-H., Won, J.-S., Park, H.-J., 2004. Determination and application of the weights for landslide susceptibility mapping using an artificial neural network. Engineering Geology 71, 289–302. doi:10.1016/S0013-7952(03)00142-X

Légier, A., 1977. Mouvements de terrain et évolution récente du relief dans la région de Barcelonnette (Alpes-de-Haute-Provence). Thèse de doctorat, Université Scientifique et Médicale de Grenoble, Institut Dolomieu.

Leone, F., Asté, J.-P., Leroi, E., 1996. Vulnerability assessment of elements exposed to mass-movement: working toward a better risk perception, in: Senneset, K. (Ed.), Landslides - Glissements de Terrain. A. A. Balkema, Rotterdam, pp. 1:263–270.

Leprince, S., Berthier, E., Ayoub, F., Delacourt, C., Avouac, J.-P., 2008. Monitoring earth surface dynamics with optical imagery. Eos, Transactions American Geophysical Union 89, 4. doi:doi:10.1029/2008EO010001

Leroi, E., 1996. Landslide hazard – Risk maps at different scales: objectives, tools and developments, in: Senneset, K. (Ed.), Landslides, Proc. Int. Symp. on Landslides. Trondheim, pp. 35–52.

Leroi, E., Bonnard, C., Fell, R., McInnes, R., 2005. Risk assessment and management, in: Hungr, O., Fell, R., Couture, R., Eberhardt, E. (Eds.), Landslide Risk Management. Taylor and Francis, London, pp. 159–198.

Li, A.H., Li, Y.H., Luo, Z.X., Li, Z.G., Pang, Y.G., 2001. Preliminary design for the stabilization of the Baota landslide group in Yunyang County, Chongqing City, Three-Gorge Reservoir Zone, No. 2. Survey & Design Institute, Ministry of Railways, Chengdu, China.

Li, C., Ma, T., Zhu, X., 2010. aiNet- and GIS-based regional prediction system for the spatial and temporal probability of rainfall-triggered landslides. Natural Hazards 52, 57–78. doi:10.1007/s11069-009-9351-x

Liébault, F., Piégay, H., 2002. Causes of 20th century channel narrowing in mountain and piedmont rivers of southeastern France. Earth Surface Processes and Landforms 27, 425–444. doi:10.1002/esp.328

Lin, P.-S., Lin, J.-Y., Hung, J.-C., Yang, M.-D., 2002. Assessing debris-flow hazard in a watershed in Taiwan. Engineering Geology 66, 295–313. doi:10.1016/S0013-7952(02)00105-9

Lineback Gritzner, M., Marcus, W.A., Aspinall, R., Custer, S.G., 2001. Assessing landslide potential using GIS, soil wetness modeling and topographic attributes, Payette River, Idaho. Geomorphology 37, 149–165. doi:10.1016/S0169-555X(00)00068-4

Lopez-Saez, J., Corona, C., Stöffel, M., Astrade, L., Berger, F., Malet, J.-P., 2011. Dendrogeomorphic reconstruction of past landslide reactivation with seasonal precision: the Bois Noir landslide, southeast French Alps. Landslides 9, 189–203. doi:10.1007/s10346-011-0284-6

Lopez-Saez, J., Corona, C., Stöffel, M., Berger, F., 2013a. High-resolution fingerprints of past landsliding and spatially explicit, probabilistic assessment of future reactivations: Aiguettes landslide, southeastern French Alps. Tectonophysics 602, 355–369. doi:10.1016/j.tecto.2012.04.020

Lopez-Saez, J., Corona, C., Stöffel, M., Berger, F., 2013b. Climate change increases frequency of shallow spring landslides in the French Alps. Geology 41, 619–622. doi:10.1130/G34098.1

Lopez-Saez, J., Corona, C., Stöffel, M., Schoeneich, P., Berger, F., 2012. Probability maps of landslide reactivation derived from tree-ring records: Pra Bellon landslide, Southern French Alps. Geomorphology 138, 189–202. doi:10.1016/j.geomorph.2011.08.034

Lu, P., Stumpf, A., Kerle, N., Casagli, N., 2011. Object-oriented change detection for landslide rapid mapping. Geoscience and Remote Sensing Letters, IEEE. doi:10.1109/LGRS.2010.2101045

Luckman, P.G., Gibson, R.D., Derose, R.C., 1999. Landslide erosion risk to New Zealand pastoral steeplands productivity. Land Degradation & Development 10, 49–65. doi:10.1002/(SICI)1099-145X(199901/02)10:1<49::AID-LDR320>3.0.CO;2-J

Malamud, B.D., Turcotte, D.L., Guzzetti, F., Reichenbach, P., 2004a. Landslide inventories and their statistical properties. Earth Surface Processes and Landforms 29, 687–711. doi:10.1002/esp.1064

Malamud, B.D., Turcotte, D.L., Guzzetti, F., Reichenbach, P., 2004b. Landslides, earthquakes, and erosion. Earth and Planetary Science Letters 229, 45–59. doi:10.1016/j.epsl.2004.10.018

Malczewski, J., 1999. GIS and multi-criteria decision analysis. Wiley, New York.

Malet, J.-P., 2003. Les “glissements de type écoulement” dans les marnes noires des Alpes du Sud. Morphologie, fonctionnement et modélisation hydro-mécanique. PhD Thesis, University Louis Pasteur, Strasbourg.

Malet, J.-P., Auzet, A.-V., Maquaire, O., Ambroise, B., Descroix, L., Esteves, M., Vandervaere, J.-P., Truchet, E., 2003. Soil surface characteristics influence on infiltration in black marls: application to the Super-Sauze earthflow (southern Alps, France). Earth Surface Processes and Landforms 28, 547–564. doi:10.1002/esp.457

Malet, J.-P., Maquaire, O., 2003. Black marl earthflows mobility and long-term seasonal dynamic in southeastern France, in: Picarelli, L. (Ed.), Fast Slope Movements: Prediction and Prevention for Risk Mitigation; Proc. Intern. Conf., Napoli, 11-13 May 2003. Bologna: Patron Editore.

Malet, J.-P., Maquaire, O., Calais, E., 2002. The use of Global Positioning System techniques for the continuous monitoring of landslides: application to the Super-Sauze earthflow (Alpes-de-Haute-Provence, France). Geomorphology 43, 33–54. doi:10.1016/S0169-555X(01)00098-8

Malet, J.-P., Puissant, A., Mathieu, A., van den Eeckhaut, M., Fressard, M., 2013. Integrating spatial multi-criteria evaluation and expert knowledge for country-scale landslide susceptibility analysis: application to France, in: Margottini, C., Canuti, P., Sassa, K. (Eds.), Landslide Science and Practice SE - 40. Springer Berlin Heidelberg, pp. 303–311. doi:10.1007/978-3-642-31325-7_40

Malet, J.-P., Remaître, A., Maquaire, O., Durand, Y., Etchevers, P., Guyomarch, G., Déqué, M., van Beek, L.P.H., 2007. Assessing the influence of climate change on the activity of landslides in the Ubaye Valley, in: Proceedings International Conference on Landslides and Climate Change - Challenges and Solutions, Wiley, London. p. 10.

Malet, J.-P., Thiery, Y., Hervás, J., Günther, A., Puissant, A., Grandjean, G., 2009. Landslide susceptibility mapping at 1:1M scale over France: exploratory results with heuristic model, in: Proc. of Landslide Process, from Geomorphologic Mapping to Dynamic Modelling. A Tribute to Dr. Theo van Asch. Strasbourg, France, Feb. 2009, pp. 315–320.

Malet, J.-P., Thiery, Y., Puissant, A., 2006. Analyse spatiale, évaluation et cartographie du risque « glissement de terrain » 1–29.

Malet, J.-P., van Asch, T.W.J., van Beek, R., Maquaire, O., 2005. Forecasting the behaviour of complex landslides with a spatially distributed hydrological model. Natural Hazards and Earth System Sciences 5, 71–85. doi:10.5194/nhess-5-71-2005

Malgot, J., Mahr, T., 1979. Engineering geological mapping of the West Carpathian landslide areas. Bulletin of the International Association of Engineering Geology 19, 116–121. doi:10.1007/BF02600461

Manné, S., Schwin, L.-C., 1998. Etude morphologique et evolution historique du glissement-coulée de Poche. Mémoire de Maîtrise de Géographie Physique, Université Louis Pasteur.

Mantovani, F., Soeters, R., van Westen, C.J., 1996. Remote sensing techniques for landslide studies and hazard zonation in Europe. Geomorphology 15, 213–225. doi:10.1016/0169-555X(95)00071-C

Maquaire, O., 2002. Aléas géomorphologiques (mouvements de terrain) : processus, fonctionnement, cartographie. Mémoire d'habilitation à diriger des recherches. Thèse de Doctorat, Université Louis Pasteur, Strasbourg I.

Maquaire, O., Malet, J.-P., Remaître, A., Locat, J., Klotz, S., Guillon, J., 2003. Instability conditions of marly hillslopes: towards landsliding or gullying? The case of the Barcelonnette Basin, South East France. Engineering Geology 70, 109–130. doi:10.1016/S0013-7952(03)00086-3

Mark, R.K., Ellen, S.D., 1995. Statistical and simulation models for mapping debris-flow hazard, in: Carrara, A., Guzzetti, F. (Eds.), Assessing Natural Hazards. Kluwer Academic Publishers, Dordrecht, The Netherlands, pp. 93–106.

Martha, T.R., Kerle, N., Jetten, V., van Westen, C.J., Kumar, K.V., 2010a. Characterising spectral, spatial and morphometric properties of landslides for semi-automatic detection using object-oriented methods. Geomorphology 116, 24–36. doi:10.1016/j.geomorph.2009.10.004

Martha, T.R., Kerle, N., van Westen, C.J., Jetten, V., Kumar, K.V., 2010b. Effect of sun elevation angle on DSMs derived from Cartosat-1 data. Photogrammetric Engineering & Remote Sensing 76, 429–438. doi:10.14358/PERS.76.4.429

Martha, T.R., Kerle, N., van Westen, C.J., Jetten, V., Vinod Kumar, K., 2012. Object-oriented analysis of multi-temporal panchromatic images for creation of historical landslide inventories. ISPRS Journal of Photogrammetry and Remote Sensing 67, 105–119. doi:10.1016/j.isprsjprs.2011.11.004

Martha, T.R., van Westen, C.J., Kerle, N., Jetten, V., Vinod Kumar, K., 2013. Landslide hazard and risk assessment using semi-automatically created landslide inventories. Geomorphology 184, 139–150. doi:10.1016/j.geomorph.2012.12.001

Mason, S.J., Graham, N.E., 2002. Areas beneath the relative operating characteristics (ROC) and relative operating levels (ROL) curves: statistical significance and interpretation. Quarterly Journal of the Royal Meteorological Society 128, 2145–2166. doi:10.1256/003590002320603584

Massonnet, D., Feigl, K.L., 1998. Radar interferometry and its application to changes in the Earth's surface. Reviews in Geophysics 36, 441–500. doi:10.1029/97RG03139

MATE/METL, 1999. Plan de Prévention des Risques (PPR) : risques de mouvement de terrain, Ministère. ed. La documentation française, Paris.

Mathieu, A., 2009. Cartographie d'inventaire et morphodynamique des mouvements de versant dans le bassin du Riou-Bourdoux (Alpes-de-Haute-Provence, France). Approche qualitative au 1/10.000. Mémoire de Master, Université de Strasbourg, Strasbourg, France.

Mathieu, A., Malet, J.-P., Stumpf, A., 2014. Characterization of rockslide dynamics by the joint analysis of airborne LiDAR and stereo-photogrammetric point clouds. Geophysical Research Abstracts 16, 9989.

Matsuoka, N., Sakai, H., 1999. Rockfall activity from an alpine cliff during thawing periods. Geomorphology 28, 309–328. doi:10.1016/S0169-555X(98)00116-0

Maury, P., Ricou, L.E., 1983. Le décrochement subbriançonnais : une nouvelle interprétation de la limite externe-interne des Alpes franco-italiennes. Revue de Géographie physique et de Géologie dynamique 24, 3–22.

Mazeau, A., 2013. Analyse cinématique du glissement-coulée de Poche : soixante ans de déplacements étudiés via des données multi-sources.

McCalpin, J., 1984. Preliminary age classification of landslides for inventory mapping. Proceedings of the Annual Symposium on Engineering Geology and Soil Engineering 21, 99–111.

McCullagh, P., Nelder, J.A., 1989. Generalized linear models, second edition, Generalized Linear Models Second Edition.

McKean, J., Roering, J., 2004. Objective landslide detection and surface morphology mapping using high-resolution airborne laser altimetry. Geomorphology 57, 331–351. doi:10.1016/S0169-555X(03)00164-8

Meijerink, A.M.J., 1988. Data acquisition and data capture through terrain mapping units. ITC Journal 1, 23–44.

Melchiorre, C., Matteucci, M., Azzoni, A., Zanchi, A., 2008. Artificial neural networks and cluster analysis in landslide susceptibility zonation. Geomorphology 94, 379–400. doi:10.1016/j.geomorph.2006.10.035

Menard, S.W., 1995. Applied logistic regression analysis. SAGE Publication, Inc. Series: Quantitative Applications in the Social Sciences, No. 106., Thousand Oaks, CA.

Merle, O., Brun, J.-P., 1984. The curved translation path of the Parpaillon Nappe (French Alps). Journal of Structural Geology 6, 711–719. doi:10.1016/0191-8141(84)90010-5

Metternicht, G., Hurni, L., Gogu, R., 2005. Remote sensing of landslides: an analysis of the potential contribution to geo-spatial systems for hazard assessment in mountainous environments. Remote Sensing of Environment 98, 284–303. doi:10.1016/j.rse.2005.08.004

Miles, S.B., Ho, C.L., 1999. Rigorous landslide hazard zonation using Newmark's method and stochastic ground motion simulation. Soil Dynamics and Earthquake Engineering 18, 305–323.

Miramont, C., 1998. Morphogenèse, activité érosive et détritisme alluvial holocènes dans le bassin de la moyenne Durance (Alpes françaises du Sud). Thèse de Doctorat en Géographie, Université d'Aix-Marseille I.

Mondini, A.C., Chang, K., 2014. Combining spectral and geoenvironmental information for probabilistic event landslide mapping. Geomorphology 213, 183–189. doi:10.1016/j.geomorph.2014.01.007

Mondini, A.C., Chang, K.-T., Yin, H.-Y., 2011. Combining multiple change detection indices for mapping landslides triggered by typhoons. Geomorphology 134, 440–451. doi:10.1016/j.geomorph.2011.07.021

Mondini, A.C., Guzzetti, F., Reichenbach, P., Rossi, M., Cardinali, M., Ardizzone, F., 2011. Semi-automatic recognition and mapping of rainfall induced shallow landslides using optical satellite images. Remote Sensing of Environment 115, 1743–1757.

Mondini, A.C., Marchesini, I., Rossi, M., Chang, K.-T., Pasquariello, G., Guzzetti, F., 2013. Bayesian framework for mapping and classifying shallow landslides exploiting remote sensing and topographic data. Geomorphology 201, 135–147. doi:10.1016/j.geomorph.2013.06.015

Montgomery, D.R., Sullivan, K., Greenberg, H.M., 1998. Regional test of a model for shallow landsliding. Hydrological Processes 12, 943–955. doi:10.1002/(SICI)1099-1085(199805)12:6<943::AID-HYP664>3.0.CO;2-Z

Mostyn, G.R., Fell, R., 1997. Quantitative and semiquantitative estimation of probability of landsliding, in: Cruden, D.M., Fell, R. (Eds.), Landslide Risk Assessment. Balkema, Rotterdam, pp. 297–315.

Motamedi, M., Liang, R.Y., 2013. Probabilistic landslide hazard assessment using Copula modeling technique. Landslides 11, 565–573. doi:10.1007/s10346-013-0399-z

Mulder, H.F.H.M., 1991. Assessment of landslide hazard. Netherlands Geographical Studies 124, 149.

Nefeslioglu, H.A., Gokceoglu, C., Sonmez, H., 2008. An assessment on the use of logistic regression and artificial neural networks with different sampling strategies for the preparation of landslide susceptibility maps. Engineering Geology 97, 171–191. doi:10.1016/j.enggeo.2008.01.004

Nichol, J., Wong, M.S., 2005a. Detection and interpretation of landslides using satellite images. Land Degradation & Development 16, 243–255. doi:10.1002/ldr.648

Nichol, J., Wong, M.S., 2005b. Satellite remote sensing for detailed landslide inventories using change detection and image fusion. International Journal of Remote Sensing 26, 1913–1926. doi:10.1080/01431160512331314047

Nikolaeva, E., Walter, T.R., Shirzaei, M., Zschau, J., 2014. Landslide observation and volume estimation in central Georgia based on L-band InSAR. Natural Hazards and Earth System Sciences 14, 675–688. doi:10.5194/nhess-14-675-2014

Ohlmacher, G.C., Davis, J.C., 2003. Using multiple logistic regression and GIS technology to predict landslide hazard in northeast Kansas, USA. Engineering Geology 69, 331–343. doi:10.1016/S0013-7952(03)00069-3

Oppikofer, T., Jaboyedoff, M., Blikra, L., Derron, M.-H., Metzger, R., 2009. Characterization and monitoring of the Åknes rockslide using terrestrial laser scanning. Natural Hazards and Earth System Sciences 9, 1003–1019. doi:10.5194/nhess-9-1003-2009

Pancioli, V., Raetzo, H., Campolmi, T., Casagli, N., 2008. Terrafirma landslide services for Europe based on space-borne InSAR data, in: Proceedings of the First World Landslide Forum, Tokyo, Japan. pp. 81–84.

Pardeshi, S.D., Autade, S.E., Pardeshi, S.S., 2013. Landslide hazard assessment: recent trends and techniques. SpringerPlus 2, 523. doi:10.1186/2193-1801-2-523

Parker, P.N., Densmore, A.L., Rosser, N.J., de Michele, M., Li, Y., Huang, R., Whadcoat, S., Petley, D.N., 2011. Mass wasting triggered by the 2008 Wenchuan earthquake is greater than orogenic growth. Nature Geoscience 4, 449–452. doi:10.1038/ngeo1154

Pascale, S., Sdao, F., Sole, A., 2010. A model for assessing the systemic vulnerability in landslide prone areas. Natural Hazards and Earth System Sciences 10, 1575–1590. doi:10.5194/nhess-10-1575-2010

Pašek, J., 1975. Landslide inventory. International Association Engineering Geologist Bulletin 12, 73–74. doi:10.1007/BF02635432

Peduto, D., Cascini, L., Fornaro, G., 2010. Satellite radar, in: Tofani, V., Segoni, S., Catani, S.F., Casagli, N. (Eds.), Evaluation Report on Innovative Monitoring and Remote Sensing Methods and Future Technology. Oslo: Norwegian Geotechnical Institute, pp. 42–43.

Pelletier, J.D., Malamud, B.D., Blodgett, T., Turcotte, D.L., 1997. Scale-invariance of soil moisture variability and its implications for the frequency-size distribution of landslides. ARXIV 20.

Pereira, S., Zêzere, J.L., Bateira, C., 2012. Technical note: assessing predictive capacity and conditional independence of landslide predisposing factors for shallow landslide susceptibility models. Natural Hazards and Earth System Sciences 12, 979–988. doi:10.5194/nhess-12-979-2012

Petley, D., 2012. Global patterns of loss of life from landslides. Geology 40, 927–930. doi:10.1130/G33217.1

Peyret, M., Djamour, Y., Rizza, M., Ritz, J., Hurtrez, J., Goudarzi, M.A., Nankali, H., Chéry, J., Le Dortz, K., Uri, F., 2008. Monitoring of the large slow Kahrod landslide in Alborz mountain range (Iran) by GPS and SAR interferometry. Engineering Geology 100, 131–141. doi:10.1016/j.enggeo.2008.02.013

Picarelli, L., Urciuoli, G., Ramondini, M., Comegna, L., 2005. Main features of mudslides in tectonised highly fissured clay shales. Landslides 2, 15–30. doi:10.1007/s10346-004-0040-2

Pieraccini, M., 2013. Real beam vs. Synthetic Aperture Radar for slope monitoring, in: Progress In Electromagnetics Research Symposium Proceedings. Stockholm, Sweden, pp. 1627–1632.

Pradhan, B., 2010. Remote sensing and GIS-based landslide hazard analysis and cross-validation using multivariate logistic regression model on three test areas in Malaysia. Advances in Space Research 45, 1244–1256. doi:10.1016/j.asr.2010.01.006

Pradhan, B., Singh, R.P., Buchroithner, M.F., 2006. Estimation of stress and its use in evaluation of landslide prone regions using remote sensing data. Advances in Space Research 37, 698–709. doi:10.1016/j.asr.2005.03.137

Prokop, A., Panholzer, H., 2009. Assessing the capability of terrestrial laser scanning for monitoring slow moving landslides. Natural Hazards and Earth System Sciences 9, 1921–1928. doi:10.5194/nhess-9-1921-2009

Raucoules, D., de Michele, M., Malet, J.-P., Ulrich, P., 2013. Time-variable 3D ground displacements from High-Resolution Synthetic Aperture Radar (SAR). Application to La Valette landslide (South French Alps). Remote Sensing of Environment 139, 198–204. doi:10.1016/j.rse.2013.08.006

Ray, R.L., Jacobs, J.M., 2007. Relationships among remotely sensed soil moisture, precipitation and landslide events. Natural Hazards 43, 211–222. doi:10.1007/s11069-006-9095-9

Razak, K.A., Straatsma, M.W., van Westen, C.J., Malet, J.-P., de Jong, S.M., 2011. Airborne laser scanning of forested landslides characterization: terrain model quality and visualization. Geomorphology 126, 186–200. doi:10.1016/j.geomorph.2010.11.003

Reichenbach, P., Galli, M., Cardinali, M., Guzzetti, F., Ardizzone, F., 2005. Geomorphologic mapping to assess landslide risk: concepts, methods and applications in the Umbria Region of central Italy, in: Glade, T., Anderson, M., Crozier, M.J. (Eds.), Landslide Hazard and Risk. John Wiley & Sons, Ltd, Chichester, pp. 429–468.

Reichenbach, P., Günther, A., Guzzetti, F., 2007. Criteria for the identification of landslide risk areas in Europe: the Tier 2 approach, in: Hervás, J. (Ed.), Guidelines for Mapping Areas at Risk of Landslides in Europe. Proc. Experts Meeting, Ispra, Italy, 23-24 October 2007. JRC Report EUR 23093 EN. Office for Official Publications of the European Communities, Luxembourg.

Reid, L.M., Page, M.J., 2003. Magnitude and frequency of landsliding in a large New Zealand catchment. Geomorphology 49, 71–88. doi:10.1016/S0169-555X(02)00164-2

Reigber, A., Scheiber, R., Jäger, M., Prats-Iraola, P., Hajnsek, I., Jagdhuber, T., Papathanassiou, K.P., Nannini, M., Aguilera, E., Baumgartner, S., Horn, R., Nottensteiner, A., Moreira, A., 2012. Very-high-resolution airborne synthetic aperture radar imaging: signal processing and applications, in: Proceedings of the IEEE. p. 25.

Remaître, A., 2006. Morphologie et dynamique des laves torentielles : applications aux torrents des Terres Noires du bassin de Barcelonnette (Alpes du Sud). Thèse de doctorat de Géographie physique, humaine, économique et régionale de l'Université de Caen Basse-Normandie.

Remaître, A., Malet, J., Maquaire, O., 2005. Morphology and sedimentology of a complex debris flow in a clay-shale basin. Earth Surface Processes and Landforms 30, 339–348. doi:10.1002/esp.1161

Remaître, A., Malet, J.-P., 2010. The effectiveness of torrent check dams to control channel instability: example of debris-flow events in clay shales, in: Garcia, C.C., Lenzi, M.A. (Eds.), Check Dams, Morphological Adjustments and Erosion Control in Torrential Streams. Nova Science Publishers, pp. 211–237.

Remaître, A., Malet, J.-P., Maquaire, O., 2009. Sediment budget and morphology of the 2003 Faucon debris flow (South French Alps): scouring and channel-shaping processes, in: Landslide Processes: From Geomorphological Mapping to Dynamic Modelling, CERG, Strasbourg, France (2009). CERG Editions, Strasbourg, pp. 75–80.

Remaître, A., Maquaire, O., Pierre, S., 2002. Analyse d'une lave torrentielle dans le torrent de Faucon (bassin de Barcelonnette, Alpes-de-Haute-Provence). Détermination des zones de déclenchement et de contribution. Géomorphologie : relief, processus, environnement 1, 71–84.

Rib, H.T., Liang, T., 1978. Recognition and identification, in: Schuster, R.L., Krizek, R.J. (Eds.), Landslide Analysis and Control. Washington, D.C., pp. 34–80.

Rickenmann, D., 2000. Debris flows and torrent floods: methods for hazard assessment, in: Proceedings of the International Conference on Avalanches, Landslides, Rock Falls, Debris Flows (CALAR). Vienna.

Roberds, W., 2005. Estimating temporal and spatial variability and vulnerability, in: Hungr, O., Fell, R., Couture, R., Eberhardt, E. (Eds.), Landslide Risk Management. A. A. Balkema Publishers, pp. 129–157.

Rocca, F., 2003. 3D motion recovery with multi-angle and/or left right interferometry, in: Proc. 3rd International Workshop on ERS SAR Interferometry (FRINGE 2003), Frascati (Italy), 2–5 December 2003. pp. 1–5.

Rosen, P.A., Hensley, S., Peltzer, G., Simons, M., 2004. Updated repeat orbit interferometry package released. Eos, Transactions American Geophysical Union 85, 47–47. doi:10.1029/2004EO050004

Rossi, M., Ardizzone, F., Cardinali, M., Fiorucci, F., Marchesini, I., Mondini, A.C., Santangelo, M., Ghosh, S., Riguer, D.E.L., Lahousse, T., Chang, K.T., Guzzetti, F., 2012. A tool for the estimation of the distribution of landslide area in R. Geophysical Research Abstracts 14, EGU2012–9438–1.

Rossi, M., Guzzetti, F., Reichenbach, P., Mondini, A.C., Peruccacci, S., 2010. Optimal landslide susceptibility zonation based on multiple forecasts. Geomorphology 114, 129–142. doi:10.1016/j.geomorph.2009.06.020

Rucci, A., Ferretti, A., Monti-Guarnieri, A., Rocca, F., 2012. Sentinel 1 SAR interferometry applications: the outlook for sub millimeter measurements. Remote Sensing of Environment 120, 156–163. doi:10.1016/j.rse.2011.09.030

Rupke, J., Cammeraat, E., Seijmonsbergen, A.C., van Westen, C.J., 1988. Engineering geomorphology of the Widentobel catchment, Apenzell and Sankt Gallen, Switzerland. A geomorphological inventory system applied to geotechnical appraisal of slope stability. Engineering Geology 26, 33–68. doi:10.1016/0013-7952(88)90005-1

Saba, S.B., van der Meijde, M., van der Werff, H., 2010. Spatiotemporal landslide detection for the 2005 Kashmir earthquake region. Geomorphology 124, 17–25. doi:10.1016/j.geomorph.2010.07.026

Saito, H., Nakayama, D., Matsuyama, H., 2009. Comparison of landslide susceptibility based on a decision-tree model and actual landslide occurrence: The Akaishi Mountains, Japan. Geomorphology 109, 108–121. doi:10.1016/j.geomorph.2009.02.026

Sandersen, F., Bakkehoi, S., Hestnes, E., Lied, K., 1996. The influence of meteorological factors on the initation of debris flows, rockfalls, rockslides and rockmass stability, in: Senneset (Ed.), Landslides. Balkema, pp. 97–114.

Sandwell, D.T., Myer, D., Mellors, R., Shimada, M., Member, S., Brooks, B., Foster, J., 2008. Accuracy and resolution of ALOS interferometry: vector deformation maps of the Father's Day intrusion at Kilauea. IEEE Transactions on Geoscience and Remote Sensing 46, 3524–3534.

Santangelo, M., Cardinali, M., Rossi, M., Mondini, A.C., Guzzetti, F., 2010. Remote landslide mapping using a laser rangefinder binocular and GPS. Natural Hazards and Earth System Sciences 10, 2539–2546. doi:10.5194/nhess-10-2539-2010

Sarkar, S., Kanungo, D., Patra, A., Kumar, P., 2006. Disaster mitigation of debris flows, slope failures and landslides. GIS based landslide susceptibility mapping - a case study in Indian Himalaya. Universal Academy Press, Tokyo, Japan.

Savage, S.B., Hutter, K., 1991. The dynamics of avalanches of antigranulocytes materials from initiation to runout. Acta Mechanica 86, 201–223. doi:10.1007/BF01175958

Schlögel, R., 2009. Detection of recent landslides in Maily-Say Valley, Kyrgyz Tien Shan, based on field observations and remote sensing data. Mémoire de Master en Sciences géologiques, Université de Liège.

Schlögel, R., Doubre, C., Malet, J.-P., Masson, F., 2015a. Landslide deformation monitoring with ALOS/PALSAR imagery: a D-InSAR geomorphological interpretation method. Geomorphology 231, 314–330. doi:10.1016/j.geomorph.2014.11.031

Schlögel, R., Malet, J.-P., Doubre, C., Lebourg, T., 2015b. Structural control on the kinematics of the deep-seated La Clapière landslide revealed by L-band InSAR observations. Landslides 1–14. doi:10.1007/s10346-015-0623-0

Schlögel, R., Malet, J.-P., Remaître, A., Reichenbach, P., Doubre, C., 2015c. Analysis of a landslide multi-date inventory in a complex mountain landscape: the Ubaye valley case study. Natural Hazards and Earth System Sciences 15, 2369–2389. doi:10.5194/nhess-15-2369-2015

Schlögel, R., Torgoev, I., De Marneffe, C., Havenith, H.-B., 2011. Evidence of a changing size-frequency distribution of landslides in the Kyrgyz Tien Shan, Central Asia. Earth Surface Processes and Landforms 36, 1658–1669. doi:10.1002/esp.2184

Schmutz, M., 2000. Apport des méthodes géophysiques à la connaissance des glissements-coulées développés dans les marnes noires. Application à Super Sauze (Alpes-de-Haute-Provence, France). Thèse de Doctorat, Université Louis Pasteur, Strasbourg, France.

Schmutz, M., Albouy, Y., Guérin, R., Maquaire, O., Vassal, J., Schott, J.-J., Descloîtres, M., 2000. Joint electrical and Time Domain Electromagnetism (TDEM) data inversion applied to the Super Sauze earthflow (France). Surveys in Geophysics 21, 371–390. doi:10.1023/A:1006741024983

Sidle, R.C., Ochiai, H., 2006. Landslide processes, prediction, and land use, Washington D.C. American Geophysical Union 1–312.

Simonett, D.S., 1967. Landslide distribution and earthquakes in the Bewani and Torricelli mountains, New Guinea, in: Jennings, J.N., Mabbutt, J.A. (Eds.), Landform Studies from Australia and New Guinea. Cambridge University Press, Cambridge, pp. 64–84.

Singhroy, V., 1995. SAR integrated techniques for geohazard assessment. Advances in Space Research 15, 67–78. doi:10.1016/0273-1177(95)00076-Q

Singhroy, V., Mattar, K.E., Gray, A.L., 1998. Landslide characterization in Canada using interferometric SAR and combined SAR and TM images. Advances in Space Research 21, 465–476. doi:10.1016/S0273-1177(97)00882-X

Singhroy, V., Molch, K., 2004. Characterizing and monitoring rockslides from SAR techniques. Advances in Space Research 33, 290–295. doi:10.1016/S0273-1177(03)00470-8

Singleton, A., Li, Z., Hoey, T., Muller, J.-P., 2014. Evaluating sub-pixel offset techniques as an alternative to D-InSAR for monitoring episodic landslide movements in vegetated terrain. Remote Sensing of Environment 147, 133–144. doi:10.1016/j.rse.2014.03.003

Smyth, C.G., Royle, S.A., 2000. Urban landslide hazards: incidence and causative factors in Niterói, Rio de Janeiro State, Brazil. Applied Geography 20, 95–118. doi:10.1016/S0143-6228(00)00004-7

Soeters, R., van Westen, C.J., 1996. Slope instability recognition, analysis, and zonation, in: Turner, A.K., Schuster, R.L. (Eds.), Landslides: Investigation and Mitigation. Transportation Research Board Special Report 247. National Academy Press. National Research Council., Washington, D.C., pp. 129–177.

Squarzoni, C., Delacourt, C., Allemand, P., 2003. Nine years of spatial and temporal evolution of the La Valette landslide observed by SAR interferometry. Engineering Geology 68, 53–66. doi:10.1016/S0013-7952(02)00198-9

Squarzoni, C., Delacourt, C., Allemand, P., 2005. Differential single-frequency GPS monitoring of the La Valette landslide (French Alps). Engineering Geology 79, 215–229. doi:10.1016/j.enggeo.2005.01.015

Stark, C.P., Hovius, N., 2001. The characterization of landslide size distributions. Geophysical Research Letters 28, 1091–1094. doi:10.1029/2000GL008527

Stark, T., Choi, H., McCone, S., 2005. Drained shear strength parameters for analysis of landslides. Journal of Geotechnical and Geoenvironmental Engineering 131, 575–588. doi:10.1061/(ASCE)1090-0241(2005)131:5(575)

Sterlacchini, S., Ballabio, C., Blahut, J., Masetti, M., Sorichetta, A., 2011. Spatial agreement of predicted patterns in landslide susceptibility maps. Geomorphology 125, 51–61. doi:10.1016/j.geomorph.2010.09.004

Stien, D., 2001. Glissements de terrains et enjeux dans la vallée de l'Ubaye et le pays de Seyne. Rapport ONF-RTM, Division de Barcelonnette, France.

Strozzi, T., Delaloye, R., Kääb, A., Ambrosi, C., Perruchoud, E., Wegmüller, U., 2010. Combined observations of rock mass movements using satellite SAR interferometry, differential GPS, airborne digital photogrammetry, and airborne photography interpretation. Journal of Geophysical Research: Earth Surface 115, F01014. doi:doi:10.1029/2009JF001311

Strozzi, T., Farina, P., Corsini, A., Ambrosi, C., Thüring, M., Zilger, J., Wiesmann, A., Wegmüller, U., Werner, C., 2005. Survey and monitoring of landslide displacements by means of L-band satellite SAR interferometry. Landslides.

Strozzi, T., Werner, C., Wiesmann, A., Wegmüller, U., 2012. Topography mapping with a portable real-aperture radar interferometer. IEEE Geoscience and Remote Sensing Letters 9, 277–281. doi:10.1109/LGRS.2011.2166751

Stumpf, A., 2013. Landslide recognition and monitoring with remotely sensed data from passive optical sensors. Thèse de Doctorat en Géophysique. Ecole doctorale des Sciences de la Terre, de l'Univers et de l'Environnement, Université de Strasbourg.

Stumpf, A., Kerle, N., 2011. Object-oriented mapping of landslides using Random Forests. Remote Sensing of Environment 115, 2564–2577. doi:10.1016/j.rse.2011.05.013

Stumpf, A., Malet, J.-P., Allemand, P., Ulrich, P., 2014. Surface reconstruction and landslide displacement measurements with Pléiades satellite images. ISPRS Journal of Photogrammetry and Remote Sensing 95, 1–12. doi:10.1016/j.isprsjprs.2014.05.008

Stumpf, A., Malet, J.-P., Kerle, N., Niethammer, U., Rothmund, S., 2013. Image-based mapping of surface fissures for the investigation of landslide dynamics. Geomorphology 186, 12–27. doi:10.1016/j.geomorph.2012.12.010

Tarchi, D., Casagli, N., Fanti, R., Leva, D.D., Luzi, G., Pasuto, A., Pieraccini, M., Silvano, S., 2003. Landslide monitoring by using ground-based SAR interferometry: an example of application to the Tessina landslide in Italy. Engineering Geology 68, 15–30. doi:10.1016/S0013-7952(02)00196-5

Tarolli, P., Sofia, G., Dalla Fontana, G., 2012. Geomorphic features extraction from high-resolution topography: landslide crowns and bank erosion. Natural Hazards 61, 65–83. doi:10.1007/s11069-010-9695-2

Tatard, L., Grasso, J.-R., Helmstetter, A., Garambois, S., 2010. Characterization and comparison of landslide triggering in different tectonic and climatic settings. Journal of Geophysical Research 115, F04040. doi:10.1029/2009JF001624

Terlien, M.T.J., 1996. Modelling spatial and temporal variations in rainfall-triggered landslides. ITC Publ., ITC publication 32, 50.

Teza, G., Atzeni, C., Balzani, M., Galgaro, A., Galvani, G., Genevois, R., Luzi, G., Mecatti, D., Noferini, L., Pieraccini, M., Silvano, S., Uccelli, F., Zaltron, N., 2008. Ground-based monitoring of high-risk landslides through joint use of laser scanner and interferometric radar. International Journal of Remote Sensing. doi:10.1080/01431160801942227

Teza, G., Galgaro, A., Zaltron, N., Genevois, R., 2007. Terrestrial laser scanner to detect landslide displacement fields: a new approach. International Journal of Remote Sensing 28, 3425–3446. doi:10.1080/01431160601024234

Thiery, Y., 2007. Susceptibilité du Bassin de Barcelonnette (Alpes du sud, France) aux “mouvements de versant” : cartographie morphodynamique, analyse spatiale et modélisation probabiliste. Thèse de Doctorat, Université de Caen Basse-Normandie.

Thiery, Y., Malet, J.-P., Sterlacchini, S., Puissant, A., Maquaire, O., 2007. Landslide susceptibility assessment by bivariate methods at large scales: application to a complex mountainous environment. Geomorphology 92, 38–59. doi:10.1016/j.geomorph.2007.02.020

Thiery, Y., Maquaire, O., Fressard, M., 2014. Application of expert rules in indirect approaches for landslide susceptibility assessment. Landslides 11, 411–424. doi:10.1007/s10346-013-0390-8

Thouvenot, F., Fréchet, J., 2006. Seismicity along the northwestern edge of the Adria microplate, in: Pinter, N., Grenerczy, G., Weber, J., Stein, S., Medak, D. (Eds.), The Adria Microplate: GPS Geodesy, Tectonics and Hazards. Springer, Dordrecht, Netherlands, pp. 335–349. doi:10.1007/1-4020-4235-3_23

Tibaldi, A., Ferrari, L., Pasquarè, G., 1995. Landslides triggered by earthquakes and their relations with faults and mountain slope geometry: an example from Ecuador. Geomorphology 11, 215–226. doi:10.1016/0169-555X(94)00060-5

Tofani, V., Raspini, F., Catani, F., Casagli, N., 2013. Persistent Scatterer Interferometry (PSI) technique for landslide characterization and monitoring. Remote Sensing 5, 1045–1065. doi:10.3390/rs5031045

Tolomei, C., Taramelli, A., Moro, M., Saroli, M., Aringoli, D., Salvi, S., 2013. Analysis of the deep-seated gravitational slope deformations over Mt. Frascare (Central Italy) with geomorphological assessment and DInSAR approaches. Geomorphology 201, 281–292. doi:10.1016/j.geomorph.2013.07.002

Tonnellier, A., Helmstetter, A., Malet, J.-P., Schmittbuhl, J., Corsini, A., Joswig, M., 2013. Seismic monitoring of soft-rock landslides: the Super-Sauze and Valoria case studies. Geophysical Journal International 193, 1515–1536. doi:10.1093/gji/ggt039

Travelletti, J., Delacourt, C., Allemand, P., Malet, J.-P., Schmittbuhl, J., Toussaint, R., Bastard, M., 2012. Correlation of multi-temporal ground-based optical images for landslide monitoring: application, potential and limitations. ISPRS Journal of Photogrammetry and Remote Sensing 70, 39–55. doi:10.1016/j.isprsjprs.2012.03.007

Travelletti, J., Malet, J.-P., 2012. Characterization of the 3D geometry of flow-like landslides: a methodology based on the integration of heterogeneous multi-source data. Engineering Geology 128, 30–48. doi:10.1016/j.enggeo.2011.05.003

Travelletti, J., Malet, J.-P., Delacourt, C., 2010. Multi-dates correlation of Terrestrial Laser Scanning data for the characterization of landslide kinematics 1–23.

Travelletti, J., Malet, J.-P., Delacourt, C., 2014. Image-based correlation of Laser Scanning point cloud time series for landslide monitoring. International Journal of Applied Earth Observation and Geoinformation 32, 1–18. doi:10.1016/j.jag.2014.03.022

Travelletti, J., Malet, J.-P., Hibert, C., Grandjean, G., 2009. Integration of geomorphological, geophysical and geotechnical data to define the 3D morpho-structure of the La Valette mudslide, Ubaye Valley, French Alps, in: Malet, J.-P., Remaître, A., Boogard, T. (Eds.), Proceedings of the International Conference on Landslide Processes: From Geomorpho- Logic Mapping to Dynamic Modelling. Strasbourg, CERG Editions, pp. 203–208.

Travelletti, J., Malet, J.-P., Samyn, K., Grandjean, G., Jaboyedoff, M., 2013. Control of landslide retrogression by discontinuities: evidence by the integration of airborne- and ground-based geophysical information. Landslides 10, 37–54. doi:10.1007/s10346-011-0310-8

Travelletti, J., Oppikofer, T., Delacourt, C., Malet, J.-P., Jaboyedoff, M., 2008. Monitoring landslide displacements during a controlled rain experiment using a long-range Terrestrial Laser Scanning (TLS), in: The International Archives of the Photogrammetry, Remote Sensing and Spatial Information Sciences. Vol. XXXVII. Part B5. Beijing. Universität Karlsruhe, pp. 485–490.

Turcotte, D.L., 1997. Fractals and chaos in geology and geophysics. Cambridge University Press, Cambridge, New York, Melbourne, 2nd Ed.

Turkington, T., Ettema, J., van Westen, C.J., Breinl, K., 2014. Empirical atmospheric thresholds for debris flows and flash floods in the Southern French Alps. Natural Hazards and Earth System Sciences 14, 1517–1530. doi:10.5194/nhess-14-1517-2014

Utasse, M., 2009. Cartographie morpho-dynamique et évolution historique de trois glissements actifs dans le bassin versant du Riou-Bourdoux (Alpes-de-Haute-Provence, Vallée de l'Ubaye). MSc Thesis, Université de Strasbourg, France.

Valagussa, A., Frattini, P., Crosta, G.B., 2014. Earthquake-induced rockfall hazard zoning. Engineering Geology 182, 213–225. doi:10.1016/j.enggeo.2014.07.009

van Asch, T.W.J., Tang, C., Alkema, D., Zhu, J., Zhou, W., 2014. An integrated model to assess critical rainfall thresholds for run-out distances of debris flows. Natural Hazards 70, 299–311. doi:10.1007/s11069-013-0810-z

van Beek, L.P.H., 2002. Assessment of the influence of changes in climate and land use on landslide activity in a Mediterranean environment. PhD Thesis, University of Utrecht, Netherlands.

van den Eeckhaut, M., Hervás, J., 2012. Geomorphology state of the art of national landslide databases in Europe and their potential for assessing landslide susceptibility, hazard and risk. Geomorphology 139-140, 545–558. doi:10.1016/j.geomorph.2011.12.006

van den Eeckhaut, M., Hervás, J., Jaedicke, C., Malet, J.-P., Montanarella, L., Nadim, F., 2012. Statistical modelling of Europe-wide landslide susceptibility using limited landslide inventory data. Landslides 9, 357–369. doi:10.1007/s10346-011-0299-z

van den Eeckhaut, M., Poesen, J., Verstraeten, G., Vanacker, V., Moeyersons, J., Nyssen, J., van Beek, L.P.H., 2005. The effectiveness of hillshade maps and expert knowledge in mapping old deep-seated landslides. Geomorphology 67, 351–363. doi:10.1016/j.geomorph.2004.11.001

van den Eeckhaut, M., Reichenbach, P., Guzzetti, F., Rossi, M., Poesen, J., 2009. Combined landslide inventory and susceptibility assessment based on different mapping units: an example from the Flemish Ardennes, Belgium. Natural Hazards and Earth System Sciences 9, 507–521. doi:10.5194/nhess-9-507-2009

van Westen, C.J., 1993. Application of geographic information systems to landslide hazard zonation. PhD Dissertation Technical University Delft. ITC-Publication Number 15, ITC, Enschede, The Netherlands.

van Westen, C.J., 2004. Geo-information tools for landslide risk assessment: an overview of recent developments, in: Lacerda, W.A., Ehrlich, M., Fontoura, A.B., Sayo, A. (Eds.), Landslides Evaluation and Stabilization. Balkema, pp. 39–56.

van Westen, C.J., Castellanos, E., Kuriakose, S.L., 2008. Spatial data for landslide susceptibility, hazard, and vulnerability assessment: an overview. Engineering Geology 102, 112–131. doi:10.1016/j.enggeo.2008.03.010

van Westen, C.J., Rengers, N., Soeters, R., 2003. Use of geomorphological information in indirect landslide susceptibility assessment. Natural Hazards 30, 399–419. doi:10.1023/B:NHAZ.0000007097.42735.9e

van Westen, C.J., Rengers, N., Terlien, M.T.J., Soeters, R., 1997. Prediction of the occurrence of slope instability phenomenal through GIS-based hazard zonation. Geologische Rundschau 86, 404–414. doi:10.1007/s005310050149

van Westen, C.J., Seijmonsbergen, A.C., Mantovani, F., 1999. Comparing landslide hazard maps. Natural Hazards 137–158. doi:10.1023/A:1008036810401

van Westen, C.J., Soeters, R., Sijmons, K., 2000. Digital geomorphological landslide hazard mapping of the Alpago area, Italy. International Journal of Applied Earth Observation and Geoinformation 2, 51–60. doi:10.1016/S0303-2434(00)85026-6

van Westen, C.J., van Asch, T.W.J., Soeters, R., 2006. Landslide hazard and risk zonation – why is it still so difficult? Bulletin of Engineering Geology and the Environment 65, 167–184. doi:10.1007/s10064-005-0023-0

van Westen, C.J., Van Duren, I., Kruse, H.M.G., Terlien, M.T.J., 1993. GISSIZ: training package for geographic information systems in slope instability zonation. ITC Publ. 15, 245+359,10 diskettes.

Varnes, D.J., 1978. Slope movement types and processes, in: Schuster, R.L., Krizek, R.J. (Eds.), Special Report 176: Landslides: Analysis and Control. Transportation and Road Research Board, National Academy of Science, Washington, D.C., pp. 11–33.

Varnes, D.J., IAEG, 1984. Landslide hazard zonation: a review of principles and practice. United Nations Scientific and Cultural Organization, Paris.

Vaunat, J., Leroueil, S., 2002. Analysis of post-failure slope movements within the framework of hazard and risk analysis. Natural Hazards 26, 81–107. doi:10.1023/A:1015224914845

Verhaagen, P., 1988. Dendrogeomorphological investigations on a landslide in the Riou-Bourdoux Valley. Utrecht.

Wasowski, J., Bovenga, F., 2014. Investigating landslides and unstable slopes with satellite Multi Temporal Interferometry: current issues and future perspectives. Engineering Geology 174, 103–138. doi:10.1016/j.enggeo.2014.03.003

Wasowski, J., Del Gaudio, V., Pierri, P., Capolongo, D., 2002. Factors controlling seismic susceptibility of the Sele valley slopes: the case of the 1980 Irpinia earthquake reexamined. Surveys in Geophysics 23, 563–593. doi:10.1023/A:1021230928587

Weber, D., 1994. Rechearch into earth movements in the Barcelonnette Basin.

Weber, D., 2001. Contribution de la géomorphologie à la connaissance des mouvements de terrains dans les "Terres noires" alpines : le glissement-coulée de Super-Sauze (Alpes de Haute Provence, France). Thèse de Doctorat, Université Louis Pasteur, Strasbourg.

Westoby, M.J., Brasington, J., Glasser, N.F., Hambrey, M.J., Reynolds, J.M., 2012. "Structure-from-Motion" photogrammetry: a low-cost, effective tool for geoscience applications. Geomorphology 179, 300–314. doi:10.1016/j.geomorph.2012.08.021

Wieczorek, G.F., 1984. Preparing a detailed landslide-inventory map for hazard evaluation and reduction. Bulletin Association of Engineering Geologists 21, 337–342.

Wieczorek, G.F., 2002. Catastrophic rockfalls and rockslides in the Sierra Nevada, USA, in: Evans, S.G., DeGraff, J. V (Eds.), Catastrophic Landslides: Effects, Occurrence, and Mechanisms: Boulder, Colorado, Geological Society of America Reviews in Engineering Geology, v. XV. pp. 165–190. doi:10.1130/REG15-p165

Wieczorek, G.F., Gori, P.L., Jager, S., Kappel, W.M., Negussy, D., 1996. Assessment and management of landslide hazards near Tully Valley landslide, Syracuse, New York, USA, in: Proc VII Int. Symp. Landslides, Trondheim, June 1966, 1. Balkema, Rotterdam, pp. 411–416.

Wills, C.J., McCrink, T.P., 2002. Comparing landslide inventories: the map depends on the method. Environmental & Engineering Geoscience 8, 279–293.

Witten, I.H., Frank, E., 2005. Data Mining: practical machine learning tools and techniques, Machine Learning.

Wood, J.L., Harrison, S., Reinhardt, L., 2015. Landslide inventories for climate impacts research in the European Alps. Geomorphology 228, 398–408. doi:10.1016/j.geomorph.2014.09.005

Yager, R.R., 1988. On ordered weighted averaging aggregation operators in multicriteria decision making. IEEE Transactions on Systems, Man and Cybernetics 18, 183–190. doi:10.1109/21.87068

Yeon, Y.-K., Han, J.-G., Ryu, K.H., 2010. Landslide susceptibility mapping in Injae, Korea, using a decision tree. Engineering Geology 116, 274–283. doi:10.1016/j.enggeo.2010.09.009

Yesilnacar, E., Topal, T., 2005. Landslide susceptibility mapping: a comparison of logistic regression and neural networks methods in a medium scale study, Hendek region (Turkey). Engineering Geology 79, 251–266. doi:10.1016/j.enggeo.2005.02.002

Yin, Y., Wang, F., Sun, P., 2009. Landslide hazards triggered by the 2008 Wenchuan earthquake, Sichuan, China. Landslides 6, 139–152. doi:10.1007/s10346-009-0148-5

Zebker, H.A., Rosen, P.A., Hensley, S., 1997. Atmospheric effects in interferometric synthetic aperture radar surface deformation and topographic maps. Journal of Geophysical Research: Solid Earth 102, 7547–7563. doi:10.1029/96JB03804

Zweig, M.H., Campbell, G., 1993. Receiver-operating characteristic (ROC) plots: a fundamental evaluation tool in clinical medicine. Clinical chemistry 39, 561–577.

APPENDIX 1:

Synthetic Aperture Radar (SAR)

for landslide surface displacement monitoring

A. Synthetic Aperture Radar (SAR)

The spatial resolution of an orbiting satellite radar instrument observing from 1,000 km is ≈ 10 km on the ground. The spatial resolution is proportional to the ratio of the wavelength to the aperture, which is ≈ 10^{-3} for a large-aperture radar system with an antenna size of ≈ 10 m. As it is impossible to increase physically the antenna size to several tens of kilometers to obtain similar resolutions as optical sensors, Synthetic Aperture Radar (SAR) microwave imaging systems have been proposed. In a SAR imaging system, the satellite carries a radar with the antenna pointed to the Earth's surface in the plane perpendicular to the orbit (Ferretti et al., 2007). It works by illuminating the Earth with beam of coherent microwave radiation (wavelength: 1 mm-1 m). Since it is an active imaging system, it has cloud-penetrating capabilities and night operational capabilities.

B. SAR image properties

The SAR image is a two-dimensional array formed by columns and rows of pixels. Each pixel gives a complex number that carries amplitude and phase information about the microwave backscattered by all the scatterers (i.e. rocks, vegetation, buildings etc.) within the corresponding resolution cell projected on the ground (Ferretti et al., 2007).

Phase

The radiation transmitted from the radar has to reach the scatterers on the ground and then come back to the radar. Therefore, this two-way travel constitutes the SAR image. The different slant ranges (i.e. distances from the radar) induce different delays between transmission and reception of the radiation. Due to the sinusoidal nature of the transmitted signal, the delay is equivalent to a phase change Φ between both signals. The phase change is proportional to the two-way travel distance $2R$ of the radiation divided by the transmitted wavelength λ such as:

$$\Phi = (4\Pi/\lambda)R \qquad \text{(a-1)}$$

Speckle effect

The echo of an individual resolution cell is the result of the echoes vector combination of the elementary scatterers inside the pixel (Froger, 2003). The echoes are not necessarily in phase and the result is highly random for each resolution cell and gives a noisy appearance to the image, namely speckle. A solution to attenuate the speckle effect is a spatial filtering, or better a multilook filtering, obtained by staking several amplitude images.

Geometric distortion

A drawback of the radar imagery comes from the oblique geometry to sort the echoes by their distance from the antenna. A distortion is observed in the radar images when the ground areas slope away from the radar and are affected by shadowing. In addition, several points in a pulse line can share the same distance to the instrument inducing a mixing of their contributions in the same range pixel. This phenomenon, called layover (i.e. the extreme limit of the foreshortening effect), occurs where the average topographic slope between two points exceeds the incidence angle of the radar.

C. SAR Interferometry (InSAR)

Different phase contributions

An interferogram consists on the difference of the phase of the two SAR images, called the interferometric phase ($\Delta\Phi_{int}$):

$$\Delta\Phi_{int} = \Phi(t_0) - \Phi(t_1) = \Delta\Phi_{def} + \Delta\Phi_{orb} + \Delta\Phi_{topo} + \Delta\Phi_{atm} + \Delta\Phi_{noise} \quad \text{(a-2)}$$

Before any corrections, $\Delta\Phi_{int}$ contains the signal related to the ground deformation ($\Delta\Phi_{def}$) between the two acquisition times, the orbital contribution ($\Delta\Phi_{orb}$) due to change of the orbital geometry, the topographic contribution ($\Delta\Phi_{topo}$), the atmospheric contribution ($\Delta\Phi_{atm}$) due to the difference of propagation delay in the atmosphere, and a noise term ($\Delta\Phi_{noise}$) corresponding to the eventual variations of scattering, thermal noise or inaccurate image coregistration (Massonnet & Feigl, 1998).

Ignoring any signal propagation delays, and assuming that the scattering characteristics are equals during both acquisitions ($\Phi scat,1 = \Phi scat,2$), the estimated interferometric phase $\Delta\Phi_{int}$ can be directly related to the difference in path length to a target from the imaging platform in the line of sight (LOS) direction:

$$\Delta\Phi_{int} = (4\Pi/\lambda)\Delta R \quad \text{(a-3)}$$

Contribution of the ground displacements ($\Delta\Phi_{def}$). Ground displacements along the Line-of-Sight (LoS) between the radar and the target appears directly as a phase shift with respect to the rest of the scene. Moving along the LoS by half the wavelength creates a deformation fringe.

Contribution of the baseline between the orbital trajectories ($\Delta\Phi_{orb}$). Most of the observed path difference corresponds to the difference in viewpoint caused by any shift in orbital trajectory between the two image acquisitions. The convergence or divergence, even if less than 1 m, of the orbital trajectories over the length of the image can also create along-track fringes. Once all the a priori knowledge of the orbits has been used to eliminate this type of contribution, there may be residual fringes, which can be eliminated by an orbital tuning (Massonnet & Feigl, 1998), or by removing a linear trend, assumed to be the residual orbital phase signal.

Contribution of the topography ($\Delta\Phi_{topo}$). Eliminating the orbital contribution reveals an underlying stereoscopic effect, as the radar observes the relief from two slightly different points of view. This topographic contribution induces fringes according to the relief, similarly as topographic contour lines. To quantify these topographic fringes, we use the notion of height of ambiguity, h_{amb}, which is the shift in altitude needed to produce one topographic fringe (Hanssen, 2001):

$$h_{amb} = \left| \frac{\lambda R_1 \sin\theta}{2B_\perp} \right| \quad \text{(a-4)}$$

where $B_\perp$ is the perpendicular baseline. This sensitivity to topographic relief can be used to generate a Digital Elevation Model (DEM). In this work, we are interested in ground displacements, thus we will remove the topographic contribution thanks to an external DEM (IGN DSM ≈ 25 m). The possible residual topographic fringes will therefore be considered as an artifact i.e. noise. However, lower is the $B_\perp$ lower will be the geometrical decorrelation.

Contribution of the atmosphere ($\Delta\Phi_{atm}$). If the two images are acquired at different times, the atmosphere characteristics are not identical. Differences in the troposphere or the ionosphere properties between the two times will affect the apparent path length between the radar and the surface. Over small spatial scales, the phase delay is mainly due to the spatial variation of water vapor in the troposphere. The ionospheric effects are due to variation of the Total Electron Content. Longer wavelength, such as L-band, is more sensitive to ionospheric effects. Using more than two SAR images can allow us to identify which SAR image is affected by an atmospheric phase delay. The different interferometric combinations of images enable the unambiguous identification of the image containing anomalies (Hanssen, 2001) and a selection of proper interferograms with low temporal baselines.

Other contributions ($\Delta\Phi_{noise}$). Other phenomena include instrumental artifacts such as the oscillator instability. Changes in the reflective characteristics of the ground can also modify the phase of an interferogram (Massonnet & Feigl, 1998).

Phase unwrapping

In SAR interferometry, the measured interferometric phase represents the absolute interferometric phase modulo 2π. It may be related directly to the topographic height and amount of deformation. To estimate the absolute phase, a two-step process is required: phase unwrapping and absolute phase determination.

Coherence

The phase noise can be estimated from the interferometric SAR pair by means of the local coherence γ. The local coherence is the cross-correlation coefficient of the SAR image pair estimated over a small window, once all the deterministic phase components (especially due to the elevation) are compensated for. This deterministic phase components are linear both in azimuth and slant-range. They can be estimated from the interferogram by means of methods of frequency detection of complex sinusoid in noise, such as a 2-D Fast Fourier Transform.

The calculation of the absolute value of γ by a moving window that covers the whole SAR image allows creating the coherence map. The coherence values ranges from 0 (only noise on the interferogram) to 1 (complete absence of noise).

Source of decorrelation

The baseline or geometric (surface) decorrelation (γ_{geom}) is caused by the two different local incidence angles. The amount of decorrelation increases linearly with the amount of spectral shift between the two SAR acquisitions. The amount of spectral shift can be due to topography or atmosphere or deformation. The fundamental condition for interferometry, which expresses that a pixel must not stretch or shrink by more than a fraction of the wavelength from one image to another, is (Massonnet and Feigl, 1998):

$$2L\,(\sin\theta_1 - \sin\theta_2) < \lambda \qquad \text{(a-4)}$$

where L is the length perpendicular to the trajectory of a pixel on the ground and θ_1 and θ_2 are the local incidence angles.

For the topography, the baseline decorrelation depends on the critical baseline, which is the baseline causing a spectral shift equal to the bandwidth. The formula of baseline decorrelation depending on the critical baseline and geometric decorrelation due to topography are found in Hanssen (2001).

D. D-InSAR processing algorithms

The SAR images were processed at full resolution with the ROI-PAC software (Repeat Orbit Interferometry PACkage, Jet Propulsion Laboratory, Rosen et al., 2004) and some NSBAS commands for DSM co-registration and atmospheric corrections (Ducret et al., 2011).

ROI_PAC software

ROI_PAC has been used stepwise according to the flowchart of Figure a.

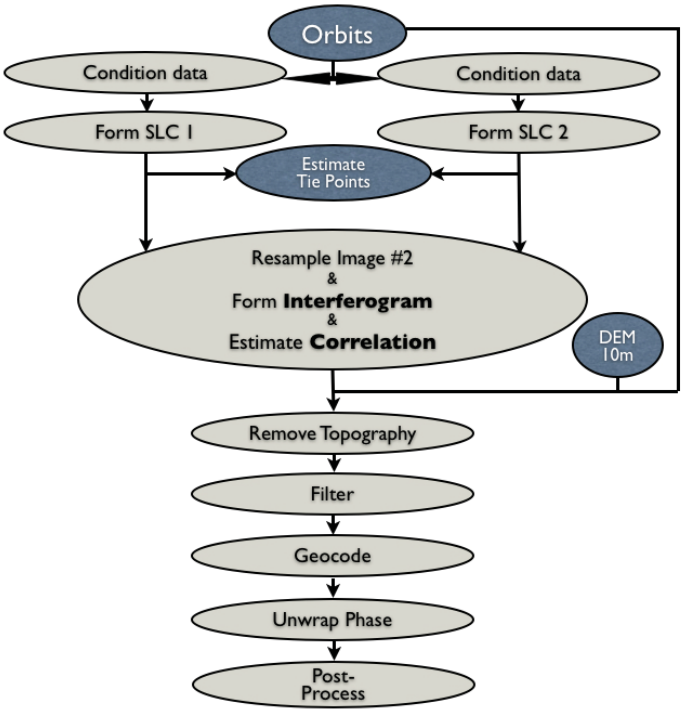

Figure a: ROI_PAC simplified two-pass processing flowchart as used in this study (modified after Fielding, 2010).

In this research, we started from raw images. Therefore the ROI_PAC focusing is an actual Doppler algorithm. In order to obtain high-spatial deformation images from the two available image modes, FBD images are oversampled to the pixel spacing of FBS images during the creation of raw images. Full resolution Single Look Complex images in radar geometry are created. Then, 2D field of offsets are calculated from orbits and scene parameters. For ALOS/PALSAR, the orbits information used are in the image header file.

After the initial flattening of the interferograms, ROI_PAC calculates the spatial correlation of the phase as an estimate of the interferometric coherence. The topographic phase is calculated after a simulation of the radar image amplitude from the DEM and the orbit phase for the master scene. This allows the projection of the elevations into the radar coordinates of the interferograms. Then, the topographic contribution can be subtracted from the original interferograms.

A power spectrum filtering is applied replacing the amplitude of the interferogram, which is heavily blurred by the filtering, with the average SAR amplitude of the coherence image (i.e. a filter strength of 0.7). The filtered interferogram is calculated by a two-dimensional inverse Fourier transform. This procedure is repeated for all interferograms patches. To alleviate discontinuities at patch boundaries, the patches are overlapped and a triangular weighted sum of the overlapping patches is used (Goldstein and Werner, 1998).

Unwrapping is the most difficult processing step in numerous studies due to the high topography, the

changing meteorological conditions and the position of the satellites. The phase unwrapping is not always possible because the interferograms are not be spatially equally coherent due to steep slopes and wavelength-scale surface changes between the observation times (Sandwell et al., 2008). According to the displacement rates of some landslides, we encountered difficulties to correctly unwrap by starting the 'Branch-Cut' unwrapping process (Goldstein et al., 1988) at a point located nearby but outside of the expected deformation area. The unwrapped phase was then checked to detect any errors related to the phase ambiguity, and in particular cases, started again guided by cuts and bridges knowing the landslide limits.

NSBAS software

Some algorithms of the NSBAS software were used to improve interferograms created with ROI_PAC. Co-registration between two SLCs images is based on a classical image correlation method. Offsets between pixels are estimated by correlation of amplitude images of the two SLCs. The transformation of a slave image in the geometry of the master image in azimuth and range is function of the following function:

$$f(x,y)=Ax^2 +Bx+Cy^2 +Dy+Exy+F \quad \text{(a-5)}$$

where x is the range, y the azimuth and *A, B, C, D, E, F* parameters to be estimated.

The range terms are estimated from the DTM and satellites orbits with NSBAS in order to increase the coherence of the interferograms. Another algorithm was used to correct atmospheric noises. We created ramps to avoid stratified atmosphere below 4000 m according to a mean fit degree in azimuth or in elevation.

APPENDIX 2:

A routine for the analysis of interferometric phase values at the slope scale in GIS

A procedure to interpret the wrapped interferograms based on a phase shifting at the slope-scale has been proposed in order to deal with the atmospheric contribution (Table a; Fig. b). Indeed, the traditional differential InSAR has some limitations, mainly due to the atmospheric contribution, which varies according to the elevation. This procedure allows us to interpret the wrapped interferograms at slope-scale by fixing the phase difference values at zero in stable areas.

Table a: Methodological framework to interpret wrapped and unwrapped interferometric phases for landslide kinematic analysis at slope-scale.

1) Selection of the interpretable interferograms

Based on:

- Preview of the interferograms to qualitatively see its quality (discontinuous evolution of phase value)
- Thresholds of coherence values (defined for each interferogram)

OUTPUT → interferograms selected for kinematic analysis

Cause: correlation btw bad quality of the interferograms and particular factors to define why there is high decorrelation

- high PBL
- high TempBL
- intense rainfall

2-3) Recalculation of the interferograms

A. Distribution of phase value

- out of landslide: normal curve (Gaussian)
- into landslide: heterogeneous curve
- median of the phase values histogram for the entire scene

B. Operation on the interferograms

- move the curve in order to position the median at the middle (i.e. 0 between -π and π) meaning a subtraction or an addition of the median value to all the data;
- reclassification to extract values lower than –π or upper than π (and assigning values of 0 or 1);
- multiply by those values to individualize zones out of the 2π interval;
- subtract or add the phase values (out of the 2π interval) by 2π;
- cut the extracted values at the beginning or at the end of the histogram (–π or π +median);
- selection of part of the curve to move those extracted values;
- add them, that will keep the interval between -π and π.

OUTPUT → new interferograms without extended phase jumps in which:

* stable zones corresponding to a phase value around '0';
* positive values corresponding to an ablation zone;
* negative values meaning accumulated materials.

4-5) Identification of homogeneous sliding compartments

A. *Draw interpretable signal on the interferogram* (i.e. *ablation* and *accumulation* zones) with:

- clear difference in phase values (positive or negative);
- a few noise.

B. Create profiles crossing the interpretable 'spot' with phase value in y-axis and distance in x-value

- detection of sudden 'phase jumps'
- definition of the different motion compartments

OUTPUT → Profiles and maps with a cartography of compartments (where decorrelation is acceptable)

C. Calculation of displacement along slope

- Profiles of displacement along slope (cm) vs. distance
- Correlation to GPS measurements
- Trend and definition of zones along the landslide

OUTPUT → Maps of displacement along slope and their corresponding profiles

6) Characterization of landslide kinematics evolution

A. Comparison between the interferograms (and thus, the period)

B. Calculation of area, percentage, quantity of:

- Depletion zones (less material)
- Accumulation zones (more material)

OUTPUT → statistics on evolution of kinematics function of the period considered

7) Creation of velocity map

- Remove highly decorrelated zones with thresholds of the coherence values

OUTPUT → raster in which each pixel has an exploitable velocity value

Perspectives: Estimation of trend for the future

E.g. trend to the extension of transit zone downstream, less accumulation, trend to increasing of the translational component (displacement along the slope)/to the decreasing of the vertical component (more rotational)

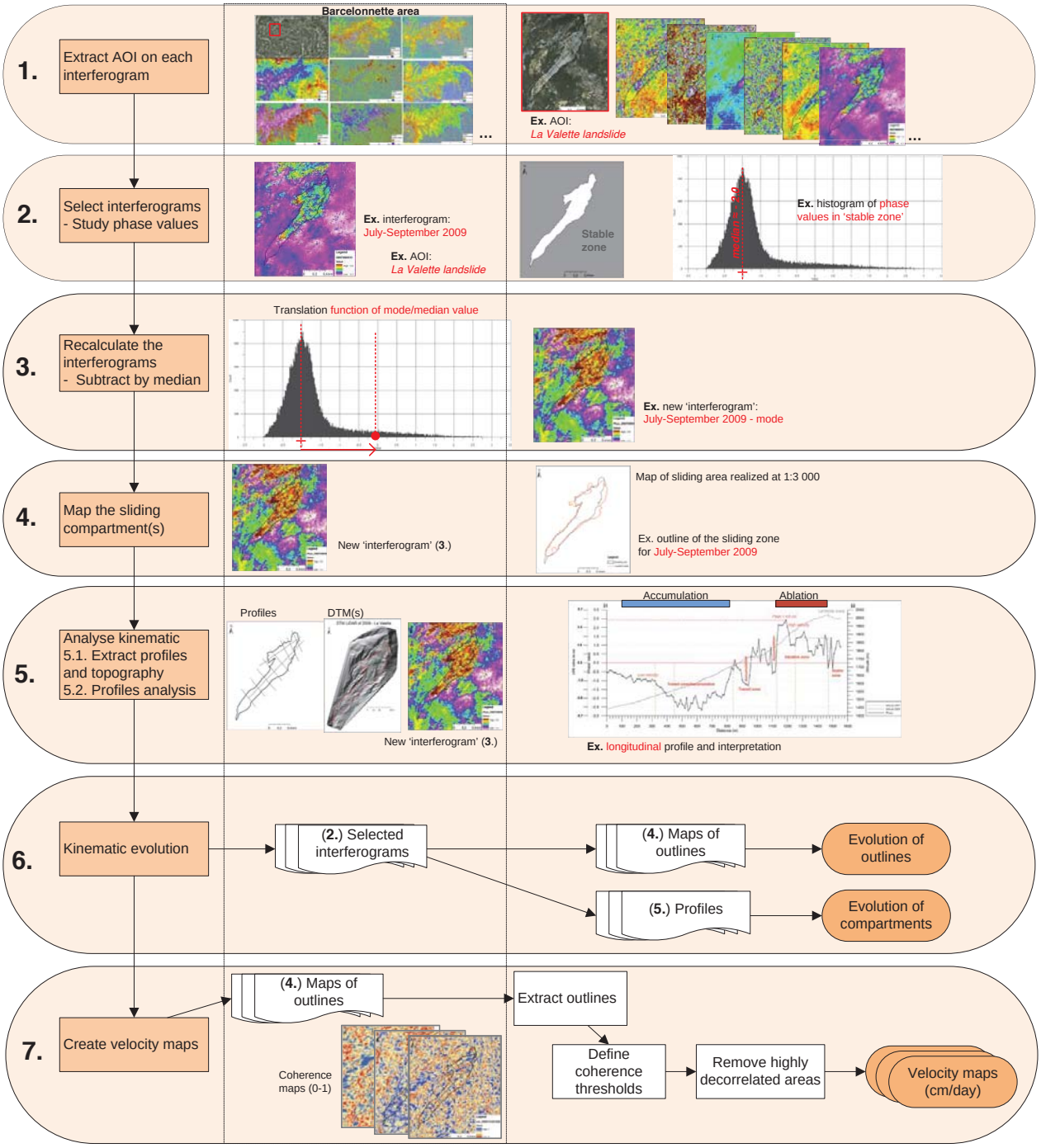

Figure b: Flowchart of the wrapped and unwrapped InSAR signal interpretation method for landslide kinematic analysis at slope-scale. (AOI: Area of Interest).

When it was possible to unwrap the interferograms, the phase shifting is kept even if the stable zone surroundings the landslide is already close to a phase value of 0. The second step of Table a and Figure b is based on the development of a GIS toolbox to post-process automatically the results at slope-scale (Fig. c). The aim is to shift the phase value to zero for the areas considered as stable on the basis of the previous inventory, by subtracting the median phase value (Φ_{med}) of the zone surrounding the landslide to the phase values of the whole cropped area. The resulting phase range for the wrapped interferograms is thus [$-\pi-\Phi_{med}$, $\pi-\Phi_{med}$] allowing the creation of velocity maps in LoS, vertical and slope directions.

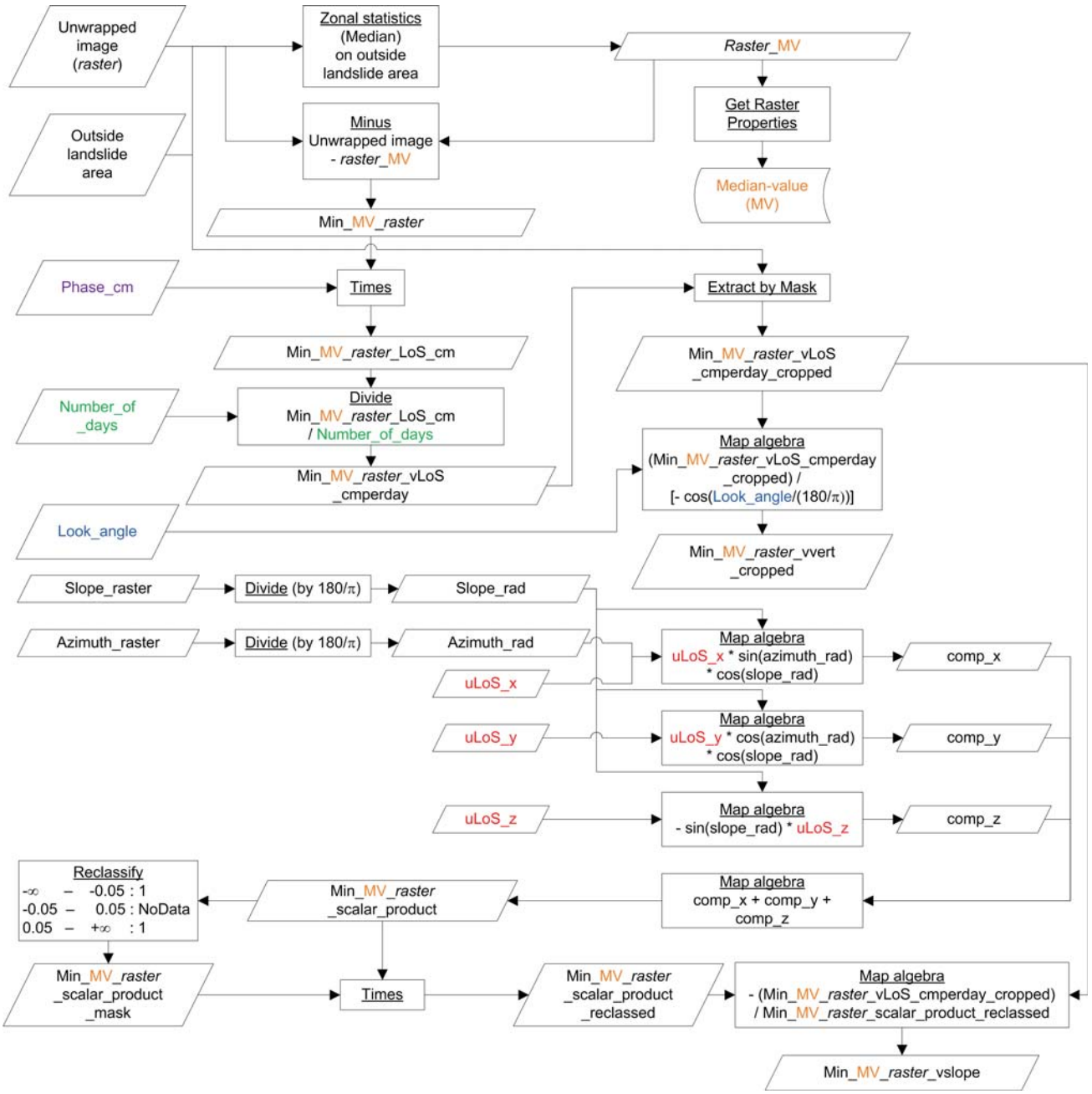

Figure c: Flowchart for the post-processing of unwrapped interferograms.

APPENDIX 3:

Complement of information about the interpretation of DInSAR signal at regional-scale

Using InSAR for mapping landslides over a large area is not a simple task as the different phase contributions to remove may be important. Although the SAR system is capable of penetrating the cloud cover, the SAR phase signal is significantly influenced by the atmospheric conditions, in particular by the water vapour distribution in the troposphere (Zebker et al., 1997; Hanssen et al., 1999). While the previous studies are focused on the local changes, the atmospherical contribution does not influence the quality of the results. Looking at regional scale induces an atmospherical phase distortion correlated in space within each individual SAR images, varying in function of range and azimuth (Colesanti and Wasowski, 2006). Therefore, even classical DInSAR is flexible to provide quantitative information on deformations without persistent scatterers, it has limitations according to the atmospheric phase delay variation (Ferretti et al., 2001).

The method that we propose to map the signal corresponding to phase deformation is based on a visual observation of the InSAR footprints over the scene covering the Ubaye valley. It considers the SAR geometric properties (Fig. 3-3a) to take into account the slopes hidden or affected by layover (i.e. with a NE, E, SE azimuth; see masked zone in Fig. 2 of the following paper). We also decided to analyse all the interpretable wrapped interferograms even with a temporal baseline overpassing 46 days (see Fig. 6 in Schlögel et al., 2014). According to Sandwell et al. (2008), the main advantages of the L-band PALSAR are as follows: the deeper penetration of vegetated areas results in less temporal decorrelation, enabling interferograms to have longer time separation; and the longer wavelength increases the critical baseline, resulting in more usable interferometric pairs. However, we noticed that in these mountainous conditions, meteorological conditions affect a lot the coherence of the signal and the lower fringe rate may result in less precise crustal-motion measurements comparing to C-band sensors.

Theoretically, the resulting interferogram is a contour map of the change in distance between the ground and the radar instrument. They record measurements in the crust, perturbations in the atmosphere, dielectric modifications in the soil, and relief in the topography (Massonnet and Feigl, 1998). As all these phenomena contribute to an interferogram, it is not straightforward to detect only the landslides. The procedure of landslide recognition looking at the unwrapped interferograms (see examples n°16 in Fig. 2) is the following:

- To select the reliable interferograms (with acceptable coherence values on more than one third of the territory);
- To detect the areas which are shadowed or affected by layover or foreshortening effects (Fig. 3-3a) and therefore, understandable with difficulties or even not considered for the analysis;
- To map the InSAR signals which can correspond to a deformation of the ground according to:
  - (i) The colours contrast in comparison to the plain of the valley, i.e. an InSAR footprint with different colour(s) comparing the main colour(s) observed;
  - (ii) The geomorphology and land use where the InSAR signal is observed (e.g. some recently ploughed fields, erosion processes or new infrastructures observed on the 2009 orthophotograph);
- To compare the mapped signal with the landslide inventory updated from Thiery (2007) in order to see if it corresponds to a landslide which is already known;
- To (in)validate the signals corresponding to landslides after a field survey;
- To introduce the information (if validated by field observations) into the multi-date inventory as followed:
  - (i) Re-mapping properly the contours considering the geomorphology of the field;
  - (ii) Introducing the new polygons corresponding to landslides into the 2009 inventory;
  - (iii) Reporting the existing landslides as active between 2004 and 2009 for the InSAR signals that already correspond to landslides;
  - (iv) Fulfilling the table of attributes with qualitative (landslide type, degree of activity, change in vegetation index);
  - (v) Calculating the size related parameters (area, perimeter, run out distance, maximal elevation, etc.).

Among all the InSAR signals detected on the interferograms, some of them correspond to creep (or solifluxion) processes or sackung landslides. They are indicated in the attribute table but are not

considered in the last version of the multi-date inventory as they have different mechanisms comparing to the slide processes (Cruden and Varnes, 1996) mapped so far.

Even if radar interferometry seems very promising for landslide hazard mapping, the geometric distortion due to foreshortening and the speckling give rather poor quality images in mountainous regions (Mantovani et al., 1996). Despite it is not able to cover the entire valley; it allows us to detect unknown very slow slides (sackung) and landslides in forested areas. Advanced InSAR techniques combining both ascending and descending tracks could cover the whole scene but unfortunately only the ascending track is available for this area in L-band PALSAR. Therefore, DInSAR must be combined to other traditional mapping techniques for landslide investigation.

Summary: The analysis of landslide inventories is the basis for quantitative hazard assessment. Landslide inventory maps are prepared using conventional methods (field surveys, visual interpretation of aerial photographs) and new remote sensing techniques. One of the most promising techniques for landslide detection and mapping is related to the measurement of the ground deformation by satellite radar interferometry (InSAR). This doctoral thesis is dedicated to the preparation of a multi-date inventory, from multi-source data, including InSAR, for a quantitative assessment of landslide hazard. The methods associate the analysis of Earth Observation products and statistical modelling for the characterization of landslide hazard in a rural and mountainous region of the South French Alps. They have been developed at the slope (1:5000-1:2000) and the regional (1:25.000-1:10.000) scales. For the creation of a multi-date inventory, this study developed a combined interpretation of time series of SAR images, aerial photographs, geomorphological maps, historical reports and field surveys. At the slope-scale, a geomorphologically-guided methodology using InSAR was proposed to identify landslide displacement patterns and measure their kinematic evolution. At regional scale, spatio-temporal distribution of landslides is characterised and hazard is assessed by computing spatial and temporal probabilities of occurrence for a given intensity of the phenomena. The spatial occurrence is evaluated using a multivariate model (logistic regression). The temporal occurrence of landslide is estimated with a Poisson probability model to compute exceedance probabilities for several return periods. Different mapping units were used in the modelling, and their influence on the results is discussed. Analysis of landslide hazard is then proposed for some particular hotspots. Relationships between landslide (re)activations and triggering factors are envisaged.

Keywords: Landslide, Mapping, Inventory, Radar remote sensing, Kinematic analysis, Susceptibility zonation, Hazard assessment, Ubaye valley

Résumé : La création d'inventaires de glissements de terrain sert de base à l'évaluation quantitative de l'aléa et à la gestion du risque. Les cartes d'inventaires de mouvements gravitaires sont produites en utilisant des méthodes conventionnelles (campagnes de mesures de terrain, interprétation visuelle de photographies aériennes) et par des techniques de télédétection plus innovantes. Une des techniques les plus prometteuses pour la détection et la cartographie des glissements de terrain fait appel à la mesure de la déformation du sol par interférométrie radar satellitaire (InSAR). Cette thèse est consacrée à la constitution d'un inventaire multi-dates à partir de données multi-sources (incluant les données InSAR) en vue d'évaluer de façon quantitative l'aléa glissement de terrain. Les méthodes associent l'analyse de produits d'Observation de la Terre et des modélisations statistiques pour la caractérisation de l'aléa dans la vallée de l'Ubaye, une région rurale et montagneuse des Alpes du Sud. Elles ont été développées à l'échelle du versant (1:5.000-1:2.000) et à l'échelle régionale (1:25.000-1:10.000). Pour la création des inventaires, cette étude propose une interprétation combinée de séries temporelles d'images SAR, de photographies aériennes, de cartes géomorphologiques, de rapports historiques et de campagnes de terrain. A l'échelle locale, une méthodologie d'interprétation guidée par la géomorphologie et utilisant l'InSAR a été proposée pour identifier les champs de déplacement des glissements de terrain et mesurer leur évolution. A l'échelle régionale, la distribution spatio-temporelle des glissements de terrain a été caractérisée et l'aléa a été calculé à partir des probabilités d'occurrence spatiale et temporelle pour une intensité donnée des phénomènes. L'occurrence spatiale est estimée grâce à un modèle multivarié (régression logistique). L'occurrence temporelle des mouvements gravitaires est évaluée grâce à un modèle de probabilité de Poisson permettant de calculer la probabilité de dépassement (incluant ou non un seuil de surface) pour plusieurs périodes de retour. Plusieurs unités d'analyse spatiale ont été utilisées pour la modélisation ; les résultats démontrent clairement leur influence sur les résultats. L'analyse de l'aléa a été réalisée sur quelques cas spécifiques. Des relations entre les (ré)activations de glissements de terrain et les facteurs déclenchants sont proposées.

Mots-clés : Glissement de terrain, Inventaire, Cartographie, Télédétection radar, Analyse cinématique, Zonage de susceptibilité, Évaluation de l'aléa, Vallée de l'Ubaye